E. Inan
D. Sengupta
M.M. Banerjee
B. Mukhopadhyay
H. Demiray
Editors

SPRINGER PROCEEDINGS IN PHYSICS 126

Vibration Problems ICOVP 2007

Springer

SPRINGER PROCEEDINGS IN PHYSICS 126

SPRINGER PROCEEDINGS IN PHYSICS

For other titles published in this series, go to www.springer.com/series/361

The Eighth International Conference on

Vibration Problems ICOVP-2007

01-03 February 2007, Shibpur, India

Edited by

Esin İnan
Işık University, İstanbul, Turkey

Dipak Sengupta
Bengal Engineering and Science, Shibpur, West Bengal, India

Muralimohan Banerjee
Founder Member ICOVP

Basudeb Mukhopadhyay
Bengal Engineering and Science, Shibpur, West Bengal, India

and

Hilmi Demiray
Işık University, İstanbul, Turkey

Springer

Editors
Esin İnan
Işık University
Kumbaba Mevkii
Şile, İstanbul 34980
Turkey

Dipak Sengupta
Department of Chemistry
Bengal Engineering and Science University
Shibpur, Howrah 711103
India

Muralimohan Banerjee
Department of Mathematics
A.C. College
Jalpaiguri 735101
India

Basudeb Mukhopadhyay
Department of Chemistry
Bengal Engineering and Science University
Shibpur, Howrah 711103
India

Hilmi Demiray
Işık University
Kumbaba Mevkii
Şile, İstanbul 34980
Turkey

ISBN: 978-1-4020-9091-2 e-ISBN: 978-1-4020-9100-1

Library of Congress Control Number: 2008934143

Printed on acid-free paper.

9 8 7 6 5 4 3 2 1

springer.com

The Eighth International Conference on

Vibration Problems

ICOVP-2007

Editors

Esin İNAN (Editor-in Chief)

Muralimohan BANERJEE

Hilmi DEMİRAY

Basudeb MUKHOPADHYAY

Dipak SENGUPTA

Springer

PREFACE

Vibration problems dealing with advanced Mathematical and Numerical Techniques have extensive application in a wide class of problems in aeronautics, aerodynamics, space science and technology, off-shore engineering and in the design of different structural components of high speed space crafts and nuclear reactors. Different classes of vibration problems dealing with complex geometries and non-linear behaviour require careful attention of scientists and engineers in pursuit of their research activities. Almost all fields of Engineering, Science and Technology, ranging from small domestic building subjected to earthquake and cyclone to the space craft venturing towards different planets, from giant ship to human skeleton, encounter problems of vibration and dynamic loading.

This being truly an interdisciplinary field, where the mathematicians, physicists and engineers could interface their innovative ideas and creative thoughts to arrive at an appropriate solution, Bengal Engineering and Science University, Shibpur, India, a premier institution for education and research in engineering, science and technology felt it appropriate to organize 8th International Conference on "Vibration Problems (ICOVP-2007)" as a part of its sesquicentenary celebration. The conference created a platform and all aspects of vibration phenomenon with the focus on the state-of-the art in theoretical, experimental and applied research areas were addressed and the scientific interaction, participated by a large gathering including eminent personalities and young research workers, generated many research areas and innovative ideas.

This proceedings being published by Spinger containing good number of scientific research articles and state-of-the art lecture by the distinguished scientists and engineers across the globe will definitely be a good reference for the scientists who would be working in the relevant field in theoretical, experimental and applied research areas.

We express our sincere thanks and gratitude to all the guests, participants, speakers, sponsors and supporters for their kind patronage and valued cooperation to make the conference a grand success. Special thanks are due to Ministry of Human Resources, Department of Science and Technology (DST), Council for Scientific and Industrial Research (CSIR), Indian Space Research Organization (ISRO), Govt. of India, Centre for Applied Mathematics and Computational

Science, Saha Institute of Nuclear Physics (SINP), Kolkata, India for their kind cooperation and support for the conference and making the publication of the proceeding a reality.

Prof. D. Sengupta	Prof. N. R. Bandyopadhyay	Prof. B. Mukhopadhyay
Chairperson	Co-Ordinator	Secretary
Organizing Committee	Organizing Committee	Organizing Committee
ICOVP-2007	*ICOVP-2007*	*ICOVP-2007*

"International Conference on Vibration Problems"

ICOVP-2007 and a short history

The 8th International Conference on Vibration Problems (ICOVP-2007) took place in Shibpur, West Bengal, India, between 1-3 February, 2007.

First ICOVP was held during October 27-30, 1990 at A.C. College, Jalpaiguri, under the co-Chairmanship of two scientists, namely, Professor M. M. Banerjee from the host Institution and Professor P. Biswas from the sister organization, A.C. College of Commerce, in the name of "International Conference on Vibration Problems of Mathematics and Physics". The title of the Conference was changed to the present one during the third conference.

The Conferences of these series are:

1. ICOVP-1990, 20-23 October 1990, A.C. College, Jalpaiguri-India,
2. ICOVP-1993, 4-7 November 1993, A.C. College, Jalpaiguri-India,
3. ICOVP-1996, 27-29 November 1996, University of North Bengal, India,
4. ICOVP-1999, 27-30 November 1999, Jadavpur University, West Bengal, India,
5. ICOVP-2001, 8-10 October 2001, (IMASH), Moscow, Russia,
6. ICOVP-2003, 8-12 September 2003, Tech. Univ. of Liberec, Czech Republic,
7. ICOVP-2005, 5-9 September 2005, Işik University, Şile, İstanbul, Turkey,
8. ICOVP-2007, 1-3 February 2007, Bengal Engineering and Science University, Shibpur, West Bengal, India.

There was also a pre-conference tutorial for the faculty members of Colleges, Universities Scientists from Research Laboratories, Research Scholars and for Post-Graduate students. Foreign and Indian scientists delivered lectures in pre-conference tutorial which was held on January 30-31, 2007.

Fifteen very well-known scientists were very kind in accepting our invitation to give General Lecture in the conference. These lectures were followed by 44 Research Communications. 15 General Lectures and 24 Research Communications are included to this Proceedings. There was 13 Session in the conference and 5 Technical Sessions in the Pre-Conference Colloquium.

As with the earlier Conferences of the ICOVP series, the purpose of ICOVP-2005 was to bring together scientists with different backgrounds, actively working on vibration problems of engineering both in theoretical and applied fields. The main objective did not lie, however, in reporting specific results as such, but rather in joining different languages, questions and methods developed

in the respective disciplines and to stimulate thus a broad interdisciplinary research. Judging from the lively discussions, the friendly, unofficial and warm atmosphere created both in side and outside Conference rooms, this goal was achieved.

The following broad fields have been chosen by the International Scientific Committee to be special importance for the ICOVP-2007.

- Mathematical modeling and computational techniques in sound and vibration analysis,
- Instrumentation and experimental techniques in sound and vibration engineering,
- Structural dynamics: seismic effect, fluid structure interaction, soil structure interaction, sensitivity problems,
- Vibration problems in structural dynamics, structural vibration in non-linear range and damage mechanics, fracture mechanics, composite and granular materials,
- Analysis of deterministic and stochastic vibration phenomena,
- Uncertainties in structural dynamics and acoustics,
- Nonlinear dynamics, stability, bifurcation and chaos and its application,
- Vibration of transport system,
- Vibration problems related to Bio-mechanics and Bio-engineering,
- Vibration in micro-systems,
- Vibrational Technology in industrial devices and processes, dynamic materials of second kind,
- Nanotechnology in vibration-phononic band gap structures and materials,
- Signal processing and analysis,
- Other topics related to vibration problems.

Other topics concerned with vibration problems, in general, were also open as well, but the bulk of presentations were within the above fields. All of the lecturers were carefully reviewed by the International Scientific Committee, so as to illustrate the newest trends, ideas and the results.

As the Editor-in-Chief, I would like to express my deep gratitude to the Faculty of Bengal Engineering and Science University (BESU) and the Scientific Committee and functional committees of the conference for their immeasurable efforts to organize this conference. They did a wonderful job for the realization of this traditional conference.

In the meantime, I would like to express my great sympathy, regards and thanks to my very best friend Professor M. M. Banerjee who is the “father” of these conference series. His efforts are immeasurable to keep this conference series as going on successfully.

I would also like to thank to Dr. Ahmet KIRIŞ for his great help on the editing of the book.

Finally, on behalf of the Editorial Board, I would like to send our cordial thanks to all lecturers for their excellent presentations and careful preparation of the manuscripts. We are looking forward to come together at 9th ICOVP conference, which will tentatively take place in India in 2009.

Esin İNAN,
Editor-in-Chief
Şile, İstanbul, December 2007

CONTENTS

FREE VIBRATIONS OF DELAMINATED COMPOSITE CYLINDRICAL SHELL ROOFS

A. KUMAR ACHARYYA*
AND DIPANKAR CHAKRABORTY
Department of Civil Engineering, Jadavpur University
Kolkata-700032, India

AMIT KARMAKAR
Department of Mechanical Engineering, Jadavpur University
Kolkata-700032, India

Abstract. Recently laminated composites are widely used in civil engineering, which may suffer from delamination damage resulting from improper fabrication and overloading at service. A review of literature that exists on composite shells reveals that the research reports on delaminated shells are very few in number. Hence the present endeavor is to work on delaminated simply supported cylindrical shell with different extents of delaminations. An eight noded isoparametric element with five degrees of freedom per node is used together with Sander's strain displacement relationships and multipoint constraint equations to satisfy the compatibility of displacements and rotations along the cracked edges. The study reveals that there is a consistent decrease in the fundamental frequency value as the area of the delamination damage increases. Further the fundamental frequency of angle ply shells undergo relatively more prominent decrease compared to that of cross ply shells. It seems that delamination damage brings about greater reduction in frequency values as the number of layers increases for angle ply shells, especially for symmetric ones.

Keywords: delamination, cylindrical shell, finite element, laminated composite, fundamental frequency

*Corresponding author, anjanboni@rediffmail.com

E. İnan et al. (eds.), *Vibration Problems ICOVP-2007*,

1. Introduction

Gim[1] worked on delaminated plates including the effect of transverse shear deformation. He employed the finite element technique and to ensure the compatibility of deformation and equilibrium of forces and moments at the delamination crack tip, a multiple constraint algorithm was developed and incorporated in the code. He considered delaminations at tips of cantilever plates and reported the strain energy release rate. Dynamic analysis of composite plates and shells with mutiple delamination was reported by Parhi and his colleagues[2] using an 8-noded finite element to study the free vibration and transient response with different parametric variations. Effects of delamination on free vibration characteristics of graphite-epoxy composite pretwisted shallow cylindrical shells were reported by Karmakar et al[3]. Although among civil engineering shells cylindrical configuration is commonest but delamination problems of commonly used composite cylindrical shells received very limited attentions only. Hence in this paper a free vibration analysis of simply supported delaminated composite cylindrical shells with different delamination areas and stacking sequences are presented.

2. Mathematical formulation

An eight noded curved quadratic isoparametric finite element with five degrees of freedom u, v, w, α, β at each node is employed for solution, where u, v, w are displacements at any general point at a distance z from the midplane within the shell thickness and α and β are rotations about Y- and X- axes respectively. The corresponding midplane displacement components are u^0, v^0, w^0. R is the radius of the shell surface.

For shallow cylindrical shells the linear inplane strains $\varepsilon_x, \varepsilon_y, \gamma_{xy}$ are expressed as

$$\begin{aligned}
\varepsilon_x &= u_{,x} = u^0_{,x} - z\alpha_{,x} \\
\varepsilon_y &= v_{,y} - \frac{w}{R} = v^0_{,y} - z\beta_{,y} - \frac{w}{R} \\
\gamma_{xy} &= u_{,y} + v_{,x} = u^0_{,y} + v^0_{,x} - z(\alpha_{,y} + \beta_{,x})
\end{aligned} \tag{1}$$

Multipoint constraint equations, used here in the finite element formulation, are to satisfy the compatibility of displacements and rotations. These are suggested by Gim[1].

3. Numerical examples

The numerical examples solved in this paper include a benchmark problem and number of other problems, which are authors' own. In each problem, E_{11}, E_{22} (elastic moduli), G_{12}, G_{13}, G_{23} (shear moduli), ν_{12} (Poisson's ratio) and ρ (density) represent material properties. Length and width of the cylindrical shell are represented by a and b along x (beam) and y (arch) directions respectively. Similarly length and width of central delamination area of the shell are represented by c and d parallel to x and y directions respectively. Shell thickness is h. Natural frequency is ω and non-dimensional natural frequency is $\overline{\omega} = \left[\omega a^2 \left(\rho / E_{22} h^2\right)^{1/2}\right]$. Fundamental frequencies (Hz) of cylindrical shells for different centrally located mid-plane delaminations, solved by Parhi[2] and obtained by the present method are compared in Table 1 as benchmark problem. Authors' own problems are about simply supported cylindrical shells. The area of delamination zone is varied from zero to 56.25% of the total plan area of the shell. Twelve different types of laminations are considered including orthotropic, anisotropic, cross and angle plies, both antisymmetric and symmetric, furnished in Table 2.

TABLE 1. Fundamental frequencies (Hz) of cylindrical shells for different centrally located (area = $c \times d$) midplane delaminations for simply supported boundary conditions.

c/a	Parhi[2]	Present approach
0	175.55	175.26
0.25	167.62	167.37
0.5	158.67	158.40
0.75	127.39	127.03

Material: Carbon-epoxy composite
E_{11}=172.5GPa, E_{22}=6.9GPa, G_{12}=G_{13}=3.45GPa, G_{23}=1.38GPa,
ν_{12}=0.25, ρ=1600 kg/m^3, a=b=0.5m, R=1.5m, h=5mmz.
Lamination: $(0^o/90^o)_2$

4. Results and discussions

The results of the fundamental frequencies as obtained by Parhi[2] and the present method show excellent agreement as evident from Table 1. The other problems are studied from different angle and discussed hereafter (Table 2).

TABLE 2. Non-dimensional fundamental frequencies of cylindrical shells for different centrally located (area = $c \times d$) midplane delaminations for simply supported boundary conditions.

Stacking sequence	c/a			
	0	0.25	0.5	0.75
0^o	24.252	23.079	21.556	20.765
90^o	22.957	22.509	19.118	16.301
$+45^o$	37.161	36.377	30.618	25.836
-45^o	37.161	36.377	30.618	25.836
$0^o/90^o$	24.520	24.403	24.182	23.994
$0^o/90^o/0^o$	27.050	26.001	24.641	23.959
$+45^o/-45^o$	32.150	32.013	30.860	29.036
$+45^o/-45^o/+45^o$	40.195	38.694	29.901	12.245
$(0^o/90^o)_2$	26.513	25.321	23.963	19.218
$(0^o/90^o)_S$	27.135	26.081	24.696	24.055
$(+45^o/-45^o)_2$	44.891	43.056	33.348	26.634
$(+45^o/-45^o)_S$	43.383	41.245	10.519	24.241

E_{11}=25, E_{22}, G_{12}=G_{13}=0.5E_{22}, G_{23}=0.2 E_{22}, ν_{12}=0.25,
a=b, h=0.01b, R=3b.

4.1. EFFECT OF EXTENT OF DELAMINATION ON NATURAL FREQUENCY VALUES

Firstly introduction of delamination reduces the bending stiffness in the damaged zone without any change in mass and hence a decrease in the value of the fundamental frequency is quite expected. But for $(+45°/-45°)_S$ laminate, the fundamental frequency value for c/a = 0.5 is even less than that when c/a = 0.75. This observation makes the author more curious to study the higher mode frequencies for this laminate, which are shown in Table 3. It is found that the second and third natural frequencies show a consistent decay as the area of damage increases. These observations leaves the room for further research to exactly determine the cause of such behaviour. Apparently it seems that the fundamental vibration mode in this case has its highest point of bending curvature within the delamination zone and hence the reduction of bending stiffness in the area of damage has affected the fundamental frequency to a very great extent. Secondly orthotropic and cross ply shells are less susceptible to frequency loss with introduction of delamination. In fact the fundamental frequency of 0°/90° is hardly affected by delamination and three and four layered symmetric cross

TABLE 3. Non-dimensonal natural frequencies of (+45°/– 45°)s laminate (area of damage = $c \times d$, centrally located at the midplane) for simply supported boundary conditions.

Natural frequency	c/a			
	0	0.25	0.5	0.75
First mode	43.383	41.245	10.519	24.241
Second mode	62.335	60.969	37.648	31.895
Third mode	69.196	66.744	56.463	37.542

E_{11}=25 E_{22}, G_{12}=G_{13}=0.5E_{22}, G_{23}=0.2 E_{22}, ν_{12}=0.25, a=b, h=0.01b, R=3b.

ply laminates exhibit a marginal loss of about 10% only even when 56.25% of the total shell area is damaged. Among angle ply laminates only +45°/–45° shell has the frequency value not much affected with the introduction of damage. But one observation is true in general that introduction of small area of damage (c/a = 0.25) hardly affects the fundamental frequency value and in no case, considered here, the loss is more than 5%.

4.2. EFFECT OF STACKING SEQUENCE ON FUNDAMENTAL FREQUENCY VALUES

Firstly the single layered anisotropic laminates perform considerably better than orthotropic ones. In the same way, angle ply laminates for undelaminated (c/a = 0) and slightly delaminated (c/a = 0.25) turn out to be better than cross ply ones. So relative performances of orthotropic and anisotropic laminates can form the basis of predicting that of multi-layered laminates for undelaminated and slightly delaminated shells. Secondly among two and four layered antisymmetric laminates four layered ones show higher frequency values than two layered ones for undelaminated and slightly delaminated shells. Among three and four layered symmetric laminates four layered ones show increased frequency values for c/a = 0 and c/a = 0.25. For higher delamination areas some deviation is noted. Thirdly symmetric cross ply and antisymmetric angle ply laminates are preferable than the other types in case of four layered laminates. Comparing three layered symmetric and four layered antisymmetric laminates, symmetric cross ply and antisymmetric angle ply laminates show higher values, as before.

5. Conclusion

Firstly the formulation, presented here, can successfully analyze problems of cylindrical laminates as established through solution of benchmark problems. Secondly for simply supported shells, the fundamental frequency values of

delaminated shells are always less than the corresponding undelaminated shells for all types of stacking sequences. Thirdly the relative performances of single layered anisotrpic laminates are better than the orthotropic ones. Fourthly undamaged (c/a = 0) and slightly damaged shells (c/a = 0.25) show that variation of fundamental frequencies is not more than 5%. Also for the same case it is seen that angle ply shells perform better than cross ply shells. So performances of multi-layered shells can be predicted from single layered shells. Moreover in this case increase in number of layers has positive effect on frequency values and symmetric cross ply and antisymmetric angle ply laminates show better performances that the other types. Fifthly moderately damaged (c/a = 0.5) and highly damaged (c/a = 0.75) shells show cross ply shells are less susceptible to frequency loss than angle ply ones. Among the angle ply laminates frequency loss is more for symmetric ones.

References

1. C. K. Gim, 1994. *Plate finite element modeling of laminated plates*, Computers & Structures **52**,157-168.
2. P. K. Parhi, 2000. *Finite element dynamic analysis of multiple delaminated composite plates and shells*, PhD Thesis.
3. A. Karmakar, H. Roy and K. Kishimoto, 2005. *Free vibration analysis of delaminated composite pretwisted shells,* Aircraft Engineering and Aerospace Technology: An International Journal, **77**, 486-490.

COMPUTATIONAL DYNAMIC ANALYSIS OF SINGLE-MASS FREELY SHAKING CONVEYERS WITH CENTRIFUGAL VIBRATION EXCITER

FÜSUN ALIŞVERİŞÇİ*
Department of Mechanical Engineering, Yıldız Technical University, 34349, Istanbul, Turkey

Abstract. Single-mass freely shaking (vibrational) conveyers with a centrifugal vibration exciter transmit their load based on the jumping method. The trough is oscillated by a common unbalanced-mass driver. This vibration causes the load to move forward and upward. The moving loads jump periodically and move forward with relatively small vibration. The movement is strictly related to the vibrational parameters. This is applicable in laboratory conditions in the industry that accommodate a few grams of loads, up to those that accommodate tons of loading capacity. In this study, the variation of motional parameters has been represented graphically using the software *Mathematica* with respect to i) vibrational parameters, ii) parameter of the unbalanced mass, iii) operation mode, iv) friction coefficient, and v) angle of attack. The proper parameters for the transport of the numerous loads and the transportation velocity can be chosen with the help of the graphics. The results obtained in this study have been compared with the experimental results in the pertaining literature, and have been found to be well matched.

Keywords: shaking (vibrational) conveyers, operation mode, unbalanced mass

1. Introduction

In the shaking conveyers, the load moves relative to the trough and the force of the load pressure on the trough's bottom is variable. The load periodically rises

*afusun@yildiz.edu.tr

E. İnan et al. (eds.), *Vibration Problems ICOVP-2007*,

(‘*jumps*’) above the trough and moves in small jerks. For the load to move in the desired direction, the drive must be mounted so that the line of action of the excitation force is at an angle of β to the longitudinal axis of the conveyer.

A suspended shaking conveyer with a freely oscillating single-mass system (Fig. 1a) consists of a load-carrying element (pipe or trough) (1) which is freely suspended on the elastic tie-dampers (3) from a stationary structure, and is oscillated in a directed manner by a centrifugal driver (4). The conveyer is equipped with a safety belt to hold the trough in the event of occasional breakage of the elastic ties. The loading and unloading connections of a vibrating pipe of a shaking conveyer are connected to stationary structures, such as bunkers or funnels, by means of flexible corrugated pipe connections (2) made of strong fabric, rubber, or plastics. The drive is in the form of a doubled centrifugal (inertia-type unbalanced) vibration exciter (Fig. 1b). The drive may be arranged above or below the load-carrying element.

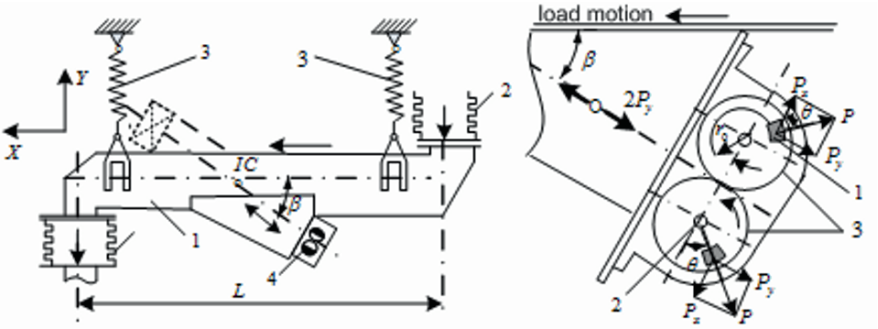

(a) (b)

Fig. 1 (a) Single-mass freely shaking conveyers with centrifugal vibration exciter (*IC* – inertia centre) (b) Two equal unbalanced centrifugal vibration exciters.

2. Dynamics of the motion

The following derivation can be made for the maximum velocity attained by the load on the trough. When the equation of motion is written according to the Newton’s second law along the horizontal axis ($X-$axis) for the load on the trough, the following equation is obtained:

$$\sum F_X = m\,a_x \quad \rightarrow f = m\,a_x \tag{1}$$

were f represents the frictional force affecting the load, m is the mass of the load, and a_X is the horizontal component of the trough’s acceleration.

If ma_X is greater than the maximum value of the frictional force $(f_{\max})$, the load starts to slide on the trough. Therefore, the maximum friction force can be expressed as follows:

$$f_{\max} = \mu_s N \tag{2}$$

where μ_s represents the static friction and N is the normal force.

The equation of motion along the vertical axis ($Y-$axis) for the load on trough can be written as

$$N = m\,g + m\,a_Y \tag{3}$$

If equation (3) is substituted into equation (2) at the beginning of the slide of the load, $f_{\max}$ is obtained as follows:

$$f_{\max} = \mu_s m(g + a_Y). \tag{4}$$

Recalling that the load starts to slide on the trough when $ma_x > f_{\max}$ and using equation (4), the condition of sliding of the load on the trough may be expressed with the following inequality:

$$a_X > \mu_s\,(g + a_Y). \tag{5}$$

By arranging inequality (5), the horizontal component of the acceleration of the load is obtained by using the kinetic friction constant μ_k as follows:

$$a_X = \mu_k\,(g + a_Y). \tag{6}$$

If equation (6) is integrated as shown below, the horizontal component of the velocity of the load can be expressed as[1,2]

$$V_X = \int_0^t \mu_k\,(g + a_Y)\,dt. \quad \rightarrow \quad V_X = \mu_k\,g\,t + \int_0^t \mu_k\,a_Y\,dt. \tag{7}$$

The vertical motion of the load is the same as the motion of the trough until the normal force vanishes or the acceleration of trough reaches the value of $-g$. Thereafter, the load is separated from the trough.

3. Forced vibration of the motion

In a doubled centrifugal driver (Fig. 1b), the two equal unbalanced masses (1) are mounted on two gear wheels (3) (or on two shafts (2)) which are engaged

with each other. As the wheels rotate, the centrifugal force P appears. The longitudinal components of the centrifugal forces of the two unbalanced masses P_y are added together and the transverse components of the centrifugal forces of the two unbalanced masses P_x counter balance each other. The equation of motion according to the Newton's second law along the y-axis for the shaking conveyer[3] can be obtained as:

$$\ddot{y} + \frac{c}{m}\dot{y} + \frac{k}{m}y = \frac{m_0 r_0 \omega^2}{m}\sin \omega t, \tag{8}$$

where k is the stiffness of the elastic ties, c is the internal resistance, m_0 is the total unbalanced mass of a centrifugal exciter, r_0 is the eccentricity of the unbalanced masses, and m is the total mass of vibrating elements of the conveyer including the attached mass of the load. If the natural frequency, viscous damping factor, forced amplitude, and the angular frequency ratio in this equation are defined as

$$\omega_n^2 = k/m, \quad \zeta = c/(2m\omega_n), \quad A = (m_0 r_0)/m, \quad \eta = \omega/\omega_n, \tag{9}$$

respectively, then the differential equation (8) can be expressed as:

$$\ddot{y} + 2\zeta\omega_n\dot{y} + \omega_n^2 y = \omega_n^2 (\eta)^2 A \sin \omega t. \tag{10}$$

The solution of the differential equation (10) is obtained as[4]:

$$y = \Phi(\omega)\sin(\omega t - \phi). \tag{11}$$

The amplitude of vibrations of the load-carrying element of a freely shaking conveyer can be determined by solving the differential equation of the forced oscillations of the inertia centre of the system (Fig. 1). The amplitude function, and the phase difference can be expressed as

$$\Phi(\omega) = AG(\omega), \ \phi = \arctan\left(\frac{2\varsigma\eta}{1-\eta^2}\right) \tag{12}$$

respectively, where $G(\omega)$ is the amplitude magnification factor

$$G(\omega) = \frac{\eta^2}{\sqrt{(1-\eta^2)^2 + (2\varsigma\eta)^2}}. \tag{13}$$

The components of y along the trough and perpendicular to the trough with β (the angle of attack) can be obtained as:

$$y_X = \Phi(\omega)\sin(\omega t - \phi)\cos\beta,\ y_Y = \Phi(\omega)\sin(\omega t + \phi)\sin\beta. \qquad (14)$$

The components of the velocity and acceleration can be found by taking the first and second derivatives of the equation (14).

4. The graphics of the motion

The graphical representations of the dynamic analysis obtained by Mathematica software are shown in Figs. 2-5 below.

For the values close to 1 of the angular frequency ratio $\eta = \omega/\omega_n$ (resonance region), it is observed that the amplitude at small viscous damping factor increases (Fig. 2a). Even though the load transmission velocity is higher in this region, the lifetime of the system is shorter as a result of the additional dynamic loads.

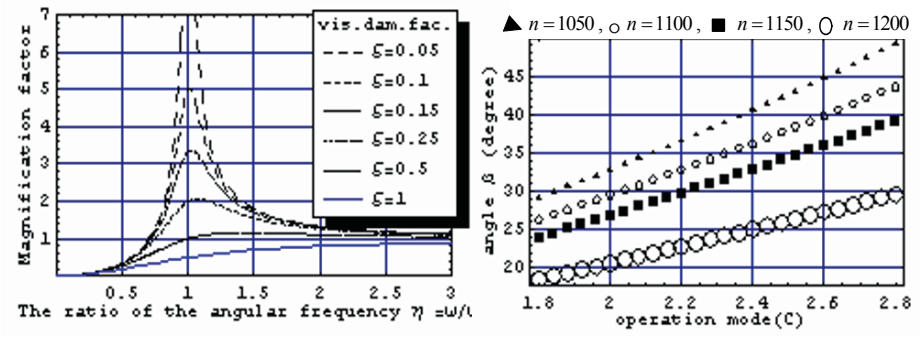

(a) (b)

Fig. 2 (a) The change in the amplitude magnification factor depending on the angular frequency ratio (b) Diverse velocity of rotating unbalanced mass according to attack angle-operation mode.

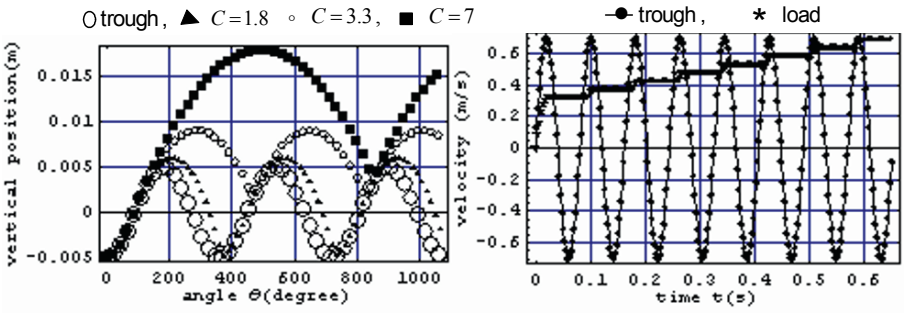

(a) (b)

Fig. 3 (a) The vertical position of the trough and the load at diverse operation modes (b) The velocity-time graph of the trough and the load in horizontal direction from the first movement until the steady state.

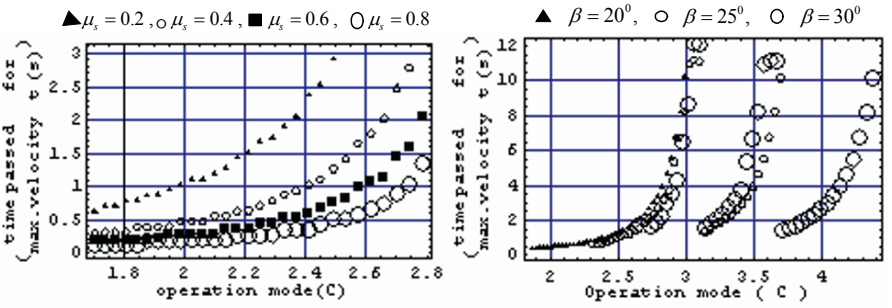

(a) (b)

Fig. 4 (a) The time passed for the load to reach maximum velocity at diverse friction coefficients according to the C operation mode (b) The time passed for the load to reach maximum velocity at diverse angles of attack depending on the C operation mode.

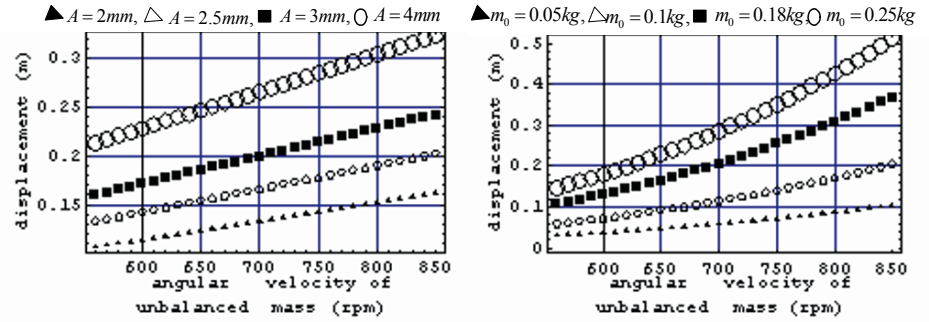

(a) (b)

Fig. 5 (a) Displacement of the load in one second at diverse amplitude values depending on velocity of the rotating unbalanced mass (b) at diverse unbalanced mass values.

C is the coefficient defining the dynamic working conditions (dynamic forces acting on the driver and other conveyer elements) of an oscillating conveyer and the motion style of the load particles. If $C < 1$, the load is always in contact with the trough of the conveyer and the load is not disengaged from the trough. If $C > 1$, the load is disengaged from its conveyer trough at some instants and moves in micro-jumps. For the values $1 < C < 3.3$, the load particle will be launched upward as soon as it reaches the trough ground (Fig. 3a). The most efficient movement of the load particles on a shaking conveyer $(C > 1)$ depends on the correct chosen time, when a particle falls on the trough. During the forward motion of the plane, the particle must be caught by the plane, and it must move with the plane until it is disengaged from the plane in the shortest possible time period. The most suitable displacement of the load and the most suitable style of transportation are achieved through the equivalence of the disengagement time interval from the trough to one complete oscillation period (Fig. 3a).

The velocity of the load increases until it equals to the velocity of the trough and the motion continues at this velocity (Fig. 3b).

The following values are used for drawing of the graphics [3, 4] (Fig. 3, 4): the spring constant $k = 62550N/m$, the friction coefficient $\mu_s = 0.5$, the operation mode $C = [(a_Y)_{\max} sin(\beta)]/g$, the eccentricity of the unbalanced masses $r_0 = 0.2m$, and the angular frequency ratio $\eta = \omega/\omega_n = 1$.

5. Conclusions

In this study, the graph of the displacement by the load in one second depending on the velocity of the rotating unbalanced mass (Fig. 5a, b) is drawn for numerous amplitude values and the unbalanced mass values. Fig. 2, 3, 4 illustrate the changes necessary for the load to reach the maximum velocity, depending on the static friction coefficient and the angle of attack (Fig. 4a, b). The numerical calculations are performed with the help of the software *Mathematica*[4-5] The graphs drawn in this study are compared with the experimental results in the literature, and it has been observed that they are well-matched. Using these graphs, the most proper parameters can be chosen. In this system at the load transmission; especially the coefficient of friction, the coefficient of spring, the coefficient of amortization of the elastic ties, the angle of attack, the values of the unbalanced mass, the radius of rotation, and the velocity of rotation must be well-arranged.

References

1. A. O. Spivakovsky, V. K. Dyachkov, 1985. *Conveying Machines*, Volume (I, II), Mir Publishers, Moskow.
2. J. E. Shigley, J. J. Uicker, Jr., 1980. *Theory of Machines and Mechanisms*, McGraw-Hill.
3. L. Meirovitch, 1986. *Element of Vibration Analysis*, McGraw-Hill.
4. I. P. Stavroulakis, S. A. Tersian, 2002. *Partial Differential Equations (2e) An Introduction with Mathematica and Maple*, World Scientific.
5. S. C. Chapra, R. P. Canale, 2002. *Numerical Method for Engineers: with Software and Programming Applications*, McGraw-Hill, Boston.

ON THE APPLICATION OF CONSTANT DEFLECTION CONTOUR METHOD TO NON-LINEAR VIBRATION ANALYSIS OF ELASTIC PLATES AND SHELLS

M. M. BANERJEE*
202 Nandan Apartment, Hillview (N), S B Gorai Road, Asansol-713304, W.B., India
Retired Reader, Department of Mathematics, A.C. College, Jalpaiguri-735101, W.B., India

Abstract. The present paper aims at establishing the validity of the constant deflection contour (CDC) method to the nonlinear analysis of plates of arbitrary shapes vibrating at large amplitude. It begins with a review of the basic ideas developed earlier by the present author. The deduction of the governing differential equations have been established. The author has made an attempt here to develop the concept of constant deflection contour method and specifically to make its introduction into the nonlinear analysis of plates. A combination of the constant deflection contour method and the Galerkin procedure has been employed for solution. The numerical results obtained for the illustrative problems are in excellent agreement with those of available studies. Application of the present analysis to structures with complicated geometry has also been attempted in this paper. It has been demonstrated that this method provides a powerful tool to tackle problems involving structures with uncommon boundaries. The comparison of the present results with others strongly supports this. The analysis carried out in this paper may readily be applied to other geometrical structures and as a byproduct the static deflection is also obtainable.

Keywords: constant deflection contours, iso-deflection curves, contour, integration and Green's function

* dgp_muralimb@sancharnet.in

E. İnan et al. (eds.), *Vibration Problems ICOVP-2007*,

1. Introduction

The paucity of literature concerning nonlinear (large amplitude) vibration analysis is, probably, due to the fact that the two basic Von Kármán field equations extended to the dynamic case, involved the deflection and the stress functions in a coupled form. Moreover, these equations are of fourth order, posing analytical problems and necessitating a numerical approach. Large amplitude vibration analysis has been treated well by many authors mostly for plates and shells having regular shapes[1-3] and almost all problems involved considerable amount of mathematical computation. Simplified approaches had been attempted[4,5] but later on some reservations were made and the accuracy of the modifications were questioned.[6,7] Recently a new idea has been put forward by Banerjee[8] to study the dynamic response of structures of arbitrary shapes based on "constant Deflection Contour" method. Mazumdar and others[9-13] have previously developed the method. However, the application of this method has been restricted to linear cases only.

2. Some preliminary remarks on the Constant Deflection Contour Method

The fundamental concept of the constant deflection contour method may be best explained by considering transverse vibrations of a plate, referred to a system of orthogonal coordinates *Oxyz* for which *Oz* is the transverse direction (positively downward). The horizontal plane *Oxy* coincides with the middle plane of the plate. Consider such a plate statically deflected, vibrating freely or forced to vibrate, all due to normal static or dynamic loads.

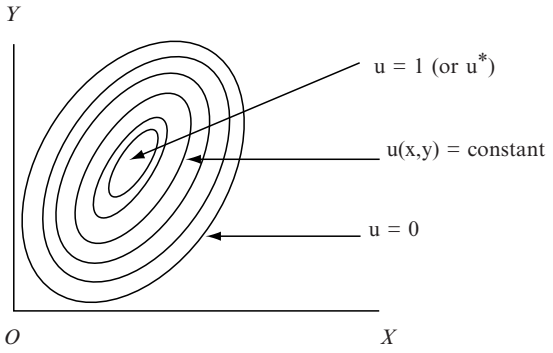

Fig. 1 Iso-deflection Curves.

When the plate vibrates in a normal mode then at any instant t_θ, the intersections between the deflected surface and the parallels *z = constant* will yield contours which after projection onto z = 0 surface are a set of level curves, *u(x,y) = constant*, called the "Lines of Equal Deflections"[10], which are iso-amplitude contours.

The boundary of the plate, irrespective of any combination of support, is also a simple curve C_u belonging to the family of lines of equal deflections.

As defined by Mazumdar[9] the family of nonintersecting curves may be denoted by C_u, for $C_u, 0 \le u \le u^*$, so that $C_u (u = 0)$ is the boundary and C_u coincides with the point(s) at which the maximum $u = u^*$ is obtained.

3. Deduction of basic equations (a different approach)

The usual procedure is to consider Kármán type field equations extended to the dynamic case

$$D\nabla^4 w = hS(\phi, w) + q - \rho h w_{tt} \tag{1}$$

$$\nabla^4 \phi = -(E/2)S(w, w), \tag{2}$$

in which the flexural rigidity D and the two-dimensional Laplacian operator ∇^2 are defined by

$$D = \frac{Eh^3}{12(1-\nu^2)}, \qquad \frac{\partial^2}{\partial x^2} + \frac{\partial^2}{\partial y^2} \equiv \nabla^2 \tag{3}$$

with *h* the thickness of the plate, E the Young's modulus, q the uniform normal load, ρ the material density, w is the deflection function and ϕ the Airy stress function. In addition a suffix is taken as an indication of partial differentiation with respect to the implied variable and the operator S is defined by

$$S(I, J) = I_{xx} J_{yy} - 2I_{xy} J_{xy} + I_{yy} J_{xx} \tag{4}$$

It should be noted here that the use of the stress function is equivalent to disregard of inertia terms in the equations of in-plane motions of the particles of the plate. This assumption is legitimate when the oscillations primarily take place in the transverse direction, perpendicular to the middle plane of the plate. We choose the deflection function and the stress function in the separable form[3]

$$w(x, y, t) = h\ W(x, y)\ F(t),\ \phi(x, y, t) = h\ \Phi(x, y)\ F^2(t) \tag{5}$$

where *F(t)* is an unknown function of time to be determined.

We consider a different approach to that used by Mazumdar[9] in establishing the Governing equations. Consider a thin elastic plate, which vibrates with moderately large amplitude in the transverse direction; under the action of a uniform load *q*. Let us now make the following transformations

$$\frac{\partial w}{\partial x} = w_x = \frac{dw}{du}u_x, \qquad w_{xx} = \frac{d^2w}{du^2}u_x^2 + \frac{dw}{du}u_{xx}, \tag{6.1}$$

$$w_y = \frac{dw}{du}u_y, \qquad w_{xy} = \frac{d^2w}{du^2}u_x u_y + \frac{dw}{du}u_{xy}, \text{ etc.} \tag{6.2}$$

With transformations exemplified by those shown in Eqns. (5) and (6), Eqns. (1) and (2) are transformed to

$$\begin{aligned} &D\sum_{i=1}^{4}\lambda_i \frac{d^{5-i}W}{du^{5-i}}hF(t) \\ &= h^3\left[\lambda_5\frac{d^2W}{du^2}\frac{d\Phi}{du} + \lambda_6\frac{d^2\Phi}{du^2}\frac{dW}{du} + \lambda_7\frac{d\,W}{du}\frac{d\Phi}{du}\right]F^3(t) + q - \rho h^2 W\ddot{F}, \end{aligned} \tag{7}$$

where $\ddot{F} = \dfrac{d^2F}{dt^2}$.

$$\sum_{i=1}^{4}\lambda_i\frac{d^{5-i}\Phi}{du^{5-i}} = Eh\left[\lambda_8\frac{d^2W}{du^2}\frac{dW}{du} + \lambda_9\left(\frac{dW}{du}\right)^2\right] \tag{8}$$

in which λ_i's are functions *of* u_x , u_y , u_{xx} , u_{yy} and u_{xy} only (See Ref. 24).

Since Eqns. (7) and (8) are valid for all points of the whole domain, it is clear that

$$\begin{aligned} \iint_\Omega \Bigg[&D\sum_{i=1}^{4}\lambda_i\frac{d^{5-i}W}{du^{5-i}}hF(t) - h^3\left\{\lambda_5\frac{d^2W}{du^2}\frac{d\,\Phi}{du} + \lambda_6\frac{d^2\Phi}{du^2}\frac{d\,W}{du}\right. \\ &\left. + \lambda_7\frac{dW}{du}\frac{d\Phi}{du}\right\}F^3(t) - q + \rho h^2 W\ddot{F}\Bigg]d\Omega = 0 \end{aligned} \tag{9a}$$

$$\iint_\Omega\left[\sum_{i=1}^{4}\lambda_i\frac{d^{5-i}\Phi}{du^{5-i}} - Eh\left\{\lambda_8\frac{d^2W}{du^2}\frac{d\,W}{du} + \lambda_9\left(\frac{dW}{du}\right)^2\right\}\right]d\Omega = 0 \tag{9b}$$

where the region of integration is taken over the region enclosed by the contour C_u. To integrate Eqns. (9a) and (9b) previous authors have usually employed

Green's Theorem. However, we pursue a different approach and change the variables using the general formula

$$\iint_{\Omega_u} f\left(u, u_x, u_{xx}\, 'u_{xy} \ldots\ldots, \frac{dW}{du}, \frac{d^2W}{du^2}, \ldots\ldots, \frac{d^nW}{du^n}\right) d\Omega = -\int_{u^*}^{u} F_1(u) \left\{ \oint_{C_u} F_2(x,y) \frac{dS}{\sqrt{\lambda_1}} \right\} du \tag{10}$$

which is a generalization of the formula adopted in Ref. [9]. Often it has been encountered that the contour integral in (10) turns out to be dependent on *u*, and hence care should be taken to evaluate first the contour integral to avoid any confusion that may arise. On evaluation of integrals (9a) and (9b), they may be further reduced to the forms

$$hF(t)\sum_{i=1}^{4} f_{1i} \frac{d^{4-i}W}{du^{4-i}} + \frac{h^3}{2D} f_{15} \frac{dW}{du}\frac{d\Phi}{du} F^3(t) + \frac{f_{16}}{D} q + \frac{\rho h^2}{D} f_{17} \ddot{F}(t) \int_{u^*}^{u} W du_0 = 0, \tag{11}$$

and

$$\sum_{i=1}^{4} g_{1i} \frac{d^{4-i}\Phi}{du^{4-i}} + \frac{Eh}{2} g_{15} \left(\frac{dW}{du}\right)^2 = 0 \tag{12}$$

where f_{1i} and g_{1i} are functions of *u* and *u** only. To avoid the integral appearing in Eqn. (11), Mazumdar et al[11] have taken the derivative of it making the equation of order four again, viz.,

$$hF(t)\sum_{i=1}^{5} f_{2i} \frac{d^{5-i}W}{du^{5-i}} + h^3 \frac{f_{25}}{2D} \frac{d}{du}\left(\frac{dW}{du}\frac{d\Phi}{du}\right) F^3(t) + \frac{f_{26}}{D} q + \frac{\rho h^2}{D} f_{27} W \ddot{F}(t) = 0 \tag{13}$$

yielding a similar result.

Eqns. (11) and (12) or Eqns. (12) and (13) may be utilized to form the basic equations governing the motion of the structure. Although a combination of Eqns. (11) and (12) or Eqns. (12) and (13) may be utilized as the basic governing equations, the later combination has been found to yield better results. The above equations have been derived without specifying the geometry of the structure and they may therefore be specialized to deal with any type of geometry, of course, provided the contour *u(x,y) = 0* is known. Moreover, Eqns. (11-13) form a system of ordinary differential equations, which may be solved for a variety of structures and subjected to several forms of boundary conditions. Different boundary conditions have already been established in Ref. 14.

4. Method of solution

The method of solution associated with real variables may be considered in a two ways: Considering (11) and (12) as the basic equations with appropriate boundary conditions, it starts with finding the exact or approximate solution for Φ from Eqn. (12). However, obtaining an exact solution for Φ may only be feasible for linear analysis, similar to the method followed by Mazumdar[9]. For nonlinear analysis one may have to seek an approximate solution for which the form of the deflected function must be first assumed compatible with the boundary conditions. Next we solve for Φ from equation (12) in conjunction with a Galerkin procedure. With this expression for Φ and previously assumed form of *W* yield an ordinary time differential equation when the Galerkin procedure is applied again. Mathematically, the above steps may also be explained in the following way. Let *u(x,y) = u* be the representative of one of the family of the iso-deflection curves, then for any prescribed boundary conditions the deflection function *w(u,t)* can be assumed to take the form

$$W = h\sum_{i=1}^{n} A_i \Gamma(u) \tag{14}$$

and

$$\phi = h\Phi(u) \tag{15}$$

Equation (12), in combination with (14) and (15), will yield $\Phi = \Phi(u)$. Substituting this value of Φ with W as in (14), Eqn. (11) or Eqn. (13) will yield the error function

$$\varepsilon = \Lambda_1\left[u, F(t), \ddot{F}(t)\right] \tag{16}$$

Since equation (14) is not an exact expression for *W*, rather an approximation, the associated error function may be minimized using Galerkin method. The appropriate orthogonality condition applied to Eqn. (16) will yield the following "*Time Differential Equation*" with known constants C_1 and C_2, e.g.,

$$\ddot{F}(t) + C_1 F(t) + C_2 F^3(t) = C_3 q \tag{17}$$

the solution of which is well known (Duffing Type Eqation) from which the required investigations can be carried out. A detailed outline and illustrations are cited in Ref. [14]. For brevity details have been omitted.

5. Illustrations

5.1. CLAMPED RIGID CIRCULAR (RCP) AND ANNULAR PLATES (AP)

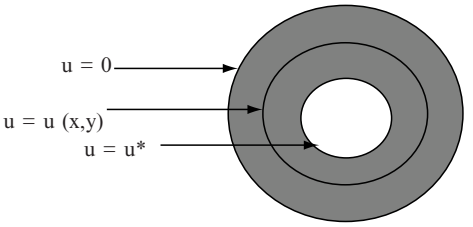

$$u(x,y)=1-(x^2+y^2)/a^2,\ u_0=0,\quad u^*=1-(b/a)^2,$$
$$a=outher\ radius,\quad b=inner\ radius$$
$$For\ rigid\ circular\ plate\ b=0$$

Fig. 2 Annular plate.

$$w=\sum_{i=2}^{\infty}A_i u^i F(t)\cong Au^2F(t),\qquad \phi\cong\Phi(u)F^2(t)$$

TABLE 1. Frequency parameter $\Omega^* = \omega a^2\sqrt{\rho h/D}$ for a clamped annular plate.

Frequency				
Parameter	Finite Strip[18]	FEM[21]	REF. [1]	Present
Ω	17.747	17.85	17.70	17.693

5.1.1. *Static Case*

$$\frac{qa^4}{Eh^4}=\begin{cases}5.8489\xi+2.754\xi^3 & \text{Ref. [3]}\\ 5.861\xi+2.762\xi^3 & \text{(RCP, present)}\\ 17.655\xi+44.3237\xi^3 & \text{(AP, present)}\end{cases}$$

The results for static deflection of annular plates cannot be compared for non-availability of such studies. However, for the linear case the result can be compared with those given in Ref. [15], e.g.,

$$W_{\max}/h=0.0575\frac{qa^4}{Eh^4}\text{(Ref. [15])},\ W_{\max}/h=0.0566\frac{qa^4}{Eh^4}\text{(Present)},$$

Moreover, in the nonlinear static case the results for RCP are even better than those of Yamaki[4], in the sense that the present results are closer to those of Way[16].

TABLE 2. Relative Time Period (T*/T)Vs Relative amplitude (ζ=A/h) (RCP & AP).

Dynamic response [T*/T]			Static deflection		
	RCP	AP		(qa^4/Eh^4)	
Relative Amplitude (ξ)	Present & Ref. [3]	Present	W_{max}/h	(RCP)	(AP)
0.25	0.9891	0.9459	0.25	1.3084	5.1063
0.50	0.9585	0.8246	0.50	3.2758	14.3680
0.75	0.9133	0.6969	0.75	5.5610	31.9400
1.00	0.8596	0.5890	1.0	8.6230	61.9787
				8.6020[3]	
				9.0000[16]	
1.25	0.8026	0.5037	1.25	12.7208	108.6385
1.50	0.7463	0.4370	1.50	18.1133	176.0750
1.75	0.6930	0.3844	1.75	25.0593	268.4436
2.00	0.6437	0.3424	2.00	33.8180	389.9000

5.2. ANNULAR PLATE WITH SS-OUTER BOUNDARY FREE INNER BOUNDARY

$$u(x,y) = 1-(x^2+y^2)/a^2, \quad W(u) = A(u+0.325u^2-0.1632u^3),$$
$$u^* = 1-(b/a)^2, \quad a = outer\ radius, \quad b = inner\ radius$$

5.2.1. *Numerical Results*

TABLE 3. Comparison of frequency parameter (AP).

ω = Circular frequency	Ref. [12]	FEM[17]	Present (CDC)
$\Omega^* = \omega a^2\sqrt{\rho h/D}$ =	5.138	4.990	5.169

TABLE 4. Relative Time Period (T*/T)Vs Relative amplitude (ζ=A/h) (SS-F AP).

ζ =(A/h)	0.25	0.50	0.75	1.00	1.25	1.50	1.75	2.00
T*/T	0.9392	0.8073	0.6739	0.5646	0.4801	0.4149	0.3640	0.3236

5.3. ELIPTIC PLATES CLAMPED ALONG THE EDGES

$$u(x,y) = 1-(x^2+y^2)/a^2, \quad u=0 \textit{ defines the boundary}$$

$$w = \sum_{i=2}^{\infty} A_i u^i \psi(t) \cong Au^2\psi(t), \qquad \phi \cong Au^2\Theta(t)$$

5.3.1. *Numerical Results*

$$\Omega^* = \omega a^2\sqrt{\frac{\rho h}{D}} = \sqrt{12\left(3m^4+2m^2+3\right)},$$

$m = a/b = 9.797$ (for m = 1, i.e., a Circular plate of radius a)

TABLE 5. Vibration characteristics for Elliptic Plate with uniform thickness: $\nu = 0.3$.

Relative time period T*/T					Load Function (qa^4/Eh^4)				
$\xi\downarrow$	b/a = 1.0	1.5	2.0	2.5	$\xi\downarrow$	b/a = 1.0	1.5	2.0	2.5
0.0	0	0	0	0	0	0	0	0	0
					0.2	1.19	3.35	8.68	19.48
0.5	0.97	0.98	0.99	0.996	0.4	2.47	6.87	17.55	39.17
					0.6	3.93	10.71	26.83	58.61
1.0	0.89	0.93	0.96	0.98	0.8	5.67	15.05	36.71	80.06
					1.0	7.78	20.04	47.38	101.72
1.5	0.80	0.86	0.93	0.96	1.2	10.34	25.85	59.05	124.42
					1.4	13.47	32.65	71.92	148.43
2.0	0.70	0.78	0.88	0.93	1.6	17.24	40.60	86.19	173.95
					2.0	27.08	60.60	119.72	230.40
2.5	0.62	0.71	0.83	0.91	2.4	40.60	87.17	161.24	295.45

5.4. APPLICATION TO ELASTIC-PLASTIC SHALLOW SHELL STRUCTURES

For brevity the analysis on large vibration of shallow shell structures is being restricted to its linear analysis. The governing differential equations on application of CDC method have already been established in Ref. [18] as

$$\frac{d^3W}{du^3}\oint(1-\Omega)Rds+\frac{d^2W}{du^2}\oint(1-\Omega)Fds+\frac{d\ W}{du}\oint(1-\Omega)Gds$$
$$+\frac{d^2W}{du^2}\oint D\left(\frac{\partial\Omega}{\partial x}\frac{\partial u}{\partial x}+\frac{\partial\Omega}{\partial y}\frac{\partial u}{\partial y}\right)t^{1/2}ds+\frac{d\ W}{du}\oint\ \frac{D}{t^{1/2}}\left(\frac{\partial\Omega}{\partial x}K+\frac{\partial\Omega}{\partial y}L\right)ds \quad (18)$$
$$+\iint\left[\ \rho h\Omega^{2W}+\frac{1}{R_x}\frac{\partial^2\Phi}{\partial y^2}+\frac{1}{R_y}\frac{\partial^2\Phi}{\partial x^2}-\frac{2}{R_{xy}}\frac{\partial^2\Phi}{\partial x\partial y}\right]dxdy=0$$

$$\frac{d^3\Phi}{du^3}\oint\ Rds+\frac{d^2\Phi}{du^2}\oint\ Fds+\frac{d\ W}{du}\oint\ Gds$$
$$-\frac{12D\left(1-\nu^2\right)}{h^2}(1-\Omega)\frac{d\ W}{du}\oint\frac{K_x(\frac{\partial u}{\partial y})^2+K_y(\frac{\partial u}{\partial x})^2}{\sqrt{t}}ds=0 \quad (19)$$

where

$$\Omega=\begin{cases}0 & \text{in the elastic region, when e}\le 1\\ \lambda[1-(3/2e)+(1/2e^3)] & \text{in the plastic region, when e}\ge 1\end{cases} \quad (20)$$

and

$$e=\frac{h}{e_s\sqrt{3}}\sqrt{\left[M\left(\frac{dw}{du}\right)^2+N\frac{dw}{du}\frac{d^2w}{du^2}+t^2\left(\frac{d^2w}{du^2}\right)^2\right]} \quad (21)$$

e_s is the yield strain, λis a material constant and the quantities *t, R, F, G, L* and *H* are taken directly from Ref. [19]. K_x and K_y denote the curvatures at a point.

Illustration

Consider the vibration of a dome of non-zero curvature upon an elliptic base.

$$u=1-(x/a)^2-(y/b)^2,\quad W=\sum_{j=2}^{n}A_ju^j,\quad \Phi=\sum_{j=2}^{n}B_ju^j \quad (22)$$

Observations

When three classes e < 1, e = 1 and e > 1, corresponding to elastic, elastic-perfectly plastic and elastic-plastic with strain hardening materials respectively, are considered it is evident that the value of e affects the separation between curves for differing values of aspect ratio (a/b). All graphs are

contained between two asymptotes, the Rayleigh-Ritz solution[20] to the problem and a constant multiple of the ratio of the shallowness parameter (2γ) to the thickness of the shell (h). Before $2\gamma / h = 3$ the graphs approach the Rayleigh-Ritz solution. After this point they tend towards the other asymptotes[18].

6. Conclusion

A simple method for the analysis of large vibration of elastic plates has been presented. The beauty of this method lies in the fact the basic governing equations come out to be a set of ordinary differential equations. The comparison of results shows that even a moderately approximated assumption for the expression of the deflected function yields results close to the standard results in all cases, sometimes better than those obtained from other methods. In conclusion it may be accepted that the CDC method may become a simple tool to deal with the problem of nonlinear vibration of plates of arbitrary shapes and shells.

References

1. G. Herrmann, 1955. *Influence of the large amplitude on flexural motion of elastic plates*, NASA Tech. Note **3578**.
2. H. N. Chu and G. Herrmann, 1956. *Influence of large amplitude on free flexural vibrations of rectangular elastic plates*, J. Appl. Mech. **23**, 532-540.
3. N. Yamaki, 1961. *Influence of large amplitude on flexural vibrations of elastic plates*, ZAMM, **41**, 501-510.
4. H. M. Berger, 1955. *A new approach to the analysis of large deflections of plates*, J. Appl. Mech., **22**, 465-472.
5. G. C. Sinharay and B. Banerjee, 1985. *Large amplitude free vibrations of shallow spherical shell and cylindrical shell A new approach*, Intl. J. Nonlinear Mech., **20**, 69-78.
6. J. Nowinski and H. Ohanabe, 1972. *On certain inconsistencies in Berger equations for large deflections of plastic plates*, Intl. J. Mech. Sci., **14**, 165-170.
7. M. M. Banerjee, P. Biswas and S. Sikder, 1993. *Temperature effect on the dynamic response of spherical shells*, SMIRT-12 Trans., Vol. B, Paper No. **B06/3**, 159-163.
8. M. M. Banerjee, 1997. *A new approach to the nonlinear vibration analysis of plates and shells*, Trans. 14th Intl. Conf. On Struc. Mech. In Reactor Tech., *(SMIRT-13),* (Lyon, France) Divn. B, Paper No. **247**.
9. J. Mazumdar, 1970. *A method for solving problems of elastic plates of arbitrary shapes*, J. Aust. Math. Soc., **11**, 95-112.
10. J. Mazumdar, 1971. *Buckling of elastic plates by the method of constant deflection lines*, J. Aust. Math. Soc., **13**, 91-103.
11. R. Jones and J. Mazumdar, 1997. *Transverse vibration of shallow shells by the method of constant deflection contours*, J. Accoust. Soc. Am., **56**, 1487-1492.

12. D. Bucco and J. Mazumdar, 1979. *Vibration analysis of plates of arbitrary shape A new approach*, J. Sound Vib., **67**, 253-262.
13. J. Mazumdar and D. Bucco, 1978. *Transverse vibrations of visco-elastic shallow shells*, J. Sound Vib., **57**, 323-331.
14. M. M. Banerjee and G. A. Rogerson, 2002. *An application of the constant contour deflection method to non-linear vibration*. Archive of Applied Mechanics. **72**, 279-292.
15. S. P. Timoshenko and S. Woinowisky-Krieger, 1959. *Theory of plates and shells*, 2nd Edn., McGraw-Hill, New York.
16. S. Way, 1934. *Bending of circular plates with large deflection*, Trans. ASME, **56**, 627-636.
17. G. Anderson, B. M. Irons and O. C. Zienkiwicz, 1978. *Vibration and stability of plates using finite elements*, Intl. J. Solids and Struc., **4**, 1031-1055.
18. M. M. Banerjee, S. Chanda, J. Mazundar and B. Pincombe, 2000. *On the free vibration of elastic-plastic shells*, Proc. Fourth Biennial Engg. Maths. and Applications Conf. RMIT University, Melbourne, Australia, 10-13 September, 59-62.
19. J. Mazumdar and R. K. Jain, 1989. *Elastic-plastic analysis of plates of arbitrary shape—A new approach*, Int. Jl. of Plasticity, **5**, 463-475.
20. R. Jones and J. Mazumdar, 1974. *Transverse vibration of elastic plates by the method of Constant Deflection Line*, Journal of the Acoustical Society of America, **56**, 1487-1492.

CRACK DETECTION IN CANTILEVER BEAM USING VIBRATION RESPONSE

A. K. BATABYAL
Dept. of Mechanical Engineering, Haldia Institute of Technology, Haldia 721657, West Bengal, India

P. SANKAR AND T. K. PAUL*
Condition Monitoring Group, Central Mechanical Engineering Research Institute, Durgapur 713209, West Bengal, India

Abstract. In the present work, a methodology for predicting crack parameters (crack depth and its location) in a thin cantilever beam using vibration response has been developed. Parametric studies have been carried out using ANSYS Software to evaluate modal parameters (natural frequencies and mode shapes) for different crack parameters. From the analysis, it has been observed that both crack location and crack depth have noticeable effects on the modal parameters of the cracked beam. Also, a certain frequency may correspond to different crack depths and its locations. Based on this, the contour lines of the cracked beam frequencies have been plotted having crack location and crack depth as its axis. The location and depth corresponding to any point on this curve becomes a possible crack location and depth. The identification procedure presented in this study is believed to provide a useful tool for detection of medium size crack in a beam.

Keywords: crack detection, vibration response, cantilever beam, natural frequency. mode shape

1. Introduction

A crack in a structural member introduces local flexibility that would affect its vibration response. This property may be used to detect existence of a crack together its location and depth in a structural member. The effect of a crack on

*Corresponding author, tkp7494@yahoo.com

E. İnan et al. (eds.), *Vibration Problems ICOVP-2007*,

the deformation of a beam has been considered as an elastic hinge by Chondros[1]. Gudmundson[2] proposed a theoretical procedure to identify the crack using measured eigenfrequency changes. Rizos[3] measured the amplitude at two points and proposed an algorithm to identify the location of crack. Pandey[4] suggested another parameter, namely curvature of the deflected shape of beam instead of change in frequencies to identify the location of crack. Ostachowicz[5] proposed a procedure for identification of a crack based on the measurement of the deflection shape of the beam. Nandwana[6] extended work carried out by Rizos[3] for stepped beam and cantilever beams with inclined edge cracks to detect crack based on natural frequency measurement. Lakshminarayana[7] carried out analytical work to study the effect of crack at different location and depth on mode shape behaviour. Nahvi[8] established analytical as well as experimental approach to the crack detection in cantilever beams. Contours of the normalized frequency in terms of the normalized crack depth and location were plotted.

In the present work, a methodology for predicting crack parameters (crack depth and its location) in a thin cantilever beam using vibration response has been developed. Parametric studies have been carried out using ANSYS Software to evaluate modal parameters (natural frequencies and mode shapes) for different crack parameters. Contour lines of the cracked beam frequencies have been plotted to identify crack location and crack depth in the above beam.

2. Results and discussions

Fig. 1 shows a cantilever beam made of mild steel with a U notched crack. To find out natural frequency and mode shapes, FE analysis has been carried out using ANSYS Software (version 8.1) for uncracked and cracked beam.

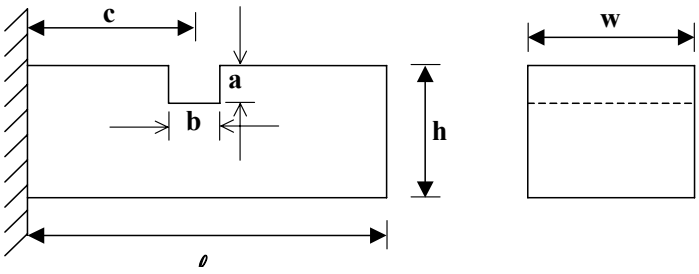

Fig. 1 Cantilever beam with crack.

The natural frequencies and mode shapes of the cracked cantilever beams are obtained for cracks located at normalized distance c/l from the fixed end with a normalized depth a/h, for thin beam. The normalized natural frequencies Fr1, Fr2 are defined as the ratio of frequency for cracked and un-cracked beam in 1st, 2nd mode respectively.

Fig. 2 shows the discretised model (zoomed near the position of crack) of thin beam with U-notch. Parametric studies have been carried out for thin beam having length $l = 260mm$, $w = 25mm$ and thickness $h = 4.4mm$. The breadth (b) of U notch has been kept as $0.32mm$. Crack depth (a) has been varied from $0.6mm$ to $3mm$ in steps of $0.6mm$. The crack location from the fixed end (c) has been varied from $30mm$ to $230mm$ in steps of $20mm$.

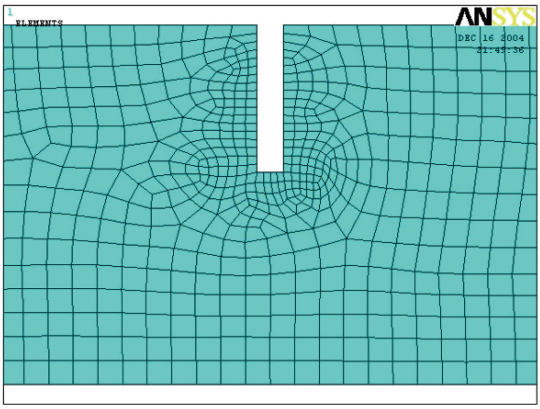

Fig. 2 Discretised model of beam with U-notch.

The variation of first two normalized natural frequencies (Fr1 & Fr2) with crack depth ratios for different crack location ratios have been shown in Figs. 3(a) & 3(b) respectively. It has been observed that the values of Fr1, Fr2 of the cracked beam decrease, as crack grow deeper. In Fig. 3(a), it is observed that the decrement rate of Fr1 is maximum for $c/l = 0.1$ and reduces as c/l increases from 0.1 to 0.7. So it can be inferred that the value of Fr1 is mostly affected when crack is located near the fixed end. Fig. 4(a) also supplements the above observation.

In Fig. 3(b), it is observed that the rate at which Fr2 decreases is not significant when the crack location is near the fixed end ($c/l = 0.1$ & $c/l = 0.3$), but decreases rapidly between $c/l = 0.5$ and $c/l = 0.7$. The above phenomenon has also been observed in Fig. 4(b). An important phenomenon

has been observed in Fig. 3(b) that the decrement rate of Fr2 is more with $c/l = 0.5$ compared to $c/l = 0.7$. As the node for second mode ($c/l = 0.783$) is closer to the point $c/l = 0.7$ compared to $c/l = 0.5$, the effect of crack is more significant at $c/l = 0.5$. The above observation has been concluded from Fig. 4(b).

From the above results it can be seen that decrease in the frequencies is greatest when the crack is located at peak/through positions of the corresponding mode shape. It can be seen in Fig. 4(b) that the trends of changes of the 2nd natural frequency with crack location are not monotonic as in the 1st natural frequency shown in Fig. 4(a). The minimum value of normalized frequency for 1st mode & 2nd mode are 0.6, 0.9 respectively. So, the effect of crack is maximum at 1st mode.

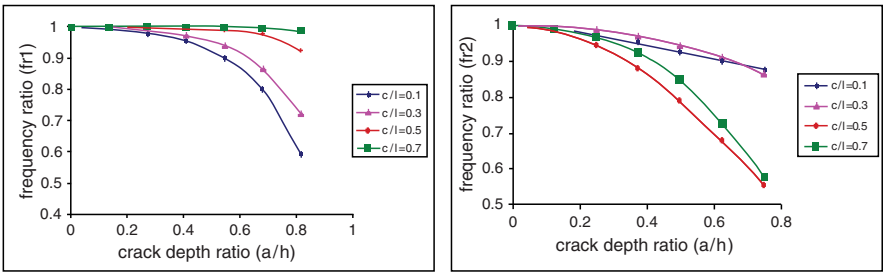

Fig. 3 Variation of frequency ratio with crack depth ratio for different crack location ratios (a) 1st mode, (b) 2nd mode.

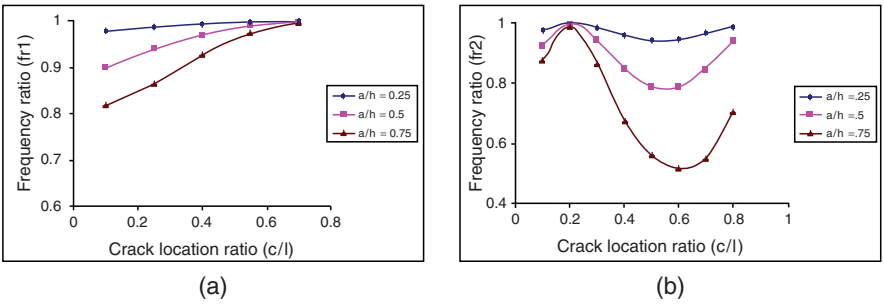

Fig. 4 Variation of frequency ratio with crack location ratio for different crack depth ratios (a) 1st mode, (b) 2nd mode.

From the observations in Figs. 3-4, it can be inferred that both crack location and crack depth have influence on the frequencies of the cracked beam. Also a certain frequency can correspond to different crack depths and locations.

Based on this, contour lines with constant normalized frequency can be plotted having crack location and crack depth as its axis. The location and depth corresponding to any point on this curve become a possible location and depth.

Figs. 5(a) & 5(b) show frequency contour plot for 1st mode and 2nd mode respectively. Two different frequency ratios (0.95 & 0.97) have been chosen for both the modes. If from experimental measurement, it is found that normalized frequency for 1st mode and 2nd mode are 0.95 and 0.97 respectively, then the actual location and depth of the crack can be predicted from the intersection point of frequency contour plot for Fr1 = 0.95 and Fr2 = 0.97.

Figs. 6(a) & 6(b) show mode shapes for uncracked beam & cracked beam ($c/l = 0.5$) for 1st mode and 2nd mode respectively. No significant shift in displacement for the cracked beam has been observed. Figs. 7(a) & 7(b) show deviation in mode shapes for cracked beam ($c/l = 0.5$) compared to uncracked beam for 1st mode and 2nd mode respectively. It has been observed that the maximum deviations are 0.16 (1st mode) and 0.6 (2nd mode).

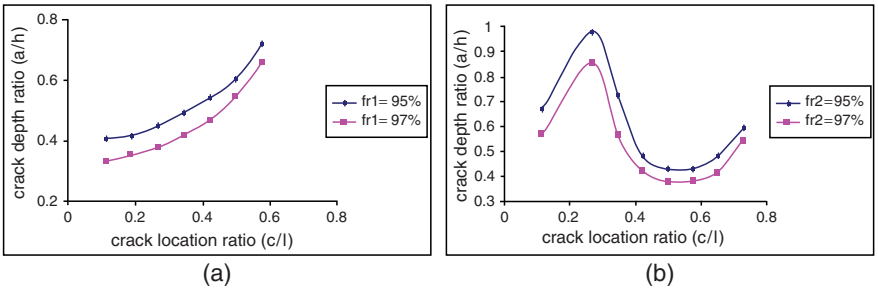

Fig. 5 Frequency contour plots (a) 1st mode, (b) 2nd mode.

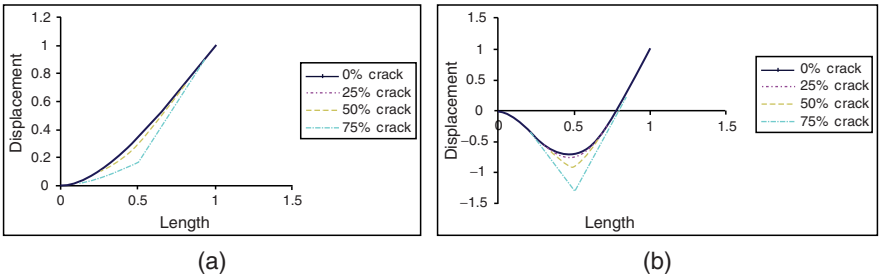

Fig. 6 Mode shape of uncracked and cracked beam ($c/l = 0.5$) (a) 1st mode, (b) 2nd mode.

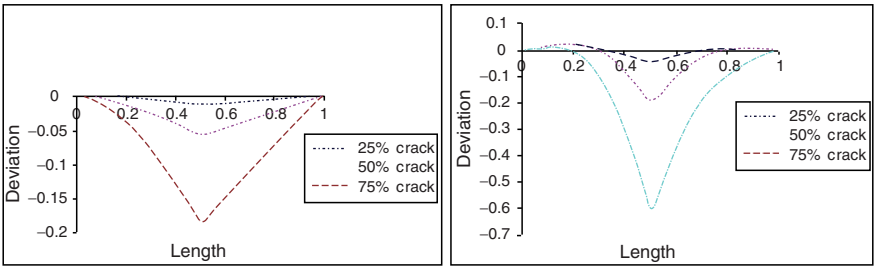

Fig. 7 Deviation in mode shape of cracked beam ($c/l = 0.5$) w.r.t. uncracked beam (a) 1st mode, (b) 2nd mode.

3. Conclusion

A method for identifying crack parameters (crack depth and its location) in a cantilever beam using vibration response has been attempted in the present work. Parametric studies have been carried out using ANSYS Software to evaluate modal parameters (natural frequencies and mode shapes) for different crack parameters. From the analysis, it has been observed that both crack location and crack depth have noticeable effects on the modal parameters of the cracked cantilever beam. Contour lines of the cracked beam frequencies have been plotted having crack location and crack depth as its axis to identify the crack. The identification procedure presented in this study is believed to provide a useful tool for detection of medium size crack in a beam.

ACKNOWLEDGEMENTS

The authors are grateful to the Director, CMERI, for the kind permission to publish the paper. They are also grateful to all the staff members of Condition Monitoring Group who have helped in carrying out the development work.

References

1. T. G. Chondros, A. D. Dimarogonas, 1980. *Identification of cracks in welded joints of complex structures*, Journal of Sound and Vibration, **69**, 531.
2. P. Gudmundson, 1982. *Eigenfrequency changes of structures due to crack, notches or other geometrical changes*, Journal of the Mechanics and Physics of Solids, **30**, 339.

3. P. F. Rizos, N. Aspragathos, A. D. Dimarogonas, 1990. *Identification of crack location and magnitude in a cantilever beam from the vibration modes*, Journal of Sound and Vibration, **138**, 381.
4. A. K. Pandey, M. Biswas, M. M. Samman, 1991. *Damage detection from change in curvature mode shapes*, Journal of Sound and Vibration, **145**, 321.
5 W. M. Ostachowicz, M. Krawczuk, 1991. *Analysis of the effect of cracks on natural frequencies of a cantilever beam*, Journal of Sound and Vibration, **150**, 191.
6. B. P. Nandwana, S. K. Maiti, 1997. *Detection of the location and size of a crack in stepped cantilever beams based on measurement of natural frequencies*, Journal of Sound and Vibration, **203**, 435.
7. K. Lakshminarayana, C. Jebaraj, 1999. *Sensitivity analysis of local/global modal parameters for identification of a crack in a beam*, Journal of Sound and Vibration, **228**, 977.
8. H. Nahvi, M. Jabbari, 2005. *Crack detection in beams using experimental modal data and finite element model*, International Journal of Mechanical Sciences, **47**, 1477.

LARGE AMPLITUDE FREE VIBRATION OF A ROTATING NON-HOMOGENEOUS BEAM WITH NON-LINEAR SPRING AND MASS SYSTEM

RASAJIT KUMAR BERA*
Department of Mathematics, Heritage Institute of Technology Anandapur, Kolkata-700107, India

P. C. RAY
Dept. of Math., Government College of Engineering & Leather Technology, Block-LB, Salt Lake City, Kolkata-70098, India

A. CHAKRABARTI
1A/14, Ramlal Agarwala Lane, Calcutta-700050, India

B. MUKHOPADHYAY
Bengal Eng. and Science University, Howrah-711103, India

Abstract. Free, out of plane vibration of a rotating non-homogeneous beam with non-linear spring mass system has been investigated. The non-linear constraint and non-homogeneity appear in the boundary condition. Solution is obtained by applying method of multiple time scale directly to the non-linear partial differential equations and the boundary conditions. The results of the linear frequencies match well with those obtained in open literature. Subsequent non-linear study indicates that there is a pronounced effect of spring and its mass. The stability of non-linear vibration of non-homogeneous beam has also been discussed at length. The influence of spring-mass location on frequencies is also investigated on non-linear frequencies of rotating non-homogeneous beam.

Keywords: non-homogeneous, non-linear, spring-mass system, rotating beam, multiple time scale

*Corresponding author, rasajit@yahoo.com

E. İnan et al. (eds.), *Vibration Problems ICOVP-2007*,

1. Introduction

Beam theories for moderate deformation have been developed by several researchers.[1-3] This approach yields non-linear analytical models, which are ultimately used to obtain the equilibrium positions and subsequent linearized solution.

Anderson[4] formulated the non-linear equation of motion of a rotating bar and obtained the natural frequencies from the linearized equation. Using a harmonic balance technique, the non-linear structural dynamic analysis of blade model was performed by Minguet and Dugundji[5]. Nayfeh and his associates[6-7] reported several studies to determine non-linear response of stationary beams under large deflection. Nayfeh et al[7] proposed a numerical perturbation method for the determination of non-linear response of a continuous beam having complicated boundary conditions. The non-linear response of a simple supported beam with an attached spring mass system was also investigated by Pakdemirli and Nayfeh[8]. Nayfeh and Nayfeh[9] obtained the non-linear modes and frequencies of a simply supported Euler Bernoulli beam resting on an elastic foundation having quadratic and cubic non-linearity. Recently, non-linear normal mode shapes were determined for a cantilever beam by using the method of multiple time scale, Nayfeh et al[10], Pohit et al[11-13] have modeled the characteristic of an elastomeric material and investigated the effect of non-linear elastomeric constraint on rotating blade. They applied a numerical perturbation technique to determine the frequency amplitude relationship of a rotating beam under transverse vibration. Recently Pesheck et al[14] proposed a method for determining reduced order models for rotating uniform cantilever Euler-Bernoulli beams.

Most of the studies on helicopter blades have focused primarily on the linear or non-linear dynamic analysis of homogeneous beams. Very little information is available on the influence of the elastomer on the structural dynamic characteristics of a rotor blade when the elastomer is included as a subsystem and the beam is non-homogeneous. In references of Nayfeh[9] and Pofit et al.[12] attempts have been made to study the effect of a non-linear constraint on a simply supported and rotating homogeneous beam respectively.

The major objectives of the present study are as follows:

(i) The formulation of the equation of motion of a rotating non-homogeneous beam with a non-linear constraint starting from transverse/axial coupling through axial strain. The non-linear constraint appears in the boundary condition and its mass is considered during the analysis.

(ii) The determination of a non-linear solution by applying methods of multiple time scale directly to the partial differential equations and boundary conditions.

(iii) The study of the influence of the location of the non-linear constraint on non-linear frequencies.

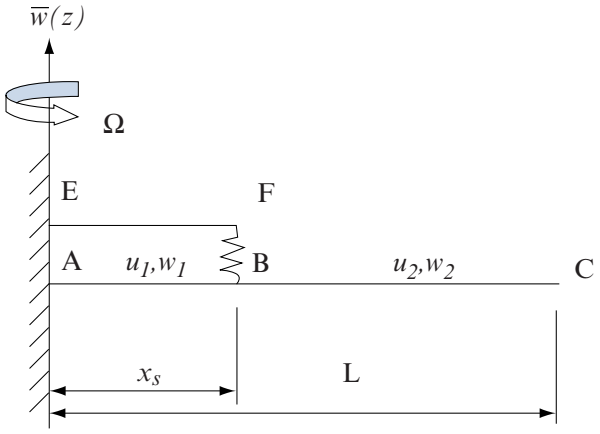

Fig. 1 Rotating beam with spring-mass system.

2. Formulation

The dynamics of a rotating beam differs from that of non-rotating one due to the addition of centrifugal stiffness. The differential equations of motion for a rotating non-homogeneous beam have variable coefficient while those for a non-rotating non-homogeneous beam have constant coefficients. Additionally, in the present problem, there is a transverse constraint at the point B (Fig. 1) in the form of a non-linear spring of mass M. The other end of the spring is attached to a rigid beam EF which is also rotating along with the beam AC. The deformation of the spring-mass system depends on the deflection of the beam at point B. Here x_s is the distance between A and B. The motion is restricted to the transverse direction only, thereby eliminating lead lag and tensional motion, and allows axial strain. The effect of rotary inertia is also neglected.
Introducing

$(') \equiv$ space derivative with respect to the distance x
$(.) \equiv$ time derivative with respect to time t

The expressions for the kinetic energy and the potential energy of the rotating non-homogeneous beam are given in equations (1) and (2) respectively.

$$K.E. = T(t) = \frac{1}{2}\int_0^{x_s} m[\{(\frac{\partial u_1}{\partial t})^2 + (\frac{\partial w_1}{\partial t})^2\} + \Omega^2 (x+u_1)^2]dx + \frac{1}{2}\int_{x_s}^{L} m[(\frac{\partial u_2}{\partial t})^2$$

$$+(\frac{\partial w_2}{\partial t})^2 + \Omega^2 (x+u_1)^2]dx + [\frac{1}{2}M[\dot{w}_1^2(x_s,t)] + \frac{1}{2}M\Omega^2\{x_s + u_1(x_s,t)\}^2] \tag{1}$$

$$PE = U(T) = \frac{1}{2}\int_0^{x_s} EI(w_1'')^2 dx + \frac{1}{2}\int_{x_s}^{L} EI(w_2'')^2 dx + \frac{1}{2}\int_0^{x_s} EA(u_1' + \frac{1}{2}w_1'^2)^2 dx$$
$$+ \frac{1}{2}\int_{x_s}^{L} EA(u_2' + \frac{1}{2}w_2'^2)^2 dx + \frac{1}{2}\alpha w_1^2(x_s,t) + \frac{1}{4}\gamma w_1^4(x_s,t) \quad (2)$$

Here t denotes time, m denotes mass per unit length of beam, EI the variable flexural rigidity of the beam cross-section, Ω the angular velocity, A the cross-sectional area of the beam, $w_i(i=1,2)$ the transverse deflection at the two segments of the beam AC, $u_i(i=1,2)$ are the left and right axial beam displacements, α and γ are the coefficients of the linear and non-linear terms of the spring respectively and M is the mass of the non-linear spring.
Inserting equations (1) and (2) into variational principle

$$\delta\int_{t_1}^{t_2}(T-U)dt = 0\,, \quad (3)$$

one can obtain the governing equations and boundary conditions as follows:

$$-m\ddot{u}_1 + m\Omega^2(x+u_1) + [EA(u_1' + \frac{1}{2}w_1'^2)]' = 0,$$
$$-m\ddot{w}_1 - [EIw_1'']'' + [EA\{(u_1' + \frac{1}{2}w_1'^2)w_1'\}]' = 0, \quad \text{for } 0 \le x \le x_s, \quad (4)$$
$$w_1(0,t) = w_1'(0,t) = 0$$

and

$$-m\ddot{u}_2 + m\Omega^2(x+u_2) + [EA(u_2' + \frac{1}{2}w_2'^2)]' = 0,$$
$$-m\ddot{w}_2 - [EIw_2'']'' + [EA\{(u_2' + \frac{1}{2}w_2'^2)w_2'\}]' = 0 \quad \text{for} \quad x_s \le x \le L \quad (5)$$
$$w_2''(L,t) = w_2'''(L,t) = 0, \quad w_1(x_s,t) = w_2(x_s,t),$$
$$w_1'(x_s,t) = w_2'(x_s,t), \quad w_1''(x_s,t) = w_2''(x_s,t)$$

$$[EIw_1''(x_s,t)]' - [EIw_2''(x_s,t)]' - EA[u_1'(x_s,t) + \frac{1}{2}w_1'^2(x_s,t)]w_1'(x_s,t)$$

$$+ EA[(u_2'(x_s,t) + \frac{1}{2}w_2'^2(x_s,t)]w_2'(x_s,t) - \alpha w_1(x_s,t) - \gamma w_1^3(x_s,t) - M\ddot{w}_1 = 0$$

$$u_1(0,t) = 0, \quad u_2' + \frac{1}{2}w_2'^2 = 0 \quad \text{at} \quad x = L \tag{6}$$

$$\begin{aligned} &-EA(u_1' + \frac{1}{2}w_1'^2) + EA(u_2' + \frac{1}{2}w_2'^2) + M\Omega^2(x_s + u_1) = 0 \\ &u_1(x_s,t) = u_2(x_s,t) \quad \text{at} \quad x = x_s \end{aligned} \tag{7}$$

Let us now introduce the following non-dimensional quantities to the above results:

$$\begin{aligned} &x^* = \frac{x}{L}; w_1^* = \frac{w_1}{r}; w_2^* = \frac{w_2}{r}; u_1^* = \frac{u_1}{\varepsilon r}; u_2^* = \frac{u_2}{\varepsilon r}; \eta = \frac{x_s}{L}; \\ &a = \frac{EAr^2}{m\Omega^2L^4} = \frac{EI}{m\Omega^2L^4}; \varepsilon = \frac{r}{L}; t^* = \Omega t \end{aligned} \tag{8}$$

where r is the radius of gyration of the cross-section of the beam and L is the length of the beam. Introducing (8) in equations (4) to (7) and removing stars (*) from all the quantities for convenience and after simplification, the following equations are obtained :

$$\varepsilon^2(u_1 - \ddot{u}_1) + x + \bar{a}[f(x)(u_1' + \frac{1}{2}(w_1')^2)]' = 0 \tag{8a}$$

and

$$-\ddot{w}_1 - \bar{a}[f(x)w_1'']'' + \bar{a}[f(x)(u_1' + \frac{1}{2}(w_1')^2)w_1']' = 0, \quad 0 \le x \le \eta \tag{8b}$$

from (4), where $E=E_0f(x)$. Similarly, the equations (5) can be written as

$$\varepsilon^2(u_2 - \ddot{u}_2) + x + \bar{a}[f(x)(u_2' + \frac{1}{2}(w_2')^2)]' = 0 \tag{9a}$$

and

$$-\ddot{w}_2 - \overline{a}[f(x)w_2'']'' + \overline{a}[f(x)(u_2' + \frac{1}{2}(w_2')^2)w_2']' = 0, \quad \eta \le x \le 1, \quad (9b)$$

The corresponding dimensionless star free boundary conditions are

$$w_1(0,t) = w_1'(0,t) = 0; \; w_2''(1,t) = w_2'''(1,t) = 0; \text{ etc.} \quad (9c)$$

where

$$\alpha_1 = \frac{\alpha L^3}{E_0 I}, \alpha_2 = \frac{\gamma r^2 L^3}{E_0 I}, \alpha_3 = \frac{\Omega^2 M L^3}{E_0 I} \quad (9d)$$

Neglecting ε^2-order terms in (8a) and (9a) and carrying out necessary integration, we obtain

$$\frac{1}{2}x^2 + \overline{a}[f(x)(u_1' + \frac{1}{2}(w_1')^2)] = f_1(t), \; 0 \le x \le \eta \quad (10a)$$

and

$$\frac{1}{2}x^2 + \overline{a}[f(x)(u_2' + \frac{1}{2}(w_2')^2)] = f_2(t), \; \eta \le x \le 1 \quad (10b)$$

By virtue of (9e), we get at x = η

$$\frac{1}{2}\eta^2 + \overline{a}[f(\eta)(u_1' + \frac{1}{2}(w_1')^2)] = \frac{1}{2}\eta^2 + \overline{a}[f(\eta)(u_2' + \frac{1}{2}(w_2')^2)] \quad (10c)$$

This implies that $f_1(t) = f_2(t)$ at $x = \eta$

At x = 0, we get from (10a),

$$\overline{a}[f(0)u_1'(0,t)] = f_1(t).$$

At x = 1,

$$\frac{1}{2} + \overline{a}[f(1)\{u_2'(1,t) + \frac{1}{2}(w_2'(1,t))^2\}] = f_2(t) \quad (10d)$$

But from (9e), we have

$$u_2'(1,t) + \frac{1}{2}(w_2'^2(1,t)) = 0 \quad (10e)$$

Therefore, from (10d) and (10e), we get $f_2(t) = ½$, which implies that

$$f_1(t) = f_2(t) = 1/2 \quad (10f)$$

Now the equations (10a) and 8(b) reduce to

$$\bar{a}f(x)[u_1' + \frac{1}{2}w_1'^2] = \bar{a}\alpha_3\eta + \frac{1}{2}(1-x^2) \tag{11a}$$

and

$$-\frac{\partial^2 w_1}{\partial t^2} - \bar{a}[f(x)w_1'']'' + \bar{a}[f(x)\{u_1' + \frac{1}{2}(w_1'^2)\}'w_1']' = 0, \quad \text{for} \quad 0 \le x \le \eta \tag{11b}$$

The equations (10b) and (9b) reduce to

$$\bar{a}f(x)[u_2' + \frac{1}{2}w_2'^2] = \frac{1}{2}(1-x^2) \tag{12a}$$

and

$$-\frac{\partial^2 w_2}{\partial t^2} - \bar{a}[f(x)w_2'']'' + \bar{a}[f(x)[u_2' + \frac{1}{2}w_2'^2)w_2']' = 0, \quad \text{for} \quad \eta \le x \le 1 \tag{12b}$$

Eliminating u_1' and u_2' from equations (11) and (12), we have the following governing equations in transverse mode as

$$-\ddot{w}_1 - \bar{a}[f(x)w_1'']'' + \bar{a}\alpha_3\eta w_1'' - xw_1' + \frac{1}{2}(1-x^2)w_1'' = 0, \quad \text{for} \quad 0 \le x \le \eta \tag{13}$$

and

$$-\ddot{w}_2 - \bar{a}[f(x)w_2'']'' - xw_2' + \frac{1}{2}(1-x^2)w_2'' = 0, \quad \text{for} \quad \eta \le x \le 1 \tag{14}$$

The corresponding boundary conditions (9) are now given by

$$\begin{aligned} &w_1(0,t) = 0 = w_1'(0,t), \quad w_2''(1,t) = 0 = w_2'''(1,t), \quad \text{etc.} \\ &w_1(\eta,t) = w_2(\eta,t), \quad w_1'(\eta,t) = w_2'(\eta,t), \quad w_1''(\eta,t) = w_2''(\eta,t) \end{aligned} \tag{15}$$

In the above equations, coefficients α_1, α_2 and α_3 are defined as follows:

$$\alpha_1 = \frac{\alpha L^3}{EI}, \alpha_2 = \frac{\gamma r^2 L^3}{EI} \text{ and } \alpha_3 = \frac{M\Omega^2 L^3}{EI}.$$

Let us now assume

$$f(x) = 1 + \beta x \tag{16}$$

for the **non-homogeneous** beam, where β is a constant.

Then the equations (13) and (14) can be rewritten as

$$-\ddot{w}_1 - \bar{a}[(1+\beta x)w_1^{iv} + 2\beta w_1'''] + \bar{a}\alpha_3\eta w_1'' - xw_1' + \frac{1}{2}(1-x^2)w_1'' = 0, \quad \text{for} \quad 0 \le x \le \eta \tag{17}$$

$$-\ddot{w}_2 - \bar{a}[(1+\beta x)w_2^{iv} + 2\beta w_2'''] - xw_2' + \frac{1}{2}(1-x^2)w_2'' = 0, \text{ for } \eta \le x \le 1 \tag{18}$$

The boundary conditions (15) are rewritten as

$$w_1(0,t) = 0 = w_1'(0,t)\,,\ w_2''(1,t) = 0 = w_2'''(1,t)\,, \text{ etc.} \tag{19}$$

If β = 0, the equations (17), (18) and (19) of the present analysis exactly coincide with the results (7) and (8) respectively of Das et al[15].

2.1. SOLUTION METHODOLOGY

Assuming the expansions for the displacements in the form

$$\begin{aligned} w_1(x,t;\varepsilon) &= \varepsilon w_{11}(x,T_0,T_2) + \varepsilon^3 w_{13}(x,T_0,T_2) + \varepsilon^5 w_{15}(x,T_0,T_2) + \ldots \\ w_2(x,t;\varepsilon) &= \varepsilon w_{21}(x,T_0,T_2) + \varepsilon^3 w_{23}(x,T_0,T_2) + \varepsilon^5 w_{25}(x,T_0,T_2) + \ldots \end{aligned} \tag{20}$$

where w_{1n} and w_{2n} are 0(1); ε is a small dimensionless parameter (defined earlier); $T_0 = t$ is a first time scale characterizing changes occurring at the frequency ω_n, where ω_n's are the natural frequencies of the non-homogeneous beam-spring system and $T_2 = \varepsilon^2 t$ is a slow time scale, characterizing the modulation of the amplitudes and phases due to damping, non-linearity, and possible resonance[9].

Substituting equation (20) in equations (17), (18) and (19), one obtains the different order equations of ε.

Order: ε

$$-D_0^2 w_{11} - \bar{a}[(1+\beta x)w_{11}^{iv} + 2\beta w_{11}'''] - xw_{11}' + (\bar{a}\alpha_3\eta)w_{11}'' + \frac{1}{2}(1-x^2)w_{11}'' = 0 \quad \text{for} \quad 0 \le x \le \eta\,, \tag{21a}$$

$$-D_0^2 w_{21} - \bar{a}[(1+\beta x)w_{21}^{iv} + 2\beta w_{21}'''] - x w_{21}' + \frac{1}{2}(1-x^2)w_{21}'' = 0, \text{ for } \eta \le x \le 1 \tag{21b}$$

and the corresponding boundary conditions are as follows:

$$\begin{aligned} &w_{11}(0,t) = 0, w_{11}'(0,t) = 0, \quad w_{21}''(1,t) = 0, w_{21}'''(1,t) = 0, \\ &w_{11}(\eta,t) = w_{21}(\eta,t), \quad w_{11}'\eta,t) = w_{21}'(\eta,t) \quad \text{etc.} \end{aligned} \tag{22}$$

Order: ε^3

$$\begin{aligned} &-D_0^2 w_{13} - \bar{a}[(1+\beta x)w_{13}^{iv} + 2\beta w_{13}'''] - x w_{13}' + (\bar{a}\alpha_3\eta)w_{13}'' \\ &+ \frac{1}{2}(1-x^2)w_{13}'' = 2D_0 D_2 w_{11}, \quad \text{for } 0 \le x \le \eta \end{aligned} \tag{23a}$$

$$\begin{aligned} &-D_0^2 w_{23} - \bar{a}[(1+\beta x)w_{23}^{iv} + 2\beta w_{23}'''] - x w_{23}' \\ &+ \frac{1}{2}(1-x^2)w_{21}'' = 2D_0 D_2 w_{21} \quad \text{for } \eta \le x \le 1 \end{aligned} \tag{23b}$$

and the corresponding boundary conditions are as follows:

$$w_{13}(0,t) = 0, \; w_{13}'(0,t) = 0, \; w_{23}''(1,t) = 0, \; w_{23}'''(1,t) = 0 \text{ etc.} \tag{24}$$

where

$$D_0 \equiv \frac{\partial}{\partial T_0} \text{ and } D_2 \equiv \frac{\partial}{\partial T_2}$$

If β = 0, the equations (21a,b), (22), (23a,b) and (24) exactly coincide with the results (10), (11), (12) and (13) respectively of Das et al[15].

2.2. LINEAR SOLUTION

At order ε, the equations and boundary conditions are linear and hence the solution is assumed in the following form:

$$\begin{aligned} w_{11} &= \{A(T_2)e^{i\omega T_0} + c.c.\}y_1(x) \\ w_{21} &= \{A(T_2)e^{i\omega T_0} + c.c.\}y_2(x) \end{aligned} \tag{25}$$

where c.c. is the complex conjugate of the preceding terms.

Introducing (25) in equations (21) and (22), one gets

$$\overline{a}[(1+\beta x)y_1^{iv}+2\beta y_1'''] - \frac{1}{2}(1-x^2)y_1'' - (\overline{a}\alpha_3\eta)y_1'' + xy_1' - \omega^2 y_1 = 0, \text{ for } 0 \le x \le \eta$$

$$\overline{a}[(1+\beta x)y_2^{iv}+2\beta y_2'''] + xy_2' - \frac{1}{2}(1-x^2)y_2'' - \omega^2 y_2 = 0 \text{ for } \eta \le x \le 1 \qquad (26)$$

and the corresponding boundary conditions are as follows:

$$y_1(0) = 0\,, \quad y_1'(0) = 0, \quad y_2''(1) = 0, \quad y_2'''(1) = 0 \text{ etc.} \qquad (27)$$

If β = 0, the equations (26) and (27) exactly coincide with the deductions (15) and (16) respectively of Das et al[15].

The power series solutions of the equations (26) and (27), can be expressed as

$$\begin{aligned} y_1(x) &= \sum_{k=1}^{\infty} A_k x^{k-1}, \quad \text{for} \quad 0 \le x \le \eta \\ y_2(x) &= \sum_{1}^{\infty} B_k x^{k-1}, \quad \text{for} \quad \eta \le x \le 1 \end{aligned} \qquad (28)$$

Substituting equations (28) in equations (26) and (27), one obtains the following recurrence relationships and the boundary conditions:

$$1.A_{j+4} + \frac{[(j-1)j\overline{a}+2j]\beta A_{j+3}}{j(j+3)\overline{a}} - \frac{0.5+\overline{a}\alpha_3\eta}{(j+2)(j+3)\overline{a}} A_{j+2} + \frac{0.5[(j-1)j-2\omega^2]}{j(j+1)(j+2)(j+3)\overline{a}} A_j = 0$$

$$1.B_{j+4} + \frac{[(j-1)j\overline{a}+2j]\beta B_{j+3}}{j(j+3)\overline{a}} - \frac{0.5}{(j+2)(j+3)\overline{a}} B_{j+2} + \frac{0.5[(j-1)j-2\omega^2]}{j(j+1)(j+2)(j+3)\overline{a}} B_j = 0 \qquad (29)$$

From (27) and (28), the boundary conditions yield

$$\begin{aligned} &A_1 = 0, \quad A_2 = 0 \\ &\sum_{k=1}^{\infty}(k-1)(k-2)B_k = 0, \quad \sum_{k=1}^{\infty}(k-1)(k-2)(k-3)B_k = 0 \quad \text{etc.} \end{aligned} \qquad (30)$$

If the power series is truncated at the pth term, then there are altogether 2p unknown coefficients. From the recurrence relations (29) and the boundary conditions (30), one obtains 2p simultaneous linear homogeneous equations. For a non-trivial solution, the determinant of the coefficient matrix must vanish. Thus, setting this determinant equal to zero, one gets the frequency equation which is solved numerically for unknown frequency ω.

2.3. NON-LINEAR SOLUTION

Since the homogeneous part of equations (23) along with the boundary conditions (24) has a non-trivial solution, the inhomogeneous equations (23) along with (24) have a solution, only if, a solvability condition is satisfied[6]. In order to find this condition their solutions are expressed in the form:

$$\left.\begin{aligned} w_{13}(x,t) &= [A(T_2)e^{i\omega T_0} + c.c.]\phi_1(x) + \bar{W}_1(x,T_0,T_2) \\ w_{23}(x,t) &= [A(T_2)e^{i\omega T_0} + c.c.]\phi_2(x) + \bar{W}_2(x,T_0,T_2) \end{aligned}\right\} \tag{31}$$

Substituting equations (31) in equations (23) and (24) and collecting the coefficients of $e^{i\omega T_0}$ and equating to zero (i.e, removing the secular term), one can obtain

Equations and corresponding boundary conditions. Solving we get

$$\theta = (\frac{3\bar{a}\alpha_2}{8\omega_L}) y_1^4(\eta).\frac{1}{b_1 + a_4 y_1^2(\eta)} \hat{A}^2 t \tag{32}$$

From equation (40), frequency-amplitude relationship can be given by

$$\omega_{nt} = \omega + (\frac{3a\alpha_2}{8\omega}) y_1^4(\eta).\frac{1}{b_1 + a_4 y_1^2(\eta)} \hat{A}^2 \tag{33}$$

3. Results and discussion

The numerical results obtained by using the methods outlined in the previous section are presented below in two parts. The data used are given in Table 1.

TABLE 1. Data for the beam to obtain the numerical results.

m = 9.7 kg m^{-1}, L = 6.6 meter, $\bar{a}$ = 0.0106 ,
Ω = 32.8 *rad* s^{-1}, $\alpha_1 = 10^3$, $\beta = 0.0, 0.01, -0.01$

3.1. LINEAR ANALYSIS

The natural frequencies of the rotating beam are obtained by using the power series method. First the analysis is carried out without spring. The roots of the frequency equations (equations 29 and 30) are obtained by the power series method following an iterative search procedure. The results are presented in

Table 2. It is observed that these results so obtained are in excellent agreement with those presented in References[11,16-17]. Here in this problem, we have used order of determinant 300 × 300 to make convergence guaranteed for our numerical calculation (convergence occurred in the order of 240×240). For calculating ω we have taken tolerance limit for error as 10^{-7}.

TABLE 2. The first three linear natural frequencies of the beam without the spring ($\forall_1 = 0.0$, $\exists = 0.0$) in comparison with other references.

	First Mode	Second Mode	Third Mode
Present Study	1.124412	3.407313	7.617049
Das et al[15]	1.1244	3.4073	7.6170
Pohit et al[11]	1.1245	3.4073	7.6218
Friedman et al[16]	1.1250	---------	--------
Gupta et al[17]	1.1247	3.4098	7.6376

Next, the lowest four frequencies of the non-homogeneous rotating beam with spring attached at different locations ($\eta = 0.1, 0.15, 0.20$ and 0.25) are determined. In this case, the mass of the spring is neglected. The value of dimensionless spring constant α_1 is assumed to be 1000. The same analysis is also carried out taking the mass of the spring into account. To compare the mass of the spring with the total mass of the beam, we have introduced a new non-dimensional number α_4 replacing α_3 as $\alpha_4 = a\alpha_3 = (M / mL)$. It is observed that due to presence of the mass, the first natural frequencies for different spring locations ($\eta = 0.1, 0.15, 0.20$ and 0.25) have increased whereas those of the higher modes have diminished. It is evident that, influence of mass of the spring on natural frequency is not very pronounced when the spring is located near the root (up to $\eta = 0.2$). However, when the spring is located at $\eta = 0.25$, the mass of the spring should not be neglected while determining the linear frequencies as these values deviate from that of mass less spring by considerable amount.

3.2. NON-LINEAR ANALYSIS

It has been observed elastomeric material exhibits non-linear characteristics so far the amplitude of the motion is concerned of the non-homogeneous beam. As

the amplitude increases, the degree of non-linearity becomes more predominant. In this section, we address the aspect of the non-linear frequency with respect to the amplitude of motion of the non-homogeneous rotating beam.

The non-linear frequency-amplitude of the non-homogeneous rotating non-homogeneous beam with spring-mass system is given in equation (33). Calculations are performed with a value of non-linear spring constant (α_2) as 10^7. It may be noted that non-linear spring constant of the damper material actually used in helicopter rotor blade exhibits even higher value[11].

In order to obtain the non-linear frequencies of the blade-spring-mass system, the value of b_1 and $y_1(\eta)$ are calculated for the first three modes of vibrations.

4. Conclusions

Large amplitude "free vibration" analysis of a non-homogeneous rotating beam with attached spring mass system has been investigated. Formulation of the rotating non-homogeneous beam includes the mass and variation of rigidity of the non-linear constraint that appear in the boundary condition.

The method of multiple time scale is directly applied to the partial differential equations and boundary conditions to determine the non-linear frequencies of the system. The first four linear frequencies are also calculated for a few location of the spring mass system. It is revealed that the effect of spring mass and non-homogeneity is quite prominent on certain spring locations, and it is not advisable to neglect spring mass and non-homogeneity and non-homogeneity and non-homogeneity while calculating natural frequencies of the system.

In the non-linear analysis, a closed form frequency-amplitude relationship of the rotating non-homogeneous beam is obtained. The effect of the mass and non-homogeneity of the spring on non-linear frequencies is investigated. It may be concluded that mass of the spring and non-homogeneity play a significant role in predicting frequency-amplitude relationship and stability of non-linear vibration. Further study is conducted to highlight the influence of the location of the spring-mass system on the rotating frequencies of the non-homogeneous beam and it is noted that spring location has pronounced effect on frequencies.

References

1. A. Rosen and P. P. Friedmann, 1979. The non-linear behavior of elastic slender straight beams undergoing small strains and moderate relations, Journal of applied mechanics **46**, 161-168.
2. K. R. Kaza and R. G. Kvaternik, 1977. *Non-linear aero elastic equations for combined flap wise bending, chord wise bending, torsion and extension of twisted non-uniform rotor blades in forward flight*, NASA TM-**74059**.

3. O. A. Bauchau, 1985. *A beam theory for anisotropic materials*. Journal of applied Mechanics **52**, 416-422.
4. G. L. Anderson, 1975. *On the extensional and flexural vibrations of rotating bars*, International Journal for Non-linear mechanics **10**, 223-236.
5. P. Minguet and J. Dugundji, 1990. *Experiments and analysis for composite blades under large deflection: part 2-dynamic behavior*, AIAA Journal **28**, 1580-1588.
6. A. H. Nayfeh, 1981, *Introduction of Perturbation technique*, Wiley, New York.
7. A. H. Nayfeh, D. T. Mook and D. W. Lobiz, 1974. *Numerical-perturbation method for the non-linear analysis of structural vibrations*, AIAA Journal **12**, 1222-1228.
8. M. Pakdemirli and A. H. Nayfeh, 1994. *Non-linear vibration of a beam-spring-mass system*, Journal of vibration and Acoustics **116**, 433-439.
9. A. H. Nayfeh and S. A. Nayfeh, 1994. *Non-linear normal modes of a continuous system with quadratic non-linearities* Journal of vibration and acoustics **117**, 199-205.
10. A. H. Nayfeh, A. H. C. Chin and S. A. Nayfeh, 1995. *Non-linear normal modes of a cantilever beam*, Journal of vibration and acoustics **117**, 477-481.
11. G. Pohit, C. Venkatesan and A. K. Mallik, 2000. *Elastomeric damper model and limit cycle oscillation in bearingless helicopter rotor blade* Journal of Aircraft **37**, 923-926.
12. G. Pohit, A. K. Mallik and C. Venkatesan, 1999. *Free out of plane vibration of a rotating beam with non-linear elastomeric Constraints*, Journal of sound and vibration **220**, 1-25.
13. G. Pohit, C. Venkatesan and A. K. Mallik, 2004. *Influence of non-linear elastomer on isolated lag dynamics and rotor/fuselage aeromechanical stability*. Journal of Aircraft **41**, 1449-1464.
14. E. Pesheck, C. Pierre and S. W. Shaw, 2002. *Modal Reduction of a non-linear rotating beam through normal modes*, Journal of vibration and acoustics, **124**, 229.
15. S. K. Das, P. Ray and G. Pohit, 2005. *Large Amplitude Free Vibration Analysis of a Rotating Beam with Non-linear Spring and Mass System*, Journal of Vibration and Control, **11**, 1511-1533.
16. P. Friedmann, K. Yuan, T. Millott and C. Venkatesan, 1994. *Gorrelation studies for hingless rotors in forward flight*, AIAA Dynamics specialists conference, USA, AIAA **94**-1722.
17. P. K. Gupta, C. Venkatesan and O. Singh, 1997. *Structural dynamics of rotor blades with precon-presweep-predoor-pretwist and torque offset including hub motion*, Proceedings of 48th AGM, Aeronautical society of India.

NON-TRIVIAL HIGH FREQUENCY EFFECTS (HFE) ON MECHANICAL OSCILLATORS WITH NON-LINEAR DISSIPATION

S. CHATTERJEE*
Department of Mechanical Engineering, Bengal Engineering and Science University, Shibpur, P.O. Botanic Garden, Howrah-711103, West Bengal, India

Abstract. The present article focuses on some interesting aspects of the effect of high frequency excitation on non-linear dissipative forces, like, non-linear viscous damping, coulomb dry friction damping, Elasto-Plastic dynamic friction. It is shown that non-linear viscous damping as well as friction damping characteristics can be considerably changed by the application of high-frequency excitation. A very useful application of HFE is vibroengine, where a rigid slider is made to move with constant average velocity along a friction surface under the action of high-frequency vibration. A new mechanism of vibroengine is proposed in the article. The proposed vibroengine consists of a rigid slider on a tangentially vibrating friction surface. The movement of the slider is made possible by modulating the normal load between two constant values in an on-off fashion depending upon the time-delayed, measured acceleration signal of the vibrating support.

Keywords: high frequency effect, non-linear damping, elasto-plastic friction, vibro engine

1. Introduction

Engineers are primarily aware of the detrimental effects of vibration, like, professional diseases, unpredictable breakdowns, annoying noises, lack of precision etc. However, the recent knowledge of the effect of high-frequency vibration on nonlinear systems, which are sometimes very strange and counter-intuitive, has made engineers think otherwise. In a growing number of industrial applications,

* shy@mech.becs.ac.in

E. İnan et al. (eds.), *Vibration Problems ICOVP-2007*,

the effects of high-frequency vibration are exploited to aid dynamical processes and devices. Uses include the vibrational transport of material (based on the change in effective rheological characteristics such as dry friction and viscosity coefficients), the vibrational sinking of piles, vibrational cutting, the vibrational separation of granular mixtures, and the vibration of liquid or granular material in order to enhance chemical reaction. Scientists believe that more research will lead to the discovery of many unknown forms of high-frequency effects in future. Only an individual's creativity is the limit to this highly potent field of research.

In general, linear mechanical oscillators act as band-pass filters, which atenuate all input frequencies away from the natural frequencies. However, this is, in general, not true for non-linear systems. Research reveals that *high-frequency effects* (HFE) may be non-trivial for some non-linear systems. Most of the known HFEs are characterized by the existence of two components of motion; one operates on a time scale comparable to the natural time scale of the system and the other operates as fast as the imposed excitation. In general, the fast component of the excitation remains imperceptible on the slow time scale, but as the system is nonlinear, this fast force/motion may leave a qualitatively perceptible effect on the slow characteristics of the motion. Thus, the interaction of the forces on two different time scales, the natural time scale (slow) of the system and the faster time scale of the excitation, is important in the understanding of HFE.

The non-trivial characteristics of HFE strictly depend on the nature of nonlinearity of the system concerned and the type and strength of the excitation. An extensive review of the research activities (mainly Russian) in this area is available in the book by Blekhman[1]. A large number of HFE problems have been studied[1-5]. These involve formation and annihilation of equilibrium configurations, change of stability of equilibrium and oscillatory motion, change in resonant characteristics, vibration-induced displacement and drift, vibrorheological effects, smoothening of discontinuity etc.

In the present article, the high-frequency effects on non-linear dissipative forces are discussed. Various types of dissipative forces, like, viscous friction, dry friction, controlled dry frictions etc. are considered. Towards the end, a new architecture of vibroengine is proposed.

2. Mathematical background

It is pertinent to discuss the mathematical formalism used for analyzing the effect of HF excitation on non-linear mechanical systems. Though several mathematical formalisms (which seem to be more general) are available, it is

convenient to make use of the *Method of Direct Partition of Motion (MDPM)* for number of reasons, and the most important one is the simplicity. A detailed discussion of the method is available in the book by Blekhman[1] who is responsible for its development. In what follows, a simplified outline of the method is given.

An oscillatory non-linear mechanical system with single-degree-of-freedom and a high-frequency excitation is conveniently modeled by the following ordinary differential equation:

$$\ddot{x} + f(\dot{x}) + \lambda(x) = q\Omega^2 \sin(\Omega t), \tag{1}$$

where x is the motion co-ordinate, $f(\dot{x})$ is the dissipative force and $\lambda(x)$ is the conservative force acting on the system. The term $q\Omega^2 \sin(\Omega t)$ represents the HF excitation on the system, where Ω is the frequency of excitation. By virtue of the class of the problem under consideration, one assumes $f(\dot{x})$ and $\lambda(x) \sim O(1)$ and $\Omega >> 1$, $q << 1$ such that $q\Omega \sim O(1)$. Thus, the system is subject to an excitation that is stronger compared to the natural forces of the original system. According to the theory of MDMP, the motion of the system is partitioned into two components, namely the slow component z and the small overlay of a fast component ϕ. The response is thus, written as

$$x(t) = s(t) + \varepsilon\phi(t, \Omega t), \tag{2}$$

where $\varepsilon = \Omega^{-1}$ is a small quantity. One easily observes that s represents the slow motion operating on the slow natural time scale t of the system, whereas the fast motion ϕ takes place on the fast time scale Ωt. Though, one is only interested in the slow motion s, the effect of the fast motion ϕ on s is also a matter of interest. As (2) represents a co-ordinate transformation, one should ask for a suitable constraining relationship that makes the transformation unique. The assumption that the fast-time average of the fast motion (with the slow time t remaining fixed) is zero is quite appropriate and this is mathematically recast as

$$\left\langle \phi(t, \Omega t) \right\rangle \equiv \frac{1}{2\pi} \int_0^{2\pi} \phi(t, \Omega t) d(\Omega t) = 0. \tag{3}$$

(3) signifies that the fast motion is periodic and that as such no bias term is associated with it. Inserting (2) in (1), one obtains

$$\phi'' = -\Omega^{-1} \left\{ \ddot{s} + 2\dot{\phi}' + f(\dot{s} + \phi') + \lambda(s) \right\} + q\Omega \sin(\Omega t) + O(\Omega^{-2}), \tag{4}$$

where dot(.) and dash ($'$) denote differentiation with respect to t and Ωt, respectively.

The first order form of (4) is given by

$$\phi'' = q\Omega \sin(\Omega t) + O(\Omega^{-1}). \tag{5}$$

An approximate solution of the fast component is obtained from (5) as

$$\phi = -q\ \Omega \sin(\Omega t).$$

Now taking average of both sides of (5) and using (3) one obtains the following autonomous equation:

$$\ddot{s} + f_{eff}(\dot{s}) + \lambda(s) = 0, \tag{6}$$

where

$$f_{eff}(\dot{s}) = < f(\dot{s} - q\Omega\cos(\Omega t)) > = \frac{1}{2\pi}\int_0^{2\pi} f(\dot{s} - q\Omega\cos\theta)d\theta\,.$$

(6) describes the average dynamics of the system on the slow natural time scale t of the system where the effective dissipative force $f_{eff}(\dot{s})$ carries the imprint of the fast excitation.

Therefore, it may be concluded that the effective dissipative forces of a nonlinear system is modified by the application of a sufficiently strong high-frequency vibration, and this modification is perceived only on a slow time scale.

3. Some examples of HFE on nonlinear friction

3.1. p^{th} POWER DAMPING

p^{th} power viscous damping is described by

$$f(\dot{x}) = \dot{x}\left|\dot{x}\right|^{p-1} \tag{7}$$

p^{th} power law models a wide class of non-linear damping $p = 0$ signifies Coulomb's dry friction damping, whereas $p = 1$, $p = 2$ and $p = 3$ signifies linear, quadratic and cubic damping, respectively. For odd integer values of p, on obtains the following expression for the effective damping characteristics:

$$< f >= \frac{1}{2\pi} \sum_{r=0,2,4}^{p-1} \binom{p}{r} (q\Omega)^r 2\sqrt{\pi} \frac{\Gamma\left(\frac{r+1}{2}\right)}{\Gamma\left(\frac{r+2}{2}\right)} \dot{s}^{p-r} \tag{8}$$

The effective-damping functions $f_{eff}(\dot{s})$ under HF excitation are shown in Fig. 1(a)-(c). Significant changes in the damping value can be observed. By extending the analysis further, it can be shown[2] that low-velocity damping of soft-dampers ($p < 1$) decreases due to fast vibration, where as, that of hard-dampers ($p > 1$) increases. It is interesting to note form Fig. 1(c) that the Coulomb dry friction damping effectively changes to viscous like damping characteristics under the action of HF excitation. However, one must admit that the effect of fast excitation on friction is more complex in nature. A thorough and rigorous analysis will be presented elsewhere in the article.

In the above analysis, fast vibration is restricted to only harmonic excitation. For complex forms of damping function and fast excitation, one can numerically compute the effective damping function Details of the method are available in [3].

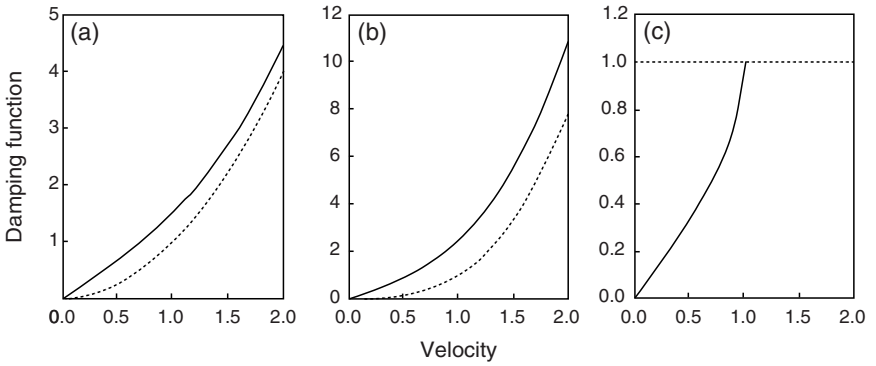

Fig. 1 Effect of harmonic fast vibration on pth power damping. ——, with fast vibration; - - -, without fast vibration. $q\,\Omega = 1$: (a) $p = 2$; (b) $p = 3$; (c) $p = 0$.

3.2. ELASTO-PLASTIC FRICTION

Using a rigorous model of dry friction it is possible to analyze the underlying physical mechanism of conversion of dry friction force into viscous-like force under HF excitation. Elasto-plastic friction model[6], which is a modified form LugGre friction model, is considered below. The system considered in shown in Fig. 2 where a single degree of freedom system is driven along a frictional

interface at a constant velocity v_m. The frictional surface is vibrated at a very high frequency and the mass M is subject to a relatively slower sinusoidal force. Non-dimensional equation of motion reads as:

$$\ddot{X} + X + F = f_s(\tau) + v_m^* \tau \tag{9}$$

Friction force F is described by Elasto-plastic model as follows:

$$\begin{aligned} F &= \sigma_0 z + \sigma_1 \frac{dz}{dt} + \sigma_2 v, \qquad \sigma_0, \sigma_1, \sigma_2 > 0, \\ \frac{dz}{dt} &= v - \frac{\sigma_0 \alpha(z,v) |v| z}{g(v)}, \end{aligned} \tag{10}$$

where v is the relative velocity between the matting surfaces and z is the average deflection of the bristles. σ_0 and σ_1 represents stiffness and damping of the interface bristles, respectively. σ_2 is viscous damping coefficient. $g(v)$ models the Stribeck effect. Introduction of the function $\alpha(z,v)$, henceforth termed as Elasto-Plastic function (EP-function), makes possible the rigorous detection of the phases of motion like sticking ($\alpha = 0$), pre-sliding ($0 < \alpha < 1$) and sliding ($\alpha = 1$).

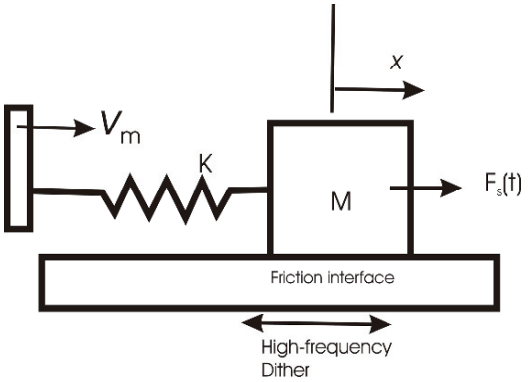

Fig. 2 Mathematical model of a positioning stage with friction.

The effective friction curves are plotted in Figs. 3(a)-(d), for different velocity amplitudes of HF excitation of frequency 100. The zero velocity vertical line in the effective friction plots, shown in Figs. 3(a)-(b), indicates the existence of long-duration sticking phases in the motion history. The extent of the vertical line along the friction-axis represents the magnitude of friction force during friction. Obviously, sticking force decreases with the increasing strength of HF excitation. For stronger HF excitation, sticking phases disappear, and the

corresponding low-velocity effective friction curves resemble linear viscous damping characteristics as observed from Figs. 3(c)-(d). With the HF excitation amplitude (velocity) fixed and the frequency changing, stick-slip motion reappears after a critical value of the excitation frequency, which is a function of the velocity amplitude of the HF excitation.

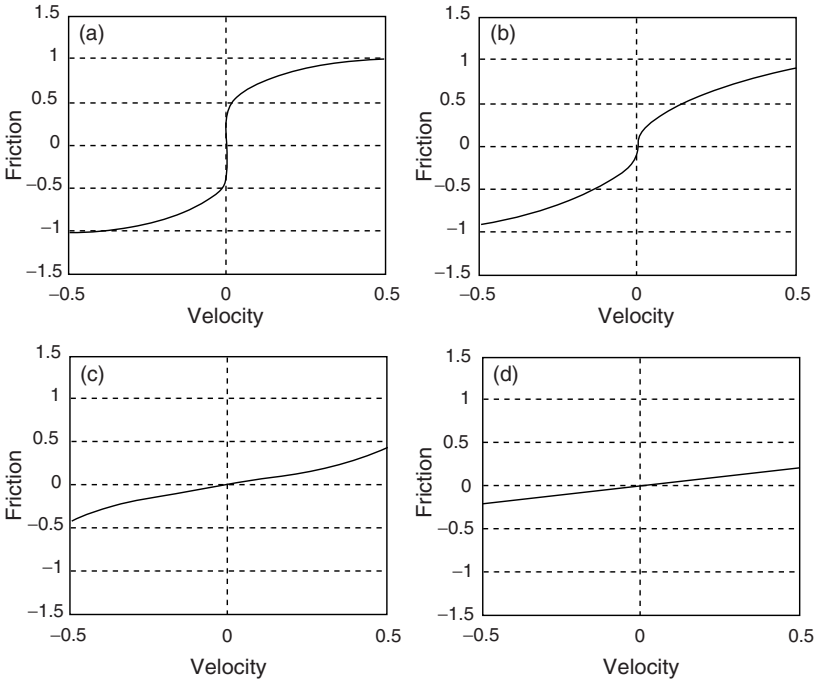

Fig. 3 Effective friction plot. $v_m^* = 0$, $f_s(\tau) = 1.7\sin(0.3\tau)$: (a) HF velocity = 0.5, (b) HF velocity = 0.8, (c) HF velocity = 1.5, (d) HF velocity = 2.

Time history of the EP-function $\alpha(.)$ and the corresponding histogram of the sample values of $\alpha(.)$ are plotted in Figs. 4(a)-(f). The time history of the EP-function without the action of HF excitation, shown in Fig. 4(a), demonstrates the existence of long-duration sticking and slipping phases interposed by pre-sliding phases. From the corresponding histogram, shown in Fig. 4(b), one concludes that the sticking and slipping phases have almost equal shares out of the total number of 18805 samples. From Figs. 4(c) and 4(e), one observes that under the action of HF excitation, long-duration stick-slip is replaced by short-duration stick-slip phases. Corresponding histograms are plotted for samples taken over integration time (100). 50162 and 55937 samples are used in Figs. 4(d) and 4(f), respectively. From Figs. 4(d) and 4(f), one may conclude that the relative shares of the slipping time increases with the strength of excitation.

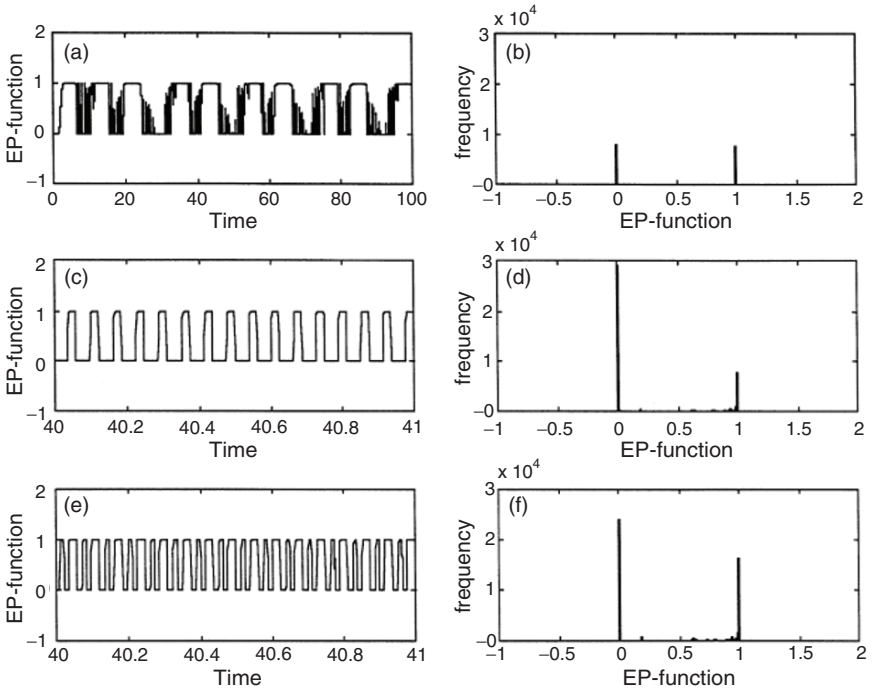

Fig. 4 Time evolution of the EP-function and the corresponding sample histograms with and without HF excitation (a) and (b) without HF excitation, (c) and (d) HF velocity amplitude = 1.5, frequency = 100, (e) and (f) HF velocity amplitude = 2.5, frequency = 100.

4. Concept of vibroengine

Vibroengines are mechanisms to produce steady motion of a rigid slider/rotor with the help of HF excitation. Different alternative models of vibroengines are discussed by Blekhman[1] and others[7,8]. Chatterjee et al[7]. have shown that under the simultaneous action of high frequency tangential and normal excitations bearing a constant phase difference, a rigid slider moves with constant average velocity (with a small high frequency fluctuation) on a frictional surface. Fidlin and Thomsen[8] consider an almost similar system, where instead of two phase shifted excitations, the motion is generated due to the asymmetry of co-efficient of friction in forward and backward movements. The principles of vibroengines considered here and also in [1,7,8] are different from that of surface-wave propelled movement utilized in ultrasonic motors. An alternative mechanism is shown in Fig. 5, where the normal load switches between 0 and N_d according to the following on-off strategy:

$$\Delta N(t) = N_d U(-\ddot{\eta}(t-\tau_d)), \tag{11}$$

where U is the Heaviside's step function and τ_d is the time delay. Non-dimensional equation of motion is written as:

$$\ddot{X} + \mu \operatorname{sgn}(\dot{X})\{N_m + \alpha U(-\sin(\Omega\tau - \phi))\} = q\Omega^2 \sin\Omega\tau - L, \qquad (12)$$

where $X = Y/x_0$ represents non-dimensional displacement of the slider relative to the vibrating base. One normalizes all displacements by some characteristic length x_0, frequencies by $\omega_0 = \sqrt{g/x_0}$, loads by Mg. $(\cdot)$ denotes differentiation with respect to the non-dimensional time $\tau = \omega_0 t$. In (12), μ denotes coefficient of friction, $q = A/x_0$, $N_m = N_0/Mg$, $L = P/Mg$ and $\alpha = N_d/N_0$. The phase ϕ of the normal load modulation is related to the time delay τ_d. Displacement time history of the vibroengine is shown in Fig. 6.

For strong HF excitation with $q << 1, \quad \Omega >> 1, \quad q\Omega \sim O(1)$, one analytically computes the average linear velocity V of the slider form the following equation:

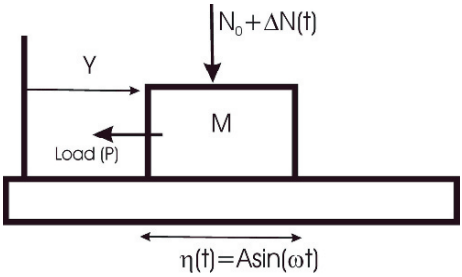

Fig. 5 Mathematical model of vibroengine.

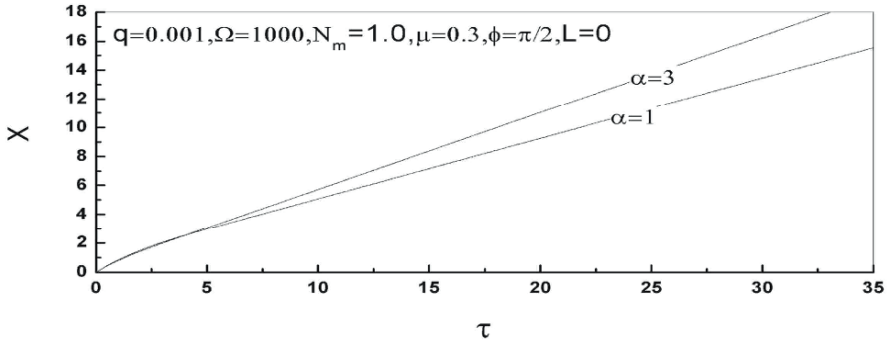

Fig. 6 Numerically simulated displacement time history of the vibroengine.

$$\mu N_m\left(1-\frac{2}{\pi}\theta_1\right)+\mu\alpha f(\theta_1,\phi)+L=0\,, \tag{13}$$

where

$$\theta_1=\cos^{-1}\left(\frac{V}{\Omega}\right)$$

and

$$f(\theta_1,\phi)=\begin{cases}-\dfrac{\phi}{\pi}+\dfrac{1}{2}-\dfrac{\theta_1}{\pi}, \phi<\theta_1, \theta_1+\phi<\pi\\ -\dfrac{1}{2}, \phi<\theta_1, \theta_1+\phi>\pi\\ \dfrac{1}{2}-\dfrac{2\theta_1}{\pi}, \phi>\theta_1, \theta_1+\phi<\pi\\ \dfrac{\phi}{\pi}-\dfrac{1}{2}-\dfrac{\theta_1}{\pi}, \phi>\theta_1, \theta_1+\phi>\pi\end{cases}$$

Characteristic plots of the vibroengine, computed form (13), are shown in Fig. 7. From Fig. 7 it can be observed that velocity of the vibroengine can be regulated over a wide range by changing the phase ϕ. The maximum velocity

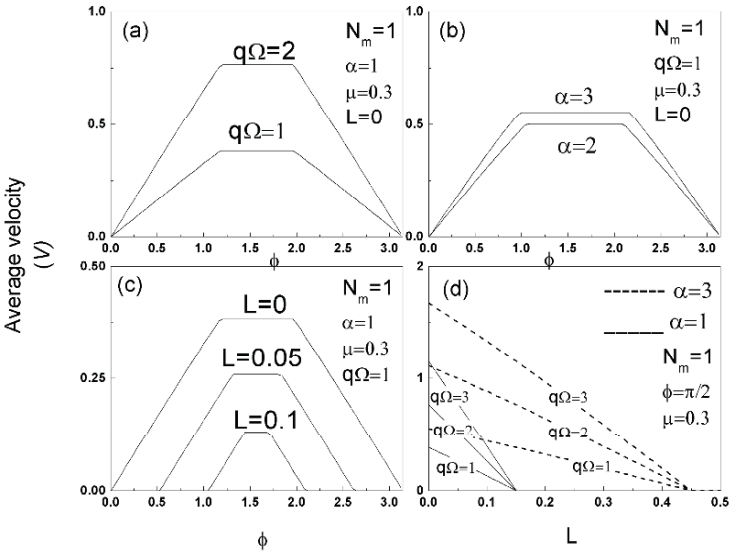

Fig. 7 Characteristic plots of the proposed vibroengine.

is generated for the phase value around $\pi/2$. The direction of movement also reverses (not shown) upon inversion of the phase. The engine can negotiate finite constant external load. It is observed from Fig. 7(d) that the vibroengine stalls at a particular value of external load, which is termed as the ***blocking force***. The exact value of the blocking force depends on the strength of normal load modulation α.

5. Conclusions and outlook

A few examples are discussed to demonstrate the strange effects of high-frequency excitation on non-linear dissipative systems. Example of a potential application of HFE on non-linear systems is also discussed. Further research is expected to reveal stranger and technologically useful effects of high-frequency excitation.

References

1. I. I. Blekhman, 2000. *Vibrational Mechanics-Nonlinear Dynamics Effects, General Approach, Applications*, World Scientific, Singapore.
2. J. J. Thomsen, 2002. *Some general effects of strong high-frequency excitation: stiffening, biasing, and smoothening*, Journal of Sound and Vibration, **253**, 807-831.
3. S. Chatterjee, T. K. Singha, S. K. Karmakar, 2003. *Non-trivial effect of fast vibration on the dynamics of a class of non-linearly damped mechanical systems*, Journal of Sound and Vibration **260,** 711-730.
4. S. Chatterjee, T. K. Singha, S. K. Karmakar, 2004. *Effect of high-frequency excitation on a class of mechanical systems with dynamic friction*, J. Sound and Vibration **269**, 61-89.
5. J. J. Thomsen, 1999. *Using fast vibrations to quench friction-induced oscillations*, Journal of Sound and Vibration **228**, 1079-1102.
6. P. Dupont, V. Hayward, B. Armstrong, F. Alpeter, 2002. Single state Elasto-Plastic friction models, IEEE Transactions on Automatic Control, preprint.
7. S. Chatterjee, S. Chatterjee, T. K. Singha, 2005. *On the generation steady motion using fast-vibration*, Journal of Sound and Vibration **283**, 1187-1204.
8. A. Fidlin, J. J. Thomsen, 2001. *Predicting vibration-induced displacement for a resonant friction slider*, European Journal of Mechanics of Solids, **20**, 155-166.

WIRE ROPE BASED VIBRATION ISOLATION FIXTURE FOR ROAD TRANSPORTATION OF HEAVY DEFENCE CARGO

SANJAY CHAUDHURI* AND BHARAT KUSHWAHA
Vehicles Research & Development Establishment (VRDE), Ahmednagar-41400 Maharastra State, India

Abstract. A fixture assembly has been designed for vibration isolation during transportation of heavy extra long cargo by road. The fixture is supported on numbers of heavy-duty metallic wire rope isolators. These isolators are very effective for both vibration and shock isolation and specifically developed for this application. The fixture has been designed based on static, modal and random analysis by finite element method. The strain measurement has been conducted on fixture for specified payload. Vibrations are recorded at various speeds on many locations for determining percentage isolation and system characteristics. The finite element analysis results and measured strain and vibration data are correlated for validation.

Keywords: vibration isolation, wire rope isolators, modal analysis, random vibration, finite element analysis, spectrum analysis, isolation effectiveness

1. Introduction

Isolation of the road bound shock and vibration are of most important requirement of transportation of defence cargo. The cargo was rested on specially designed and developed vibration isolation fixture and complete assembly was transported on a low bed semi trailer. The requirement of low shock and vibration vis-à-vis transportation of such cargo calls for design and development of special isolation fixture assembly. The restriction on maximum moving dimension (MMD) of vehicle for road transportation, overall low system natural frequencies, dynamic/shock load etc. govern the selection of isolators and

* vrde_san@rediffmail.com

E. İnan et al. (eds.), *Vibration Problems ICOVP-2007*,

structural design of isolator frame. Various types of isolators for e.g. rubber based, laminated rubbers, felts, air bellows, metallic spring type, wired mesh, metallic wire rope etc. are reported in many literatures but selection of right isolators depends on performance characteristics, nature of application and the environmental conditions. Metallic wire rope isolators are found most suitable for this application due to its high payload carrying capacity, compactness, low natural frequency and high deflection under shock. The weight of the frame assembly with cargo is 41T approximately and is supported on total 18 nos. of such isolators. The isolators have 3-D non-linear force-deflection characteristics and capable of isolating in three planes. The natural frequencies are obtained by modal analysis. The prototype isolator fixture assembly has been developed and integrated on semi-trailer along with load for experimental validation. The strains are measured at various locations of fixture and correlated with stress results from FEA. Limited road trails with full load have been conducted for assessment of structural integrity, mobility aspects and vibration characteristics. The vibrations are recorded for various speeds of transportation at different locations on frame before and after isolators. The spectrum analyses of these data are carried out to identify system natural frequencies, performance characteristics and to evaluate isolation effectiveness.

2. Characteristics of wire rope isolators

Wire rope or cable isolators use multistrand stainless steel cables as flexible elements. The static load-deflection characteristics of these isolators are hardening non-linear at low loads. At higher load the cable elements tends to buckle in a controlled way results in softening non-linear characteristics, which is beneficial for shock absorption. The softening behaviour causes decrease in natural frequency with increase in load. The contact between the cables increases with increase in load in compression and lubricant, if any between the wires, squeezed out and the friction between the wires exhibits characteristics of dry friction. Both stiffness and energy dissipation does not depend on frequency but strongly depends on vibration amplitudes. Under vibratory loading, slippage of wires relative to one another dissipates the energy of motion[1]. Because of this feature, cable isolators are often used in cases where both vibration and shock protection are required, e.g. for packaging fragile components into containers, cargo sensitive to vibration etc. These isolators have 3-D non-linear force-deflection characteristics. Fig. 1 shows performance characteristics of the isolator in the vertical direction. Curve fitting of these data yields in third order polynomial of deflection u as given in Fig. 1(a) and load $\mathbf{P}$ is represented as function of deflection $\mathbf{u}$ in (1). Stiffness K_{ii} and natural frequency ω_n, derived from (2) and (3) respectively, depends on $\mathbf{u}$.

$$\{\mathbf{P}_i\} = \{f_i(\mathbf{u})\}; \quad (i = 1,2,3 \text{ for three principal directions}) \tag{1}$$

$$\frac{d(\mathbf{P}_i)}{du} = K_{ii} \tag{2}$$

$$\omega_n = \sqrt{K_{ii} * g / \mathbf{P}_i} \tag{3}$$

It can be seen from Fig. 1(b) that ω_n reduces with increase in deflection. The longitudinal and lateral stiffness (K_{22}, K_{33}) of these isolators are same. The natural frequency of the isolation is $4.4\,Hz$ approx. for the rated static load.

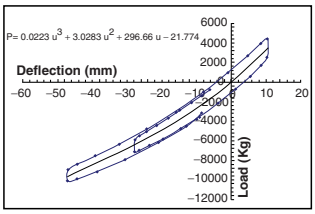

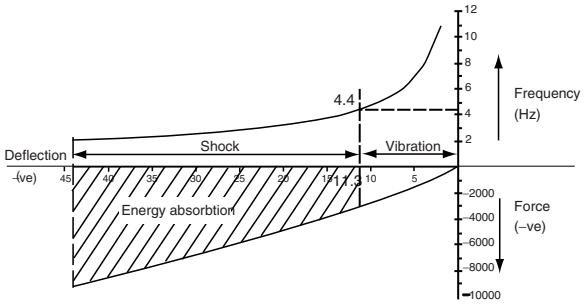

Fig. 1 Performance characteristics of Isolator; (a) curve fitting of vertical Load-deflection data, (b) frequency and load deflection curve.

3. Finite element analysis of isolation fixture

Solid model of Cargo rested on isolation fixture on trailer platform is shown in Fig. 2. Initially finite element analysis (FEA) of isolation fixture was done by using three dimensional beam elements having six degrees of freedom (three translations and three rotations). The cross members of the frame are joined to the longitudinal members through the nodes. The isolators are also modelled using 3D non-linear spring using load–deflection curve shown in Fig. 1 and joined to the frame through nodes. Generally nodes are positioned at points where members are connected although nodes are also required at load positions and at points where displacements are to be found. The exact position of the node representing a joint is usually the point of intersection of the centroidal axis of the members. Idealisation of this kind makes the joint stiff and has practical limitation due to dimensional differences of various sections. Many

local openings are provided on the longitudinal and cross members for easy maintenance and accessibility of isolator bolts. Beam element has limitation of accurate modelling of these details.

The foregoing discussion brings out the necessity of three-dimensional shell (six degree of freedom) model for the frame that can work accurately and efficiently. The area model of the frame is meshed by shell element. The isolators are modelled in similar way as in beam model. The weight of cargo is modelled as lumped mass at C.G. location and appropriate joints in FE model represent the connection between cargo and fixture. Translation d.o.f. of bottom nodes of spring elements are constrained. Static, modal analysis are carried out by using ABAQUS solvers for both beam and shell model. Mises' stress for shell model (Fig. 3) is shown for static load.

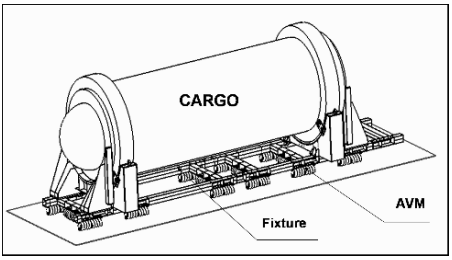

Fig. 2 Solid model of Fixture with CARGO.

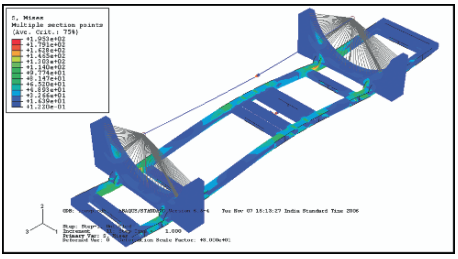

Fig. 3 Mises' stress plots of FEA.

It is observed from Table 1 that beam model is comparatively stiffer and hence shell model generates more local modes in comparison to beam model. Random response analysis is carried out to find out the spectra of different variables caused by road bound random vibration. Random vibration is usually represented by Power spectral density (PSD) of signal and published in MIL - 810-F[2] for various modes of road transportation. Common carrier transportation mode, which is typically applicable for paved roadway is considered for this application and PSD values are provided as input (Fig. 4) to FE model at base (where the nodes are constrained). The contribution of vibration above 100 *Hz*

TABLE 1. Comparison of frequencies for beam and shell model.

Mode no		1	2	3	4	5	6	7	8	10	50	60	72
Frequency (Hz)	BEAM model	2.6	4.3	11.6	18.5	24	26.8	27.6	31.6	47.5	298	354	455
	SHELL model	2.5	4.0	10	15.5	15.9	19.3	20.6	28.9	36.6	268	301	350

is caused by local modes though PSD values are considered up to 350 *Hz* in analysis. The peak acceleration of cargo is at $4.3Hz$. Isolation up to $100Hz$ on RMS (root mean square) acceleration is observed (Fig. 5) and the increase in vibration from fixture to saddle and to cargo is due to their spatial location. One $40mm$ thick rubber pad (not modelled in FEA) is used between cargo and saddle and reduction in vibration on cargo is observed in measurement (Fig. 7).

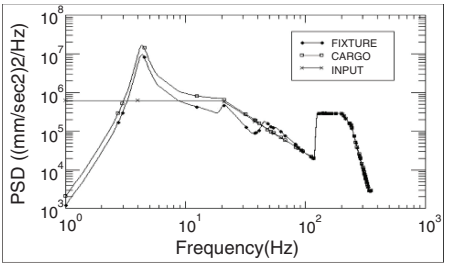

Fig. 4 Input and output acceleration PSD.

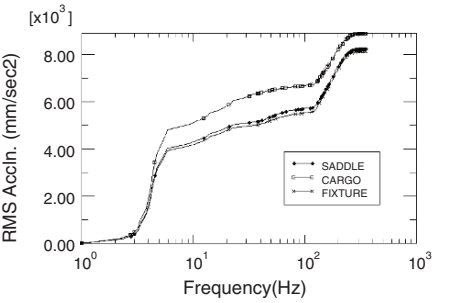

Fig. 5 RMS acceleration spectra from analysis.

4. Results and experimental validation

After prototype development, all systems are integrated on vehicle and have been subjected to strain, deflection and vibration measurement with full payload to assess structural adequacy, integrity and other performance parameters. Experimental scheme and locations of various sensors is shown in Fig. 6. The

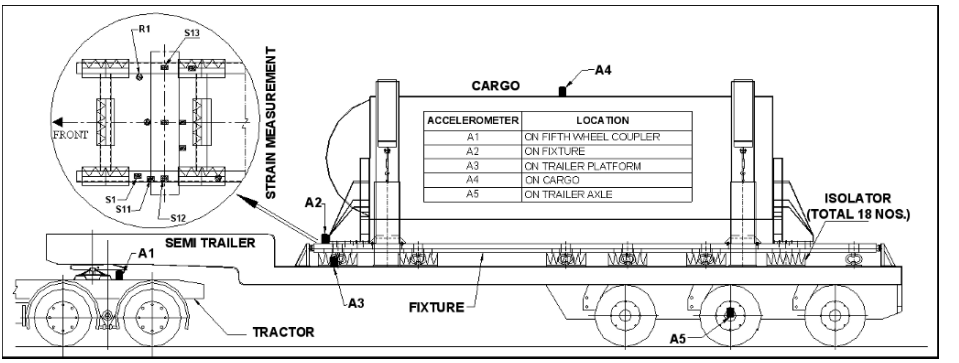

Fig. 6 Experimental scheme and location of strain and vibration sensors.

strain locations are selected based on results of FEA. Single element strain gauge (S) is used where the direction of stress is known; otherwise strain rosette (R) is used. Environmental and other effect has been taken care appropriately.

The measured strains are converted into Von Misses stress for comparison. The comparative stresses on various locations are shown in Table 2. Variation in stress levels is observed due to welding, local reinforcement and inaccessibility to exact location for measurement. Vibrations are measured for three speeds of vehicle in vertical direction only and spectrum analysis of signals is done. Though acceleration increases with increase in speed (Fig. 7), isolation observed on cargo up to 62.2% (Table 3). The effect of speed on vibration and system frequencies measured on cargo is shown in Fig. 8. Peaks are observed at $2.56\,Hz$, $4.39\,Hz$, $13.18\,Hz$ etc. caused by tractor and semi-trailer suspension. Peaks at higher frequency are structural modes.

TABLE 2. Comparison of stress from measurement and analysis.

Stress (Kg/mm^2)	R1	S1	S11	S12	S13
FEA	9.1-10.0	5.4-6.8	6.7-6.8	8.3-10.6	8.3-10.6
Measured	12.53	8.91	8.45	9.84	11.02

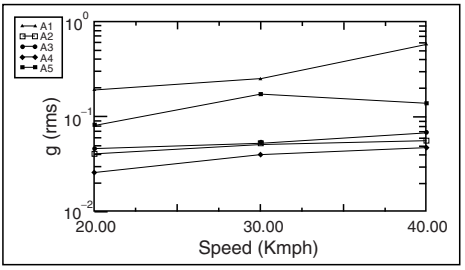

Fig. 7 RMS acceleration vs. frequency plot.

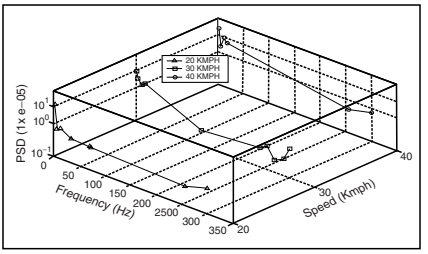

Fig. 8 Effect of Speed on vibration.

TABLE 3. Comparison of isolation at various speeds.

Speed (KMPH)	G (RMS) at major locations			Isolation (%) w.r.t platform	
	A3 (Platform)	A2 (Fixture)	A4 (Cargo)	On Fixture	On cargo
20	0.046	0.04	0.021	13	54.3
30	0.053	0.05	0.02	5.7	62.2
40	0.068	0.055	0.028	19.1	58.8

5. Conclusions

It is observed that measured stress values are in close agreement with that of FEA. The contribution of vibration beyond $350\,Hz$ is not observed and hence response analysis using frequency envelope up to $350\,Hz$ is justifiable. The RMS vibration increases with increase in vehicle speed. Wire rope isolators are very effective and yielded isolation up to 62%. Study of interlinking of modes in low frequencies and effect of damping by wire rope isolators on dynamic response needs to be studied as future course of work. The prototype system has been developed and used successfully for its intended application.

ACKNOWLEDGEMENT

The authors are indebted to Dr C. L. Dhamejani, Director, VRDE, for his encouragement and Shri Manmohan Singh, Head and other members of VRDE team and team of RCI, Hyderabad for their active efforts and involvement during measurement.

References

1. M. L. Tinker, M. A. Cutchins, 1992. *Damping phenomena in a wire rope vibration isolation system*, Journal of Sound and Vibration, **157**, 7-18.
2. Military standards handbook MIL-STD-810-F.

A COMPARISON OF VIBRATION AMPLITUDES OF A ROTOR BEARING SYSTEM DUE TO VARIOUS TYPES OF DEFECTS IN ROLLING ELEMENT BEARINGS

A. CHOUDHURY*
Department of Mechanical Engineering, Sikkim Manipal Institute of Technology, Majitar, Rangpo, 737132, Sikkim, India

N. TANDON
ITMMEC, Indian Institute of Technology Hauz Khas, New Delhi, 110016, India

Abstract. A comparative study for the prediction of amplitudes of a rotor bearing system for both localized and distributed defects in rolling element bearings has been reported in this paper. The rotor bearing system has been modeled as a multiple degree of freedom system and the excitation to the system has been assumed to be caused due to the presence of defects in inner race of the bearing. The types of defect studied include local defect such as pits and spalls and distributed defect in the form of race waviness. Discrete spectra have been obtained for both the types of defects. Significant components have been predicted at the harmonics of inner race characteristic defect frequency for both the types of defect and sidebands about the characteristic defect frequency have been predicted at the multiples of shaft frequency. Amplitudes of all these spectral components have also been obtained. Numerical results for all these components have been calculated for NJ 204 bearing. A comparison of these results for the two types of defects concludes the paper.

Keywords: vibration amplitudes, bearings, local defect, distributed defect

*Corresponding author, achintya01@rediffmail.com

E. İnan et al. (eds.), *Vibration Problems ICOVP-2007*,

1. Introduction

Spectral analysis of vibration signal has found wide applications in Industries for quality inspection and condition monitoring. The frequency spectra obtained from a defective bearing contain peaks at the characteristic defect frequencies of various bearing elements and can thus readily identify whether the defect is on the outer race, inner race or on a rolling element. The expressions for characteristic frequencies are well-established (Table 1). It has been found that many of these defect frequencies of localized and distributed type coincide with each other. As a result it becomes difficult to identify from frequency information whether the peak at a particular frequency is due to localized or distributed defect. Hence a study of the amplitude in addition to the frequency information of vibration response of defective bearings assumes importance.

In separate studies[1,2], the authors have attempted to predict amplitudes of spectral components for vibration response from a rotor bearing system due to distributed and localized defects in various bearing elements. In the present study, the authors' approach to predict vibration amplitudes of rotor bearing system due to localized and distributed defects have been compared with specific application of inner race defect in both the cases. Numerical results for these spectral components have been calculated and a comparison of these results for different types of defects has been presented in the paper.

TABLE 1. Characteristic defect frequencies for a stationary outer race; ω_s: shaft rotation frequency; d: rolling element diameter; D: pitch diameter; Z: number of rolling elements; α: contact angle.

Characteristic frequency	Expression
Cage frequency, ω_c	$(\omega_s/2)[1-(d/D)\cos\alpha]$
Outer race defect frequency, ω_{od}	$(Z\omega_s/2)[1-(d/D)\cos\alpha]$
Inner race defect frequency, ω_{id}	$(Z\omega_s/2)[1+(d/D)\cos\alpha]$
Rolling element defect frequency, ω_{red}	$(D\omega_s/d)[1-(d^2/D^2)\cos^2\alpha]$

2. Problem formulation and solution

The rotor bearing system has been modeled as a discrete spring-mass-dashpot system following the model developed by White[3] in which the races have been assumed to be rigidly mounted on the shaft and housing and their flexural vibration has been neglected. The rotor bearing system shown in Fig. 1 has been considered for the present work and the same has been modeled as a three DOF system as shown in Fig. 2.

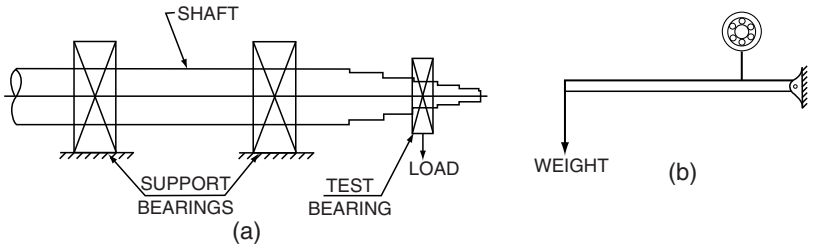

Fig. 1 A schematic diagram of (a) the rotor bearing system; and (b) the loading arrangement.

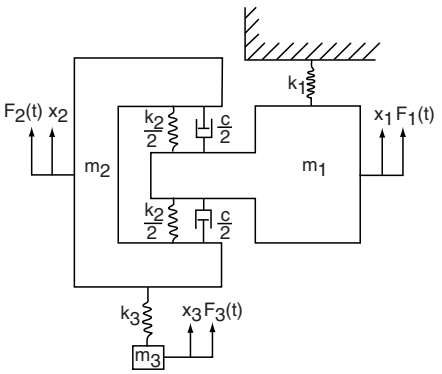

Fig. 2 The three-DOF model representing the rotor bearing set up.

2.1. ELEMENTS OF VIBRATORY SYSTEM

For the measurement of radial vibration at the test bearing, the shaft may be assumed to be fixed at the right support bearing (Fig. 1) and the extended portion may be assumed to act as a cantilever. Stiffness, k_1, of the present model represents the stiffness of the cantilever portion of the shaft. The mass at the inner race, m_1, is the sum of the mass of the inner race and the effective mass of the extended portion of the shaft at the point of suspension of the test bearing. k_2 and c represent the stiffness and damping coefficient of the bearing. The stiffness is dependent on the load distribution among various elements and on the relationship between maximum rolling element load and the applied load. Damping coefficient, c, depends on the oil film that builds up during rotation under elasto-hydrodynamic lubrication and the extent of the load zone in the bearing. The expressions for k_2 and c have been developed in [1] and [2]. The mass, m_2, is the combined effect of the mass of outer race and

the mass of the housing. The loading arrangement of the rotor bearing system has considerable deflection in the bending mode. Therefore the lever has been assumed as a spring in the vibratory system under consideration. The stiffness of this spring, k_3, can be determined by assuming the lever to be a cantilever rigidly attached at one end to the test bearing housing. The mass, m_3, is the sum of the mass due to the load actually applied at the free end of the lever and the effective mass of the cantilever portion at that point.

2.2. EQUATIONS OF MOTION

Taking care of the different elements used in the physical model (Fig. 2), the equation of motion can be expressed as

$$\begin{bmatrix} m_1 & 0 & 0 \\ 0 & m_2 & 0 \\ 0 & 0 & m_3 \end{bmatrix} \begin{Bmatrix} \ddot{x}_1 \\ \ddot{x}_2 \\ \ddot{x}_3 \end{Bmatrix} + \begin{bmatrix} c & -c & 0 \\ -c & c & 0 \\ 0 & 0 & 0 \end{bmatrix} \begin{Bmatrix} \dot{x}_1 \\ \dot{x}_2 \\ \dot{x}_3 \end{Bmatrix} + \begin{bmatrix} k_1+k_2 & -k_2 & 0 \\ -k_2 & k_2+k_3 & -k_3 \\ 0 & -k_3 & k_3 \end{bmatrix} \begin{Bmatrix} x_1 \\ x_2 \\ x_3 \end{Bmatrix} = \begin{Bmatrix} F_1(t) \\ F_2(t) \\ F_3(t) \end{Bmatrix} \quad (1)$$

where F_i, $(i = 1, 2, 3)$ is the excitation force caused due to the defect at time t and x_i is the resultant displacement at the same time t.

2.3. EXCITATION DUE TO LOCAL DEFECT

The excitation to the system is caused by pulses generated due to the interaction of the defect with the mating element. When a defect on the inner race is struck by a rolling element, excitation force F_1 is resulted by generation of a pulse on the inner race or mass m_1. F_2 and F_3 are zero because a localized defect on the inner race can not cause any force to be exerted on the masses m_2 and m_3. Under this condition the pulses are generated at the inner race defect frequency, ω_{id} and the defect itself moves at the shaft speed ω_s. The load at the point of excitation and the location of the defect certainly influence the excitation force. Therefore the excitation force can be expressed as (2):

$$F_1(t) = f(\omega_{id} t)\, P(\omega_s t) \cos \omega_s t \quad (2)$$

Pulse form f and the load P have periodicity of ω_{id} and ω_s respectively. The resultant $F_1(t)$ is, therefore, a sum of harmonic components at ω_s, ω_{id} and their multiples and the sidebands about ω_{id} at multiples of shat frequency ω_s.

The excitation force vector for an inner race defect is also a sum of harmonic components having the same frequencies as that of $F_1(t)$.

2.4. EXCITATION DUE TO DISTRIBUTED DEFECT

The distributed defect on a bearing element causes additional deflection (in addition to the static deflection due to the applied load) of a rolling element and this, in turn, results in additional spring force which is exerted on both the races. The additional spring force is time dependent and acts as the source of excitation. The excitation force applied by a rolling element at angle φ can be expressed as [1]:

$$F_{e\varphi} = K_d n \delta^{n-1}(\varphi)\, w(\varphi) \tag{3}$$

where K_d is deformation constant[4], $n = 3/2$ for ball bearing and $10/9$ for roller bearing, $\delta(\varphi)$ is the deflection of a rolling element at angle[4] φ and $w(\varphi)$ is the additional deflection at the same angle φ due to race waviness. Due to waviness of order m and amplitude β at a the inner race which rotates at a speed of ω_s, the additional deflection of a rolling element at position $\omega_c t$ has a frequency of $m(\omega_c - \omega_s)$ and can be expressed as

$$w(\omega_c t) = \beta \cos m(\omega_c - \omega_s)t \tag{4}$$

Deflection $\delta(\varphi)$ and $\delta^{n-1}(\varphi)$ are periodic and even. At $\varphi = \omega_c t - \delta^{n-1}(\varphi)$ can be expressed as[1]:

$$\delta^{n-1}(\varphi) = \delta_0 + \sum \delta_r \cos \omega_c t \tag{5}$$

The forces exerted by a rolling element on the inner and outer races are equal and opposite. Therefore the total excitation forces F_1 and F_2 are also equal and opposite and are obtained by linearly adding the additional spring forces applied by all the rolling elements in the direction of radial load. F_1 and F_2, thus obtained are sum of the harmonic components and the amplitudes of these components for various frequencies are given by[1]:

$$F_1(r\omega_s) = K_d n \beta Z \frac{(\delta_{r-1} + \delta_{r+1})}{4}, \; for \quad m = r = 1, 2, 3, ... \tag{6a}$$

$$F_1(i\omega_{id}) = K_d n\beta Z \frac{\delta_1}{2}, \qquad for \quad m = iZ \tag{6b}$$

$$F_1(i\omega_{id} \pm r\omega_s) = K_d n\beta Z \frac{(\delta_{r-1} + \delta_{r+1})}{4}, \quad for \quad m \pm r = iZ \tag{6c}$$

As discussed before, for any frequency ω, $F_2(\omega) = -F_1(\omega)$.

2.5. CALCULATION OF RESPONSE

Substituting the values of $F_1(\omega)$, $F_2(\omega)$ and $F_3(\omega)$ in (1), and applying the mechanical impedance method, the solution for any frequency ω can be found out from the following equation:

$$\{\bar{x}\} = [Z(\omega)]^{-1} \{F\} \tag{7}$$

where $\{\bar{x}\}$ is the phasor of the displacement vector $\{x\}$ and $[Z(\omega)]$ is the impedance matrix for frequency ω and its elements may be obtained as

$$Z_{ij} = k_{ij} - \omega^2 m_{ij} + j\omega c_{ij} \qquad for \ i, j = 1, 2, 3 \tag{8}$$

The amplitude of the velocity of the housing or mass m_2 at frequency ω can be obtained as the product of ω and the displacement amplitude of the housing at the same frequency.

3. Results and discussion

In order to obtain numerical results for the velocity of the housing, an NJ 204 cylindrical roller bearing with normal clearance has been considered. The bearing has been assumed to be mounted on a shaft rotating at $1500\,rpm$ and operating at a radial load of $750\,N$. For the geometry of the above bearing and spindle speed as mentioned, the important frequency components ω_s, ω_c, ω_{od} and ω_{id} are $25\,Hz$, $9.47\,Hz$, $107.14\,Hz$ and $167.83\,Hz$ respectively. For localized defect, a defect width of $500\,\mu$ on the inner race and for distributed defect, 30 orders of waviness having the same amplitude of $0.01\mu m$ on the inner race have been considered. The results thus obtained have been plotted in Fig. 3.

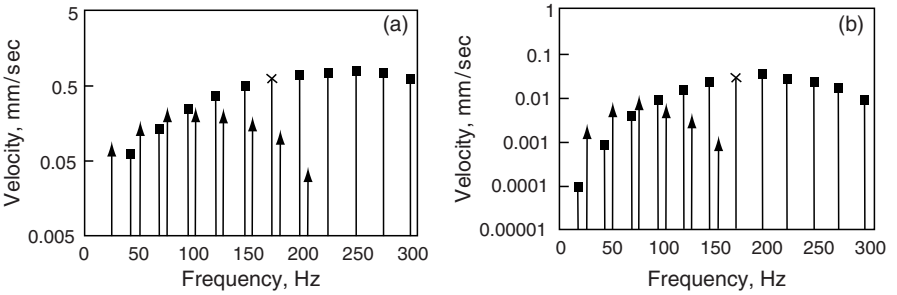

Fig. 3 Frequency spectra for the velocity of the housing for (a) local and (b) distributed defects.

It is observed from these figures that the spectral components for both the types of defects appear at the same frequencies. Further examination of these spectra leads to the following inferences:

1. The magnitude of the response is of the same order as found in the literature for vibration response of rotor bearing system.
2. Velocity response for distributed defect seems to be more evenly distributed about the characteristic frequency in comparison that for localized defect.
3. The pattern of spectra for distributed defects from actual experimental measurements will be different because the amplitudes for various orders of waviness are likely to be different.

4. Conclusions

A comparative study of amplitude prediction for bearings in a rotor bearing system with localized and distributed defects on the inner race, has been presented in this paper. The study justifies the need for prediction of amplitudes in addition to frequency information for a defective bearing. The work can be extended in future to include multiple localized defects as well as varying amplitudes for different orders of waviness in case of distributed defects.

References

1. N. Tandon, A. Choudhury, 2000. *A Theoretical Model to Predict the Vibration Response of Rolling Bearings in a Rotor Bearing System to Distributed Defects under Radial Load*, Transactions of ASME: Journal of Tribology, **122**, 609-615.

2. A. Choudhury, N. Tandon, 2006. *Vibration Response of Rolling Element Bearings in a Rotor Bearing System to a Local Defect under Radial Load*, Transactions of ASME: Journal of Tribology, **128**, 252-261.
3. M. F. White, 1979. *Rolling Element Bearing Vibration Transfer Characteristics: Effect of Stiffness*, Transactions of ASME: Journal of Applied Mechanics, **46**, 677-684.
4. T. A. Harris, 1966. *Rolling Bearing Analysis*, John Wiley and Sons, New York.

ASYMPTOTIC LIMITS OF THE FREQUENCY OF VIBRATIONS OF A GENERALIZED THERMOELASTIC INFINITE PLATE

N. C. DAS, S. SARKAR, AND R. MITRA*
Department of Mathematics, Jadavpur University, Calcutta, 700032, India

Abstract. The model of generalized Thermoelasticity as developed by Green and Nagdhi has been used in this paper to investigate the symmetric and anti-symmetric mode of free oscillation of an infinite plate. The frequency equations are analysed for the case of small and large wave lengths, and the results are compared with the corresponding elastic cases.

Keywords: generalized thermoelasticity, symmetric and antisymmetric modes, Rayleigh–Lamb equation, asymptotic limits

1. Introduction

Lord and Shulman[1] introduced a flux–rate term into the Fourier law of heat conduction which results a finite speed of thermal signals. Green and Lindsay[2] included a temperature rate dependent term in the constitutive equations that does not violet the classical Fourier law of heat conduction. This also predicts finite speed for heat propagation. As such, the heat propagation is to be viewed as a wave phenomenon rather than a diffusion one. Suhubi[3] referred to this wave like disturbances as "second sound". In order to apply the heat flow theory in more wider class of heat flow problems Green and Nagdhi[4] made certain basic modifications to this generalized theory. During the last three decades, a host of papers have been published following these models of generalized theormoelasticity. A review article by Chandrasekharaiah[5] may be

*Corresponding author, smita1308@gmail.com

E. İnan et al. (eds.), *Vibration Problems ICOVP-2007*,

referred to in this context. Sharma[6,7] considered the reflection of generalized thermoelasticelastic waves in a half space and the propagation of thermoelastic waves in an infinite plate respectively. Following Green and Nagdhi[4] theory, Taheri, H., et al[8] studied the one–dimensional disturbances in a layer using Laplace transform technique.

In the present article, we considered a similar layer problem as in [8, 9]. Following Green and Nagdhi[4] model, we have investigated the problem of oscillation of an infinite plate/layer for different modes of wave propagation. Asymptotic limits of the frequency equations for long and short wave lengths in both the cases of symmetric and antisymmetric vibrations have been analyzed.

2. Formulation and solution of the problem

We consider the rectangular Cartesian Coordinate system with origin at a point at the middle plane of a homogeneous, isotropic, thermally conducting plate. The plate is bounded by the planes $y = \pm H$ and extending to infinity in the $\pm(x, z)$ directions.

Let T_0 be the uniform absolute temperature in the undisturbed state. If we restrict our analysis to plane strain parallel to the $x - y$ plane with displacement components $u = u(x, y, t)$, $v = v(x, y, t)$, $w = 0$ and the temperature change $\theta(x, y, t)$ then the fundamental equations of motion and heat conduction, in the absence of body forces and heat sources, in generalized thermoelasticity developed by Green and Nagdhi[4] are given by

$$\left(\lambda + \mu\right)\vec{\nabla}(\vec{\nabla}.\vec{u}) + \mu\nabla^2\vec{u} - \gamma\vec{\nabla}\theta = \rho\ddot{\vec{u}} \tag{1}$$

$$\rho c_e\ddot{\theta} + \gamma \mathrm{T}_\mathrm{o}\vec{\nabla}.\ddot{\vec{u}} = k * \nabla^2\theta\,. \tag{2}$$

The stresses can be written as

$$\tau_{ij} = \lambda\delta_{ij}u_{k,k} + \mu(u_{i,j} + u_{j,i}) - \gamma\theta\delta_{ij} \tag{3}$$

where λ and μ are Lame's constants, $\gamma = (3\lambda + 2\mu)\beta^*$, β^* is the coefficient of volume expansion, k^* is a characteristic constant of the medium, ρ and c_e are respectively the mass density and specific heat at constant strain, and τ_{ij} is the stress tensor. The superposed dot represents the time differentiation. It may be noted that equations (1) and (2) are hyperbolic and hence permit finite speed for both the elastic and thermal waves.

We now define the following quantities:

$$x' = \frac{x}{l},\ y' = \frac{y}{l},\ \mathrm{t}' = \frac{\mathrm{Vt}}{l},\ \theta' = \frac{\theta}{\mathrm{T_o}},$$
$$u' = \frac{\lambda + 2\mu}{l\gamma T_o}u,\ v' = \frac{\lambda + 2\mu}{l\gamma T_o}v,\quad \tau'_{\mathrm{ij}} = \frac{\tau_{ij}}{\gamma T_o} \tag{4}$$

where l and V are respectively the standard length and standard speed.

Introducing the quantities (4) in equations (1-3) and suppressing the primes, we obtain

$$C_1^2\frac{\partial^2 u}{\partial x^2} + C_2^2\frac{\partial^2 u}{\partial y^2} + \left(C_1^2 - C_2^2\right)\frac{\partial^2 v}{\partial x \partial y} - C_1^2\frac{\partial \theta}{\partial x} = \frac{\partial^2 u}{\partial t^2} \tag{5}$$

$$C_2^2\frac{\partial^2 v}{\partial x^2} + C_1^2\frac{\partial^2 v}{\partial y^2} + \left(C_1^2 - C_2^2\right)\frac{\partial^2 u}{\partial x \partial y} - C_1^2\frac{\partial \theta}{\partial y} = \frac{\partial^2 v}{\partial t^2} \tag{6}$$

$$C_3^2\left(\frac{\partial^2 \theta}{\partial x^2} + \frac{\partial^2 \theta}{\partial y^2}\right) - \frac{\partial^2 \theta}{\partial t^2} - \in\left(\frac{\partial^3 u}{\partial x \partial t^2} + \frac{\partial^3 v}{\partial y \partial t^2}\right) = 0 \tag{7}$$

$$\tau_{yy} = \left(1 - \frac{2C_2^2}{C_1^2}\right)\frac{\partial u}{\partial x} + \frac{\partial v}{\partial y} - \theta \tag{8}$$

$$\tau_{xy} = \frac{C_2^2}{C_1^2}\left(\frac{\partial u}{\partial y} + \frac{\partial v}{\partial x}\right) \tag{9}$$

where

$$c_1^2 = \frac{\lambda + 2\mu}{\rho},\quad c_2^2 = \frac{\mu}{\rho},\quad C_1^2 = \frac{c_1^2}{V^2},\quad C_2^2 = \frac{c_2^2}{V^2},\quad C_3^2 = \frac{k^*}{\rho c_e V^2},$$
$$\text{and}\quad \in = \frac{\gamma^2 T_o}{\rho c_e(\lambda + 2\mu)} \tag{10}$$

Introducing the thermoelastic potential functions through the relations

$$\vec{u} = grad\,\phi + curl\,\vec{\psi},\quad \vec{\psi} = (\psi_1, \psi_2, \psi_3),\quad div\,\vec{\psi} = 0 \tag{11}$$

in equations (5-7), we obtain the following:

$$\nabla^2\phi - \frac{1}{C_1^2}\frac{\partial^2 \phi}{\partial t^2} = \theta \tag{12}$$

$$\nabla^2\psi = \frac{1}{C_2^2}\frac{\partial^2\psi}{\partial t^2} \tag{13}$$

$$C_3^2\nabla^2\theta - \frac{\partial^2\theta}{\partial t^2} = \in \frac{\partial^2}{\partial t^2}\left(\nabla^2\phi\right) \tag{14}$$

where $\psi_1 = \psi_2 = 0, \quad \psi_3 = \psi$ and $\nabla^2 = \frac{\partial^2}{\partial x^2} + \frac{\partial^2}{\partial y^2}$.

Eliminating θ from the equations (12) and (14) we get,

$$C_1^2C_3^2\nabla^4\phi - \left[C_1^2(1+\in) + C_3^2\right]\nabla^2\ddot{\phi} + \frac{\partial^4\phi}{\partial t^4} = 0 \tag{15}$$

To investigate wave motion in the thermoelastic layer, we consider the solution of ϕ, ψ and θ in the form:

$$(\phi, \psi, \theta) = \left(\Phi(y), \Psi(y), \Theta(y)\right)\exp\left\{ik(x - Ct)\right\} \tag{16}$$

Substituting (16) in (15), (13) and (12) we obtain

$$\Phi(y) = A_1 \sinh\ m_1 y + B_1 \cosh\ m_1 y + A_2 \sinh m_2 y + B_2 \cosh m_2 y \tag{17}$$

$$\Psi(y) = D_1 \sinh m_3 y + D_2 \cosh m_3 y \tag{18}$$

$$\Theta(y) = \left(m_1^2 - k^2 + \frac{k^2C^2}{C_1^2}\right)\left(A_1 \sinh m_1 y + B_1 \cosh m_1 y\right) + \left(m_2^2 - k^2 + \frac{k^2C^2}{C_1^2}\right)\left(A_2 \sinh m_2 y + B_2 \cosh m_2 y\right)$$

where $m_1^2 = k^2(1 - C^2q^2)$, $m_2^2 = k^2(1 - C^2p^2)$, $m_3^2 = k^2\left(1 - \frac{C^2}{C_2^2}\right)$ and p^2, q^2 are determined from

$$p^2, q^2 = \frac{1}{2C_1^2C_3^2}\left[C_3^2 + C_1^2(1+\in) \mp \sqrt{M}\right],$$

and

$$M = \left[C_3^2 - C_1^2(1+\in)\right]^2 + 4 \in C_1^2C_3^2 \tag{19}$$

The following figure demonstrates the nature of the modes of oscillation.

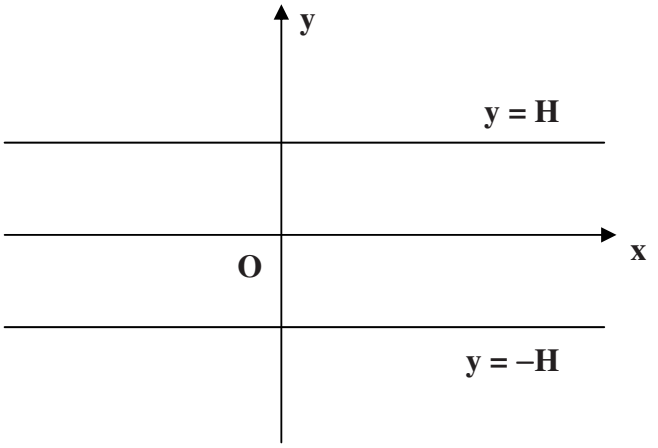

Fig. 1 The nature of the modes of oscillation.

We note that the displacement in the x–direction u is symmetric (or antisymmetric) with respect to $y = 0$ (x–axis) if u contains cosh (or sinh) term. The displacement in the y–direction v is symmetric (or antisymmetric) if v contain sinh (or cosh) terms. The choice of terms in θ are made accordingly for different modes.

The wave propagation in the thermoelastic layer may thus be split into two systems of symmetric and antisymmetric modes respectively.

Symmetric modes (omitting the factor $exp\{ik(x - Ct)\}$)

$$\begin{aligned}
&\phi = B_1 \cosh m_1 y + B_2 \cosh m_2 y,\\
&\psi = D_1 \sinh m_3 y,\\
&u = ik(B_1 \cosh m_1 y + B_2 \cosh m_2 y) + D_1 m_3 \cosh m_3 y,\\
&v = m_1 B_1 \sinh m_1 y + m_2 B_2 \sinh m_2 y - i D_1 k \sinh m_3 y,\\
&\theta = \left(m_1^2 - k^2 + \frac{k^2 C^2}{C_1^2}\right) B_1 \cosh m_1 y + \left(m_2^2 - k^2 + \frac{k^2 C^2}{C_1^2}\right) B_2 \cosh m_2 y
\end{aligned} \tag{20a}$$

The stresses can now be written from (8) and (9) as

$$\begin{aligned}
&\tau_{yy} = \frac{k^2}{C_1^2}\left(2C_2^2 - C^2\right)(B_1 \cosh m_1 y + B_2 \cosh m_2 y) - 2iD_1 k m_3 \frac{C_2^2}{C_1^2} \cosh m_3 y\\
&\frac{C_1^2}{C_2^2}\tau_{xy} = 2ik(m_1 B_1 \sinh m_1 y + m_2 B_2 \sinh m_2 y) + D_1(k^2 + m_3^2)\sinh m_3 y
\end{aligned} \tag{20b}$$

Antisymmetric modes (omitting the factor $\exp\{ik(x-Ct)\}$)

$$\phi = A_1 \sinh m_1 y + A_2 \sinh m_2 y,$$
$$\psi = D_2 \cosh m_3 y,$$
$$u = ik(A_1 \sinh m_1 y + A_2 \sinh m_2 y) + D_2 m_3 \sinh m_3 y, \tag{21a}$$
$$v = m_1 A_1 \cosh m_1 y + m_2 A_2 \cosh m_2 y - i D_2 k \cosh m_3 y,$$
$$\theta = \left(m_1^2 - k^2 + \frac{k^2 C^2}{C_1^2} \right) \mathrm{A}_1 \sinh m_1 y + \left(m_2^2 - k^2 + \frac{k^2 C^2}{C_1^2} \right) A_2 \sinh m_2 y$$

The stresses can be calculated from above relation as

$$\tau_{yy} = \frac{k^2}{C_1^2}\left(2C_2^2 - C^2\right) A_1 \sinh m_1 y + \frac{k^2}{C_1^2}(2C_2^2 - C^2) A_2 \sinh m_2 y$$
$$- 2iD_2 k m_3 \frac{C_2^2}{C_1^2} \sinh m_3 y \tag{21b}$$
$$\tau_{xy} = 2iA_1 k m_1 \cosh m_1 y + 2iA_2 k m_2 \cosh m_2 y + (m_3^2 + k^2) D_2 \cosh m_3 y$$

If the boundaries are free from stresses and zero temperature is maintained, then the boundary conditions may be written as

$$\tau_{yy} = \tau_{xy} = \theta = 0 \quad \text{on} \quad y = \pm H \tag{22}$$

For the symmetric mode, the boundary conditions yield three homogeneous linear equations involving B_1, B_2 and D_1 namely,

$$k^2(2C_2^2 - C^2)(B_1 \cosh m_1 H + B_2 \cosh m_2 H) - 2iD_1 k m_3 C_2^2 \cosh m_3 H = 0$$

$$2k(m_1 B_1 \sinh m_1 H + m_2 B_2 \sinh m_2 H) - iD_1(k^2 + m_3^2) \sinh m_3 H = 0$$

$$\left(m_1^2 - k^2 + \frac{k^2 C^2}{C_1^2} \right) B_1 \cosh m_1 H + \left(m_2^2 - k^2 + \frac{k^2 C^2}{C_1^2} \right) B_2 \cosh m_2 H = 0$$

Eliminating B_1, B_2 and D_1 from the above equations we get

$$-\left(2 - \frac{C^2}{C_2^2}\right)^2 k^2 (p^2 - q^2) = 4m_3 \left[m_1 \left(\frac{1}{C_1^2} - p^2 \right) \frac{\tanh m_1 H}{\tanh m_3 H} - m_2 \left(\frac{1}{C_1^2} - q^2 \right) \frac{\tanh m_2 H}{\tanh m_3 H} \right] \tag{23}$$

which is the frequency equation of the symmetric mode of vibration of the plate.

Similarly, using the boundary condition (22) we obtain from equations (21b), the frequency equation for the antisymmetric mode in the form:

$$\left(2-\frac{C^2}{C_2^2}\right)^2 k(p^2-q^2)=4\left(1-\frac{C^2}{C_2^2}\right)^{1/2}\left[m_2\left(\frac{1}{C_1^2}-q^2\right)\frac{\tanh m_3 H}{\tanh m_2 H}-m_1\left(\frac{1}{C_1^2}-p^2\right)\frac{\tanh m_3 H}{\tanh m_1 H}\right] \tag{24}$$

If we put $\in=0$ in equation (19), we get $p=\frac{1}{C_1}$ and taken the limit as $q\to\infty$ in the frequency equations (23) and (24), we get

$$\frac{\tanh\left(1-\frac{C^2}{C_1^2}\right)^{1/2} kH}{\tanh\left(1-\frac{C^2}{C_2^2}\right)^{1/2} kH}=\frac{\left(2-\frac{C^2}{C_2^2}\right)^2}{4\left(1-\frac{C^2}{C_1^2}\right)^{1/2}\left(1-\frac{C^2}{C_2^2}\right)^{1/2}} \tag{25}$$

and

$$\frac{\tanh\left(1-\frac{C^2}{C_1^2}\right)^{1/2} kH}{\tanh\left(1-\frac{C^2}{C_2^2}\right)^{1/2} kH}=\frac{4\left(1-\frac{C^2}{C_1^2}\right)^{1/2}\left(1-\frac{C^2}{C_2^2}\right)^{1/2}}{\left(2-\frac{C^2}{C_2^2}\right)^2} \tag{26}$$

Choosing $c=CV$ and using (10), the dimensional form of the equations (25-26) are no other than the well known Rayleigh–Lamb frequency equations for vibration of a plate in absence of the thermal field for symmetric and antisymmetric mode respectively, vide, Achenbach[10].

Asymptotic limits of the frequency equation for long and short wavelengths

We now proceed to determine the asymptotic limits of the frequency for both the cases of symmetric and antisymmetric modes of vibration in the case of generalized thermoelasticity and compare our results with those of the corresponding elastic case in absence of the temperature field.

Symmetric vibrations

In this case the frequency equation (23) can be written as

$$(C^2-2C_2^2)\left(2-\frac{C^2}{C_2^2}\right)(p^2-q^2)$$

$$=4C_2^2(1-C^2q^2)^{1/2}\left(1-\frac{C^2}{C_2^2}\right)^{1/2}\left(\frac{1}{C_1^2}-p^2\right)\times\frac{\tanh\{1-C^2q^2)^{1/2}kH}{\tanh\left\{\left(1-\frac{C^2}{C_2^2}\right)^{1/2}kH\right\}} \quad (27)$$

$$-4C_2^2(1-C^2q^2)^{1/2}\left(1-\frac{C^2}{C_2^2}\right)^{1/2}\left(\frac{1}{C_1^2}-p^2\right)\times\frac{\tanh\{1-C^2p^2)^{1/2}kH}{\tanh\left\{\left(1-\frac{C^2}{C_2^2}\right)^{1/2}kH\right\}}$$

where $C<\min(C_2,1/q)$.

This is an equation involving the phase velocity C and the wave length $\frac{2\pi}{k}$.

***Case I*:**

For wave length large compared with the thickness $2H$ of the plate, we can write $kH<<1$. From (19) we see that $M>0$ and hence $q>p$. Thus, if we choose $C<\min\left(C_2,\frac{1}{q}\right)$, then $(1-C^2q^2)^{1/2}kH$, $(1-C^2p^2)^{1/2}kH$ and $\left(1-\frac{C^2}{C_2^2}\right)^{1/2}kH$ may be taken to be very small quantities. Using the result, that

$$\tanh z=z(1-\frac{z^2}{3}+\frac{2z^4}{15}-.....)\approx z \quad (28)$$

when z is small, we simplify the equation (27) and write down the expression for phase velocity as

$$C^2=\frac{4C_2^2\left(C_1^2-C_2^2\right)}{C_1^2} \quad \text{or} \quad c^2=\frac{4c_2^2\left(c_1^2-c_2^2\right)}{c_1^2} \quad (29)$$

which is the phase velocity equation in dimensional form in the elastic case[10].

Thus the phase velocity is independent of thermal parameters and we need have to retain more terms in the expansion of (28) for the determining the effect of the thermal field.

***Case II*:**

For wave length very small compared with the thickness of the plate, $kH >> 1$ and if $C < \min(C_2, 1/q)$, the quantities $(1-C^2q^2)^{1/2}kH$, $(1-C^2p^2)^{1/2}kH$ and $(1-C^2/C_2^2)^{1/2}kH$ are also very large. Hence, using the result that $\tanh z \approx 1$ for large z, we get from the equation (27) the frequency equation in this case as,

$$\left(2-\frac{C^2}{C_2^2}\right)^2 (p^2-q^2) - 4\left(1-\frac{C^2}{C_2^2}\right)^{1/2} \times\left[\left(1-C^2p^2\right)^{1/2}\left(\frac{1}{C_1^2}-q^2\right)-\left(1-C^2q^2\right)^{1/2}\left(\frac{1}{C_1^2}-p^2\right)\right]=0 \tag{30}$$

In the absence of the thermal field, performing the same operations as we have done earlier, the equation (30) results in

$$\left(2-\frac{C^2}{C_2^2}\right)^2 - 4\left(1-\frac{C^2}{C_1^2}\right)^{1/2}\left(1-\frac{C^2}{C_2^2}\right)^{1/2}=0 \tag{31}$$

In dimensional form this becomes

$$\left(2-\frac{c^2}{c_2^2}\right)^2 - 4\left(1-\frac{c^2}{c_1^2}\right)^{1/2}\left(1-\frac{c^2}{c_2^2}\right)^{1/2}=0$$

which is the velocity equation of Rayleigh wave as in [10] in an elastic semi–infinite medium.

***Case III*:**

For $C_2 < C < 1/q$ and for $kH >> 1$, the first term on the r.h.s. of equation (23) can be expressed as

$$4m_1m_3\left(\frac{1}{C_1}-p^2\right)\frac{\tanh m_1H}{\tanh m_3H} = 4k^2\left(1-C^2q^2\right)^{1/2}\left(\frac{C^2}{C_2^2}-1\right)^{1/2}\left(\frac{1}{C_1^2}-p^2\right)\frac{1}{\tan\left\{\left(\frac{C^2}{C_2^2}-1\right)^{1/2}kH\right\}}$$

The second term on the r.h.s. can also be written similarly.
Thus, in this case, the frequency equation (23) becomes

$$\tan\left\{\left(\frac{C^2}{C_2^2}-1\right)^{1/2} kH\right\}$$

$$= \frac{4\left(\frac{C^2}{C_2^2}-1\right)^{1/2}\left[\left(1-C^2q^2\right)^{1/2}\left(\frac{1}{C_1^2}-p^2\right)-\left(1-C^2p^2\right)^{1/2}\left(\frac{1}{C_1^2}-q^2\right)\right]}{\left(2-\frac{C^2}{{}_2C^2}\right)^2\left(q^2-p^2\right)} \quad (32)$$

In the absence of the thermal field, the equation (32) becomes,

$$\tan\left\{\left(\frac{C^2}{C_2^2}-1\right)^{1/2} kH\right\} = \frac{4\left(1-\frac{C^2}{C_1^2}\right)^{1/2}\left(\frac{C^2}{C_2^2}-1\right)^{1/2}}{\left(2-\frac{C^2}{C_2^2}\right)^2} \quad (33)$$

which in the dimensional form takes the form:

$$\tan\left\{\left(\frac{c^2}{c_2^2}-1\right)^{1/2} kH\right\} = \frac{4\left(1-\frac{c^2}{c_1^2}\right)^{1/2}\left(\frac{c^2}{c_2^2}-1\right)^{1/2}}{\left(2-\frac{c^2}{c_2^2}\right)^2} \quad (34)$$

as in [10].

Now, if $\left(\frac{C^2}{C_2^2}-1\right)^{1/2} \to \frac{\pi}{kH}$ which tends to zero as $kH \to \infty$ then the l.h.s. of equation (32) becomes

$$\tan\left\{\left(\frac{C^2}{C_2^2}-1\right)^{1/2} kH\right\} \to \tan\pi \to 0$$

and the r.h.s. $\to 0$, because $\left(\frac{C^2}{C_2^2}-1\right)^{1/2} \to 0$. Thus the equation is satisfied. Therefore, for $C > C_2$, $C \to C_2$ as $kH >> 1$.

Antisymmetric vibrations

***Case IV*:**

The frequency equation for antisymmetric vibration has been given by equation (24). If kH is very small, i.e. the waves are long compared to the thickness $2H$ and if $C < \min(C_2, \frac{1}{q})$, then retaining the first two terms in the expansion of $\tanh z$ in (28), we get for small value of z,

$$\tanh z = z\left(1-\frac{z^2}{3}\right)$$

Thus the frequency equation (24) becomes,

$$\left(2-\frac{C^2}{C_2^2}\right)^2\left(p^2-q^2\right) = 4\left(\frac{1}{C_1^2}-q^2\right)\left(1-\frac{C^2}{C_2^2}\right)\frac{\left[1-\frac{1}{3}k^2H^2\left(1-\frac{C^2}{C_2^2}\right)\right]}{\left[1-\frac{1}{3}k^2H^2\left(1-C^2p^2\right)\right]} - 4\left(\frac{1}{C_1^2}-p^2\right)\left(1-\frac{C^2}{C_2^2}\right)\frac{\left[1-\frac{1}{3}k^2H^2\left(1-\frac{C^2}{C_2^2}\right)\right]}{\left[1-\frac{1}{3}k^2H^2\left(1-C^2q^2\right)\right]} \tag{35}$$

We simplify the equation (35) by neglecting terms containing $(kH)^4$ which are very small, and obtain

$$k^2H^2\left(p^2+q^2\right)\left(\frac{C}{C_2}\right)^4 + \left[2k^2H^2\left(\frac{3}{C_2^2}-\frac{2}{C_1^2}\right)+\frac{3}{C_2^2}\right]\left(\frac{C}{C_2}\right)^2 - 4k^2H^2\left(\frac{1}{C_2^2}-\frac{1}{C_1^2}\right) = 0 \tag{36}$$

The corresponding equation in the elastic field is

$$\frac{k^2H^2}{C_1^2}\left(\frac{C}{C_2}\right)^4+\left[k^2H^2\left(\frac{3}{C_2^2}-\frac{4}{C_1^2}\right)+\frac{3}{C_2^2}\right]\left(\frac{C}{C_2}\right)^2-4k^2H^2\left(\frac{1}{C_2^2}-\frac{1}{C_1^2}\right)=0 \quad (37)$$

Equations (36) and (37) are quadratic equations in $(C/C_2)^2$ which when solved separately gives $(C/C_2)^2$ and hence C/C_2.

It is interesting to note that, if further, we neglect terms which are smaller than C^4/C_2^4, then both the equations (36) and (37) can be simplified to,

$$\frac{C}{C_2}=2kH\left\{\frac{1}{3}\left(1-\frac{C_2^2}{C_1^2}\right)\right\}^{1/2} \quad (38)$$

In the equation (38), there is no thermal parameters. Equations (36-38) are dispersive in nature and from (38) it is clear that the phase velocity C decreases to zero with increasing wave length.

***Case V*:**

For $kH\to\infty$, i.e. for waves with very short length compared to thickness, equation (24) again reduces to the Rayleigh wave equation (30).

***Case VI*:**

$C>C_2$ but $C<1/q<1/p,$ then in the case when $kH\to\infty$, equation (24) becomes,

$$\frac{\left(2-\frac{C^2}{C_2^2}\right)^2(p^2-q^2)}{\tan\left(\frac{C^2}{C_2^2}-1\right)^{1/2}kH}=-4\left(\frac{C^2}{C_2^2}-1\right)^{1/2}\left[\left(1-C^2p^2\right)^{1/2}\left(\frac{1}{C_1^2}-q^2\right)-\left(1-C^2q^2\right)^{1/2}\left(\frac{1}{C_1^2}-p^2\right)\right] \quad (39)$$

We notice that if $\left(\frac{C^2}{C_2^2}-1\right)^{1/2}\to\frac{\pi/2}{kH}$ which tends to zero as $kH\to\infty$, then the l.h.s. of (40) becomes zero. The r.h.s. is also zero because $\left(\frac{C^2}{C_2^2}-1\right)^{1/2}\to 0.$ Thus we find that as $kH\to\infty$, $C\to C_2$ if $C_2<C\frac{1}{q}$.

3. Concluding remarks

The Rayleigh–Lamb frequency equations as given by the equations (23) and (24) for longitudinal and flexural modes respectively are transcendental in nature and as such there are infinite number of branches. The corresponding equations (25) and (26) for the elastic case have been graphed[10] for four lowest longitudinal and flexural modes, where, the symbols used are different. In our case, we prefer to determine asymptotic limits for our equations for both the cases of longitudinal and flexural modes of vibration in terms of algebraic equations.

References

1. H. W. Lord, Y. Shulman, 1967. *A generalized dynamical theory of Thermoelasticity*, J. Mech. Phys. Solids, **15**, 229–309.
2. A. E. Green, K. A. Lindsay, 1972. *Thermoelasticity*, J. Elasticity, **2**, 1–7.
3. E. S. Suhubi, 1975. *Thermoelastic solids in 'Continuum Physics II'*, (ed. A. C. Eringen), Academic Press, New York.
4. A. E. Green, P. N. Nagdhi, 1983. *Thermoelasticity without energy disscicpation*, J. Elasticity, **31**, 189–208.
5. D. S. Chandrasekharaiah, 1986. *Thermoelasticity with second sound: A review*, Applied. Mech. Rev., **39**, 355–376.
6. J. N. Sharma, V. Kumar, Dayal Chand, 2003. *Reflection of Generalized Thermoelastic waves from the boundary of a half space*, J. Therm. Stress, **26**, 925–942.
7. J. N. Sharma, 2004. On the *propagation of thermoelastic waves in homogeneous isotropic plates*, Ind. Jour. Pure and Appld. Maths. Vol. 32, 1329–1342, 2001.
8. H. Taheri, S. J. Fariborz, M. R. Eslami, 2004. *Thermoelasticity solution of a layer using the Green–Nagdhi model*, J. Therm. Stress, **27**, 795–809.
9. R. B. Hetnarski, J. Ignaczak, 1999. *Generalized Thermoelasticity*, J. Therm. Stress, **22**, 451–476.
10. J. D. Achenbach, *Wave propagation in Elastic solids*, North–Holland Pub. Co., New York.

FREE VIBRATION ANALYSIS OF A ROTATING BEAM WITH NON-LINEAR SPRING AND MASS SYSTEM

S. K. DAS AND P. C. RAY*
Department of Mechanical Engineering, Government College of Engineering and Leather Technology, Block-LB, Salt Lake City, Kolkata-700098, India

G. POHIT
Department of Mechanical Engineering, Jadavpur University, Kolkata-700032, India

Abstract. Free, out of plane vibration of a rotating beam with non-linear spring mass system has been investigated. The non-linear constraint is connected to the beam between two points on the beam through a rigid rod. Formulation of the equation of motion is obtained starting from transverse/axial coupling through axial strain. Solution is obtained by applying method of multiple time scale directly to the non-linear partial differential equations and the boundary conditions. The results of the linear frequencies match well with those obtained in open literature. Subsequent non-linear study indicates that there is a pronounced effect of spring and its mass. The influence of rigid rod location on frequencies is also investigated on non-linear frequencies of rotating beam.

Keywords: rotating beam, non-linear spring mass system, multiple time scale method

1. Introduction

With the advancement in technology, the design and construction of helicopter rotors has become very simple with the introduction of specialized elastomer with high loss factor, thus replacing the external hydraulic damper in the blade. A comprehensive review of the development of modern helicopter rotors in which elastomer plays an important role. The mechanical arrangement of the

* raypratab1@yahoo.co.in

E. İnan et al. (eds.), *Vibration Problems ICOVP-2007*,

elastomeric damper leads to additional non-linear constraint during the deformation of the blade. Consequently, the dynamic analysis of advanced helicopter rotors (known as bearingless rotor) becomes complicated due to multiple load paths and highly non-linear characteristics of the elastomeric damper. Beam theories for moderate deformation have been developed by several researchers. Independent of the above studies related to helicopter blades, several researchers have made significant contribution to the study of non-linear dynamics of beams using perturbation techniques. Anderson[1] formulated the non-linear equation of motion of a rotating bar and obtained the natural frequencies from the linearized equation. Using a harmonic balance technique, the non-linear structural dynamic analysis of blade model was performed by Minguet and Dugundji[2]. Nayfeh and his associates reported several studies to determine non-linear response of stationary beams under large deflection. Nayfeh et al[3,4]. proposed a numerical perturbation method for the determination of non-linear response of a continuous beam having complicated boundary conditions.

In a recent paper[5], formulation of equation of motion of a rotating beam with non-linear constraint has been presented starting from transverse/axial coupling through axial strain. The non-linear constraint with its mass appears in the boundary condition, thus making it possible to study the influence of spring-mass on the dynamic characteristic of the system. The major objectives of the present paper are to determination of non-linear solution by applying methods of multiple time scale directly to the partial differential equations and the boundary conditions and study the influence of the location of the non-linear constraint and its mass on non-linear frequencies.

2. Formulation

The present problem is shown in Fig. 1 in the form of a non-linear spring of mass M. The other end of the spring is attached to a rigid massless link EC, which is also rotating along with the beam AC. One end of the link being free and the other end is attached to the beam at C. It is to be noted that the deformation of the spring-mass system depends not only on the deflection of the beam at point B, but also on the deflection and slope at the point C. The motion is restricted to the transverse direction only, thereby eliminating lead lag and torsional motion, and allows axial strain. The effect of rotary inertia is also neglected.

Introducing, $(')$ ≡ space derivative with respect to x and $(\dot{})$ ≡ time derivative, and using the following non-dimensional quantities,

$$x^* = \frac{x}{L}; \qquad w_i^* = \frac{w_i}{r}; \qquad u_i^* = \frac{u_i}{r}; \qquad \eta_1 = \frac{L_1}{L}; \qquad \eta_2 = \frac{L_2}{L};$$

$$a=\frac{EAr^2}{m\Omega^2L^4}=\frac{EI}{m\Omega^2L^4};\qquad \varepsilon=\frac{r}{L};\ t^*=\Omega t;\qquad i=1,2,3,$$

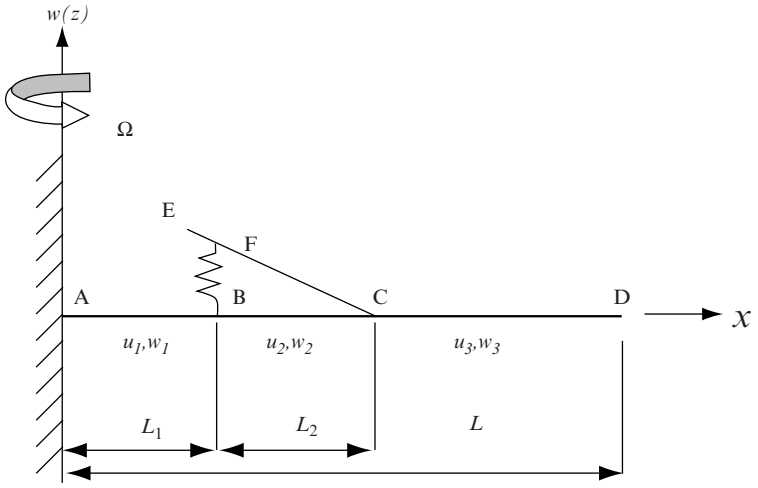

Fig. 1 Rotating beam with spring-mass system.

governing equations and boundary conditions can be written as

$$\varepsilon^2\left(-\frac{\partial^2u_1}{\partial t^2}+u_1\right)+x+a\left(u_1'+\frac{1}{2}w_1'^2\right)'=0$$
$$-\frac{\partial^2w_1}{\partial t^2}-aw_1''''+a.\left\{\left(u_1'+\frac{1}{2}w_1'^2\right)w_1'\right\}'=0,\quad for\quad 0\le x\le\eta_1 \tag{1}$$

$$\varepsilon^2\left(-\frac{\partial^2u_2}{\partial t^2}+u_2\right)+x+a\left(u_2'+\frac{1}{2}w_2'^2\right)'=0,$$
$$-\frac{\partial^2w_2}{\partial t^2}-aw_2''''+a.\left\{\left(u_2'+\frac{1}{2}w_2'^2\right)w_2'\right\}'=0,\quad for\quad \eta_1\le x\le\eta_2 \tag{2}$$

$$\varepsilon^2\left(-\frac{\partial^2u_3}{\partial t^2}+u_3\right)+x+a\left(u_3'+\frac{1}{2}w_3'^2\right)'=0,$$
$$-\frac{\partial^2w_3}{\partial t^2}-aw_3''''+a.\left\{\left(u_3'+\frac{1}{2}w_3'^2\right)w_3'\right\}'=0,\quad for\quad \eta_2\le x\le 1 \tag{3}$$

$$-\left(u_1^{'}+\frac{1}{2}w_1^{'2}\right)+\left(u_2^{'}+\frac{1}{2}w_2^{'2}\right)+\alpha_3\left(\eta_1+\varepsilon^2 u_1\right)=0,\quad x=\eta_1$$

$$u_1(0,t)=0,\quad u_1(\eta_1,t)=u_2(\eta_1,t),\quad u_2(\eta_2,t)=u_3(\eta_2,t),$$

$$u_2^{'}(\eta_2,t)=u_3^{'}(\eta_2,t),\quad u_3^{'}+\frac{1}{2}w_3^{'2}=0\quad at\quad x=1;$$

$$w_1(0,t)=0,\quad w_1^{'}(0,t)=0;\quad w_1(\eta_1,t)=w_2(\eta_1,t);\quad w_1^{'}(\eta_1,t)=w_2^{'}(\eta_1,t);$$

$$w_1^{'''}(\eta_1,t)-w_2^{'''}(\eta_1,t)-\left(u_1^{'}+\frac{1}{2}w_1^{'2}\right)w_1^{'}+\left(u_2^{'}+\frac{1}{2}w_2^{'2}\right)w_2^{'}$$

$$+\alpha_1\Delta_1(\eta_1,t)+\alpha_2{\Delta_1}^3(\eta_1,t)+\alpha_3\ddot{\Delta}_1=0$$

$$w_1^{''}(\eta_1,t)=w_2^{''}(\eta_1,t)=0,\quad w_2(\eta_2,t)=w_3(\eta_2,t),\quad w_2^{'}(\eta_2,t)=w_3^{'}(\eta_2,t);$$

$$-w_2^{''}-w_3^{''}+(\eta_2-\eta_1)\alpha_1\Delta_1+(\eta_2-\eta_1)\alpha_2{\Delta_1}^3+(\eta_2-\eta_1)\alpha_3\ddot{\Delta}_1=0,\quad at\quad x=\eta_2$$

$$w_2^{'''}-w_3^{'''}-\alpha_1\Delta_1-\alpha_2{\Delta_1}^3-\alpha_3\ddot{w}_1=0,\ at\ x=\eta_2,\ w_3^{''}(1,t)=0,\ w_3^{'''}(1,t)=0;\quad (4)$$

It is to be noted that stars (*) are removed from all the quantities for convenience.

In the above equations, co-efficient α_1, α_2, α_3, Δ_1 and $\ddot{\Delta}_1$ are defined as follows:

$$\alpha_1=\frac{\alpha L^3}{EI},\ \alpha_2=\frac{\gamma r^2L^3}{EI},\ \alpha_3=\frac{M\Omega^2L^3}{EI},\ \Delta_1=\frac{\Delta}{r},\ \ddot{\Delta}_1=\frac{\ddot{\Delta}}{r\Omega^2}\ \text{and}\ \alpha_4\left(=a\alpha_3=\frac{M}{mL}\right)$$

3. Solution methodology

For the subsequent solution of the above non-linear equations, one may uses the method of multiple scale and seeks expansions of the solution for frequency-amplitude in the form

$$
\begin{aligned}
w_1(x,t;\varepsilon) &= \varepsilon w_{11}(x,T_0,T_2) + \varepsilon^3 w_{13}(x,T_0,T_2) + \varepsilon^5 w_{15}(x,T_0,T_2) + \ldots \\
w_2(x,t;\varepsilon) &= \varepsilon w_{21}(x,T_0,T_2) + \varepsilon^3 w_{23}(x,T_0,T_2) + \varepsilon^5 w_{25}(x,T_0,T_2) + \ldots \\
w_3(x,t;\varepsilon) &= \varepsilon w_{31}(x,T_0,T_2) + \varepsilon^3 w_{32}(x,T_0,T_2) + \varepsilon^5 w_{35}(x,T_0,T_2) + \ldots
\end{aligned} \tag{5}
$$

where, w_{1n}, w_{2x} and w_{3n} are $O(l)$; ε is a small dimensionless parameter (defined earlier); $T_0 = t$ is a first time scale characterizing changes occurring at ω_n, where ω_n are the natural frequencies of the beam-spring system; and $T_2 = \varepsilon^2 t$ is a slow time scale, characterizing the modulation of the amplitudes and phases due to nonlinearity[4].

4. Linear solution

At order ε, the equations and boundary conditions are linear and hence the solution is assumed of the form

$$
\begin{aligned}
&w_{11} = \left\{ A(T_2) e^{i\omega T_0} + c.c. \right\} y_1(x),\ w_{21} = \left\{ A(T_2) e^{i\omega T_0} + c.c. \right\} y_2(x), \\
&w_{31} = \left\{ A(T_2) e^{i\omega T_0} + c.c. \right\} y_3(x)
\end{aligned} \tag{6}
$$

where $c.c.$ is the complex conjugate of the preceding terms.

The power series solutions of the linear part of Equations (1-4) can be expressed as

$$
y_1(x) = \sum_{k=1}^{\infty} A_k x^{k-1}, \quad y_2(x) = \sum_{k=1}^{\infty} B_k x^{k-1}, \quad y_3(x) = \sum_{k=1}^{\infty} C_k x^{k-1} \tag{7}
$$

$$
\text{for} \quad 0 \le x \le \eta_1, \quad \eta_1 \le x \le \eta_2 \quad \text{and} \quad \eta_2 \le x \le 1
$$

From the above linear system we find the linear frequencies for different position of the torque tube.

TABLE 1. Data for the beam to obtain the numerical results.

$m = 9.7\,kg/m$; $L = 6.6\,m$; $a = 0.0106$; $\Omega = 32.8\,rad/\sec$; $\alpha_1 = 1000$

TABLE 2. The first three linear natural frequencies of the rotating beam without spring ($\alpha_1 = 0.0$) with comparison of the other references.

	1st mode	2nd mode	3rd mode
Present study	1.1244	3.4073	7.6170
Pohit et al[6]	1.1245	3.4073	7.6218
Gupta et al[7]	1.1247	3.4089	7.6376

5. Non-linear solution

Since the ε^3 order of the problem has a non-trivial solution, the inhomogeneous part of those equations have a solution only if a solvability condition is satisfied[4]. In order to find this condition, their solution is expressed in the form:

$$\begin{aligned} w_{13}(x,t) &= \left[A(T_2) e^{i\omega T_0} + c.c \right] \Phi_1(x) + \bar{W}_1(x, T_0, T_2), \\ w_{23}(x,t) &= \left[A(T_2) e^{i\omega T_0} + c.c \right] \Phi_2(x) + \bar{W}_2(x, T_0, T_2), \\ w_{33}(x,t) &= \left[A(T_2) e^{i\omega T_0} + c.c \right] \Phi_3(x) + \bar{W}_3(x, T_0, T_2). \end{aligned} \tag{8}$$

After some algebraic manipulation we get

$$\begin{aligned} &\frac{3}{4} a\alpha_2 \sigma^2 {\delta_{11}}^4 - 2\omega a\alpha_3 \theta' {\delta_{11}}^2 = 2\omega\theta' \left(\int_0^{\eta_1} {y_1}^2 dx + \int_{\eta_1}^{\eta_2} {y_2}^2 dx + \int_{\eta_2}^{1} {y_3}^2 dx \right), \\ &\delta_{11} = y_2(\eta_2) - (\eta_2 - \eta_1) y_2'(\eta_2) - y_1(\eta_1), \\ &A(T_2) = \frac{1}{2} \sigma(T_2) e^{i\theta(T_2)}, \quad A\bar{A} = \frac{1}{4}\sigma^2. \end{aligned} \tag{9}$$

Here $A(T_2)$ is the amplitude of vibration. Using

$$b_1 = \int_0^{\eta_1} {y_1}^2 dx + \int_{\eta_1}^{\eta_2} {y_2}^2 dx + \int_{\eta_2}^{1} {y_3}^2 dx ,$$

here y_1, y_2 and y_3 are the solutions of the linear problems. Then (9) becomes

$$\theta' = \left(\frac{3a\alpha_2}{8\omega} \sigma^2 \right) {\delta_{11}}^4 \frac{1}{b_1 + a\alpha_3 {\delta_{11}}^2} \tag{10}$$

On integration, finally one obtains

$$\omega_{nl} = \omega + \left(\frac{3a\alpha_2}{8\omega} \right) {\delta_{11}}^4 \frac{1}{b_1 + \alpha_4 {\delta_{11}}^2} \hat{A}^2 ;$$

here ω and ω_{nl} are the linear and nonlinear frequencies.

6. Results and discussion

The first three natural frequencies of the rotating beam (Table 1 and 2) with spring mass attached at different locations ($\eta_2 = 0.15, 0.20,$ and 0.25) are determined (Table 3). It is observed that due to the presence of the mass, the first natural frequencies for different spring locations ($\eta_2 = 0.15, 0.20,$ and 0.25) have increased whereas those of the higher modes have diminished. It is evident that influence of mass of the spring on natural frequency is not very pronounced when the spring is located near the root (up to $\eta_2 = 0.15$). However, when the spring is located at $\eta_2 = 0.20$ or above, the mass of the spring should not be neglected while determining the linear frequencies as these values deviate from that of massless spring by considerable amount. In order to obtain the non-linear frequencies of the blade-spring-mass system, the value of b_1 and $y_1(\eta)$ are calculated for the first three modes of vibrations. They are presented in Table 4. The dynamic characteristics of the rotating beam are analyzed for different torque tube locations. Fig. 2 shows the variation of the third non-linear frequency with tip amplitudes for different values of torque tube locations ($\eta_2 = 0.15, 0.20,$ and 0.25) and for $\eta_1 = 0.1$.

TABLE 3. The first three linear natural frequencies of the rotating beam with spring with mass system for various locations (η_2) of the torque tube with $\alpha_4 = 0.15$.

η_2	1st mode	2nd mode	3rd mode
0.15	1.12494	3.40874	7.61962
0.20	1.12685	3.40943	7.62175
0.25	1.12998	3.40844	7.64637

TABLE 4. The values of b_1 and $y_2(\eta_2)$ for the first three modes and for various locations of the torque tube on the beam with spring mass system ($\alpha_4 = 0.15$).

η_2		1st mode	2nd mode	3rd mode
0.15	b_1	0.50197 e-004	0.15138 e-005	0.15794 e-007
	$y_2(\eta_2)$	-8.36419 e-004	4.87704 e-004	1.06267 e-004
0.20	b_1	0.43622 e-004	0.14552 e-005	0.16323 e-007
	$y_2(\eta_2)$	-0.00127	7.44880 e-004	1.51596 e-004
0.25	b_1	0.36045 e-004	0.15355 e-005	0.19655 e-007
	$y_2(\eta_2)$	0.00169	-0.00103	1.9631 e-004

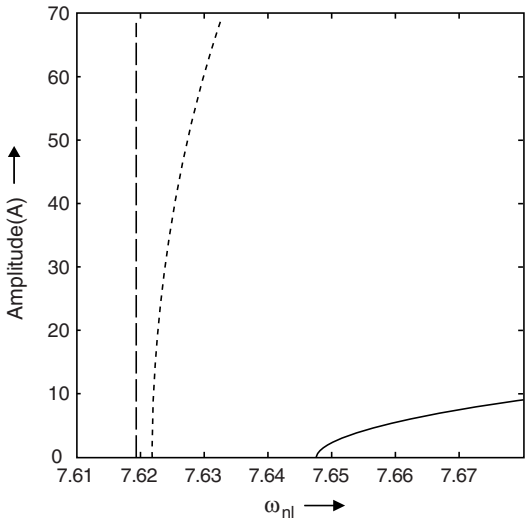

Fig. 2 Variation of third non-linear frequency with amplitude of oscillation for different location of the torque tube with spring-mass $(\alpha_4 = 0.15)$. $\eta_2 = 0.15$, $\eta_2 = 0.20$, $\eta_2 = 0.25$.

7. Conclusions

A closed form frequency-amplitude relationship of the rotating beam along with spring mass system is obtained. The effect of the mass of the spring on non-linear frequencies is investigated. It may be concluded that mass of the spring plays a significant role in predicting frequency-amplitude relationship.

References

1. G. L. Anderson, 1975. *On the extensional and flexural vibrations of rotating bars*, International Journal for Non-linear Mechanics, **10**, 223-236.
2. P. Minguet, J. Dugundji, 1990. *Experiments and analysis for composite blades under large deflection part 2-dynamic behavior*, AIAA Journal, **28**, 1580-1588.
3. A. H. Nayfeh, D. T. Mook, D. W. Lobitz, 1974. *Numerical-perturbation method for the non-linear analysis of structural vibrations*, AIAA Journal, **12**, 1222-1228.
4. M. Pakdemirli, A. H. Nayfeh, 1994. *Non-linear vibration of a beam-spring-mass system*, Journal of Vibration and Acoustics, **116**, 433-439.

5. S. K. Das, P. C. Ray, G. Pohit, 2005. *Large Amplitude Free Vibration Analysis of a Rotating Beam with Non-Linear Spring and Mass System*, Journal of Vibration and Control, **11**, 1511-1533.
6. G. Pohit, A. K. Mallik, C. Venkatesan, 1999. *Free out-of-plane vibration of a rotating beam with non-linear elastomeric constraints*, Journal of Sound and Vibration, **220**, 1-25.
7. P. K. Gupta, C. Venkatesan, O. Singh, 1997. *Structural dynamics of rotor blades with precone-presweep-predoor-pretwist and torque offset including hub motion*, Proceedings of 48th AGM, Aeronautical Society of India, India.

TRAVELLING WAVES IN A PRESTRESSED ELASTIC TUBE FILLED WITH A FLUID OF VARIABLE VISCOSITY

HİLMİ DEMİRAY*
Department of Mathematics, Işık University, Istanbul, Turkey
TAY KIM GAIK
Science Study Center, Universiti Teknologi Tun Hussein Onn Malaysia, Johor, Malaysia

Abstract. In this work, treating the artery as a prestressed thin elastic tube with variable radius and the blood as an incompressible Newtonian fluid with variable viscosity, the propagation of nonlinear waves in such a composite medium is studied, in the long wave approximation, through the use of the reductive perturbation method and the Forced Korteweg-de Vries-Burgers (FKdVB) equation with variable coefficients is obtained as the evolution equation. A progressive wave type of solution is presented for this evolution equation and the result is discussed.

Keywords: prestressed elastic tube, fluid of variable viscosity, FKdVB equation

1. Introduction

The propagation of small-but finite amplitude waves in distensible tubes has been studied by Johnson[1], Hashizume[2], Yomosa[3], Demiray[4-6]. Such problems have been investigated, especially, in view of their applications to biological problems involving pulse propagation in large blood vessels. In all these works, the blood is modelled as an inviscid or a Newtonian fluid with constant viscosity. In the majority of these research works, blood is treated as an inviscid

*Corresponding author, demiray@isikun.edu.tr

E. İnan et al. (eds.), *Vibration Problems ICOVP-2007*,

fluid since it is almost impossible to satisfy the non-slip boundary conditions on the tube wall. To circumvent this difficulty the researchers averaged the field equations or used the boundary layer approximation[7].

As is well known, in essence, blood is an incompressible non-Newtonian fluid. In the course of flow in large arteries, the red blood cells in the vicinity of the arterial wall move to the central region of the artery and the hematocrit ratio becomes quite low near the arterial wall, which results in lower viscosity in this region. As is seen from the Poiseuille flow in the cylindrical tubes, the shear rate is quite large near the arterial wall. Due to these factors, the blood viscosity near the arterial wall is quite small as compared to the viscosity at the central region. Because of these flow properties of blood in large blood vessels, researchers modelled the blood as a layered fluid, where the outer layer is an inviscid fluid and the inner layer is a viscous fluid[8]. The drawbacks of this model are the discontinuity of shear stress on the interface of the layers and the arbitrariness of the thickness of the layers.

In the present work, motivated with the layered fluid models, we treat blood as a Newtonian fluid with variable viscosity which vanishes on the boundary and reaches to its maximum value at the center and the artery as a prestressed thin elastic tube with variable radius and studied the propagation of nonlinear waves in such a composite medium, in the long wave approximation, through the use of reductive perturbation method and the evolution equation is obtained as the Forced Korteweg-de Vries-Burgers equation with variable coefficients. Progressive wave type of solution is presented for such an evolution equation and the result is discussed.

2. Theoretical preliminaries and basic equations

2.1. EQUATION OF A TUBE

We consider a circularly cylindrical tube of radius R_0, subjected to an inner pressure $P_0(Z^*)$. The position vector of a generic point on the tube may be given by

$$\mathbf{r_0} = [r_0 - f^*(z^*)]\mathrm{e}_r + z^*\mathrm{e}_z, \quad z^* = \lambda_z Z^*. \tag{1}$$

where λ_z is the axial stretch ratio, r_0 is the deformed radius at the origin and $f^*(z^*)$ characterizes the variable radius along the tube axis. In the course of blood flow a radial displacement u^* will be superimposed on this static field. Due to external tethering in the axial direction, the effect of axial displacement

is neglected. Then the position vector of the corresponding generic point in the final configuration will be

$$\mathbf{r} = [r_0 - f^*(z^*) + u^*]\mathrm{e}_r + z^*\mathrm{e}_z, \quad z^* = \lambda_z Z^*. \tag{2}$$

Then, the stretch ratios along the meridional and circumferential curves may be given, respectively, by

$$\lambda_1 = \lambda_z[1 + (-f^{*'} + \partial u^*/\partial z^*)^2]^{1/2}, \quad \lambda_2 = \frac{r_0 - f^* + u^*}{R_0}, \tag{3}$$

where the prime denotes the differentiation of the corresponding quantity with respect to z^*.

Now considering a small tube element and writing the Newton's equation of motion in the radial direction, we obtain

$$-\frac{\mu}{\lambda_z}\frac{\partial \Sigma}{\partial \lambda_2} + \lambda_z \mu R_0 \frac{\partial}{\partial z^*}\left[\left(-f^{*'} + \frac{\partial u^*}{\partial z^*}\right)\frac{1}{\lambda_1}\frac{\partial \Sigma}{\partial \lambda_1}\right] + \frac{R_0 P_r^*}{\lambda_z H}\lambda_1\lambda_2 = \rho_0 \frac{R_0}{\lambda_z}\frac{\partial^2 u^*}{\partial t^{*2}}. \tag{4}$$

2.2. EQUATION OF FLUID

Blood is known to be an incompressible non-Newtonian fluid. However, in the course of flow on large arteries, the red blood cells in the vicinity of arterial wall move to the central region of the artery so that the hematocrit ratio becomes quite low near the arterial wall, which results in lower viscosity in this region. Moreover, due to high shear rate near the arterial wall, the viscosity of blood is further reduced. Therefore, for flow problems in large blood vessels, the blood may be treated as Newtonian fluid with variable viscosity, which vanishes on the arterial wall and takes its maximum value at the center of the artery. Because of the vanishing viscosity on the arterial wall, the tangential velocity of the fluid on the boundary will not set equal to zero.

Let V_r^* and V_z^* denote the radial and axial velocity components of the fluid. The equations of axially symmetric motion of fluid may be given by

$$\begin{aligned} &\frac{\partial V_r^*}{\partial t^*} + V_r^*\frac{\partial V_r^*}{\partial r} + V_z^*\frac{\partial V_r^*}{\partial z^*} + \frac{1}{\rho_f}\frac{\partial \overline{p}}{\partial r} \\ &-\hat{\upsilon}\gamma(r)\left[\frac{\partial^2 V_r^*}{\partial r^2} + \frac{1}{r}\frac{\partial V_r^*}{\partial r} - \frac{V_r^*}{r^2} + \frac{\partial^2 V_r^*}{\partial z^{*2}}\right] - 2\hat{\upsilon}\gamma'(r)\frac{\partial V_r^*}{\partial r} = 0, \end{aligned} \tag{5}$$

$$\frac{\partial V_z^*}{\partial t^*}+V_r^*\frac{\partial V_z^*}{\partial r}+V_z^*\frac{\partial V_z^*}{\partial z^*}+\frac{1}{\rho_f}\frac{\partial \bar{p}}{\partial z^*}$$
$$-\hat{\upsilon}\gamma(r)\left[\frac{\partial^2 V_z^*}{\partial r^2}+\frac{1}{r}\frac{\partial V_z^*}{\partial r}+\frac{\partial^2 V_z^*}{\partial z^{*2}}\right]-\hat{\upsilon}\gamma'(r)\left(\frac{\partial V_r^*}{\partial z^*}+\frac{\partial V_z^*}{\partial r}\right)=0, \tag{6}$$

$$\frac{\partial V_r^*}{\partial r}+\frac{V_r^*}{r}+\frac{\partial V_z^*}{\partial z^*}=0, \tag{7}$$

and the boundary conditions

$$V_r^*\,|_{r=r_f}=\frac{\partial u^*}{\partial t^*}+\left(-f^{*'}+\frac{\partial u^*}{\partial z^*}\right)V_z^*\,|_{r=r_f},$$
$$P_r^*=\frac{\lambda_z}{\lambda_1}\left[\bar{p}-2\rho_f\hat{\upsilon}\gamma(r)\frac{\partial V_r^*}{\partial r}+\rho_f\hat{\upsilon}\gamma(r)\left(-f^{*'}+\frac{\partial u^*}{\partial z^*}\right)\left(\frac{\partial V_z^*}{\partial r}+\frac{\partial V_r^*}{\partial z^*}\right)\right]|_{r=r_f}. \tag{8}$$

where ρ_f is the fluid mass density, $\hat{\upsilon}$ is the kinematic viscosity and γ(r) represants variable viscosity. The dimensionless form of these field equations and the boundary conditions are given by

$$P_r=\frac{1}{\lambda_\theta-f+u}\left[\frac{m}{\lambda_z}\frac{\partial^2 u}{\partial t^2}+\frac{1}{\lambda_z}\frac{\partial \Sigma}{\partial \lambda_2}-\frac{\partial}{\partial z}\left\{\frac{-f'+\dfrac{\partial u}{\partial z}}{\left[1+\left(-f'+\partial u/\partial z\right)^2\right]^{1/2}}\frac{\partial \Sigma}{\partial \lambda_1}\right\}\right], \tag{9}$$

$$\frac{\partial V_r}{\partial t}+V_r\frac{\partial V_r}{\partial x}+V_z\frac{\partial V_r}{\partial z}+\frac{\partial \bar{p}}{\partial x}$$
$$-\bar{\upsilon}\gamma(x)\left[\frac{\partial^2 V_r}{\partial x^2}+\frac{1}{x}\frac{\partial V_r}{\partial x}-\frac{V_r}{x^2}+\frac{\partial^2 V_r}{\partial z^2}\right]-2\bar{\upsilon}\gamma'(x)\frac{\partial V_r}{\partial x}=0, \tag{10}$$

$$\frac{\partial V_z}{\partial t}+V_r\frac{\partial V_z}{\partial x}+V_z\frac{\partial V_z}{\partial z}+\frac{\partial \bar{p}}{\partial z}$$
$$-\bar{\upsilon}\gamma(x)\left[\frac{\partial^2 V_z}{\partial x^2}+\frac{1}{x}\frac{\partial V_z}{\partial x}+\frac{\partial^2 V_z}{\partial z^2}\right]-\bar{\upsilon}\gamma'(x)\left(\frac{\partial V_r}{\partial z}+\frac{\partial V_z}{\partial x}\right)=0, \tag{11}$$

$$\frac{\partial V_r}{\partial r}+\frac{V_r}{x}+\frac{\partial V_z}{\partial z}=0, \tag{12}$$

with the boundary conditions

$$V_r\,|_{x=\lambda_\theta - f+u} = \frac{\partial u}{\partial t} + \left(-f' + \frac{\partial u}{\partial z}\right) V_z\,|_{x=\lambda_\theta - f+u},$$
$$P_r = \left[\bar{p} - 2\bar{\upsilon}\gamma(x)\frac{\partial V_r}{\partial x} + \bar{\upsilon}\gamma(x)\left(-f' + \frac{\partial u}{\partial z}\right)\left(\frac{\partial V_z}{\partial x} + \frac{\partial V_r}{\partial z}\right)\right]|_{x=\lambda_\theta - f+u}. \tag{13}$$

The equations (9)-(13) give sufficient relations to determine the field quantities u, V_r, V_z and $\bar{p}$ completely.

3. Long wave approximation

In this subsection, we shall examine the propagation of small-but-finite amplitude waves for fluid-filled prestressed elastic tubes in the long wave approximation. For this, we adopt the long wave approximation and employ the reductive perturbation method[9]. For that purpose we shall introduce the following stretched coordinates

$$\xi = \varepsilon^{1/2}(z - ct), \quad \tau = \varepsilon^{3/2} z, \tag{14}$$

where ε is a small parameter measuring the weakness of nonlinearity, dispersion and disipation and c is a scale parameter to be determined from the solution.

Solving z in terms of τ, we get $z = \varepsilon^{-3/2}\tau$. Then the function $f(z)$ becomes $f(z) = f(\varepsilon^{-3/2}\tau)$. In order to take the effect of stenosis into account, the order of $f(z)$ should be $\varepsilon^{5/2}$. For the present problem, we shall approximate $f(z)$ as $f(z) = \varepsilon h(\tau)$. We shall assume that field variables may be expanded into asymptotic series of ε as

$$u = \varepsilon u_1 + \varepsilon^2 u_2 + \ldots, \quad V_r = \varepsilon^{1/2}\left(\varepsilon V_r^{(1)} + \varepsilon^2 V_r^{(2)} + \ldots,\right),$$
$$V_z = \varepsilon V_z^{(1)} + \varepsilon^2 V_z^{(2)} + \ldots, \quad P_r = P_r^{(0)} + \varepsilon P_r^{(1)} + \varepsilon^2 P_r^{(2)} + \ldots, \tag{15}$$
$$\bar{p} = \bar{p}_0 + \varepsilon \bar{p}_1 + \varepsilon^2 \bar{p}_2 + \ldots, \quad \gamma(x) = \gamma_0(x) + \varepsilon\gamma_1(x) + \varepsilon^2\gamma_2(x) + \ldots,$$

where $\gamma_0(x)$, $\gamma_1(x)$ and $\gamma_2(x)$ are defined by

$$\gamma_0(x) = 1 - \frac{x}{\lambda_\theta}, \quad \gamma_1(x) = \frac{x}{\lambda_\theta^2}(u_1 - h), \quad \gamma_2(x) = \frac{x}{\lambda_\theta^2}\left(u_2 - \frac{(u_1 - h)^2}{\lambda_\theta}\right). \tag{16}$$

Here, we assume that the function $\gamma(x)$, characterizing the variation of the viscosity, is of the form

$$\gamma(x) = 1 - \frac{x}{\lambda_\theta - \varepsilon h + u}, \tag{17}$$

Introducing the expansions (15) and (16) into the equations (9)-(13), the following sets of differential equations are obtained

$0(\varepsilon)$ equations

$$\begin{aligned} &-c\frac{\partial V_z^{(1)}}{\partial \xi} + \frac{\partial \bar{p}_1}{\partial \xi} - \upsilon\gamma_0(x)\left[\frac{\partial^2 V_z^{(1)}}{\partial x^2} + \frac{1}{x}\frac{\partial V_z^{(1)}}{\partial x}\right] - \upsilon\gamma_0'(x)\frac{\partial V_z^{(1)}}{\partial x} = 0, \\ &\frac{\partial \bar{p}_1}{\partial x} = 0, \qquad \frac{\partial V_r^{(1)}}{\partial x} + \frac{V_r^{(1)}}{x} + \frac{\partial V_z^{(1)}}{\partial \xi} = 0, \end{aligned} \tag{18}$$

with the boundary conditions

$$V_r^{(1)}\,|_{x=\lambda_\theta} = -c\frac{\partial u_1}{\partial \xi}, \quad \bar{p}_1\,|_{r=\lambda_\theta} = P_r^{(1)}. \tag{19}$$

$0(\varepsilon^2)$ equations

$$\begin{aligned} &-c\frac{\partial V_r^{(1)}}{\partial \xi} + \frac{\partial \bar{p}_2}{\partial x} - \upsilon\gamma_0(x)\left[\frac{\partial^2 V_r^{(1)}}{\partial x^2} + \frac{1}{x}\frac{\partial V_r^{(1)}}{\partial x} - \frac{V_r^{(1)}}{x^2}\right] - 2\upsilon\gamma_0'(x)\frac{\partial V_r^{(1)}}{\partial x} = 0, \\ &-c\frac{\partial V_z^{(2)}}{\partial \xi} + \frac{\partial \bar{p}_2}{\partial \xi} + \frac{\partial \bar{p}_1}{\partial \tau} + V_r^{(1)}\frac{\partial V_z^{(1)}}{\partial x} + V_z^{(1)}\frac{\partial V_z^{(1)}}{\partial \xi} - \upsilon\gamma_0(x)\left[\frac{\partial^2 V_z^{(2)}}{\partial x^2} + \frac{1}{x}\frac{\partial V_z^{(2)}}{\partial x} + \frac{\partial^2 V_z^{(1)}}{\partial \xi^2}\right] \\ &-\upsilon\gamma_1(x)\left[\frac{\partial^2 V_z^{(1)}}{\partial x^2} + \frac{1}{x}\frac{\partial V_z^{(1)}}{\partial x}\right] - \upsilon\gamma_0'(x)\left[\frac{\partial V_r^{(1)}}{\partial \xi} + \frac{\partial V_z^{(2)}}{\partial x}\right] - \upsilon\gamma_1'(x)\frac{\partial V_z^{(1)}}{\partial x} = 0, \\ &\frac{\partial V_r^{(2)}}{\partial x} + \frac{V_r^{(2)}}{x} + \frac{\partial V_z^{(2)}}{\partial \xi} + \frac{\partial V_z^{(1)}}{\partial \tau} = 0, \end{aligned} \tag{20}$$

with the boundary conditions

$$\begin{aligned} &\left[V_r^{(2)} + (u_1 - h)\frac{\partial V_r^{(1)}}{\partial x}\right]|_{r=\lambda_\theta} = -c\frac{\partial u_2}{\partial \xi} + \frac{\partial u_1}{\partial \xi}V_z^{(1)}\,|_{x=\lambda_\theta}, \\ &P_r^{(2)} = \left[\bar{p}_2 + (u_1 - h)\frac{\partial \bar{p}_1}{\partial x} - 2\upsilon\gamma_0(r)\frac{\partial V_r^{(1)}}{\partial x}\right]|_{x=\lambda_\theta}. \end{aligned} \tag{21}$$

Here, it is assumed that the viscosity is of order of $0(\varepsilon^{1/2})$, i.e. $\bar{\upsilon} = \varepsilon^{1/2}\upsilon$.

In order to complete the equations, one must know the expression of $P_r^{(1)}$ and $P_r^{(2)}$ in terms of the radial displacement u. For that purpose, we need the series expansion of the stretch ratios λ_1 and λ_2, which read

$$\lambda_1 \approx \lambda_z, \quad \lambda_2 = \lambda_\theta + \varepsilon(u_1 - h) + \varepsilon^2 u_2. \tag{22}$$

Using the expansion (22) in the expression of P_r given in (13), we have

$$P_r^{(1)} = \beta_1(u_1 - h), \tag{23}$$

$$P_r^{(2)} = \left(\frac{mc^2}{\lambda_\theta \lambda_z} - \beta_0\right)\frac{\partial^2 u_1}{\partial \xi^2} + \beta_1 u_2 + \beta_2[u_1 - h(\tau)]^2. \tag{24}$$

Here the coefficients β_0, β_1 and β_2 are defined by

$$\beta_0 = \frac{1}{\lambda_\theta}\frac{\partial \Sigma}{\partial \lambda_z}, \quad \beta_1 = \frac{1}{\lambda_z \lambda_\theta}\frac{\partial^2 \Sigma}{\partial \lambda_\theta^2} - \frac{1}{\lambda_z \lambda_\theta^2}\frac{\partial \Sigma}{\partial \lambda_\theta}, \quad \beta_2 = \frac{1}{2\lambda_z \lambda_\theta}\frac{\partial^3 \Sigma}{\partial \lambda_\theta^3} - \frac{\beta_1}{\lambda_\theta}. \tag{25}$$

4. Solution of the field equations

From the solution of the equation (18) under the boundary conditions (19), we have

$$u_1 = U(\xi, \tau), \quad \bar{p}_1 = \beta_1(U - h), \quad V_z^{(1)} = \frac{\beta_1}{c}U, \quad V_r^{(1)} = -\frac{\beta_1}{2c}\frac{\partial U}{\partial \xi}x, \quad \beta_1 = \frac{2c^2}{\lambda_\theta}. \tag{26}$$

Here $U(\xi, \tau)$ is an unknown function whose governing equation will be obtained later and c is the phase velocity in the long wave approximation.

Solving $0(\varepsilon^2)$ equations (20) under the associated boundary conditions (21), the following evolution equation is obtained

$$\frac{\partial U}{\partial \tau} + \mu_1 U\frac{\partial U}{\partial \xi} - \mu_2\frac{\partial^2 U}{\partial \xi^2} + \mu_3\frac{\partial^3 U}{\partial \xi^3} - \mu_4 h(\tau)\frac{\partial U}{\partial \xi} = \frac{1}{2}\frac{dh}{d\tau}, \tag{27}$$

where the coefficients μ_1, μ_2, μ_3 and μ_4 are defined by

$$\mu_1 = \frac{\beta_2}{\beta_1} + \frac{5}{2\lambda_\theta}, \quad \mu_2 = \frac{\upsilon}{2c}, \quad \mu_3 = \frac{m}{4\lambda_z} + \frac{\lambda_\theta^2}{16} - \frac{\beta_0}{2\beta_1}, \quad \mu_4 = \left[\frac{1}{2\lambda_\theta} + \frac{\beta_2}{\beta_1}\right]. \tag{28}$$

This evolution equation is known as the Forced Korteweg-de Vries-Burgers (FKdVB) equation with variable coefficients.

5. Progressive wave solution to the FKDVB equation

In this subsection, we shall present a progressive wave solution to the evolution equation given in (27). For that purpose, we introduce the following new dependent variable V as

$$U(\xi,\tau)=V(\xi,\tau)+\frac{1}{2}h(\tau). \tag{29}$$

Introducing this expression of U into the equation (27), we have

$$\frac{\partial V}{\partial \tau}+\mu_1 V\frac{\partial U}{\partial \xi}-\mu_2\frac{\partial^2 V}{\partial \xi^2}+\mu_3\frac{\partial^3 V}{\partial \xi^3}-\kappa h(\tau)\frac{\partial U}{\partial \xi}=0. \tag{30}$$

where the coefficient κ is defined by

$$\kappa=\mu_4-\frac{\mu_1}{2}=\frac{\beta_2}{2\beta_1}-\frac{3}{4\lambda_\theta}. \tag{31}$$

Now, we introduce the following coordinate transformation

$$\tau'=\tau,\qquad \xi'=\xi+\kappa\int_0^\tau h(s)ds. \tag{32}$$

In the new coordinate system, the evolution equation reduces to the conventional Korteweg-de vries-Burgers equation

$$\frac{\partial V}{\partial \tau'}+\mu_1 V\frac{\partial U}{\partial \xi'}-\mu_2\frac{\partial^2 V}{\partial \xi'^2}+\mu_3\frac{\partial^3 V}{\partial \xi'^3}=0. \tag{33}$$

Following Demiray[10], the solution of equation (33) may be given as follows

$$V=\frac{a}{\mu_1}+\frac{3\mu_2^2}{25\mu_1\mu_3}(\sec h^2\zeta+2\tanh\zeta), \tag{34}$$

where a is a constant and the phase function ζ is defined by

$$\zeta=\frac{\mu_2}{10\mu_3}(\xi'-a\tau'). \tag{35}$$

Using the coordinate transformation (32), the phase function takes the following form

$$\zeta = \frac{\mu_2}{10\mu_3}[\xi - a\tau + \kappa\int_0^\tau h(s)ds]. \tag{36}$$

As is seen from the expression of the phase function ζ, the trajectory ($\zeta = \cos nt$), of the wave is not a straight line anymore, it is rather a curve in the (ξ, τ) plane. This is the result of the stenosis in the tube. As a matter of fact, the existence of a stenosis causes the variable wave speed. Noting that τ is the spatial variable and ξ is a temporal variable, the wave speed may be defined by

$$v_p = \frac{d\tau}{d\xi} = \frac{1}{a - \kappa h(\tau)}. \tag{37}$$

As in seen from equation (37), due to the existence of stenosis, the wave speed is variable along the axis.

6. Conclusion

By employing the nonlinear field equations of an elastic tube with and the Newtonian fluid with variable viscosity, we have studied the propagation of nonlinear waves in such a composite medium, in the long wave approximation and obtained the Forced Korteweg-de Vries-Burgers equation with variable coefficient. It is observed that the wave trajectory is not a straight line anymore. It is rather a curve is the (ξ, τ) plane. Furthermore, we observe that the wave speed changes with axial distance of the tube. The wave speed takes its maximum value at the center of stenosis and its gets smaller and smaller as we go away from the center of stenosis.

References

1. R. S. Johnson, 1970. *A non-linear equation incorporating damping and dispersion*, Journal of Fluid Mechanics, **42**, 49-60.
2. Y. Hashizume, 1985. *Nonlinear Pressure Waves in a Fluid-Filled Elastic Tube*, J. Phys. Soc. Japan, **54**, 3305-3312.
3. S. Yomosa, 1987. *Solitary Waves in Large Blood Vessels*, J. Phys. Soc. Japan, **56**, 506-520.
4 H. Demiray, 1996. *Solitary waves in prestressed elastic tubes*, Bull. Math. Biol, **58**, 939-955.
5. H. Demiray, 1998. *Slowly varying solitary waves in an elastic tube filled with a viscous fluid*, ARI (formely, the Bulletin of Technical University of Istanbul), **51**, 98-102.

6 H. Demiray, 2004. *Solitary waves in a tapered prestressed fluid-filled elastic tube*, Z. angew. Mat. Phys, **55**, 282-294.
7. N. Antar and H. Demiray, 2000. *The Boundary layer approximation and nonlinear waves in elastic tubes*, Int. J. Eng. Sci, **38**, 1441-1457.
8. H. Demiray, 2001. *Solitary waves in elastic tubes filled with a layered fluid*, Int. J. Eng. Sci, **39**, 629-640.
9. A. Jeffrey and T. Kawahara, 1981. *Asymptotitc methods in nonlinear wave theory*, Pitman, Boston.
10. H. Demiray, 2003. *A note on the travelling wave solution to the KdV-Burgers equation*, Wave Motion, **38**, 367-369.

MEASUREMENT OF FLOW INDUCED VIBRATION OF REACTOR COMPONENT

N. DHARMARAJU*, K. K. MEHER, AND A. RAMA RAO
Vibration Laboratory Section, Reactor Engineering Division, Bhabha Atomic Research Centre Mumbai-400085, India

Abstract. The effect of flow-induced vibration on class I components in the reactor is a very important design factor for its qualifications worthy of loading inside the core. In this regard, a clear definition of the flow excitation and the dynamic characteristics of the component are the two primary inputs required to make an estimation of vibration severity. Though there are general guidelines available, more often it has been seen that they only help in arriving at a first approximation. There are many instances wherein a component has failed to perform as per design in spite of sufficient margin provided in the calculations. There are also instances wherein some components have failed even after successful testing under close to simulated flow condition. The paper deals with qualification procedure followed to flow test an in core component in an out of pile facility. The adopted procedure is considered to be a best approach especially in this field where in there are many gray areas.

The effort was to qualify new type of fuel bundle under simulated flow conditions in a specially erected flow test facility. The facility is meant to cater for testing new fuel design for upcoming reactors. To start with, 37 element PHWR bundles have been tested in the facility. The paper deals with the procedure of dynamic measurement, analysis and interpretation of the results, which helped in optimizing the assembly design for final acceptance.

Keywords: flow induced vibration, wall pressure, fuel bundle qualification

*Corresponding author, drajugn@yahoo.com

E. İnan et al. (eds.), *Vibration Problems ICOVP-2007*,

1. Introduction

In many applications in nuclear and process industries, structural members such as fuel bundles, heating elements, etc. are subjected to flow excitation[1-3], which need to be qualified for flow induced vibration before being put to actual use. Such qualifications need exact understanding of the nature and level of excitation, which depends on the flow characteristics. As there is no definite excitation pattern or protocol to suit all application, it is always better to generate such information in-situ for individual application, which depends on the nature of the fluid, flow speed, size of channel, process variables, etc. Many researchers have carried out studies to understand many such flow excitation phenomena and their effect on structures subjected to flow induced vibration[1-3]. Fluid forces on structure and their phase relationship have been discussed by Sinha et al[4]. In-situ direct measurement on such structural member is not always practicable because of the constraints of a direct approach. However, the surrounding fluid medium can be accessed through the flow channel wall or other means, which serves as an indirect route to it[5-7]. The vibrating structure in a fluid medium generates pressure ripples of identical nature in the fluid, which can be correlated directly to the structural vibration. An exact correlation between the structural vibration and the dynamic fluid pressure (which is generally picked up using a hydrophone and/or a dynamic pressure transducer) will prove very helpful in such quantification[8]. This work has been done in the context of quantifying vibration level on a nuclear fuel bundle for the exact nature and level of flow induced vibration.

1.1. VIBRATION AND PRESSURE MEASUREMENTS ON FLOW TEST SECTION

The Flow test section (FTS) is more than $9\,m$ long supported at locations identical to in core component conditions. The bottom of the fuel cluster is free where as the top of the fuel assembly is supported on the inside diameter (ID) of the test section. The flow enters the channel from the bottom and leaves from the top through a set of tail pipes. Throttling the pump discharge valve can vary the flow through the channel. Due to free bottom end of the fuel and the flow entering from the bottom, there was a need to assess the cluster vibration during rated flow in the channel. The radial clearance between the fuel and the ID of the test section is about $500\,microns$. The normal method is to measure the vibration on the channel and estimate the vibration of the fuel inside. Such an approach involves errors and especially when it is required to make correct estimation of fuel vibration for long term use in the reactor core it is important

to device a reliable method. In order to meet the objective, the test section was instrumented with accelerometers and dynamic pressure transducers as explained below.

The test section was instrumented with 7 accelerometers covering its entire length and the accelerometer signals were used for characterizing the channel and to identify the principle modes of vibration excited by the flow. In addition, two dynamic pressure transducers were installed on the test section. The transducer (probe) mounting arrangement is shown in Figure 1. The face of the pressure transducer is flushed to the internal diameter of the test section. The transducer senses the dynamic pressure pulsations in the flow caused by the vibration of fuel bundle due to the flow. Before installing, the pressure transducers were calibrated in the laboratory by simulating the gap between the sensor and a vibrating member in a water medium. The dynamic characteristic of the flow test station is identified by experimental modal analysis. The identified modal frequencies of the test channel with out the fuel inside were $6.0\,Hz$, $14.5\,Hz$ and $24\,Hz$. With the fuel assembly loaded the modal frequencies decrease. The identified modal frequencies were $3.6\,Hz$, $7.5\,Hz$ and $17.5\,Hz$. Vibration of the flow test section was checked at different flow in the channel by throttling the flow inlet valve of the test section. 100% flow corresponded to 1600 LPM whereas the required flow for vibration estimation was 900 LPM. Vibration of the test section and the fuel were measured at 38%, 47%, 55%, 69% and 100% flow. The vibration sensors directly measured the vibration of the test section where as fuel vibration was measured by the pressure sensor. Vibration of the fuel in micron units was estimated by calibrating the pressure signal with respect to channel vibration.

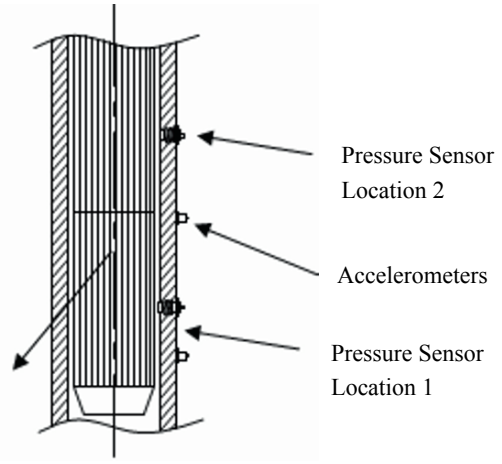

Fig. 1 Dynamic pressure transducers measuring fluid pulsation.

1.2. CALIBRATION OF PRESSURE SIGNAL IN TERMS OF VIBRATION AMPLITUDE

The test set-up for calibrating the pressure signal is essentially a cylindrical drum filled with water, which has embedded standard dynamic pressure transducer at different level as shown in Fig. 2. In front of the pressure transducers stands a cantilever dipped into the drum, which is connected at one end to a vibration shaker. The cantilever beam is sufficiently rigid in the frequency range of test. Moving the shaker closer/nearer to them can vary the gap between the cantilever and the sensors. Standard tiny accelerometers (Strain gauge type) are mounted directly on the cantilever beam to record the exact vibration level of the beam induced by the shaker.

The dynamic calibration was conducted by giving sinusoidal excitation at different frequencies and level of excitation. The gap between the cantilever beam and the dynamic pressure sensors was varied and the frequency range was kept between $5-40\,Hz$, which was a reasonably good in view of the structural frequencies and the involved flow excitation. Figure 3 shows the linear relationship between pressure and displacement at different frequencies obtained from a calibration test in an open container. Similar correlation was obtained between channel displacement (microns) and pressure (Pascal) at different frequencies. The displacement of the FTS test section and amplitude of pressure signal was found to have linear relationship similar to one established for an open container except that the pressure amplitudes were higher per unit displacement. By applying the appropriate correlation, displacement of the fuel bundle was estimated.

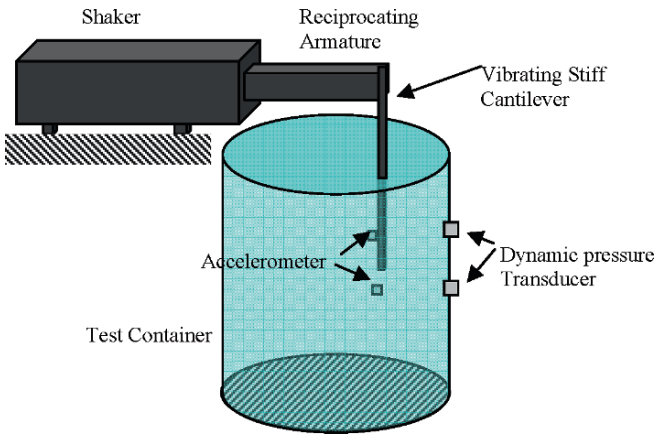

Fig. 2 Laboratory Test Set-up for calibrating fluid pressure signal in an open container.

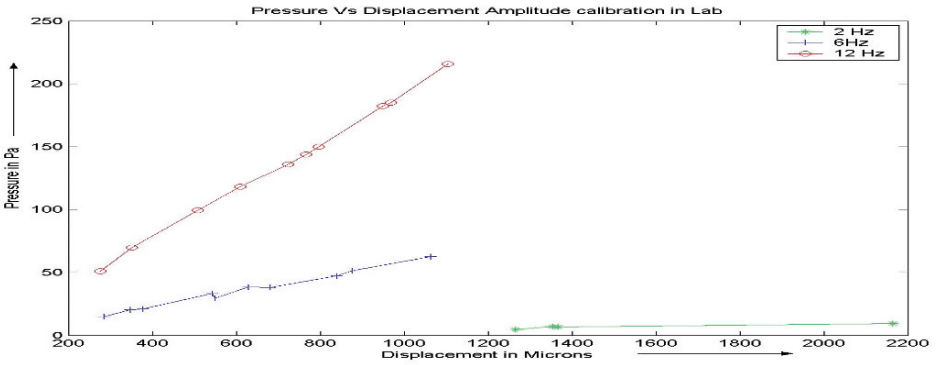

Fig. 3 Calibration of pressure and displacement amplitudes in an open container.

2. Results

The over all vibration of the fuel cluster for different flow inside the test section as measured from the dynamic pressure signal is given in Table 1. The maximum vibration velocity is $5.1\,mm/\sec$ and maximum displacement is $150\,microns$ at around 900 LPM flow. At other flows the measured vibration amplitudes were low. Figure 4 shows the spectra of the pressure signal at 900 LPM. Both the

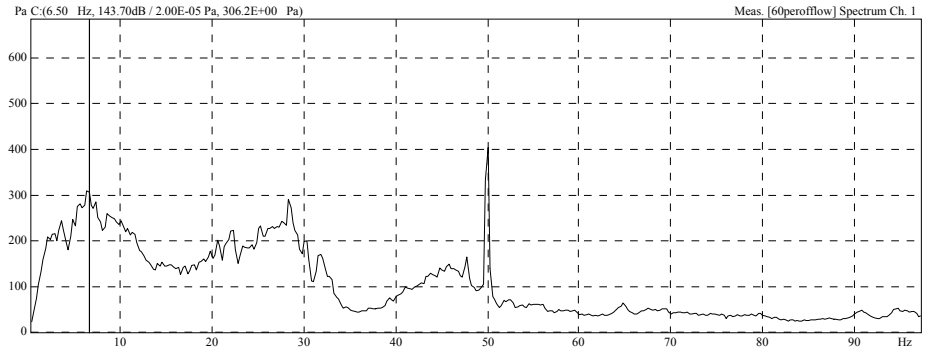

Fig. 4 Spectrum of pressure signal at flow rate of 60% (Pa).

TABLE 1. Overall vibration of test section.

Flow rate (%)	Velocity (mm/sec)		Displacement (microns)	
	Location 1	Location 2	Location 1	Location 2
38	2.2	1.9	76.3	71.3
47	3.3	3.3	**147.6**	141.8
55	**5.1**	3.1	112.1	83.9
70	3.0	2.5	112.1	83.9

pressure signals show identical frequencies. The peaks in the spectra of the pressure signal are associated with the vibration frequency of the bundle and the test section.

3. Conclusions

Estimating fuel vibration due to flow excitation inside a channel is an important safety issue in a nuclear plant. Normally fuel resides in a channel for very long operating days and hence its structural integrity is very important. High vibration could lead to fret and fatigue related failures. Direct measurements inside the reactor are very difficult and not advisable due to complication of instrumentation. Flow test stations with simulating structural and flow conditions are the best way of qualifying fuel and other in core components. A method was devised to measure the fuel vibration directly using dynamic pressure signals sensed in close proximity to the fuel cluster. A correlation was obtained between the pressure signal and vibration amplitude by carrying out calibration test in the laboratory. The calibration indeed helped in estimating the fuel vibration accurately.

References

1. R. D. Blevins, 1977. *Flow-induced vibrations*, Van Nostrand Reinhold Company, New York.
2. X. Q. Wang, R. M. C. So, Y. Liu, 2001. *Flow-induced vibration of an Euler-Bernoulli Beam*, Journal of Sound and Vibration, **234**, 241-268.
3. G. S. Baarholm, C. M. Larsen, H. Lie, 2000. *On fatigue damage accumulation from in-line and cross-flow vortex-induced vibrations on risers*, Journal of Fluid and Structures, **22**, 109-127.
4. J. M. Clinch, 1969. *Measurement of the wall pressure field at the surface of a smooth walled pipe containing turbulent water flow*, Journal of Sound and Vibration, **9**, 319-348.
5. J. K. Sinha, A. R. Rao, R. K. Sinha, 2005. *Prediction of flow-induced excitation in a pipe conveying fluid*, Nuclear Engng. and Design, **235**, 627-636.
6. N. Dharamraju, K. K. Meher, P. Kumar, A. R. Rao, 2005. *Study of Fuel and Channel vibration in Flow* Test Station of 2 MW In-pile Loop of Dhruva, BARC internal report No. RED/VLS/09-05/8, Ref. RED/VLS/3591/2005.
7. K. K. Meher, A. R. Rao, 2004. *Vibration Analysis of modified D3 & D5 cluster of AHWR under single phase and two phase (air-water) flow in FTF*, BARC internal report No.RED/VLS/07-04/02, Ref:RED/VLS/2792/2004.
8. K. K. Meher, A. R. Rao, 2003. *Vibration Analysis of AHWR modified D3 cluster under single phase and air-water flow in FTF*, BARC internal report. Ref:RED/VLS/2550/2003.

BEHAVIOR OF HIGH AND INTERMEDIATE FREQUENCY MODES OF STRUCTURES SUBJECTED TO HARMONIC EXCITATION

M. DHILEEP*
Department of Civil Engineering, Royal Bhutan Institute of Technology, Rinchending, Phuentsholing, Bhutan, India

Abstract. Dynamic analysis of structures subjected to harmonic and seismic loads shows that the contributions of high frequency modes are essentially static. The modal responses of the structures subjected to harmonic excitation are generally combined using square root of sum of squares (SRSS) rule for well separated modes. The combination of modal response s using SRSS will results in erroneous results for even well separated modes, if the high frequency modes having frequency greater than operating frequency are included. This paper makes an attempt to identify the behavior of the modes which have a frequency greater than the operating frequency. The rigid and periodic part of the response are assumed to be statically independent and the behavior of high frequency and intermediate frequency modes of structures subjected to harmonic loads are studied with the help of an example. The problems involved in using the available modal combination rules in combining the modal responses, when high and intermediate frequency modes are included are discussed.

Keywords: high frequency modes, intermediate frequency modes, harmonic analysis, mode superposition method, modal response combination, dynamic magnification factor

1. Introduction

The structural systems which support heavy machineries like turbo generators and crushers etc are subjected to harmonic excitation. The analysis and design of such structural systems involves dynamic analysis using mode super position

* dhileep@rbit.edu.bt

E. İnan et al. (eds.), *Vibration Problems ICOVP-2007*,

method. In dynamic analysis of structures subjected to harmonic loads, a modal analysis with all the modes is considered to yield the "exact" response of a structure. The physical interpretation of truncation of modes[1] shows that truncation of even a single mode may result in incorrect response. To satisfy such a requirement all the modes have to be included in the analysis or the contribution of truncated high frequency modes should be taken into account using appropriate technologies developed[1]. Consideration of all high frequency modes may introduce additional inaccuracies in mode super position method of harmonic analysis, if the modal responses are not combined correctly.

For high frequency modes, the inertial resistance of the structure becomes negligible and the elastic response is the predominant part[2,3]. For the low frequency modes of the system the elastic resistance is negligible and the resistance becomes purely inertial[2]. In seismic analysis of structures the combined response of high frequency rigid modes can be calculated by summing algebraically the responses[3]. The modal responses of harmonic analysis are generally combined using square root of sum of squares (SRSS) for well separated modes[1]. For structures subjected to harmonic excitation as the frequency ratio of excitation frequency to the natural frequency tends to zero, the resistance of the system tends towards static[2]. The behavior of the response in high and intermediate frequency modes of a structure subjected to harmonic excitation towards modal response combination is not known and is the subject of this paper.

This paper focuses on the behavior of high and intermediate frequency modes with the objective of illustrating the reasons as to why it can be inappropriate to simply consider all high frequency modes. The purpose of this part is to address the myth that a dynamic analysis would always give correct structural response when all the modes are considered.

2. Dynamic analysis: Mode superposition method

The equation of motion for an N degrees of freedom, viscously damped system can be written as,

$$\mathbf{M}\ddot{\mathbf{U}} + \mathbf{C}\dot{\mathbf{U}} + \mathbf{K}\mathbf{U} = \mathbf{F}(t) = \mathbf{F}_o \mathbf{R}_b \mathrm{Sin}\omega_{\mathrm{op}}(\mathrm{t}) \tag{1}$$

where **M**, **C** and **K** are the mass, damping and stiffness matrices, respectively, **U** is the displacement vector; and the vector $\mathbf{F}_o$ is the maximum amplitude of the force with an operating frequency, ω_{op} and $\mathbf{R_b}$ is its spatial distribution. The displacement **U** of the system can be expressed as the super position of modal contributions[4] $\mathbf{U}_i$.

$$\mathbf{U} = \sum_{i=1}^{N} \mathbf{U}_i = \sum_{i=1}^{N} \phi_i \, \mathbf{cf}_i \tag{2}$$

where ϕ are determined from the general eigen value problem $\mathbf{K}\phi_i = \omega_i^2 \mathbf{M}\phi_i$ and cf_i is the contribution factor of the response corresponding to mode *i*, is given by,

$$\mathbf{cf}_i = \mathbf{DMF}_i \frac{\phi_i^T \mathbf{F}_o}{\phi_i^T \mathbf{K}\phi_i} \tag{3}$$

where $\mathbf{DMF}_i$ is the dynamic magnification factor of the i^{th} mode, is given by,

$$\mathbf{DMF}_i = \frac{1}{\sqrt{\left(1-\left(\omega_{op}/\omega_i\right)^2\right)^2 + \left(2\varsigma\,\omega_{op}/\omega_i\right)^2}} \tag{4}$$

where ω_i is the natural frequency of the i^{th} mode and $\frac{\omega_{op}}{\omega_i}$ is the frequency ratio β. The combination of the response contributions of all the modes gives the total response Eqn. (2). Generally the modal responses are combined using SRSS and the method is fundamentally sound when the frequencies are well separated[2].

2.1. DYNAMIC MAGNIFICATION FACTOR

The ratio of the resultant harmonic response amplitude to the static displacement which would be produced by the force $\mathbf{F}_o$ is called the dynamic amplification factor. In mode super position method, the individual modes respond to the applied loading independently, so that the dynamic magnification effects can of the applied loading can be evaluated for each mode as a single degree of freedom system. Fig. 1 shows the variation of dynamic magnification factor with respect to the frequency ratio β, for an undamped case. For values of β greater than one, the plot shows the negative of the curve, showing that the response is 180° out of phase with the applied load for these larger frequency ratios. For frequency ratio $\beta = 0$, the **DMF** is equal to one which shows that the harmonic response is equal to static response produced by the maximum amplitude of harmonic force.

The study on response in terms of the ratio of the modal elastic resistance to the harmonic modal applied force with respect to the frequency ratio[2] shows that the applied force is directly balanced by the elastic resistance for a frequency ratio zero. The curve resembles the curves shown in Fig. 1. The ratio of modal inertial resistance to the harmonic modal load decreases from zero for $\beta = 0$ to negative infinity at resonance (i.e. $\beta = 1$), negative sign indicating that the inertial resistance acts in the direction opposing elastic resistance. For the frequency ratio $\beta > 1$, the inertial resistance undergoes a phase reversal equivalent to that shown for the elastic resistance and as β increases the inertial resistance ratio approaches unity asymptotically. The inertial force ratio and the elastic force ratio always are of opposite sign, and they vary with respect to frequency ratio β in such a way that their combined effect is equal to unity. This shows that all the modal responses having a frequency ratio in between $\beta = 0$ and $\beta = \infty$, contains a rigid and a periodic part.

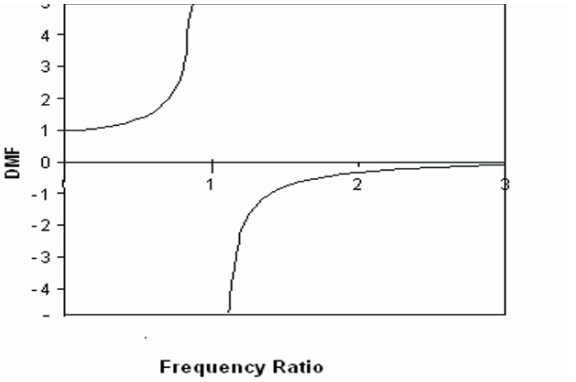

Fig. 1 Dynamic Magnification Factor Vs Frequency ratio response curve.

3. Response of high frequency

At higher frequencies **DMF** is equal to one (Fig. 1), and the corresponding response becomes static. Therefore for a frequency ratio $\beta = 0$, the behavior of high frequency modes is essentially static, i.e. the transient part of the response, the damped periodic response becomes negligible and only the steady state (rigid) part of response remains. The combined response of these rigid modes can be calculated by summing algebraically the responses. The response in rigid modes combines algebraically irrespective of how close or apart the modes are.

Fig. 1 shows that as the frequency ratio increases from zero to one, the **DMF** increases from 1 to infinity for an undamped case, which shows that there is a gradual increase in the periodic part and the rigid content will be equal to zero, when **DMF** is equal to infinity.

A three degrees of freedom system with five percentage damping, as shown in Fig. 2 is considered to illustrate the behavior of high frequency modes. The system is subjected to harmonic excitation with an operating frequency of $2\,Hz$ and $F_o = 100N$ and the spatial distribution of the force is given by $[1\ 1\ 0]^T$. The frequencies of the modes are $38.5\,Hz$, $71.21\,Hz$, $93.04\,Hz$ respectively. The corresponding frequency ratios and corresponding **DMF** are 0.051948, 0.02808, 0.021496 and 1.005, 1.002, 1.001 respectively. The percentage of rigid content in the response corresponding to first, second and third modes are 98.9, 99.68 and 99.82 percentage respectively which shows that the behavior of structure in these modes are essentially static than dynamic. The percentage of rigid content is calculated assuming that rigid and periodic parts are statically independent[3]. Furthermore it is observed that the effect of damping is negligible. The system is analyzed statically using force $\mathbf{F}_o$ and the results are compared with the modal responses which are combined algebraically and SRSS (Table 1). It is observed that the modal responses which are algebraically combined matches with the static analysis results.

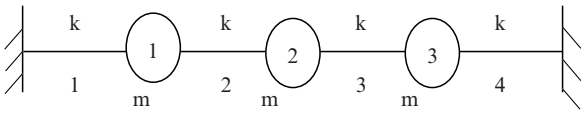

Fig. 2 Three degrees of freedom system.

TABLE 1. Response in mm at corresponding nodes.

Node	Static Analysis using $\mathbf{F}_o$	Modal Analysis	
		SRSS	Algebraic
Node 1	1.250	1.066	1.256
Node 2	1.500	1.466	1.508
Node 3	0.750	1.066	0.755

To study the behavior further, the operating frequency is varied and the results are tabulated in Table 2. The variation of percentage of rigid content with respect to frequency ratio is shown in Fig. 3.

The results in Table 2 shows that as the modes moves near towards the resonance the algebraic combination is not valid. From Fig. 3 it can be observed that even though the rigid content is reducing as the frequency ratio increases. The Periodic part of the response combines algebraically while the periodic part combines as per modal combination rules. Therefore the results may not be correct if the rigid part is ignored or not combined properly and further investigation is required to formulate the appropriate modal response combination rules.

TABLE 2. Response in mm for different excitation frequencies.

Operating frequency Hz	Node number	Static Analysis using $\mathbf{F}_o$	Modal Analysis	
			SRSS	Algebraic
5	Node 1	1.250	1.0956	1.287
	Node 2	1.500	1.507	1.5503
	Node 3	0.750	1.0956	0.7827
10	Node 1	1.250	1.21	1.41
	Node 2	1.500	1.67	1.72
	Node 3	0.750	1.21	0.89
15	Node 1	1.250	1.45	1.67
	Node 2	1.500	2.02	2.07
	Node 3	0.750	1.45	1.12

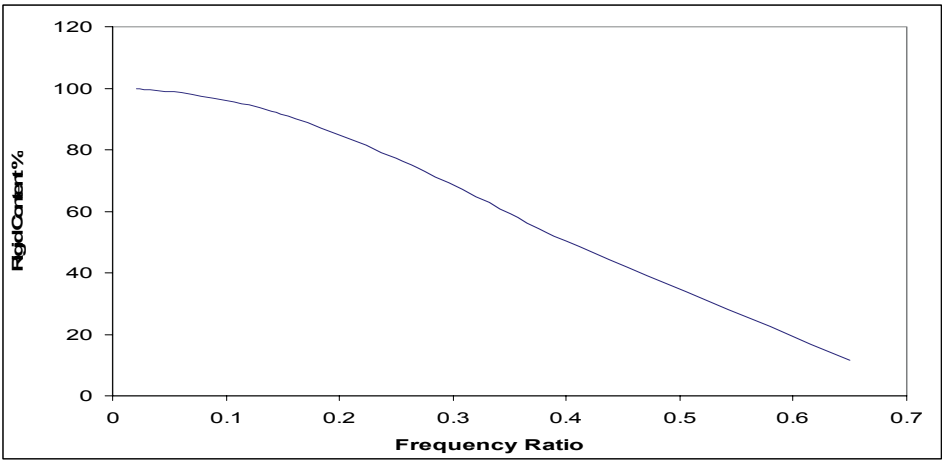

Fig. 3 Rigid Content Vs Frequency Ratio.

4. Conclusions

Dynamic analysis of Structural systems subjected to harmonic excitation involves mode super position method. It is observed that the modal analysis with all the modes of structures subjected to harmonic excitation can lead to incorrect results if the modes are not combined appropriately. Generally the modal response of structures subjected to harmonic excitation is combined using SRSS. It is observed that the behavior of high frequency modes with respect to resonance is static and their modal responses combine algebraically. The modes having frequency less than rigid modes (intermediate frequency modes) contain a rigid part as well as a periodic part. Rigid parts combine algebraically while periodic parts combine according to modal combination rules. Further studies are required regarding the effect of combination of modal responses, for structures subjected to harmonic excitation.

References

1. M. Dhileep, R. B. Pratima, 2006. *Effect of Mode Truncation in Structures Subjected to Harmonic Forces: Physical Interpretation*, Proceedings of the Tenth Asia Pacific conference on Structural Engineering and Construction, 151-156, Bangkok.
2. R. W. Clough, J. Penzein, 1993. *Dynamics of Structures* 2e, Mc-Graw Hill, Singapore.
3. A. K. Gupta, 1992. *Response Spectrum Method: In seismic analysis and design of structures*, Blackwell Scientific Publications, Boston, Mass.
4. M. Dhileep, S. Nagan, 2002. *Synthesis of modes towards the Dynamic Analysis of Turbo – Generator Foundations*, Power Engineer Journal (Institute of Power Engineers, India), **49**, 1-9.

LIMIT CYCLE OSCILLATIONS

DEBABRATA DUTTA*
S.N. Bose National Centre for Basic Sciences, Saltlake, Kolkata 700098, India

J. K. BHATTACHARJEE
Indian Association for the Cultivation of sciences, Kolkata 700032, India

Abstract. We discuss the origin of different kinds of limit cycle oscillations. Limit cycle is a trajectory for which energy of the system would be constant over a cycle - i.e. on an average there is no loss or gain of energy. Limit cycle is an outcome of delicate energy balance due to the presence of nonlinear term in the equation of motion. In practise most systems are dissipative and we require this delicate energy balance between the energy dissipation and the energy input of the system to draw it to the attractor, which in principle can both be stable fixed point or limit cycle. It is generally believed that limit cycle can only be produced by the nonlinearity of the system. We will demonstrate here that linear systems under memory effects can lead to similar scenario. The memory dependent model suggests the possibility of other types of dynamical systems that produces limit cycles.

Keywords: limit cycle, oscillations

1. Introduction

The most natural motion for confined conservative systems is oscillatory. Conservative systems are characterized by the existence of a potential and the two most common potentials are those of the oscillator and the gravitational force. The oscillator potential for a particle of mass 'm' is written as

*Corresponding author, debabrata@bose.res.in

E. İnan et al. (eds.), *Vibration Problems ICOVP-2007*,

$V(x) = \frac{1}{2} m x^2 \omega^2 x^2$ for one dimensional simple harmonic motion with frequency ω and as $V(x) = \frac{1}{2} m\omega^2 x^2 + \frac{\lambda}{2\mu} x^{2\mu}$ for symmetric anharmonic motion ($\mu \geq 2$). If we want to include asymmetry then an odd power of x has to enter the potential. In two or higher dimension, we need to replace x^2 by $r^2 = \sum x_{i^2}$ where $i = 1, 2, \ldots, D$; D being the dimensionality of space. The gravitational potential is pertinent in three dimensions, where the potential created by a mass M located at the origin is $\frac{-GMm}{r}$. The orbits as we know from celestial mechanics are in general periodic. In fact, oscillatory motion is ubiquitous feature in conservative systems. The most sophisticated method of dealing with these systems uses variables called action and angle - the latter making it amply clear that periodicity is essential. The characteristic feature of the simple harmonic oscillator potentials is that the frequency is a constant determined by the characteristics of the system, while the size of the orbit (amplitude of motion) is determined by initial conditions (energy of the system), while for the nonlinear oscillation and the gravitational potential, the frequency of the motion can depend on the initial condition. An example will clarify what we mean. For the one dimensional simple harmonic motion the equation of motion is $\ddot{x} + \omega^2 x = 0$ leading to the solution $x = A\cos\omega t + B\sin\omega t$, where A and B are constants of motion. If we use the initial condition $x = a$ at $t = 0$ and $\dot{x} = 0$ at $t = 0$, The solution is $x = a\cos\omega t$. The first integral of the equation of motion is the energy per unit mass that can be written as $E = \frac{1}{2}\dot{x}^2 + \frac{1}{2}\omega^2 x^2 = \frac{1}{2}\omega^2 a^2$ according to the given initial conditions and hence $x = \sqrt{2E/\omega}\cos\omega t$. The frequency ω is fixed by the system characteristic (applied potential) while the amplitude is fixed by the initial condition. For the gravitational potential (a typical example of anharmonic oscillator!) on the other hand, if we focus on the circular orbit, then we can write the equation of motion for an orbit of radius R as $\frac{mv^2}{R} = \frac{GMm}{R^2}$ with the energy given by $E = \frac{mv^2}{2} - \frac{GMm}{2R}$. As expected, the size of the orbit is determined by the energy. The frequency ω is found from $v = \omega R$ and is easily seen to be $\omega^2 = \frac{GM}{R^3}$, so that we find that ω is dependent in the size of the orbit and thence on the initial condition.

The oscillations that we encounter in many practical situations are however, oscillations in dissipative systems because friction is an almost indispensable part of natural processes. Now dissipative systems would in general try to cause cessation of motion and hence sustaining oscillations in such systems require a rather delicate balance. These oscillations in dissipative systems are called limit cycles and are stable attractors of the dynamical systems. This would imply that all initial conditions (or at least an infinite subset of initial conditions) would be drawn to the attractor which would consequently be independent of initial condition which constitute the basin of attraction. While this is indeed true for a large class of limit cycle oscillations, it is not as universal phenomenon, as we shall see below, Further it is generally believed that limit cycles can only be produced in systems with nonlinearity - the nonlinear term being essential to produce the delicate balance between dissipation and supply of energy that will sustain the limit cycle. However, we shall demonstrate below that memory effects in a linear system can also produce a limit cycle.

2. The Vander Pol oscillator

The natural language for discussing limit cycles is that of dynamical systems - a set of coupled ordinary differential equations. If $\{x_i\}, i = 1,2,...,N$ is the set of variables describing the system, then the dynamical system has the form

$$\dot{x}_i = f_i\left(\{x_i\}\right) \tag{1}$$

This system is conservative if $\sum \frac{\partial \dot{x}_i}{\partial x_i} = 0$. If the sum is negative we have a dissipative system and an energy generating one if the sum is positive. This can be understood by following the trajectories of a bunch of initial conditions. The dynamics of a single particle obeying Newton's laws of motion can always be cast as a dynamical system since $m\ddot{x} = F\left(x,t\right)$ can be written as

$$\dot{v} = \frac{F\left(x,t\right)}{m} \tag{2}$$

Clearly x and v are the x_1 and x_2 of (2). The long time dynamics of (1) can settle down on a stable fixed point of the system or on an oscillatory state called the limit cycle. For dimensionality (N) greater than two, we can have more complicated trajectories - quasi-periodic or even chaotic. The fixed points or the limit cycles are the usual attractors of the systems. The fixed points are found

from $f\left(\left\{x_i^*\right\}\right)$ and stable implies that the determinant $\left.\frac{\partial f_i\left(\left\{x_i^*\right\}\right)}{\partial x_j}\right| = 0$ gives rise to eigenvalues with negative real parts. In two dimensions an unstable fixed point together with a bounded orbit generally signals a limit cycle. A very common method of producing a limit cycle in a physical system is to have positive and negative damping in different regions of the space spanned by x_i (the phase space). We begin with a linear oscillator. A damped linear oscillator has the equation of motion

$$m\ddot{x} = -k\left(x^2 - 1\right)\dot{x} - m\omega^2 x \tag{3}$$

Writing $\Gamma = \frac{k}{m}$ and using the prescription of (2) with $x_1 = x$ and $x_2 = v$, we have

$$\begin{aligned} \dot{x}_1 &= x_2, \\ \dot{x}_2 &= -\Gamma x_2 - \omega^2 x_1 \end{aligned} \tag{4}$$

there is only one fixed point $x_2 = x_1 = 0$. The stability matrix is

$$\begin{pmatrix} 0 & 1 \\ -\omega^2 & \Gamma \end{pmatrix}$$

leading to the eigenvalue eq. $\lambda\left(\Gamma + \lambda\right) + \omega^2 = 0$ or $2\lambda = -\Gamma \pm i\sqrt{4\omega^2 - \Gamma^2}$. For $\Gamma > 0$ (positive damping) and $\omega > \Gamma/2$, we have a stable spiral and the motion eventually comes to rest at the origin ($x_2 = x_1 = 0$), while for $\Gamma < 0$ (negative damping), we have an unstable spiral and the trajectory is unbounded as $t \to \infty$. This is in exact conformity with one's usual experience.

We now consider the nonlinear Vander Pol oscillator with the equation of motion

$$m\ddot{x} = -k\dot{x} - m\omega^2 x \tag{5}$$

The corresponding dynamical system is

$$\dot{x}_1 = x_2 \tag{6}$$

$$\dot{x}_2 = -\Gamma\left(x^2 - 1\right)x_2 - \omega^2 x_1 \tag{7}$$

There is only one fixed point $x_2 = x_1 = 0$. The stability of the fixed point is found from the eigenvalues of the matrix (7)

$$\begin{pmatrix} 0 & 1 \\ -\omega^2 & -\Gamma \end{pmatrix}.$$

The fixed point is an unstable spiral. However trajectories starting close to $x_2 = x_1 = 0$ and spiraling outwards cannot go indefinitely as the trajectories are damped for all $|x_1| > 1$. Thus we have the recipe for a limit cycle. For $k \ll 1$, we can find the limit cycle from a physical argument. The energy of an oscillator can be written as (8) $E = \frac{1}{2}\dot{x}^2 + \frac{1}{2}\omega^2 x^2$ and from (5), we note that

$$\frac{dE}{dt} = m\{\dot{x}\{\ddot{x} + \omega^2 x\} = -k\left(x^2 - 1\right)\dot{x}^2 . \tag{8}$$

Clearly (10) $\frac{dE}{dt} < 0$ for $|x| > 1$ and $\frac{dE}{dt} > 0$ for $|x| < 1$. A limit cycle would be a trajectory for which E would be constant over a cycle - i.e. on an average there is no loss or gain of energy. For $k \ll 1$, we expect from (5), the frequency to be ω and hence we require

$$\oint_{cycle} \frac{dE}{dt} dt = 0, \quad \int_0^{2\pi/\omega} \left(x^2 - 1\right)\dot{x}^2 = 0 \tag{9}$$

If we try an orbit $x = A\cos\omega t$, then (9) implies

$$\begin{aligned} \int_0^{2\pi/\omega} A^4\omega^2 \sin^2\omega t \cos^2\omega t dt &= \int_0^{2\pi/\omega} A^2\omega^2 \sin^2\omega t dt \\ \Rightarrow A^2 = 4, \quad \text{i.e.} \quad A &= 2 \end{aligned} \tag{10}$$

The limit cycle is fixed, independent of the initial conditions. For $k \ll 1$ the limit cycle has the fixed frequency ω and the fixed amplitude 2.

A more systematic approach to finding the limit cycle is to seek a solution for $x(t)$ of the form $x(t) = A(t)\cos\left(\omega t + \theta(t)\right)$, where $A(t)$ and $\theta(t)$ are slowly varying functions of t for $k \ll 1$ and the limit cycle would correspond to $A(t)$ and $\theta(t)$ becoming constants. We insert this solution in (5) and use [1]

$$\dot{x} = \dot{A}\cos(\omega t + \theta) - A(\omega + \dot{\theta})\sin(\omega t + \theta)$$

$$\ddot{x} = \ddot{A}\cos(\omega t + \theta) - 2\dot{A}(\omega + \dot{\theta})\sin(\omega t + \theta) - A\ddot{\theta}\sin(\omega t + \theta)$$
$$- A(\omega + \dot{\theta})^2\cos(\omega t + \theta) - 2\dot{A}\omega\sin(\omega t + \theta) - A\omega^2\cos(\omega t + \theta)$$
$$- 2A\omega\dot{\theta}\cos(\omega t + \theta)$$

to write

$$-2\dot{A}\omega\sin(\omega t + \theta) - A\omega^2\cos(\omega t + \theta) - 2A\omega\dot{\theta}\cos(\omega t + \theta)$$
$$-\Gamma\omega[\frac{A^2}{2}(1 + \cos 2(\omega t + \theta)) - 1]A\sin(\omega t + \theta) + A\omega^2\cos 2(\omega t + \theta) = 0$$

or

$$-2\dot{A}\omega\sin(\omega t + \theta) - 2A\omega\dot{\theta}\cos(\omega t + \theta) - \Gamma\omega\frac{A^3}{2}\sin(\omega t + \theta)$$
$$-\Gamma\omega\frac{A^3}{4}[\sin 3(\omega t + \theta) - \sin(\omega t + \theta)] + \omega\Gamma A\sin(\omega t + \theta) = 0$$

Equating coefficients of sine and cosine separately

$$2\dot{A} = \Gamma A - \frac{\Gamma A^3}{4}$$

Clearly A is a constant for $A^2 = 4$ and it is stable situation. Thus, we have the same oscillator as before but now additionally we know its stability.

3. Predator-Prey oscillator

3.1. INTRODUCTION

Lotka-Volterra dynamics describes a predator-prey system where the prey thrives on the naturally available resources while predator thrives only on its interaction with the prey and would be extinct in a non interacting system. It is easy to realize that in such a system the prey population would thrive of the predators decrease while an increase in the predator number would cause the prey population to diminish. The predator cannot flourish for ever because a decreasing number of prey would lead to fewer interaction and would drive the predator towards extinction. This produces the limit cycle like oscillations. The Lotka Volterra limit cycle is however very different from the usual limit cycles in that it depends on the initial conditions. This makes Lotka Volterra dynamics interesting. The unbounded growth of the prey population in the absence of the

predator depends on a constant source of nutrients. In any practical situation, there will be some periodic fluctuations in the nutrients because of natural causes. If it is a wolf-rabbit situation, then the rabbit's supply of grass will have a seasonal variation. Interestingly enough, the periodic variation in the growth rate of the prey has not been studied in literature. There has been study of random variation but not periodic ones. In this work, we study the effect of periodic variations [1].

4. Dependence of initial condition

In this section, we focus on the limit cycle of the Lotka-Volterra model. As is well known, this limit cycle is unusual in the sense that it depends on the initial conditions. We show how the Poincare-Linstedt technique can be applied to the model to obtain an initial condition dependent frequency for the limit cycle. This calculation is valid for small amplitudes and our numerical calculation supports the validity of this result.

We take the simplest form of two species Lotka-Volterra system;

$$\begin{aligned} \dot{x} &= x - xy \\ \dot{y} &= -y + xy \end{aligned} \tag{11}$$

According to a linear stability analysis, the fixed point at (1,1) is a center. We first transform (11) to the variables $x_1 = x - 1$ and $y_1 = y - 1$ to write,

$$\begin{aligned} \dot{x}_1 &= -y_1 - x_1 y_1 \\ \dot{y}_1 &= x_1 + x_1 y_1 \end{aligned} \tag{12}$$

We note immediately that if we drop the nonlinear terms, then we have a simple harmonic oscillator of frequency unity. We are now in a position to carry out a Poincare-Linstedt analysis. We imagine the existence of a parameter λ multiplying the non-linear terms in (13) and introducing the frequency ω of the full dynamics, rewrite (12) in the form;

$$L\begin{pmatrix} x_1 \\ y_1 \end{pmatrix} = \begin{pmatrix} \dfrac{\partial}{\partial t} & \omega \\ -\omega & \dfrac{\partial}{\partial t} \end{pmatrix} \begin{pmatrix} x_1 \\ y_1 \end{pmatrix} = \lambda \begin{pmatrix} -1 \\ 1 \end{pmatrix} x_1 y_1 + (\omega - 1) \begin{pmatrix} y_1 \\ -x_1 \end{pmatrix} \tag{13}$$

For $\lambda << 1$ we expand

$$\begin{aligned} \omega &= 1 + \lambda\omega_1 + \lambda^2\omega_2 + ... \\ x_1 &= x_{10} + \lambda x_{11} + \lambda^2 x_{12} + ... \\ y_1 &= y_{10} + \lambda y_{11} + \lambda^2 y_{12} + ... \end{aligned} \tag{14}$$

The right hand side of (14) has term of order λ and higher. At order unity, the solution is $x_{10} = \Re e^{i\omega t}$, $y_{10} = \Re \frac{A}{i} e^{i\omega t}$, where A is the amplitude of motion. At $O(\lambda)$, we have

$$L\begin{pmatrix} x_{11} \\ y_{11} \end{pmatrix} = \begin{pmatrix} -1 \\ 1 \end{pmatrix} x_{10}\, y_{10} + \omega_1 \begin{pmatrix} y_{10} \\ -x_{10} \end{pmatrix} \tag{15}$$

The solvability condition for an inhomogeneous second order differential equation now leads to $\omega_1 = 0$. The solution for x_{11} and y_{11} is found to be

$$\begin{aligned} x_{11} &= \Re \frac{A^2}{12i\omega}(1+2i)e^{2i\omega t} \\ y_{11} &= \Re \frac{A^2}{12i\omega}(1-2i)e^{2i\omega t} \end{aligned} \tag{16}$$

At $O(\lambda^2)$

$$L\begin{pmatrix} x_{12} \\ y_{12} \end{pmatrix} = \begin{pmatrix} -1 \\ 1 \end{pmatrix}(x_{10}y_{11} + x_{11}y_{10}) + \omega_2 \begin{pmatrix} y_{10} \\ -x_{10} \end{pmatrix} \tag{17}$$

The solvability condition requires that the $e^{i\omega t}$ part of the right hand side be orthogonal to the left eigenvector of L. This leads to

$$\omega_2 = \frac{-|A|^2}{12\omega} \tag{18}$$

The perturbative result for ω up to $O(\lambda^2)$, after setting $\lambda = 1$ is

$$\omega = 1 - \frac{|A|^2}{12\omega} \tag{19}$$

where A is the amplitude of the limit cycle. If x_0 and y_0 be the initial values of x and y, then we can write

$$\omega = 1 - \frac{(x_0 - 1)^2 + (y_0 - 1)^2}{12} \tag{20}$$

The result are shown in Fig. 1. The good agreement between the computed frequencies and the obtained from (20) is apparent.

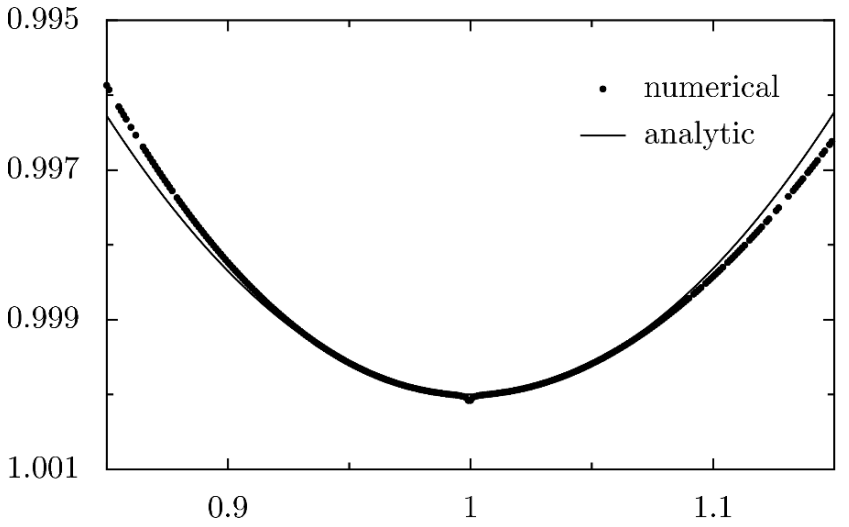

Fig. 1 Initial number of population density modifies its periodicity. Initial population density ($x_0 = y_0$) is plotted with corresponding frequency (ω) of its oscillation.

5. Limit cycle from memory effects

In this section we point out the existence of a different class of limit cycles - limit cycles produced by a memory effects [2]. we consider the damped oscillator (3)

$$\ddot{x} + \Gamma\{\dot{x}\theta\left[x(t) - x(t-\tau)\right] + \omega^2 x = 0 \tag{21}$$

In the above $\theta(y) = 1$ for $\theta > 0$ and -1 for $\theta < 0$. The time interval τ is fixed for a given system. We note that (21) implies a positive damping if the value of x decreases. This should make it qualitatively akin to the Vander Pol oscillator and a limit cycle should emerge. This is exactly what happens numerically as can be seen from the following figures.

As far as damping remains small the phase space trajectory is a limit cycle. As damping becomes larger shape of limit cycle changes and for higher damping trajectory periodicity breaks. Fig. 2a.

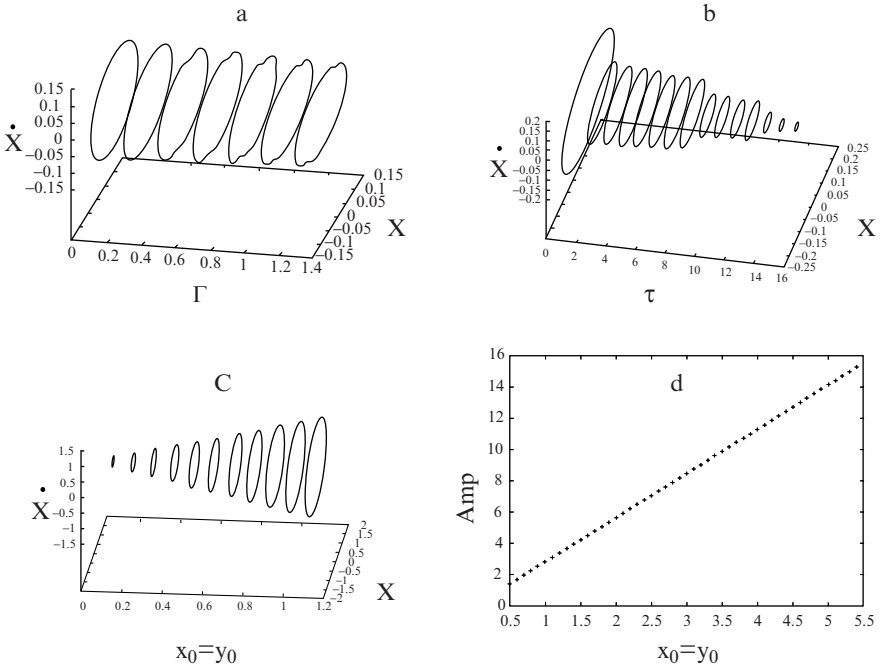

Fig. 2 With increase of damping Γ (a), limit cycle gets destabilized. As time interval τ (b) varies, amplitude of the limit cycle varies. (c) Amplitude of the limit cycle $(x_0 = y_0)$ also changes linearly (d) with initial condition.

For small damping as we change time interval τ to have delayed memory effect, though we still get perfect limit cycles, the amplitude of limit cycles changes with time interval. As the time interval increases amplitude of corresponding limit cycle decreases. Fig. 2.b. It is worth noting that As in predator prey model, here also amplitude of limit cycle is determined by initial condition. This dependence is linear and shown in Fig. 2c-d.

6. Conclusion

In conclusion, We have delineated different forms of limit cycles in non conservative systems in this article. We have also shown an example of non-standard scenarios of getting limit cycles. It suggests new possibilities of energy balance that manifests limit cycles.

References

1. Complex Systems, Eds. (J. K. Bhattacharjee and A. K. Mallik), Narosa, 1995.
2. D. Dutta and J. K. Bhattacharjee, *ArXiv*. nlin.CD/0610044.
3. D. Dutta and J. K. Bhattacharjee, *to be published*.

PUSHOVER ANALYSIS METHODOLOGIES: A TOOL FOR LIMITED DAMAGE BASED DESIGN OF STRUCTURE FOR SEISMIC VIBRATION

SEKHAR CHANDRA DUTTA*
Department of Civil Engineering, Bengal Eng. and Science University, Shibpur, Howrah 711103, West Bengal, India

SUVONKAR CHAKROBORTY
SMS DEMAG Private Limited, West Bengal, India

ANUSRITA RAYCHAUDHURI
Department of Civil Engineering, Bengal Eng. and Science University, Shibpur, Howrah 711103, West Bengal, India

Abstract. Vibration transmitted to the structure during earthquake may vary in magnitude over a wide range. Design methodology should, therefore, enumerates steps so that structures are able to survive in the event of even severe ground motion. However, on account of economic reason, the strengths can be provided to the structures in such a way that the structure remains in elastic range in low to moderate range earthquake and is allowed to undergo inelastic deformation in severe earthquake without collapse. To implement this design philosophy a rigorous nonlinear dynamic analysis is needed to be performed to estimate the inelastic demands. Furthermore, the same is time consuming and requires expertise to judge the results obtained from the same. In this context, the present paper discusses and demonstrates an alternative simple method known as Push-over method, which can be easily used by practicing engineers bypassing intricate nonlinear dynamic analysis and can be thought of as a substitute of the latter. This method is in the process of development and is increasingly becoming popular for its simplicity. The objective of this paper is to emphasize and demonstrate the basic concept, strength and ease of this state of the art methodology for regular use in design offices in performance based seismic design of structures.

*Corresponding author, scdind2000@yahoo.com

E. İnan et al. (eds.), *Vibration Problems ICOVP-2007*,

Keywords: seismic vibration, non linear dynamic analysis, pushover analysis, dual design philosophy, response reduction factor

1. Introduction

Earthquake poses a unique nature of vibration problem to the technologists and engineers which has specialities in characteristic features primarily in the following aspects.

Firstly, the pulses, with frequencies varying in a very wide range, participate in the ground excitation resulting from the earthquake and hence, neither they can be expressed in any functional form nor the same time-acceleration history is repeated ever.

Secondly, the peak magnitude of earthquake ground shaking may vary in a very wide range. For the moderate intensity of shaking, it may be feasible to design the structures to behave elastically while for the extreme range of shaking, if the structures are designed in such a way that they still remain elastic; the cost shoots up so sharply that they can not be afforded. Hence, dual design philosophy is introduced as a practical engineering solution to strike a balance between economy and safety.

In this proposition, buildings are designed and detailed in the elastic range under moderate earthquake. Under severe earthquake the structural system is allowed to have some plastic deformation in its elemental configuration. So, the philosophy ensures that no collapse or failure mechanism will occur though damage may occur in the structural and non structural elements of a particular structure under severe earthquake. Successful implementation of this philosophy needs ultimate deformation capacity of all structural elements to be more than the demand of accommodating the inelastic deformation during the expected ground excitation. Philosophy may be more clearly understood from Fig. 1.

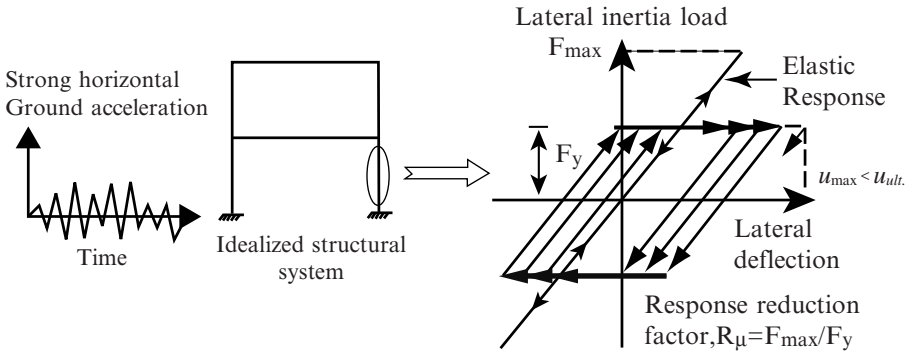

Fig. 1 Schematic representation of concept of dual design philosophy.

This requires an estimate of the maximum displacement caused due to design earthquake and in order to achieve that correctly the application of nonlinear inelastic dynamic time history analysis is resorted to. However, on account of rigor involved in the computational procedure it attracts high computational cost and time and also the difficulties involved in verification of the results obtained from analysis one needs to have a deep insight and understanding on the philosophy of how a structure behaves inelastically when subjected to severe ground motion.

In order to avoid the computational difficulties and at the same time to obtain a reliable result an easy enough user friendly method is required to be adopted. Though some parallel propositions are already made in this regard, pushover analysis, which is a typical nonlinear static analysis procedure, has been adopted, considering it to be more compatible in the design offices. In addition to this, pushover analysis is a newly developed technology in the field of seismic resistant design of structures for initial planning as well as retrofitting of existing structural systems, which also takes proper care of the performance based design philosophy. Keeping in view, the functional purposes of various types of structural systems, the ultimate performance point is evaluated in this method. This paper is an effort to provide a theoretical background with a detail discussion of various existing methodologies of Pushover Analysis in its limited scope of study.

2. Pushover analysis – a substitute for nonlinear dynamic analysis

The most basic as well as rigorous and accurate inelastic analysis method is the nonlinear response history analysis, which is a quite powerful tool in the seismic evaluation of structures under ground excitation. But, the understanding and hence application of this method requires time for developing background. Further, enormous amount of computational time and effort required for such analysis makes it a bit complex and impractical for general use by the practising engineers. Of course, this method has privilege in comparison to others from technical point of view also. In pushover analysis, incremental static lateral loads are applied at the roof level and then capacity curve, which is applied load versus roof displacement, is plotted. After first yielding occurs in any one of the elements of the structural system under consideration, the lateral loading is increased and the stiffness of the structure is revised or specifically decreased equivalently. Thus the plotting is continued till the structure becomes a mechanism i.e. total collapse occurs. So, using pushover analysis methodology, one can automatically uphold a continuous observation over the elemental yielding throughout the analysis procedure.

3. State of the art on pushover analysis

Pushover Analysis employs a static nonlinear analysis procedure using an equivalent single-degree of freedom system along with the combination of a spectrum based linear dynamic analysis, to estimate the dynamic response of multi-degree of freedom system as has been referred in ATC-40[1], FEMA-273[2] and FEMA-356[3]. The basic idea of this equivalent static nonlinear analysis procedure involves plotting of the capacity curve and the demand curve of the structural system. Capacity curve represents the resistance of the structural system under external loading. On the other hand, demand curve represents the maximum displacement which is needed to be accommodated during an earthquake excitation. In the method of Pushover Analysis the allowable deformation limit for the structure is considered to be the intersection point of the capacity curve and the demand curve, specifically known as the 'Performance Point'. Normally, for MDOF (multi-degree of freedom) systems responding in multi-mode during shaking, Pushover Analysis is able to consider the deformation only in a particular mode ignoring the change in deformed shape of the structure during vibration. The literature[4] has studied well the applicability of this analysis procedure for the first mode dominating structures. Even, the failure of this method in structures dominated by higher modal effect, has also been clarified in the same literature[4]. Further, some recent studies[5,6] presented a rigorous analysis regarding the issue of such higher mode participation. In this regard, modal pushover analysis[6], which considers the contribution of higher modes of vibration, estimates the performance parameters e.g. storey drift demands, maximum displacement etc. to sufficient accuracy in most building design and retrofit applications for low to medium rise buildings and also maintain the conceptual simplicity of pushover analysis. However, this method offers less accurate results compared to nonlinear dynamic analysis if applied in vertically irregular frames with irregularity in mass, strength and stiffness in combination and separately[7]. A new method, an upper bound pushover procedure proposed by some authors[8] takes into consideration the effect of higher mode dependence of seismic demands on the frequency contents of ground motion and characteristics of structural systems and proposes to determine a new load pattern and target displacements. The new method provides better results for high rise buildings with significant higher mode effects.

It is important to understand the central approximations linked with the procedures of Pushover Analysis methodologies. The first fold of approximation lies in the philosophy of replacing the actual but rigorous as well as complex nonlinear dynamic method through a set of relatively simple and easy to understand

equivalent nonlinear static and linear dynamic analyses. On the other hand, the second fold of approximation roots from the consideration of a single predominant mode to represent the response of a multimodal system. Extensive research[5,6] on this second fold of approximation is made.

The accuracy of pushover analysis rests to a great extent on the distribution of inertia forces along the height of the structure. A study of five load patterns as described in the literature[9] viz. first mode, inverted triangular, rectangular, code and adaptive indicates that the simplification in the first mode pushover load pattern can be made without an appreciable loss of accuracy for low to medium rise frame structure.

Incremental dynamic analysis (IDA) as has been described in the literature[10] is another performance based design for estimation of seismic demand and capacity of structure. It uses a series of nonlinear dynamic analysis under suitably multiply – scaled ground motion records. The global dynamic instability is characterised by studying an IDP curve, on two scalars – intensity measure (IM) and engineering demand parameters (EDP), where, IM represents the scaling factor of the ground motion record and EDP monitors the structural response parameters.

4. Demonstration of pushover analysis for an example problem

This relatively easier methodology is also needed to be understood philosophically as well as sequentially for its adequate application because of its novelty. This section is an effort to demonstrate this beautiful concept through a simple example problem.

4.1. DYNAMIC CHARACTERISTICS OF SYSTEM

Idealized one-story structural system with a rigid deck supported by four columns with total lateral stiffness k and rigid deck mass m has been considered. The structural system can be idealized as an equivalent single degree of freedom system as an inverted pendulum as shown in Fig. 2 with mass m concentrated at the deck level. The total stiffness of the structural components is considered to be the lateral stiffness of the stick to which the mass is connected.

4.2. GROUND MOTIONS

One artificially generated earthquake time history consistent with the design spectrum of the Indian earthquake code of practice, i.e., IS 1893-1984[11], is generated by a procedure detailed in the literature[12]. The design spectrum of the

Indian earthquake code is derived from the well accepted design spectrum developed in reference[13]. The acceleration time history as well as the response spectrum generated from it, superposed with the target codal design spectrum as presented in Fig. 2, which is extracted from the literature[14], exhibits close resemblance. Thus, this time history is expected to have the characteristics in terms of the frequency contents as intended through this well accepted spectrum and hence adopted in the present investigation likewise a few recent investigations[14,15].

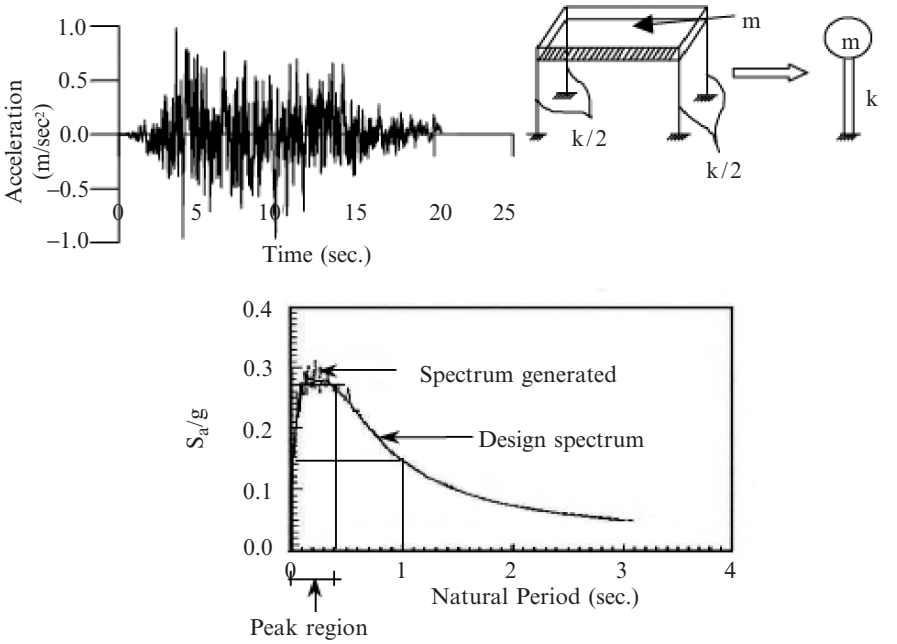

Fig. 2 Schematic representation of a single story structural system idealized as an equivalent single degree of freedom model under acceleration time history considered along with the response spectrum for the ground motion.

4.3. HYSTERESIS MODEL

A bilinear elastic - fully plastic hysteresis model has been used to analyse the inelastic behaviour of the structural system as shown in Fig. 3.

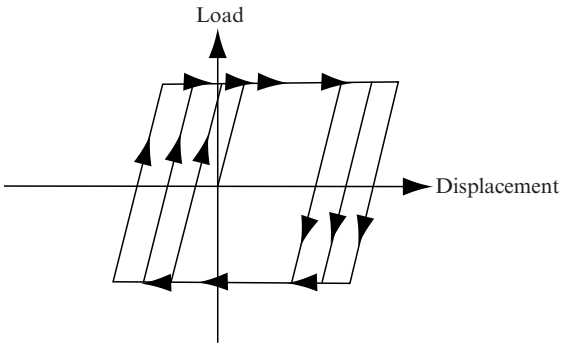

Fig. 3 Actual idealized hysteresis model of structural system.

4.4. RESPONSE REDUCTION FACTOR

The term response reduction factor, R_μ is defined as the ratio of the elastic force demand of a structure to its actual lateral strength provided. The allowable limit for the inelastic deformation of the structure under a specified load condition depends on this ratio. Structures may have response reduction factors as high as 6 and 8 depending on their functional purposes. However, for this study, structural components have been designed with $R_\mu = 4$.

4.5. DEMONSTRATION OF THE EXAMPLE

Modeling and procedural approach

An idealized SDOF (single-degree of freedom) system with mass $1kg$ and lateral stiffness of $157.91 N/m$ leading to a lateral natural period of $T = 0.5s$ is considered as an example problem. The elastic strength demand due to spectrum consistent ground motion from time history analysis is computed as $0.852N$ Subsequently, yield strength of the system, due to a response reduction factor $R_\mu = 4$, is set to $0.213N$. 5% damped elastic response spectrum has been obtained directly from the relevant Indian Standard (IS 1893: 1984[11]).

The performance points for the aforesaid structural system under specific ground excitation can be evaluated by four varieties of Pushover Analysis methodologies as has been discussed through the subsequent steps.

Performance point using Procedure A

1. The 5% damped (elastic) response spectrum corresponding to the previous code of earthquake i.e. IS 1893-1984, is developed (Fig. 4). The response spectrum for 5% damping is converted into ADRS (acceleration displacement response spectrum) format - a plot of spectral acceleration (S_a) vs. spectral displacement (S_d) considering S_d as independent variable. This conversion is achieved using the following relationships (Eqn. 1(a) and Eqn. 1(b) as specified in ATC 40[1]).

$$S_a = S'_a / g \tag{1a}$$

$$S_d = (T^2 / 4\pi^2) \times (S'_a / g) \times (g) \tag{1b}$$

2. The capacity curve is transferred into a capacity spectrum in the ADRS format (Fig. 5).

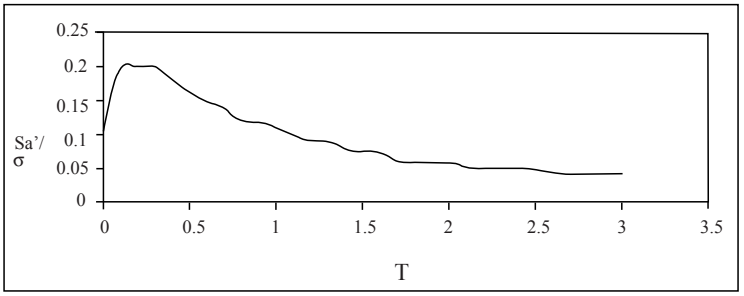

Fig. 4 Response spectrum corresponding to 5% damping in S'_a/g vs. T format.

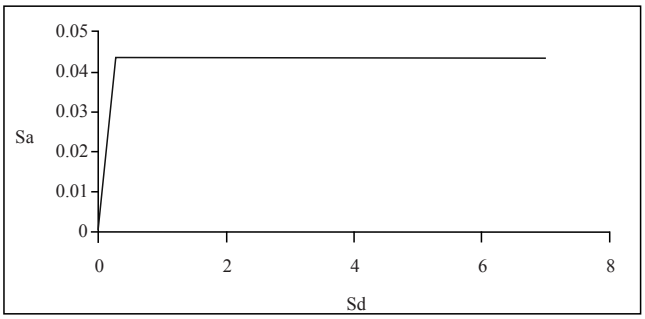

Fig. 5 Capacity curve in ADRS format.

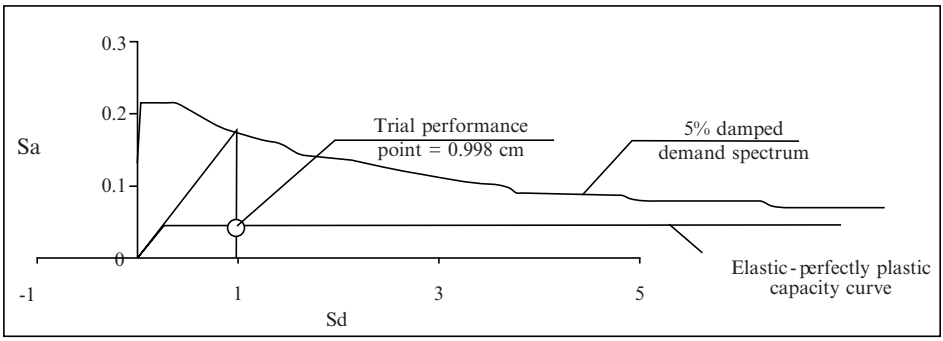

Fig. 6 Diagrammatic representation showing selection of trial performance point.

3. The capacity spectrum is superposed with the 5% damped elastic response spectrum. A trial performance point is chosen as $0.998\,cm$ (from equal displacement approximation rule) (Fig. 6).
4. Spectral Reduction Factors SR_A and SR_V are calculated to consider the effect of increased effective damping over the 5% damped response spectrum. Where, SR_A is the Reduction Factor in Constant Acceleration Region of Elastic 5% Damped Spectrum and SR_V is the Reduction Factor in Constant Velocity Region of Elastic 5% Damped Spectrum. To calculate these factors, Eqn. (2-8) are used.

$$SR_A = \frac{3.21 - 0.68 \ln\left(\frac{63.7\kappa(a_y d_{pi} - d_y a_{pi})}{a_{pi} d_{pi}} \mp 5 \right)}{2.12} \tag{2}$$

$$SR_V = \frac{2.31 - 0.41 \ln\left(\beta_{eff}\right)}{1.65} \tag{3}$$

$$\beta_{eff} = \frac{63.7\kappa(a_y d_{pi} - d_y a_{pi})}{a_{pi} d_{pi}} + 5 = \kappa \beta_0 + 5 \tag{4}$$

where, κ is a factor which depends on the structural behaviour type.

a_y, a_{pi}, d_y, d_{pi} are the spectral acceleration of yield point of the structural system, spectral acceleration of the trial performance point, spectral displacement of the yield point and spectral displacement of trial performance point respectively. β_{eff} is the effective viscous damping.

For this problem, $a_y = a_{pi}, d_{pi} = 0.998\,cm, d_y = 0.269\,cm$, hysteretic damping represented as equivalent viscous damping

$$\beta_0 = \frac{(a_y d_{pi} - d_y a_{pi})}{a_{pi} d_{pi}} \times 63.7 = 46.51\% > 16.25\% \tag{5}$$

$$\begin{aligned} \kappa &= (1.13) - \left((0.51) \times (d_{pi} - d_y)/(d_{pi})\right) \\ &= 0.76 \end{aligned} \tag{6}$$

$$\beta_{eff.} = \kappa \beta_0 + 5 = 0.76 \times 46.51 + 5 = 40.24\%$$

$$SR_A = \left(3.21 - 0.68 \ln(\beta_{eff})\right) / 2.12 = 0.33 \tag{7}$$

$$SR_V = \left(2.31 - 0.41 \ln(\beta_{eff})\right) / 1.65 = 0.48 \tag{8}$$

5. The 5% damped elastic spectrum is decreased by multiplying the ordinates of the constant acceleration range and constant velocity range of the spectrum with SR_A and SR_V respectively to draw the demand spectrum with increased damping on the same plot as has been shown pictorially in Fig. 7.
6. The intersection point of reduced demand spectrum and the capacity curve is taken to be the performance point. As obtained by analysis, the performance point is given by $1.54\,cm$. Fig. 8 will help to encompass an entire idea of the procedure mentioned above.

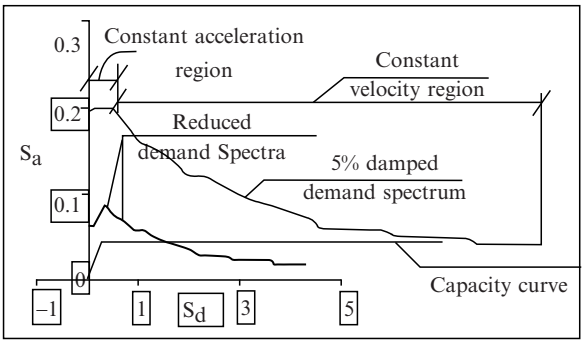

Fig. 7 Schematic representation of reduction of demand spectrum using SR_A and SR_V.

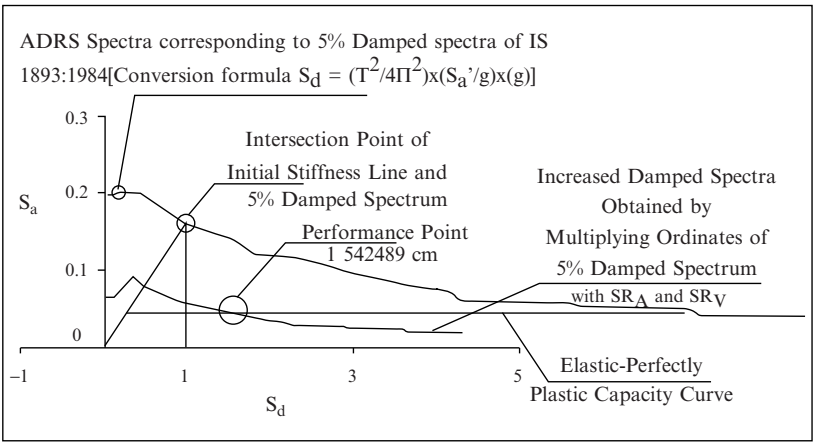

Fig. 8 Schematic representation of Procedure A.

Performance point using Procedure B

1. The 5% damped elastic spectrum and the capacity spectrum are plotted on the ADRS format (Fig. 9).
2. Series of increased damped spectra are superposed with the 5% damped spectrum as has been shown in Fig. 10.
3. From equal displacement approximation rule, the first trial performance point is considered as $0.988\,cm$.
4. A series of displacement values are assumed close to the first trial performance point. For this particular structure, nine such values have been considered.

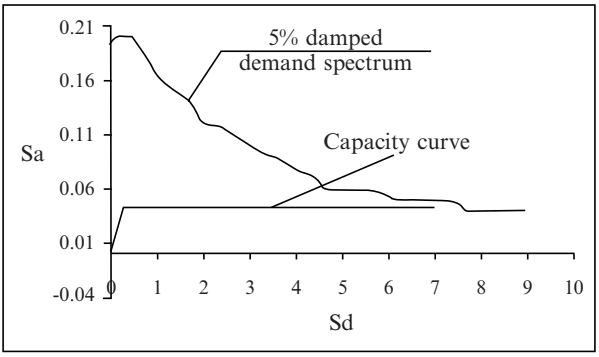

Fig. 9 Response Spectrum corresponding to 5% damping and Capacity Curve in ADRS format.

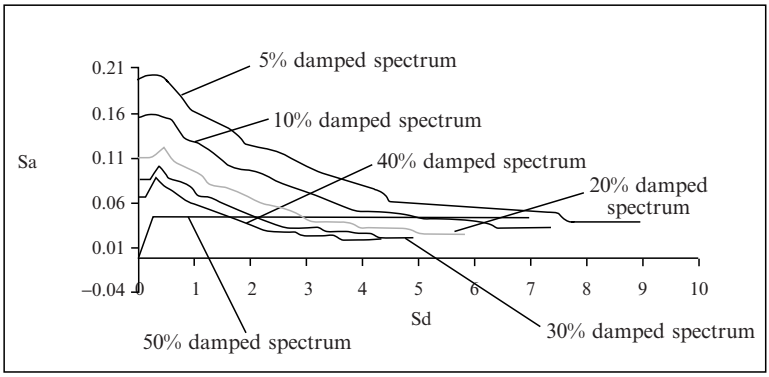

Fig. 10 Plot of series of damped spectra superposed with 5% damped response spectrum and Capacity Curve in ADRS format.

5. Corresponding to individual displacement value, the effective damping values i.e. β_{eff} are calculated. Following the same method as has been described in the Procedure A, spectral reduction factors SR_A and SR_V are determined.
6. For each of those assumed displacement values, the corresponding displacements values, S_d for 5% damping are calculated.
7. The corresponding accelerations S_a/g are interpolated and hence, the respective reduced spectral acceleration and spectral displacement values are calculated with the help of corresponding SR_V values. It is obvious that spectral displacement values (designated as D_{pi} in Fig. 11) obtained must be equal to the initial assumed displacement values.

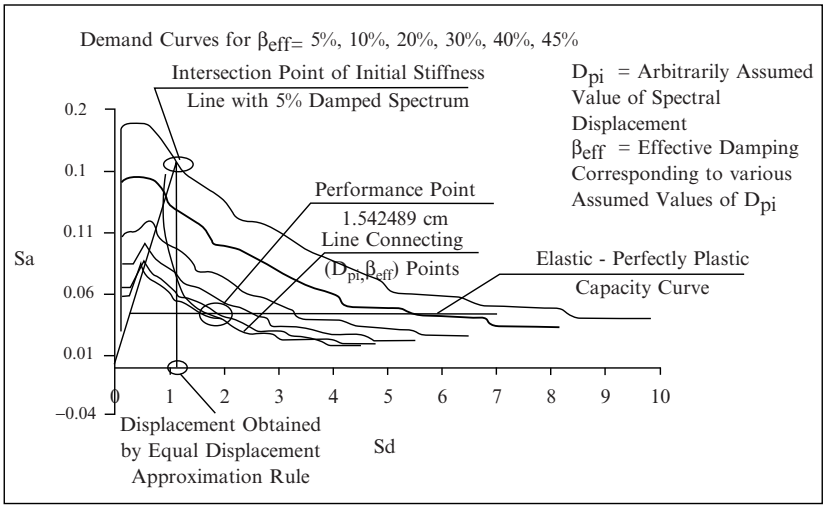

Fig. 11 Schematic representation of Procedure B.

8. These points (D_{pi} vs. β_{eff}) obtained through step 3 to step 7 are plotted in the same ADRS format. All these points are joined with a line and the intersection of this line with the capacity curve produces the performance point.
9. Thus, the final performance point is obtained as $1.54\,cm$ and has been shown in the Fig. 11.

Performance point using Procedure C

In contrast to Procedure A and B, Procedure C is purely a graphical method and hence it is the most convenient methodology for hand analysis. The steps involved are stated hereafter.

1. The 5% damped elastic spectrum and the structural capacity spectrum are plotted over the same ADRS format.
2. On the same plot, family of reduced response spectra corresponding to the increased effective damping are drawn as shown in Fig. 12.
3. An initial displacement is assumed as 1.5 times the displacement obtained by equal displacement approximation and is expressed as $1.5 \times 0.998 = 1.49\,cm$.
4. The yield displacement as obtained from the capacity spectrum is given by $0.269\,cm$.

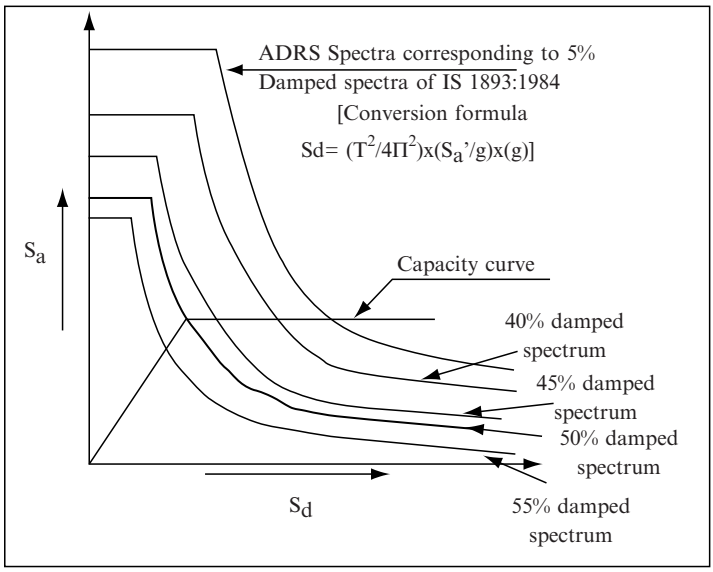

Fig. 12 Schematic representation of Procedure C after step 2.

5. The effective damping β_{eff} is now calculated using the similar formula as has been illustrated in the Procedure A and is given by $\beta_{eff} = 42.18\%$ (Fig. 13).
6. Subsequently, the initial stiffness line i.e. the line with same stiffness as that of the structural system, designated as line 1 is extended to intersect the 5% damped elastic response spectrum (Fig. 14).

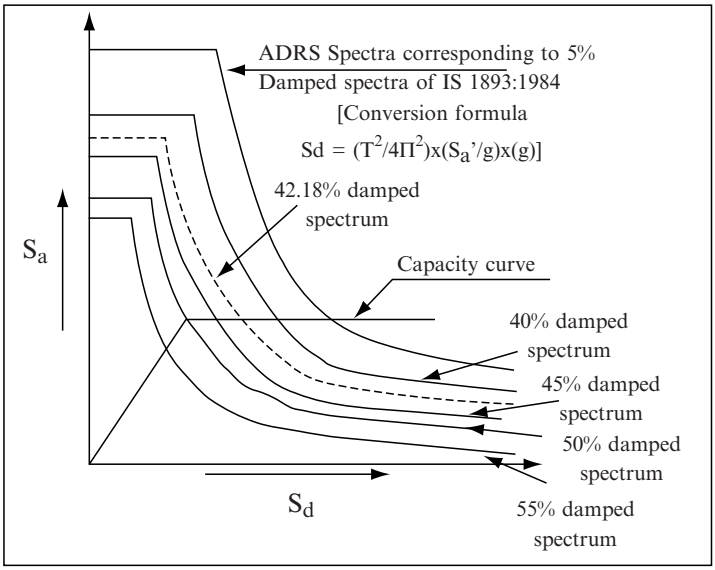

Fig. 13 Schematic representation of Procedure C after step 5.

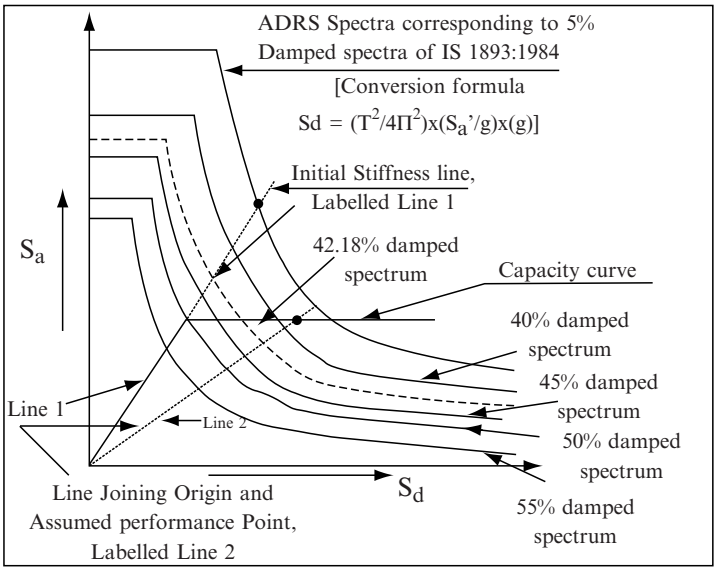

Fig. 14 Pictorial representation of Procedure C after step 7.

7. A line, symbolized as line 2 is drawn connecting the origin and the assumed initial point. (Fig. 14).
8. A line joining the intersection point of line 1 and the 5% damped response spectrum to the intersection point of line 2 and reduced spectrum corresponding to β_{eff} is plotted on the same chart. This line is designated as line 3.
9. The point, where, line 3 crosses the capacity curve, yields the final performance point. Thus, the performance point obtained by Procedure C is given by $1.522\,cm$. The following pictographic view (Fig. 15) will facilitate the detailed understanding of the steps cited above.

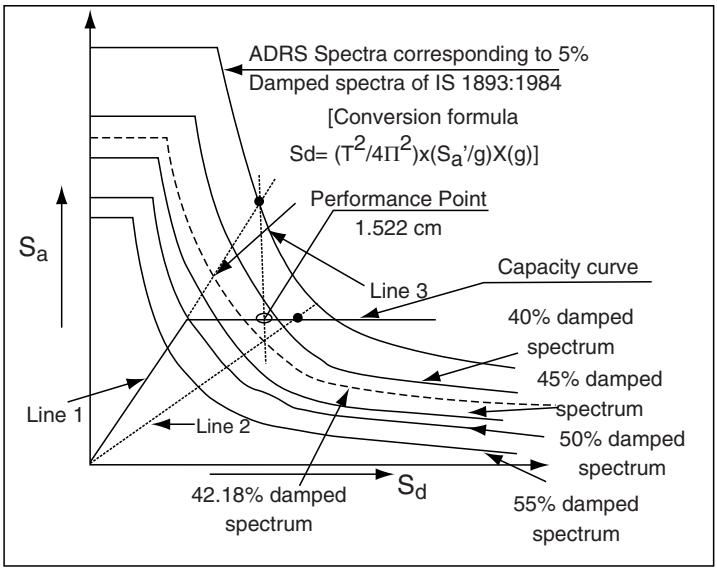

Fig. 15 Schematic representation of Procedure C.

Performance point using Displacement Coefficient Method

Another standard method of pushover analysis is Displacement coefficient method (Fig. 16). This does not involve capacity and demand curves. On the other hand, this method uses elastic spectrum based on the equivalent lengthened period which can account for the large period behaviour arising due to the inelastic excursions, even using an elastic spectral ordinate. Further, various factors are multiplied with the spectral abscissa corresponding to such empirically estimated lengthened period to incorporate the effect of changing modal displacement to roof displacement, the effect of continued plastic yielding, the effect of the shape of hysteresis model and that due to increased second order effect. This

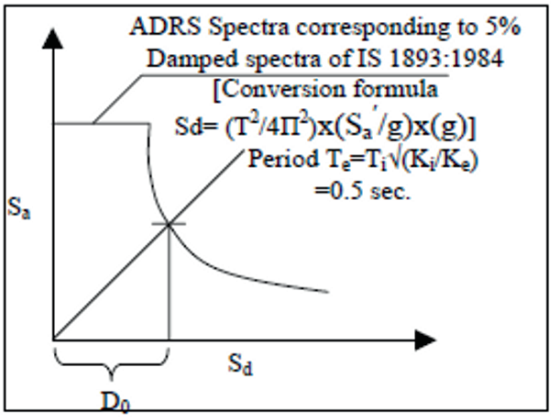

Fig. 16 Schematic Representation of Displacement Coefficient Method.

method is applicable precisely for regular buildings and buildings, which are dominated by first mode and without any adverse torsion effect. It is a pure numerical process for calculating the performance point.

The steps involved in this procedure can be pointed out as follows:

1. 5% damped elastic spectrum of IS 1893:1984 is plotted in the ADRS format.
2. The effective fundamental period, T_e is calculated as, $T_e = T_i\sqrt{(K_i / K_e)}$ where, T_i is elastic fundamental period $= 0.5\,s$, K_i and K_e are defined as elastic and effective lateral stiffness of the structural system respectively.

$$K_i = K_e, \quad T_e = T_i = 0.5\,s$$

3. The evaluation of the performance point D_{DCM} involves presence of some modification factors, like C_0, C_1, C_2 and C_3 as has been shown in Eq. (9).

$$D_{DCM} = C_0 C_1 C_2 C_3 S_a (T_e^2 / 4\pi^2) \tag{9}$$

where,

C_0 = Factor converting spectral displacement to roof displacement $= 1.0$

C_1 = Factor incorporating the effect of inelasticity $= 1.0$

C_2 = Factor incorporating the effect of hysteresis shape $= 1.0$

C_3 = Factor incorporating the second order effect $= 1.0$

S_a = Response spectrum acceleration $= 0.161$

T_e = Effective fundamental period $= 0.5\,s$

Thus,

$$\begin{aligned} D_{DCM} &= 1.0 \times 1.0 \times 1.0 \times 1.0 \times D_0 \\ &= 1.0 \times 1.0 \times 1.0 \times 1.0 \times 0.00999867\, m \\ &= 0.00999867 \times 100\, cm \\ &= 0.99\, cm \end{aligned}$$

Demand obtained using inelastic dynamic analysis

The same example problem has also been analyzed by inelastic dynamic analysis for the sake of comparison with pushover analysis methodologies described earlier. For the purpose of rigorous nonlinear time history analysis, the general governing differential equation of motion is converted to incremental form and is expressed over a small time step as Eq. (10).

$$m\,\Delta\ddot{u}_i + c\,\Delta u_i' + k_i\,\Delta u_i = -m\,\ddot{u}_{gi}(t) \tag{10}$$

where, u, u', $\ddot{u}$ and $\ddot{u}_g(t)$ represent the displacement, velocity, acceleration of the structural system and ground acceleration respectively. To analyze the inelastic range behaviour, this incremental equation is solved numerically in the time domain by Newmark's $\beta - \gamma$ method. Newmark's parameters are taken as $\beta = 0.5$ and $\gamma = 0.5$ to achieve unconditional stability. The change in stiffness of the elements is upgraded in each time steps as has been detailed in the literature[16]. Further, to ensure accuracy at each step and to eliminate cumulative error, the incremental displacement value at the corresponding time step is calculated from modified Newton-Raphson's technique. The Time duration for the spectrum consistent ground motion is about $20\,s$ and the time step, which also involves lots of iterations, is considered less than $T/1000\,s$ to avoid stability problem and non-convergence of the procedure. Thus, one can easily feel the computational rigor and the time required in this procedure. To judge the error creeped in due to lack of stability and convergence, the expertise and insight of a numerical is required for successful routine application. This is really difficult issue to be ensured in design office.

However, analyzing the same problem with this procedure, the demand obtained is given by $1.75\,cm$.

4.6. PERFORMANCE OF PUSHOVER ANALYSIS

The inelastic displacement demands obtained by different varieties of Pushover Analysis procedures, namely Procedure A, Procedure B, Procedure C and Displacement Coefficient Method are $1.54\,cm$, $1.54\,cm$, $1.522\,cm$, and $0.99\,cm$

respectively. These results seem to be reasonably close to the results obtained from rigorous inelastic dynamic analysis, except the Displacement Coefficient Method, which gives quite a lower estimate of the inelastic demand.

5. Concluding remarks

The demonstration presented in this paper with its theoretical background explaining the novel procedure of dual design philosophy is an effort to develop understanding of this philosophy with its advantage as well as bottlenecks.

The demonstration clearly indicates the relative ease of this philosophy. The semiphysical as well as semiempirical formulation employed in this method in various steps help to develop physical intuition and facilitate tracking out error from the nature of the results at different steps. On the other hand, detecting error seems to be too much difficult in its counterpart: nonlinear dynamic analysis which is a rigorous computational procedure which yields results at the end of running a program. In fact, the insight as well as expertise of a numerical analyst (which is generally seldom available in a design office) is necessary to ensure a result free from error due to instability and nonconvergence.

The graphical representation is another possible advantageous point of Pushover Analysis as it helps to have much more picturesque representation of the problem developing a clear physical insight in the mind of the designer, providing more behavioural information about the structure.

References

1. Applied Technology Council (ATC), 1996. *Seismic evaluation and retrofit of concrete buildings, Report ATC–40*, Applied Technology Council, Redwood City, California Seismic Safety Commission.
2. Building Seismic Safety Council (BSSC), 1997. *NEHRP guidelines for the seismic rehabilitation of buildings. Report FEMA–273*: October. Applied Technology Council (ATC-33 Project), Redwood City, California.
3. Building Seismic Safety Council (BSSC), 2000. *Prestandard and commentary for the seismic rehabilitation of buildings. Report FEMA–356*, Federal Emergency Management Agency, Washington, D.C.
4. H. Krawinkler, G. D. P. K. Seneviratna, 1998. *Pros and cons of a pushover analysis of seismic performance evaluation*. Engineering Structures, **20**, 452-464.
5. A. K. Chopra, R. Goel, 2002. *A Modal Pushover Analysis Procedure for Estimating Seismic Demands for Buildings*. Earthquake Engineering Structural Dynamics, **31**, 561-582.
6. A. K. Chopra, R. Goel, 2003. *A Modal Pushover Analysis Procedure to estimate Seismic Demands for Buildings: Summary and evaluation*. Fifth National Conference on Earthquake Engineering, 26-30, May. Istanbul, Turkey.

7. C. Chintanapakadee, A. K. Chopra, 2004. *Seismic Response of Vertically Irregular Frames: Response History and Modal Pushover Analyses*, Journal of Structural Engineering, ASCE, **130**, 1177-1185.
8. T. S. Jan, M. W. Liu, Y. C. Kao, 2004. *An Upper Bound Pushover Analysis Procedure for Estimating the Seismic Demands of High-Rise Buildings*, Engineering Structures, **26**, 117-128.
9. M. Inel, T. Tjhin, M. A. Aschheim, 2003. *The Significance of Lateral Load Pattern in Push-over Analysis*, Fifth National Conference on Earthquake Engineering, Istanbul, Turkey, Paper No. AE-009, 26-30, Istanbul, Turkey.
10. D. Vamvatsikos, C. A. Cornell, 2004. *Applied incremental dynamic analysis*. Earthquake Spectra, **20**, 523-553.
11. Indian standard code of practice for earthquake resistant design of structures. IS: 1893 (Part 1):1984. Bureau of Indian Standards, New Delhi.
12. M. R. Khan, 1987. *Improved method of generation of artificial time-histories, rich in all frequencies*. Earthquake Engineering Structural Dynamics, **15**, 985-992.
13. G. W. Housner, 1959. *Behaviour of structures during earthquakes*. Proc. Engineering Mechanics Division, ASCE, **85**(EM-4), 109-129.
14. S. C. Dutta, K. Bhattacharya, R. Roy, 2004. *Response of low-rise buildings under seismic ground excitation incorporating soil-structure interaction*. Soil Dynamics and Earthquake Engineering, **24**, 893-914.
15. S. C. Dutta, P. K. Das, R. Roy, 2005. *Seismic behavior of code-designed bidirectionally eccentric systems.* Journal of Structural Engineering, ASCE, **131**, 1497-1514.
16. A. K. Chopra, 1995. *Dynamic of structures: theory and applications to earthquake engineering*. Englewood Cliffs, NJ: Prentice-Hall.

NONLINEAR WAVES IN A STENOSED ELASTIC TUBE FILLED WITH VISCOUS FLUID: FORCED PERTURBED KORTEWEG-DE VRIES EQUATION

TAY KIM GAIK*
Science Study Center, Universiti Teknologi Tun Hussein Onn Malaysia, Johor, Malaysia

HİLMİ DEMİRAY
Department of Mathematics, Işık University, Istanbul, Turkey

ONG CHEE TIONG
Faculty of Science, Universiti Teknologi Malaysia, Johor, Malaysia

Abstract. In the present work, treating the artery as a prestressed thin-walled and long circularly cylindrical elastic tube with a mild symmetrical stenosis and the blood as an incompressible Newtonian fluid, we have studied the propagation of weakly nonlinear waves in such a composite medium, in the long wave approximation, by use of the reductive perturbation method. By introducing a set of stretched coordinates suitable for the boundary value type of problems and expanding the field variables into asymptotic series of the smallness parameter of nonlinearity and dispersion, we obtained a set of nonlinear differential equations governing the terms at various order. By solving these nonlinear differential equations, we obtained the forced perturbed Korteweg-de Vries equation with variable coefficient as the nonlinear evolution equation. By use of the coordinate transformation, it is shown that this type of nonlinear evolution equation admits a progressive wave solution with variable wave speed.

Keywords: prestressed elastic tube, Korteweg-de Vries equation

*Corresponding author, tay@uthm.edu.my

E. İnan et al. (eds.), *Vibration Problems ICOVP-2007*,

1. Introduction

Due to its application in arterial mechanics, the propagation of pressure pulse in fluid-filled distensible tubes has been studied by several researchers[1-2]. Most of the early works on wave propagation in compliant tubes have considered small amplitude waves ignoring the nonlinear effects and focused on the dispersive character of waves[3-5]. However, the nonlinear term must be taken into consideration if one considers the finite amplitude, or small-but-finite amplitude waves, depending on the order of nonlinearity.

The propagation of finite amplitude waves in fluid-filled elastic or viscoelsatic tubes has been examined, for instance, by Rudinger[6], Ling and Atabek[7], Anliker et al.[8] and Tait and Moodie[9] by using the method of characteristics, in studying the shock formation. On the other hand, the propagation of small-but-finite amplitude waves in distensible tubes has been investigated by Johnson[10], Hashizume[11], and Yomosa[12]. In all these works[10-12], the effect of initial deformation is neglected. Recently in a series of works of Demiray and Antar[13-15] in which they treated artery as an incompressible, prestressed thin isotropic elastic tube filled with inviscid, viscous or layered fluid as blood, using approximate method on fluid equations and reductive perturbation method, in the long-wave approximation, they obtained various evolution equations of Korteweg-de Vries and Korteweg-de Vries-Burgers equations. In all previous works, they treated the arteries as circularly cylindrical long thin tubes with a constant cross-section. However due to decomposition of fat or cholesterol in artery over the time, the artery become narrower and may have variable radius along the axis of the tube.

Thus, in this work, treating the arteries as an incompressible prestressed thin walled elastic tube with a mild symmetrical stenosis and the blood as a Newtonian fluid, we have studied the propagation of weakly nonlinear waves in such a composite medium, in the long wave approximation, by use of the reductive perturbation method. We obtained the forced Korteweg-de Vries perturbed equation with variable coefficients as the evolution equation.

2. The governing equations

The non-dimensional governing equations of an thin-walled, prestressed, incompressible, stenosed elastic tube (artery) and the averaged viscous fluid (blood) are given by

$$P_r = \frac{1}{\lambda_\theta - f(z) + u}\left[\begin{array}{l} \dfrac{m}{\lambda_z}\dfrac{\partial^2 u}{\partial t^2} + \dfrac{1}{\lambda_z}\dfrac{\partial \Sigma}{\partial \lambda_2} - \dfrac{\partial}{\partial z}\left\{\dfrac{(-f'(z)+\partial u/\partial z)}{\left[1+(-f'(z)+\partial u/\partial z)^2\right]^{1/2}}\dfrac{\partial \Sigma}{\partial \lambda_1}\right\} \\ +4\bar{\upsilon}\left(-f'+\dfrac{\partial u}{\partial z}\right)w \end{array}\right],$$

$$2\frac{\partial u}{\partial t} + 2w\left[-f'(z)+\frac{\partial u}{\partial z}\right] + [\lambda_\theta - f(z) + u]\frac{\partial w}{\partial z} = 0, \tag{1}$$

$$\frac{\partial w}{\partial t} + w\frac{\partial w}{\partial z} + \frac{\partial \bar{p}}{\partial z} - \bar{\upsilon}\left[\frac{\partial^2 w}{\partial z^2} - \frac{8w}{(\lambda_\theta - f(z)+u)^2}\right] = 0,$$

where z and t are axial and time parameters, u is the radial displacement of the tube, λ_z and λ_θ are the initial stretch ratios in the axial and circumferential directions, λ_1 and λ_2 are the final stretch ratios in the circumferential and tangential directions, $f(z)$ is a stenosis function, Σ is the strain energy density function, w and p are the averaged axial fluid velocity and averaged fluid pressure function and υ is the kinematic viscosity.

3. Longwave approximation

In this subsection, we shall examine the propagation of small-but-finite amplitude waves for fluid-filled elastic tubes in the longwave approximation whose non-dimensional governing equations are given in equation (1). For this, we adopt the long wave approximation and employ the reductive perturbation method[16]. For this type of problem, it is convenient to introduce the following type of stretched coordinates

$$\xi = \varepsilon^{1/2}(z - ct), \quad \tau = \varepsilon^{3/2} z, \tag{2}$$

where ε is a small parameter measuring the weakness of nonlinearity and dispersion and c is a scale parameter to be determined from the solution. Solving z in terms of τ and introducing it into the expression of $f(z)$, we obtain

$$f(z) = f(\varepsilon^{-3/2}\tau) = \varepsilon g(\tau) \tag{3}$$

in order to take into account of the stenosis effect. From the stretch coordinates, we can get the following differential relations

$$\frac{\partial}{\partial t} = -\varepsilon^{1/2} c \frac{\partial}{\partial \xi}, \quad \frac{\partial}{\partial z} = \varepsilon^{1/2} \left(\frac{\partial}{\partial \xi} + \varepsilon \frac{\partial}{\partial \tau} \right). \tag{4}$$

For the long wave limit, it is assumed that the field quantities may be expanded into asymptotic series of

$$u = \varepsilon u_1 + \varepsilon^2 u_2 + ..., \quad w = \varepsilon w_1 + \varepsilon^2 w_2 + ..., \quad p = p_0 + \varepsilon p_1 + \varepsilon^2 p_2 ..., \tag{5}$$

Introducing equations (3)-(5) into (1), the following sets of differential equations are obtained

$0(\varepsilon)$ equations

$$p_1 = \beta_1 [u_1 - g(\tau)], \quad -2c \frac{\partial u_1}{\partial \xi} + \lambda_\theta \frac{\partial w_1}{\partial \xi} = 0, \quad -c \frac{\partial w_1}{\partial \xi} + \frac{\partial p_1}{\partial \xi} = 0. \tag{6}$$

$0(\varepsilon^2)$ equations

$$\begin{aligned} p_2 &= \left(\frac{mc^2}{\lambda_\theta \lambda_z} - \beta_0 \right) \frac{\partial^2 u_1}{\partial \xi^2} + \beta_1 u_2 + \beta_2 [u_1 - g(\tau)]^2, \\ -2c \frac{\partial u_2}{\partial \xi} &+ 2w_1 \frac{\partial u_1}{\partial \xi} + \lambda_\theta \frac{\partial w_2}{\partial \xi} + \lambda_\theta \frac{\partial w_1}{\partial \tau} + [u_1 - g(\tau)] \frac{\partial w_1}{\partial \xi} = 0, \\ -c \frac{\partial w_2}{\partial \xi} &+ w_1 \frac{\partial w_1}{\partial \xi} + \frac{\partial p_2}{\partial \xi} + \frac{\partial p_1}{\partial \tau} + \frac{8 \upsilon w_1}{\lambda_\theta^2} = 0. \end{aligned} \tag{7}$$

Here, it is assumed that the viscosity is of order of $0(\varepsilon^{3/2})$, i.e. $\bar{\upsilon} = \varepsilon^{3/2} \upsilon$ and the coefficients β_0, β_1 and are defined by

$$\beta_0 = \frac{1}{\lambda_\theta} \frac{\partial \Sigma}{\partial \lambda_z}, \quad \beta_1 = \frac{1}{\lambda_z \lambda_\theta} \frac{\partial^2 \Sigma}{\partial \lambda_\theta^2} - \frac{1}{\lambda_z \lambda_\theta^2} \frac{\partial \Sigma}{\partial \lambda_\theta}, \quad \beta_2 = \frac{1}{2 \lambda_z \lambda_\theta} \frac{\partial^3 \Sigma}{\partial \lambda_\theta^3} - \frac{\beta_1}{\lambda_\theta}. \tag{8}$$

4. Solution of the field equations

From the solution of the equation (6), we get

$$u_1 = U(\xi, \tau), \quad w_1 = \frac{2c}{\lambda_\theta} U \quad \bar{p}_1 = \beta_1 [U - g(\tau)], \quad \beta_1 = \frac{2c^2}{\lambda_\theta}. \tag{9}$$

Here $U(\xi, \tau)$ is an unknown function whose governing equation will be obtained later and c is the phase velocity in the long wave approximation. Introducing equation (9) into (7), we obtain

$$
\begin{aligned}
&p_2 = \left(\frac{mc^2}{\lambda_z\lambda_\theta} - \beta_0\right)\frac{\partial^2 U}{\partial \xi^2} + \beta_1 u_2 + \beta_2[U - g(\tau)]^2,\\
&-2c\frac{\partial u_2}{\partial \xi} + \frac{4c}{\lambda_\theta}U\frac{\partial U}{\partial \xi} + \lambda_\theta\frac{\partial w_2}{\partial \xi} + 2c\frac{\partial U}{\partial \tau} + \frac{2c}{\lambda_\theta}[U - g(\tau)]\frac{\partial U}{\partial \xi} = 0, \qquad (10)\\
&-c\frac{\partial w_2}{\partial \xi} + \left(\frac{2c}{\lambda_\theta}\right)^2 U\frac{\partial U}{\partial \xi} + \frac{\partial p_2}{\partial \xi} + \beta_1\frac{\partial U}{\partial \tau} - \beta_1 g'(\tau) + \frac{16c\upsilon U}{\lambda_\theta^3} = 0,
\end{aligned}
$$

Inserting equation $(10)_1$ into $(10)_3$ yields

$$
\begin{aligned}
&-c\frac{\partial w_2}{\partial \xi} + \left(\frac{2c}{\lambda_\theta}\right)^2 U\frac{\partial U}{\partial \xi} + \left(\frac{mc^2}{\lambda_z\lambda_\theta} - \beta_0\right)\frac{\partial^3 U}{\partial \xi^3} + \beta_1\frac{\partial u_2}{\partial \xi}\\
&+2\beta_2[U - g(\tau)]\frac{\partial U}{\partial \xi} + \beta_1\frac{\partial U}{\partial \tau} - \beta_1 g'(\tau) + \frac{16c\upsilon U}{\lambda_\theta^3} = 0,
\end{aligned} \qquad (11)
$$

Eliminating for w_2 between equations $(10)_2$ and (11), the following forced perturbed Korteweg-de Vries equation with variable coefficients is obtained

$$
\begin{aligned}
&\frac{\partial U}{\partial \tau} + \mu_1 U\frac{\partial U}{\partial \xi} + \mu_3\frac{\partial^3 U}{\partial \xi^3} + \mu_4(\tau)\frac{\partial U}{\partial \xi} + \mu_5 U = \mu(\tau),\\
&\mu_1 = \frac{\beta_2}{\beta_1} + \frac{5}{2\lambda_\theta}, \quad \mu_3 = \frac{m}{4\lambda_z} - \frac{\beta_0}{2\beta_1}, \quad \mu_4 = -\left[\frac{1}{2\lambda_\theta} + \frac{\beta_2}{\beta_1}\right]g(\tau), \qquad (12)\\
&\mu_5 = \frac{4\upsilon}{c\lambda_\theta^2}, \quad \mu(\tau) = \frac{1}{2}g'(\tau).
\end{aligned}
$$

5. Progressive wave solutions

In this sub-section, we shall present a progressive wave solution to the evolution equation given in (12). For that purpose, we introduce the following coordinates transformation on dependent and independent variables

$$
\begin{aligned}
&U(\xi,\tau) = V(\xi,\tau) + e^{-\mu_5\tau}\int_0^\tau \mu(s)e^{\mu_5 s}ds,\\
&\tau' = \tau, \quad \xi' = \xi - \int_0^\tau\left[\mu_4(q) + \mu_1 e^{-\mu_5 q}\int_0^q \mu(s)e^{\mu_5 s}ds\right]dq.
\end{aligned} \qquad (13)
$$

In the new coordinate system, the evolution equation reduces to the conventional perturbed Korteweg-de Vries equation

$$\frac{\partial V}{\partial \tau'} + \mu_1 V \frac{\partial V}{\partial \xi'} + \mu_3 \frac{\partial^3 V}{\partial \xi'^3} + \mu_5 V = 0. \tag{14}$$

Following Demiray[17], the solution of the nonlinear evolution equation (14) may be given by

$$V = a(\tau')\mathrm{sech}^2\zeta,\ a(\tau') = a_0 e^{-\frac{4}{3}\mu_5\tau'},\ \zeta = \left(\frac{\mu_1 a(\tau')}{12\mu_3}\right)^{1/2}\left(\xi' - \frac{\mu_1 a_0}{4\mu_5}\left[1 - e^{-\frac{4}{3}\mu_5\tau'}\right]\right), \tag{15}$$

where a_0 is the wave speed. Inserting the equation (15) into (13), the solution of forced perturbed Korteweg-de Vries equation with variable coefficients (11) is given by

$$\begin{aligned} U &= a_0 e^{-\frac{4}{3}\mu_5\tau}\mathrm{sech}^2\zeta + e^{-\mu_5\tau}\int_0^\tau \mu(s)e^{\mu_5 s}ds, \\ \zeta &= \left(\frac{\mu_1 a(\tau)}{12\mu_3}\right)^{1/2}\left(\xi - \frac{\mu_1 a_0}{4\mu_5}\left[1 - e^{-\frac{4}{3}\mu_5\tau}\right] - \int_0^\tau\left[\mu_4(q) + \mu_1 e^{-\mu_5 q}\int_0^q \mu(s)e^{\mu_5 s}ds\right]dq\right). \end{aligned} \tag{16}$$

As is seen from the expression of the phase function ζ, the trajectory of the wave is not a straight line anymore, it is rather a curve in the (ξ, τ) plane. This is the result of the stenosis in the tube. Noting that τ is the spatial variable and ξ is a temporal variable, the wave speed is defined by

$$V_p = \frac{d\tau}{d\xi} = \left(\frac{\mu_1 a_0}{3}e^{-\frac{4}{3}\mu_5\tau} + \mu_4(\tau) + \mu_1 e^{-\mu_5\tau}\int_0^\tau \mu(s)e^{\mu_5 s}ds\right)^{-1}. \tag{17}$$

Due to the existence of a stenosis, the wave speed is variable along the tube axis.

6. Conclusion

By employing the nonlinear field equations of an elastic tube of variable radius, and the averaged equation for incompressible Newtonian fluid, we have studied the propagation of nonlinear waves in such medium, in the long wave approximation by use of reductive perturbation method. We obtained the forced

perturbed Korteweg-de Vries equation with variable coefficient as the evolution equation. Seeking a progressive wave solution to this evolution equation, we observed that the wave speed changes with the axial distance parameter.

References

1. T. J. Pedley, 1980. *Fluid Mechanics of Large Blood Vessels*, Cambridge University Press, Cambridge 1980.
2. Y. C. Fung, 1981. *Biodynamics: Circulation*, Springer Verlag, New York.
3. H. B. Atabek, H. S. Lew, 1966. *Wave propagation through a viscous incompressible fluid contained in an initially stressed elastic tube*, Biophys. J, **7**, 486-503.
4. A. J. Rachev, 1980. *Effects of transmural pressure and muscular activity on pulse waves in arteries*, J. Biomech. Engng., ASME, **102**, 119-123.
5. H. Demiray, 1992. *Wave propagation through a viscous fluid contained in a prestressed thin elastic tube*, Int. J. Engng. Sci., **30**, 1607-1620.
6. G. Rudinger, 1970. *Shock waves in a mathematical model of aorta*, J. Appl. Mechanics, **37**, 34-37.
7. S. C. Ling, H. B. Atabek, 1972. *A nonlinear analysis of pulsatile blood flow in arteries*, J. Fluid Mech., **55**, 492-511.
8. M. Anliker, R. L. Rockwell, E. Ogden, 1968. *Nonlinear analysis of flow pulses and shock waves in arteries*, Z. Angew. Math. Phys., **22**, 217-246.
9. R. J. Tait, T. B. Moodie, 1984. *Waves in nonlinear fluid filled tubes*, Wave Motion, **6**, 197-203.
10. R. S. Johnson, 1970. *A non-linear equation incorporating damping and dispersion*, J. Fluid Mech., **42**, 49-60.
11. Y. Hashizume, 1985. *Nonlinear Pressure Waves in a Fluid-Filled Elastic Tube*, J. Phys. Soc. Japan, **54**, 3305-3312.
12. S. Yomosa, 1987. *Solitary Waves in Large Blood Vessels*, J. Phys. Soc. Japan, **56**, 506-520.
13. H. Demiray, 1996. *Solitary waves in prestressed elastic tubes*, Bull. Math. Biol, **58**, 939-955.
14. N. Antar, H. Demiray, 1999. *Weakly nonlinear waves in a prestressed thin elastic tube containing a viscous fluid*, Int. J. Eng. Sci., **37**, 1859-1876.
15. H. Demiray, 2002. *Nonlinear waves in prestressed elastic tubes filled with a layered fluid*, Int. J. Eng. Sci., **40**, 713-726.
16. A. Jeffrey, T. Kawahara, 1981. *Asymptotitc methods in nonlinear wave theory*, Pitman, Boston.
17. H. Demiray, 2002. *A note on the solution of perturbed Korteweg-de Vries equation*, App. Math. Comp., **132**, 643-647.

DETERMINATION OF MECHANICAL PROPERTY OF SYNTHETIC RUBBER USING OPTICAL MOUSE AS A VIBRATION SENSOR

N. GUPTA*
Department of Electrical Engineering, Motilal Nehru National Institute of Technology, Allahabad, 211004, India

M. SHARMA
Department of Mechanical Engineering, National Institute of Technology, Warangal, India

S. SARANGI AND R. BHATTACHARYYA
Department of Mechanical Engineering, Indian Institute of Technology, Kharagpur, 721302, India

Abstract. Synthetic rubber is an incompressible isotropic hyper-elastic material. Its mechanical property is described only by rigidity modulus at undeformed configuration which is one third of Young's modulus at the same configuration. This paper describes an indirect method to determine its rigidity modulus by measuring the frequency of oscillation of a loaded rubber string. Small super-imposed oscillation at static equilibrium stretch is measured with an optical mouse. The obtained data is processed to determine the frequency of oscillation. This process of acquiring data and processing it to obtain the desired information is known as Data Acquisition. Post processing and interpretation of the signal is done with help of MATLAB. The rigidity modulus of synthetic rubber is thus determined.

Keywords: small superimposed oscillation, rigidity modulus, hyper-elastic material, optical mouse, Fast Fourier transformation, data acquisition

* Corresponding author, neha.1608@gmail.com

E. İnan et al. (eds.), *Vibration Problems ICOVP-2007*,

1. Introduction

Synthetic rubber is a type of artificially made polymer material commonly known as elastomer. An elastomer can undergo much more elastic deformation under stress than most materials and still return to its previous size without permanent set. Thus it is extensively used in machine and structural foundation. Its improved material properties enable it to serve as a good substitute for natural rubber. Some of the uses of synthetic rubber are as in plumbing fixtures, mechanical seal, mechanical belt, tires etc. In sheet form, it is used to make diving suit, glove, protective clothing, and radar absorbing material.

The synthetic rubber is considered to be incompressible isotropic hyperelastic material. Its mechanical property is defined through its rigidity modulus G in the reference configuration. The incompressibility condition leads the rigidity modulus as one third of the Young's modulus in such a configuration. The non linear stress-stretch relation often makes it difficult to determine the initial slope in the ground state. This work gives an indirect method to determine the rigidity modulus by measuring frequency at different steady state stretch. The method shows an effective agreement with the theory, thus determining the rigidity modulus effectively.

The experiment is conducted with an optical mouse. The optical mouse uses a tiny camera to take 1,500 pictures every second. The mouse has a small, red light-emitting diode (LED) that bounces light off that surface onto a complimentary metal-oxide semiconductor (CMOS) sensor. The CMOS sensor sends each image to a digital signal processor (DSP) for analysis. The DSP, operating at 18 MIPS (million instructions per second), is able to detect patterns in the images and see how those patterns have moved since the previous image. Based on the change in patterns over a sequence of images, the DSP determines how far the mouse has moved and sends the corresponding coordinates to the computer. The optical mouse has been demonstrated to be an optical displacement sensor beyond its use as a pointing device. It has been shown that optical mouse may be applied to measuring vibratory displacements with reasonable accuracy. Here, an experiment is done to measure low frequency mechanical oscillations using optical mouse.

The dynamic analysis of loaded rubber string was studied by Beatty and Chow[1]. They derived analytical solutions for the finite amplitude oscillations of the mass. Several important conclusions can be drawn from their work. Lawton and King[2] did an experimental investigation on rubber and tissue strip. However, authors have not come across any previous work on finding the mechanical property of rubberlike material. In the proceeding sections, formulation of the problem, brief description of the experimental procedure with observations, result and detailed discussion are given.

2. Formulation of the problem

A rubber string subjected to end load and other end fixed can be described with principle stress component as $T_{11} = T_{22} = T_{33} = 0$, where $\mathbf{T}$ is Cauchy's stress. The stress field defines traction free condition on the lateral surface. The above description of stress is satisfied identically with the equilibrium equation $div\,\mathbf{T} = 0$, in absence of body force. Beatty and Stalnaker[3] defines this deformation as *simple* extension. The detailed derivation is omitted and one can follow Ogden[4] to get the detail derivations.

The constitutive model of the rubber is based on network chain orientation and statistical mechanics model. There are several material models to describe constitutive relation. Neo-Hookean, Mooney-Rivlin, Arruda Boyace[5], James Guth[6], and Gent[7] are a few to mention. In these models neo-Hookean provides a simple functional form and has good agreement for lower stretch ($\lambda < 4$). In this work the constitutive model is considered as neo-Hookean.

An incompressible, isotropic, hyperelastic neo-Hookean rubber string of undeformed length L, cross-sectional area A and modulus of rigidity G is fixed at one end and the other end is tied to mass M such that the mass-string configuration is inclined to angle θ on the air track. At time t the stretch length is $l(t)$ and stretch $\lambda(t) = l(t)/L$. Following Ogden[4] the engineering longitudinal stress follows

$$\sigma = G(\lambda - \frac{1}{\lambda^2}), \tag{1}$$

which leads to the expression for tension in the string as

$$T(\lambda) = AG(\lambda - \frac{1}{\lambda^2}). \tag{2}$$

To study the dynamics of the mass attached to the rubber string the assumptions are made such that mass of the string is negligible compared to *M*, dynamical system is conservative, deformation in the string is uniform and homogeneous, loading and unloading is independent of stretch rate, $\dot{\lambda}$.

Introduce a Cartesian frame as shown in the system schematic with origin at the fixed end of the string and oriented inclined such that the **i** being the unit vector directed along the length of the string and parallel to the air track which is inclined at an angle θ to the horizontal plane. The motion will take place in **i** direction only as the lateral movement is restrained by the linear air track. The effective load on the string is due to gravity and equals to $M\,g\sin\theta$ The Fig. 1 describes the set up configuration. The governing equation of motion for the mass attached to neo-Hookean rubber string is given by

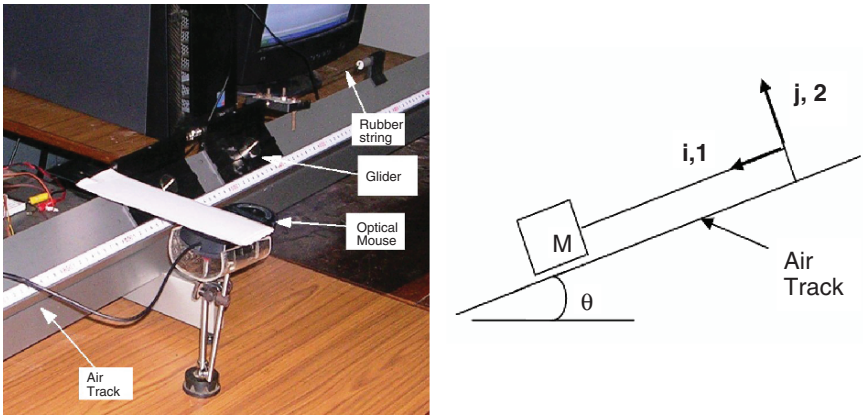

Fig. 1 Experimental setup and Schematic diagram of the setup.

$$\ddot{\lambda}(t)+\frac{T(\lambda)}{ML}=p_0^2, \tag{3}$$

where $p_0 = p_0 = (g\sin\theta/L)^{1/2}$, $T(\lambda)$ is the tensions in the string at time t.

The static equilibrium stretches for a given value of static load $Mg\sin\theta$ mentioned above are obtained from the solution of the simple equation $T(\lambda_e) = Mg\sin\theta$, where the λ_e is the equilibrium stretches and $T(\lambda)$ is the tension. Thus the equilibrium equations follow from (2)

$$\lambda_e^3 - \frac{1}{2\kappa}\lambda_e^2 - 1 = 0. \tag{4}$$

In (4) the stiffness parameter $\kappa = AG/2Mg\sin\theta$

3. Small superimposed oscillation about finite static stretch

To obtain linearized equation for small superimposed oscillation about finite static equilibrium stretch, $\lambda = \lambda_e + \delta$ is substituted in equations (3), where $\delta \ll 1$ and λ_e is the static equilibrium stretches. Linearization of expressions in (2) with $\lambda = \lambda_e + \delta$ and use of equation (3) gives the linear differential equation of motion as

$$\ddot{\delta}+\frac{AG}{ML}\left[\frac{d\{T(\lambda)/AG\}}{d\lambda}\right]_{\lambda=\lambda_e}\delta = 0 \tag{5}$$

The equation (5) is reduced to

$$\ddot{\delta} + (2\kappa Z_v) p_0^2 \delta = 0, \qquad \text{where} \quad Z_v = \left[(1 + \frac{2}{\lambda_e^3}) \right] \tag{6}$$

By substituting the $2\kappa = \dfrac{1}{(\lambda_e - \dfrac{1}{\lambda_e^2})}$ above equation reduces to

$$\ddot{\delta} + \omega_v^2 \delta = 0, \qquad \text{where,} \quad \frac{\omega_v}{p_0} = \left[\frac{(\lambda_e^3 + 2)}{\lambda_e (\lambda_e^3 - 1)} \right]^{1/2}. \tag{7}$$

In order to compare the small oscillation frequencies (7) for a fixed value of the normalized static load $Mg\sin\theta / AG$ suspended by a neo-Hookean rubber string-mass system with about their corresponding static stretches, the variation of the non-dimensional frequencies ω_v/p_0 is much relevant with respect to $1/\kappa (= 2Mg\sin\theta / AG)$ instead of λ_e. It may be observed from (4) and (7) that as $1/\kappa \to 0$, $\lambda_e \to 1 \to 1$, $\omega_v \to \infty$.

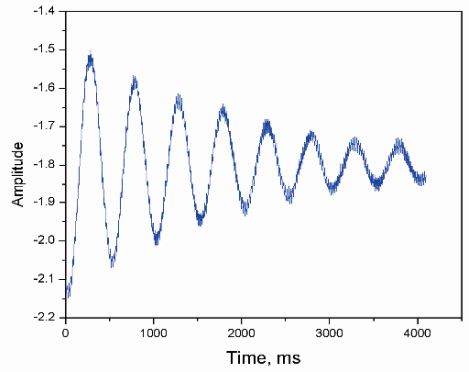

Fig. 2 Typical time response curve from the optical mouse.

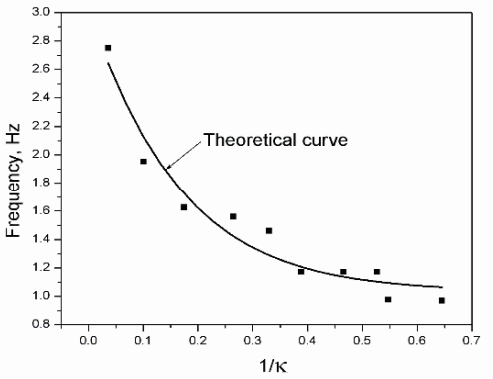

Fig. 3 Variation of natural frequency with $1/\kappa$. Solid curve represents the theoretical relation. Square blocks show the experimental data points.

4. Experiment

The experimental arrangement used to illustrate the aim is shown in Fig. 1. Gliders are placed on the air track. Different masses can be introduced on the gliders for varying the load. The synthetic rubber is attached to a fixed end of the air track and the other end of rubber is attached to the glider. Care must be

taken to ensure that the rubber does not stretch prior to giving it a displacement as this may result in breaking of sulphur bonds. Incline the air track to desired angle. Put on the power supply and adjust the air flow until the gliders just glide freely on the track. The new position of the glider is noted. Slight displacement is provided to the glider such that small oscillations are produced. The rubber string attached provides damping and in some seconds the glider comes to rest. This displacement is measured using optical mouse. Once the setup is ready, the connector of the optical mouse is plugged into computer's USB port. On the computer a program[8] that polls and stores the inclined position from the optical mouse is activated when the glider is set into oscillatory motion (Fig. 2). It should be made sure that the plain surface of the mouse touches the oscillating flag, i.e. this sensor works only when the two bodies are in physical contact with each other. The data is transferred to notepad and thus fed in MATLAB for FFT. The process is repeated with different weights. Each time the position of the glider is noted down and similar operation is performed.

5. Results

			Using Equation (4)		Using Equation (7)	
M(gm)	λ_e	ω_n (Hz)	κ	G(Pa)*10^6	κ	G(Pa)*10^6
236	1.006	2.751	27.994	4.1079	10.1667	1.4945
420	1.017	1.954	9.9696	2.6082	5.2407	1.3710
609	1.03	1.627	5.7206	1.1701	3.7247	1.4129
709	1.046	1.5616	3.7873	1.6726	3.5345	1.5610
809	1.058	1.461	3.0370	1.5304	3.1614	1.5931
909	1.069	1.171	2.5783	1.4599	2.0707	1.1724
1009	1.084	1.173	2.1461	1.3488	2.1320	1.3399
1109	1.096	1.1725	1.8975	1.3107	2.1733	1.5013
1209	1.1	0.976	1.8275	1.3765	1.5158	1.1415
1396	1.12	0.9707	1.5489	1.3469	1.5483	1.3463
1496	1.13	0.9013	1.4415	1.3433	1.3558	1.2634

6. Conclusions

This work presents an experiment to determine the Rigidity Modulus of a synthetic rubber using optical mouse. In this simple test, all the experimentally produced data shows a good correspondence with the expected values (Fig. 3). Care

must be taken to eliminate any kind of friction between the optical mouse and oscillating body. An advantage of using the optical mouse is that it can measure not only small superimposed oscillations but also finite amplitude oscillations thus extending its application in other mechanical oscillator experiments.

References

1. M. F. Beatty and A. C. Chow, 1984. *Free Vibration of a Loaded Rubber String*, International Journal of Non-Linear Mechanics, **1**, 69-84.
2. R. W. Lawton and A. L. King, 1951. *Free longitudinal vibrations of rubber and soft strips*, Journal of Applied Physics, **22**, 1340-1343.
3. M. F. Beatty and D. O. Stalnaker, 1986. *The Poisson function of finite elasticity*, Journal of Applied Mechanics, **53**, 807-813.
4. R. W. Ogden, 2001. *Nonlinear Elasticity: Theory and Applications*, Cambridge University Press.
5. E. M. Arruda and M. C. Boyce, 1993. *A three-dimensional constitutive model for the large stretch behavior of rubber elastic materials*, Journal of Mechanics and Physics of Solids, **41**, 389-412.
6. H. M. James and E. Guth, 1943. *Theory of the elastic properties of rubber*, Journal of Chemical Physics, **10**, 455-481.
7. A. N. Gent, 1996. A new constitutive relation for rubber, rubber chemistry and technology, **69**, 59-61.
8. http://twng.eng.nus.edu.sg/course/ResearchOM/mousetrackerdynamic.html

LARGE AMPLITUDE VIBRATIONS OF NONCIRCULAR CYLINDRICAL SHELLS

S. M. IBRAHIM, B. P. PATEL, AND Y. NATH*
Department of Applied Mechanics, Indian Institute of Technology Delhi, New Delhi-110016, India

Abstract. The aim of this paper is to review the literature on the large amplitude vibration of circumferentially closed shells and to study the nonlinear forced response characteristics of noncircular cylindrical shells. The study is carried out using semi-analytical method with the meridional approximation of the displacement field as the superposition of the linear free vibration modal functions and the three noded quadratic finite element approximation in the circumferential direction. The Sander's type strain-displacement relations are used. The governing equations are solved using Newmark's time integration approach coupled with the Newton-Raphson iterative technique. The forced response curves in the frequency domain are obtained from the steady state dynamic response of the shells. Some of the interesting characteristics pertaining to the noncircular shells are highlighted.

Keywords: semi-analytical, noncircular, large amplitude, forced response, shell

1. Introduction

Cylindrical shells are extensively used as structural elements in modern engineering industry such as aerospace, marine, nuclear and power, etc. Although circular cylindrical shell is a simple structural component, the cross-section of such cylinders may become noncircular due to either the fabrication process or special design requirements like external shape/internal storage compartments

*Corresponding author, nathyogendra@hotmail.com

E. İnan et al. (eds.), *Vibration Problems ICOVP-2007*,

in aerospace and submersible systems. The presence of out of roundness in the shell geometry not only increases the level of geometrical complexity but also may adversely affect the dynamic behaviour. With increasing flight vehicle speed and more powerful propulsion systems, the dynamic environment on vehicle structures becomes severe. Hence, there is a growing appreciation of the importance of nonlinear effects in determining the response characteristics of these shells under dynamic loading.

The early development on the topic of nonlinear vibrations of isotropic circular cylindrical shells has been reported in [1]. Recently, Moussaoui and Benemar[2] and Amabili and Paidoussis[3] presented reviews on nonlinear shell vibrations. Based on the available review studies, it is clear that the behaviour of open shells is quite well understood, but there are only few studies available on the behaviour of closed shells such as closed cylinders and they are reviewed here.

The origin of the large amplitude vibration study of circular cylindrical shallow shells is attributed to the Reissner[4], who isolated a single half-wave (lobe) of the vibration mode and analyzed it for simply supported open shells using Donnell's shallow-shell theory. It was found that the nonlinearity could either be of the hardening or softening type, depending upon the geometry of the lobe. Other investigators who followed the same technique to analyse simply supported circular cylindrical shell were Chu[5], Nowinski[6] and Cummings[7] and their results indicated a hardening type of non-linearity. Evensen[8] performed a series of experiments in which shells were subjected to vibration amplitudes up to three or four times the wall thickness and observed a definite softening type of nonlinear behaviour. This has led him to reexamine Chu[5] and Nowinski[6] analyses, according to which the shell nonlinearity is of hardening type. It was noticed that Chu's[5] approximate solution did not satisfy the periodicity condition for circumferential displacement and that Nowinski's[6] analysis was not accurate, as it did not maintain a zero transverse deflection at the ends of the shell. Using the Galerkin's approach, Evensen[9] analyzed the free and forced non-linear vibrations of thin circular rings by assuming two vibration modes (driven and companion modes). The analytical and experimental results exhibited several features that are characteristics of non-linear vibrations of axisymmetric systems in general, and of circular cylindrical shells in particular. Evensen and Fulton[10] extended the original investigations in studying the nonlinear dynamic response of thin circular cylindrical shells. They found that the nonlinearity might either be of hardening type or softening type depending upon the ratio of the number of axial waves to the number of circumferential waves. A series of experimental studies on the large amplitude vibration of rings by Evensen[11, 12] gave an insight in choosing the mode shape, as it was found that in large amplitude vibrations:

(i) the shell does not spend equal time intervals in outward and inward motions,
(ii) inward maximum deflection is larger than outward one.

Hence, the idea for mode expansion to add to the asymmetric linear mode an axisymmetric mode giving a contraction to the shell was proposed. Evensen[13] chose a mode shape such that the periodicity condition for circumferential displacement was satisfied a priori and it amounted to an assumption of in-extensionality in the circumferential direction. Specifically, he included the companion mode, as well as an axisymmetric contraction having twice the frequency of the driven mode in the assumed mode shape. His results indicated softening type of nonlinearity, which is in agreement with Olson's experiments[14]. The experimental results of Olson[14] clearly indicated softening type of non-linearity, the presence of the double frequency nodal contraction, wherein the axisymmetric response occurs at twice the frequency of asymmetric response, and the occurrence of jump phenomenon associated with the nonlinear theory. Matsuzaki and Kobayashi studied theoretically simply supported circular shells[15], and theoretically and experimentally clamped circular cylindrical shells[16]. The method used was similar to that of Evensen's[13] and the results showed a softening type of nonlinearity. Ginsberg used a different approach to solve the problem of asymmetric[17] and axisymmetric[18] large amplitude vibrations of circular cylindrical shells. In fact, he avoided the assumptions of mode shapes and employed, instead, an asymptotic analysis to solve the nonlinear problem of a simply supported circular cylindrical shell. Both softening and hardening nonlinearities were found, depending on some system parameters. Ginsberg[17] studied the damped response to an excitation and its stability, considering both the driven and companion modes. Chen and Babcock[19] used the perturbation method to solve the nonlinear equations obtained by Donnell's nonlinear shallow shell theory, without selecting a particular deflection solution. They solved the classical simply supported case and studied the driven mode response, the companion mode participation, and the appearance of a travelling wave. They also presented experimental results in good agreement with their theory, showing a softening type of nonlinearity.

Prathap[20] pointed out some inconsistencies in the mathematical analysis of Evensen[13] and the physical behaviour of the model suggested by Dowell and Ventres[21]. Subsequently, based on the comments of Prathap[20], a three term model without any mathematical physical deficiencies was suggested by Ramani[22]. For the aspect ratio of shells around unity, the type of nonlinearity predicted in [13] and [22] were opposite in nature. Ramani[22] and Varadan et al[23] concluded in their analytical studies that the term pertaining to the axisymmetric mode should be independent and proportional to the square of the asymmetric mode.

The nonlinear free vibration characteristics of conical shells, including both circular cylinders and annular plates as special cases, have been investigated by Ueda[24] using Donnell-type shell theory. Each shell element was reduced to a nonlinear system of two degrees of freedom by using an expansion similar to Evensen's[13] analysis but without companion mode participation. Ueda concluded that the discrepancy in the results of the earlier analyses, stemmed from the choice of the trial functions that were assumed for the mode shape in solving the equations, rather than from differences in shell theories or other assumptions.

Amabili[25] investigated large-amplitude vibrations of circular cylindrical shells with different boundary conditions and subjected to radial harmonic excitation in the spectral neighbourhood of the lowest resonances. In particular, simply supported shells with either allowed or constrained axial displacements at the edges were studied; in both cases the radial and circumferential displacements at the shell edges were constrained. Elastic rotational constraints were assumed; they allow simulating any condition from simply supported to perfectly clamped, by varying the stiffness of this elastic constraint. Two different nonlinear, thin shell theories, namely Donnell's and Novozhilov's, were used to calculate the elastic strain energy. Geometric imperfections were taken into account. The non-linear free and forced vibrations of a simply supported, circular cylindrical shell, in contact with an incompressible and inviscid, quiescent and dense fluid have been investigated by Amabili et al[26]. The problem was reduced to a system of ordinary differential equations by means of Galerkin's method, and the effects of both internal and external dense fluid have been examined. In a series of papers (four parts) presented recently by Amabili et al[27-30], the non-linear dynamics and stability of simply supported circular cylindrical shells containing inviscid incompressible fluid flow was investigated in detail. The nonlinearity due to large amplitude shell motion has been considered using the nonlinear Donnell's shallow shell theory, taking into account the effect of viscous structural damping. Part I deals with a detailed study of the stability of the structure[27], Part II deals with large vibration amplitudes without flow[28], Part III deals with truncation effects without flow and experiments[29], and Part IV deals with large vibration amplitudes with flow[30]. Nonlinear vibration of an empty and fluid filled circular cylindrical shell with clamped edges subjected to radial harmonic load was investigated by Karagiozis et al[31]. Two different models, based on classical form and full form of the Donnell's nonlinear shallow-shell equations, derived using Galerkin's approach and Hamiltonian principle, respectively, were used in the study and both were found to agree well with experimental results of Chiba[32]. Also, the

non-linear supersonic flutter of circular cylindrical shells has been investigated by Amabili and Pellicano[33], using the Donnell non-linear shallow-shell theory. The effect of equivalent viscous damping has been taken into account and results show that the system loses stability by standing-wave flutter through specific bifurcation. A very good agreement between theoretical and experimental data has been found for flutter amplitudes.

The studies on the vibration characteristics of noncircular cylindrical shells are rather limited in literature[34] even for the linear case. The available studies reveal that the spatially fixed asymmetric vibration modes of doubly symmetric cross-section noncircular shells are classified as SS, SA, AS, AA depending on whether they are symmetric (S) or anti-symmetric (A) about the semi-major and the semi-minor axes. The investigations of nonlinear vibration behaviour of noncircular structural elements are sparsely treated in the literature. Few contributions are available concerning with the nonlinear vibration of noncircular shells and they are reviewed here.

Using the Galerkin method and assumed modes, Pandalai and Sathyamoorthy[35] analyzed the non-linear flexural vibrations of thin elastic orthotropic oval cylindrical shells. Patel et al[36,37] investigated the nonlinear free flexural vibration behaviour of isotropic/laminated orthotropic noncircular rings, using finite element approach. The formulation includes in-plane and rotary inertia effects, and the nonlinearity due to the finite deformation of the ring. Authors brought out that the information on the participation of various asymmetric modes in addition to the axisymmetric one while vibrating the oval ring at large amplitude in particular asymmetric mode, which is useful for accurate modelling of the closed noncircular structures.

It is evident from the above literature review that the studies on the nonlinear vibration of noncircular cylindrical shells are sparse in the literature in spite of their importance in the design of modern aerospace structures and transport vehicles. In particular, there is no literature available concerning the investigation on whether the phenomena such as the participation of companion mode and travelling wave response etc., observed in the large amplitude vibrations of circular cylindrical shells, are also present in the noncircular shells. Here, the finite strip method is used so as to workout a practicable solution of the problem in a reasonable computational time as the full finite element discretization of the problem like this one requires a large number of elements and hence become computationally inefficient.

The detailed parametric studies are being carried out to investigate the influences of the noncircularity parameter, load magnitude and location and geometrical parameters on the large amplitude forced vibration of doubly symmetric cross-section noncircular shells.

2. Formulation

The geometry of the noncircular cylindrical shell is shown in Figure 1. The coordinates x, y and z having origin at the mid-plane of the shell are considered along the meridional, circumferential and thickness directions, respectively. The displacements u, v, w at a point (x, y, z) are expressed as functions of the mid-plane displacements u_0 v_0, and w_0, and the independent rotations θ_x and θ_y of the normal in the xz and yz planes, respectively, as

$$\begin{aligned} u(x,y,z,t) &= u_0(x,y,t) + z\theta_x(x,y,t) \ ; \\ v(x,y,z,t) &= v_0(x,y,t) + z\theta_y(x,y,t) \ ; \ w(x,y,z,t) = w_0(x,y,t) \end{aligned} \tag{1}$$

where t is the time.

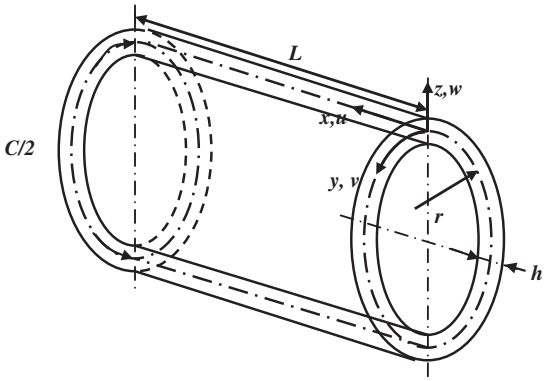

Fig. 1 Geometry of the noncircular cylindrical shell.

Using the semi-analytical approach, u_0, v_0, w_0, θ_x and θ_y are represented as the superposition of modal function in the meridional coordinate x and are written as:

$$\begin{aligned} u_0(x,y,t) &= \sum_{i=1}^{M} u_0^i(y,t)\, U_i(x); \quad v_0(x,y,t) = \sum_{i=1}^{M} v_0^i(y,t)\, V_i(x); \\ w_0(x,y,t) &= \sum_{i=1}^{M} w_0^i(y,t)\, W_i(x); \quad \theta_x(x,y,t) = \sum_{i=1}^{M} \theta_x^i(y,t)\, \Theta_{xi}(x); \\ \theta_y(x,y,t) &= \sum_{i=1}^{M} \theta_y^i(y,t)\, \Theta_{yi}(x) \end{aligned} \tag{2}$$

where $U_i(x)$, $V_i(x)$, $W_i(x)$, $\Theta_{xi}(x)$ and $\Theta_{yi}(x)$ are the modal function obtained from the linear free vibration analysis of the shell. For instance, for a movable simply-supported shell at its two ends, these functions are obtained as:

$$\begin{aligned} &U_i(x)=\cos(i\pi x/L),\ V_i(x)=\sin(i\pi x/L),\ W_i(x)=\sin(i\pi x/L),\\ &\Theta_{xi}(x)=\cos(i\pi x/L),\quad \Theta_{yi}(x)=\sin(i\pi x/L) \end{aligned} \tag{3}$$

Using the Sander's type kinematic relations, Green's strains can be written in terms of mid-plane deformations as,

$$\{\boldsymbol{\varepsilon}\}=\begin{Bmatrix}\boldsymbol{\varepsilon}_{\mathbf{p}}^{\mathbf{L}}\\ 0\end{Bmatrix}+\begin{Bmatrix}z\boldsymbol{\varepsilon}_{\mathbf{b}}\\ \boldsymbol{\varepsilon}_{\mathbf{s}}\end{Bmatrix}+\begin{Bmatrix}\boldsymbol{\varepsilon}_{\mathbf{p}}^{\mathbf{NL}}\\ 0\end{Bmatrix} \tag{4}$$

where, the membrane strains $\{\boldsymbol{\varepsilon}_{\mathbf{p}}^{\mathbf{L}}\}$, bending strains $\{\boldsymbol{\varepsilon}_{\mathbf{b}}\}$, transverse shear strains $\{\boldsymbol{\varepsilon}_{\mathbf{s}}\}$ and nonlinear in-plane strains $\{\boldsymbol{\varepsilon}_{\mathbf{p}}^{\mathbf{NL}}\}$ in the Eq. (4) are written as

$$\{\boldsymbol{\varepsilon}_{\mathbf{p}}^{\mathbf{L}}\}=\begin{Bmatrix}\dfrac{\partial u_o}{\partial x}\\ \dfrac{\partial v_o}{\partial y}+\dfrac{w_o}{r}\\ \dfrac{\partial u_o}{\partial y}+\dfrac{\partial v_o}{\partial x}\end{Bmatrix};\qquad \{\boldsymbol{\varepsilon}_{\mathbf{b}}\}=\begin{Bmatrix}\dfrac{\partial \theta_x}{\partial x}\\ \dfrac{\partial \theta_y}{\partial y}\\ \dfrac{\partial \theta_x}{\partial y}+\dfrac{\partial \theta_y}{\partial x}\end{Bmatrix};$$

$$\{\boldsymbol{\varepsilon}_{\mathbf{s}}\}=\begin{Bmatrix}\theta_x+\dfrac{\partial w_o}{\partial x}\\ \theta_y+\dfrac{\partial w_o}{\partial y}-\dfrac{v_o}{r}\end{Bmatrix};\qquad \{\boldsymbol{\varepsilon}_{\mathbf{p}}^{\mathbf{NL}}\}=\begin{Bmatrix}\dfrac{1}{2}\left(\dfrac{\partial w_o}{\partial x}\right)^2\\ \dfrac{1}{2}\left(\dfrac{\partial w_o}{\partial y}-\dfrac{v_o\cos\phi}{r}\right)^2\\ \dfrac{\partial w_o}{\partial x}\left(\dfrac{\partial w_o}{\partial y}-\dfrac{v_o\cos\phi}{r}\right)\end{Bmatrix} \tag{5}$$

where r is the radius of curvature and is the function of y coordinate for a noncircular cylindrical shell.

The membrane stress resultants $\{N\}$ and the bending stress resultants $\{M\}$ can be related to membrane strains $\{\varepsilon_p\} = \{\varepsilon_p^L + \varepsilon_p^{NL}\}$ and bending strains (curvatures) $\{\varepsilon_b\}$, through the constitutive relation as

$$\begin{Bmatrix} \{N\} \\ \{M\} \end{Bmatrix} = \begin{bmatrix} [A] & [B] \\ [B] & [D] \end{bmatrix} \begin{Bmatrix} \{\varepsilon_p\} \\ \{\varepsilon_b\} \end{Bmatrix} \tag{6}$$

where $[A],[B]$ and $[D]$ are extensional, bending, and bending-extensional coupling stiffness coefficients matrices of the composite laminate shell.

Similarly, the transverse shear stress resultants $\{Q\}$ is related to the transverse shear strains $\{\varepsilon_s\}$ as

$$\{Q\} = [E]\{\varepsilon_s\} \tag{7}$$

The potential energy functional (due to strain energy and transverse load) is given by

$$U(\delta) = \frac{1}{2}\int_A \begin{bmatrix} \{\varepsilon_p\}^T [A]\{\varepsilon_p\} + \{\varepsilon_p\}^T [B]\{\varepsilon_b\} + \{\varepsilon_b\}^T [B]\{\varepsilon_p\} \\ + \{\varepsilon_b\}^T [D]\{\varepsilon_b\} + \{\varepsilon_s\}^T [E]\{\varepsilon_s\} \end{bmatrix} dA - \int_A q w_0 dA \tag{8}$$

where δ is the vector of degrees of freedom associated to the displacement field and q is the applied external load.

The total potential energy functional can be expressed as

$$U(\delta) = \{\delta\}^T [(1/2)\,[K] + (1/6)[K_1(\delta)] + (1/12)[K_2(\delta)]\,]\,\{\delta\} - \{\delta\}^T \{F_M\} \tag{9}$$

where $[K]$ is the linear stiffness matrix, $[K_1]$ and $[K_2]$ are nonlinear stiffness matrices linearly and quadratically dependent on the field variables, respectively. $\{F_M\}$ is the load vector.

The kinetic energy of the shell is given by

$$T(\delta) = \frac{1}{2}\int_A \left[p\left(\dot{u}_0^2 + \dot{v}_0^2 + \dot{w}_0^2\right) + I\left(\dot{\beta}_s^2 + \dot{\beta}_\theta^2\right) \right] dA \tag{10}$$

where $p = \sum_{k=1}^{N} \int_{z_{k-1}}^{z_k} \rho^k dz$, $I = \sum_{k=1}^{N} \int_{z_{k-1}}^{z_k} z^2 \rho^k dz$ and ρ^k is the mass density. The dot over the variable denotes the derivative with respect to time.

Substituting Eqs. (9) and (10) in the Lagrange's equation of motion and incorporating the energy dissipation through the proportional damping, the governing equations for the shell are obtained as:

$$[M]\{\ddot{\delta}\}+[C]\{\dot{\delta}\}+\left[[K]+\frac{1}{2}[K_1\{\delta\}]+\frac{1}{3}[K_2\{\delta\}]\right]\{\delta\}=\{F\} \quad (11)$$

where $[M]$, $[C]$, $[K]$ and $\{F\}$ are the consistent mass matrix, damping matrix, stiffness matrix and external force vector, respectively. The governing equation (11) can be employed to study the linear/nonlinear free or forced response of the shells by neglecting the appropriate terms. The governing equation (11) for the nonlinear dynamic response analysis is solved using Newmark's time integration approach coupled with the Newton-Raphson iterative technique.

3. Element description

The field variables in the circumferential direction (y) are expressed in terms of their nodal values using shape functions as

$$\left(u_o^i, v_o^i, w_o^i, \theta_x^i, \theta_y^i\right)=\sum_{k=1}^{3}\bar{N}_k^0\left(u_{ok}^i, v_{ok}^i, w_{ok}^i, \theta_{xk}^i, \theta_{yk}^i\right) \quad (12)$$

where $\bar{N}_1^0=(\zeta^2-\zeta)/2$, $\bar{N}_2^0=(1-\zeta^2)$, $\bar{N}_3^0=(\zeta^2+\zeta)/2$; ζ is the local natural circumferential coordinate of the element. Here, $\bar{N}_k^0$ are the original shape functions.

If the interpolation functions for the three noded element are used directly to interpolate the field variables $\left(u_o^i, v_o^i, w_o^i, \theta_x^i, \theta_y^i\right)$ in deriving the transverse shear and membrane strains, the element will lock and show oscillations in the transverse shear and membrane stresses. Field consistency requires that the membrane and the transverse shear strains must be interpolated in a consistent manner. Thus, to eliminate the locking syndrome, while substituting the variables θ_y and v_0 (defined in Eq. (2)) in the expression for second component of $\{\boldsymbol{\varepsilon}_\mathbf{s}\}$ Eq. (4), the terms v_o^i, θ_y^i have to be consistent with the field function $\partial w_o^i/\partial y$. Similarly, while substituting the variables w_0 and v_0 in Eq. (4) for second and third components of membrane strain $\{\boldsymbol{\varepsilon}_\mathbf{p}^\mathbf{L}\}$, respectively, the terms w_o^i and v_o^i have to be consistent with the field functions $\partial v_o^i/\partial y$ and $\partial u_o^i/\partial y$, respectively. This

is achieved by using the field redistributed substitute shape functions obtained using the method of least squares and are given as

$$\bar{N}_1^1 = (1/3 - \zeta)/2; \quad \bar{N}_2^1 = 2/3; \quad \bar{N}_3^1 = (1/3 + \zeta)/2 \tag{13}$$

where $\bar{N}_1^1$, $\bar{N}_2^1$, and $\bar{N}_3^1$ are consistent with $\bar{N}_{1,\zeta}^0$, $\bar{N}_{2,\zeta}^0$, and $\bar{N}_{3,\zeta}^0$, respectively.

Using the smoothed interpolation functions, the constrained membrane and transverse shear strain components are expressed as

$$\begin{aligned}
\frac{\partial v_o}{\partial y} + \frac{w_o}{r} &= \sum_{i=1}^{M}\sum_{k=1}^{3}\left[\frac{\partial \bar{N}_k^0}{\partial y} V_i(x)\, v_{0k}^i + \bar{N}_k^1 W_i(x) \frac{w_{0k}^i}{r}\right] \\
\frac{\partial u_o}{\partial y} + \frac{\partial v_o}{\partial x} &= \sum_{i=1}^{M}\sum_{k=1}^{3}\left[\frac{\partial \bar{N}_k^0}{\partial y} U_i(x)\, u_{0k}^i + \bar{N}_k^1 \frac{\partial V_i}{\partial x} v_{0k}^i\right] \\
\theta_y + \frac{\partial w_o}{\partial y} - \frac{v_o}{r} &= \sum_{i=1}^{M}\sum_{k=1}^{3}\left[\bar{N}_k^1 \Theta_{yi}(x)\theta_{yk}^i + \frac{\partial \bar{N}_k^0}{\partial y} W_i(x)\, w_{0k}^i - \bar{N}_k^1 V_i(x) v_{ok}^i\right]
\end{aligned} \tag{14}$$

The other strain fields are expressed in terms of original shape functions ($\bar{N}_i^0$) and their derivatives.

The elements derived in this fashion behaves very well for both thick and thin situations, and permits the greater flexibility in the choice of integration order for the energy terms. It has good convergence and has no spurious rigid modes.

Based on the convergence study for the evaluation of the various energy terms, 5-point Gauss quadrature numerical integration scheme is used with respect to the circumferential coordinate (y). The integration in the meridional direction is carried out explicitly using the symbolic software MATHEMATICA.

4. Results

The study is carried out for the oval shell: $r = r_0/[1 + \zeta\cos(2y/r_0)]$. The geometrical and material properties are: $L = 0.2\,\text{m}$, $r_0 = 0.1\,\text{m}$, $h = 0.247\,\text{mm}$, $E = 71.02\,\text{GPa}$, $\rho = 2796\,\text{kg/m}^3$ and $v = 0.31$. The shell is subjected to point harmonic force at the mid length of the shell $(x = L/2)$: $F = F_0 \sin(\omega_F t)$. The proportional modal damping with damping factor $\delta_{mn} = 0.002$ is assumed. The forcing frequency ω_F is varied in the neighbourhood of linear free vibration frequency corresponding to first SS mode ($\zeta = 0$: $\omega_{mn} = 489.6615\,\text{Hz}$,

$\zeta = 0.2$: $\omega_{mn} = 476.5911\,\text{Hz}$, $\zeta = 0.4$: $\omega_{mn} = 443.7239\,\text{Hz}$, $\zeta = 0.6$: $\omega_{mn} = 394.4065\,\text{Hz}$. The forcing frequency versus amplitude curves obtained from the steady state response evaluated from the time integration approach are shown in Fig. 2 for two loading conditions of the oval shells with different noncircularity parameter (ζ). The steady state response versus time curves for two forcing frequencies are shown in Fig. 3 and the corresponding phase plane plots are shown in Fig. 4. It can be seen from Fig. 2 that the noncircular shells reveal softening type of nonlinear behaviour.

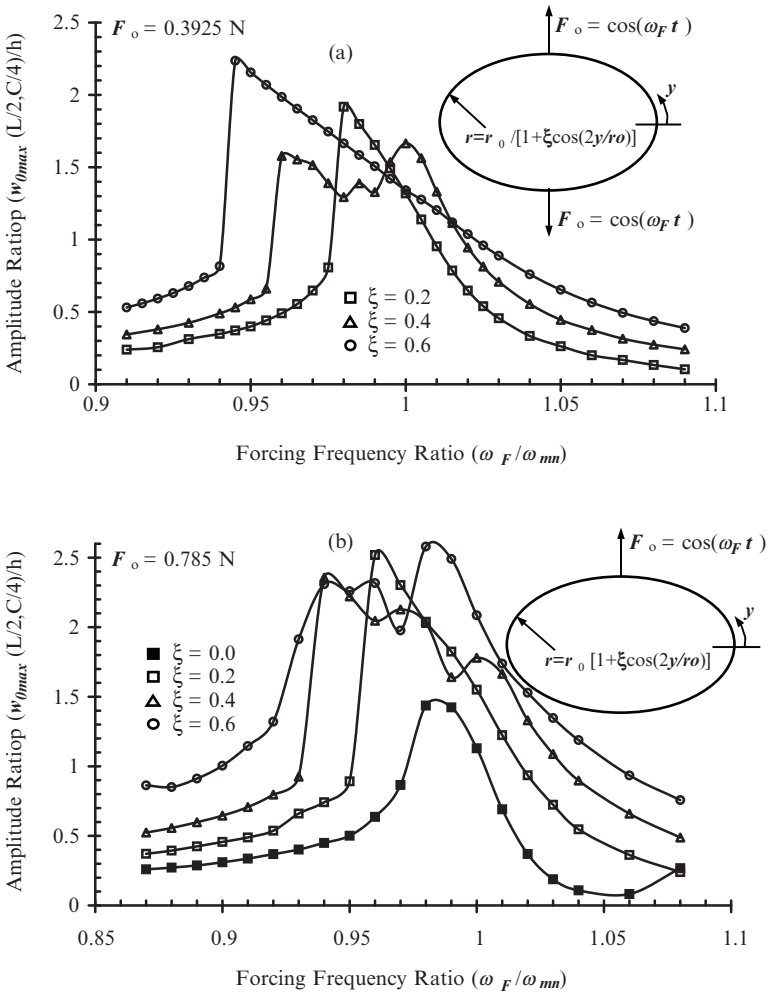

Fig. 2 Forcing frequency versus steady state amplitude for oval cylindrical shell under different loading conditions (a) two-point loading, (b) single-point loading.

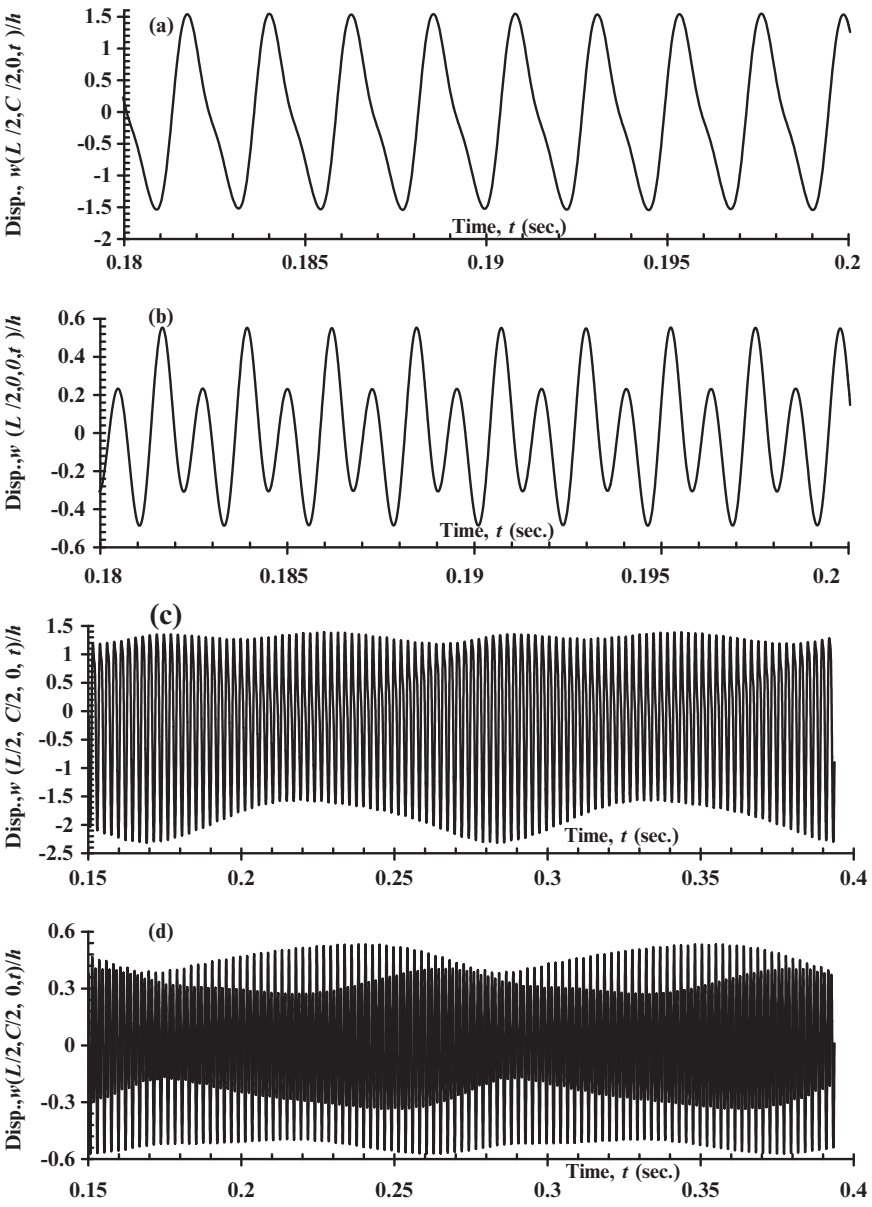

Fig. 3 Steady state response versus time curves for oval cylindrical shell subjected two-point force excitation: (a) response at loading point (semi-minor axis), ω_F/ω_{mn} = 0.995 (b) response at semi-major axis ω_F/ω_{mn} = 0.995 (c) at semi-minor axis, ω_F/ω_{mn} = 0.985 (d) at semi-major axis, ω_F/ω_{mn} = 0.985.

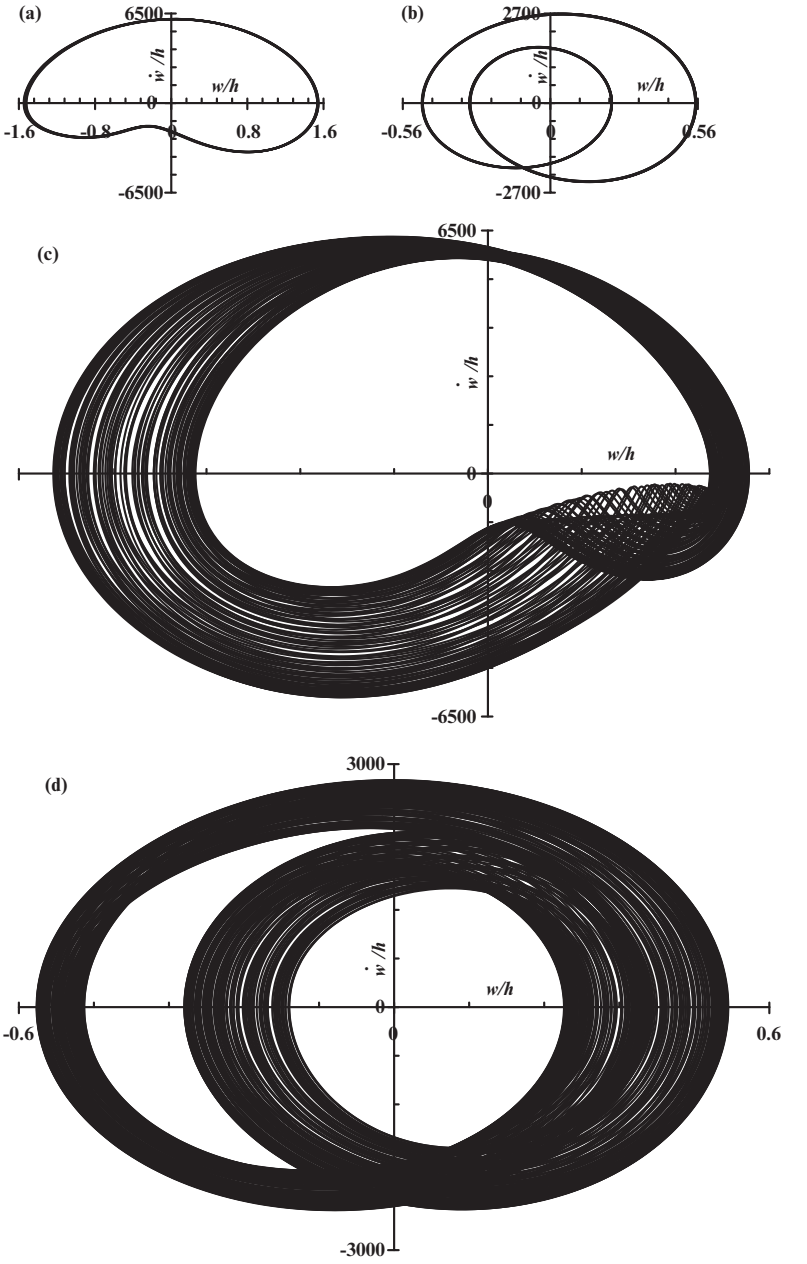

Fig. 4 Phase-plane plot of steady state response of oval cylindrical shell subjected two-point force excitation: (a) response at loading point (semi-minor axis), $\omega_F/\omega_{mn} = 0.995$ (b) response at semi-major axis, $\omega_F/\omega_{mn} = 0.995$ (c) at semi-minor axis, $\omega_F/\omega_{mn} = 0.985$ (d) at semi-major axis, $\omega_F/\omega_{mn} = 0.985$.

The degree of softening nonlinearity increases with the increase in the non-circularity parameter. The detailed study shows that the response of noncircular shells with $\zeta > 0.2$ reveals different temporal variation near to the semi-major axis region compared to that in the semi-minor axis region (see Fig. 3 and 4).

5. Conclusions

It is concluded from the literature that the woks on the circular shells based on the mode approximation reveal companion mode participation and traveling wave response as the distinct features. This work reveals softening type of nonlinearity. The degree of the nonlinearity increases with the increase in the noncircularity parameter. The response of noncircular shells, $\zeta > 2$ reveals different temporal variation near to the semi-major axis region compared to that in the semi-minor axis region.

References

1. D. A. Evensen, 1974. *Nonlinear vibrations of circular cylindrical shells*, *Thin-Shell Structures: Theory, Experiment and Design*, YC Fung and EE Sechler (eds), Prentice Hall, Englewood Cliffs, NY, 133–155.
2. F. Moussaoui, R. Benamar, 2002. *Nonlinear vibrations of shell-type structures: A review with bibliography*, Journal of Sound and Vibration, **255**, 161–184.
3. M. Amabili, M. P. Paidoussis, 2003. *Review of studies on geometrically nonlinear vibrations and dynamics of circular cylindrical shells and panels, with and without fluid–structure interaction*, Applied Mechanics Reviews, **56**, 105–125.
4. E. Reissner, 1955. *Nonlinear effects in vibrations of cylindrical shells*, Ramo Wooldridge Corporation Report *AM 5-6.*
5. H. N. Chu, 1961. *Influence of large-amplitudes on flexural vibrations of a thin circular cylindrical shell*, Journal of Aerospace Sciences, **28**, 602–609.
6. J. Nowinski, 1963. *Nonlinear transverse vibrations of orthotropic cylindrical shells*, AIAA Journal, **1**, 617–620.
7. B. E. Cummings, 1964. *Large-amplitude vibration and response of curved panels*, AIAA Journal, **2**, 709–716.
8. D. A. Evensen, 1963. *Some observations on the nonlinear vibration of thin cylindrical shells*, AIAA Journal, **1**, 2857–2858.
9. D. A. Evensen, 1966. *Nonlinear flexural vibrations of thin circular rings*, ASME Journal of Applied Mechanics, **33**, 553–560.
10. D. A. Evensen, E. Fulton, 1967. *Some studies on the nonlinear dynamic response of shell-type structures*, Proceedings of the International Conference on Dynamic Stability of Structures, Evanston, IL, Oct 18–20 1965, Pergamon Press, 237–254.
11. D. A. Evensen, 1964. *Non-linear flexural vibrations of thin circular rings*, PhD Thesis, California Institute of Technology, Pasadena, CA.

12. D. A. Evensen, 1965. *A theoretical and experimental study of nonlinear flexural vibrations of thin circular rings*, NASA TR R-227, Washington, DC, Government Printing Office.
13. D. A. Evensen, 1967. *Nonlinear flexural vibrations of thin-walled circular cylinders*, NASA TN D-4090.
14. M. D. Olson, 1965. *Some experimental observations on the nonlinear vibration of cylindrical shells*, AIAA Journal, **3**, 1775-1777.
15. Y. Matsuzaki, S. Kobayashi, 1970. *A theoretical and experimental study of the nonlinear flexural vibration of thin circular cylindrical shells with clamped ends*, Trans. of the Japan Society for Aeronautical and Space Sciences, **12**, 55–62.
16. Y. Matsuzaki, S. Kobayashi, 1969. *An analytical study of the nonlinear flexural vibration of thin circular cylindrical shells (in Japanese)*, Journal of the Japan Society for Aeronautical and Space Sciences, **17**, 308–315.
17. J. H. Ginsberg, 1973. *Large-amplitude forced vibrations of simply supported thin cylindrical shells*, ASME J. Appl. Mech., **40**, 471–477.
18. J. H. Ginsberg, 1974. *Nonlinear axisymmetric free vibration in simply supported cylindrical shells*, ASME J. Appl. Mech., **41**, 310–311.
19. J. C. Chen, C. D. Babcock, 1975. *Nonlinear vibration of cylindrical shells*, AIAA Journal, **13**, 868–876.
20. G. Prathap, 1978. *Comments on the large-amplitude asymmetric vibrations of some thin shells of revolution*, Journal of Sound and Vibration, **56**, 303–305.
21. E. H. Dowell, C. S. Ventres,1968. *Modal equations for the nonlinear flexural vibrations of a cylindrical shell*, International Journal of Solids and Structures, **4**, 975–991.
22. H. V. Ramani, 1985. *An analytical investigation of large amplitude free flexural vibration of thin circular cylindrical shells*, M. S. Thesis, Department of Aerospace Engineering, IIT Madras, India.
23. T. K. Varadhan, G. Prathap, H. V. Ramani, 1989. *Nonlinear free flexural vibrations of thin circular cylindrical shells*, AIAA Journal, **27**, 1303–1304.
24. T. Ueda, 1979. *Non-linear free vibrations of conical shells*, Journal of Sound and Vibration, **64**, 85–95.
25. M. Amabili, 2003. *Nonlinear vibrations of circular cylindrical shells with different boundary conditions*, AIAA Journal, **41**, 1119–1130.
26. M. Amabili, F. Pellicano, M. P. Paidoussis, 1998. *Nonlinear vibrations of simply supported, circular cylindrical shells, coupled to quiescent fluid*, Journal of Fluids and Structures, **12**, 883–918.
27. M. Amabili, F. Pellicano, M. P. Paidoussis, 1999. *Non-linear dynamics and stability of circular cylindrical shells containing flowing fluid. Part I: stability*, Journal of Sound and Vibration, **225**, 655-699.
28. M. Amabili, F. Pellicano, M. P. Paidoussis, 1999a. *Non-linear dynamics and stability of circular cylindrical shells containing flowing fluid. Part II: Large-amplitude vibrations without flow*, Journal of Sound and Vibration, **228**, 1103-1124.
29. M. Amabili, F. Pellicano, M. P. Paidoussis, 2000. *Non-linear dynamics and stability of circular cylindrical shells containing flowing fluid. Part III: Truncation effect without flow and experiments*, Journal of Sound and Vibration, **237**, 617-640.
30. M. Amabili, F. Pellicano, M. P. Paidoussis, 2000a. *Non-linear dynamics and stability of circular cylindrical shells containing flowing fluid. Part IV: Large-amplitude vibrations with flow*, Journal of Sound and Vibration, **237**, 641-666.
31. K. N. Karagiozis, M. Amabili, M. P. Paidoussis, A. K. Misra, 2005. *Nonlinear vibrationm of fluid filled clamped circular circular cylindrical shells*, Journal of Fluids and Structures, **21**, 579–595.

32. M. Chiba, 1993. *Experimental studies on a nonlinear hydroelastic vibration of a clamped cylindrical tank partially filled with liquid*, ASME Journal of Pressure Vessel Technology, **115**, 381–388.
33. M. Amabili, F. Pellicano, 2001. *Nonlinear supersonic flutter of circular cylindrical shells*, AIAA Journal, **39**, 564–573.
34. K. P. Soldatos, 1999. *Mechanics of Cylindrical Shells with Non-Circular Cross-Section*, Applied Mechanics Review, **52**, 237–274.
35. K. A. V. Pandalai, M. Sathyamoorthy, 1970. *Non-linear flexural vibrations of orthotropic oval cylindrical shells*, Studies in Structural Mechanics (K. A. V. Pandalai, editor), 47-74.
36. B. P. Patel, M. Ganapathi, D. P. Makhecha, S. S. Gupta, 2002. *On the nonlinear free flexural vibrations problem for thin elastic rings*, Journal of The Aeronautical Society of India, **54**, 298–309.
37. B. P. Patel, M. Ganapathi, D. P. Makhecha, P. Shah, 2003. *Large amplitude free flexural vibration of rings using finite element approach*, International Journal of Nonlinear Mechanics, **37**, 911–921.

3-D VIBRATION ANALYSIS OF MICROSTRETCH PLATES

ESİN İNAN*
Faculty of Arts and Sciences, Işık University, 34398, Maslak, Istanbul, Turkey

AHMET KIRIŞ
Faculty of Science and Letters, Istanbul Technical University, 34469, Maslak, Istanbul, Turkey

Abstract. In the present work, rectangular plates with various boundary conditions are studied, which are modeled by the microstretch theory. Wave propagation problem is investigated and new waves are observed which do not appear in the classical theory of elasticity. Ritz method is used for this investigation. Triplicate Chebyshev series, multiplied by boundary functions, are used as admissible functions and the frequency equations of the microstretch plate are obtained by the use of Chebyshev-Ritz method. The additional frequencies due to the microstructure of the plate are observed among the values of the frequencies obtained from the classical theory of elasticity. We observed that these additional frequencies disappear while the all microstretch constants are taken as zero.

Keywords: microstretch theory, plate vibration, natural frequencies, Ritz method

1. Introduction

Although materials are defined as homogeneous in the classical theory of continuum mechanics, in practical engineering problems, materials have lots of defects with different sizes and forms which violate the assumption of continuity at micro scales. However, the classical theory of elasticity gives reliable

*Corresponding author, inan@isikun.edu.tr

results to define firmly materials having more unyielding structure like steel, but the inconsistency between the results obtained from the classical theory and experiments shows that the classical theory of elasticity is unable to explain the behavior of materials that possess granular and heterogeneous structures like polymers or damaged materials in general.

Microstretch theory defined by Eringen[1] relies on the idea that every particles of the material can make both micro rotation and volumetric micro elongation in addition to the bulk deformation of the material. Since this theory includes the effects of micro structure which could affect the overall behavior of the medium, it reflects the physical realities much better than the classical theory for the engineering materials.

In the present work, plates having microstructure are modeled by the microstretch theory. The kinetic and the potential energies are calculated and the Ritz method is extended to the microstretch theory. The triplicate Chebyshev polynomial series which are multiplied by proper boundary functions, are used to describe the plate deflections[2]. The frequency equations of the microstretch plate for various boundary conditions are obtained in the matrix form and an analysis is realized to identify the relation between the frequencies of the microstretch plate and the microstretch material constants.

The vibration analysis of the plates modeled by microstretch theory shows that some additional frequencies due to the microstretch property of the plate appears among the values of the frequencies obtained in the classical theory of elasticity, as expected. We also observed that when the microstretch material constants vanish, these additional frequencies disappear and only the classical frequencies remain. More importantly, we also observed that these additional frequencies are more sensitive to the change of the micro elastic constants than the classical frequencies. Therefore, the values of the additional frequencies rapidly increase by the change of the micro constants and then considerable amount of additional frequencies move out among the classical frequencies under consideration. And more, if these constants get bigger than their threshold values, the classical frequencies also begin to deviate from their original values. We think that these threshold values may be considered as upper bounds for each of the constants and therefore this observation may guide us to identify the microstretch material constants for different materials for future works.

2. Vibration analysis in microstretch theory

The constitutive equations for a linear isotropic microstretch elastic solid are given as

$$
\begin{aligned}
t_{kl} &= \lambda\, \varepsilon_{mm}\, \delta_{kl} + (\mu + \kappa)\, \varepsilon_{kl} + \mu\, \varepsilon_{lk} + \lambda_0\, \theta\, \delta_{kl}, \\
m_{kl} &= \alpha\, \gamma_{mm}\, \delta_{kl} + \beta\, \gamma_{kl} + \gamma\, \gamma_{lk}, \\
m_k &= a_0\, \theta_{,k}, \\
s - t &= \lambda_1\, \theta + \lambda_0\, \varepsilon_{kk}.
\end{aligned}
\tag{1}
$$

Here, t_{kl}, m_{kl} are the stress and couple stress tensors, m_k is the microstretch vector, δ_{kl} is the Kronecker delta and $s = s_{kk}$, $t = t_{kk}$. The strain tensors in a microstretch medium are given by Eringen[1] as

$$
\varepsilon_{kl} = u_{l,k} + e_{lkm}\phi_m, \quad \gamma_{kl} = \phi_{k,l}, \quad \gamma_k = \theta_{,k} \tag{2}
$$

Here, λ, μ are Lamé constant and shear modulus respectively, κ, α, β, γ are the micropolar constants, λ_0, λ_1 and a_0 are the microstretch constants, ρ is the mass density per unit volume, j is the micro-inertia, e_{ijk} is the permutation symbol. $\mathbf{u}, \boldsymbol{\phi}$ and θ are displacement, microrotation vectors and microstretch scalar, respectively.

Here, we only give the results of the wave propagation analysis in a linear isotropic microstretch medium for brevity. There are five types of wave propagation with different phase velocities; coupled "longitudinal microstretch wave" and "longitudinal displacement wave", coupled "transverse displacement wave" and "transverse micro rotational wave", uncoupled "longitudinal micro rotational wave" which the last two waves do not appear in classical theory of elasticity while the first wave also disappear in both micropolar theory and classical theory[3,4].

We consider an isotropic rectangular plate with length a, width b and thickness h and the origin of a Cartesian Coordinate system (x_1, x_2, x_3) is located at the middle of the plate whose normal is in the positive direction of the axes x_3.

Here, the maximum energy functional is,

$$
\Pi = V_{\max} - T_{\max}. \tag{3}
$$

Assuming harmonic-time dependence, $\mathbf{u}, \boldsymbol{\phi}$ and θ may be written in terms of the amplitude functions as follows

$$
\left\{\mathbf{u}(x,y,z,t), \boldsymbol{\phi}(x,y,z,t), \theta(x,y,z,t)\right\} = \left\{\mathbf{U}(x,y,z,t), \boldsymbol{\Phi}(x,y,z,t), \Theta(x,y,z,t)\right\} e^{i\omega t} \tag{4}
$$

where ω denotes the natural frequency. Now introducing the following non dimensional parameters

$$\xi = \frac{2x}{a}, \quad \eta = \frac{2y}{b}, \quad \zeta = \frac{2z}{h} \tag{5}$$

the linear elastic strain energy $V_{\max}$ and the kinetic energy $T_{\max}$ may be written in terms of the non dimensional parameters as

$$\begin{aligned}
V &= \frac{h}{4\alpha_1}\int_{-1}^{1}\int_{-1}^{1}\int_{-1}^{1}\Big[\lambda\bar{\Lambda}_1^2 + (2\mu+\kappa)\bar{\Lambda}_2 + 2\mu\bar{\Lambda}_3 + (\mu+\kappa)\bar{\Lambda}_4 + \alpha\bar{\Lambda}_5^2 + (\beta+\gamma)\bar{\Lambda}_6 \\
&\quad + 2\beta\bar{\Lambda}_7 + \gamma\bar{\Lambda}_8 + a_0\bar{\Lambda}_9\Big]d\zeta\, d\eta\, d\xi \\
&\quad + \frac{bh}{8}\int_{-1}^{1}\int_{-1}^{1}\int_{-1}^{1}\Big[\kappa\bar{\bar{\Lambda}}_3 + 2\lambda_0\Theta\bar{\Lambda}_1\Big]d\zeta\, d\eta\, d\xi + \frac{abh}{16}\int_{-1}^{1}\int_{-1}^{1}\int_{-1}^{1}\Big[\kappa\bar{\bar{\bar{\Lambda}}}_3 + \lambda_1\Theta^2\Big]d\zeta\, d\eta\, d\xi \\
T &= \frac{\rho}{16}abh\omega^2\int_{-1}^{1}\int_{-1}^{1}\int_{-1}^{1}\Big\{\Big[U_1^2 + U_2^2 + U_3^2\Big] + j\Big[\Phi_1^2 + \Phi_2^2 + \Phi_3^2\Big] + 3j\Theta^2\Big\}d\zeta\, d\eta\, d\xi
\end{aligned} \tag{6}$$

where

$$\begin{aligned}
&\bar{\Lambda}_1 = \bar{\varepsilon}_{\xi\xi} + \bar{\varepsilon}_{\eta\eta} + \bar{\varepsilon}_{\zeta\zeta}, \quad \bar{\Lambda}_2 = \bar{\varepsilon}_{\xi\xi}^2 + \bar{\varepsilon}_{\eta\eta}^2 + \bar{\varepsilon}_{\zeta\zeta}^2, \\
&\bar{\Lambda}_3 = {}_1\bar{\varepsilon}_{\xi\eta}\,{}_1\bar{\varepsilon}_{\eta\xi} + {}_1\bar{\varepsilon}_{\xi\zeta}\,{}_1\bar{\varepsilon}_{\zeta\xi} + {}_1\bar{\varepsilon}_{\eta\zeta}\,{}_1\bar{\varepsilon}_{\zeta\eta}, \\
&\bar{\bar{\Lambda}}_3 = \left({}_1\bar{\varepsilon}_{\xi\eta} - {}_1\bar{\varepsilon}_{\eta\xi}\right){}_2\bar{\varepsilon}_{\xi\eta} + \left({}_1\bar{\varepsilon}_{\xi\zeta} - {}_1\bar{\varepsilon}_{\zeta\xi}\right){}_2\bar{\varepsilon}_{\xi\zeta} + \left({}_1\bar{\varepsilon}_{\eta\zeta} - {}_1\bar{\varepsilon}_{\zeta\eta}\right){}_2\bar{\varepsilon}_{\eta\zeta}, \\
&\bar{\bar{\bar{\Lambda}}}_3 = {}_2\bar{\varepsilon}_{\xi\eta}^2 + {}_2\bar{\varepsilon}_{\xi\zeta}^2 + {}_2\bar{\varepsilon}_{\eta\zeta}^2, \quad \bar{\Lambda}_4 = {}_1\bar{\varepsilon}_{\xi\eta}^2 + {}_1\bar{\varepsilon}_{\eta\xi}^2 + {}_1\bar{\varepsilon}_{\xi\zeta}^2 + {}_1\bar{\varepsilon}_{\zeta\xi}^2 + {}_1\bar{\varepsilon}_{\eta\zeta}^2 + {}_1\bar{\varepsilon}_{\zeta\eta}^2, \\
&\bar{\Lambda}_5 = \bar{\gamma}_{\xi\xi} + \bar{\gamma}_{\eta\eta} + \bar{\gamma}_{\zeta\zeta}, \quad \bar{\Lambda}_6 = \bar{\gamma}_{\xi\xi}^2 + \bar{\gamma}_{\eta\eta}^2 + \bar{\gamma}_{\zeta\zeta}^2, \\
&\bar{\Lambda}_7 = \bar{\gamma}_{\xi\eta}\,\bar{\gamma}_{\eta\xi} + \bar{\gamma}_{\xi\zeta}\,\bar{\gamma}_{\zeta\xi} + \bar{\gamma}_{\eta\zeta}\,\bar{\gamma}_{\zeta\eta}, \quad \bar{\Lambda}_8 = \bar{\gamma}_{\xi\eta}^2 + \bar{\gamma}_{\eta\xi}^2 + \bar{\gamma}_{\xi\zeta}^2 + \bar{\gamma}_{\zeta\xi}^2 + \bar{\gamma}_{\eta\zeta}^2 + \bar{\gamma}_{\zeta\eta}^2, \\
&\bar{\Lambda}_9 = \bar{\Theta}_{,\xi}^2 + \bar{\Theta}_{,\eta}^2 + \bar{\Theta}_{,\zeta}^2
\end{aligned} \tag{7}$$

and

$$\bar{\varepsilon}_{\xi\xi}=\frac{\partial U_1}{\partial\xi},\ \bar{\varepsilon}_{\eta\eta}=\alpha_1\frac{\partial U_2}{\partial\eta},\ \bar{\varepsilon}_{\zeta\zeta}=\frac{\alpha_1}{\alpha_2}\frac{\partial U_3}{\partial\zeta},\ {}_1\bar{\varepsilon}_{\xi\eta}=\frac{\partial U_2}{\partial\xi},\ {}_1\bar{\varepsilon}_{\eta\xi}=\alpha_1\frac{\partial U_1}{\partial\eta},\ {}_1\bar{\varepsilon}_{\xi\zeta}=\frac{\partial U_3}{\partial\xi},$$

$${}_1\bar{\varepsilon}_{\zeta\xi}=\frac{\alpha_1}{\alpha_2}\frac{\partial U_1}{\partial\zeta},\ {}_1\bar{\varepsilon}_{\eta\zeta}=\alpha_1\frac{\partial U_3}{\partial\eta},\ {}_1\bar{\varepsilon}_{\zeta\eta}=\frac{\alpha_1}{\alpha_2}\frac{\partial U_2}{\partial\zeta},\ {}_2\bar{\varepsilon}_{ij}=e_{jik}\Phi_k,\quad (i,j,k=\xi,\eta,\zeta),$$

$$\bar{\gamma}_{\xi\xi}=\frac{\partial\Phi_1}{\partial\xi},\ \bar{\gamma}_{\eta\eta}=\alpha_1\frac{\partial\Phi_2}{\partial\eta},\ \bar{\gamma}_{\zeta\zeta}=\frac{\alpha_1}{\alpha_2}\frac{\partial\Phi_3}{\partial\zeta},\ \bar{\gamma}_{\xi\eta}=\alpha_1\frac{\partial\Phi_1}{\partial\eta},\ \bar{\gamma}_{\eta\xi}=\frac{\partial\Phi_2}{\partial\xi},\ \bar{\gamma}_{\xi\zeta}=\frac{\alpha_1}{\alpha_2}\frac{\partial\Phi_1}{\partial\zeta},$$

$$\bar{\gamma}_{\zeta\xi}=\frac{\partial\Phi_3}{\partial\xi},\ \bar{\gamma}_{\eta\zeta}=\frac{\alpha_1}{\alpha_2}\frac{\partial\Phi_2}{\partial\zeta},\ \bar{\gamma}_{\zeta\eta}=\alpha_1\frac{\partial\Phi_3}{\partial\eta},\ \bar{\Theta}_{,\xi}=\frac{\partial\Theta}{\partial\xi},\ \bar{\Theta}_{,\eta}=\alpha_1\frac{\partial\Theta}{\partial\eta},\ \bar{\Theta}_{,\zeta}=\frac{\alpha_1}{\alpha_2}\frac{\partial\Theta}{\partial\zeta},$$

$$\alpha_1=\frac{a}{b},\ \alpha_2=\frac{h}{b}.$$

(8)

Here, following[3] , we used Chebyshev polynomials multiplied by a proper boundary function as admissible functions for each amplitude functions of the Eqn. (3), i. e.,

$$U_1(\xi,\eta,\zeta)=F_{u_1}(\xi,\eta)\sum_{i,j,k=1}^{\infty}A_{ijk}P_i(\xi)P_j(\eta)P_k(\zeta),\ \ \Phi_1(\xi,\eta,\zeta)=F_{\Phi_1}(\xi,\eta)\sum_{\hat{i},\hat{j},\hat{k}=1}^{\infty}\hat{A}_{\hat{i}\hat{j}\hat{k}}P_{\hat{i}}(\xi)P_{\hat{j}}(\eta)P_{\hat{k}}(\zeta),$$

$$U_2(\xi,\eta,\zeta)=F_{u_2}(\xi,\eta)\sum_{l,m,n=1}^{\infty}B_{lmn}P_l(\xi)P_m(\eta)P_n(\zeta),\ \Phi_2(\xi,\eta,\zeta)=F_{\Phi_2}(\xi,\eta)\sum_{\hat{l},\hat{m},\hat{n}=1}^{\infty}\hat{B}_{\hat{l}\hat{m}\hat{n}}P_{\hat{l}}(\xi)P_{\hat{m}}(\eta)P_{\hat{n}}(\zeta),$$

$$U_3(\xi,\eta,\zeta)=F_{u_3}(\xi,\eta)\sum_{p,q,r=1}^{\infty}C_{pqr}P_p(\xi)P_q(\eta)P_r(\zeta),\ \Phi_3(\xi,\eta,\zeta)=F_{\Phi_3}(\xi,\eta)\sum_{\hat{p},\hat{q},\hat{r}=1}^{\infty}\hat{C}_{\hat{p}\hat{q}\hat{r}}P_{\hat{p}}(\xi)P_{\hat{q}}(\eta)P_{\hat{r}}(\zeta),$$

$$\Theta(\xi,\eta,\zeta)=F_{\Theta}(\xi,\eta)\sum_{\hat{i},\hat{j},\hat{k}=1}^{\infty}\hat{\hat{A}}_{\hat{i}\hat{j}\hat{k}}P_{\hat{i}}(\xi)P_{\hat{j}}(\eta)P_{\hat{k}}(\zeta)$$

(9)

where the one dimensional i^{th} Chebyshev polynomial is given as

$$P_i(\chi)=\cos\left[(i-1)\arccos(\chi)\right].\tag{10}$$

The boundary functions are

$$F_\delta(\xi,\eta)=f_\delta^1(\xi)f_\delta^2(\eta),\quad (\delta=u_i,\phi_i,\theta,\quad i=1,...,3).\tag{11}$$

The boundary functions due to the classical deformation are given in[2] for different boundary conditions. And the boundary functions due to micro deformation for all types , are considered as

$$f_\delta^1(\xi)=f_\delta^2(\eta)=1,\ (\delta=\phi_i,\theta,\ i=1,...,3).\tag{12}$$

Finally, substituting the series expansions (9) into the potential energy and into the kinetic energy (6) and using these results in the maximum energy functional (3) of the microstretch plate and then minimizing this functional with respect to the coefficients of the Chebyshev polynomials, we find the final equations in the form of an eigenvalue problem as

$$\left(\mathbf{K}-\Omega^2\,\mathbf{M}\right)\mathbf{Z}=\mathbf{0}. \tag{13}$$

Here, $\Omega=\omega a\sqrt{\rho}$ and the stiffness and the diagonal mass matrices are given by the use of its-sub-matrices;

$$\mathbf{K}=\begin{pmatrix}
\left[K_{u_1u_1}\right] & \left[K_{u_1u_2}\right] & \left[K_{u_1u_3}\right] & \mathbf{0} & \left[K_{u_1\phi_2}\right] & \left[K_{u_1\phi_3}\right] & \left[K_{u_1\theta}\right] \\
\left[K_{u_1u_2}\right]^T & \left[K_{u_2u_2}\right] & \left[K_{u_2u_3}\right] & \left[K_{u_2\phi_1}\right] & \mathbf{0} & \left[K_{u_2\phi_3}\right] & \left[K_{u_2\theta}\right] \\
\left[K_{u_1u_3}\right]^T & \left[K_{u_2u_3}\right]^T & \left[K_{u_3u_3}\right] & \left[K_{u_3\phi_1}\right] & \left[K_{u_3\phi_2}\right] & \mathbf{0} & \left[K_{u_3\theta}\right] \\
\mathbf{0} & \left[K_{u_2\phi_1}\right]^T & \left[K_{u_3\phi_1}\right]^T & \left[K_{\phi_1\phi_1}\right] & \left[K_{\phi_1\phi_2}\right] & \left[K_{\phi_1\phi_3}\right] & \mathbf{0} \\
\left[K_{u_1\phi_2}\right]^T & \mathbf{0} & \left[K_{u_3\phi_2}\right]^T & \left[K_{\phi_1\phi_2}\right]^T & \left[K_{\phi_2\phi_2}\right] & \left[K_{\phi_2\phi_3}\right] & \mathbf{0} \\
\left[K_{u_1\phi_3}\right]^T & \left[K_{u_2\phi_3}\right]^T & \mathbf{0} & \left[K_{\phi_1\phi_3}\right]^T & \left[K_{\phi_2\phi_3}\right]^T & \left[K_{\phi_3\phi_3}\right] & \mathbf{0} \\
\left[K_{u_1\theta}\right]^T & \left[K_{u_2\theta}\right]^T & \left[K_{u_3\theta}\right]^T & \mathbf{0} & \mathbf{0} & \mathbf{0} & \left[K_{\theta\theta}\right]
\end{pmatrix} \tag{14}$$

and

$$\mathbf{M}=\begin{pmatrix}
\left[M_{u_1u_1}\right] & \mathbf{0} & \mathbf{0} & \mathbf{0} & \mathbf{0} & \mathbf{0} & \mathbf{0} \\
\mathbf{0} & \left[M_{u_2u_2}\right] & \mathbf{0} & \mathbf{0} & \mathbf{0} & \mathbf{0} & \mathbf{0} \\
\mathbf{0} & \mathbf{0} & \left[M_{u_3u_3}\right] & \mathbf{0} & \mathbf{0} & \mathbf{0} & \mathbf{0} \\
\mathbf{0} & \mathbf{0} & \mathbf{0} & \left[M_{\phi_1\phi_1}\right] & \mathbf{0} & \mathbf{0} & \mathbf{0} \\
\mathbf{0} & \mathbf{0} & \mathbf{0} & \mathbf{0} & \left[M_{\phi_2\phi_2}\right] & \mathbf{0} & \mathbf{0} \\
\mathbf{0} & \mathbf{0} & \mathbf{0} & \mathbf{0} & \mathbf{0} & \left[M_{\phi_3\phi_3}\right] & \mathbf{0} \\
\mathbf{0} & \mathbf{0} & \mathbf{0} & \mathbf{0} & \mathbf{0} & \mathbf{0} & \left[M_{\theta\theta}\right]
\end{pmatrix} \tag{15}$$

The column vector $\mathbf{Z}$ may be denoted as $\mathbf{Z}=\{\mathbf{A},\mathbf{B},\mathbf{C},\hat{\mathbf{A}},\hat{\mathbf{B}},\hat{\mathbf{C}},\hat{\hat{\mathbf{A}}}\}$ and each sub-column vector is given as $\mathbf{A}=\{A_{111},\ldots,A_{11N},\ldots,A_{1k1},\ldots,A_{1kN},\ldots,A_{I11},\ldots,A_{IJK}\}$. Here, the elements of the stiffness and the mass matrix are found as

$$\left[K_{u_1u_1}\right]=(\lambda+2\mu+\kappa)D^{1,1}_{u_1iu_1\underline{i}}G^{0,0}_{u_1ju_1\underline{j}}H^{0,0}_{k\underline{k}}+(\mu+\kappa)\alpha_1^2\left(D^{0,0}_{u_1iu_1\underline{i}}G^{1,1}_{u_1ju_1\underline{j}}H^{0,0}_{k\underline{k}}+\frac{1}{\alpha_2^2}D^{0,0}_{u_1iu_1\underline{i}}G^{0,0}_{u_1ju_1\underline{j}}H^{1,1}_{k\underline{k}}\right),$$

$$\left[K_{u_2u_2}\right]=\alpha_1^2\left((\lambda+2\mu+\kappa)D^{0,0}_{u_2lu_2\underline{l}}G^{1,1}_{u_2mu_2\underline{m}}H^{0,0}_{n\underline{n}}+(\mu+\kappa)\frac{1}{\alpha_2^2}D^{0,0}_{u_2lu_2\underline{l}}G^{0,0}_{u_2mu_2\underline{m}}H^{1,1}_{n\underline{n}}\right)$$
$$+(\mu+\kappa)D^{1,1}_{u_2lu_2\underline{l}}G^{0,0}_{u_2mu_2\underline{m}}H^{0,0}_{n\underline{n}},$$

$$\left[K_{u_3u_3}\right]=\alpha_1^2\left(\frac{1}{\alpha_2^2}(\lambda+2\mu+\kappa)D^{0,0}_{u_3pu_3\underline{p}}G^{0,0}_{u_3qu_3\underline{q}}H^{1,1}_{r\underline{r}}+(\mu+\kappa)D^{0,0}_{u_3pu_3\underline{p}}G^{1,1}_{u_3qu_3\underline{q}}H^{0,0}_{r\underline{r}}\right)$$
$$+(\mu+\kappa)D^{1,1}_{u_3pu_3\underline{p}}G^{0,0}_{u_3qu_3\underline{q}}H^{0,0}_{r\underline{r}},$$

$$\left[K_{u_1u_2}\right]=\alpha_1\left(\lambda D^{1,0}_{u_1iu_2l}G^{0,1}_{u_1ju_2m}H^{0,0}_{kn}+\mu D^{0,1}_{u_1iu_2l}G^{1,0}_{u_1ju_2m}H^{0,0}_{kn}\right),\quad\left[K_{u_1\phi_2}\right]=-\frac{a}{4}\kappa\frac{\alpha_1}{\alpha_2}D^{0,0}_{u_1i\phi_2\hat{l}}G^{0,0}_{u_1j\phi_2m}H^{1,0}_{kn},$$

$$\left[K_{u_1u_3}\right]=\frac{\alpha_1}{\alpha_2}\left(\lambda D^{1,0}_{u_1iu_3p}G^{0,0}_{u_1ju_3q}H^{0,1}_{kr}+\mu D^{0,1}_{u_1iu_3p}G^{0,0}_{u_1ju_3q}H^{1,0}_{kr}\right),\quad\left[K_{u_1\phi_3}\right]=\frac{a}{4}\kappa\alpha_1D^{0,0}_{u_1i\phi_3\hat{p}}G^{1,0}_{u_1j\phi_3\hat{q}}H^{0,0}_{k\hat{r}},$$

$$\left[K_{u_1\theta}\right]=\frac{a}{2}\lambda_0D^{1,0}_{u_1i\theta\hat{i}}G^{0,0}_{u_1j\theta\hat{\underline{j}}}H^{0,0}_{k\hat{\underline{k}}},\quad\left[K_{u_2u_3}\right]=\frac{\alpha_1^2}{\alpha_2}\left(\lambda D^{0,0}_{u_2lu_3p}G^{1,0}_{u_2mu_3q}H^{0,1}_{nr}+\mu D^{0,0}_{u_2lu_3p}G^{0,1}_{u_2mu_3q}H^{1,0}_{nr}\right),$$

$$\left[K_{u_2\phi_1}\right]=\frac{a}{4}\kappa\frac{\alpha_1}{\alpha_2}D^{0,0}_{u_2l\phi_1\hat{i}}G^{0,0}_{u_2m\phi_1\hat{\underline{j}}}H^{1,0}_{n\hat{k}},\quad\left[K_{u_2\phi_3}\right]=-\frac{a}{4}\kappa D^{1,0}_{u_2l\phi_3\hat{p}}G^{0,0}_{u_2m\phi_3\hat{q}}H^{0,0}_{n\hat{r}},$$

$$\left[K_{u_2\theta}\right]=\frac{a}{2}\lambda_0\alpha_1D^{0,0}_{u_2l\theta\hat{\underline{i}}}G^{1,0}_{u_2m\theta\hat{\underline{j}}}H^{0,0}_{n\hat{\underline{k}}},\quad\left[K_{u_3\phi_1}\right]=-\frac{a}{4}\kappa\alpha_1D^{0,0}_{u_3p\phi_1\hat{\underline{i}}}G^{1,0}_{u_3q\phi_1\hat{\underline{j}}}H^{0,0}_{r\hat{k}},$$

$$\left[K_{u_3\phi_2}\right]=\frac{a}{4}\kappa D^{1,0}_{u_3p\phi_2\hat{l}}G^{0,0}_{u_3q\phi_2\hat{\underline{m}}}H^{0,0}_{r\hat{n}},\quad\left[M_{u_1u_1}\right]=\frac{1}{4}D^{0,0}_{u_1iu_1\underline{i}}G^{0,0}_{u_1ju_1\underline{j}}H^{0,0}_{k\underline{k}},$$

$$\left[M_{\phi_1\phi_1}\right]=\frac{1}{4}jD^{0,0}_{\phi_1\hat{i}\phi_1\hat{\underline{i}}}G^{0,0}_{\phi_1\hat{j}\phi_1\hat{\underline{j}}}H^{0,0}_{\hat{k}\hat{\underline{k}}},\quad\left[M_{u_2u_2}\right]=\frac{1}{4}D^{0,0}_{u_2lu_2\underline{l}}G^{0,0}_{u_2mu_2\underline{m}}H^{0,0}_{n\underline{n}},$$

$$\left[M_{\phi_2\phi_2}\right]=\frac{1}{4}jD^{0,0}_{\phi_2\hat{l}\phi_2\hat{\underline{l}}}G^{0,0}_{\phi_2\hat{m}\phi_2\hat{\underline{m}}}H^{0,0}_{\hat{n}\hat{\underline{n}}},\quad\left[M_{u_3u_3}\right]=\frac{1}{4}D^{0,0}_{u_3pu_3\underline{p}}G^{0,0}_{u_3qu_3\underline{q}}H^{0,0}_{r\underline{r}},$$

$$\left[M_{\phi_3\phi_3}\right]=\frac{1}{4}jD^{0,0}_{\phi_3\hat{p}\phi_3\hat{\underline{p}}}G^{0,0}_{\phi_3\hat{q}\phi_3\hat{\underline{q}}}H^{0,0}_{\hat{r}\hat{\underline{r}}},\quad\left[M_{\theta\theta}\right]=\frac{3}{4}jD^{0,0}_{\theta\hat{i}\theta\hat{\underline{i}}}G^{0,0}_{\theta\hat{j}\theta\hat{\underline{j}}}H^{0,0}_{\hat{k}\hat{\underline{k}}}\tag{16}$$

where

$$D^{s,\bar{s}}_{\beta_1\tau_1\beta_2\tau_2}=\int_{-1}^{1}\left\{\frac{d^s\left(f^1_{\beta_1}(\xi)P_{\tau_1}(\xi)\right)}{d\xi^s}\frac{d^{\bar{s}}\left(f^1_{\beta_2}(\xi)P_{\tau_2}(\xi)\right)}{d\xi^{\bar{s}}}\right\}d\xi,\quad H^{s,\bar{s}}_{\tau_1\tau_2}=\int_{-1}^{1}\left\{\frac{d^sP_{\tau_1}(\zeta)}{d\zeta^s}\frac{d^{\bar{s}}P_{\tau_2}(\zeta)}{d\zeta^{\bar{s}}}\right\}d\zeta,$$

$$G^{s,\bar{s}}_{\beta_1\tau_1\beta_2\tau_2}=\int_{-1}^{1}\left\{\frac{d^s\left(f^2_{\beta_1}(\eta)P_{\tau_1}(\eta)\right)}{d\eta^s}\frac{d^{\bar{s}}\left(f^2_{\beta_2}(\eta)P_{\tau_2}(\eta)\right)}{d\eta^{\bar{s}}}\right\}d\eta,$$

$$(s,\bar{s}=0,1,\quad \beta_1,\beta_2=u_1,u_2,u_3,\phi_1,\phi_2,\phi_3,\theta,\quad \tau_1,\tau_2=i,j,k,l,m,n,p,q,r,...). \tag{17}$$

3. Comparison and numerical results

To our knowledge, there is no other result found for the frequencies of free vibration of a plate modeled by microstretch theory in the literature. Therefore we had to compare our results with only the results obtained in the classical theory of elasticity by taking all microstretch material constants zero in Table 1. We may investigate the vibration modes of the plate as symmetric (**S**) and antisymmetric (**A**) modes in the directions ξ, η and ζ as **AAA, AAS, ASA, ASS, SAA, SAS, SSA,** and **SSS**. Here, the non-dimensional frequency parameter is given as $\Delta=b/a\,h\,\pi^2\sqrt{12(1-\nu^2)/E}\;\Omega$. In Table 2, we used Gauthier material[5] (ν=0.4 , $E=5.29\,GPa$, $a=1\,m$, $j=1.96\times10^{-7}\,m^2$, $\alpha_1=1$, $\alpha_2=0.1$).

TABLE 1. Comparison of the frequency parameter.

Cond.-Sym $\alpha_1-\alpha_2$ no.terms	Comparison	Δ_1	Δ_2	Δ_3	Δ_4	Δ_5	Δ_6
Sim.Sup.SSS 1-0.2 6x6x2	3-D Ritz[3] Pre.results*	4.6127 4.61275	7.7465 7.74654	10.314 10.3144	10.314 10.3144	13.838 13.8382	16.632 16.6318
Clamped AAS 1.5-0.3 8x8x4	3-D Ritz[3] Pre.results*	4.2234 4.2235	5.1628 5.1633	6.3962 6.3962	8.0677 8.0687	8.8143 8.8143	9.0568 9.0569
Sim.Sup. NoSym. 1-0.1 8x8x4	3-D Ritz[3] Pre.results*	1.9342 1.9342	4.6222 4.6224	4.6222 4.6224	6.5234 6.5234	6.5234 6.5234	7.1030 7.1038
Clamped SSS 2-0.5 8x8x4	3-D Ritz[3] Pre.results*	2.4682 2.4685	3.8884 3.8888	3.9131 3.9135	4.0559 4.0564	4.3534 4.3536	4.5282 4.5283
Sim.Sup. NoSym. 1-0.2 8x8x4	3-D Ritz[3] Pre.results*	1.7558 1.7759	3.2617 3.2617	3.2617 3.2617	3.8991 3.9010	3.8991 3.9010	4.6128 4.6128

TABLE 2. Frequency parameter for simply supported plates.

Micro Mat. Constant	class., micropolar, microelongation and deviated class. freq. are written in normal, italic, underline and bold, respectively.
$all = 0$	1.9273, 4.5858, 4.5858, 6.0395, 6.0395, 7.0226, 8.5411, 8.5483, 8.5483, 10.7084, 10.7084, 12.079, 12.079, 13.5049
$all = 10^{-12}$	*0.7127,* 1.9273, 4.5858, 4.5858, 6.0395, 6.0395, 7.0226, 8.5411, 8.5483, 8.5483, 10.7084, 10.7084, 12.079, 12.079, 13.5049
$\alpha = \beta = \gamma = \kappa = 10^{-11}$ $a_0 = \lambda_0 = \lambda_1 = 0$	*0.0.5412, 0.7754, 0.8263, 1.2888, 1.3586, 1.4264, 1.6010, 1.9273, 2.2798, 2.3054*, 4.5858, 4.5858, 6.0395, 6.0395, 7.0226, 8.5411, 8.5483, 8.5483, 10.7084, 10.7084, 12.079, 12.079, 13.5049
$\alpha = \beta = \gamma = \kappa = 10^{-10}$ $a_0 = \lambda_0 = \lambda_1 = 0$	*0.4822, 0.5216, 0.6536, 0.7803, 0.8017, 0.9286, 1.0103, 1.1529, 1.2404, 1.3200, 1.4032, 1.5208, 1.6065, 1.7289, 1.8235,* 1.9273, *2.0763, 2.1854, 2.2688, 2.347, 2.5849, 2.6499, 2.7740, 2.8608, 2.9458, 3.161, 3.2336, 3.3514, 3.5103, 3.7664, 3.8530, 3.9580, 4.0418, 4.1192, 4.2677, 4.3671*, 4.5858, 4.5858, *4.6787, 4.7948, 4.8422, 4.9590, 5.0671, 5.1358, 5.3554, 5.4584, 5.5957*, 6.0395, 6.0395, 7.0226, *7.1556, 7.2658, 7.3245, 7.4185*, 8.5411, 8.5483, 8.5483, 10.7084, 10.7084, 12.079, 12.079, 13.5049
$\alpha = \beta = \gamma = \kappa = 10^{-8}$ $a_0 = \lambda_0 = \lambda_1 = 0$	*0.3153, 0.8885, 0.9093, 1.0647, 1.2745, 1.3343, 1.436, 1.5611, 1.6207, 1.7086, 1.8681*, 1.9273, *2.0004, 2.2907, 2.4994, 2.5639, 2.6947, 2.8196, 2.9162, 3.1638, 3.2013, 3.3990, 3.4501, 3.5878, 3.6726, 3.7504, 3.9294, 4.1562, 4.2191, 4.397*, 4.5858, 4.5858, *4.6530, 4.8224, 5.0812, 5.2161, 5.3302, 5.4675, 5.5492, 5.6791, 5.8206, 5.9456*, 6.0395, 6.0395, *6.1246, 6.4403, 6.5367, 6.6438, 6.7735, 6.8439, 6.9550*, 7.0226, *7.2230, 7.6489, 7.8036, 8.0170, 8.1792, 8.2903, 8.3980, 8.4216*, 8.5411, 8.5483, 8.5483, *8.6307, 8.7547, 8.9151, 9.2865, 9.8998, 10.0288, 10.1028, 10.166, 10.2517, 10.4159, 10.5435, 10.6561*, 10.7084, 10.7084, *10.836, 11.0445, 11.2786, 11.3208, 11.444, 11.5297*, 12.079, 12.079, *12.1772, 12.2797, 12.3637, 12.4039, 12.6479, 12.743, 12.8939, 13.2007, 13.3125*, 13.5049
$\alpha = \beta = \gamma = \kappa = 10^{-6}$ $a_0 = \lambda_0 = \lambda_1 = 0$	1.9273, *3.1532, 3.7111, 4.2811*, 4.5858, 4.5858, *4.6666, 5.8085*, 6.0395, 6.0395, 7.0226, 8.5411, 8.5483, 8.5483, *8.8846, 9.0938, 9.8004, 10.6473*, 10.7084, 10.7084, 12.079, 12.079, *12.7452, 13.3431*, 13.5049

$\alpha = \beta = \gamma = \kappa = 10^{-5}$ $a_0 = \lambda_0 = \lambda_1 = 0$	**1.9274, 4.5860, 4.5860,** 6.0395, 6.0395, **7.0228,** 8.5411, **8.5485, 8.5485,** *9.9713*, **10.7085, 10.7085,** *11.7357*, 12.079, 12.079, 13.5049
$\alpha = \beta = \gamma = \kappa = 10^{-3}$ $a_0 = \lambda_0 = \lambda_1 = 0$	**1.9384, 4.6035, 4.6035, 6.0399, 6.0399, 7.0399, 8.5418, 8.5656, 8.5656, 10.7253, 10.7253, 12.0802, 12.0802, 13.5064**
$\alpha = \beta = \gamma = \kappa = 0$ $a_0 = \lambda_1 = \lambda_0 = 10^{-11}$	0.4460, 0.7529, 1.9273, 4.5858, 4.5858, 6.0395, 6.0395, 7.0226, 8.5411, 8.5483, 8.5483, 10.7084, 10.7084, 12.079, 12.079, 13.5049
$\alpha = \beta = \gamma = \kappa = 0$ $a_0 = \lambda_1 = \lambda_0 = 10^{-10}$	0.3028, 0.5723, 0.6697, 0.7239, 0.8718, 1.0190, 1.1926, 1.4615, 1.5738, 1.6600, 1.9273, 2.3773, 2.4665, 2.5224, 2.6052, 4.5858, 4.5858, 6.0395, 6.0395, 7.0226, 8.5411, 8.5483, 8.5483, 10.7084, 10.7084, 12.079, 12.079, 13.5049
$\alpha = \beta = \gamma = \kappa = 0$ $a_0 = \lambda_1 = \lambda_0 = 10^{-8}$	0.1820, 0.6002, 0.8291, 1.1582, 1.2917, 1.6279, 1.7257, 1.8180, 1.9273, 2.0704, 2.3660, 2.4342, 2.6280, 2.9229, 3.0286, 3.2375, 3.4811, 3.8390, 4.2793, 4.5858, 4.5858, 5.7523, 5.837, 5.9755, 6.0395, 6.0395, 6.1909, 6.2172, 6.4243, 6.5781, 6.6768, 6.7982, 6.8896, 6.9883, 7.0226, 7.1443, 7.2395, 8.4345, 8.5411, 8.5483, 8.5483, 8.6073, 8.7582, 8.8851, 9.0313, 9.2271, 9.3010, 10.1916, 10.2557, 10.3351, 10.4611, 10.6307, 10.7084, 10.7084, 10.9196, 11.9268, 12.079, 12.079, 12.1288, 13.2279, 13.5049
$\alpha = \beta = \gamma = \kappa = 0$ $a_0 = \lambda_1 = \lambda_0 = 10^{-6}$	1.8205, 1.9273, 4.5858, 4.5858, 6.0395, 6.0395, 7.0226, 8.2906, 8.5411, 8.5483, 8.5483, 10.7084, 10.7084, 11.5828, 12.079, 12.079, 12.9179, 13.5049
$\alpha = \beta = \gamma = \kappa = 0$ $a_0 = \lambda_1 = \lambda_0 = 10^{-5}$	1.9273, 4.5858, 4.5858, 5.7569, 6.0395, 6.0395, 7.0226, 8.5411, 8.5483, 8.5483, 10.7084, 10.7084, 12.079, 12.079, 13.5049
$\alpha = \beta = \gamma = \kappa = 0$ $a_0 = \lambda_1 = \lambda_0 = 10^{-4}$	1.9273, 4.5858, 4.5858, 6.0395, 6.0395, 7.0226, 8.5411, 8.5483, 8.5483, 10.7084, 10.7084, 12.079, 12.079, 13.5049
$\alpha = \beta = \gamma = \kappa = 0$ $\lambda_0 = 10^{-3}, a_0 = \lambda_0 = 0$	**1.9404, 4.5913, 4.5913,** 6.0395, 6.0395, **7.02261**, 8.5411, **8.5511, 8.5511, 10.7105, 10.7105,** 12.079, 12.079, 13.5049
$all = 10^{-11}$	0.4460, *0.5412*, 0.7529, *0.8263, 1.2887, 1.3586, 1.4265, 1.6016*, 1.9273, *2.2798, 2.3054,* 4.5858, 4.5858, 6.0395, 6.0395, 7.0226, 8.5411, 8.5483, 8.5483, 10.7084, 10.7084, 12.079, 12.079, 13.5049

$all = 10^{-10}$	0.3028, *0.4822, 0.5216*, 0.5723, *0.6536*, 0.6697, 0.7239, *0.7803, 0.8017*, 0.8718, *0.9286, 1.0103*, 1.0190, *1.1529*, 1.1926, *1.2404, 1.3200, 1.4032*, 1.4615, *1.5208*, 1.5738, *1.6065*, 1.6600, *1.7289, 1.8235*, 1.9273, *2.0763, 2.1854, 2.2688,* 2.3773, *2.347*, 2.4665, 2.5224, *2.5849*, 2.6052, *2.6499, 2.7740, 2.8608, 2.9458, 3.161, 3.2336, 3.3514, 3.5103, 3.7664, 3.8530, 3.9580, 4.0418, 4.1192, 4.2677, 4.3671*, 4.5858, 4.5858, *4.6787, 4.7948, 4.8422, 4.9590, 5.0671, 5.1358, 5.3554, 5.4584, 5.5957*, 6.0395, 6.0395, 7.0226, *7.1556, 7.2658, 7.3245, 7.4185*, 8.5411, 8.5483, 8.5483, 10.7084, 10.7084, 12.079, 12.079, 13.5049
$all = 10^{-7}$	0.5756, *0.9971, 1.1735, 1.3538, 1.4757, 1.8368*, 1.8980, 1.9273, 2.6217, *2.8095, 3.0991, 3.3669*, 3.6628, *4.0303*, 4.085, *4.2194, 4.3511*, 4.5858, 4.5858, *4.9368, 5.0405, 5.1251*, 5.1479, *5.4032*, 5.4574, *5.6412,* 5.7493, *5.9074,* 6.0395, 6.0395, *6.3258,* 6.5473, *6.6058*, 7.0226, *7.2439*, 7.4822, 7.6964, *7.9035, 8.1077*, 8.3107, *8.3614, 8.4901*, 8.5411, 8.5483, 8.5483, *8.8981, 8.9164, 9.2220*, 9.2431, 9.5775, 9.7468, *10.0051, 10.1237, 10.2285*, 10.2379, *10.3785*, 10.5658, 10.7084, 10.7084, *10.9101*, 11.0082, *11.3456, 11.6139, 11.8601*, 12.079, 12.079, *12.426, 13.1431, 13.3422*, 13.5049
$\kappa = 0.00001$, $\alpha = \beta = \gamma = 10^{-6}$ $a_0 = \lambda_0 = \lambda_1 = 10^{-4}$	**1.9274, 4.5859, 4.5859,** 6.0395, 6.0395, **7.0228,** 8.5411, **8.5485, 8.5485,** *9.9713, 10.1616, 10.3833, 10.5481*, **10.7085, 10.7085,** *11.1006*, 12.079, 12.079, *12.9778, 13.1218*, 13.5049
$all = 10^{-5}$	**1.9274, 4.5860, 4.5860,** *5.7569*, 6.0395, 6.0395, **7.0228,** 8.5411, **8.5485, 8.5485,** *9.9713*, **10.7085, 10.7085,** *11.7357*, 12.079, 12.079, 13.5049
$\kappa = 0.0149$, $\alpha = \beta = \gamma = 2.63 \times 10^{-6}$ $a_0 = \lambda_0 = \lambda_1 = 10^{-6}$	1.8205, **2.0620, 4.7193, 4.7193,** 6.0020, **6.0454, 6.0454, 7.1541, 8.5495, 8.6788, 8.6788, 10.8375, 10.8375,** 11.5828, **12.0909, 12.0909,** 12.9179, **13.5182**
$\kappa = 0.0149$, $\alpha = \beta = \gamma = 2.63 \times 10^{-6}$ $a_0 = \lambda_0 = \lambda_1 = 10^{-5}$	**2.0620, 4.7193, 4.7193,** 5.7569, **6.0454, 6.0454, 7.1541, 8.5495, 8.6788, 8.6788, 10.8375, 10.8375, 12.0909, 12.0909**
$\kappa = 0.0149$, $\alpha = \beta = \gamma = 2.63 \times 10^{-6}$ $a_0 = \lambda_0 = \lambda_1 = 10^{-4}$	**2.0620, 4.7193, 4.7193, 6.0454, 6.0454, 7.1541, 8.5495, 8.6788, 8.6788, 10.8375, 10.8375, 12.0909, 12.0909, 13.5182**

4. Conclusions

In the present work, we investigate the vibration problem of a rectangular plate having micro defects which is modeled by the microstretch theory. This analysis is realized by the use of Ritz method on the microstretch plates and Chebyshev polynomial series multiplied by a proper boundary function are used for admissible function. Some additional frequencies due to the microstretch property are observed among the classical frequencies. When all microstretch constants are taken as zero, these additional frequencies disappear and only classical frequencies remain. Further, these additional frequencies also begin to move out among the classical frequencies under consideration when the microstretch constants get bigger and finally completely disappear among the classical frequencies when the constants exceed some threshold values. And, if these constants get bigger than their threshold values, the classical frequencies also begin to deviate from their original values. We believe that this observation may be used to determine microstretch material constants in future works by combining this analysis with some optimization methods.

References

1. A. C. Eringen, 1990. *Theory of thermo-microstretch elastic solids*, International Journal of Engineering Science, **28**, 1291-1301.
2. D. Zhou, Y. K. Cheung, F. T. K. Au, S. H. Lo, 2002. *Three-dimensional vibration analysis of thick rectangular plates using Chebyshev polynomial and Ritz method*, International Journal of Solids and Structures, **39**, 6339-6353.
3. B. Singh, R. Kumar, 1998. *Wave propagation in a generalized thermo-microstretch elastic solid*, International Journal of Engineering Science, **36**, 891-912.
4. V. R. Parfitt, A. C. Eringen, 1969. *Reflection of plane waves from the flat boundary of a micropolar elastic half space*, Journal of Acoustical Society of America, **45**, 1258-1272.
5. R. D. Gauthier, 1974. *Analytical and experimental investigations in linear isotropic micropolar elasticity*, University of Colorado, PhD Thesis.

FINITE ELEMENT FORMULATION FOR PASSIVE SHAPE CONTROL OF THIN COMPOSITE PLATES WITH INTEGRATED PIEZOELECTRIC LAYER

RAVIKIRAN KADOLI* AND RAVINDRA G. KENDRI
Department of Mechanical Engineering, National Institute of Tech., Karnatak, Surathkal, PO Srinivasnagar 575025, India

Abstract. The Hamilton's principle for piezoelectric materials and the strain displacement relations based on the classical laminate theory's kinematics of deformation are utilized in deriving the piezoelectroelastic finite element equations of motion. Lagrange interpolation functions for in-plane displacement and Hermite cubic shape functions (conforming type) for transverse deflection are implemented through a four noded rectangular element. The formulation does not account voltage as the nodal degree of freedom. The computer code developed for composite plates with integrated piezoelectric sensors and actuator layers has been extensively validated for piezoelectric behaviour, static deflection and free vibration. The laminate deflection suppressed depends on the magnitude of the voltage applied, and this is a passive method of shape control. The effect of fibre orientation, stacking sequence and number of plies has been part of the numerical exercise on passive shape control.

Keywords: electric enthalpy, fibre-reinforced composite plate, Lagrange and Hermite cubic shape functions, actuating voltage, passive shape control

1. Introduction

A smart structure or "intelligent" structural system possesses self-sensing, diagnosis and control capabilities. Literature on the finite element formulation for the analysis of application of piezoelectric material for vibration, buckling and

*Corresponding author, rkkadoli@rediffmail.com

E. İnan et al. (eds.), *Vibration Problems ICOVP-2007*,

deflection suppression is quite vast. Variational principle which incorporates piezoelectric effect has been used to develop tetrahedral finite element for the electroelastic vibration analysis of piezoelectric continuum[1]. The shape control and active vibration suppression of laminated composite plate with piezoceramic layers has been analyzed using non-conforming laminate finite element[2]. Based on the element free Galerkin method a mesh free finite element based on first order shear deformation theory for the static analysis of laminated composite beams and plates with integrated piezoelectric layers has been the focus of study in [3]. A new piezoelectric plate bending element with electric degree of freedom was developed for analysis of static shape control[4].

2. Theoretical Formulation: Finite element formulation for thin laminates with piezolayers and finite element equations for passive shape control

The dynamic equations of a piezoelectric continuum can be derived from the Hamilton's principle in conjunction with the linear piezoelectric constitutive equations[1,5]. The Lagrangian L of the Hamiltonian is the sum of kinetic energy J and electrical enthalpy H (the sum of the strain and electric energies for piezoelectric materials) and also includes the virtual work of mechanical and electrical forces. Using the standard finite element procedure: The shape functions $\mathbf{N_u}$ relating the displacement field, $\mathbf{u}$, to the nodal displacement values $\bar{\mathbf{u}}$ and the shape function $\mathbf{N}_\phi$ relating the electric field to the nodal electric potential are used to derive the finite element equation of motion for piezoelectric continuum. The strain field $\boldsymbol{\varepsilon}$ are expressed in terms of the derivatives of the nodal displacement vector $\bar{\mathbf{u}}$ by using the differential operator matrix, and the electric field vector $\mathbf{E}$ is defined by the electric potential $\bar{\phi}$ by the gradient operator. The corresponding statement for a finite element is:

$$
\begin{aligned}
0 = &-\delta\dot{\bar{\mathbf{u}}}^T \int_V \rho \mathbf{N}_u{}^T \mathbf{N}_u \, dV \ddot{\bar{\mathbf{u}}} - \delta\bar{\mathbf{u}}^T \int_V \mathbf{B}_u{}^T \mathbf{c}^{\mathbf{E}} \mathbf{B}_u dV \bar{\mathbf{u}} - \delta\bar{\mathbf{u}}^T \int_V \mathbf{B}_u{}^T \mathbf{e} \mathbf{B}_\phi dV \bar{\phi} - \delta\bar{\phi}^T \int_V \mathbf{B}_\phi{}^T \mathbf{e}^T \mathbf{B}_u dV \bar{\mathbf{u}} \\
&+ \delta\bar{\phi}^T \int_V \mathbf{B}_\phi{}^T \boldsymbol{\chi} \mathbf{B}_\phi dV \{\phi_i\} + \delta\bar{\mathbf{u}}^T \int_V \mathbf{N}_u{}^T \mathbf{F}_b dV + \delta\bar{\mathbf{u}}^T \int_{S_1} \mathbf{N}_u{}^T \mathbf{F}_S dS + \delta\bar{\mathbf{u}}^T \mathbf{N}_u{}^T \mathbf{F}_P \qquad (1) \\
&- \delta\bar{\phi}^T \int_{S_2} \mathbf{N}_\phi{}^T \varsigma dS - \delta\bar{\phi}^T \mathbf{N}_\phi{}^T Q
\end{aligned}
$$

$\boldsymbol{\sigma}$ and $\boldsymbol{\varepsilon}$ are the stress and strain vectors, $\mathbf{c}$ is the elastic constant matrix, $\mathbf{e}$ is the piezoelectric stress coefficient matrix ($\mathbf{e}^T$ is the transpose of $\mathbf{e}$), $\boldsymbol{\chi}$ is the

dielectric permittivity matrix, $\dot{\mathbf{u}}$ is the velocity field, and ρ is the mass density. The virtual work of the external mechanical forces ($\mathbf{F_b}$, $\mathbf{F_S}$, $\mathbf{F_P}$ are the body force vector, surface force vector, and point force vector respectively) and the applied electric charges (ς is the surface charge and Q is the localized electric charge) for an arbitrary variation of displacement, $\delta\mathbf{u}$, and electrical potential, $\delta\Phi$, is also included. In the above Eqn. (1) all variations over the time $t=t_1$ and $t=t_2$ must vanish. The resulting equilibrium equations for a finite element of piezoelectric continuum can be written as

$$\mathbf{m}^e_{uu}\ddot{\overline{\mathbf{u}}} + \mathbf{k}^e_{uu}\overline{\mathbf{u}} + \mathbf{k}^e_{u\phi}\overline{\phi} = \mathbf{f}^e \tag{2}$$

$$\mathbf{k}^e_{\phi u}\overline{\mathbf{u}} + \mathbf{k}^e_{\phi\phi}\overline{\phi} = \mathbf{g}^e \tag{3}$$

The above formulation can be utilized for the vibration and static shape control analysis of laminate with integrated piezo layers, a typical configuration is illustrated in Fig. 1. Based on the kinematics of deformation for thin lamina(te) and the plane stress conditions, the converse piezoelectric constitutive equations can be expressed in terms of stress and moment resultants considering the material axis of piezo layer or laminae oriented arbitrarily in relation to laminate axis, Eqn. (4). It is assumed that polarization is along the thickness coordinate, hence, $E_1 = E_2 = 0$ and electric displacement, $\overline{D}_1 = \overline{D}_2 = 0$, and therefore the electric field vector reduces to $E_3 = -\phi_k / h_k$. Similarly, the direct piezoelectric constitutive equation for the piezo laminae oriented at arbitrary orientation has its detailed form as in Eqn. (5)[5].

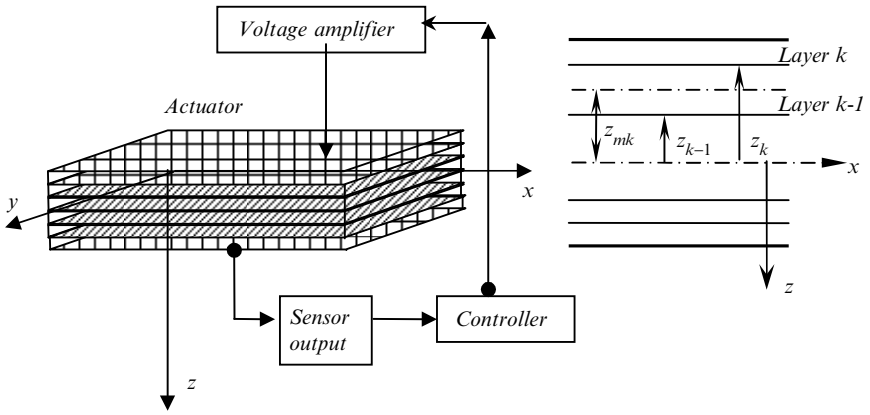

Fig. 1 Laminate with integrated piezo layers for sensing and actuation incorporating feedback controller. $z_{mk} = (z_{k-1} + z_k)/2$, $h_k = (z_k - z_{k-1})$.

$$\begin{Bmatrix} N_x \\ N_y \\ N_{xy} \\ M_x \\ M_y \\ M_{xy} \end{Bmatrix} = \begin{bmatrix} A_{11} & A_{12} & A_{16} & B_{11} & B_{12} & B_{16} \\ A_{12} & A_{22} & A_{26} & B_{12} & B_{22} & B_{26} \\ A_{16} & A_{26} & A_{66} & B_{16} & B_{26} & B_{66} \\ B_{11} & B_{12} & B_{16} & D_{11} & D_{12} & D_{16} \\ B_{12} & B_{22} & B_{26} & D_{12} & D_{22} & D_{26} \\ B_{16} & B_{26} & B_{66} & D_{16} & D_{26} & D_{66} \end{bmatrix} \begin{Bmatrix} \varepsilon_{x0} \\ \varepsilon_{y0} \\ \varepsilon_{xy0} \\ \mathrm{k}_x \\ \mathrm{k}_y \\ \mathrm{k}_{xy} \end{Bmatrix} - \begin{bmatrix} 1 & 0 & 0 \\ 0 & 1 & 0 \\ 0 & 0 & 1 \\ z_{mk} & 0 & 0 \\ 0 & z_{mk} & 0 \\ 0 & 0 & z_{mk} \end{bmatrix} \left[R_T\right]^{-1} \begin{bmatrix} 0 & 0 & e \\ 0 & 0 & e_{32} \\ 0 & 0 & 0 \end{bmatrix} \begin{Bmatrix} 0 \\ 0 \\ \phi_k \end{Bmatrix} \quad (4)$$

$$\begin{Bmatrix} 0 \\ 0 \\ \overline{D}_3 \end{Bmatrix} = \begin{bmatrix} 0 & 0 & 0 \\ 0 & 0 & 0 \\ e_{31} & e_{32} & 0 \end{bmatrix} \left[R_S\right] \begin{bmatrix} 1 & 0 & 0 & z_{mk} & 0 & 0 \\ 0 & 1 & 0 & 0 & z_{mk} & 0 \\ 0 & 0 & 1 & 0 & 0 & z_{mk} \end{bmatrix} \begin{Bmatrix} \varepsilon_{x0} \\ \varepsilon_{y0} \\ \varepsilon_{xy0} \\ \mathrm{k}_x \\ \mathrm{k}_y \\ \mathrm{k}_{xy} \end{Bmatrix} + \begin{bmatrix} 0 & 0 & 0 \\ 0 & 0 & 0 \\ 0 & 0 & \chi_{33} \end{bmatrix} \begin{Bmatrix} 0 \\ 0 \\ E_3 \end{Bmatrix} \quad (5)$$

$\left[R_T\right]$ and $\left[R_s\right]$ are the transformation matrices relating the stress and strains in the material axes (1-2-3) to the stresses and strains in the laminate axis (*xyz*). $\varepsilon_{x0}, \varepsilon_{y0}, \varepsilon_{xy0}$ are the normal strains and $\mathrm{k}_x, \mathrm{k}_y, \mathrm{k}_{xy}$ are the curvatures. A_{ij}, B_{ij}, D_{ij} are the transformed reduced stiffnesses for each laminae. In-plane displacement u and v of each element is expressed using the linear shape functions N_{inpl} obtained using the polynomial of the second degree. The cubic Hermite conforming shape functions $N_{hmtconf}$ for bending displacement field w, is obtained using the polynomial function with 16 terms i.e. a complete quartic (fourth order) polynomial. The electric voltage applied is assumed to act over surface area of the actuator or in case of sensor, the charge developed by electrodes deposited over piezo layer is considered as spatial summation of all point charges developed over the surface area of the piezo sensor layer. The finite element matrices are derived using the shape functions for a four node rectangular element. The finite element static equations for piezoelectric continuum can be reduced from Eqn. (2) and Eqn. (3) by ignoring the mass matrix. In the passive control the deformations are controlled by applying electrical voltage to piezo actuator layer bonded on to the top and bottom surfaces. To minimize the deformation of the laminate due to external mechanical load the electric voltages are applied continuously to the actuators. Thus the new deflection field is obtained as follows:

$$\overline{\overline{\mathbf{u}}} = \mathbf{K}_{uu}^{-1} \left(\mathbf{f} - \mathbf{K}_{u\phi} \phi \right) \quad (6)$$

where $\mathbf{f}$ is the external applied load vector, $\overline{\overline{\mathbf{u}}}$ is the modified displacement field due to actuating voltage ϕ.

3. Results and discussions

Numerical studies are presented on the passive static shape control of simply supported laminated plates. Composite plates with various fibre orientation (cross ply and angle ply), stacking sequence (symmetric and asymmetric layup) and number of plies were the parameters considered for the study.

3.1. VALIDATION OF DISPLACEMENT OF A CANTILEVERED KYNAR AND PVDF BIMORPH BEAM

Fig. 2 shows the tip deflections of KYNAR bimorph cantilever beam for the external applied voltages, the results obtained by the present FE (conforming laminate plate element) solution are in good agreement with those of Liu et al[2] (non-conforming rectangular plate element). Tip deflection of PVDF bimorph beam for various applied voltages between 0 to 200V closely tally with the results from analytical solution[3].

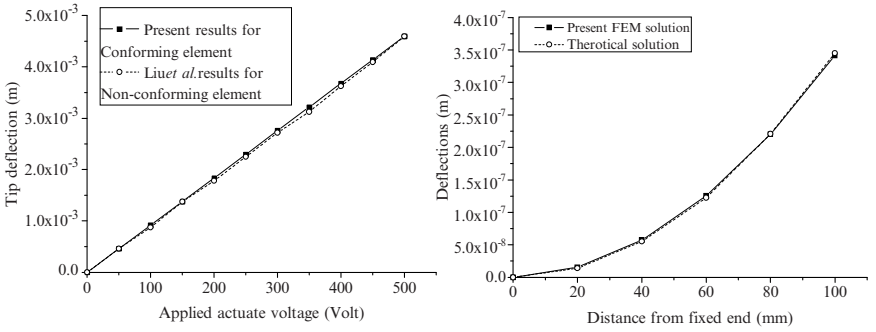

Fig. 2 Validation: tip deflections of KYNAR beam for different actuating voltages and deflection along the length of PVDF bimorph beam for unit actuation voltage.

3.2. PASSIVE SHAPE CONTROL OF ANTI-SYMMETRIC AND SYMMETRIC CROSS PLY LAMINATED PLATES

Fig. 3 illustrates the control of static deflections achieved depending on the applied voltage to the piezo actuator layers. Similar plots were obtained for laminate with a/h=20, 15 with 6 and 8 plies respectively. Also studies were extended to symmetric and asymmetric laminate of a/h=33 (4 plies), a/h=20 (6 plies) and a/h=15 (8 plies).

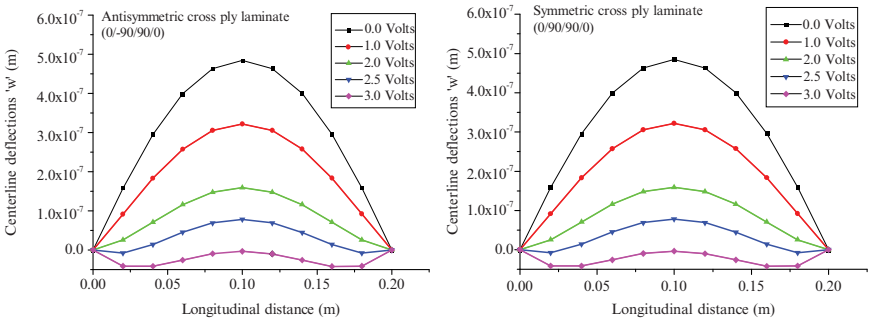

Fig. 3 Shape control of simple supported piezolaminated cross ply composite plates subjected to a uniformly distributed load under various applied voltages. a/h=33, laminate thickness 2.0mm and PZT4 layer thickness 2×1.0mm.

4. Conclusion

The finite element code for the laminated composite plate with integrated piezoelectric layers based on the formulation presented was successfully implemented to study the behaviour of piezoelectric effect and application of piezoelectric material for passive shape control. Numerical studies were presented to illustrate passive shape control for a composite laminate with piezo actuators bonded on the top and bottom surfaces of the laminate.

References

1. H. Allik, T. J. R. Hughes, 1970. *Finite element method for piezoelectric vibration*, International Journal of Numerical Methods in Engineering, **2**, 151-157.
2. G. R. Liu, X. Q. Peng, K. Y. Lam, 1998. *Vibration control simulation of laminated composite plates with integrated piezoelectrics*, Journal of Sound and Vibration, **220**, 827-846.
3. K. M. Liew, H. K. Lim, M. J. Tan, X. Q. He, 2002. *Analysis of laminated composite beams and plates with piezoelectric patches using the element-free Galerkin method*, Computational Mechanics, **29**, 486-497.
4. Z. Wang, S.-H. Chen, W. Han, 1997. *The static shape control for intelligent structures*, Finite Elements in Analysis and Design, **26**, 303-314.
5. V. Piefort, 2001. *Finite Element Modelling of Piezoelectric Active Structures*, Ph.D. thesis, Université Libre de Bruxelles, Belgium.

3-D VIBRATION ANALYSIS OF THE RECTANGULAR MICRO DAMAGED PLATES

AHMET KIRIŞ
Faculty of Science and Letters, Istanbul Technical University, 34469, Maslak, Istanbul, Turkey

ESİN İNAN*
Faculty of Arts and Sciences, Işık University, 34398, Maslak, Istanbul, Turkey

Abstract. In the present work, damaged plates are modeled by the micro-elongation theory which neglects the micropolar effects in Eringen's microstretch theory. The wave propagation problem is studied and a new wave which does not appear in the classical theory of elasticity is observed. The Ritz method is extended to the microelongation theory and triplicate Chebyshev series multiplied by a boundary function are used as admissible functions to approximate plate deflection, and the frequency equations of the microelongated plate are obtained by using Chebyshev-Ritz method. The additional frequencies due to the micro-structure of the plate are observed among the values of the classical frequencies. We examined the relation between these additional frequencies and the material constants of the microelongated medium and observed that these additional frequencies disappear while the all microelongational constants are taken as zero.

Keywords: microelongation theory, micro damaged plate, natural frequencies

1. Introduction

In the present work, micro damaged plates are modeled by the microelongation theory which can be considered as a special case of microstretch theory[1]. The microelongation theory is based on the fact that the material particles can make

*Corresponding author, inan@isikun.edu.tr

E. İnan et al. (eds.), *Vibration Problems ICOVP-2007*,

only volumetric micro elongation in addition to the classical deformation of the medium while micropolar effects are discarded in the microstretch theory.

The vibration analysis of the microelongated plates shows that some additional frequencies due to the microelongation property of the damaged plate occur, as expected. We also observed that when the microelongational material constants are taken as zero, these additional frequencies disappear and only the classical frequencies remain. More importantly, these additional frequencies also begin to move out among the classical frequencies under consideration, while the microelongational material constants get bigger and finally completely disappear among the classical frequencies when the constants exceed some threshold values. If these constants get bigger than their threshold values, the classical frequencies also begin to deviate from their original values. We think that these threshold values may be considered as upper bounds for each of the constants and therefore this observation may guide us to identify the microelongational material constants for different materials for future works.

2. Vibration analysis in microelongation theory

The constitutive equations for a linear isotropic microelongated elastic solid are obtained from microstretch theory[1] by taking all micropolar quantities zero as

$$\begin{aligned} t_{kl} &= \lambda\, \varepsilon_{mm}\, \delta_{kl} + \mu\, \varepsilon_{kl} + \mu\, \varepsilon_{lk} + \lambda_0\, \theta\, \delta_{kl}, \\ m_k &= a_0\, \theta_{,k}, \\ s - t &= \lambda_1\, \theta + \lambda_0\, \varepsilon_{kk} \end{aligned} \tag{1}$$

Here, t_{kl}, m_{kl} are the stress and couple stress tensors, m_k is the microstretch vector, δ_{kl} is the Kronecker delta and $s = s_{kk}$, $t = t_{kk}$. The strain tensors in a microstretch medium are given by Eringen[1] as

$$\varepsilon_{kl} = u_{l,k} + e_{lkm}\phi_m, \quad \gamma_{kl} = \phi_{k,l}, \quad \gamma_k = \theta_{,k} \tag{2}$$

Here t_{kl} is the stress tensor, m_k is the microstretch vector, $s = s_{kk}$, $t = t_{kk}$. $\varepsilon_{kl} = u_{l,k}$, $\gamma_k = \theta_{,k}$ and $e = 3\theta$ are the strain tensors, λ_0, λ_1 and a_0 are the microelongational material constants, ρ is the mass density per unit volume, j is the micro-inertia and $\mathbf{u}$ and θ are the displacement vector and the microelongation scalar, respectively and the other quantities are given as usual manner.

In this work, we only present the results of the wave propagation analysis in a linear isotropic microelongated medium for brevity. There are three types of wave propagation with different phase velocities. They are; coupled "longitudinal microstretch wave" and "longitudinal displacement wave" and uncoupled "transverse displacement wave" which the last two waves appear in the classical theory of elasticity, while the first wave does not appear in the classical theory[2].

We consider a homogeneous isotropic rectangular plate with length a, width b and thickness h and the origin of a Cartesian coordinate system (x_1, x_2, x_3) is located at the middle of the plate whose normal is in the positive direction of the axes x_3.

The energy functional of the microelongated plate under free vibration may be written as

$$\Pi = V_{\max} - T_{\max}. \tag{3}$$

Assuming harmonic-time dependence, the periodic displacement and the microelongation components of the microelongated plate undergoing free vibration may be written in terms of the amplitude functions as follows

$$\left\{\mathbf{u}(x,y,z,t), \theta(x,y,z,t)\right\} = \left\{\mathbf{U}(x,y,z,t), \Theta(x,y,z,t)\right\} e^{i\omega t} \tag{4}$$

where ω denotes the natural frequency. Now introducing the following non dimensional parameters

$$\xi = \frac{2x}{a}, \quad \eta = \frac{2y}{b}, \quad \zeta = \frac{2z}{h} \tag{5}$$

the linear elastic strain energy $V_{\max}$ and the kinetic energy $T_{\max}$ take the following forms:

$$\begin{aligned} V &= \frac{h}{4\alpha_1} \int_{-1}^{1}\int_{-1}^{1}\int_{-1}^{1} \left[\lambda\, \overline{\Lambda}_1^2 + 2\mu\, \overline{\Lambda}_2 + 2\mu\, \overline{\Lambda}_3 + \mu\, \overline{\Lambda}_4 + a_0\, \overline{\Lambda}_5\right] d\zeta\, d\eta\, d\xi \\ &\quad + \frac{b\,h}{8} \int_{-1}^{1}\int_{-1}^{1}\int_{-1}^{1} 2\lambda_0\, \Theta\, \overline{\Lambda}_1\, d\zeta\, d\eta\, d\xi + \frac{a\,b\,h}{16} \int_{-1}^{1}\int_{-1}^{1}\int_{-1}^{1} \lambda_1 \Theta^2\, d\zeta\, d\eta\, d\xi \\ T &= \frac{\rho}{16} a\,b\,h\,\omega^2 \int_{-1}^{1}\int_{-1}^{1}\int_{-1}^{1} \left\{\left[U_1^2 + U_2^2 + U_3^2\right] + 3\, j\, \Theta^2\right\} d\zeta\, d\eta\, d\xi \end{aligned} \tag{6}$$

where

$$\bar{\Lambda}_1=\bar{\varepsilon}_{\xi\xi}+\bar{\varepsilon}_{\eta\eta}+\bar{\varepsilon}_{\zeta\zeta},\quad \bar{\Lambda}_2=\bar{\varepsilon}_{\xi\xi}^2+\bar{\varepsilon}_{\eta\eta}^2+\bar{\varepsilon}_{\zeta\zeta}^2,\quad \bar{\Lambda}_3=\bar{\varepsilon}_{\xi\eta}\bar{\varepsilon}_{\eta\xi}+\bar{\varepsilon}_{\xi\zeta}\bar{\varepsilon}_{\zeta\xi}+\bar{\varepsilon}_{\eta\zeta}\bar{\varepsilon}_{\zeta\eta},$$

$$\bar{\Lambda}_4=\bar{\varepsilon}_{\xi\eta}^2+\bar{\varepsilon}_{\eta\xi}^2+\bar{\varepsilon}_{\xi\zeta}^2+\bar{\varepsilon}_{\zeta\xi}^2+\bar{\varepsilon}_{\eta\zeta}^2+\bar{\varepsilon}_{\zeta\eta}^2,\quad \bar{\Lambda}_5=\bar{\Theta}_{,\xi}^2+\bar{\Theta}_{,\eta}^2+\bar{\Theta}_{,\zeta}^2,\quad \bar{\varepsilon}_{\xi\xi}=\frac{\partial U_1}{\partial\xi},\quad \bar{\varepsilon}_{\eta\eta}=\alpha_1\frac{\partial U_2}{\partial\eta},$$

$$\bar{\varepsilon}_{\zeta\zeta}=\frac{\alpha_1}{\alpha_2}\frac{\partial U_3}{\partial\zeta},\quad \bar{\varepsilon}_{\xi\eta}=\frac{\partial U_2}{\partial\xi},\quad \bar{\varepsilon}_{\eta\xi}=\alpha_1\frac{\partial U_1}{\partial\eta},\quad \bar{\varepsilon}_{\xi\zeta}=\frac{\partial U_3}{\partial\xi},\quad \bar{\varepsilon}_{\zeta\xi}=\frac{\alpha_1}{\alpha_2}\frac{\partial U_1}{\partial\zeta},\quad \bar{\varepsilon}_{\eta\zeta}=\alpha_1\frac{\partial U_3}{\partial\eta},\tag{7}$$

$$\bar{\varepsilon}_{\zeta\eta}=\frac{\alpha_1}{\alpha_2}\frac{\partial U_2}{\partial\zeta},\quad \bar{\Theta}_{,\xi}=\frac{\partial\Theta}{\partial\xi},\quad \bar{\Theta}_{,\eta}=\alpha_1\frac{\partial\Theta}{\partial\eta},\quad \bar{\Theta}_{,\zeta}=\frac{\alpha_1}{\alpha_2}\frac{\partial\Theta}{\partial\zeta},\quad \alpha_1=\frac{a}{b},\quad \alpha_2=\frac{h}{b}.$$

Following[3], we use Chebyshev polynomials multiplied by a boundary function as admissible functions for each amplitude functions of the Eqn. (3), i. e.,

$$U_1(\xi,\eta,\zeta)=F_{u_1}(\xi,\eta)\sum_{i,j,k=1}^{\infty}A_{ijk}P_i(\xi)P_j(\eta)P_k(\zeta),\ U_2(\xi,\eta,\zeta)=F_{u_2}(\xi,\eta)\sum_{l,m,n=1}^{\infty}B_{lmn}P_l(\xi)P_m(\eta)P_n(\zeta),$$
$$U_3(\xi,\eta,\zeta)=F_{u_3}(\xi,\eta)\sum_{p,q,r=1}^{\infty}C_{pqr}P_p(\xi)P_q(\eta)P_r(\zeta),\ \Theta(\xi,\eta,\zeta)=F_{\Theta}(\xi,\eta)\sum_{\hat{i},\hat{j},\hat{k}=1}^{\infty}\hat{A}_{\hat{i}\hat{j}\hat{k}}P_{\hat{i}}(\xi)P_{\hat{j}}(\eta)P_{\hat{k}}(\zeta).\tag{8}$$

Here the one dimensional i^{th} Chebyshev polynomial and the boundary functions are given as

$$P_i(\chi)=\cos\left[(i-1)\arccos(\chi)\right],\quad F_\delta(\xi,\eta)=f_\delta^1(\xi)f_\delta^2(\eta),\quad (\delta=u_i,\theta,\quad i=1,...,3)\tag{9}$$

The values of the boundary functions of Eqn. (9) related to the classical deformation are given in Zhou et al.[3] for different boundary conditions, while the boundary functions due to micro deformation for all types are considered as $f_\theta^1(\xi)=f_\theta^2(\eta)=1$.

$$f_\delta^1(\xi)=f_\delta^2(\eta)=1,\ (\delta=\phi_i,\theta,\ i=1,...,3).\tag{10}$$

Finally, substituting the series expansions (7) into the potential and kinetic energy expressions (5), and using these results in the maximum energy functional (2) of the microelongated plate, and then minimizing this functional with respect to the coefficients of the Chebyshev polynomials, we obtain the eigenvalue problem in matrix form as

$$\left(\mathbf{K}-\Omega^2\,\mathbf{M}\right)\mathbf{Z}=\mathbf{0}.\tag{11}$$

Here, $\Omega=\omega\,\mathrm{a}\sqrt{\rho}$ and the stiffness and the diagonal mass matrices are given by the use of with its-sub-matrices as

$$\mathbf{K}=\begin{pmatrix} \left[K_{u_1u_1}\right] & \left[K_{u_1u_2}\right] & \left[K_{u_1u_3}\right] & \left[K_{u_1\theta}\right] \\ \left[K_{u_1u_2}\right]^T & \left[K_{u_2u_2}\right] & \left[K_{u_2u_3}\right] & \left[K_{u_2\theta}\right] \\ \left[K_{u_1u_3}\right]^T & \left[K_{u_2u_3}\right]^T & \left[K_{u_3u_3}\right] & \left[K_{u_3\theta}\right] \\ \left[K_{u_1\theta}\right]^T & \left[K_{u_2\theta}\right]^T & \left[K_{u_3\theta}\right]^T & \left[K_{\theta\theta}\right] \end{pmatrix}, \mathbf{M}=\begin{pmatrix} \left[M_{u_1u_1}\right] & \mathbf{0} & \mathbf{0} & \mathbf{0} \\ \mathbf{0} & \left[M_{u_2u_2}\right] & \mathbf{0} & \mathbf{0} \\ \mathbf{0} & \mathbf{0} & \left[M_{u_3u_3}\right] & \mathbf{0} \\ \mathbf{0} & \mathbf{0} & \mathbf{0} & \left[M_{\theta\theta}\right] \end{pmatrix} \tag{12}$$

The column vector $\mathbf{Z}$ may be shown as $\mathbf{Z}=\{\mathbf{A},\mathbf{B},\mathbf{C},\hat{\mathbf{A}}\}$ and each sub-column vector is given like $\mathbf{A}=\{A_{111},...,A_{11N},...A_{1k1},...,A_{1kN},...,A_{I11},...,A_{IJK}\}$. The elements of the stiffness and the mass matrix are found as

$$\left[K_{u_1u_1}\right]=(\lambda+2\mu)D^{1,1}_{u_1iu_1\underline{i}}G^{0,0}_{u_1ju_1\underline{j}}H^{0,0}_{kk}+\mu\alpha_1^2\left(D^{0,0}_{u_1iu_1\underline{i}}G^{1,1}_{u_1ju_1\underline{j}}H^{0,0}_{kk}+\frac{1}{\alpha_2^2}D^{0,0}_{u_1iu_1\underline{i}}G^{0,0}_{u_1ju_1\underline{j}}H^{1,1}_{kk}\right),$$

$$\left[K_{u_2u_2}\right]=\alpha_1^2\left((\lambda+2\mu)D^{0,0}_{u_2lu_2\underline{l}}G^{1,1}_{u_2mu_2\underline{m}}H^{0,0}_{nn}+\mu\frac{1}{\alpha_2^2}D^{0,0}_{u_2lu_2\underline{l}}G^{0,0}_{u_2mu_2\underline{m}}H^{1,1}_{nn}\right)+\mu D^{1,1}_{u_2lu_2\underline{l}}G^{0,0}_{u_2mu_2\underline{m}}H^{0,0}_{nn},$$

$$\left[K_{u_3u_3}\right]=\alpha_1^2\left(\frac{1}{\alpha_2^2}(\lambda+2\mu)D^{0,0}_{u_3pu_3\underline{p}}G^{0,0}_{u_3qu_3\underline{q}}H^{1,1}_{rr}+\mu D^{0,0}_{u_3pu_3\underline{p}}G^{1,1}_{u_3qu_3\underline{q}}H^{0,0}_{rr}\right)+\mu D^{1,1}_{u_3pu_3\underline{p}}G^{0,0}_{u_3qu_3\underline{q}}H^{0,0}_{rr},$$

$$\left[K_{\theta\theta}\right]=a_0\left(D^{1,1}_{\theta i\theta\underline{i}}G^{0,0}_{\theta j\theta\underline{j}}H^{0,0}_{kk}+\alpha_1^2D^{0,0}_{\theta i\theta\underline{i}}G^{1,1}_{\theta j\theta\underline{j}}H^{0,0}_{kk}+\frac{\alpha_1^2}{\alpha_2^2}D^{0,0}_{\theta i\theta\underline{i}}G^{0,0}_{\theta j\theta\underline{j}}H^{1,1}_{kk}\right)+\frac{a^2}{4}\lambda_1D^{0,0}_{\theta i\theta\underline{i}}G^{0,0}_{\theta j\theta\underline{j}}H^{0,0}_{kk},$$

$$\left[K_{u_1u_2}\right]=\alpha_1\left(\lambda D^{1,0}_{u_1iu_2\underline{l}}G^{0,1}_{u_1ju_2\underline{m}}H^{0,0}_{kn}+\mu D^{0,1}_{u_1iu_2\underline{l}}G^{1,0}_{u_1ju_2\underline{m}}H^{0,0}_{kn}\right),\quad \left[K_{u_1\theta}\right]=\frac{a}{2}\lambda_0D^{1,0}_{u_1i\theta\hat{i}}G^{0,0}_{u_1j\theta\hat{j}}H^{0,0}_{kk},$$

$$\left[K_{u_1u_3}\right]=\frac{\alpha_1}{\alpha_2}\left(\lambda D^{1,0}_{u_1iu_3p}G^{0,0}_{u_1ju_3q}H^{0,1}_{kr}+\mu D^{0,1}_{u_1iu_3p}G^{0,0}_{u_1ju_3q}H^{1,0}_{kr}\right),\quad \left[K_{u_2\theta}\right]=\frac{a}{2}\lambda_0\alpha_1D^{0,0}_{u_2l\theta\hat{i}}G^{1,0}_{u_2m\theta\hat{j}}H^{0,0}_{n\hat{k}},$$

$$\left[K_{u_2u_3}\right]=\frac{\alpha_1^2}{\alpha_2}\left(\lambda D^{0,0}_{u_2lu_3p}G^{1,0}_{u_2mu_3q}H^{0,1}_{nr}+\mu D^{0,0}_{u_2lu_3p}G^{0,1}_{u_2mu_3q}H^{1,0}_{nr}\right),\quad \left[K_{u_3\theta}\right]=\frac{a}{2}\lambda_0\frac{\alpha_1}{\alpha_2}D^{0,0}_{u_3p\theta\hat{i}}G^{0,0}_{u_3q\theta\hat{j}}H^{1,0}_{r\hat{k}},$$

$$\left[M_{u_1u_1}\right]=\frac{1}{4}D^{0,0}_{u_1iu_1\underline{i}}G^{0,0}_{u_1ju_1\underline{j}}H^{0,0}_{kk},\quad \left[M_{u_2u_2}\right]=\frac{1}{4}D^{0,0}_{u_2lu_2\underline{l}}G^{0,0}_{u_2mu_2\underline{m}}H^{0,0}_{nn},$$

$$\left[M_{u_3u_3}\right]=\frac{1}{4}D^{0,0}_{u_3pu_3\underline{p}}G^{0,0}_{u_3qu_3\underline{q}}H^{0,0}_{rr},\quad \left[M_{\theta\theta}\right]=\frac{3}{4}jD^{0,0}_{\theta i\theta\underline{i}}G^{0,0}_{\theta j\theta\underline{j}}H^{0,0}_{kk} \tag{13}$$

where

$$D^{s,\bar{s}}_{\beta_1\tau_1\beta_2\tau_2}=\int_{-1}^{1}\left\{\frac{d^s\left(f^1_{\beta_1}(\xi)P_{\tau_1}(\xi)\right)}{d\xi^s}\frac{d^{\bar{s}}\left(f^1_{\beta_2}(\xi)P_{\tau_2}(\xi)\right)}{d\xi^{\bar{s}}}\right\}d\xi,\quad H^{s,\bar{s}}_{\tau_1\tau_2}=\int_{-1}^{1}\left\{\frac{d^sP_{\tau_1}(\zeta)}{d\zeta^s}\frac{d^{\bar{s}}P_{\tau_2}(\zeta)}{d\zeta^{\bar{s}}}\right\}d\zeta,$$

$$G^{s,\bar{s}}_{\beta_1\tau_1\beta_2\tau_2}=\int_{-1}^{1}\left\{\frac{d^s\left(f^2_{\beta_1}(\eta)P_{\tau_1}(\eta)\right)}{d\eta^s}\frac{d^{\bar{s}}\left(f^2_{\beta_2}(\eta)P_{\tau_2}(\eta)\right)}{d\eta^{\bar{s}}}\right\}d\eta,\quad (s,\bar{s}=0,1,\quad \beta_1,\beta_2=u_1,u_2,u_3,\theta,\quad (14)$$

$\tau_1,\tau_2=i,j,k,l,m,n,p,q,r,...).$

3. Comparison and numerical results

To our knowledge, there are no other results on the frequencies of free vibration of the plate modeled by microelongation theory in the literature. Therefore we had to compare our results with only the results obtained with the classical theory of elasticity by taking all microelongational material constants are zero (Table 1). Here, the non-dimensional frequency parameter is given as $\Delta = b\sqrt{12\,(1-\nu^2)/E}\;\Omega/(a\,h\,\pi^2)$. We summarized the results in the following tables (Table 2 and 3). Here (S) and (A) symmetric and antisymmetric modes respectively, in the directions ξ, η and ζ as AAA, AAS, ASA, ASS, SAA, SAS, SSA, and SSS. In Table 2, an aluminum-epoxy composite are considered. Here $\nu=0.4$, $E=5.29\,GPa$, $j=1.96\times10^{-7}m^2$, $\alpha_1=1$, $\alpha_2=0.1$ and $a=1m$ and the number of terms is taken $8\times8\times4$.

TABLE 1. Comparison of the frequency parameter.

Cond.-Sym $\alpha_1-\alpha_2$ no.terms	Comparison	Δ_1	Δ_2	Δ_3	Δ_4	Δ_5	Δ_6
Sim.Sup.SSA	3-D Ritz[3]	1.9993	9.9826	9.9826	17.944	25.883	25.883
1-0.01 10x10x3	Pre.results*	1.9993	9.98255	9.98255	17.9436	25.8827	25.8827
Clamped AAA	3-D Ritz[3]	6.8456	10.924	15.910	16.877	19.021	23.830
1.5-0.1 8x8x4	Pre.results*	6.8482	10.9282	15.915	16.8825	19.0269	23.8372
Sim.Sup. NoSym.	3-D Ritz[3]	1.9972	4.9999	4.9999	7.9996	9.9995	9.9995
1-0.001 13x13x3	Pre.results*	1.9999	4.9999	5.0002	8.0005	9.9997	9.9998
Clamped AAS	3-D Ritz[3]	4.2234	5.1628	6.3962	8.0677	8.8143	9.0568
1.5-0.3 8x8x4	Pre.results*	4.2235	5.1632	6.3962	8.0687	8.8143	9.0569
Sim.Sup. NoSym.	3-D Ritz[3]	1.2590	1.3047	1.3047	1.8451	2.3312	2.3312
1-0.5 7x7x5	Pre.results*	1.2590	1.3046	1.3046	1.8451	2.3315	2.3315

TABLE 2. Frequency parameter for simply supported plates.

Micro Mat. Constant	class., microelongation and deviated class. freq. are written in normal, italic and bold, respectively.
$all = 0$	1.9273, 4.5858, 4.5858, 6.0395, 6.0395, 7.0226, 8.5411, 8.5483, 8.5483, 10.7084, 10.7084, 12.079, 12.079
$a_0 = \lambda_0 = \lambda_1 = 10^{-7}$	*0.5767, 1.9016, 1.9016,* 1.9273, *2.6267, 3.6697, 3.6697, 4.0927, 4.0927,* 4.5858, 4.5858, *5.1576, 5.4677, 5.4677, 5.7601, 5.7601,* 6.0395, 6.0395, *6.5597, 6.5597,* 7.0226, *7.4963, 7.4963, 7.7109, 7.7122, 7.7122, 8.3264, 8.3264*, 8.5411, 8.5483, 8.5483, *9.2606, 9.2606, 9.5956, 9.5956, 9.7652, 9.7652, 10.2572, 10.2572, 10.5858*, 10.7084, 10.7084, *11.029, 11.029*, 12.079, 12.079
$a_0 = \lambda_0 = \lambda_1 = 10^{-6}$	*1.8239,* 1.9273, 4.5858, 4.5858, *6.0134, 6.0134,* 6.0395, 6.0395, 7.0226, *8.3063*, 8.5411, 8.5483, 8.5483, 10.7084, 10.7084, *11.6047*, *11.6047,* 12.079, 12.079
$a_0 = \lambda_0 = \lambda_1 = 10^{-5}$	1.9273, 4.5858, 4.5858, *5.7678*, 6.0395, 6.0395, 7.0226, 8.5411, 8.5483, 8.5483, 10.7084, 10.7084, 12.079, 12.079
$a_0 = \lambda_0 = \lambda_1 = 10^{-4}$	1.9273, 4.5858, 4.5858, 6.0395, 6.0395, 7.0226, 8.5411, 8.5483, 8.5483, 10.7084, 10.7084, 12.079, 12.079
$a_0 = 2 \times 10^{-6}$, $\lambda_0 = \lambda_1 = 10^{-6}$	*1.8239*, 1.9273, 4.5858, 4.5858, 6.0395, 6.0395, 7.0226, *8.3063, 8.3063,* 8.5411, 8.5483, 8.5483, 10.7084, 10.7084, *11.6045,* 12.079, 12.079
$a_0 = 2 \times 10^{-5}$, $\lambda_0 = \lambda_1 = 5 \times 10^{-5}$	1.9273, 4.5858, 4.5858, 6.0395, 6.0395, 7.0226, 8.5411, 8.5483, 8.5483, 10.7084, 10.7084, 12.079, 12.079

4. Conclusions

In this work, micro damaged plates are modeled by the microelongation theory. A 3-D vibration analyses is realized by using the Ritz method on the micro damaged plates having various boundary conditions modeled by the microelongation theory. Chebyshev polynomial series multiplied by a boundary function are used for admissible function. Some additional frequencies due to the microelongation theory are observed among the frequencies due to the classical theory for various boundary conditions of the micro damaged plate. Further, we examined the relation between these additional frequencies and the microelongational material constants and observed that these additional frequencies begin to disappear among the classical frequencies under consideration, while

TABLE 3. Freq. parameter for damaged plates with different boundary and symmetry conditions.

Cond.	Micro Mat. Constant	class., microelongation and deviated class. freq. are written in normal, italic and bold, respectively.
Clamped SSS 1-0.2 7*x*7*x*3	$all = 0$	9.9421, 11.529, 12.1653, 14.5793, 16.3016, 17.2705, 18.587, 19.7459, 19.9161, 21.1693
	$a_0 = \lambda_0 = \lambda_1 = 5\times10^{-7}$	*2.9764, 6.4060, 8.5565,* 9.9421, *10.2661,* 11.529, *11.729,* 12.1653, *14.21, 14.21,* 14.5793, *15.3004,* 16.3016, 17.2705, *17.2819, 18.1834,* 18.587, *19.053,* 19.7459, *19.8958,* 19.9161, *20.6886,* 21.1693
	$a_0 = \lambda_0 = \lambda_1 = 5\times10^{-6}$	*9.4124,* 9.9421, 11.529, 12.1653, 14.5793, 16.3016, 17.2705, 18.587, 19.7459, 19.9161, *20.2576,* 21.1693
Free-Clamped SSS 1-0.2 7*x*7*x*3	$all = 0$	5.7366, 8.6833, 10.5378, 11.7335, 13.7748, 14.5377, 15.2991, 16.4593, 18.1419, 19.2461, 19.3147
	$a_0 = \lambda_0 = \lambda_1 = 5\times10^{-7}$	*2.9764,* 5.7366, *6.4060 8.5565,* 8.6833, *10.2661,* 10.5378, *11.729,* 11.7335, 13.7748, *14.21, 14.21,* 14.5377, 15.2991, *15.3004,* 16.4593, *17.2819*, 18.1419, *18.1834,* 19.2461, 19.3147
	$a_0 = \lambda_0 = \lambda_1 = 5\times10^{-6}$	5.7366, 8.6833, *9.4124,* 10.5378, 11.7335, 13.7748, 14.5377, 15.2991, 16.4593, 18.1419, 19.2461,19.3147

the microelongational constants get bigger. We believe that this observation may be used to determine microelongational material constants in future works by combining this analysis with some optimization methods.

References

1. A. C. Eringen, 1990. *Theory of thermo-microstretch elastic solids*, International Journal of Engineering Science, **28**, 1291-1301.
2. B. Singh, R. Kumar, 1998. *Wave propagation in a generalized thermo-microstretch elastic solid*, International Journal of Engineering Science, **36**, 891-912.
3. D. Zhou, Y. K. Cheung, F. T. K. Au, S. H. Lo, 2002. *Three-dimensional vibration analysis of thick rectangular plates using Chebyshev polynomial and Ritz method*, International Journal of Solids and Structures, **39**, 6339-6353.

NOISE REDUCTION OF AIR BLOWER CASING USING COMPOSITES

S. KOLLA* AND Y. ANIL KUMAR
R.V.R & J.C.C.E, Guntur-522019, A.P., India

S. RAJESH
S.R.K.R.C.E, Bhimavaram, A.P., India

Abstract. Sound subjectively, what is heard by the ear; objectively, is a mechanical disturbance from equilibrium in an elastic medium. The noise produced by a rotating component has two main components, the broadband noise and the discrete frequency noise. The broadband noise from a rotor is due to random loading forces on the blades, which are induced by the absorption of atmospheric turbulence. The discrete frequency noise is due to periodic interaction of incoming air with the blades of the rotor. At present the centrifugal blowers, in Naval defense application which is made of steel is generating a noise of 86dB, which causes mental imbalance to the people working near the blower on ship. Therefore in Naval defense applications the reduction of sound level from a source is very important and critical task. Hence the objective of this paper is to reduce the noise level produced by the metal air blower. The noise radiated by the casing of a centrifugal blower can be effectively reduced by the use of (1) Composite Materials, (2) Visco-Elastic material treatment and (3) Stiffness addition. In this paper it is proposed to carry out a study to evaluate the effectiveness of composites in reducing noise levels of the casing. Composite materials are those containing more than one bonded material, each with different structural properties. The advantage of composite materials is the potential for a high ratio of stiffness to weight. In order to evaluate the effectiveness of composites over metals, modal analysis (Eigen value analysis) and Static analysis was performed on both composite and metal blowers using FEA package (ANSYS). Modal analysis is performed on both metals (Alluminium and Composite) blower casing to find out the first ten natural frequencies and static analysis is performed for a pressure of 1570 Pa. This paper also describes the experimental setup of the centrifugal blower, the values of the sound levels for both metal and FRP blowers are taken at a distance of 1m from inlet of the blower, and the sound pressure values at different frequencies of both metal and composite

*Corresponding author, kolla_neha@rediffmail.com

E. İnan et al. (eds.), *Vibration Problems ICOVP-2007*,

blower were compared. This paper also describes numerical approach using SYSNOISE software. Fluid medium, boundary condition and the type of analysis was defined. A boundary mesh of sphere shaped with a radius of 1m was created and a known source was given as input in order to get the sound pressure levels for different frequencies at the boundary mesh. With blower as the noise source and noise that is radiated exterior to the casing is then estimated at various points of interest and the results were correlated with experimental data.

Keywords: noise, air-blower, composite

1. Introduction

Most noise problems can be modeled as source-path-receiver systems. It is most desirable to reduce the strength or number of the sources. For example, replacing one or both of the metal contacts with softer material such as nylon or strong durable plastic might reduce the noise from the impact of two metal machine parts in a punch press. However, it is sometimes difficult to reduce the noise at a source without extensive redesign. Sound waves have an effective range in water greater by several orders of magnitude than electromagnetic waves. These characteristics are primarily responsible for the present large-scale use of under-water sound in commercial as well as military applications. Underwater Sound is generated by many types of sources, both within and outside the, medium, natural and artificial. Natural sounds are usually considered noise and are primary constituents of the important category of ambient noise.

Tandom[1] brings out the importance of noise control measures at the design stage of machines or structures in his paper. Rao[2] describes the application of passive damping technology using viscoelastic materials to control noise and vibration in vehicle and aeroplanes in his paper. Wang et al[3]. in their article provides a critical review of computational techniques for flow-noise prediction and the underlying theories. Kim and Jung[4] in their paper presents a finite element analysis for a magnetostrictive transducer by taking into account the nonlinear behavior of the magnetostrictive material and fluid interaction. Li and Vipperman[5] discussed on the vibro-acoustic properties, sound transmission behavior and noise transmission control of a novel chamber core composite cylinder. Martin[6] presents the primary source of internal noise is due to propeller induced fuselage vibration can be reduced by minimizing the noise transmission through

the fuselage using active structural control. Asnani et al[7]. in their paper describes the side band phenomenon by applying active control to amplitude or frequency modulated sounds in a duct. An attempt is first made to attenuate these sounds using the conventional FX-LMS algorithm. Acronyms Terms.

In the present work the centrifugal blower, which is made of Aluminum is generating a noise of 86dB, which causes mental imbalance to the people who are working near the blower on ship. The noise radiated by the casing of a centrifugal blower can be effectively reduced by the use of: Composite materials, visco elastic material treatment, and Stiffness addition. Composite materials are those containing more than one bonded material, each with different structural properties. The main advantage of composite materials is the potential for a high ratio of stiffness to weight. Composites used for typical engineering applications are advanced fiber or laminated composites, such as fiberglass, glass epoxy, graphite epoxy, and boron epoxy. The unique characteristic of Fiber reinforced composite materials is high internal damping, which leads to better vibrational energy absorption within the material and results in reduced transmission of noise and vibrations to neighboring structure. It is proposed to carry out a study to evaluate the effectiveness of composites in reducing noise of the casing. The study involves both numerical and experimental approaches. In the numerical approach the casing is modeled using ANSYS software and the FE mesh is imported into SYSNOISE software to generate the boundary element mesh. With the blower as the noise source, the noise that is radiated exterior to the casing is then estimated at various points of interest. These results are then correlated with experimental data.

Material properties of metal (aluminum) blower:

Thickness of blower casing = 3 mm.
Density = 2700 kg/m^3.
Young's modulus = 70000 N/mm^2.

Material properties of composite (FRP) blower:

Thickness of blower casing = 4.8 mm, Number of layers = 6,
Density = 1650 kg/mm^3,
E_{XX}=69000 N/mm^2, E_{YY}=69000 N/mm^2, E_{zz}=9244 N/mm^2,
G_{12}=27600 N/mm^2. G_{23}=5019 N/mm^2. G_{13}=3689 N/mm^2.
μ_{12}=0.307. μ_{23}=0.307. μ_{13}=0.248

Fluid properties:

Fluid name = air, Velocity of sound = 340 m/sec, Mass density = 1.225 kg/mm^3

2. Experimental work

The alluminium blower is installed in the anechoic chamber. The exhaust of the blower is connected to the inlet of exhaust system of the chamber. The projected surface of the blower is divided into number of grids of 5x5. Each grid is 100x100 mm size. This measurement surface is scanned by intensity probe at the center of each grid segment. The data is processed by PULSE 3560 C software.

The values in Table 1 represents the various sound pressure levels at different frequencies of both metal blower and composite blower taken at a distance of 1m from suction side. Fig. 1 shows the comparison of these sound levels, it is found that there is a reduction of 25% of sound pressure level in composite blower when compared with metal blower.

TABLE 1. Comparison of sound levels.

Frequency HZ	Aluminum (dB)	GFRP (dB)
25	50.15	31.65
31.5	48.97	40.82
40	49.49	41.46
50	51.4	47.32
63	52.36	44.92
80	53.84	47.56
100	58.42	50.15
125	67.74	47
160	74.94	57.1
200	67.65	52.59

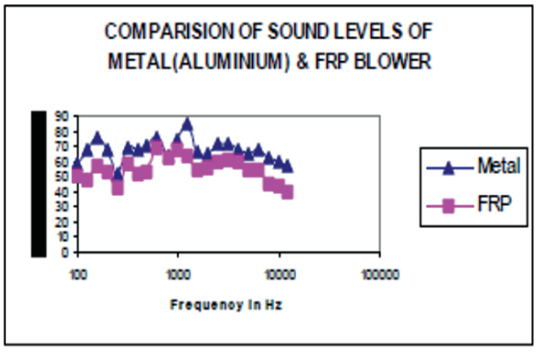

Fig. 1 Graph comparing the Sound Levels.

3. Results and discussions

To evaluate the effectiveness of composites in reducing noise of the casing, Modal analysis and static analysis of both metal and composite blower casing were performed using FEA package ANSYS. The reduction in noise level of composite blower casing over metal blower casing was performed using fluid structure interaction software SYSNOISE and the results were correlated with the experimental data.

From the Table 2 and Fig. 2 it is clear that the natural frequencies of composite (GFRP) blower casing are greater than the metal blower (Aluminum) casing which causes less deformation in composite blower casing when compared with metal blower casing.

TABLE 2. Comparison of natural frequencies.

Mode No	Aluminum (Hz)	GFRP (Hz)
1	42.762	82.625
2	48.298	93.285
3	77.425	152.43
4	233.7	471.78
5	421.94	685.81
6	446.53	829.77
7	525.16	865.84
8	656.86	991.41
9	669.41	1039
10	684.41	1260.6

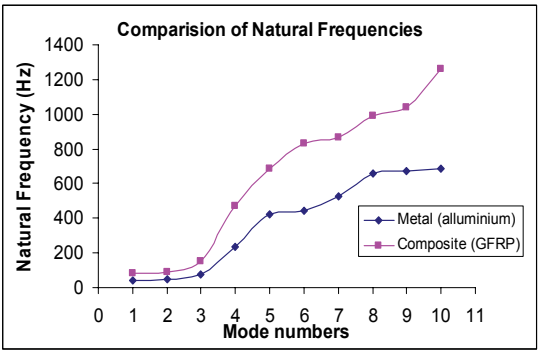

Fig. 2 Graph comparing the Natural frequencies.

Static analysis was performed for both metal and composite blower casing for a pressure of 1570 Pa and it found that maximum deformation in Metal and Composites are 1.092mm and 0.209mm and corresponding stress are 31.1MPa and 13.7 MPa. (Fig. 3 to Fig. 6).

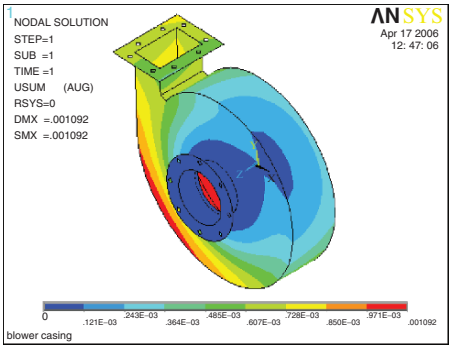

Fig. 3 Deformed shape of metal (alluminium) blower casing.

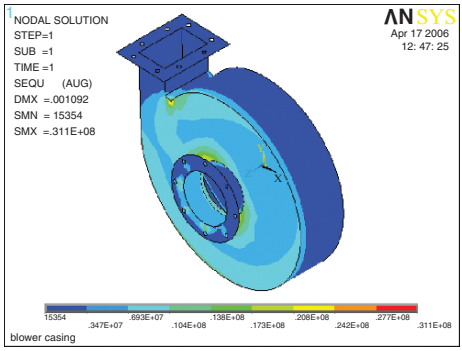

Fig. 4 Equivalent stresses of metal (alluminium) blower casing.

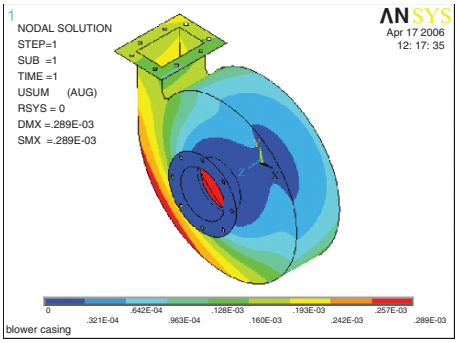

Fig. 5 Deformed shape of composite (GFRP) blower casing.

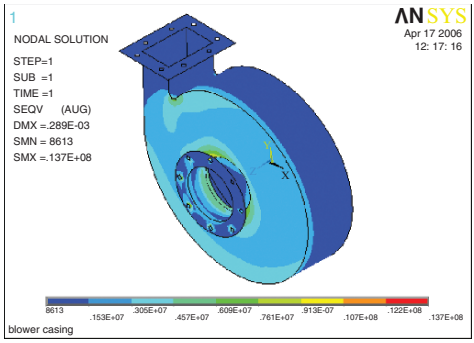

Fig. 6 Equivalent stresses of composite (GFRP) blower casing.

4. Noise level analysis using Sysnoise

In this analysis the meshed model of blower casing created in ANSYS was imported in to SYSNOISE software. Fluid medium, boundary condition and the type of analysis were defined. A boundary mesh of sphere shape with a radius of 1m was created and a known source was given as input in order to get the pressure levels for different frequencies at the boundary mesh (Fig. 7).

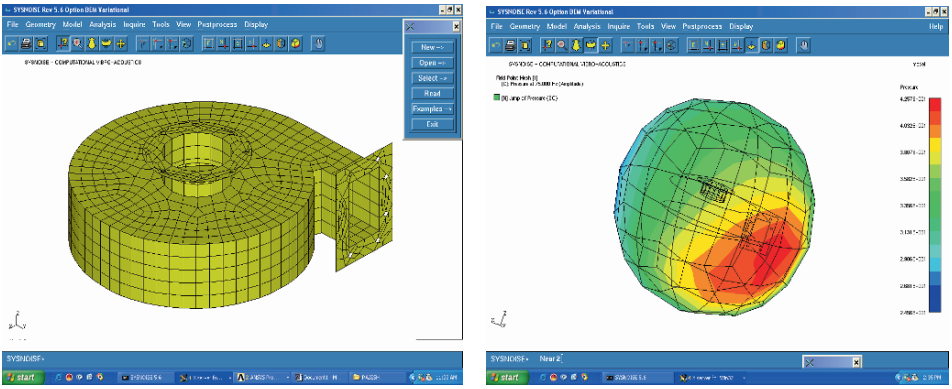

Fig. 7 SYSNOISE meshed model and pressure plot.

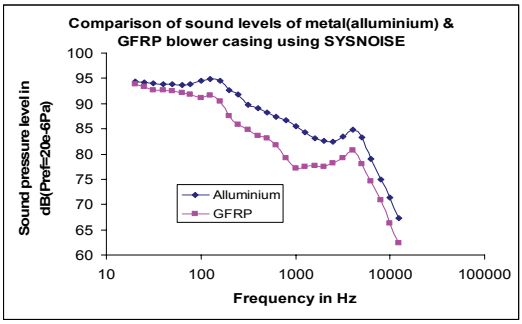

Fig. 8 Comparison of sound levels.

TABLE 3. Comparison of sound levels for metal and composite blower casing.

Frequency in Hz	Metal (Alluminium)	Composite (GFRP)
20	94.4594	93.8075
25	94.2005	93.3237
31.5	93.9874	92.7084
40	93.839	92.6669
50	93.8062	92.4315
63	93.7449	92.1285
77.44	93.8466	91.8
100	94.6161	91.1
125	94.8768	91.7
160	94.4697	90.4
200	92.6321	87.6
250	91.9121	85.9
315	89.8114	84.8
400	89.1482	83.6
500	88.2417	83.1

The above values represent the various sound pressure values at different frequencies of both metal blower and composite blower taken at boundary mesh (sphere of radius 1m) (Table 3). There is a reduction of 9.7% at 1000 Hz of sound pressure level in composite blower when compared with metal blower. From the above analysis it is concluded that composites is more effective than the metals and they produce less noise compared to metal blower casing (Fig. 8).

References

1. N. Tandom, 2000. *Noise-Reducing Designs of Machines and Structures*, Sadhana, **25**, 331-339.
2. D. R. Mohan, 2001. *Recent Applications of Viscoelastic Damping For Noise Control in Automobiles and Commercial Aeroplanes*, India-USA Symposium on Emerging Trends in Vibration and Noise Engineering, IIT Delhi, India.
3. M. Wang, J. B. Freund, K. L. Sanjiva, 2006. *Computational Prediction of Flow-Generated Sound*, Annual Review of Fluid Mechanics, **38**, 483-512.
4. J. Kim, E. Jung, *Finite element analysis for acoustic characteristics of a magnetostrictive transducer*, Struct., **14**, 1273-1280.
5. D. Li, J. S. Vipperman, 2005. *On the Noise Transmission and Control for a Cylindrical Chamber Core Composite Structure*, Journal of sound and vibration, **288**, 235-254.
6. D. G. M. Martin, *Collocated Structural Control for Reduction of Aircraft Cabin Noise*, Noise Control Engineering Journal.
7. V. Asnani, R. Singh, S. Yurkovich, 2005. *Active Control of Amplitude or Frequency Modulated Sounds in a Duct*, Noise Control Engineering Journal, **53**, 211-221.
8. L. E. Kinsler, A. R. Frey, A. B. Coppens, J. V. Sanders, 2000. *Fundamentals of Acoustics*, John Wiley and Sons, New York.
9. K. Pujara, 1977. *Vibration and Noise for Engineers*, 2nd Edn., Delhi, Dhanpat Rai.
10. G. M. Diehl, 1974. *Machinery Acoustics*, John Wiley and Sons.
11. R. J. Urick, 1975. *Principles of Underwater Sound*, 2nd Edn., McGraw-Hill Book Company, New York.
12. E. L. Kinsler, 1982. *Fundamentals of Acoustics*, John Wiley and Sons, New York.
13. A. Craggs, *A Finite Element Model for Acoustically Lined Small Rooms*, Journal of Sound and Vibration, **108**, 327-337.
14. O. C. Zienkiewicz, R. E. Newton, 1969. *Coupled Vibrations of a Structure Submerged in a Compressible Fluid*, Proceedings of the Symposium on Finite Element Techniques, University of Stuttgart, Germany.
15. K. J. Bathe, 1996. *Finite Element Procedures*, Prentice-Hall, Englewood Cliffs.
16. J. E. F. Williams, D. L. Hawkings, 1969, *Sound Generation by Turbulence and Surfaces in Arbitrary Motion*, Phil. Trans. Roy. Soc., A, **264**, pp. 321-344.

PARAMETRIC ESTIMATION OF NONLINEAR 3D OF SYSTEM USING GENETIC ALGORITHM IN TIME DOMAIN

R. KISHORE KUMAR*, S. SANDESH, AND K. SHANKAR
Dept. of Mechanical Engineering, Machine design section, Indian Institute of Technology Madras, Chennai – 600036, India

Abstract. This paper mainly concentrates on the procedural technique to identify the system parameters of multi degrees of freedom nonlinear system using Genetic Algorithm (GA) in time domain. Conventional optimization techniques are mainly calculus based, and often fails in search for global optimum. In this paper estimation has been done using continuous Genetic Algorithm (GA). In parametric estimation the difference between experimental acceleration and acceleration estimated by GA is minimized by updating the parameters. A three degrees of freedom (3-DOF) system with two pairs of non-linear spring and damper (Van der Pol–Duffing oscillator) is considered. Both hardening and softening type of nonlinear springs are considered and corresponding parameters are estimated. The system is excited by known harmonic forces at each mass to ensure enough excitation. Different combinations of hardening and softening nonlinear springs, nonlinear dampers, and single and two nonlinear springs are solved in the present study. The percentage of error in estimation of parameters is less than 5%. Perturbation analysis has been done to study the sensitivity of parameters on output.

Keywords: parametric identification, non-linear system, Van der Pol–Duffing oscillator, genetic algorithm, non-linear damper, hardening - softening nonlinear springs, perturbation analysis

1. Introduction

System identification (SI) is very important and essential for the control system engineering. System identification is the process of determining the parameters

*Corresponding author, kishoreramisetti@iitm.ac.in

E. İnan et al. (eds.), *Vibration Problems ICOVP-2007*,

of a system based on the observed input and output (I/O) of the system. In structural engineering, system identification can be applied to determine unknown parameters such as mass, stiffness and damping properties of a structure. The structural identification methods can be classified under various categories, e.g., frequency domain and time domain, parametric and nonparametric methods.

In recent years, many search methods have been developed and applied to structural identification. Identification methods may be classified into two groups, classical and non-classical. Classical methods[1] can be thought of as those derived from sound mathematical theories whereas non-classical methods based on some heuristic concepts and depend heavily on computer power for extensive and robust search. Classical methods have many drawbacks such as requires sound mathematical knowledge, a good initial guess and converging often to local optima. With the increases in available computational speed non-classical methods are becoming more popular. Genetic Algorithms, developed on Darwin's theory of survival of the fittest, have received considerable attention[2,3]. Chang[4] applied real coded GA for first-order plus dead-time non-linear system. Hanagud et al.[5] identified parameters of single DOF nonlinear dynamic system with cubic nonlinearity in stiffness using Levenberg-Marquardt (LM) method. To get better convergence in LM method, the initial guess should be good enough. If the no. of parameters to be estimated is more, it is difficult to give good initial guess values. But here in GA there is no problem of guessing good initial values. Some studies applying traditional GA with binary coding to the system identification have already been exploited[2,3].

In the present study parametric identification of multiple DOF nonlinear dynamic system has been carried out using continuous GA, which uses real numbers instead binary numbers to represent the parameters. A more complex 3-DOF nonlinear system with cubic and quadratic non-linearity[6] is considered in spring and damper (Van der Pol–Duffing oscillator) respectively. Perturbation analysis has been carried out to study the effect of each parameter on the system response and on identification of parameters.

2. Numerical studies

Numerical simulations of 3-DOF system are carried out. The structural system considered is shown in Fig. 1. The equations of the nonlinear cubic stiffness and quadratic damping are given in the Eq.(1) K_1, K_2 are nonlinear springs and C_1, C_2 are nonlinear dampers.

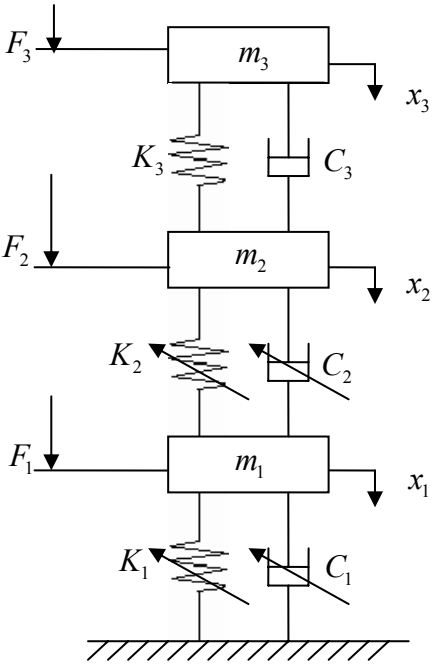

Fig. 1 3 DOF dynamic system with 2 pairs of non-linear spring, non-linear damper.

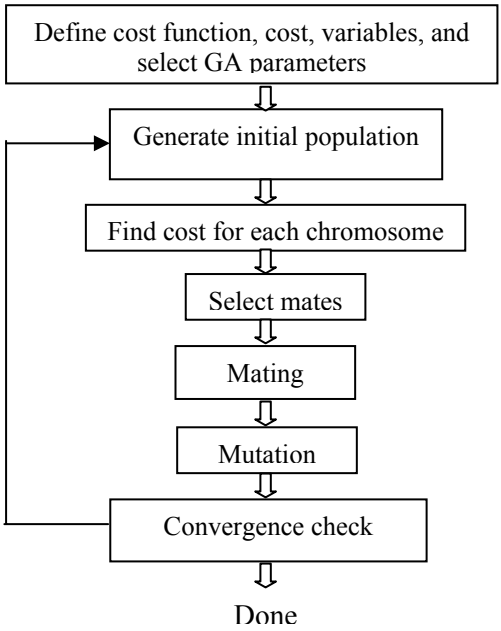

Fig. 2 Flow chart for continuous GA.

$$
\begin{aligned}
K_1(\delta_1) &= a\delta_1 + b\delta_1^3 \\
C_1(\delta_1, \dot{\delta}_1) &= c\dot{\delta}_1(\delta_1^2 + 1) \\
K_2(\delta_2) &= d\delta_2 + e\delta_2^3 \\
C_2(\delta_2, \dot{\delta}_2) &= f\dot{\delta}_2(\delta_2^2 + 1)
\end{aligned}
\tag{1}
$$

where $\delta_1 = x_1$ and $\delta_2 = (x_2 - x_1)$ are relative deflections of first and second spring respectively. K_3 and C_3 are the linear stiffness and damping coefficient for the third spring and damper pair. Governing differential equations for the above system are

$$
\begin{aligned}
&M_1\ddot{x}_1 + K_1 + C_1 + K_2 + C_2 = F_1 \\
&M_2\ddot{x}_2 - K_2 - C_2 + K_3(x_2 - x_3) + C_3(\dot{x}_2 - \dot{x}_3) = F_2 \\
&M_3\ddot{x}_3 - K_3(x_2 - x_3) - C_3(\dot{x}_2 - \dot{x}_3) = F_3
\end{aligned}
\tag{2}
$$

where x_1, x_2, x_3 are the displacements of each mass and a, b, c, d, e, *and* f are constants of the nonlinear springs and dampers. The values of structural parameters as tabulated in the Table 1[5]. Masses M_1, M_2, M_3 are considered to

be unity. Accelerations of three masses are obtained numerically by Runge-Kutta method using MATLAB.7.0. Care should be taken in selection of parameter values to avoid numerical instability.

TABLE 1. Given values of structural parameters.

Parameters	a	b	c	d	e	f	K_3	C_3
Values	25	0.5	1	25	0.5	1	25	1

3. Genetic algorithm

Genetic Algorithms are developed based on Darwin's theory of natural selection and survival of the fittest. The parametric estimation of nonlinear system using a real coded GA starts with an initial population with many chromosomes which are generated randomly from the search range of 0 to 150% of the exact values. Each chromosome in the population represents a set of possible solution to the optimization problem of parametric estimation. The chromosomes are then evolved to generate better offspring according to the values of objective function by applying three genetic operators (selection, crossover and mutation) as shown in Fig. 2. The objective function used for parametric estimation is weighted mean square difference of the actual acceleration and estimated acceleration by GA. All parameters are updated by GA till the error between actual and estimated acceleration is minimized. The objective function can be written as:

$$f(P) = \frac{1}{N}\sum_{i=1}^{N} \mu_i \varepsilon_i \tag{3}$$

where P is the vector parameters to be identified ε_i mean square error at each mass, μ_i is weight of RMS value of acceleration at each mass and N (1 to 3) is the number of measured accelerations. The values ε_i and μ_i are calculated as below: where $\ddot{x}_{exct}$ and $\ddot{x}_{esti}$ are exact acceleration with exact parameters and estimated acceleration by GA respectively and L is the number of time steps.

$$\varepsilon_i = \frac{1}{L}\sum_{j=1}^{L}\left[\ddot{x}_{exct}(i,j) - \ddot{x}_{esti}(i,j)\right]^2 \tag{4}$$

$$\mu_i = \frac{\overline{\lambda}}{\lambda_i}, \quad \overline{\lambda} = \sum_{i=1}^{N}\frac{\lambda_i}{N}, \quad \lambda_i = \sqrt{\frac{1}{L}\sum_{j=1}^{L}\ddot{x}_{exct}{}^2(i,j)} \tag{5}$$

4. Results and discussions

Parameters of 3-DOF structural dynamic system with single and two nonlinear springs with different combinations of hardening and softening type are estimated. Three harmonic forces of 50N amplitude with different frequencies (10, 8, and 6 in rad/sec) were applied at the three masses to excite the system. For exact accelerations the system parameters are considered as given in the Table 1. The accelerations are obtained for duration of one second with time step of 0.01 sec. Five different examples are studied with various combinations of hardening and softening springs as given in Table 2 and Table 3 The GA with number of generations 150 and 200 are considered for single and two nonlinear springs respectively, other GA parameters, such as, population size 700, cross-over rate 40%, mutation rate 1% are kept constant for all examples. Five trials were made for each example. Results with average errors in estimation of parameters in all examples with computational time are given in Table 2 and Table 3.

TABLE 2. 3-DOF structural dynamic system with single nonlinear spring, nonlinear damper pair.

Example 1. *Hardening spring*, Computation time: 3561 sec							
Parameters	K_1	C_1	d	e	f	K_3	C_3
Exact	25	1	25	0.5	1	25	1
Estimated	24.994	0.99996	24.997	0.51274	1.0001	24.997	1.0001
% error	0.024	0.004	0.012	-2.548	-0.01	0.012	-0.01
Example 2. *Softening spring*, Computation time: 3539 sec							
Parameters	K_1	C_1	D	e	f	K_3	C_3
Exact	25	1	25	-0.5	1	25	1
Estimated	25.006	0.99975	24.996	-0.48055	1.0002	25.003	0.99985
% error	-0.024	0.025	0.016	3.89	-0.02	-0.012	0.015

The accuracy of identification can be increased by increasing population size at the cost of computation time. It can be observed that the percentage error in estimation of nonlinear stiffness coefficient e in Table 2 and nonlinear stiffness coefficients b and e in Table 3 is high as compared to other parameters. The fact can be explained by perturbation analysis of each parameter on acceleration RMS value. Each parameter is perturbated by 10% of the exact value and change in acceleration RMS is calculated for all parameters. Fig. 3 shows the result of the perturbation analysis. Since sensitivity of the parameters b and e is very less, correspondingly error in the identification of these parameters are high. On the other hand, percentage of error in identification of parameter K_3 less than 0.004% since acceleration is very sensitive to change in K_3 as shown in Fig. 3.

TABLE 3. 3-DOF structural dynamic system with two nonlinear spring and nonlinear damper pairs.

Example 3. Combination of *hardening and softening springs*, Computational time: 4052 sec								
Parameters	A	b	c	d	e	f	K_3	C_3
Exact	25	0.5	1	25	-0.5	1	25	1
Estimated	25.001	0.49392	1.0002	24.997	-0.49515	0.99989	24.998	1
% error	-0.004	1.216	-0.02	0.012	0.97	0.011	0.008	0
Example 4. Both softening springs, Computational time: 4074 sec								
Parameters	A	b	c	d	e	f	K_3	C_3
Exact	25	-0.5	1	25	-0.5	1	25	1
Estimated	25.002	-0.50546	0.99988	25.001	-0.50034	1.0001	25.001	0.9999
% error	-0.008	-1.092	0.012	-0.004	-0.068	-0.01	-0.004	0.007
Example 5. Both hardening springs, Computational time: 4013 sec								
Parameters	A	b	c	d	e	f	K_3	C_3
Exact	25	0.5	1	25	0.5	1	25	1
Estimated	24.999	0.47869	0.99865	25.005	0.49046	1.0003	24.999	0.9995
% error	0.004	4.262	0.135	-0.02	1.908	-0.03	0.004	0.043

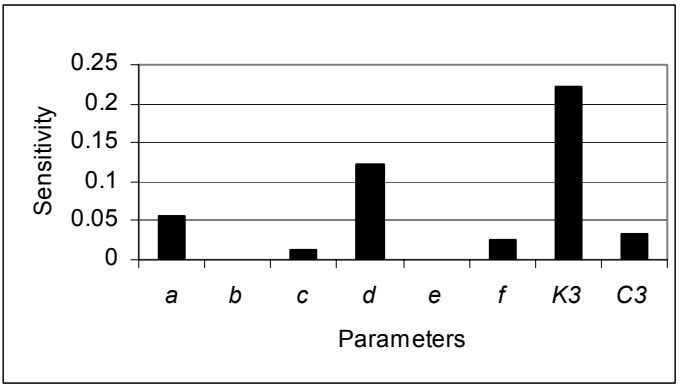

Fig. 3 Change in acceleration RMS values due to 10% perturbation in each parameter.

5. Conclusions

Parametric identification of multi DOF nonlinear system in time domain using continuous GA has been presented. Both spring and damper nonlinearities are considered. Parameters are identified for five different examples with various combinations of hardening and softening springs. The nonlinear stiffness coefficient e of Example 1 (Table 1) is identified with maximum error of 3.89% and 2.55% for softening and hardening springs, respectively. In Example 3 to 5,

error in identification of nonlinear stiffness coefficients b and e are considerably more than other parameters with maximum being 4.62% and 1.9% for b and e, respectively. Perturbation analysis has been carried out to find the effect of each parameter on the acceleration. From the above results one can conclude that GA can provide reasonable estimate for the parameters of nonlinear systems.

References

1. G. Kerschen, K. Worden, A. F. Vakakis, J. C. Golinval, 2006. *Past, present and future of nonlinear system identification in structural dynamic*, **20**, 505–592.
2. K. Kristinsson, G. A. Dumont, 1992. *System identification and control using genetic algorithms*, IEEE Transactions on Systems, Man, and Cybernetics, **22**, 1033–1046.
3. B. Jiang, B. W. Wang, 2000. *Parameter estimation of nonlinear system based on genetic algorithm*, Control Theory and Applications, **17**, 150–152.
4. W. D. Chang, 2006. *An improved real-coded genetic algorithm for parameter estimation of nonlinear systems*, Mechanical Systems and Signal Processing, **20**, 236–246.
5. S. V. Hanagud, M. Meyyappa, J. I. Craig, 1985. *Method of Multiple Scales and Identification of Nonlinear Structural Dynamic Systems*, AIAA Journal, **23**, 802–807.
6. S. J. Zhu, Y. F. Zheng, Y. M. Fu, 2004. *Analysis of non-linear dynamics of a two-degree-of-freedom vibration system with non-linear damping and non-linear spring*, Journal of Sound and Vibration, **271**, 15–24.

EFFECT OF TRENCHES ON ATTENUATION OF GROUND VIBRATION DURING PILE DRIVING

C. K. MADHESWARAN* AND K. NATARAJAN
Structural Engineering Research Centre, Chennai India

R. SUNDARAVADIVELU AND A. BOOMINATHAN
Dept. of Ocean Engineering, Indian Institute of Technology Madras, India

Abstract. The ground vibration generated from pile driving, could cause disturbances to adjacent structures and also disrupt the operation of nearby sensitive equipment. Raleigh waves that propagate in a zone close to the ground surface carries most of the vibration energy affecting near by structures. Trenches open or filled (wave barriers) are often used in engineering practice to reduce the ground vibrations caused by propagating surface (Rayleigh) waves of relatively small wavelengths. The measurement of ground vibrations during prototype pile driving at a site in Chennai was carried out. The analysis was carried using a finite element code, PLAXIS, to study the ground vibration with and without trenches during driving of steel casing with bottom shoe. This paper presents the Peak Particle Acceleration (PPA) of ground measured from prototype pile driving were compared with analytical results. This paper present the results of Finite Element (FE) analysis of concrete trench for effectiveness of screening of vertically polarized Rayleigh waves. Finite element analysis was also carried out to study the effect of parameters such as trench dimension, location of trench from the piling and strength of concrete trenches on ground vibration.

Keywords: ground vibration, field investigations, pile driving, concrete-filled trench, loose sand, Plaxis, dynamic analysis, screening effectiveness, vibration isolation

*Corresponding author, ckm@sercm.org

E. İnan et al. (eds.), *Vibration Problems ICOVP-2007*,

1. Introduction

As the land is very precious in urban areas many structures are built in close proximity. Damage to existing structures are caused by vibration induced differential settlement as well as vibrations transmitted through soil to the structures. The soil available at the site is loose to medium dense sand. Because of soil instability and high water table levels, the concrete filled trench were used for screening of ground vibrations. Athanasopoulous and Pelekis[1], studied the effect of pile driving on adjacent structures. During pile driving, the seismic waves are generated. Various authors suggest settlements can be expected for a distance up to 10 time the pile diameter and occasionally as much as 10 to 15m distance from driven pile. Where as some authors, limit the settlement distance to one length of the pile. More serious structural damage can be induced, however, in the case of loose sandy soils or silty soils from vibration-induced settlement of ground. Such settlement-induced damages, may occur as much as 400m from the source of vibration especially on a large number of piles are being driven. Vythinathan[2] has reported that piling causes ground vibrations and wave propagation through the sandy soils. It produced densification and vibration induced differential settlement that affect the near by railway buildings at the park town. It was observed that 6 feet length crack in one of the walls at second floor of the railway building. Several cases have been reported in the literature, in which significant settlement occurred as a result of pile or sheet pile driving. In some cases settlements occurred under vibration levels ($v = 2\,mm/s$) well below allowable levels usually specified by codes USBM standard (Siskind USBM)[3]. Mabsout and Tassoulas (1994)[4] studied the finite element model for the simulation of pile driving. Information on the effect of concrete-filled trenches on attenuation of ground vibration due to driven cast-insitu pile is seldom available. The problem of isolating vibration by concrete-filled trench was solved using PLAXIS[5]. The main objective of the present work is to study the effect of concrete-filled trenches on screening of ground vibration generated by pile driving.

2. Measurement of ground vibration

The measurement of ground vibration during prototype pile driving was carried out at a construction site in Chennai. The depth of borehole below the ground level was about 20m at which soil is essentially weathered rock. The soil upto the depth of 19m was loose to medium dense sand (Fig. 1). As the soil was essentially sand, a driven casing cast-insitu pile of 600mm has been recommended. A 41 kN capacity impact hammer was used to drive the 25 mm thick mild steel (MS) pipe casing[6]. The hammer was dropped from a height of 2.5 m.

During pile driving, ground accelerations was measured using seismic accelerometer from the centre of source of pile at a distance of 5D, 8.33D and 25D (where D is the diameter of the pile). TEAC instrumentation tape recorder was used to record the ground acceleration. The graduation marks at every 10cm was made on the steel casing. For each drop, the depth of penetration of steel casing and serial number of blows were noted continuously till the driving of casing for full depth of 15.8 m.

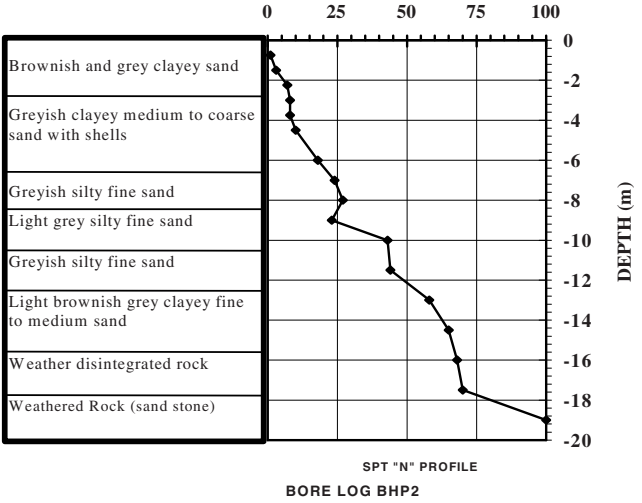

Fig. 1 Details of soil data available at the site.

3. Numerical studies

Finite element analysis was carried out to study the effect of various parameters of concrete-filled trenches on screening of wave propagation. A finite element code, PLAXIS was used to study the ground vibration with and without trenches during driving of steel casing with bottom shoe. The bore log shows the soil up to depth of 19m was mainly loose to medium dense sand. As the soil was loose sand, because of soil instability and high water table levels, the concrete-filled trench are recommended and the effect of concrete-filled trench on screening of vibrations were studied. The soil layer is idealized with 15 nodded axisymmetric triangular elements having two degree of freedom per node. The soil was modeled using hardening soil model (elasto-plastic). The discretisation of the soil layer is considered up to a depth of 80 times diameter (80D) of the pile. The steel pile is modeled by means of the linear elastic model considering non-porous behaviour. Interface elements were placed around the pile and the soil. Standard absorbent boundaries were used at the bottom and at

the side boundary to avoid spurious reflection of waves at the boundary. The pile driving i.e. hammer blow on top of pile is simulated as application of a distributed unit load on top of the pile. The forcing function applied at the top of the pile, is selected from Mabsout (1994)[4]. The dynamic Finite Element (FE) analysis was carried out using soil and pile parameters relevant to prototype pile driving. The material property of sand, Elastic modulus is 29000 kN/m^2, Poisson's ratio is 0.4, Dry weight is 17.9 kN/m^3, cohesion is 1, friction angle θ is 31º and interface strength Rinter is 0.7. The material property of steel casing pile, Elastic modulus is 2.1e+8kN/m^2, Poisson's ratio is 0.3, Dry weight is 78.9 kN/m^3, and interface strength Rinter is 1.0. The time step of 0.001s was used to study the ground response during piling. Fig. 2 shows the comparison of experimental and Finite Element Method (FEM) results of Peak Horizontal Acceleration (PHA) of ground at a distance of 3m (5D) from the centre of source. The FEM results are in good agreement with the experimental results. The variation of horizontal PPA of ground at a distance of 3m with pile penetration depth obtained from FEM and experimental results (Fig. 2) indicates that the FE analysis overestimates PPA by about 20%. Hence, the finite element analysis can be used as a conservative estimate for PPA.

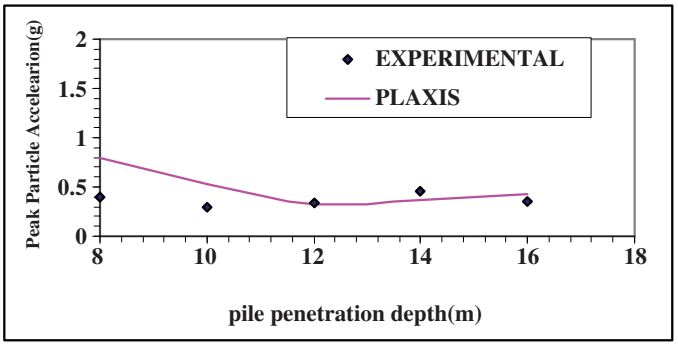

Fig. 2 Horizontal PPA of ground at a distance of 5D (3m).

3.1. EFFECT OF CONCRETE FILLED TRENCHES ON SCREENING OF GROUND VIBRATIONS

The main aim of the study is to arrive the optimal dimensions of trench, location of trench from the centre of source of piling and strength of concrete grade. This paper presents details for estimating the vibration screening effectiveness of rectangular wave barriers in homogenous soil deposits. The effect of concrete trench on attenuation of ground vibration due to pile driving was studied using finite element software PLAXIS. The parametric study is carried out

using PLAXIS. The parameters under investigation are i) trench dimensions, ii) distance of trench and iii) material strength of concrete infilled trenches. Here some of the typical results are compared with experimental results. Analysis is carried out for concrete trenches with three different sizes: 3D X 3D, 3D X 4D and 3D X 5D. The locations of the trenches considered are: 6D, 9D and 12D from the centre of the piling. Trenches with three grades of concrete M10, M15 and M20 were adopted. Fig. 3 shows the finite element discretisization of pile and ground with concrete trenches.

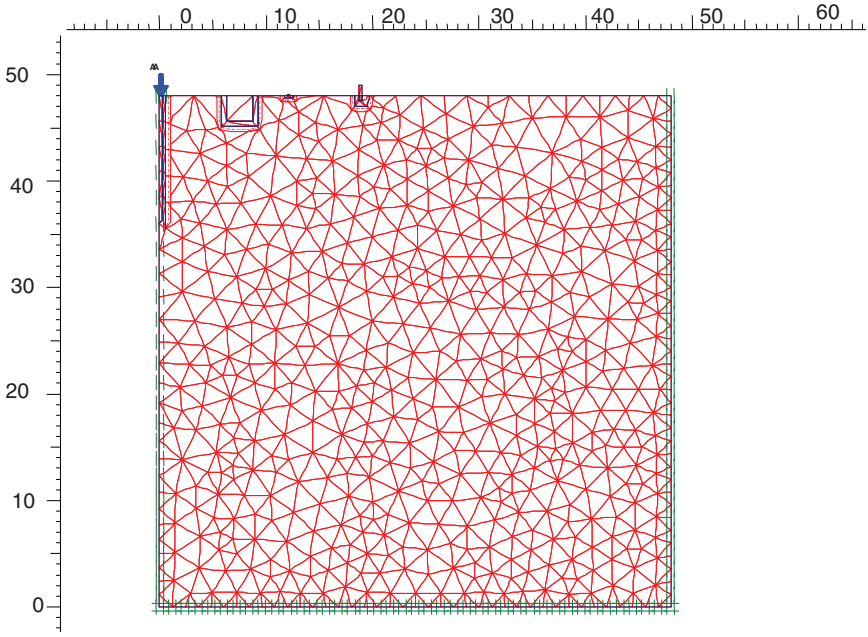

Fig. 3 Finite element discretisation of ground with concrete-infilled trench.

3.2. EFFECT OF TRENCH DIMENSIONS

The material properties of the concrete trenches M20 grade adopted in the FE analysis are, Elastic modulus is 2.23 x 10^7 kN/m^2, Poisson's ratio is 0.2, Dry weight is 24 kN/m^3, and interface strength R_{inter} is 1.0. The result of finite element analysis carried out to study the effect of trenches is presented in Figs. 4 to 6. Open trenches or piles are more effective wave barriers than concrete filled trenches. The effectiveness of trenches on reduction of vibration amplitude is commonly expressed in terms of amplitude reduction ratio, A_r which is defined as ratio of vertical PPV of ground with trench to vertical PPV of ground without trench. Another parameter called the reduction factor is defined as the

percentage reduction of the ground amplitude i.e. R_f (%) = (1- A_r) X 100% is also used to determine the effectiveness of trenches for screening of waves[5]. Open or concrete-filled trenches are more effective wave barrier than corresponding piles. Thus the trench should be used for small to medium depth and piles for large depth. The minimum depth should be 0.8 λ_R (where λ_R, Rayleigh wave length). It was concluded that for open trenches, the normalized depth 'D' is the governing factor, the normalized width W is not important. For in-filled trenches, depth and width are equally important, and effect of the shear modulus and density of the fill material must also be considered.

Fig. 4 shows the variation of vertical PPA with pile penetration depth at the ground during driving of piles with different trench sizes. In this case, the trenches are located at a distance of 9D from the source and vibrations were estimated for a distance of 20D from the centre of the piling. It can be easily observed from Fig. 4 that the PPA for trench with dimension 3D x 4D with different depth of pile penetration is less in comparison to PPA with other size of trenches. It was observed that the percentage of amplitude reduction of the ground amplitude R_f is about 50% for the trench of 3D x 4D with M20 grade concrete.

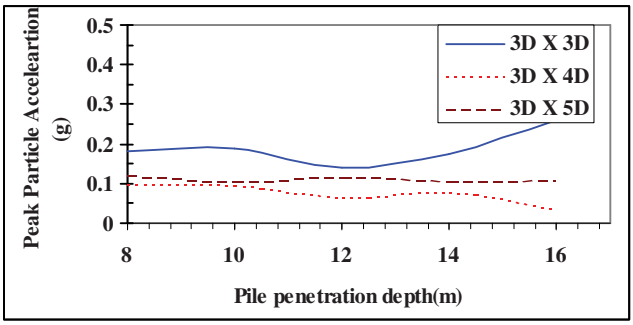

Fig. 4 Effect of dimension of concrete trench on PPA (M10 grade).

3.3. EFFECT OF LOCATION OF TRENCHES

Fig. 5 shows the variation of vertical PPA with pile penetration depth at the ground during driving of piles with different location of trenches. In this case, the trenches are located at a distance of 6D, 9D and 12D from the source and vibrations were estimated at a distance of 20D from the centre of the pile. Fig. 5 indicates that the location of trench at 9D distance was more effective for screening of seismic waves.

3.4. EFFECT OF STRENGTH OF CONCRETE

The effect of strength of concrete grade of M10, M15 and M20 was studied. Fig. 6 shows the variation of vertical PPA with pile penetration depth at the ground during driving of piles with different grades of concrete. In this case, the trenches are located at a distance of 9D from the source and vibrations were estimated at a distance of 20D from the centre of the trenches. Fig. 6 indicates that M20 grade concrete was more effective for screening of seismic waves. It can be concluded from the figures that the trench with dimension of 3D x 4D and M20 grade concrete located at 9D from the source is the most effective of screening of vertically polarized Rayleigh waves.

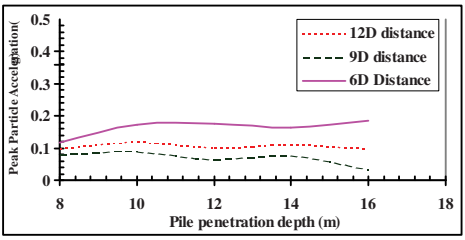

Fig. 5 Effect of location of concrete trench (3D X 4D) on PPA (M10grade).

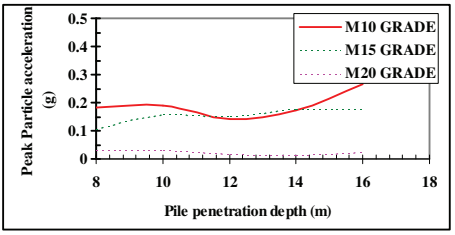

Fig. 6 Effect of strength of concrete trench (3D X 4D) on PPA.

4. Conclusions

Finite element analysis was carried out using PLAXIS software to study the effect of concrete trench parameters such as the size of trench, location of trench and grade of concrete on the isolation of vibration due to pile driving. The major conclusions arrived based on the above studies are given below.

a) The study of pile driving by PLAXIS software is carried out. The FE analysis overestimates the horizontal PPA by about 20% and hence the FE analysis using PLAXIS can be used as a conservative estimate for PPA due to pile driving in sandy strata.
b) It was observed that the percentage of amplitude reduction values is about 50% for trench of 3D x 4D with M20 grade concrete. Based on the parameter study with trench dimensions, grade of concrete and location of trench, it is concluded that the concrete trench with dimension of 3D x 4D with M20 concrete grade located at a distance of 9D from the source is found to be effective for screening of incoming vertically polarized Rayleigh waves due to pile driving.

ACKNOWLEDGEMENT

The paper is published with the permission of the Director, Structural Engineering Research Centre, Madras.

References

1. G. A. Athanasopoulos, P. C. Pelekis, 2000. *Ground vibrations from sheet pile driving in urban environment; measurements, analysis and effects on buildings and occupants*, Soil dynamics and Earthquake Engineering, **19**, 371-387.
2. Vythinathan, 2002. *Hospital complex/pile driving causes vibrations: railway building at park town under threat in the Hindu*, Chennai, February 8 2002.
3. D. E. Siskind, M. S. Stag, J. W. Copp, C. H. Dowding, 1980. *Structure response and damage Produced by ground vibration from surface mine blasting*, Report of investigations 8507 US Bureau of Mines.
4. M. E. Mabsout, J. L. Tassouals, 1994. *A finite element model for the simulation of pile driving*, International Journal of numerical Engineering, **37**, 257-278.
5. Brinkgreve, Vermeer, 1998. *PLAXIS Finite element code for soil and rock analysis*, Netherlands.
6. C. K. Madheswaran, T. S. Thandavamoorthy, 2004. *Filed Investigations on Ground and Structural Vibrations during Prototype Pile Driving*, Proceedings of 5th International Conference on Case Histories in Geotechnical Engineering, New York, Paper No. 4. 24. (CD format).

RANDOM VIBRATION OF A SIMPLE OSCILLATOR UNDER DIFFERENT EXCITATIONS

A. MAITI*
Department of Mathematics, Presidency College, Kolkata, 700073, India

G. P. SAMANTA
Department of Mathematics, Bengal Engineering and Science University, Shibpur, Howrah, 711103, India

Abstract. Many real engineering systems can be modelled adequately as single degree of freedom (SDOF) linear systems. Recently, the behaviour of such systems under random excitation has become the focus of considerable attention in their own right. The usefulness and applicability of random vibration of linear SDOF systems is discussed. The basic model we have considered in this paper is a single degree of freedom linear mass-spring-damper system, or oscillator. It is shown that in the deterministic situation, the fixed point at the origin is asymptotically stable. Our main purpose is to study the behaviour of the system under random excitation. Different stochastic specifications of the excitation are considered. It is shown that the system undergoes large fluctuations if the damping factor is small. If the system is critically damped, then the fluctuations are relatively small. In case of overdamping, the fluctuations are very small and the system is effectively deterministic. A comparative study of the results is presented through computer simulation.

Keywords: SDOF system, damping, excitation, noise, spectral density, dispersion

*Corresponding author, alekesh_maity@hotmail.com

E. İnan et al. (eds.), *Vibration Problems ICOVP-2007*,

1. Introduction

Random vibration is a phenomenon wherein random excitation applied to a mechanical system induces random response. Over the last few decades, the methods of predicting the vibration response of mechanical and structural systems to fluctuating external forces have grown rapidly in importance, in engineering design. It is now well recognized that randomness or stochasticity plays a significant role in structure and function of mechanical or structural systems. Randomness occurs so often, in almost every situation, that to ignore it is to ignore reality. For many years, engineers were mainly concerned with periodic vibration i.e. with situations where the excitations of the system are simple periodic functions of time. A very comprehensive body of classical theory for analyzing this type of vibration now exists and may be found in the classical textbook of McCallion[1].

At present, very sophisticated mathematical machinery (the theory of stochastic processes etc.) is available for handling the problem of random vibration. The development of such theory was first originated from the early work by physicists, notably Einstein[2], on the theory of Brownian motion. Numerous other investigations[3,4] extended the theme introduced by Einstein.

The linear theory of random vibration is applicable in a wide variety of engineering disciplines. Ships and other offshore structures responding to wave excitation, civil engineering structures such as tall building and bridges responding to earthquakes, and wind excitation and land-based vehicles such as cars and trains responding to irregularities in ground and track surfaces, can all be analyzed using the concepts and results of linear random vibration theory (see Ref. 5 and references cited therein).

The rapid and accelerating growth has resulted in a very extensive literature on linear random vibration, covering both theoretical and practical aspects (see the standard textbooks of Nigam[6], Roberts and Spanos[5], Soong and Grigoriu[7], Wirsching et al[8]).

In this paper, we have studied the behaviour of a linear SDOF system under different random excitations. Computer simulations are carried out and the implications of the results are explained.

2. Equation of motion and model analysis

We consider a mass-spring-damper system under the framework of the following ordinary differential equation:

$$m\ddot{y} + c\dot{y} + ky = F(t)\,. \tag{1}$$

where y is the horizontal displacement of the mass, m and $F(t)$ is the excitation force. The positive constants k and c respectively denote the stiffness of the linear spring and damping coefficient of the linear damper (parallel to the spring) (see Fig. 1).

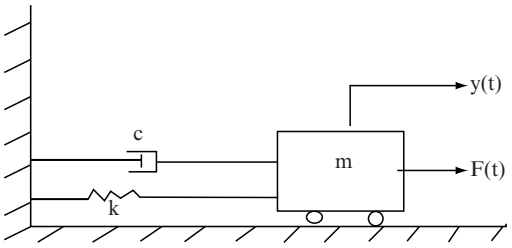

Fig. 1 The mass-spring-damper system.

Dividing throughout by the mass, m, one can write the equation (1) in the standard form of a SDOF system as

$$\ddot{y} + 2\zeta\mu\dot{y} + \mu^2 y = \eta(t)\,, \tag{2}$$

where, $\zeta = \dfrac{c}{2\sqrt{km}}$, $\mu = \sqrt{\dfrac{k}{m}}$ and $\eta(t) = \dfrac{F(t)}{m}$.

When $\eta(t) = 0$, putting $\dot{y} = z$, the system (2) can be rewritten as

$$\dot{y} = z, \qquad \dot{z} = -2\zeta\mu z - \mu^2 y\,. \tag{3}$$

The Jacobian matrix for the system (3) is $J = \begin{bmatrix} 0 & 1 \\ -2\zeta\mu & -\mu^2 \end{bmatrix}$ with $\mathrm{tr}(J) = -\mu^2 < 0$ and $\det(J) = 2\zeta\mu > 0$. Therefore, the fixed point at the origin is always asymptotically stable (see Fig. 2).

In the following, we study the behaviour of the system (2) under different stochastic specifications of the excitation process $\eta(t)$.

2.1. EXCITATION NO. 1

Suppose that the excitation process is a Gaussian white noise characterized by [9]

$$E\{\eta(t)\} = 0 \quad \text{and} \quad E\{\eta(t)\eta(t+\tau)\} = D\delta(\tau)\,,$$

where $D > 0$ is the intensity or strength of the white noise and δ is the Dirac delta function. The frequency response function $\alpha(\omega)$ is given by [5]

$$\alpha(\omega) = \frac{1}{\mu^2 - \omega^2 + 2i\zeta\mu\omega}.$$

The power spectral density function of the excitation is

$$S_\eta(\omega) = \frac{1}{2\pi}\int_{-\infty}^{\infty} E\{\eta(t)\eta(t+\tau)\}e^{-i\omega\tau}d\tau = \frac{D}{2\pi}.$$

The power spectral density function of y is given by

$$S_y(\omega) = S_\eta(\omega)\left|\alpha(\omega)\right|^2,$$

and the dispersion of y is given by

$$D_y = \int_{-\infty}^{\infty} S_y(\omega)d\omega.$$

After some calculations using Gradshteyn and Ryzhik[10], we obtain

$$D_y = \frac{D}{4\zeta\mu^3}.$$

2.2. EXCITATION NO. 2

Suppose that the excitation $\eta(t)$ is the Ornstein-Uhlenbeck process or coloured noise[4]. The mathematical expectation and autocorrelation function of the process $\eta(t)$ is given by

$$E\{\eta(t)\} = 0 \quad \text{and} \quad E\{\eta(t)\eta(t+\tau)\} = De^{-\nu|\tau|}, \quad \nu > 0.$$

The power spectral density function of the excitation is

$$S_\eta(\omega) = \frac{1}{2\pi}\int_{-\infty}^{\infty} E\{\eta(t)\eta(t+\tau)\}e^{-i\omega\tau}d\tau = \frac{D\nu}{\pi(\omega^2+\nu^2)}.$$

The power spectral density function of y is given by

$$S_y(\omega) = S_\eta(\omega)\left|\alpha(\omega)\right|^2,$$

and the dispersion of y is given by (using [10])

$$D_y = \int_{-\infty}^{\infty} S_y(\omega) d\omega = \frac{D(2\zeta\mu + \nu)}{2\zeta\mu^3(\mu^2 + 2\zeta\mu\nu + \nu^2)}.$$

2.3. EXCITATION NO. 3

Consider the excitation $\eta(t)$ as a stochastic process characterized by

$$E\{\eta(t)\} = 0 \text{ and } E\{\eta(t)\eta(t+\tau)\} = De^{-\nu|\tau|}\left(\cos\theta\tau + \frac{\nu}{\theta}\sin\theta|\tau|\right), \nu > \theta > 0.$$

The power spectral density function of the excitation and the dispersion of y are given by

$$S_\eta(\omega) = \frac{2D\nu(\nu^2 + \theta^2)}{\pi\{(\nu^2 + \theta^2 - \omega^2)^2 + 4\nu^2\omega^2\}},$$

$$D_y = \frac{D\{\zeta\mu(\mu^2 + 4\zeta\mu\nu + 4\nu^2) + \nu(\nu^2 + \theta^2)\}}{\zeta\mu^3\{\mu^3(\mu + 4\zeta\nu) + (\nu^2 + \theta^2)(\nu^2 + \theta^2 + 4\zeta^2\mu^2 + 4\zeta\mu\nu) + 2\mu^2(\nu^2 - \theta^2)\}}$$

2.4. EXCITATION NO. 4

Suppose that the mathematical expectation and autocorrelation function of the process $\eta(t)$ is given by [11]

$$E\{\eta(t)\} = 0$$

and

$$\langle\eta(t)\eta(t+\tau)\rangle = De^{-\nu|\tau|}\left(\cosh\theta|\tau| - \frac{\nu}{\theta}\sinh\theta|\tau|\right), \quad \nu > \theta > 0.$$

The power spectral density function of the excitation and the dispersion of y are given by

$$S_\eta(\omega) = \frac{2D\nu\omega^2}{\pi\{\omega^2 + (\nu - \theta)^2\}\{\omega^2 + (\nu + \theta)^2\}}$$

$$D_y = \frac{D(\zeta\mu + \nu)}{\zeta\mu\{\mu^3(\mu + 4\zeta\nu) + (\nu^2 - \theta^2)(\nu^2 - \theta^2 + 4\zeta^2\mu^2 + 4\zeta\mu\nu\} + 2\mu^2(\nu^2 + \theta^2)\}}.$$

2.5. NUMERICAL SIMULATION

When $\eta(t) = 0$, $y(0) = 1$ and $\mu = 1$, the values of y are plotted against time for different choices of the critical damping factor ζ in Fig. 2. For $D = 50000$, $\nu = 4$ and $\theta = 1$, the spectral densities of the excitations are shown in Fig. 3. The spectral densities of the process y for different excitations are shown in Fig. 4 for $\zeta = 0.2$, $\mu = 2$, $D = 50000$, $\nu = 4$ and $\theta = 1$. Fig. 5 shows the dispersions with varying ζ.

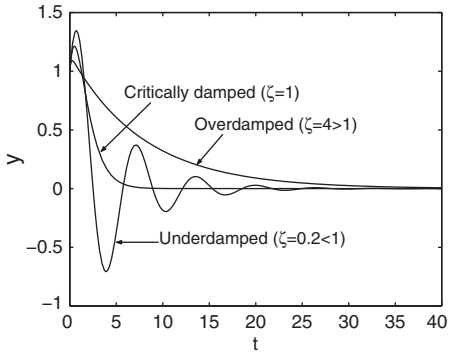

Fig. 2 y versus t for different choices of ζ when $\eta(t) = 0$ and $x(0) = 1$ and $\mu = 1$.

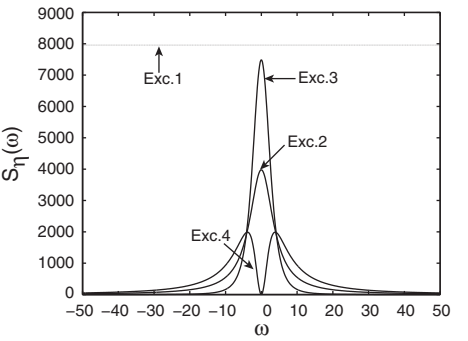

Fig. 3 Spectral densities of the different excitations when $D = 50000$, $\nu = 4$ and $\theta = 1$.

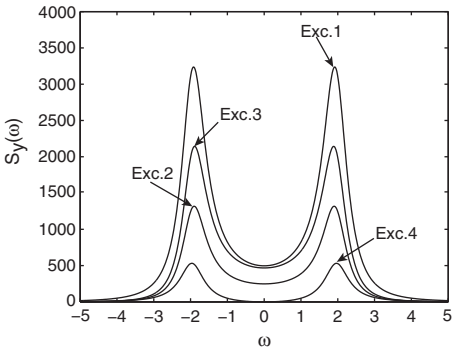

Fig. 4 $S_y(\omega)$ for different $\eta(t)$ when $\zeta = 0.2$, $\mu = 2$, $D = 50000$, $\theta = 1$ and $\theta = 1$.

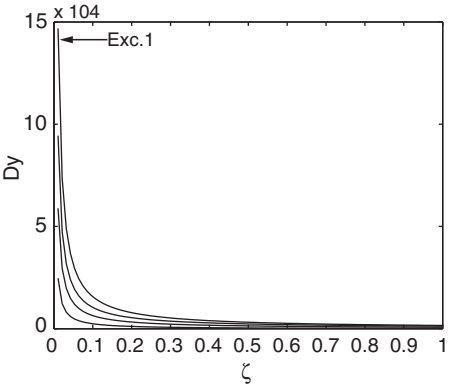

Fig. 5 D_y versus ζ for $\mu = 2$, D = 50000, $\nu = 4$ and $\theta = 1$.

3. Conclusion

The paper aims to study the behaviour of a SDOF system with different selection of random excitations. The spectral densities and dispersions of the process y are calculated for different excitations. It is observed that the system undergoes large fluctuations if the damping factor is very small ($\zeta << 1$). In this case, the system exhibits severe fluctuation for the excitation no. 1 compared to other excitations. If the system is critically damped ($\zeta = 1$), then the fluctuations are relatively small. In case of overdamping ($\zeta > 1$), the fluctuations are very small and the system is effectively deterministic.

References

1. H. McCallion, 1973. *Vibration of Linear Mechanical Systems*, Longman, London.
2. A. Einstein, 1905. *On the Movement of Small Particles Suspended in a Stationary Liquid Demanded by the Molecular-Kinetic Theory of Heat*, Ann. Phys., **17**, 549-569.
3. N. Wiener, 1930. *Generalized Harmonic Analysis*, Acta Mathematica, **55**, 118.
4. G. Uhlenbeck, L. Ornstein, 1930. *On the Theory of Brownian Motion*, Phys. Rev., **36**, 823-841.
5. J. B. Roberts, P. D. Spanos, 1990. *Random Vibration and Statistical Linearization*, John Wiley & Sons, New York.
6. N. C. Nigam, 1983. *Introduction to Random Vibration*, MIT Press, Cambridge.
7. T. Soong, M. Grigoriu, 1993. *Random Vibration of Mechanical and Structural Systems*, Prentice-Hall, New Jersey.
8. P. Wirsching, T. Paez, K. Ortiz, 1995. *Random Vibrations: Theory and Practice*, John Wiley & Sons, New York.
9. W. Horsthemke, R. Lefever, 1984. *Noise Induced Transitions*, Springer-Verlag, Berlin.
10. I. S. Gradshtyen, I. M. Ryzhik, 1980. *Table of integrals: Series and Product*, Academic Press, New York.
11. E. Wentzel, L. Ovacharov, 1986. *Applied Problems on Probability Theory*, Mir Publishers, Moscow.

EXPERIMENTAL ANALYSIS OF THERMALLY INDUCED MOTION OF U-TUBES

PRAVIN MALIK* AND RAVIKIRAN KADOLI
Department of Mechanical Engineering, National Institute of Technology Karnataka, Surathkal, Srinivasnagar, 575025, India

Abstract. The present article focuses attention on the effect of thermal load on dynamic response of the thin U-tubes. Experimental studies are carried out on thermally induced vibration of internally heated cantilevered U-tube. The dynamic response of the tube is studied in lateral and transverse direction for varying heating rates and frequencies. The analysis showed that the rate of vibration is governed by the heating rate and natural frequency of the tube. Lower the heating rates larger are the time to attain steady state amplitude and vice versa, there exist a threshold heating rate to produce thermal induced motion for tube. Displacement response of the U-tube in the lateral direction, during the initial period of the tube motion, occurred in the first mode and with progress of time the displacement response changed to second mode with amplitude of vibrations being lower than that observed in first mode.

Keywords: thermally induced vibrations, internally heated U-tube, dynamic response, lateral and transverse displacement

1. Introduction

Thin walled small circular tubes are widely found in various structural engineering applications, for example boom type antennas used on satellites, heat exchangers etc. In the present study attention is focused on the effect of thermal load on the dynamic response of thin tubes. Thermal load is likely to arise due to heating of the structure by constant exposure to heat source, passage of electric current or sudden exposure to very large amount of heat, sudden temperature changes

*Corresponding author, pravin_malik@yahoo.com

E. İnan et al. (eds.), *Vibration Problems ICOVP-2007*,

encountered by satellite structures at day-night or night-day transition in the orbit, etc. The first paper to address thermally induced vibrations was by Boley[1]. Beam[2] of NASA Ames demonstrated unstable thermally induced oscillations in the laboratory. The experiment was performed using a 3 ft long boom fixed at one end with an attached mass at the other end. Beam[2] demonstrated through experiments, thermally induced vibrations in beams due to radiant surface heating. The first published experimental data on thermally induced vibrations due to internal heating was by Baker and Mikina[3], in their article they mentioned that the thermal vibrations occur under so varied conditions that they cannot be normally controlled but can be prevented from building up by using some form of damping. Blandino and Thornton[4] have reviewed the contributions of various researchers to study thermally induced vibrations. They also carried out detailed theoretical and experimental studies on the thermally induced vibration of single tube caused by internal heating. The results from the theoretical model agreed very well with the experimental data. The authors have carried out theoretical study on thermally induced motion of internally heated tube with tip mass[5]. The main objective of present article is to carry out experimental investigations on the dynamic response of the internally heated vertical tube bent to a U shape. The ends of the two limbs of the U-tube are fixed. These two ends of the tube also serve the purpose of supplying power. The tubes were heated by means of current supplied by regulated DC power supply. The dynamic response of two different sizes of U-tubes in lateral and transverse directions was studied experimentally for different heating rates.

2. Experimental setup

The U-tube cantilever beam is shown in Fig. 1. The test specimens used for the experimental investigation were stainless steel SS304 tubes with 1.86 mm and 1.05 mm external diameter and 0.22 mm thick each bent to a U shape to form cantilever beam.

The test specimen was mounted inside a wooden test box of 300 mm wide, 300 mm long and 1100 mm high with three sides of the box covered with perspex glass. The test box performed several functions: (i) the walls of the box prevented cross currents from affecting the convection heat transfer from the surface of the tube, (ii) provided clamped support for holding the tube and (iii) allowed for the mounting of instrumentation. The ambient temperature inside the test box was measured before each experimental trial using the digital thermometer. Tube displacements were measured directly with a laser displacement sensor. The sensor head was located approximately 40 mm from the point where the displacement was measured. The sensor used had a ± 10 mm resolution with a response time of 1 ms. The output from the laser sensor was

5 VDC. The output from the laser pickup was supplied to the data acquisition system (DAQ). The data acquisition program in LABView through a closed loop controlled the acquisition of displacement data from the test specimen which was written to a data file. The power supply used to supply current to the test beam delivered up to 5 A and 65 VDC. It was capable of constant current control. The heating is achieved by using the tube as a resistance heater by connecting the either ends of the tube to power supply to form a closed circuit in conjunction with power supply. A photograph of the experimental setup with U-tube mounted inside test box, laser pickup and D.C. power supply is shown in Fig. 2.

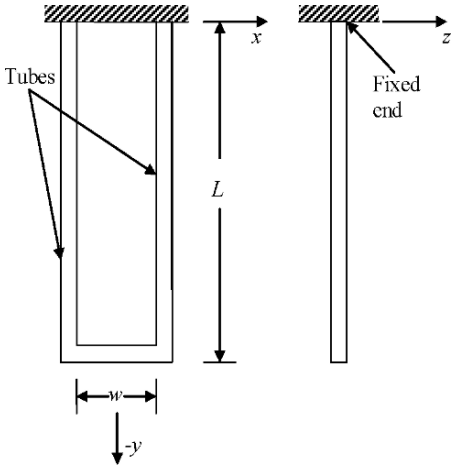

Fig. 1 Global co-ordinates for U-tube configuration.

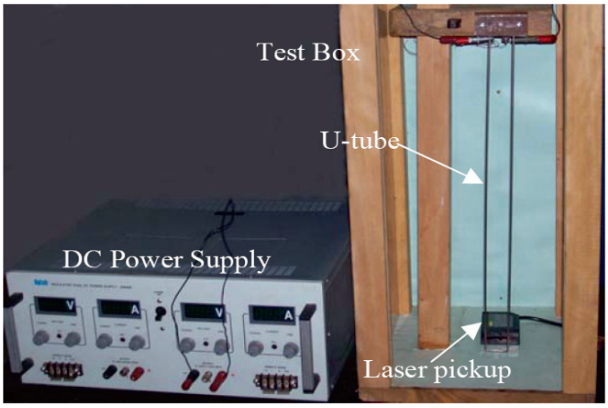

Fig. 2 Experimental setup of U-tube cantilever beam.

3. Response of 1.86 mm diameter U-Tube in transverse direction

The test specimen used for the experimental investigation was a stainless steel SS304 tube 960 mm long with 1.86 mm external diameter and 1.42 mm internal diameter bent in U form with effective length $l = 465$ mm and width $w = 30$ mm as shown in Fig. 1. Thermal-structural data for the U-tube material is as follows: $\alpha = 17.2$ μm/m/°C, $E = 193$ GPa, $K = 16.2$ W/mK, $c_p = 500$ J/kgK and $\rho = 8000$ kg/m^3. The studies were carried out for the heating rates ranging from 8.4 W to 25 W. The displacement histories at the tip (free end) of the tube were obtained in each case. The experiment was carried out for about 250 sec. The ambient temperature during the experiment was 35.5°C. The damped response of the U-tube in the transverse direction (about z-axis) in the absence of a forcing function was studied experimentally. By carrying out FFT on the experimentally obtained displacement data the natural frequency of the tube at ambient temperature was found to be equal to 10.45 Hz. Given an initial displacement of approximately 10 mm, it takes 100 sec for the tube to come to rest.

To determine the effect of heating rate on vibration growth in transverse direction, results are compared for two different heating rates of 15.6 W and 25 W as shown in Fig. 3 and Fig. 4 respectively. In both the cases the initial displacement of 4 mm was given to the U-tube. It is seen that for a higher heating rate equal to 25 W (Fig. 4) the U-tube attains rapidly within 70 sec the steady state amplitude of 3 mm whereas for lower heating rate (Fig. 3) it takes almost 150 sec to achieve steady state amplitude of 2.25 mm. It is observed from the Fig. 5 that as the heating rate is increased above 8.4 W it gives rise to self induced vibrations. This value corresponds to threshold heating rate below which the self induced vibrations will not be seen.

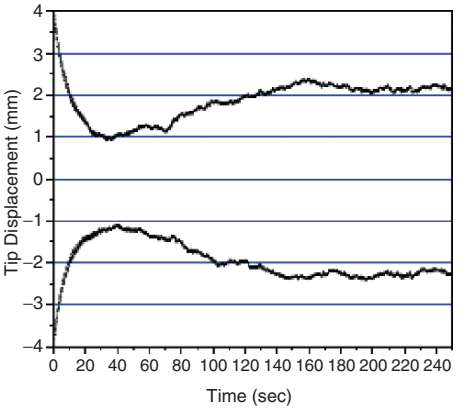

Fig. 3 Transverse displacement histories for the U-tube beam for heating rate of 15.6 W.

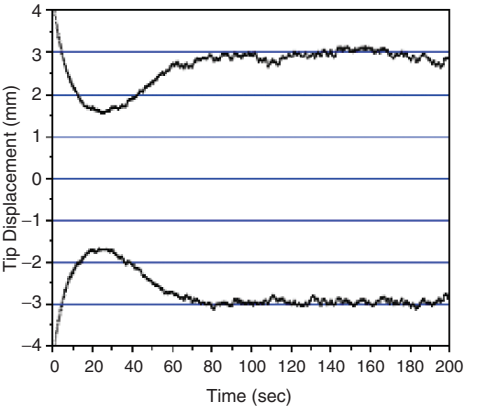

Fig. 4 Transverse displacement histories for the U-tube beam for heating rate of 25 W.

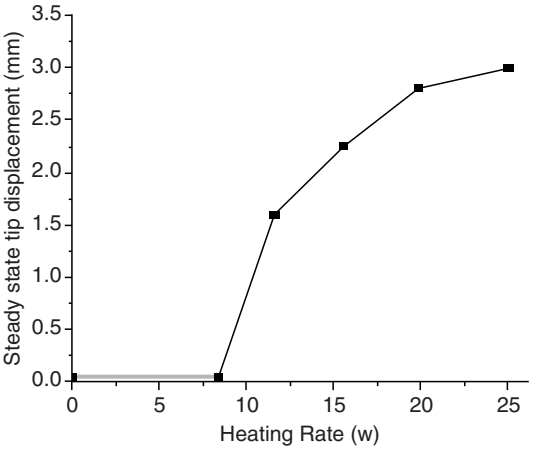

Fig. 5 Effect of heating rate on U-tube tip displacement in transverse direction.

4. Response of 1.05 mm diameter U-Tube in lateral direction

The test specimen used for the experimental investigation was a stainless steel SS304 tube 810 mm long with 1.05 mm external diameter and 0.61 mm internal diameter. The bent tube in the U shape had an effective length l = 400 mm and width w = 10 mm as shown in Fig. 1. The studies were carried out for the heating rates ranging from 1.9 W to 35.55 W. The lateral displacement histories at the tip (free end) of the U-tube were obtained in each case. The experiment was carried out for about 400 sec for each of the heating rates. The ambient temperature during the experiment was 37°C. The damped response of the U-tube in the lateral direction (about x-axis) in the absence of a forcing function was studied experimentally. By carrying out FFT on the experimentally obtained displacement data the natural frequency of the tube at ambient temperature was found to be equal to 4.7 Hz. Given an initial displacement of approximately 5mm, it takes 80 sec for the tube to come to rest.

The lateral tip displacement histories obtained from the experiment for the heating rates of 21.7 W and 35.5 W are illustrated in Fig. 6 and Fig. 7 respectively. In both the cases the initial displacement of about 5 mm was given to the U-tube. It was observed that for heating rates below 15.9 W thermal induced motions did not occur. Hence, the threshold heating rate which will cause thermally induced motion is greater than 15.9 W. It is seen that for the higher

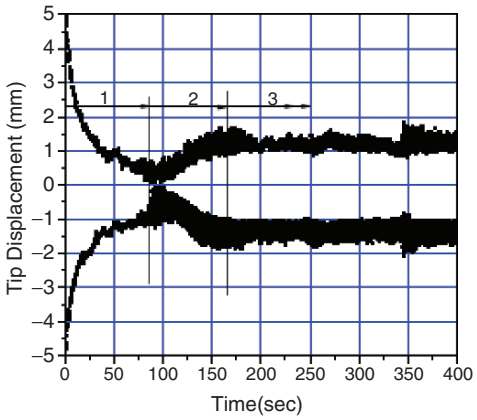

Fig. 6 Lateral displacement histories for the U-tube beam for heating rate of 21.7 W.

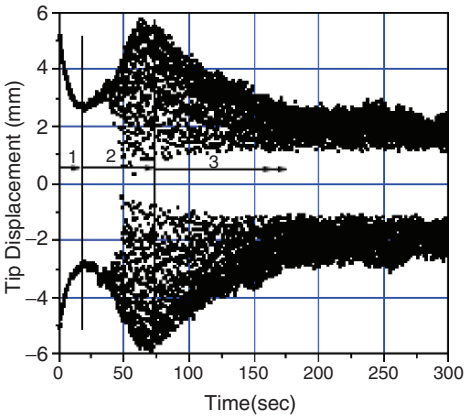

Fig. 7 Lateral displacement histories for the U-tube beam for heating rate of 35.55 W.

heating rates (Fig. 7) the amplitude of vibration first decreases to a minimum and later on as time progresses, the amplitude starts increasing to attain steady state governed by the amount of heat input. As shown in Fig. 6 and Fig. 7, it was observed during the experiments that for higher heating rates, the beam initially vibrates at the frequency of 4.7 Hz. At the same frequency it shows a damped response until the amplitude of oscillation becomes minimal. Later from this time onwards the amplitude of vibration starts increasing and attains a maximum. Refer to region 1 and 2 in Fig. 6 and Fig. 7. Further, from this time onwards the amplitude of oscillation decreases and with progress of time the amplitudes become steady, with the frequency of oscillation being 28.515 Hz, i.e. region 3. It is found that there exists a transition from first mode frequency of 4.7 Hz to a second mode frequency of 28.515 Hz during the time when the amplitude of oscillation starts decreasing towards final steady state amplitude. The amplitude of vibration at steady state occurring at beam frequency of 28.515 Hz is less than the maximum amplitude attained by the beam at frequency of 4.7 Hz. The change of mode of vibration of beam with respect to time is illustrated in Fig. 8.

5. Conclusions

Experimental results for the transverse displacement response of U-tubes had the following observations: (i) for lower heating rates, it took considerable amount of time to attain steady state amplitude when compared to higher heating rates, (ii) there exists a threshold heating rate to produce thermal induced motion for U-tube, (iii) the time required for steady state thermally induced oscillations depends on the amount of heat input. Observations on the experimental results

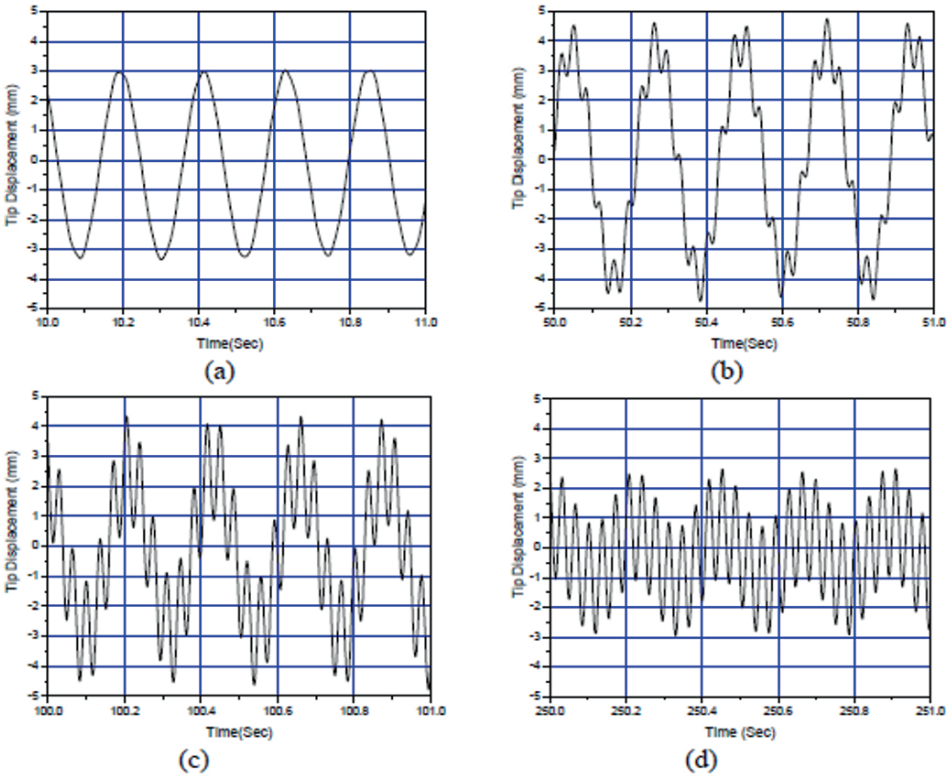

Fig. 8 Change in mode of vibration with time for a U-tube.

for the lateral displacement response of U-tube were as follows: (i) lower the heating rates larger is the time to attain steady state amplitude and vice-versa, (ii) there exists a threshold heating rate to produce thermal induced motion for U-tube, (iii) during the initial period of the response, the beam motion occurred in the first mode and with progress of time the displacement response changed to second mode with amplitude of vibration being lower than that observed in first mode.

References

1. B. A. Boley, 1956. *Thermally Induced Vibrations of Beams*, J. Aeronaut. Sci., **23**, 179–181.
2. R. M. Beam, 1969. *On the Phenomenon of Thermoelastic Instability (Thermal Flutter) of Booms with Open Cross Section*, NASA TN D-5222.

3. J. G. Baker, S. J. Mikina, 1936. *The Calculation of Dampers for Systems Subject to Self-Induced Vibration*, ASME Journal of Applied Mechanics, **59**, A121–A126.
4. J. R. Blandino, E. A. Thornton, 2001. *Thermally Induced Vibration of an Internally Heated Beam*, ASME Journal of Vibration and Acoustics, **123**, 67–75.
5. P. Malik, R. Kadoli, 2005. *Dynamic Response of Heated Tube a Theoretical Model*, Proceedings of 50th Congress of ISTAM, an International Meet., IIT Kharagpur, 45–52.

RESPONSE OF A HARMONICALLY EXCITED HARD DUFFING OSCILLATOR – NUMERICAL AND EXPERIMENTAL INVESTIGATION

A. K. MALLIK*
Department of Mechanical Engineering, Indian Institute of Technology Kanpur, 208016, India

Abstract. Response of a lightly damped hard Duffing oscillator to harmonic excitations has been investigated experimentally as well as numerically. A single degree-of-freedom torsional vibratory system has been fabricated as a mechanical analogue of Duffing equation with strong nonlinearity. Assumed linear damping and nonlinear restoring characteristics are modelled to fit the experimental results. The forced response of the system, in terms of peak-to-peak values and associated power spectrum, is studied for different levels of excitation. The excitation frequency is varied up to about five times the linearised natural frequency of the system. Both experimental and numerical results reveal complicated and chaotic motion at low frequency regime with increasing level of excitation. Unpredictable jump phenomenon, with two and three coexisting periodic attractors, with possible Wada basin boundaries, is also observed.

Keywords: hard Duffing oscillator, jump phenomenon, chaotic response

1. Introduction

The notion of classical determinism is now completely eliminated with the help of low order, simple looking nonlinear systems. Duffing oscillator is one such system, which acts as a paradigm of nonlinear ordinary differential equation representing forced, dissipative systems. Since its introduction by Duffing[1], this

*akmallik@iitk.ac.in

E. İnan et al. (eds.), *Vibration Problems ICOVP-2007*,

oscillator has been extensively studied for a wide range of parameter values. The equation of motion of a harmonically excited and viscously damped Duffing oscillator is given by

$$\ddot{x} + c\dot{x} + \alpha x + \beta x^3 = F\cos\omega t; \qquad c > 0 \tag{1}$$

The approximate periodic response for the above equation, obtained by various analytical methods, is discussed in almost all textbooks on nonlinear vibration. A representative, but by no means complete, list of such texts is included as references[2-8].

If the parameters α and β are of opposite signs, then the corresponding undamped and unforced system has three equilibrium states at $x = 0$ and $x = \pm\sqrt{-\beta/\alpha}$. Such systems are referred to as 'soft' systems. With $\alpha > 0$ and $\beta < 0$, this equation approximately represents moderately large forced oscillations of a mathematical pendulum. On the other hand, with $\alpha < 0$ and $\beta > 0$, the equation has been used to represent the vibrations of a buckled beam. The system is under a so-called double-well potential. Complicated and chaotic dynamics of such systems possessing heteroclinic and homoclinic orbits have received a lot of attention and have been studied, analytically, numerically and experimentally[9-13]. Chaotic responses in such pendulums and double-well potential systems have been obtained experimentally[9, 14-16].

Ueda[17] presented extensive numerical results for $\alpha = 0$ and $\beta > 0$ and showed the possibility of periodic and chaotic (strange) attractors, coexistence of multiple periodic attractors and coexistence of periodic and strange attractors.

When both $\alpha > 0$ and $\beta > 0$, the corresponding system, known as a "hard" system received[18-20] less attention in comparison to soft systems. It may be pointed out that a hard system has only one equilibrium point at $x = 0$ around which oscillations take place. Consequently, very high level of excitation is required to exhibit chaotic oscillation in such systems. This fact has been explicitly mentioned in reference[16], where a hard system was designed which exhibited chaotic response in numerical simulation. However, the excitation needed was too high to be achieved during experimentation.

Recently Aguirre and Sanjuan[21] have reported unpredictable behavior in the presence of Wada basins for a Duffing oscillator. Nusse et al[22,23] first discussed the possibility of Wada basin boundaries in physical systems. These refer to common fractal basin boundaries for three coexisting attractors of a system.

In the present paper, we discuss the response of a torsional, hard Duffing oscillator. Both experimental and numerical results are included. The experimental system is designed following the idea of Pippard[24]. The possibility of chaotic response, especially at low frequency regime with higher levels of

excitation, is observed both *experimentally* and numerically. Besides the usual jump phenomenon near the linearised natural frequency, non-smooth variation of the peak-to-peak value of the periodic response in the low frequency regime is exhibited. If the forcing frequency is around three times the linearised natural frequency of the system, then the response reveals unpredictable jumps between two and even three possible attractors. In such a situation, the response does not reach a steady state during experimentation.

2. Experimental set-up

Fig. 1 shows the experimental set-up for a torsional oscillatory system. A permanent magnet is held in the middle by two thin mylar strips pasted securely on to the magnet. The ends of the strips are clamped to a perspex ring on to which a coil of several hundred turns is wound. For rotational motion of the magnet about its central vertical axis, mylar strips act as a nonlinear torsional spring. The torsional stiffness characteristic of the system is measured by applying equal tensions near the ends of the magnet using pulleys and dead weights. The loading system is explained in Fig. 2.

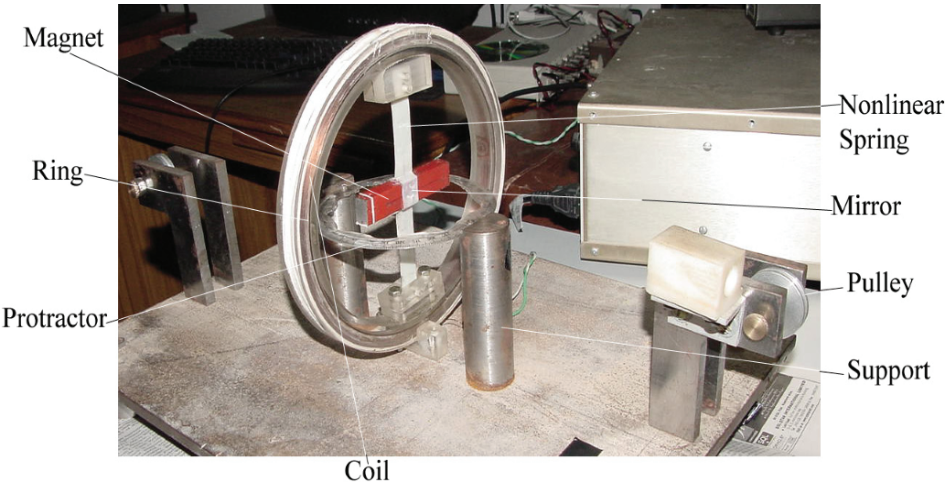

Fig. 1 Experimental set-up.

The torque about the central vertical axis of the magnet can be computed if the weights and the distances involved (moment arms) are known[25]. It may be pointed out that the moment arm of the torque due to tension in the string is dependent on the rotation (θ) of the magnet. It can be shown that the expression for the moment arm is

$$\left[a\left(l\cos\theta - a\sin\theta\right) / \sqrt{\left(l - a\sin\theta\right)^2 + \left(a - a\cos\theta\right)^2} \right],$$

where a is the distance of the string attachment point from the axis of rotation along the length of the magnet and l is the distance of the top of the pulley from the string attachment point when $\theta = 0$. The torsional stiffness characteristic is obtained from the plot of this measured torque (T_s) and the measured rotation of the magnet.

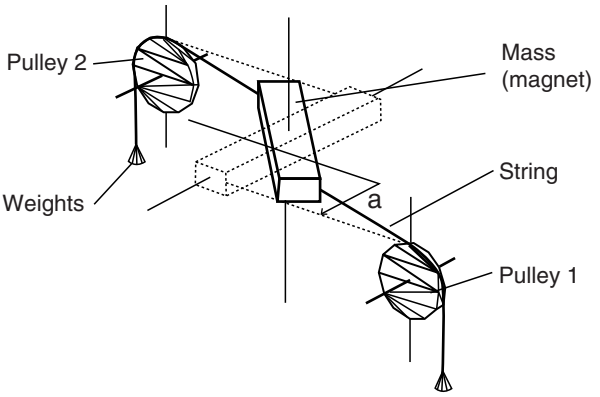

Fig. 2 Measurement of torsional stiffness.

High values of θ are measured by the protractor (Fig. 1) with a least count of 0.5 degree. For measuring low values of θ, a small mirror is attached to the side of the magnet (Fig. 1). The deflection of a reflected laser pointer incident on the mirror (at the center of the side of the magnet) is measured as explained in Fig. 3. This system has a least count of 0.1 degree. Small frictional torque at the pulley axles is estimated by assuming it to be constant and a linear relationship between the torque and rotation for very small values of θ [25]. All the torque readings were corrected by subtracting this frictional torque and plotted versus θ. This plot is shown in Fig. 4. Fitting the data of Fig. 4 as

$$T_s = k_1\theta + k_2\theta^3 \tag{2}$$

the following values are obtained:

$$k_1 = 60.14\ \mathrm{N\cdot mm/rad},$$
$$k_2 = 62.46\ \mathrm{N\cdot mm/rad^3}.$$

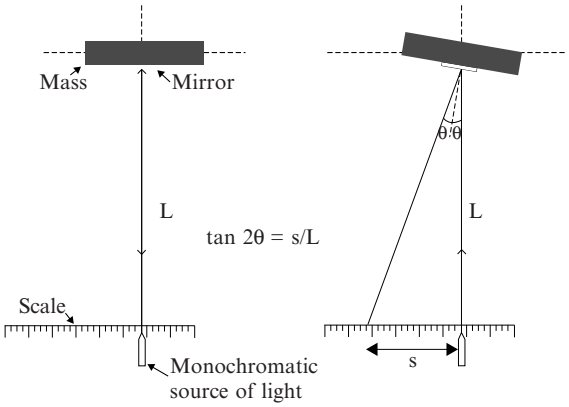

Fig. 3 Measurement of small rotation.

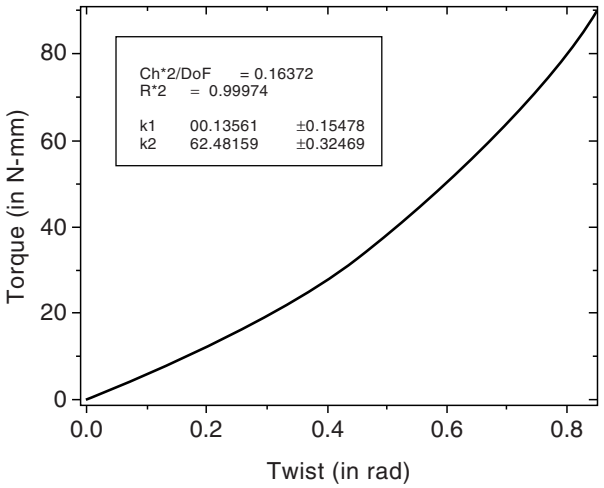

Fig. 4 Measurement of torsional stiffness.

From the mass and geometric dimensions of the magnet, its moment of inertia (J) about the central vertical axis comes out as 4.69 x 10^{-5} kg.m^2. This value is also corroborated by the measured value of the linearised natural frequency (ω_n) of small oscillations $\omega_n = 5.7$ Hz .

A small B&K 4374 accelerometer was attached near the end of the magnet. The accelerometer signal was fed to CF 3200 ONO SOKKI FFT analyzer via a B&K 2635 charge amplifier. A typical free vibration decay signal for small initial disturbance is shown in Fig. 5. From several such plots, assuming linear viscous damping, the damping factor of the system is estimated to lie between 0.014 and 0.016.

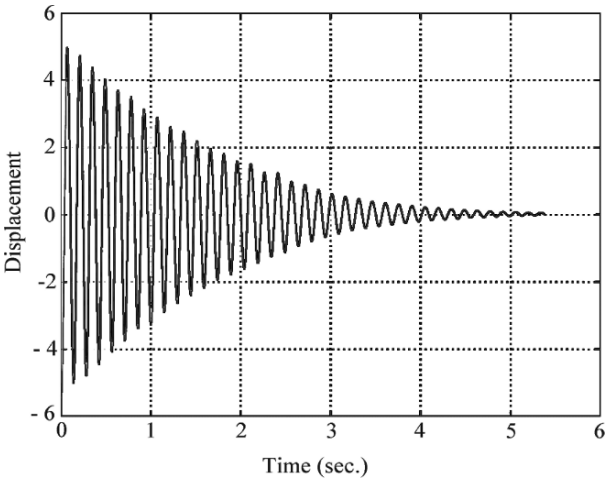

Fig. 5 Free vibration decay signal.

Current sent to the coil wound on the ring provides harmonic excitation to the torsional system. A Philips PM 5132 (0.1 Hz – 2 MHz) signal generator and a MB Dynamics SL 6000 VCF power amplifier was used for this purpose. The amplitude (Γ) and frequency (ω) of the excitation torque are controlled by setting the gains and frequency accordingly in these two instruments. The steady state peak-to-peak response and the associated power spectrum are obtained from the FFT analyzer. No attempt is made to calibrate the exciting torque.

The equation of motion of the driven oscillator can now be written as

$$\Theta'' + 0.03\Theta' + \Theta + \Theta^3 = T_1 \cos(\omega_1 \tau) \tag{3}$$

where the prime denotes differentiation with respect to τ and the other symbols are defined as given below:

$$\Theta = \sqrt{\beta/\alpha}\,\theta, \quad T_1 = \left(\sqrt{\beta/\alpha}\right)(T/\alpha), \quad \omega_1 = \omega/\sqrt{\alpha}, \quad \tau = \sqrt{\alpha}t,$$
$$\alpha = k_1/J, \quad \beta = k_2/J, \quad T = \Gamma/J.$$

3. Numerical integration

Numerical results are obtained by integrating equation (3) using a standard solver *ode45* in *MATLAB* 6.5. This solver is based on explicit Runge–Kutta (4,5) formula, the Dormand-Prince pair. It is a one step solver with adaptive step size. Integrations have been carried out with various sets of initial values (Θ_0, Θ_0').

4. Results and discussions

Fig. 6 shows some typical peak-to-peak response at different forcing frequencies for a particular level of excitation. These periodic steady-state responses are obtained by numerical integration of Eqn. (3) after starting with different sets of initial conditions. The combinations of initial conditions used are also mentioned in the figure. Three frequency regions, marked as J_1, J_2 and J_3, are delineated. In the low frequency regime J_1, the response curve is irregular. But all the sets of initial conditions produced the same response. Fig. 7(a) shows the response in the frequency range 1 – 5 Hz for three different values of excitation.

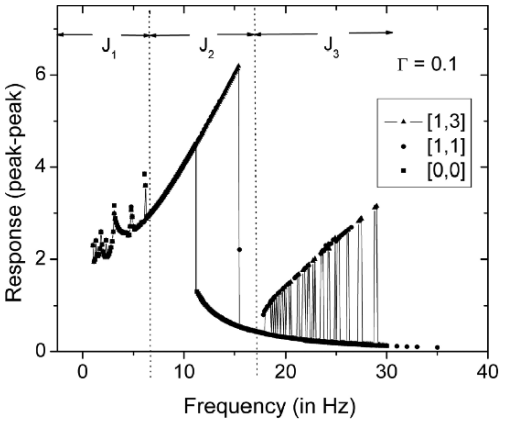

Fig. 6 Frequency response obtained numerically.

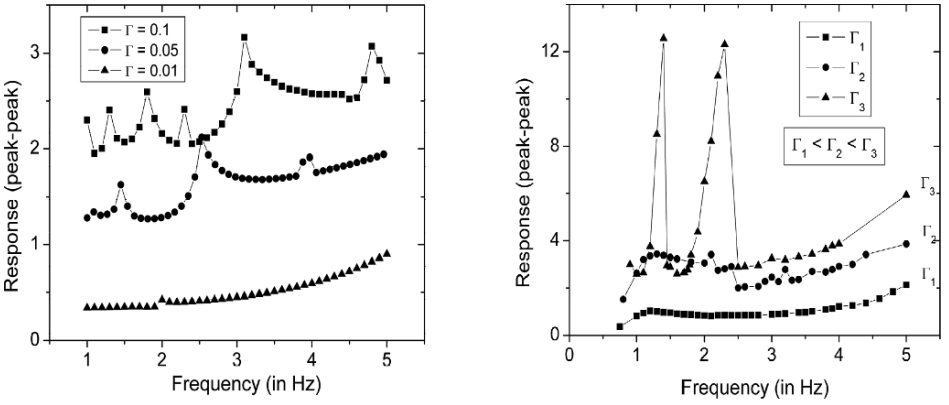

Fig. 7 Frequency response in the low frequency regime.

It is clear that the irregularities increase with increasing values of excitation. This irregular behavior can be attributed to complex interaction of higher order unstable regions of harmonic response[17]. Fig. 7(b) shows the response in the same region obtained experimentally for three levels of excitation. Again the irregularities in the response curve with higher excitation levels are apparent.

One particular frequency ($\omega = 1.8$ Hz) in this range J_1 is now considered for detailed study. Numerically obtained results are presented in Figs. 8(a)-(e) with increasing levels of excitation. The symbol n denotes the ratio of the period of the response to that of the excitation. The appearance of dual solution, indicated in Fig. 8(b), signifies the presence of even order superharmonics at that level of excitation. Stroboscopic maps have been obtained by plotting the values of Θ'

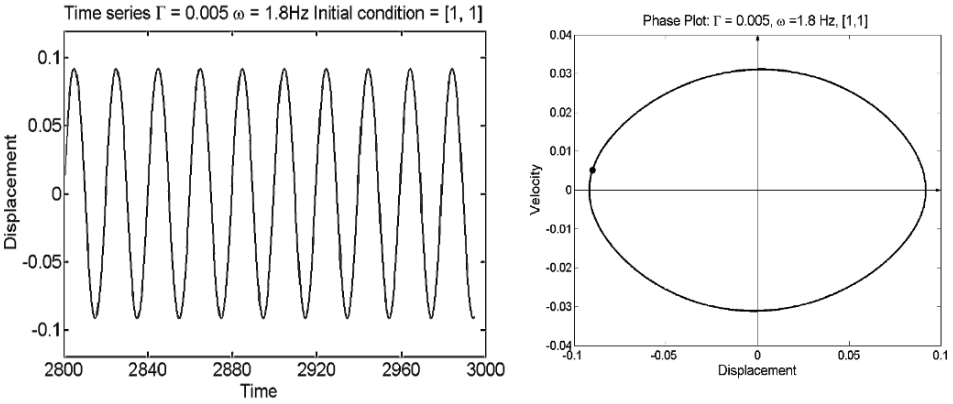

(a) Time series and phase plot for n=1. Symmetric solution

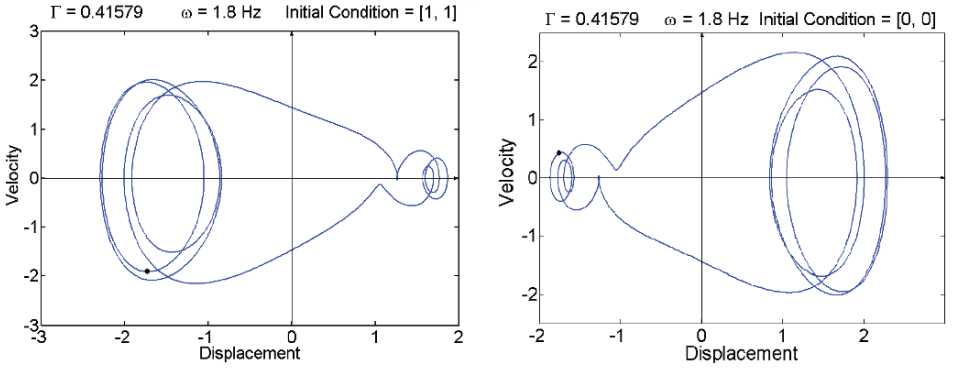

(b) Dual solution after symmetry breaking

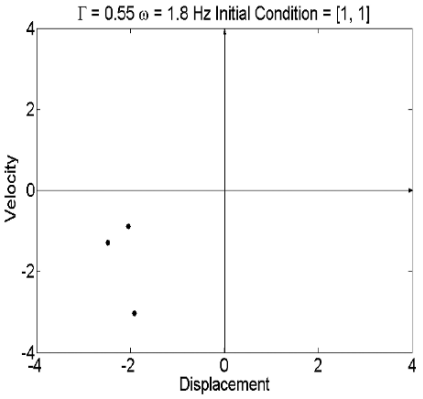

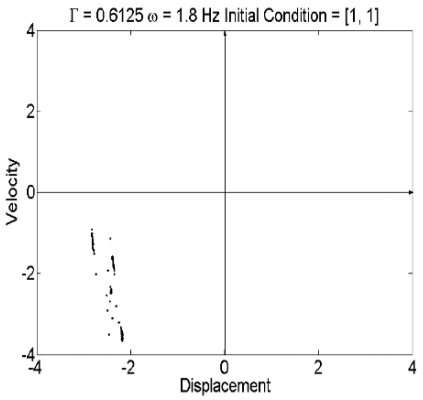

(c) Stroboscopic map for n=3 solution turning into pre-chaotic solution

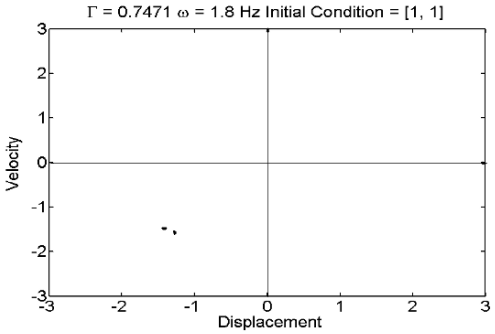

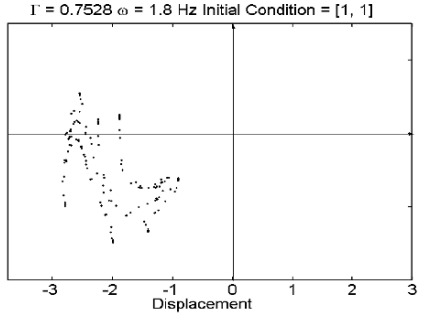

(d) Stroboscopic map of n=2 solution turning into chaotic solution

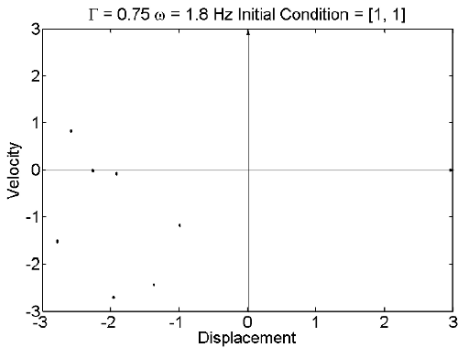

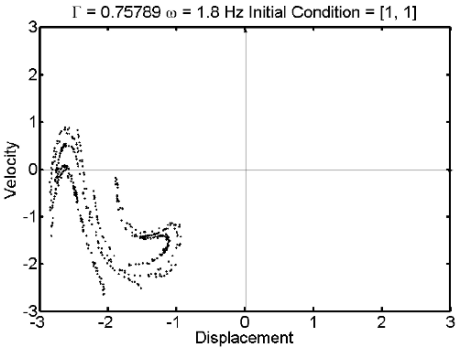

(c) Stroboscopic map of n=7 solution turning into chaotic solution

Fig. 8 Typical features of response obtained numerically at 1.8 Hz.

and Θ with a time interval equal to the time period of the excitation. It is clearly seen that periodic solutions of different periods ultimately bifurcate into chaotic response. Fig. 9 shows the time response and the corresponding power spectrum

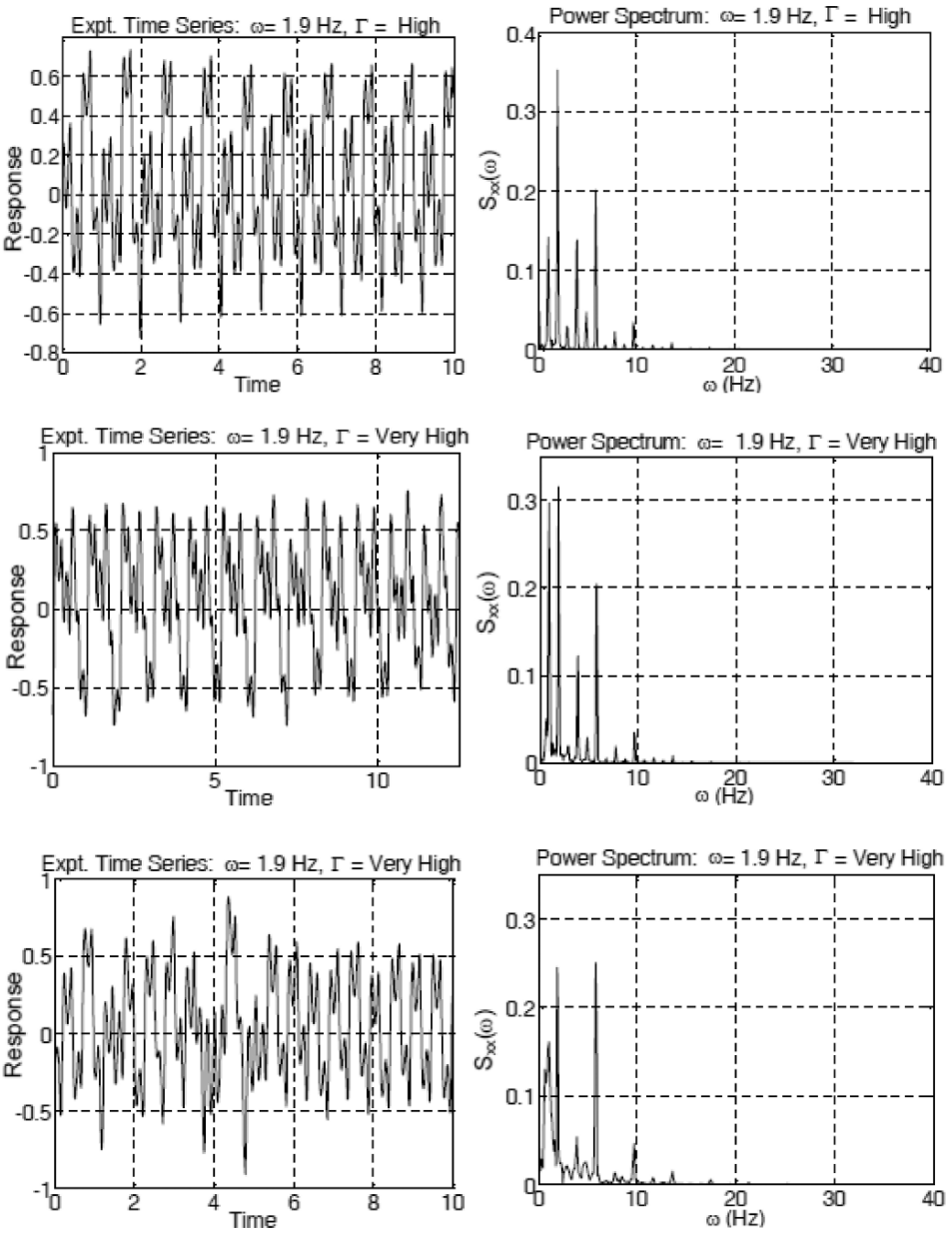

Fig. 9 Chaotic response obtained experimentally at 1.9 Hz with increasing level of excitation.

obtained experimentally at 1.9 Hz for three different levels of excitations. The top diagram shows a periodic response with a number of superharmonics. With increasing level of excitation, subharmonics start appearing with consequent increase in the period and finally all the low frequencies starting from zero appear in the response and the response turns aperiodic or chaotic.

The response characteristics obtained numerically at a frequency (6.6 Hz) of excitation in the region marked as J_2 in Fig. 6 showed coexistence of different solutions (including different dual solutions) of period 1, for the same level of excitation with different initial conditions. With increasing level of excitation, periodic solutions of $n = 2$ and $n = 3$ appeared, which with further increase in excitation turned pre-chaotic as revealed by stroboscopic maps. Such high level of excitation could not be reached in the experiment due to heating of the coil. However, the jump phenomenon in this region with increasing and decreasing excitation frequencies are revealed in the experiment as shown in Fig. 10. The size of the hysteresis loop, while jumping to and from the resonance branch, increases with increasing level of excitation. It may be pointed out that when the excitation level is below a critical value, no jump is seen in the response curve[20].

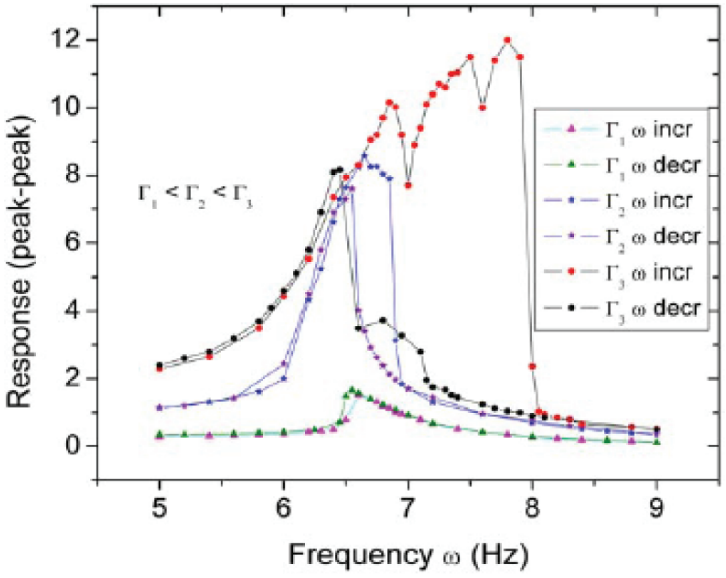

Fig. 10 Jump phenomenon in the response obtained experimentally.

The frequency range marked as J_3 in Fig. 6 is now discussed. Figures 11(a) - (b) show the response obtained numerically in this region for two different levels of excitation. Unpredictable jumps between two and possibly three (at higher level of excitation) attractors having $n = 1, 2$ and $n = 1, 2$ and 3 can be seen. In this region, the response becomes very sensitive to any minute changes in parameters like forcing amplitude or frequency. Fig. 12 clearly shows how this sensitivity changes both the phase plot and the stroboscopic map of the attractor. It may be pointed out that $53/110 = 0.4818$ is the level of excitation in the second diagram of Fig. 12.

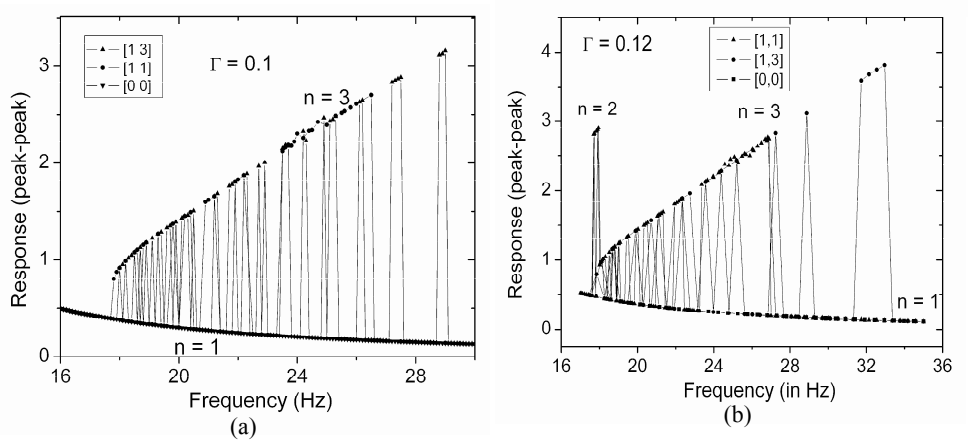

Fig. 11 Frequency response curve obtained numerically in high-frequency regime.

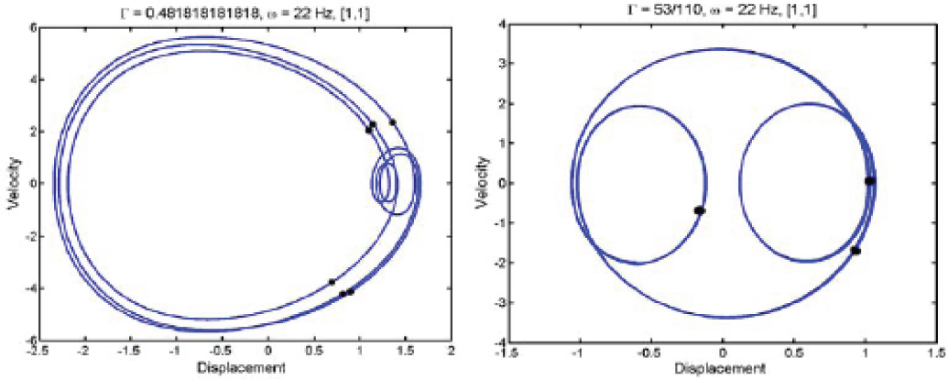

Fig. 12 Response sensitivity to parameters at 22 Hz.

It is well known that in a Duffing oscillator, when the forcing frequency is around three times the linearised natural frequency then one-third subharmonic solution can be sustained. With a high level of excitation, the normal jump from resonance to non-resonance branch can also be shifted to this high frequency. All these can give rise to complicated behavior, so far as the response is concerned. Therefore, it was decided to study the response around 18 Hz.

The effect of the unpredictable jump when the excitation frequency is around 18 Hz is studied both numerically and experimentally. Numerical integration reveals that the transients take very long to die down and finally a period two solution settles two a period one solution at 18.01 Hz. This phenomenon is clearly shown in Fig. 13. Further, around this frequency, a little change in the frequency also alters the response quite drastically as shown in

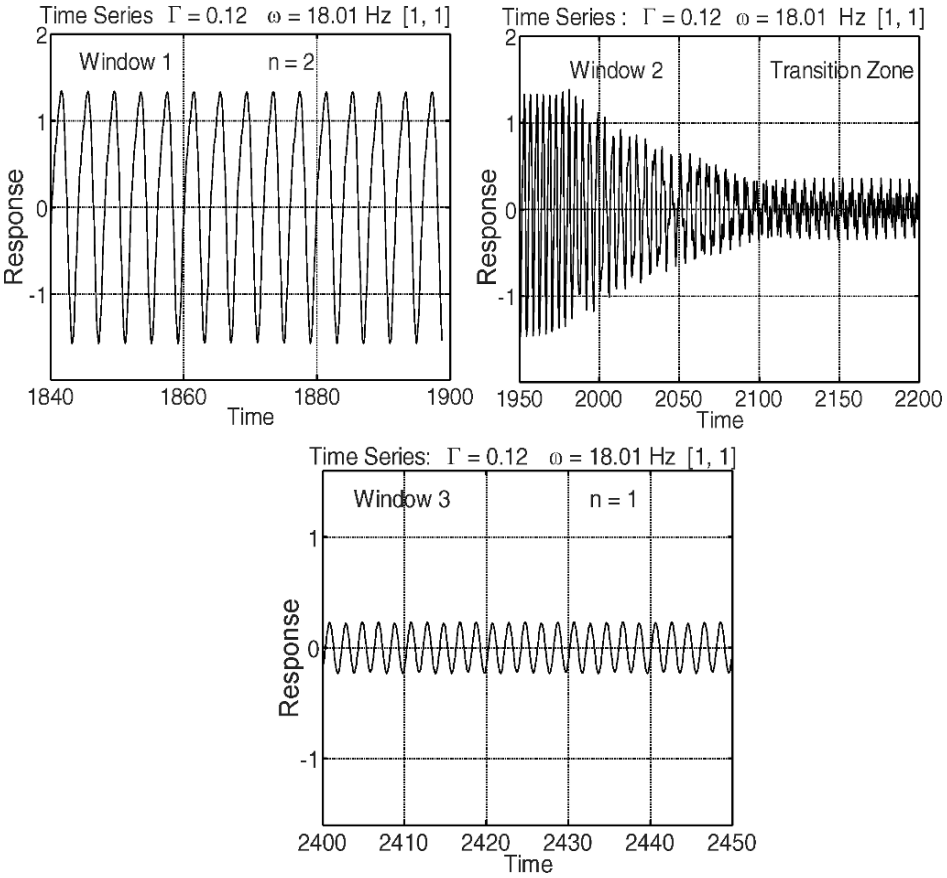

Fig. 13 Long transients in the numerically obtained response at 18.01 Hz.

Fig. 14. It is clearly seen that the response at 18.03 Hz has period one. But the response at 18.02 Hz has a strong presence of one-third subharmonic. The response at 18.01 Hz consists of almost only the one-third subharmonic.

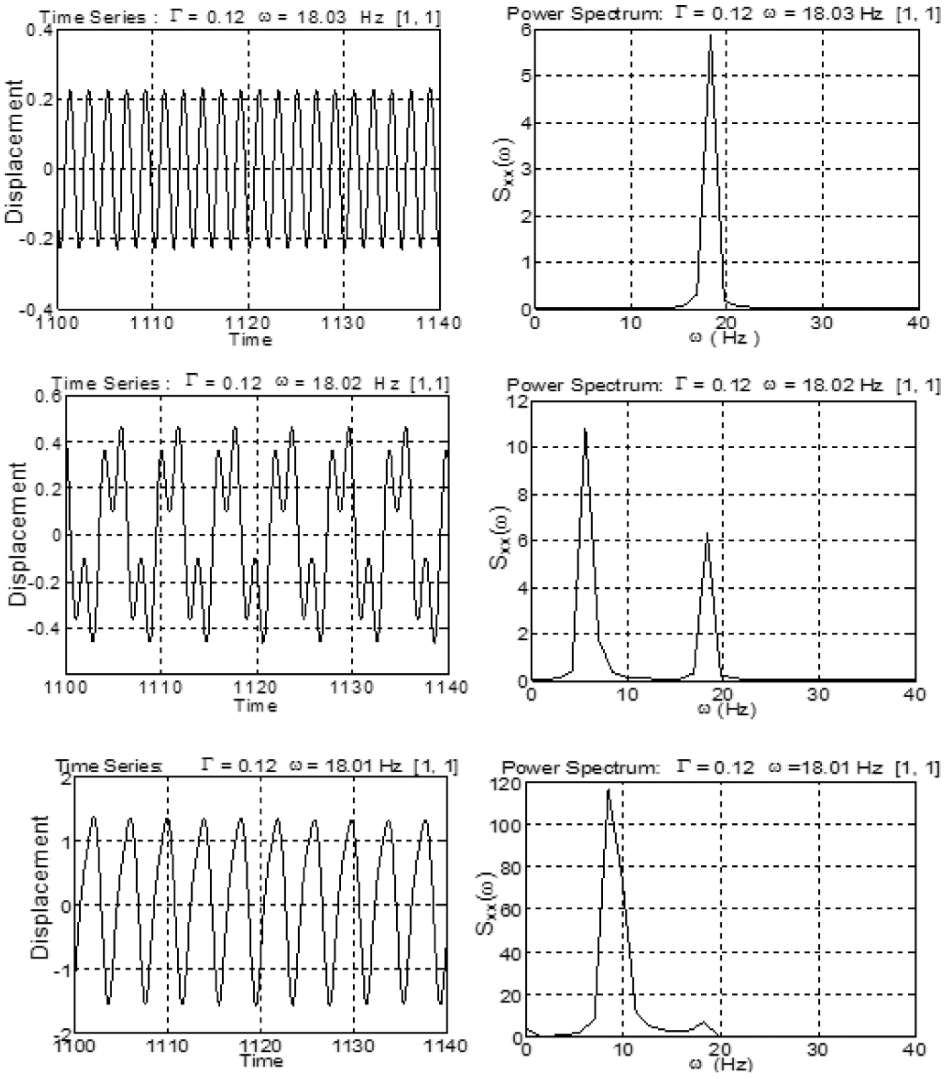

Fig. 14 Sensitivity of the response to frequency around 18 Hz.

During experimentation there are inevitable fluctuations in the forcing frequency. To see the effect of intense sensitivity of the response to the forcing frequency, experiment was conducted at 18 Hz. It was observed that the response never settles down to a steady state. Three typical time windows after a long run, by when normally periodic steady state was reached at other frequencies, are shown in Fig. 15.

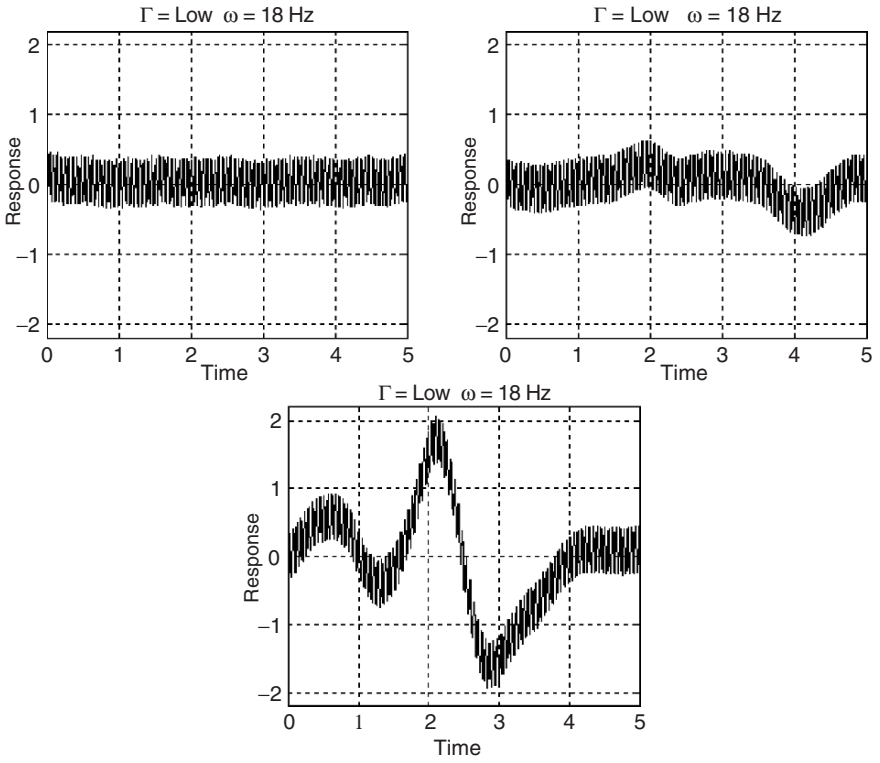

Fig. 15 Experimentally obtained response at 18 Hz showing unpredictable jumps between different solutions resulting in disappearance of steady state.

5. Conclusions

The major conclusions of this paper are listed below:

(i) A torsional, hard Duffing oscillator with strong nonlinearity has been designed and fabricated.
(ii) The nonlinear stiffness and linear damping parameters have been obtained from static and free vibration decay, respectively.

(iii) Numerical simulation and experimental results from this model exhibit non-smooth variation of the peak-to-peak value of the periodic response, finally leading to chaotic motion at low frequency regime.
(iv) Over and above the usual jump phenomenon between resonance and non-resonance branches, the response at high frequency reveals unpredictable jumps between coexisting periodic solutions of different frequencies.
(v) At excitation frequencies around three times the linearised natural frequency, the response is extremely sensitive to the forcing parameters resulting in disappearance of steady state in the experimental result.

References

1. G. Duffing, 1918. *Vieweg*, Braunschweig. Erzwungene Schwingungen bei verlaenderlicher Eigenfrequenz und ihre technische Bedeutung.
2. J. J. Stoker 1950. *Nonlinear Vibrations*, Interscience Publishers Inc., New York.
3. C. Hayashi 1964. *Nonlinear Oscillations in Mechanical and Electrical Systems*, Mc-Graw Hill, New York.
4. K. Magnus 1965. *Vibrations*, Blackie & Son Limited, Glasgow.
5. A. H. Nayfeh, D. T. Mook 1979. *Nonlinear Oscillations*, Wiley, New York.
6. P. Hagedorn 1988. *Non-Linear Oscillations* (Second Edition), Clarendon Press, Oxford.
7. W. Szemplinska-Stupnica 1990. *The behavior of Nonlinear Vibrating Systems* Vols. I and II, Kluwer Academic Publishers, London.
8. D. W. Jordan, P. Smith 1997. *Nonlinear Ordinary Differential Equations – An Introduction to Dynamical Systems* (Third Edition), Oxford University Press, Oxford.
9. F. C. Moon 1980. *Experiments on chaotic motions of forced nonlinear oscillator: Strange attractors*, Transactions of the ASME Journal of Applied Mechanics, **47**, 638-644.
10. E. H. Dowell, C. Pezeshki, 1986. *On the understanding of chaos in Duffing equation including a comparison with experiment*, Transactions of the ASME Journal of Applied Mechanics **53**, 5-9.
11. J. A. Gottwald, L. N. Virgin, E. H. Dowell, 1992. *Experimental mimicry of Duffing's equation*, Journal of Sound and Vibration, **158**, 447-467.
12. M. D. Todd, L. N. Virgin, 1997. *An experimental verification of basin metamorpheses in a nonlinear mechanical system*, International Journal of Bifurcation and Chaos, **7**, 1337-1357.
13. B. Ravindra, A. K. Mallik, 1994. *Role of nonlinear dissipation in soft Duffing oscillators*, Physical Review (E), **49**, 4950-4954.
14. H. Hatwal, A. K. Mallik, A. Ghosh, 1983. *Forced nonlinear oscillations of an autoparametric system – Part II: Chaotic responses*, *Journal of Applied mechanics, Transactions of ASME*, **50**, 663-668.
15. G. L. Baker, J. P. Gollub, 1990. *Chaotic Dynamics – An Introduction*, Cambridge University Press, Cambridge.
16. L. N. Virgin, 2000. *Introduction to Experimental Nonlinear Dynamics: A Case Study in Mechanical Vibration*, Cambridge University Press, Cambridge.
17. Y. Ueda, 1980. *Steady motions exhibited by Duffing's equation: a picture book of regular and chaotic motions*, New Approaches to Nonlinear Problems in–Dynamics, P. J. Holmes (Ed), SIAM, Philadelphia.

18. M. S. Soliman, J. M. T Thompson, 1996. *Indeterminate bifurcational phenomena in hardening systems*, Proceedings of Royal Society London **452**, 187-191.
19. M. S. Soliman, 1997. *Non-linear vibrations of hardening systems: Chaotic dynamics and unpredictable jumps to and from resonance*, Journal of Sound and Vibration **207**, 383-392.
20. A. K. Mallik, B. Ravindra, 1997. *Nonlinear mechanical vibrations*, Modelling of Complex Systems –, J. K. Bhattacharjee, A. K. Mallik (Ed), Narosa Publishing House, New Delhi.
21. J. Aguirre, M. A. F. Sanjuan, 2002. *Unpredictable behaviour in the Duffing oscillator: Wada basins*, Physica D, **171**, 41-51.
22. H. E. Nusse, E. Ott, A. Yorke, 1995. *Saddle-node bifurcations on fractal basin boundaries*, Physical Review Letters **75**, 2482-2485.
23. H. E. Nusse, A. Yorke, 1996. *Wada basin boundaries and basin cells*, Physica D, **90**, 242-261.
24. A. B. Pippard, 1985. *Response and Stability: An Introduction to the Physical Theory* Cambridge University Press, Cambridge.
25. N. S. Patil, 2004. *M. Tech. Thesis Forced vibrations of a hard Duffing oscillator – numerical and experimental investigations*, IIT Kanpur, India, University of Colorado, PhD Thesis.

IDENTIFICATION OF VISCOELASTIC MODEL OF FILLED RUBBER AND NUMERICAL SIMULATION OF ITS TIME DEPENDENT RESPONSE

BOHDANA MARVALOVA*
Technical University of Liberec, Halkova 6, 46117 Liberec, Czech Republic

Abstract. The rate-dependent behavior of filled rubber was investigated in compression regimes. The viscosity-induced rate-dependent effects are described. The parameters of a constitutive model of finite strain viscoelasticity were determined by nonlinear optimization methods. The material model was implemented into finite element code and the viscoelastic stress response of carbon black filled rubber at large strains in relaxation, creep and cyclic loading was simulated.

Keywords: viscoelasticity, relaxation, filled rubber, mechanical testing, identification of material parameters, FE simulation

1. Introduction

Rubber materials are applied in various branches of mechanical engineering because of their damping properties. One of such applications of the orthotropic cord-reinforced rubber composite in engineering practice is the sheath of air-spring used for the vibration isolation of driver seats. Hyperelastic models of the composite material at finite strains were developed and used successfully for FE simulation of deformations of a cylindrical air-spring[1,2]. However, the modeling and FE simulations of the structural response require a constitutive model which captures the complex material behaviour. In order to describe

*bohda.marvalova@tul.cz

E. İnan et al. (eds.), *Vibration Problems ICOVP-2007*,

damping effects of cord-reinforced rubber composites their dissipative viscoelastic behaviour must be explored and included into the material model. The present paper focuses on the time dependent viscoelastic behaviour of the filled rubber.

The ground-stress response of filled rubber is usually modeled in the phenomenological framework of finite elasticity by Mooney-Rivlin or Ogden models, or by Aruda and Boyce model in terms of the micromechanically based kinetic theory of polymer chain deformations.

Beside the elastic response the filled rubber shows also the finite viscoelastic overstress response which is apparent in creep and relaxation tests. Cyclic loading tests show a typical frequency-dependent hysteresis as well where the width of the hysteresis increases with increasing stretch rates. The constitutive theory of finite linear viscoelasticity is a major foundation for modeling rate dependent material behaviour based on the phenomenological approach. In this approach, a suitable hyperelasticity model is employed to reproduce the elastic response and the inelastic overstress is determined by an evolution equation.

2. Model for finite viscoelasticity

The origin of the material model of finite strain viscoelasticity used in our work is the concept of Simo[3], Govindjee and Simo[4] and Holzapfel and Simo[5]. The finite element formulation of the model was elaborated by Holzapfel[6] and used by Holzapfel and Gasser[7] to calculate the viscoelastic deformation of fiber reinforced composite material undergoing finite strains. The model is based on the theory of compressible hyperelasticity with the decoupled representation of the Helmholtz free energy function with the internal variables[8].

$$\Psi\left(\mathbf{C},\boldsymbol{\Gamma}_1,.....,\boldsymbol{\Gamma}_m\right)=\Psi_{VOL}^{\infty}\left(J\right)+\Psi_{ISO}^{\infty}\left(\overline{\mathbf{C}}\right)+\sum_{\alpha=1}^{m}\Upsilon_{\alpha}\left(\overline{\mathbf{C}},\boldsymbol{\Gamma}_{\alpha}\right),\ \overline{\mathbf{C}}=J^{-2/3}\mathbf{C}\,. \quad (1)$$

The first two terms in Eq.(1_1) characterize the equilibrium state and describe the volumetric elastic response and the isochoric elastic response when $t\to\infty$, respectively. The third term is the dissipative potential responsible for the viscoelastic contribution. The derivation of the 2nd Piola-Kirchhoff stress with volumetric and isochoric terms:

$$\mathbf{S}=2\frac{\partial\Psi\left(\mathbf{C},\boldsymbol{\Gamma}_1,.....,\boldsymbol{\Gamma}_m\right)}{\partial\mathbf{C}}=\mathbf{S}_{VOL}^{\infty}+\mathbf{S}_{ISO}^{\infty}+\sum_{\alpha=1}^{m}\mathbf{Q}_{\alpha}, \quad (2)$$

where $\mathbf{S}_{VOL}^{\infty}$ and $\mathbf{S}_{ISO}^{\infty}$ is the volumetric and the isochoric stress response respectively and the overstress $\mathbf{Q}_{\alpha}$ is stress of 2nd Piola-Kirchhoff type.

Motivated by the generalized Maxwell rheological model at Fig. 1, the evolution equation for the internal variable $\mathbf{Q}_\alpha$ takes on the form of Eq. (3_1).

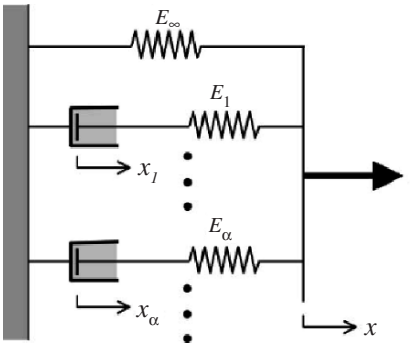

Fig. 1 Maxwell rheological model.

$$\begin{aligned}
&\dot{\mathbf{Q}}_\alpha + \frac{\mathbf{Q}_\alpha}{\tau_\alpha} = \dot{\mathbf{S}}_{ISO\alpha},\\
&\mathbf{S}_{ISO\alpha} = J^{-2/3} Dev\left[2\frac{\partial \Psi_{ISO\alpha}\left(\overline{\mathbf{C}}\right)}{\partial \overline{\mathbf{C}}} \right],\\
&\Psi_{ISO\alpha}\left(\overline{\mathbf{C}}\right) = \beta_\alpha^\infty \Psi_{ISO}^\infty\left(\overline{\mathbf{C}}\right),\\
&\mathbf{S}_{ISO\alpha} = \beta_\alpha^\infty \mathbf{S}_{ISO}^\infty\left(\overline{\mathbf{C}}\right).
\end{aligned} \tag{3}$$

The variable $\beta_\alpha^\infty \in (0,\infty)$ in the Eq. (3) is the nondimensional strain energy factor and τ_α is the relaxation time, $Dev(.)$ is the deviatoric operator in the Lagrangian description. The material is assumed slightly compressible, the volumetric and isochoric parts of Helmholtz free energy function were chosen in the form

$$\Psi_{VOL}^\infty(J) = \frac{1}{d}(J-1)^2,\ \Psi_{ISO}^\infty\left(\overline{\mathbf{C}}\right) = c_1\left(\overline{I}_1 - 3\right) + c_2\left(\overline{I}_2 - 3\right), \tag{4}$$

where the parameters c_1, c_2 and d are to be determined from experiments. The viscoelastic behavior is modeled by use of $\alpha = 2$ relaxation processes with the corresponding relaxation times τ_α and free energy factors β_α^∞.

3. Experiments

The relaxation behaviour at different strain levels is examined in detail through multi-step relaxation tests. In the compression tests, the strain rate of 0,05mm/s was applied during the loading path. The stress relaxation was recorded for 1200 s. Fig. 2 shows the time histories of stress at different strain levels in compression regime. All curves reveal the existence of a very fast stress relaxation during the first 10 seconds followed by a very slow rate of relaxation that continues in an asymptotic sense. Comparing the results obtained at different strain levels, it can be seen that relaxation tests carried out at higher strain levels possess larger over-stresses and subsequently show a faster stress relaxation than those at lower strain levels with lower over-stresses. This conforms with observations reported by Haupt and Sedlan[9] and by Amin et al[10].

In the classical approach, equilibrium states are reached if the duration of the relaxation periods is infinitely long. Thus, the stresses measured at the termination points of the relaxation periods are approximate values of the equilibrium stress. The difference between the current stress and the equilibrium stress is the so-called overstress. Fig. 2 compares the experimental data of a multi-step relaxation test and the curves fitted to the proposed material model by nonlinear least squares method. The curve at Fig. 3 approximates the equilibrium stress

$$\boldsymbol{S}_{VOL}^{\infty} + \boldsymbol{S}_{ISO}^{\infty} .$$

To characterize better the viscosity properties, a series of simple relaxation tests at different stretch levels were carried out. In this course, a stretch rate of 0.05/s followed by a hold time of 20 min was used in the tests. All tests were performed at constant temperature under strain control. Prior to an actual test, each virgin specimen was subjected to a pre-loading process to remove the

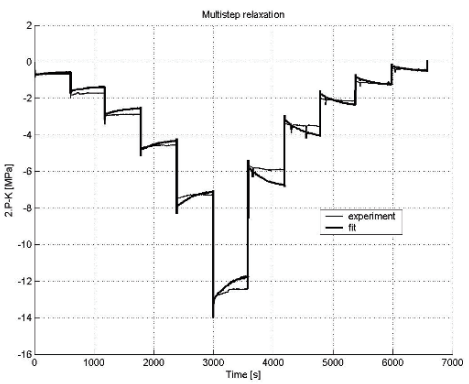

Fig. 2 Multistep relaxation.

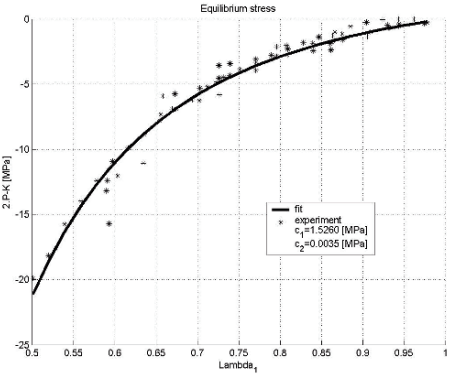

Fig. 3 Equilibrium stress.

Mullins' softening effect. The second Piola-Kirchhoff stress and the stretch in the loading direction of test specimens were determined from experimental results. The seven material parameters were calculated by nonlinear optimization methods in Matlab.

4. Finite element simulation in Comsol Multiphysics

The material model described above was implemented into Comsol Multiphysics. The Structural Mechanics and PDE modules were used for the calculation of time dependent response of a rubber block in plain strain in different loading regimes. The application mode type plane strain in Structural Mechanics Module, the time dependent analysis and the Mooney-Rivlin hyperelastic material were chosen.

The components of the isochoric stress rate $\dot{\mathbf{S}}_{ISO}^{\infty}$ were determined in Symbolic Toolbox in Matlab and added to the scalar expression table in Comsol. PDE module was used for the integration of the evolution Eqn. (3_1). The results of the simulations of creep, relaxation and cyclic loading at Figs. 4-7 show the good qualitative agreement with experimental time dependent behaviour of filled rubbers.

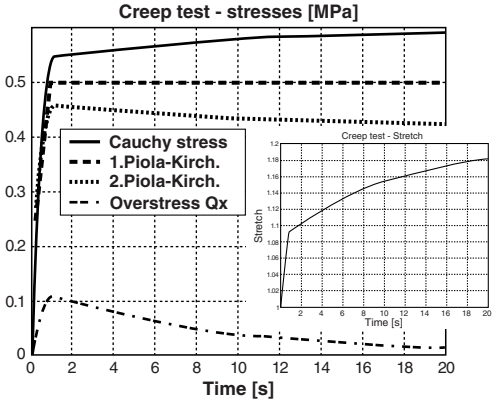

Fig. 4 Simulation of a creep test.

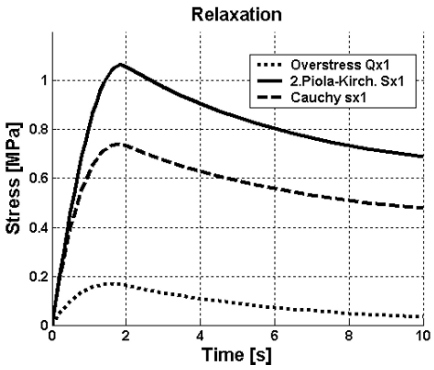

Fig. 5 Simulation of a relaxation test.

5. Conclusions

Multi-step relaxation and single relaxation of a filled rubber were modeled with viscoelastic theory. The parameters of the model were determined from relaxation data by employing nonlinear optimization methods. The proposed model

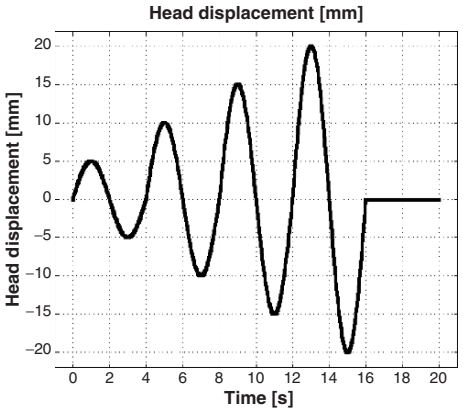

Fig. 6 Strain controled cyclic test.

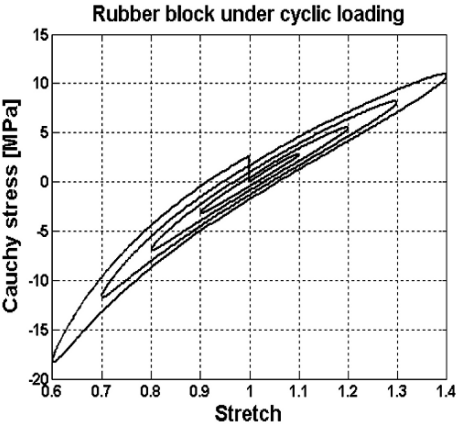

Fig. 7 Cyclic test - stress response.

is then compared with experimental data for filled rubber subjected to different loading histories. It is shown that the model gives good quantitative agreement for different time dependent behaviour. The FE implementation in Comsol Multiphysics of a viscoelastic material model in finite strain in the Lagrangian configuration was realized. Simple examples were subsequently presented, namely the relaxation, creep and time dependent loading of a rubber block. Numerical simulation of monotonic deformation processes with different strain rates, simple relaxation and multi-step relaxation tests have illustrated the adequacy of the model and the identified parameters in physical and general senses.

ACKNOWLEDGEMENT

The author gratefully acknowledges the funding provided by the Czech Grant *Agency GACR – grant No.101/05/2669.*

References

1. T. H. Nam, 2004. *Mechanical properties of the composite material with elastomeric matrix reinforced by textile cords*, PhD thesis, TUL Liberec.
2. R. Urban, 2004. *Modeling of structure elements made of cord-reinforced rubber*, PhD thesis, TUL Liberec.
3. J. C. Simo, 1987. *On a fully three dimensional finite strain viscoelastic damage model: formulation and computational aspects*, Comput. Meth. Appl. Mech. Eng., **60**, 153–173.
4. S. Govindjee, J. C. Simo, 1992. *Mullins' effect and strain amplitude dependence of the storage modulus*, Int. J. Solid Struct., **29**, 1737–1751.

5. G. A. Holzapfel, J. C. Simo, 1996. *A new viscoelastic constitutive model for continuous media at finite thermomechanical changes*, Int. J. Solid Struct., **33**, 3019–3034.
6. G. A. Holzapfel, 1996. *On large strain viscoelasticity: continuum formulation and finite element applications to elastomeric structures*, Int. J. Numer. Meth. Eng., **39**, 3903–3926.
7. G. A. Holzapfel, T. C. Gasser, 2001. *A viscoelastic model for fiber-reinforced composites at finite strains: Continuum basis, computational aspects and applications*, Comput. Meth. Appl. Mech. Eng., **190**, 4379–4430.
8. G. A. Holzapfel, 2000. *Nonlinear Solid Mechanics*, pp. 282–295, Wiley, Chichester.
9. P. Haupt, K. Sedlan, 2001. *Viscoplasticity of elastomeric materials: experimental facts and constitutive modelling*, Arch. Appl. Mech., **71**, 89–109.
10. A. F. M. S. Amin, A. Lion, S. Sekita, Y. Okui, 2006. *Nonlinear dependence of viscosity in modeling the ratedependent response of natural and high damping rubbers in compression and shear: Experimental identification and numerical verification*, Int. J. of Plasticity, **22**, 1610–1657.

ELASTIC OSCILLATIONS OF SPACE TETHERS AND THE SPACE ELEVATOR

ARUN K. MISRA* AND STEPHEN S. COHEN
Department of Mechanical Engineering, McGill University, Montreal, QC, H3A 2K6, Canada

Abstract. Many tethered satellite systems that have flown so far involve tethers that are several kilometers long. Another thin long structure that might become a reality in the future is the space elevator, which will extend from the surface of the Earth to an altitude beyond the geostationary orbit. For both of these structures, the ratio of the length to any cross-sectional dimension is very high. Hence, their flexural rigidity is negligible and they behave like strings. For both space tethers and the space elevator, an axial tension is generated due to the gravity force gradient and the centrifugal force gradient. This tension varies along the length. An exact solution is presented for the longitudinal oscillations of space tethers. The proposed space elevator is expected to have a variable area of cross-section to nominally maintain uniform stress throughout. For this case, the discretized equations governing elastic oscillations are derived using the assumed modes method. These are solved to obtain the frequencies of longitudinal and transverse oscillations.

Keywords: tethered satellites, space elevator, longitudinal oscillations, transverse vibrations

1. Introduction

Tethered satellite systems, i.e., satellites connected by long thin tethers, have been proposed for a variety of applications. Several tethered systems have already flown in space, for example, the Italian/American mission TSS, the American missions SEDS and TiPS, and the Canadian missions Oedipus A and C. A description of these and other missions can be found in [1]. All the flights mentioned above involved tethers several kilometers long (1 to 20 km).

*Corresponding author, arun.misra@mcgill.ca

E. İnan et al. (eds.), *Vibration Problems ICOVP-2007*,

Successful operation of these satellites requires the knowledge of their general dynamics, including orbital motion, librational motion and elastic oscillations. This paper examines the elastic oscillations of space tethers.

Another space structure that has a lot of similarity with space tethers regarding the elastic oscillations is the space elevator. This, if constructed, will be the longest structure with the largest aspect-ratio ever constructed by humans, and will revolutionize the launching of satellites. Even though its construction is not likely to start for decades, some researchers have started to look into its dynamics. Some preliminary results for longitudinal and transverse vibrations of the space elevator are presented in this paper. The elastic oscillations of the two systems, space tethers and the space elevator, are somewhat similar in nature. Both are subjected to a non-uniform axial tension generated due to the gravity force gradient and the centrifugal force gradient. In the following, first the space tethers will be considered, followed by the space elevator.

2. Elastic oscillations of space tethers

The system under consideration consists of the main orbiter A, subsatellite B and a tether (Fig. 1). It is assumed that the orbiter is in a circular orbit having an angular velocity Ω. The longitudinal deformation of an element of the tether at any instant t is denoted by $u(s,t)$, where s is the distance of the element from the orbiter.

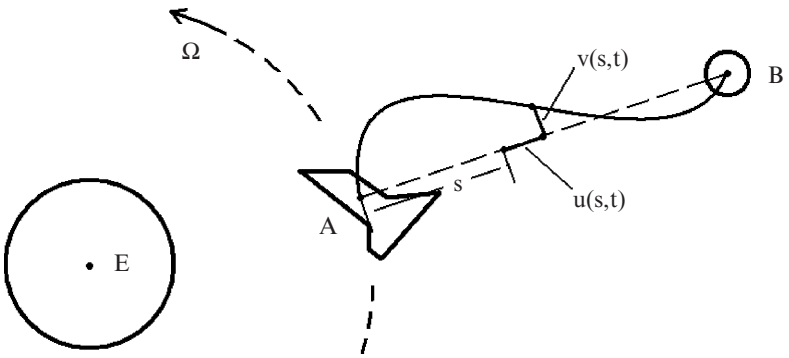

Fig. 1 Space tether system.

Using the extended Hamilton's principle (or otherwise), one can obtain the following equation of motion:

$$EA\frac{\partial^2 u}{\partial s^2}-\rho\frac{\partial^2 u}{\partial t^2}+3\rho\Omega^2\left(s+u\right)=0 \tag{1}$$

with the boundary conditions

$$u(0,t) = 0 \tag{2}$$

$$-EA\frac{\partial u}{\partial s}(L_0,t) - m_b\frac{\partial^2 u}{\partial t^2}(L_0,t) + 3m_b\Omega^2\left[L_0 + u(L_0,t)\right] = 0 \tag{3}$$

Here L_0, E and ρ stand for the nominal length, Young's modulus and mass per unit length of the tether, A the uniform area of its cross-section and m_b the mass of the subsatellite. The last term in Eqn. (1) and that in Eqn. (3) arise due to the gradient of the gravity and centrifugal effect along the tether and are more important for lower orbits. It is convenient to non-dimensionalize the equation of motion and boundary conditions by defining

$$\xi = s/L_0,\ \ \tau = \Omega t,\ \ U = u/L_0 \tag{4}$$

$$p = \left(EA/\rho L_0^2\right)^{1/2}/\Omega,\ \ r = \rho L_0/m_b \tag{5}$$

Here r is the mass ratio (tether mass to subsatellite mass), while p is a measure of the ratio of longitudinal frequencies to the orbital frequency. The equation of motion now becomes

$$p^2\frac{\partial^2 U}{\partial \xi^2} - \frac{\partial^2 U}{\partial \tau^2} + 3\left(\xi + U\right) = 0 \tag{6}$$

with boundary conditions

$$U(0,\tau) = 0 \tag{7}$$

$$-p^2 r\frac{\partial U}{\partial \xi}(1,\tau) - \frac{\partial^2 U}{\partial \tau^2}(1,\tau) + 3\left[1 + U(1,\tau)\right] = 0 \tag{8}$$

The boundary value problem described by Eqns. (6)–(8) can be solved by defining a new variable $\hat{U}$ as follows:

$$\hat{U}(\xi,\tau) = U(\xi,\tau) - U_0(\xi) \tag{9}$$

where $U_0(\xi)$ is the static non-dimensional longitudinal extension of the tether and satisfies the following equation:

$$p^2\frac{d^2 U_0}{d\xi^2} + 3U_0 = -3\xi \tag{10}$$

with boundary conditions

$$U_0(0) = 0 \text{ and } -p^2 r \frac{dU_0}{d\xi}(1) + 3\left[1 + U_0(1)\right] = 0 \tag{11}$$

In that case, the oscillations around the static extension are governed by

$$p^2 \frac{\partial^2 \hat{U}}{\partial \xi^2} - \frac{\partial^2 \hat{U}}{\partial \tau^2} + 3\hat{U} = 0 \tag{12}$$

with boundary conditions

$$\hat{U}(0,\tau) = 0 \tag{13}$$

$$-p^2 r \frac{\partial \hat{U}}{\partial \xi}(1,\tau) - \frac{\partial^2 \hat{U}}{\partial \tau^2}(1,\tau) + 3\hat{U}(1,\tau) = 0 \tag{14}$$

The solution to Eqns. (10) and (11) are given by

$$U_0 = D \sin\left[\left(\sqrt{3}/p\right)\xi\right] - \xi \tag{15}$$

where

$$D = \left(rp/\sqrt{3}\right) \Big/ \left[r\cos\left(\sqrt{3}/p\right) - \left(\sqrt{3}/p\right)\sin\left(\sqrt{3}/p\right)\right] \tag{16}$$

The equilibrium tension at any point ξ can then be calculated using

$$T_0 = EA \frac{dU_0}{d\xi} \tag{17}$$

where U_0 is as given in Eqn. (15). For most tethered satellites, p is very large.

In that case, after some algebraic manipulation, T_0 can be written as

$$T_0 = 3m_b \Omega^2 L_0 \left[1 + \left(r/2\right)\left(1 - \xi^2\right)\right] \tag{18}$$

Hence, the steady state tension varies quadratically along the length.

Now the partial differential equation (12) with boundary conditions (13) and (14) can be solved to obtain the frequency equation

$$\tan\left[\left(3 + \lambda^2\right)^{1/2} \Big/ p\right] = rp \Big/ \left(3 + \lambda^2\right)^{1/2} \tag{19}$$

where λ is the longitudinal frequency (non-dimensionalized with respect to Ω). It was observed that the lowest root λ_1 obtained from the solution of Eqn. (19) varies as $L_0^{-1/2}$, while the rest vary as L_0^{-1}.

Consider now an example of an orbiter in a circular orbit at an altitude of 400 km, carrying a 60-km long tether having a mass per unit length 4.09×10^{-3} kg/m, area of cross-section $\pi \times 10^{-6}$ m^2 and elastic modulus 4.488×10^{10} N/m^2. Two subsatellite masses are considered: 100 kg and 500 kg. The frequencies of longitudinal oscillations, obtained by solving Eqn. (19) for these parameters, are presented in Table 1.

TABLE 1. Frequencies of longitudinal oscillations (rad/sec) for a typical space tether.

Mode #	Subsatellite Mass	
	100 kg	500 kg
1	0.1112	0.0634
2	0.3644	0.3219
3	0.6495	0.6224
4	0.9466	0.9273

It may be noted that the subsatellite mass affects the lowest frequency significantly, but the higher ones are not affected very much.

The transverse oscillations of the tether are not significantly different from those for the constant tension case. Since the space is limited, these results are not shown in this paper.

3. Elastic oscillations of space elevator

The space elevator consists of a ribbon (tether) and a counterweight attached to the surface of the Earth and is assumed to be in the equatorial plane (Fig. 2). As such, the angular velocity of the tether's orbit, Ω, coincides with that of the Earth. The longitudinal and transverse displacements of an element of the ribbon are denoted by u and v, respectively and are dependent on the distance s of the element from the surface of the Earth. The ribbon can also rotate from the vertical; the libration is denoted by α.

In the optimal design of the space elevator, the stress along the ribbon must be constant (denoted here by σ_0). This requires the area of cross-section of the ribbon to vary in a specific manner. It has been shown by Cohen[2] that the appropriate variation is:

$$A(\xi) = A_m \exp\left[F(\xi)\right] \tag{20}$$

where

$$F(\xi)=\frac{R_E^2}{\bar{h}R_G\left(1+\varepsilon_0\right)}\left\{\frac{3}{2}-\frac{R_G}{\left[R_E+\xi\left(1+\varepsilon_0\right)L_0\right]}-\frac{\left[R_E+\xi\left(1+\varepsilon_0\right)L_0\right]^2}{2R_G^2}\right\} \quad (21)$$

A_m is the maximum area of cross-section of the ribbon, which occurs at the geosynchronous altitude. ξ is as defined in Eqn. (4). R_E and R_G denote the radius of the Earth and the geosynchronous radius, respectively. The characteristic height of the ribbon is $\bar{h}=\sigma_0/\gamma g_0$, where γ is the ribbon's bulk density and g_0 is the surface gravity of the Earth. ε_0 is the uniform nominal strain in the ribbon and is given by σ_0/E. It is also essential that there be a counterweight at the free end. Its mass is given by

$$m_c=\gamma A_m\bar{h}\frac{\exp\left[F(\xi)\big|_{\xi=1}\right]}{\left(R_E/R_G\right)^2\left\{\left(R_E+L\right)/R_G-\left[R_G/\left(R_E+L\right)\right]^2\right\}}. \quad (22)$$

L here is the stretched length of the ribbon, i.e., $L=L_0\left(1+\varepsilon_0\right)$.

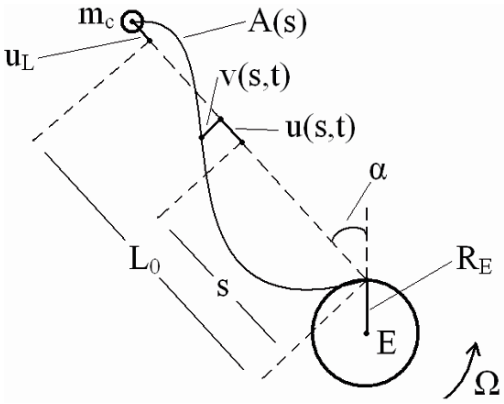

Fig. 2 A schematic diagram of the space elevator.

The equations of motion can be obtained by using the Lagrangian formulation in conjunction with the assumed modes method. The elastic displacements are expanded in series form as

$$U=u/L_0=\varepsilon_0\xi+\sum_{i=1}^{N}A_i(\tau)\psi_i(\xi) \quad (23)$$

and

$$V = v/L_0 = \sum_{i=1}^{M} B_i(\tau)\phi_i(\xi) \tag{24}$$

where ψ_i and ϕ_i are a set of basis functions satisfying the geometric boundary conditions and τ is as defined in Eqn. (4). N and M are the number of generalized coordinates A_i and B_i (and corresponding spatial basis functions) used to describe the longitudinal and transverse displacements, respectively.

3.1. LONGITUDINAL OSCILLATIONS OF THE RIBBON

The longitudinal extension of the ribbon is now examined by neglecting its transverse displacement and libration. If this is done, the equations describing the longitudinal extension of the ribbon may be expressed as [2]

$$\mathbf{M^A A''} + \mathbf{K^A A} = \mathbf{0} \tag{25}$$

where the elements of matrices $\mathbf{M^A}$ and $\mathbf{K^A}$ are given by

$$M_{ik}^{A} = M_p \int_0^1 \exp\left[F(\xi)\right]\psi_i\psi_k d\xi + M_c\left(\psi_i\psi_k\right)\Big|_{\xi=1} \tag{26}$$

and

$$\begin{aligned} K_{ik}^{A} = {} & \bar{\Omega}^2 \int_0^1 \exp\left[F(\xi)\right]\left(\frac{d\psi_i}{d\xi}\right)\left(\frac{d\psi_k}{d\xi}\right)d\xi - M_p\int_0^1 \exp\left[F(\xi)\right]\psi_i\psi_k d\xi - M_c\left(\psi_i\psi_k\right)\Big|_{\xi=1} \\ & -2\left(\frac{\beta}{\Lambda}\right)^3\left\{M_p\int_0^1 \frac{\exp\left[F(\xi)\right]\psi_i\psi_k}{\left[\left(1/\Lambda\right)+\xi\left(1+\varepsilon_0\right)\right]^3}d\xi + M_c\frac{\left(\psi_i\psi_k\right)\Big|_{\xi=1}}{\left[\left(1/\Lambda\right)+1+\varepsilon_0\right]^3}\right\} \end{aligned} \tag{27}$$

where indexes i and $k = 1, 2, 3, \ldots, N$. Non-dimensional masses are defined by $M_p = \gamma A_m L_0 / m_{tot}$ and $M_c = m_c / m_{tot}$, where m_{tot} is the total mass of the system. The nominal length of the ribbon is non-dimensionalized with respect to the radius of the Earth as $\Lambda = L_0 / R_E$. Another useful non-dimensional parameter is the ratio of the geosynchronous radius to the radius of the Earth: $\beta = R_G / R_E$. The frequency ratio associated with the axial elongation of the ribbon is defined as $\bar{\Omega} = \sqrt{EA_m/(m_{tot}L_0)}\,/\Omega$.

Now, basis functions to approximate the longitudinal extension must be chosen. They must all be zero at the base (when $\xi = 0$) to satisfy the boundary condition. Also, to allow the counterweight to move, the basis functions must be non-zero at the space end (when $\xi = 1$). A reasonable option is to use polynomials as the basis functions, i.e., $\psi_i(\xi) = \xi^i$. However, for these basis functions, $\mathbf{M^A}$ and $\mathbf{K^A}$ become very ill-conditioned as the value of N increases. In order to analyze a greater number of modes, the system is analyzed using basis functions defined by

$$\psi_i(\xi) = \sin\left[\left(i - 1/2\right)\pi\xi\right] \tag{28}$$

Clearly, these basis functions satisfy the aforementioned boundary conditions. The general eigenvalue problem in Eqns. (25)-(27) is solved using Matlab, for a 100,000 km ribbon having a taper ratio of six ($\overline{h} = 2,750$ km). The maximum area of cross-section is taken to be 10 mm^2. The bulk density and Young's modulus of the ribbon are assumed to be 1300 kg/m^3 and 10^{12} N/m^2, respectively. The first 20 non-dimensional natural frequencies are given in Table 2. The frequencies are non-dimensionalized with respect to Ω. The first mode of longitudinal extension has a frequency of 4.37, i.e., a period of approximately five and a half hours.

TABLE 2. Non-dimensional frequencies of longitudinal modes.

Mode	Freq.	Mode	Freq.	Mode	Freq.	Mode	Freq.	Mode	Freq.
1	4.37	5	49.35	9	99.62	13	149.91	17	200.27
2	12.74	6	61.89	10	112.15	14	162.42	18	212.77
3	24.45	7	74.48	11	124.76	15	175.07	19	225.53
4	36.82	8	8702	12	137.29	16	187.58	20	238.04

3.2. TRANSVERSE OSCILLATIONS OF THE RIBBON

The transverse displacement of the ribbon is now examined by neglecting its longitudinal extension (other than its nominal value given by $U = \varepsilon_0 \xi$). However, the libration of the ribbon must be included in the analysis. This is because it represents the zeroth mode of transverse motion. If this is done, the coupled system of equations governing the libration and generalized coordinates B_k may be written as [2]

$$\mathbf{M^B B''} + \mathbf{K^B B} = \mathbf{0} \tag{29}$$

where

$$\mathbf{B} = \left[\alpha,\ B_1,\ B_2, \ldots B_k\right]^T$$

and the elements of matrices $\mathbf{M^B}$ and $\mathbf{K^B}$ are given by

$$M_{11}^B = \left(1+\varepsilon_0\right)^2 \left(M_p \int_0^1 \exp\left[F(\xi)\right] \xi^2 d\xi + M_c \right) \tag{30}$$

$$K_{11}^B = \left(1+\varepsilon_0\right) \left[\frac{1}{\Lambda} \left\{ M_p \int_0^1 \exp\left[F(\xi)\right] \xi d\xi + M_c \right\} - \frac{\beta^3}{\Lambda^4} \left\{ M_p \int_0^1 \frac{\exp\left[F(\xi)\right] \xi}{\left[\left(1/\Lambda\right)+\xi\left(1+\varepsilon_0\right)\right]^3} d\xi + M_c \frac{1}{\left[\left(1/\Lambda\right)+1+\varepsilon_0\right]^3} \right\} \right] \tag{31}$$

$$M_{i1}^B = M_{1k}^B = M_p \left(1+\varepsilon_0\right) \int_0^1 \exp\left[F(\xi)\right] \xi \phi_i d\xi \tag{32}$$

$$K_{i1}^B = K_{1k}^B = M_p \left\{ \frac{1}{\Lambda} \int_0^1 \exp\left[F(\xi)\right] \phi_i d\xi - \frac{\beta^3}{\Lambda^4} \int_0^1 \frac{\exp\left[F(\xi)\right] \phi_i}{\left[\left(1/\Lambda\right)+\xi\left(1+\varepsilon_0\right)\right]^3} d\xi \right\} \tag{33}$$

$$M_{ik}^B = M_p \int_0^1 \exp\left[F(\xi)\right] \phi_i \phi_k d\xi \tag{34}$$

and

$$K_{ik}^B = \pi^2 \left(\varepsilon_0 - \varepsilon_0^2\right) ik \bar{\Omega}^2 \int_0^1 \exp\left[F(\xi)\right] \frac{d\phi_i}{d\xi} \frac{d\phi_k}{d\xi} d\xi + M_p \left\{ \left(\frac{\beta}{\Lambda}\right)^3 \int_0^1 \frac{\exp\left[F(\xi)\right] \phi_i \phi_k}{\left[\left(1/\Lambda\right)+\xi\left(1+\varepsilon_0\right)\right]^3} d\xi - \int_0^1 \exp\left[F(\xi)\right] \phi_i \phi_k d\xi \right\} \tag{35}$$

where indexes i and $k = 2, 3, 4, \ldots M$.

The basis functions used here are defined by $\phi_i(\xi) = \sin\left(i\pi\xi\right)$. Again, the generalized eigenvalue problem defined by Eqns. (29)-(35) may be solved using Matlab. The same numerical values as those in the previous example are used. Table 3 contains the non-dimensional natural frequencies of the first 20 modes

of the transverse oscillations. The first frequency (zeroth mode) is that of the libration (α). It has a value of 0.16. This corresponds to a period of about six days. The first sinusoidal mode of transverse vibration has a period of about ten hours.

TABLE 3. Non-dimensional frequencies of transverse modes.

Mode	Freq.	Mode	Freq.	Mode	Freq.	Mode	Freq.	Mode	Freq.
1	0.16	5	9.21	9	18.31	13	27.43	17	36.53
2	2.43	6	11.48	10	20.58	14	29.69	18	38.81
3	4.67	7	13.76	11	22.86	15	31.97	19	41.09
4	6.93	8	16.03	12	25.14	16	34.25	20	43.37

The modal matrix consisting of normalized eigenvectors is approximately equivalent to the identity matrix. This means that the assumed sinusoidal modes for the transverse displacement are, approximately, the actual modes for the transverse motion of the ribbon. Patamia and Jorgensen[3] have also observed this to be the case.

4. Conclusions

An analytical study has been conducted to investigate the longitudinal and transverse motion of space tethers and the space elevator ribbon. For longitudinal oscillations of space tethers, an exact solution was obtained and numerical results were presented for a typical case. For the space elevator, frequencies of longitudinal and transverse oscillations were calculated for a typical set of parameters. It was found that the period of the first longitudinal mode was about five and a half hours and that of the pendulum mode was about six days.

References

1. E. L. M. Lanoix, 1999. *A Mathematical Model for Long Term Dynamics of Tethered Satellites Systems*, M. Eng. Thesis, Dept. of Mechanical Engineering, McGill Univ., Montreal.
2. S. S. Cohen, 2006. *Dynamics of a Space Elevator*, M. Eng. Thesis, Dept. of Mechanical Engineering, McGill Univ., Montreal.
3. S. E. Patamia, A. M. Jorgensen, 2005. *Analytical Model of Large Scale Transverse Dynamics of Proposed Space Elevator*, *56th International Astronautical Congress of the International Astronautics Federation*, Paper No. IAC-05-D4.2.06, Fukuoka, Japan.

ASYMPTOTIC MODELS OF BLOCH-FLOQUET WAVES IN PERIODIC WAVEGUIDES

ALEXANDER B. MOVCHAN*
Department of Mathematical Sciences, University of Liverpool, U.K.

Abstract. This review paper outlines a class of results for Bloch-Floquet waves propagating in thin walled periodic waveguides. The emphasis is made on asymptotic approximations of low eigenvalues and corresponding eigenfunctions and on analysis of dispersion relations linking the frequency parameter to components of the Bloch vector. A particular attention is given to structures, which possess stop bands for waves within certain ranges of frequencies.

Keywords: Bloch-Floquet waves, asymptotic analysis, periodic structures

1. Background

The interest to photonic and phononic band gap structures has been generated by physicists and engineers due to a wide range of applications in the design of filters of acoustic and optical signals, communication systems and structural mechanics, as outlined in the papers[1,2].

For the case when a structure includes a sufficiently large ordered array of voids, inclusions, the filtering properties of such an array may be estimated via the analysis of Bloch-Floquet waves in an infinite periodic structure, where the corresponding spectral problem can be formulated and studied on an elementary cell of the structure. The book[3] includes the theoretical outline and a series of examples of scalar and vector problems involving propagation of acoustic and elastic waves through periodic media; this also includes asymptotic estimates for solutions associated with the so-called thin walled domains. Such approximations involve auxiliary limit problems of reduced dimensions, which

*abm@liv.ac.uk

E. İnan et al. (eds.), *Vibration Problems ICOVP-2007*,

possess closed form analytical solutions. The asymptotic analysis involved in this study is based on the method of compound asymptotic expansions presented in the two-volume monograph[4] and also discussed[5,6].

There is an extensive range of results and physical applications for models of waveguides in the framework of the linear water wave theory. Corresponding periodic structure for waveguides and trapped vibration modes for obstacles in two-dimensional waveguides were studied[7-9]. These studies have generated a substantial interest in the analysis of waves interacting with the boundaries of the waveguides.

The paper[10] presents a lattice model for Bloch-Floquet elastic waves in two dimensions. This includes inhomogeneous structures where the corresponding dispersion diagrams possess stop bands for certain ranges of frequencies. The results are applicable to thin walled elastic structures where each thin elastic ligament is approximated by a one-dimensional elastic rod, and every junction region is replaced by a point mass. Another example including a periodic system of thin walled elements is discussed[11]; this paper deals with the so-called "split-ring resonators" and the corresponding dispersion diagrams possess low frequency stop bands, whose boundaries can be evaluated analytically. The asymptotic approximations have proved to be accurate and efficient in spectral problems for multi-structures with thin walled elements, as outlined in detail[6].

The purpose of the present paper is to outline some ideas and methods of analysis of spectral problems in periodic thin walled structures that support standing waves and/or filter waves within certain range of frequencies. In Section 2, we discuss the stop band lattice structures and show the influence of inhomogeneities on the dispersion diagram. In this section, every junction region between thin ligaments is replaced by a point mass and the geometry of the structure is chosen in such a way that it is compatible with the hinge-type junctions, so that no moments are exerted at the junction regions. The detailed analysis of this problem is included in the paper[10]. It is noted that boundary layer fields may be of importance in analysis of region of junctions between several thin walled elements of the structure. Section 3 presents an analysis of a singularly perturbed problem where a boundary layer (in the vicinity of the junction region) is included as an important part of the asymptotic solution. The latter section deals with the anti-plane shear Bloch-Floquet waves propagating along a periodic waveguide containing cracks. Here we give an outline of the asymptotic solution. Detailed analysis of the Wiener-Hopf type functional equation involved in the evaluation of the boundary layer is included[12].

2. Bloch-Floquet waves in inhomogeneous lattice structures

We begin with an illustration of elastic waves in periodic structures consisting of one-dimensional elastic rods connected at junctions of the hinge type, as shown, for example, in Fig. 2. This is a limit configuration approximating a thin walled periodic structure incorporating an array of closely placed holes, where every thin ligament separating the holes is replaced by a one-dimensional elastic element.

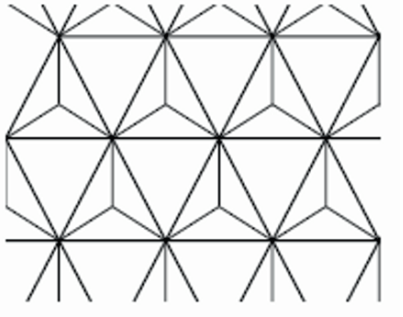

Fig. 1 Triangular lattice with a “macro-cell”.

2.1. GEOMETRY AND THE DISPERSION EQUATION

The structure is inhomogeneous, and the masses allocated to the junction regions are of two types, so that we refer to a bi-atomic lattice. Photonic/phononic band gap structures of this type, as well as more complicated structures containing macro-cells (see, for example, Fig. 1) were studied in detail[10].

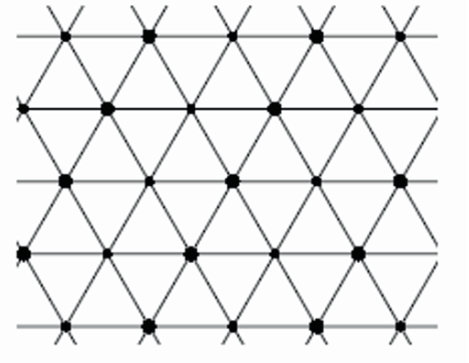

Fig. 2 A bi-atomic two-dimensional lattice.

The irreducible cell of periodicity of the structure, shown in Fig. 3, includes masses m_1 and m_2.

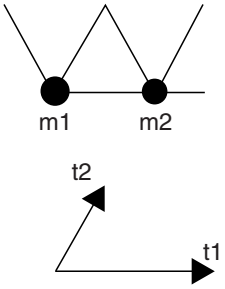

Fig. 3 The irreducible cell of the periodic structure and the corresponding lattice vectors.

The lattice vectors for this type of the discrete structure are $\mathbf{t}^{(1)} = (2l, 0)$ and $\mathbf{t}^{(1)} = (l/2, \sqrt{3}l/2)$ where l is the distance between the nearest junctions. The multi-index $\mathbf{n} = (n_1, n_2)$ characterizes the position of the cell within the lattice, whereas the index κ corresponds to the a particle of mass m_κ. Let $\mathbf{u}^{(\mathbf{n},\kappa)} = (u_1^{(\mathbf{n},\kappa)}, u_2^{(\mathbf{n},\kappa)})^T$ denote the displacement of the junction $(\mathbf{n}, \kappa)$, and let the entries of the matrix $\mathbf{T}$ be defined by $T_{ij} = t_i^{(j)}$.

As in [10], one can introduce the unit vectors

$$\mathrm{a}_j = (\cos\frac{2(j-1)\pi}{3}, \sin\frac{2(j-1)\pi}{3})^T, \quad j = 1,2,3 \tag{1}$$

so that the equations of motion for the case of harmonic oscillations (of radian frequency ω) yield

$$\begin{aligned}
\omega^2 m_1 \mathbf{u}^{(\mathbf{n},1)} &= c(\mathbf{a}_1 \otimes \mathbf{a}_1)(2\mathbf{u}^{(\mathbf{n},1)} - \mathbf{u}^{(\mathbf{n},2)} - \mathbf{u}^{(\mathbf{n}-\mathbf{e}_1,2)}) \\
&\quad + c(\mathbf{a}_2 \otimes \mathbf{a}_2)(2\mathbf{u}^{(\mathbf{n},1)} - \mathbf{u}^{(\mathbf{n}+\mathbf{e}_2,1)} - \mathbf{u}^{(\mathbf{n}-\mathbf{e}_2,2)}) \\
&\quad + c(\mathbf{a}_3 \otimes \mathbf{a}_3)(2\mathbf{u}^{(\mathbf{n},1)} - \mathbf{u}^{(\mathbf{n}-\mathbf{e}_1+\mathbf{e}_2,2)} - \mathbf{u}^{(\mathbf{n}-\mathbf{e}_2,2)}), \\
\omega^2 m_2 \mathbf{u}^{(\mathbf{n},2)} &= c(\mathbf{a}_1 \otimes \mathbf{a}_1)(2\mathbf{u}^{(\mathbf{n},2)} - \mathbf{u}^{(\mathbf{n}+\mathbf{e}_1,1)} - \mathbf{u}^{(\mathbf{n},1)}) \\
&\quad + c(\mathbf{a}_2 \otimes \mathbf{a}_2)(2\mathbf{u}^{(\mathbf{n},2)} - \mathbf{u}^{(\mathbf{n}+\mathbf{e}_2,2)} - \mathbf{u}^{(\mathbf{n}-\mathbf{e}_2,2)}) \\
&\quad + c(\mathbf{a}_3 \otimes \mathbf{a}_3)(2\mathbf{u}^{(\mathbf{n},2)} - \mathbf{u}^{(\mathbf{n}+\mathbf{e}_2,1)} - \mathbf{u}^{(\mathbf{n}+\mathbf{e}_1-\mathbf{e}_2,1)}),
\end{aligned}$$

where c is the stiffness coefficient. Let $\mathbf{k}$ be the Bloch vector. Then applying the condition of quasi-periodicity to the amplitude vector of the Bloch-Floquet waves,

$$\mathbf{u}^{(\mathbf{n}+\mathbf{m},\kappa)} = e^{i\mathbf{k}\cdot\mathbf{T}\mathbf{m}}\mathbf{u}^{(\mathbf{n},\kappa)}$$

we obtain

$$\omega^2 \mathbf{M}\,\mathbf{u}^{(\mathbf{n})} = \sigma(\mathbf{k})\mathbf{u}^{(\mathbf{n})}. \tag{2}$$

Here

$$\mathbf{u}^{(\mathbf{n})} = [\mathbf{u}^{(\mathbf{n},1)}, \mathbf{u}^{(\mathbf{n},2)}]^T \in \mathbf{R}^4,$$

is the vector of displacements for particles within an elementary cell whose position is characterized by the multi-index $\mathbf{n}$, whereas $\mathbf{M} = diag\{m_1, m_1, m_2, m_2\}$ and $\sigma(\mathbf{k})$ are the 4×4 mass matrix and the stiffness matrix, respectively. Equation (2) has non-trivial solutions if and only if

$$\det(\sigma(\mathbf{k}) - \omega^2\mathbf{M}) = 0, \tag{3}$$

which is the dispersion equation linking the radian frequency ω to the Bloch vector $\mathbf{k}$.

2.2. DISPERSION DIAGRAMS AND STOP BANDS

Although the dispersion equation (3) is polynomial in ω, it is not always possible to find its solutions analytically. In any case, the numerical treatment is straightforward and Fig. 4 includes one of the results of analysis of dispersion relations of [10]. It shows the normalized radian frequency versus the Bloch parameter, and, in particular, one can see the influence of inhomogeneities within the irreducible cell on the dispersion diagrams. The first diagram, on the left, in Fig. 4 corresponds to the case of a structure where the mass is distributed uniformly over the set of junction points $(m_1 = m_2 = 1)$; no stop bands are observed there. However, as we introduce a contrast and correspondingly a non-uniform distribution of mass $(m_1 = 1, M_2 = 10)$ through the array of junction points, a low frequency stop band appears on the second dispersion diagram (on the right) in Fig. 4. The stop bands correspond to the intervals of frequencies where the dispersion equation (3) does not have real solutions and hence propagation of the Bloch-Floquet waves of such frequencies is not supported by such a structure. This implies that an inhomogeneous lattice lattice structure can be designed as a filter of elastic waves within certain ranges of frequencies.

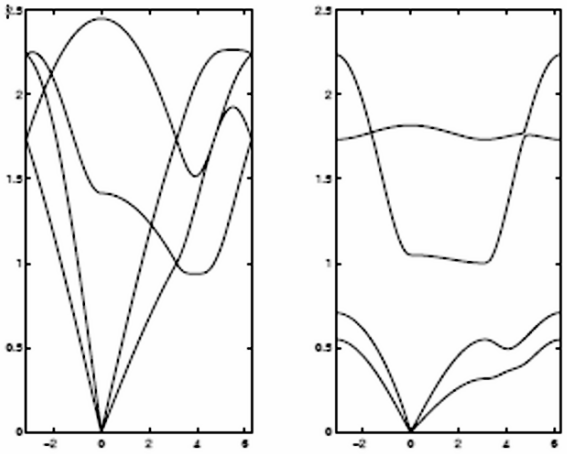

Fig. 4 Eigenfrequencies for the triangular biatomic lattice with $c = 1$ In the left graph, $m_1 = m_2 = 1$, in the right, $m_1 = 1$, $m_2 = 10$.

3. A thin periodic waveguide with longitudinal cracks

In Section 2, we have shown examples of spectral problems for inhomogeneous lattice structures that possess stop bands. The outline presented above did not involve any boundary layers, and all the junction regions were characterized as point masses. In the present section, we show a situation when a thin walled waveguide required a boundary layer analysis to characterize a certain class of singular stress fields. We give an outline, which focuses on the effect of stop bands and singular stress fields; the detailed analysis including the solution of the relevant equations of the Wiener-Hopf type is presented in [12].

In Fig. 5, we show the two-dimensional elementary cell within the waveguide. It contains a longitudinal crack, whose length is assumed to be much larger compared to the thickness of the waveguide itself. Also, it is assumed that the distance between the cracks within the array is much larger than the thickness of the waveguide.

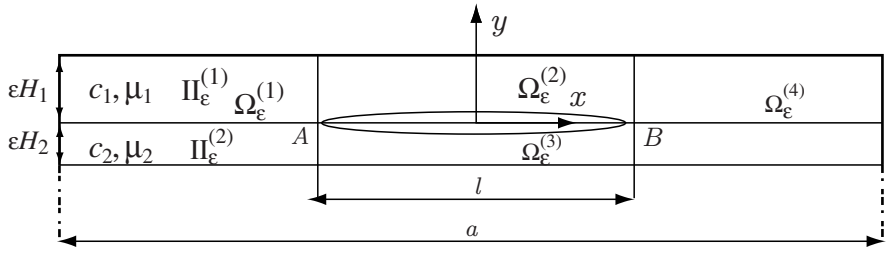

Fig. 5 The elementary cell Π_ε for a periodic waveguide with cracks.

First, we are going to refer to the "beam approximation" or the skeleton of the structure, where each thin ligament with the elementary cell is replaced by a one-dimensional segment, as shown in Fig. 6. Limit differential equations are derived for the leading order approximation of the displacement along each segment and appropriate junction conditions are set at the junction points.

Fig. 7 shows an example of a standing wave within the thin walled waveguide with cracks. For a waveguide without cracks, such a mode would not appear - the discontinuity of the displacement is clearly visible on the diagram. Furthermore, a boundary layer occurs near the vertices of the crack. It is noted that the "beam approximation" would not show any singularities in the physical fields, and one needs the analysis of the boundary layer to describe the singular stress at the crack tips.

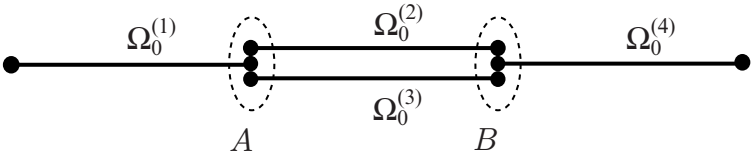

Fig. 6 Limit set: the skeleton of the thin walled structure.

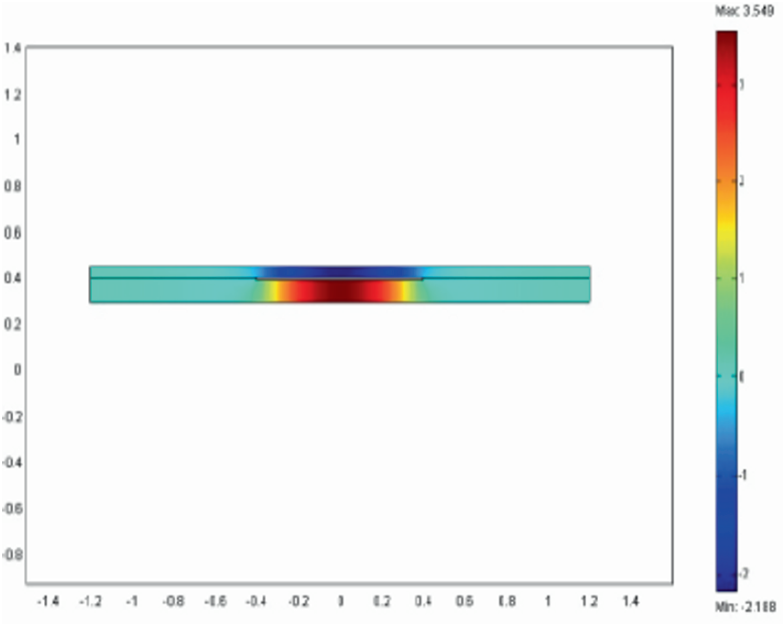

Fig. 7 A standing wave within the waveguide with cracks.

3.1. GEOMETRY AND THE GOVERNING EQUATIONS

We formulate a spectral problem of anti-plane shear in a two-phase periodic waveguide shown in Fig. 5. The elementary cell of the periodic structure is defined as $\Pi_\varepsilon = \Pi_\varepsilon^{(1)} \bigcup \Pi_\varepsilon^{(2)}$ *where*

$$\begin{aligned} \Pi_\varepsilon^{(1)} &= \{(x,y) : |x| < a/2, \quad 0 < y < \varepsilon H_1\} \\ \Pi_\varepsilon^{(2)} &= \{(x,y) : |x| < a/2, \quad -\varepsilon H_2 < y < 0\} \end{aligned} \tag{4}$$

and ε is a small positive non-dimensional parameter.

The functions $u^{(j)}(x,y)$ stand for the amplitudes of the time-harmonic anti-plane displacement, and they are defined in $\Pi_\varepsilon^{(j)}$ as solutions of the Helmholtz equations

$$\Delta u^{(j)}(x,y) + \frac{\omega^2}{c_j^2} u^{(j)}(x,y) = 0, \quad (x,y) \in \Pi_\varepsilon^{(j)}, \quad j = 1,2 \tag{5}$$

where $c_j = \sqrt{\mu_j / \rho_j}$ are the shear wave speeds in $\Pi_\varepsilon^{(j)}, j = 1,2$. We regard $u^{(j)}$ as out-of plane displacements and denote the shear modulus and the mass density in $\Pi_\varepsilon^{(j)}$ by μ_j and ρ_j, respectively. The quantity ω stands for the radian frequency of the time-harmonic vibrations with the amplitude u.

The crack M_l of length l is located on the interface between $\Pi_\varepsilon^{(1)}$ and $\Pi_\varepsilon^{(2)}$:

$$M_l = \{(x,y) : |x| < l/2, \, y = 0\}.$$

The homogeneous Neumann boundary conditions, corresponding to zero tractions, are set on the horizontal parts of the boundary of Π_ε and on the faces of the crack:

$$\sigma_{yz}^{(1)}(x, \varepsilon H_1) := \mu_1 \left. \frac{\partial u^{(1)}}{\partial y} \right|_{y=\varepsilon H_1} = 0, \quad x \in (-a/2, a/2), \tag{6}$$

$$\sigma_{yz}^{(2)}(x, -\varepsilon H_2) := \mu_2 \left. \frac{\partial u^{(2)}}{\partial y} \right|_{y=-\varepsilon H_2} = 0, \quad x \in (-a/2, a/2), \tag{7}$$

and

$$\sigma_{yz}^{(1)}(x,0^+) := \mu_1 \left.\frac{\partial u^{(1)}}{\partial y}\right|_{y=0^+} = 0, \quad x \in (-l/2, l/2), \tag{8}$$

$$\sigma_{yz}^{(2)}(x,0^-) := \mu_2 \left.\frac{\partial u^{(2)}}{\partial y}\right|_{y=0^-} = 0, \quad x \in (-l/2, l/2). \tag{9}$$

Outside the crack, along the interface between $\Pi_\varepsilon^{(1)}$ and $\Pi_\varepsilon^{(2)}$ we have

$$u^{(1)}(x,0^+) = u^{(2)}(x,0^-), \quad x \in (-a/2, -l/2) \bigcup (l/2, a/2) \tag{10}$$

$$\mu_1 \left.\frac{\partial u^{(1)}}{\partial y}\right|_{y=0^+} = \mu_2 \left.\frac{\partial u^{(2)}}{\partial y}\right|_{y=0^-}, \quad x \in (-a/2, -l/2) \bigcup (l/2, a/2). \tag{11}$$

The functions $u^{(j)}$ correspond to the amplitudes of the time-harmonic Bloch-Floquet waves, so that at the ends $x = \pm a/2$ we have

$$\begin{aligned} &u^{(j)}(-a/2, y) = e^{-iKa} u^{(j)}(a/2, y), \quad y \in (-\varepsilon H_2, \varepsilon H_1), \\ &\frac{\partial}{\partial x} u^{(j)}(-a/2, y) = e^{-iKa} \frac{\partial}{\partial x} u^{(j)}(a/2, y), \quad y \in (-\varepsilon H_2, \varepsilon H_1). \end{aligned} \tag{12}$$

The eigenfields $\{u^{(1)}, u^{(2)}\}$ are chosen in such a way that that elastic energy is fixed:

$$\varepsilon\left|(u^{(1)}; u^{(2)}) := \sum_{i=1}^{3} \left\{ \mu_i \int\limits_{\Pi_\varepsilon^{(i)}} \left|\nabla u^{(i)}\right|^2 dx \right\} = \varepsilon_0 = const \right. \tag{13}$$

We also aim to describe the dispersion relation between the Bloch parameter K and the radian frequency ω.

3.2. OUTLINE OF THE ASYMPTOTIC APPROXIMATIONS

Assuming that a radian frequency ω is within an interval adjacent to the origin, we approximate the corresponding eigenfunction $u(x,y)$ in the form

$$\begin{aligned} u(x,y,\varepsilon) = \sum_{k=0}^{N} \varepsilon^k \Bigg\{ &\sum_{m=1}^{4} \chi_m(x,y,\varepsilon) \left(v_m^{(k)}(x) + \varepsilon^2 V_m^{(k)}(x,Y) \right) \\ &+ \left(W_A^{(k)}\left(X_A, Y\right) + W_B^{(k)}\left(X_B, Y\right) \right) \Bigg\} + R_N(x,y,\varepsilon). \end{aligned} \tag{14}$$

Here, the notation $u(x,y)$ is used for eigenfunctions, which are equal to $u^{(j)}(x,y)$ in $\Pi_\varepsilon^{(j)}$ (see above Section 3.1). The scaled coordinates

$$X_A = \frac{x-x_A}{\varepsilon}, \quad X_B = \frac{x-x_B}{\varepsilon}, \quad Y = \frac{y}{\varepsilon},$$

are introduced in the vicinity of the left and right vertices of the crack. The functions $v_m^{(k)}$ represent solutions of lower-dimensional problems within limit sets $\Omega_0^{(j)}$, $j=1,2,3,4$, so that $\bigcup_{j=1}^{4}\Omega_0^{(j)}$ is referred to as the skeleton of the elementary cell, as shown in Fig. 6. The notation χ is used for the cut-off function, which vanishes in the vicinity of the origin, as shown in Fig. 8, and correspondingly the cut-off functions χ_m vanish near "junction points" A and B (vertices of the crack); these functions are defined as follows:

$$\begin{aligned} &\chi_1(x,y,\varepsilon)=\chi(-X_A), \quad \chi_2(x,y,\varepsilon)=\chi(X_A)\chi(-X_B)\mathcal{H}(y), \\ &\chi_3(x,y,\varepsilon)=\chi(X_A)\chi(-X_B)\mathcal{H}(-y), \quad \chi_4(x,y,\varepsilon)=\chi(X_B). \end{aligned} \tag{15}$$

Here $\mathcal{H}(y)$ is the Heaviside step function, and X_A, X_B are the scaled variables defined in (15).

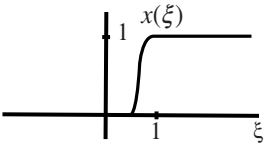

Fig. 8 Cut-off function $\chi(\xi)$.

The "fast" change of eigenfunctions in the transverse directions in $\Omega_\varepsilon^{(j)}$ is described by the functions $V_m^{(k)}(x,Y)$, whereas the terms $W_A^{(k)}(X_A,Y)$, $W_B^{(k)}(X_B,Y)$ represent the boundary layers in the vicinity of the junction points A and B. Finally, $R_N(x,y,\varepsilon)$ is a small remainder term in the asymptotic approximation. The lower-dimensional approximation (the "beam approximation") of the eigenfunctions is used in the derivation of the dispersion equation represented by the dispersion diagrams of Section 3.3.

The leading terms $v_m^{(0)}(x)$ in the asymptotic formula (14) satisfy the differential equations

$$\frac{d^2 v_m^{(0)}}{dx^2}(x)+\frac{\omega^2}{\mathsf{c}_m^2}v_m^{(0)}(x)=0, \quad x\in\Omega_0^{(m)}, \tag{16}$$

and the junction conditions at the points A and B are

$$v_1^{(0)}(-l/2)=v_2^{(0)}(-l/2)=v_3^{(0)}(-l/2),\quad v_4^{(0)}(l/2)=v_2^{(0)}(l/2)=v_3^{(0)}(l/2),$$

$$(\mu_1H_1+\mu_2H_2)\left(v_1^{(0)}\right)'(-l/2)=\mu_1H_1\left(v_2^{(0)}\right)'(-l/2)+\mu_2H_2\left(v_3^{(0)}\right)'(-l/2), \quad (17)$$

$$(\mu_1H_1+\mu_2H_2)\left(v_4^{(0)}\right)'(l/2)=\mu_1H_1\left(v_2^{(0)}\right)'(l/2)+\mu_2H_2\left(v_3^{(0)}\right)'(l/2).$$

In (16), c_m are the "effective" wave speeds defined as follows

$$\mathrm{c}_{j+1}=\mathrm{c}_j,\quad j=1,2,\quad \mathrm{c}_1=\mathrm{c}_4=c_1c_2\sqrt{\frac{\mu_1H_1+\mu_2H_2}{\mu_1H_1c_2^2+\mu_2H_2c_1^2}}\,. \quad (18)$$

Equations (16), (17) are complemented by the Bloch-Floquet conditions at $x=\pm a/2$.

$$v_1^{(0)}(-a/2)=e^{-iKa}v_4^{(0)}(a/2),\quad \left(v_1^{(0)}\right)'(-a/2)=e^{-iKa}\left(v_4^{(0)}\right)'(a/2), \quad (19)$$

where the Bloch parameter $K\in[0,2\pi/a]$.

We note that the junction conditions (17) are derived as conditions of exponential decay of the boundary layers $W_A^{(k)}$ and $W_B^{(k)}$ at infinity. The functions $W_A^{(k)}$, $W_B^{(k)}$ depend on scaled coordinates and satisfy the model boundary value problems for the Poisson equation (see Section 3.2) in unbounded domains shown in Fig. 9.

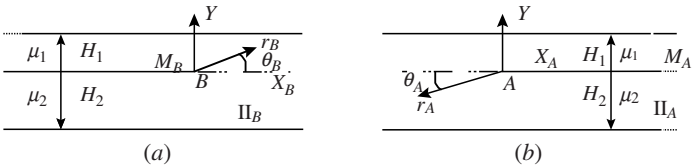

Fig. 9 Unbounded model domains corresponding to the boundary layer fields.

The notation $M_\alpha,\alpha=A,B$ stands for the semi-infinite crack with the vertex at the point α in the scaled domain $\Pi_\alpha,\alpha=A,B$. It is remarked that the displacement field (14) is not smooth: the boundary layer terms are characterized by the asymptotic formula

$$W_\alpha^{(k)}(X_\alpha,Y)\sim\frac{2\kappa_\alpha^{(k)}}{\mu_j}\sqrt{R_\alpha}\sin(\theta_\alpha/2),\quad \alpha=A,B,\ \text{as}\ R_\alpha^2=X_\alpha^2+Y^2\to0, \quad (20)$$

here $j=1$ when $Y>0$ and $j=2$ when $Y<0$. Here, $\kappa_\alpha^{(0)}=0$, and the coefficients $\kappa_\alpha^{(1)}$, have the form

$$\kappa_\alpha^{(1)}=C_\alpha(\mu_1,\mu_2,H_1,H_2)\left[\left(v_2^{(0)}\right)'(x_\alpha)-\left(v_3^{(0)}\right)'(x_\alpha)\right],\quad \alpha=A,B, \quad (21)$$

where the coefficients C_α are independent of the external load. Formula (21) implies that the "stress intensity factors" for the crack M_1 are proportional to the angle of the "opening" between the limit one-dimensional elements $\Omega_0^{(2)}$ and $\Omega_0^{(3)}$ of the skeleton structure in Fig. 6.

3.3. DISPERSION DIAGRAMS AND STOP BANDS

The presence of cracks leads to the existence of standing waves within the waveguide. We consider an example that involves a bi-material strip made of Aluminium and Iron.

TABLE 1. Material properties.

Material	Shear modulus [N/m^2]	Mass density [kg/m^3]	Shear wave speed [m/sec]
Iron	82.10^9	7860	3230
Aluminium	26.10^9	2700	3103

The corresponding material constants are given in Table 1. One important feature of this example is that the shear wave speeds in the both materials are very close in their magnitude. The geometrical parameters for the elementary cell are defined as follows:

$$l=0.8[\mathrm{m}],\quad a=2.4[\mathrm{m}],\quad h_1=0.05[\mathrm{m}],\quad h_2=0.1[\mathrm{m}].$$

The interval of frequencies used for the numerical calculations is chosen according to the constraints of the asymptotic model. We have taken the ratio of the thicknesses of the strip to the half-distance between the cracks to be 0.1875, with the average wave speed (see (18)) of $3.1789\ 10^3$[m/sec] and the half-distance between the cracks (which is also equal to the crack length) of 0.8[m]. In this case, the asymptotic model requires the frequency to be much smaller than $3.1789\ 10^3/(0.1875\times 0.8) = 2.1193\ 10^4$[Hz]. The numerical

simulations show that the asymptotic model provides a satisfactory accuracy for the whole range of frequencies up to this value.

The dispersion relations are obtained within the frame of the asymptotic approach involving the lower dimensional model (16), (17), (19). The smooth solutions $v_m^{(0)}, m = 1,2,3,4$ are sought in the form

$$v_m^{(0)}(x) = A_m \sin(x\omega / \mathrm{c}_m) + B_m \cos(x\omega / \mathrm{c}_m) \tag{22}$$

where c_m, the "effective" wave speeds, were defined in (18), and A_m, B_m are constant coefficients. The dispersion equation

$$D(\mu_1, \mu_2, \mathrm{c}_m, l, a, K, \omega) = 0\,, \tag{23}$$

is derived according to the standard algorithm.

The results of the asymptotic model are compared with the Finite Element computations (produced in FEMLAB).

In Fig. 10 we show four dispersion diagrams representing the radian frequency ω as a function of the Bloch parameter K. The diagram 10a was generated in FEMLAB for a fully two-dimensional spectral problem in the thin

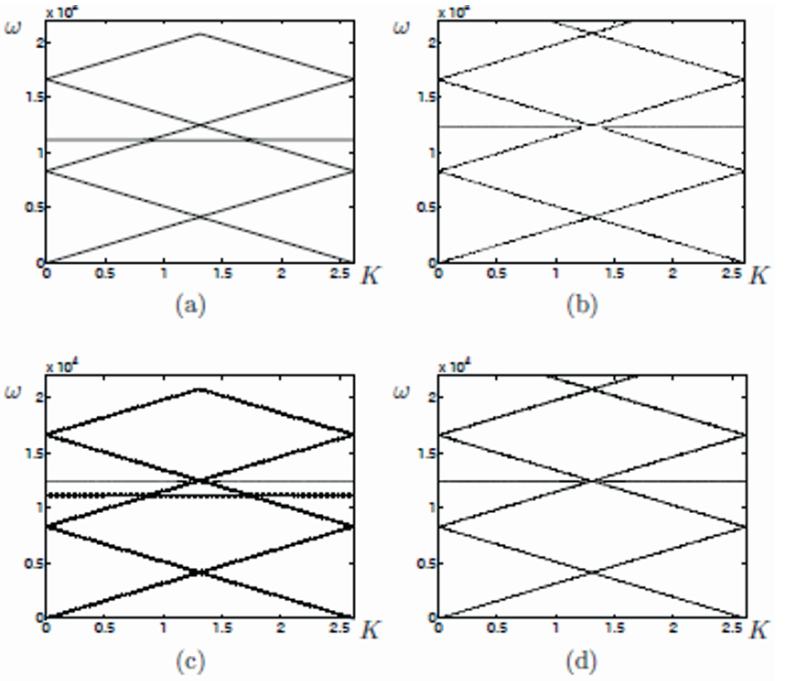

Fig. 10 Dispersion diagrams for the Iron-Aluminium bi-material strip containing the periodic array of interfacial cracks.

elementary cell with the longitudinal crack, whereas the dispersion diagram 10b was generated via the asymptotic approximation and hence it represents solutions of dispersion equation (23) (solved in MATLAB).

As shown in diagram 10c, the asymptotic model (the corresponding dispersion curves are shown by solid lines) agrees well with the finite element computation (the corresponding dispersion curves are marked by '*'), except for a small discrepancy corresponding to the standing wave (which has zero group velocity in the asymptotic model). The frequency of standing waves of this type decreases with the increase of the crack length l together with the length a of the elementary cell, and also the discrepancy between asymptotic and numerical models becomes smaller. The finite element computation also shows a narrow stop band located next to the frequency of the standing wave. The eigensolution corresponding to this standing wave is shown in Fig. 7.

Note that, in case when the wave speeds of materials are very close to each other (as in the case of the Iron-Alumunium strip), the dispersion equation (23) reduces (to the leading order) to

$$\sin(\omega l / c)(\cos(Ka) - \cos(\omega a / c)) = 0, \tag{24}$$

where $c = (c_1 + c_2)/2$. The diagram in Fig. 10d includes a comparison between the Fig. 10b and the dispersion diagram computed for materials of equal waves speeds $c = (c_1 + c_2)/2 \simeq 3167[\mathrm{m/sec}]$ according to equation (24). As shown here, these diagrams are very close, except for region of the multiple root around the frequency $1.24\ 10^4[\mathrm{Hz}]$ (see diagram 10b). A small discrepancy between the asymptotic approximation and the exact solution is noted (compare with diagram 10b) near this multiple root of the dispersion equation corresponding to the intersection of dispersion curves.

If the contrast between two materials gradually increases, then the stop band opens up near the frequency corresponding to the standing wave.

The asymptotic model illustrated here is fully analytical and it catches the effects of both singular stress fields near crack tips as well as existence of standing waves associated with discontinuities of displacements across the crack.

References

1. A. R. Parker, R. C. McPhedran, D. R. McKenzie, L. C. Botten, N. A. Nicorovici, 2001. *Photonic engineering: Aphrodite's iridescence*, Nature, **409**, 36-37.
2. P. S. Russell, E. Marin, A. Diez, S. Guenneau, A. B. Movchan, 2003. *Sonic band gaps in PCF preforms: enhancing the interaction of sound and light*, Optics Express, **11**, 2555-2560.

3. A. B. Movchan, N. V. Movchan, C. G. Poulton, 2002. *Asymptotic Models of Fields in Dilute and Densely Packed Composites*. Imperial College Press.
4. V. Maz'ya, S. Nazarov, B. Plamenevskij, 2000. *Asymptotic Theory of Elliptic Boundary Value Problems in Singularly Perturbed Domains*, Birkhäuser.
5. A. B. Movchan, N. V. Movchan, 1995. *Modelling of Elastic Solids with Non-regular Boundaries*, CRC Press.
6. V. Kozlov, V. Maz'ya, A. Movchan, 1999. *Asymptotic Analysis of Fields in Multi-structrures,* Oxford University Press.
7. D. V. Evans, C. M. Linton, F. Ursell, 1993, *Trapped mode frequencies Embedded in the continuous-spectrum*, Quart. J. Mech. Appl. Math., **46**, 253-274.
8. C. M. Linton, M. McIver, 2002. *Periodic structures in waveguides*. Proc. R. Soc. A, **458**, 3003-3021.
9. M. McIver, C. M. Linton, P. McIver, J. Zhang, R. Porter, 2001. *Embedded trapped modes for obstacles in two-dimensional waveguides*. Quart. J. Mech. Appl. Math., **54**, 273-293.
10. P. G. Martinsson, A. B. Movchan, 2003. *Vibrations of lattice structures and phononic band gaps*. Quart. J. Mech. Appl. Math., **56**, 45-64.
11. A. B. Movchan, S. Guenneau, 2004. *Split-ring resonators and localized modes*, Phys. Rev. B, **70**, 125116(1-5).
12. G. S. Mishuris, A. B. Movchan, J. P. Bercial, 2007. *Asymptotic analysis of Bloch-Floquet waves in a thin bi-material strip with a periodic array of finite-length cracks*, Waves in Random and Complex Media, **17**, 511-533.

ERROR ANALYSIS IN COMPUTATIONAL ELASTODYNAMICS

SOMENATH MUKHERJEE*
Structures Division, National Aerospace Laboratories, Bangalore 560017, India

P. JAFARALI
Air Frame Stress Group, Aeronautical Development Agency, Bangalore 560017, India

GANGAN PRATHAP
Centre for Mathematical Modelling and Computer Simulation, Bangalore 560037, India

Abstract. The Finite Element Method (FEM) is the mathematical tool of the engineers and scientists to determine approximate solutions, in a discretised sense, of the concerned differential equations, which are not always amenable to closed form solutions. In this presentation, the mathematical aspects of this powerful computational tool as applied to the field of elastodynamics have been highlighted, using the first principles of virtual work and energy conservation.

Interesting geometrical patterns arising from the errors in the computational process in finite element elastodynamic problems have been discussed, and suitably illustrated through simple bar and beam elements. The approximate Rayleigh Quotient is interpreted in a geometrically abstract, but elegant fashion. It has been shown how incorporation of variationally incorrect procedures (like mass lumping or reduced integration) in the element formulations leads to the violation of the general rules of virtual work in elastodynamic analysis. The Timoshenko beam element has been chosen for demonstrating the variational incorrectness introduced through the 'variational crime' of using reduced integration to avoid locking.

*Corresponding author, somu@css.cmmacs.ernet.in

E. İnan et al. (eds.), *Vibration Problems ICOVP-2007*,

Keywords: Finite element elastodynamics, energy-error theorems, frequency-error hyperboloid, variational incorrectness, Timoshenko beam element

1. Introduction

Finite element analysis can be regarded as a tool for obtaining approximate solutions to differential equations using piecewise assumed interpolation functions. Conventionally, the method involves the use of element equilibrium equations derived from the basic principles of variational calculus[1,2]. In a mathematical rigorous fashion, the best-fit paradigm[2] has been correlated to the projection theorems of function space algebra of elastostatics[3]. The best-fit paradigm has been extended to elastodynamic problems using the virtual work principle and the function space approach[4-6].

The Timoshenko beam theory has features that make it an interesting case study for the examination of errors that appear when a finite element discretisation of its elastodynamics is made[6]. Attempts were made to derive error convergence rates and estimates for the finite element elastodynamics of Timoshenko beam[6]. The consequences of employing lumped masses and reduced integration as variationally incorrect procedures are illustrated by projection theorem using function space algebra.

2. The elastodynamic projection theorem and the energy – error-rule – A function space review[5]

The determination of the eigenvalues of free vibration problems in structural mechanics can be expressed as variational problems using Rayleigh Quotient:

$$(\omega^h)^2 = \frac{\left\|\varepsilon^h\right\|^2}{\left|u^h\right|^2}; \quad \omega^2 = \frac{\left\|\varepsilon\right\|^2}{\left|u\right|^2}; \quad \omega^2 = \frac{<\varepsilon^h, \varepsilon>}{(u^h, u)} \qquad (1.a,b,c)$$

where, $\{u^h\}$ and $\{u\}$ respectively are the approximate and exact modal displacement, $\{\varepsilon^h\}$ and $\{\varepsilon\}$ are the resulting approximate and exact modal strain vector and $(\omega^h)^2$ and ω^2 are the corresponding approximate and exact eigenvalues. Note that equations (1a) and (1b) are expressions derived from the conservation of energy, while equation (1c) results from the virtual work principle. In equations (1.a,b,c) the stiffness and inertia inner products and the corresponding norms are given respectively by

$$< \varepsilon^h, \varepsilon > = \sum_{ele=1}^{N^e} \int_{ele} \{\varepsilon^h\}^T [D] \{\varepsilon\} dx, \quad \|\varepsilon\|^2 = < \varepsilon, \varepsilon >, \quad \|\varepsilon^h\|^2 = < \varepsilon^h, \varepsilon^h > \quad (2a)$$

$$(u^h, u) = \sum_{ele=1}^{N^e} \int_{ele} \{u^h\}^T [\rho] \{u\} dx, \quad |u|^2 = (u, u), \quad |u^h|^2 = (u^h, u^h) \quad (2b)$$

where $[D]$ is the element elasticity matrix and $[\rho]$ is the inertia density matrix.

From equations (1a) and (1c) one can derive the elastodynamic projection theorem[5] as

$$< \varepsilon^h, \varepsilon - \varepsilon^h > = (u^h, \omega^2 u - \omega^{h^2} u^h) \quad (3)$$

The energy error rule for elastodynamics, which governs the error in eigenvalues due to discretisation, can be derived[5] in the form

$$\|\varepsilon\|^2 - \|\varepsilon^h\|^2 = \omega^2 |u|^2 - \omega^{h^2} |u^h|^2 \quad (4)$$

Note that the energy rules above are valid only at the *global* level as per the inner product defined in equation (2a, b). It has been shown earlier for the linear elastostatic case that these rules also govern the error due to discretisation at the element level[2,3]. Introducing the idea of a unit generalised mass in equation (4), ($i.e. |u|^2 = |u^h|^2 = 1$), the error in the eigenvalues can be expressed in terms of strain energy norms as

$$\|\varepsilon\|^2 - \|\varepsilon^h\|^2 = \left(\omega^2 - \omega^{h^2}\right) \quad (5)$$

The following interesting geometric pattern of the errors from a variationally correct FE model of elastodynamics can be derived[5,6], (Fig. 1).

$$\frac{|u - \overline{u}|^2}{|\overline{u}|^2} + \frac{\overline{\omega}^2}{\omega^2} - \frac{\|\varepsilon - \overline{\varepsilon}\|^2}{\omega^2 |\overline{u}|^2} = 1 \quad (6)$$

i.e. the values of the Rayleigh Quotient ratio (ω^h / ω), the norms of the modal displacement error, $|u - u^h|$ and the norms of the modal strain error, $\|\varepsilon - \varepsilon^h\|$ of any variationally correct but approximate solution generates a portion of the surface of the first octant of a hyperboloid of one sheet, with $(\omega^h / \omega) \geq 1$ (Fig. 1). Furthermore, it has been justified[5,6] that the in variationally correct formulations, the approximate Rayleigh Quotient exceeds the exact value $[(\omega^h / \omega) \geq 1]$ because the angular *deviation* of the approximate modal strain vector from the exact is more than that of the approximate modal displacement.

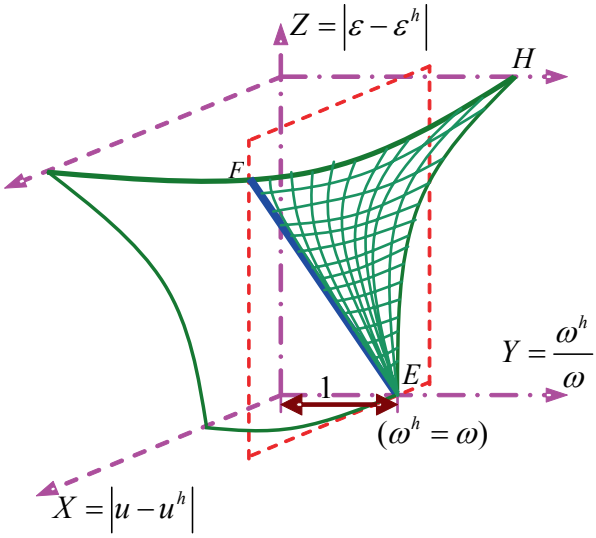

Fig. 1 Geometric interpretation of eigenvalue analysis of the variationally correct formulation using the frequency-error-hyperboloid. Variationally incorrect formulations (with, Lumped Mass Reduced Integration etc.) do not satisfy the Hyperboloid Rule.

3. Numerical experiments, results and discussions

3.1. CONSISTENT MASS VERSUS LUMPED MASS FORMULATION

Free vibration analysis of a fixed-fixed bar, performed using consistent mass and lumped mass matrices and using only two linear elements, has been studied[5] with varying position of the middle node. Variationally correct formulation (with consistent mass matrix) always yields an approximate value for the Rayleigh Quotient higher than the exact one for all positions of the middle node, but variationally incorrect formulations (with lumped masses) can yield this as lower than, equal to, or greater than the exact value, according the position of the middle node (Fig. 2). Recently, it has been demonstrated by Jafarali et al[6] that in the vibration analysis of Timoshenko beams, use of reduced integration, as a variationally incorrect step, cannot guarantee that the approximate natural frequency will always be above the exact one.

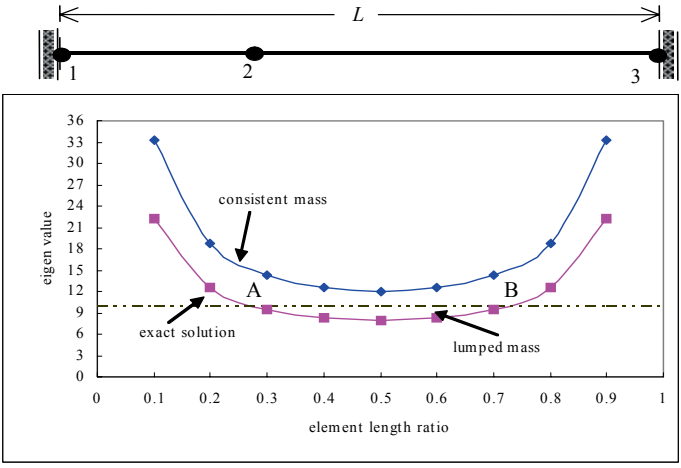

Fig. 2 Variation of eigenvalue of the first mode of a fixed-fixed bar using consistent and lumped mass formulations from a sweep test (node 2).

3.2. TIMOSHENKO BEAM ANALYSIS BASED ON THE PROJECTION THEOREM

3.2.1. *Pure shear vibration of hinged-hinged beam*

Hinged-hinged Timoshenko beam permits the pure shear vibration[6] where the section rotates without any transverse displacement and the rotation of the section is constant throughout the length of the beam; i.e., $W(x) = 0$ and $\theta(x) = c$ a constant. Table 1 shows the results of the analysis for thin and thick beams using analytical solution, virtual work principle and the finite element solution with two element discretisation. The finite element model predicts the pure shear frequency exactly in both the locked and lock-free solutions. In fact, the elastodynamic projection theorem (equation (3)) and *frequency-error-hyperboloid* (equation 6) are satisfied by both the exact and reduced integration finite element model. This is a special case, because the finite element model predicts the constant shear strain behaviour of the hinged-hinged beam without any discretisation error for both locked and lock-free finite element model.

3.2.2. *The coupled flexural and rotational vibration*

The results for the 1st mode of the bending and the shear spectra are summarised in Table 1. The 1st bending frequency obtained from a locked solution $((\omega^h)^2 = 2.7065)$ is much higher than the exact frequency ($\omega^2 = 1.5802 \times 10^{-2}$)

due to locking. However, it can be noted that ε^h from the locked finite element solution still satisfies the elastodynamic projection theorem (equation (3)) in both the cases of flexural and the shear spectra. Also we see that ε^{h}* from the reduced integrated lock-free finite element model violates the virtual work principle (Table 1). It is clear from Table 1 that, for lock-free finite element model,

TABLE 1. Results of the exact solution, virtual work principle and the finite element solution (with locked and lock-free model) of the pure shear mode ($n = 0$), bending and shear spectra for the 1st mode of simply supported beam discretised using two equal linear Timoshenko beam elements (L/d=10).

			Pure shear	Flexural spectra	Shear spectra
Exact solution (equation (1b))		$\langle \varepsilon, \varepsilon \rangle$	4.25×10^{10}	3.9817×10^{3}	3.3351×10^{9}
		(u,u)	4.1667×10^{8}	2.5198×10^{5}	3.1824×10^{7}
		$\omega^2 = \dfrac{\langle \varepsilon,\varepsilon \rangle}{(u,u)}$	102	1.5802×10^{-2}	104. 7970
Virtual work principle (equation (1c))	u^h, ε^h from the locked solution	$\langle \varepsilon^h, \varepsilon \rangle$	4.25×10^{10}	3.2262×10^{3}	2.4547×10^{9}
		(u^h, u)	4.1667×10^{8}	2.0417×10^{5}	2.3423×10^{7}
		$\omega^2 = \dfrac{\langle \varepsilon^h,\varepsilon \rangle}{(u^h,u)}$	102	1.5802×10^{-2}	104.7970
	u^{h*}, ε^{h*} from the lock-free solution	$\langle \varepsilon^{h*}, \varepsilon \rangle$	4.25×10^{10}	4.0826×10^{3}	1.5607×10^{9}
		$\langle u^{h*}, u \rangle$	4.1667×10^{8}	2.0466×10^{5}	1.8815×10^{7}
		$\hat{\omega}^2 = \dfrac{\langle \varepsilon^{h*},\varepsilon \rangle}{(u^{h*},u)}$	102	1.9948×10^{-2}	82.95
Finite element model (equation (1a))	u^h, ε^h from the locked solution	$\langle \varepsilon^h, \varepsilon^h \rangle$	1.4167×10^{9}	4.5431×10^{4}	1.8393×10^{9}
		(u^h, u^h)	1.3889×10^{7}	1.6786×10^{4}	1.7493×10^{7}
		$(\omega^h)^2 = \dfrac{\langle \varepsilon^h,\varepsilon^h \rangle}{(u^h,u^h)}$	102	2.7065	105.14
	u^{h*}, ε^{h*} from the lock-free solution	$\langle \varepsilon^{h*}, \varepsilon^{h*} \rangle$	1.4167×10^{9}	5.1710×10^{3}	9.0215×10^{8}
		$\langle u^{h*}, u^{h*} \rangle$	1.3889×10^{7}	1.6875×10^{5}	1.1292×10^{7}
		$(\omega^{h*})^2 = \dfrac{\langle \varepsilon^{h*},\varepsilon^{h*} \rangle}{(u^{h*},u^{h*})}$	102	3.0642×10^{-2}	79.89

the virtual work principle predicts an eigenvalue which is different from the exact solution. (i.e., $\hat{\omega}^2 = 1.9948 \times 10^{-2}$ is not equal to the $\omega^2 = 1.5802 \times 10^{-2}$). This violation of the elastodynamic projection theorem is attributed to the variational incorrectness of the reduced integration finite element model.

It is very interesting to note that in the case of flexural spectra, the lock-free solution is more accurate than that of the locked solution because locking has been eliminated through reduced integration. However in the case of shear dominated spectra, the locked solution is more accurate than the lock-free finite element solution. The increased accuracy of the flexural spectra by using reduced integration is actually due to cancellation of errors[6], where the error introduced by the reduced integration in the finite element model is in opposite sign of the error due to discretisation. The violation of the elastodynamic projection theorem by the reduced integration finite element model will cause the loss of boundedness of the approximate eigenvalues with the exact eigenvalues. This has been demonstrated recently by Jafarali et al[6].

4. Conclusions

The present paper highlights some significant results of error analysis of computational elastodynamics using a function space approach. The virtual work principle is employed to arrive at the fundamental theorems that govern the error in finite element computation in elastodynamic problems. It has been demonstrated that while variationally correct formulations follow the elastodynamic projection theorems, those with variationally incorrect procedures violate these. It has been shown how the upper boundedness of the Rayleigh quotient is conserved in variationally correct formulations and is lost in variationally incorrect ones. These facts have been demonstrated using the lower order one-dimensional elements like the bar and the Timoshenko beam elements.

References

1. G. Strang, G. F. Fix, 1996. *Analysis of the Finite Element Method*, Prentice Hall, Englewood Cliffs, New Jersey.
2. G. Prathap, 1993. *The Finite Element Method in Structural Mechanics*, Kluwer Academic Publishers, Dordrecht.
3. S. Mukherjee, G. Prathap, 2001. *Analysis of shear locking in Timoshenko beam elements using the function space approach*, Communications in Numerical Methods in Engineering, **17**, 385-393.
4. G. Prathap, S. Mukherjee, 2003. *The engineer grapples with Theorem 1.1 and Lemma 6.3 of Strang and Fix*, Current Science **85**, 989-994.

5. S. Mukherjee, P. Jafarali, G. Prathap, 2005. *A variational basis for error analysis in finite element elastodynamic problems*, Journal of Sound and Vibration, **285**, 615-635.
6. P. Jafarali, M. Ameen, S. Mukherjee, G. Prathap, *Variational correctness and Timoshenko beam finite element elastodynamics*, Journal of Sound and Vibration, (in press).

FINITE ELEMENT ANALYSIS OF FREE AND TRANSIENT VIBRATION IN SANDWICH FOLDED PLATES

S. PAL AND A. GUHA NIYOGI*
Civil Engineering, Jadavpur University, Kolkata-700032, India

Abstract. A 9-noded Lagrangian plate bending finite element that incorporates first-order transverse shear deformation and rotary inertia is used to predict the free and forced vibration response of sandwich folded plate structures. A 6 x 6 transformation matrix is applied to transform the system element matrices before assembly. An additional drilling degree of freedom is appended with the usual five degrees-of-freedom per node to use the transformation. The finite element results presented here show good agreement with the available semi-analytical solutions and finite element results. Parametric studies are presented for free and forced vibration response for sandwich folded plates, with reference to crank angle and different boundary conditions.

Keywords: sandwich folded plate, finite element method

1. Introduction

Folded plate structures have a wide range of engineering applications in buildings, pressure vessels, naval, automobile, and aeronautical constructions. Sandwich folded plate structure is often more effective due to their low weight, high stiffness and high strength properties. A sandwich is a three layered construction, where a low weight thick core layer (e.g., rigid polyurethane foam) of adequate transverse shear rigidity, is sandwiched between two thin laminated composite face layers of higher rigidity. This possesses high qualities, namely, high stiffness to weight ratio, high strength to weight ratio, resistance to corrosion and

* Corresponding author, agn_ju@yahoo.com

E. İnan et al. (eds.), *Vibration Problems ICOVP-2007*,

better damping qualities. In addition, these materials offer better dynamic characteristics than other conventional materials. A first order shear deformation theory is used in the present analysis to analyze the sandwich folded plates so that moderately thick plates may be taken up. The results of free vibration analysis and transient analysis of sandwich folded plates are presented. In the free vibration analysis, subspace iteration technique[1] is adopted for extraction of the eigenpairs. In the forced vibration analysis, damping is neglected. Newmark's explicit integration technique[1] is adopted for the transient analysis. Parametric studies are conducted by varying the crank angle and using different boundary conditions. The present methodology can easily be applied to the analysis of box beams and closed structures.

2. Theoretical formulation

For Mindlin plates the following relationships hold:

$$\begin{Bmatrix} u \\ v \\ w \end{Bmatrix} = \begin{Bmatrix} u_0 + z\theta_x \\ v_0 + z\theta_y \\ w_0 \end{Bmatrix} \text{ and } \begin{Bmatrix} \theta_x \\ \theta_y \end{Bmatrix} = \begin{Bmatrix} \dfrac{\partial w}{\partial x} + \phi_x \\ \dfrac{\partial w}{\partial y} + \phi_y \end{Bmatrix} \tag{1}$$

The displacements of a plate is fully described by five components, u, v, w, θ_x, θ_y, where u, v and w are displacements along the x, y, and z-directions while θ_x and θ_y are rotations about y- and x-axes. Here u_0, v_0 and w_0 are the mid-plane translations along x, y, and z-directions. The displacements δ_j at any point within the element are given in terms of nodal displacements as

$$\delta_j = N_i \, \delta_{ij} \, . \tag{2}$$

Here N_j are Lagrangian interpolation functions[1].

The stiffness matrix of the plate element assumes the form

$$[K]_e = \int_{A_e} [B]^T [D][B] dA \, , \tag{3}$$

where

$$\{\varepsilon\} = [B]\{\delta\} \, , \tag{4}$$

$\{\varepsilon\}$ being the strain vector, and $\{\delta\}$ the nodal displacement vector. $[B]$ is the strain-displacement matrix, and $[D]$ is the stiffness matrix given by

$$[D]=\begin{bmatrix} A_{ij} & B_{ij} & 0 \\ B_{ij} & D_{ij} & 0 \\ 0 & 0 & A_{lm} \end{bmatrix}, \tag{5}$$

where

$$A_{ij}, B_{ij}, D_{ij} = \sum_{k=1}^{N} \int_{z_{k-1}}^{z_k} \left(Q_{ij}\right)^k (1, z, z^2) dz, i, j = 1, 2, 6 \tag{6a}$$

and

$$A_{km} = \sum_{k=1}^{N} \int_{z_{k-1}}^{z_k} \kappa (Q_{lm})^k \, dz, l, m = 4, 5, \; \kappa = 5/6. \tag{6b}$$

Here, Q_{ij} are the elements of off-axis stress-strain relations. Q_{ij}^k relates stresses and strains in k^{th} layer by the relation, $\sigma_i^k = Q_{ij}^k \varepsilon_j^k, \quad i, j = 1, 2, 6$. Here σ_1, σ_2, and σ_6 denote σ_x, σ_y and τ_{xy} respectively and ε_1, ε_2, and ε_6 denote ε_x, ε_y and τ_{xy} respectively, whereas $\sigma_{lm}^k = Q_{lm}^k \varepsilon_m^k, \quad l, m = 4, 5$ and κ is the shear correction factor taken as $5/6$.

The mass matrix of the plate element is given by

$$[M]_e = \int_{A_e} [N]^T [\rho][N] dA, \tag{7}$$

$[\rho]$ being the density matrix functions. Finally, the element load vector is given by

$$\int_{A_e} [N]^T q dA, \tag{8}$$

where, q is the transverse load intensity on the element. The integration in every case is carried out over the area of the plate element. Generally, a 3-point Gauss quadrature is adopted to compute the bending stiffness of the elements, whereas a 2-point integration is applied to calculate the shear stiffness, mass matrix, and element force vector.

Finally, the global stiffness and mass matrices and force vector are expressed as

$$[K']_e = [T]^T [K]_e [T] \tag{9}$$

$$[M']_e = [T]^T [M]_e [T] \tag{10}$$

$$\{f'\}_e = [T]^T \{f\}_e . \tag{11}$$

Before applying the transformation, the 45×45 stiffness and mass matrices are expanded to 54×54 size, to accommodate the nine drilling degrees of freedom per element. The off-diagonal terms corresponding to the θ_z terms are set to zero, while a very small positive number, about 1000 times smaller than the smallest leading diagonal, is introduced at the corresponding leading diagonal terms[1]. The load vector is similarly enlarged by incorporating null terms in the θ_z positions

The governing equations, without damping being accounted, are

$$\text{Free Vibration: } M\ddot{x} + Kx = 0 \tag{12}$$

$$\text{Forced Vibration: } M\ddot{x} + Kx = F \tag{13}$$

3. Numerical results and discussions

The finite element formulation described in the earlier section has been used to generate numerical results to study the effects of crank angle and different boundary conditions used, on the responses and frequencies of sandwich folded

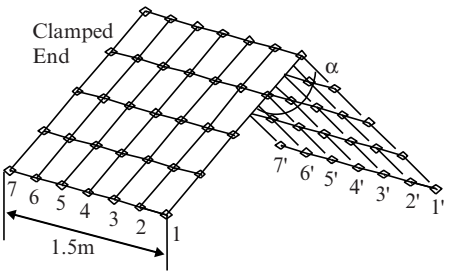

Fig. 1 Geometry of folded plate structure in case study 1.

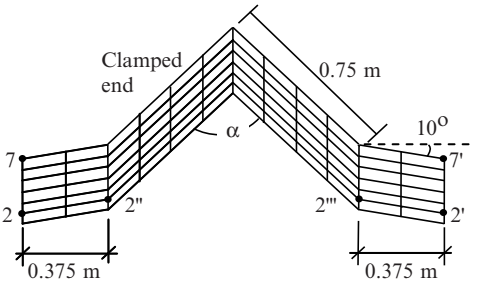

Fig. 2 Geometry of folded plate structure in case study 2 and 3.

plate structures. The validation of the code developed and the mesh convergence study has been provided elsewhere[3].

3.1. CASE STUDY 1

The free vibration behaviour of sandwich folded plate with sides along $7-7'$ being clamped and the nodes 1 and $1'$ are provided as fixed. The sandwich plate is composed of polyurethane core and three layers of E-glass epoxy surface material each at top and bottom. The overall thickness is assumed to be distributed in 15 layers (mass = 29.66 Kg/m^3). The data used for polyurethane core are $E_1 = E_2 = G_{12} = G_{13} = G_{23} = 0.896 \times 10^9$ N/m^2, $\nu_{12} = \nu_{21} = 0.35$, $\rho = 121.874$ Kg/m^3 and for E-glass epoxy surface material $E_1 = 60.7\ 10^9$ N/m^2, $E_2 = 24.8\ 10^9$ N/m^2, $G_{12} = G_{13} = G_{23} = 12.0\ 10^9$ N/m^2, $\nu_{12} = \nu_{21} = 0.23$, $\rho = 1300$ Kg/m^3. Parametric studies are conducted by shifting the point of fixity from $1-1'$ to $4-4'$. It may be observed from Table 1, that the fundamental frequencies of the single-fold folded plates are very nearly identical for different crank angles. Here it may be seen that effect of fixity is prominent when the fixity is at $2-2'$ compared to other positions.

TABLE 1. Effect of Fixity on Natural Frequency (Hz) of Sandwich One-fold Folded Plate Structure.

Crank Angle α	Mode No.	Fixity at			
		1-1'	2-2'	3-3'	4-4'
90°	1	111.9	166.6	129.1	88.8
	2	130.3	188.1	163.0	114.3
	3	211.6	218.8	208.2	243.7
	4	280.3	300.3	246.9	317.2
	5	318.6	350.7	329.2	322.4
120°	1	112.0	166.8	129.3	88.9
	2	129.5	187.1	160.8	112.9
	3	212.8	219.4	208.7	245.0
	4	266.5	290.5	242.7	294.4
	5	320.1	351.9	330.5	318.2
150°	1	112.0	166.9	129.4	88.9
	2	124.9	181.4	148.2	105.2
	3	206.6	219.6	208.8	215.2
	4	213.2	244.3	216.6	245.5
	5	311.9	349.5	295.0	318.6

3.2. CASE STUDY 2

The free vibration behaviour of sandwich folded plate structure with two stiffeners along the length is shown in Fig. 2. It will serve as chajja of a car-parking shed. The boundary conditions provided are same as before. The fixity is provided along $7-7'$ and either at $2-2'$ or at $2''-2'''$. The results are shown in Table 2. The length and material for the folded plate structure are same as previous case. From the table it can be seen that changing boundary condition and crank angle affect the natural frequency of the folded plate structure. The folded plate with crank angle 90^o shows different behaviour compared to other crank angle.

TABLE 2. Effect of Fixity and Crank Angle on Natural Frequency (Hz) of Sandwich Folded Plate Structure.

Crank Angle α	90^o		120^o		150^o	
Mode No.	Fixity along 2-2′	Fixity along 2′′-2′′′	Fixity along 2-2′	Fixity along 2′′-2′′′	Fixity along 2-2′	Fixity along 2′′-2′′′
1	173.8	161.0	132.5	158.5	100.2	146.2
2	175.1	167.9	143.8	162.5	107.0	146.4
3	236.4	219.9	214.5	203.5	163.2	178.5
4	239.0	250.5	216.8	229.2	165.5	195.3
5	275.8	254.3	250.0	246.7	237.5	239.6

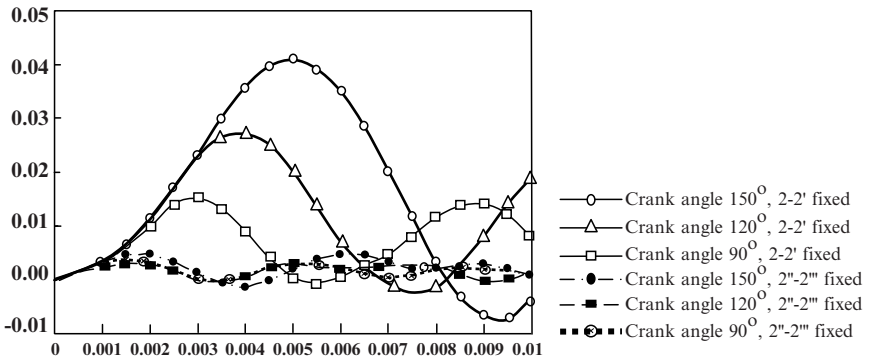

Fig. 3 Transient response of sandwich folded plate structure for crack angle 90°, 120° and 150°.

3.3. CASE STUDY 3

Study on Transient Response: Fig. 3 represent comparison of transient response of the sandwich folded plate structure for different boundary conditions and crank angle, under uniformly applied step loading of intensity, 1.0×10^5 N/m^2 acting normal to all the faces, outward and upward, for crank angle $\beta = 90°$, 120° and 150°, respectively. Here it can be seen that if fixity are provided at $2'' - 2'''$, it will produce less deflection compared to when fixity is placed at $2 - 2'$.

4. Conclusions

This paper deals with analysis of sandwich cantilever folded plate structures. For the numerical simulation of the problem finite element technique has been used. Various folded plate configurations have been considered in the present study. A set of new results for sandwich folded plate structures with various crank angles and boundary conditions are presented. In case study 3, it is observed that there is very little effect of crank angle in the deflection when the fixity is provided in the inward direction. The first order shear deformation theory is found to work well for folded plates where the five regular degrees of freedom is appended with a sixth drilling degree of freedom. It has been shown that natural frequency of sandwich folded plates varies due to variation in crank angle and boundary condition.

ACKNOWLEDGEMENT

The authors gratefully acknowledge the financial support extended by the Council of Scientific and Industrial Research, India for conducting this research, vide grant No.9/96(501) 2K6-EMR-I.

References

1. K. J. Bathe, 1996. *Finite Element Procedures*, Prentice Hall of India Pvt. Ltd, New Delhi.
2. A. G. Niyogi, P. K. Sinha, M. K. Laha, 2003. *Finite element analysis of cantilever laminated composite and sandwich folded plate structures*, Structural Engineering Convention, IIT, Mumbai.
3. S. Pal, A. G. Niyogi, *Application of folded plate formulation in analysing stiffened laminated composite and sandwich folded plate vibration*, Journal of Reinforced Plastics and Composites, (communicated).

RECENT ADVANCES IN OPTIMIZATION OF AEROSPACE STRUCTURES AND ENGINES

J. S. RAO*
Chief Science Officer, Altair Engineering, Mercury 2B Block, 5th Floor, Prestige Tech Park, Sarjapur Marathhalli Outer Ring Road, Bangalore 560087, India

Abstract. Optimization theories have been well advanced during the last few decades; however when it came to handle real life engineering structures it has been always time consuming and approximate when the structure geometry is highly complex. Design of Experiments has helped in understanding the influence of size and shape parameters on achieving a specified objective function with required constraints and a suitable analysis platform, but has its limitations in arriving at the final optimal solution. There are several commercial codes that addressed this need to handle large size structures subjected to dynamic loads. Most advanced tools in this category are *Altair OptiStruct* and *Altair HyperStudy* available in *Altair HyperWorks* suite. Application of these tools in achieving optimum solutions for linear advanced aircraft structures for minimization of weight are first explained. The application of these tools for globally elastic and locally plastic nonlinear structures to reduce local plastic strains and achieve higher life under dynamic loads will then be discussed.

Keywords: optimization, locally plastic structures, weight optimization, plastic strain minimization, topology optimization, shape optimization

1. Introduction

Optimization is the necessity of engineering designs. It may be cost driven for a product or it may be performance driven to achieve certain goals of advanced engineering applications. Machines were initially designed to be robust and

*js.rao@altair.com

E. İnan et al. (eds.), *Vibration Problems ICOVP-2007*,

followed practices with safety margins. The final designs are arrived at with extensive proto type models and testing. Engineers have begun to look at the advantages in adopting mathematical techniques in solid mechanics, fluid mechanics and thermodynamics to get improved designs that gradually eliminated the need for severe safety margins in arriving at better designs. It is the optimization process that has enabled advanced engineering designs to be arrived at; however they initially were hampered by the inability to handle large size descriptions of structures with intricate topography and shapes. Modern FEA and Optimization techniques and digital computers help in virtual simulation and virtual prototyping to decrease design cycle time to a minimum and bring the concept to a product to the market quicker.

Modern optimization techniques are described by Rao[1] and recently by Deb[2]. They can be classified as given in Table 1.

TABLE 1. Classification of Optimization Techniques.

Constraints	Design Variables	Physical Structure	Nature of Equations
Constrained Equality and Inequality Unconstrained No constraints	Parameter or Static – e.g., Minimum weight of a Prismatic beam Dynamic – e.g., Minimum weight Design variables continuous function through space Multi-objective Programming	Optimal control Two types of variables, Control (design) and state variables Non optimal	Nonlinear Programming Geometric Programming Quadratic Programming Linear Programming Stochastic Programming Genetic Algorithms

Altair HyperWorks has two codes *Altair OptiStruct* and *Altair HyperStudy* which provide optimization methods for various engineering problems. *Altair OptiStruct*[3] has been developed recently to perform structural optimization. This has been successfully applied for topology, topography, gauge and shape optimizations of automotive and airframe structures, e.g., Schuhmacher[4], Taylor et al[5]. discussed the weight optimization achieved in aircraft structures.

Altair OptiStruct uses an iterative procedure known as the local approximation method to solve an optimization problem. The design update is computed using the solution of an approximate optimization problem, which is established using the sensitivity information. It has three different methods implemented: the optimality criteria method, a dual method, and a primal feasible directions method. The primal method is more common in shape optimizations. This approach is based on the assumption that only small changes occur in the design with each optimization step. This tool is conventionally used with *Altair HyperMesh*[6] which has mesh morphing incorporated in it which allows the mesh generated for the base line geometry to be morphed with the changes in design variables automatically thus reducing considerable effort for different geometries when design variables are continually changed.

Altair HyperStudy[7] is a *multipurpose* DOE/Optimization/Stochastic tool that can be applied in multi-disciplinary optimization of a design combining different analysis types. It uses global optimization methods that use higher order polynomials to approximate the original optimization problem over a wide range of design variables that are referred to as Response Surface methods. A sequential response surface method approach is used in which, the objective and constraint functions are approximated in terms of design variables using a second order polynomial. One can create a sequential response surface update by linear steps or by quadratic response surfaces. The process can also be used for non-linear physics and experimental analysis using wrap-around software, which can link with various solvers[8].

In this paper the applications of the above tools to advanced optimization problems in aerospace industry are discussed.

2. Weight optimization of wing structure

The optimization process of a typical nose rib is illustrated in Fig. 1. Typically it starts with the base line of an operating structure in service or a component being newly designed. The base line model is defined with the design space and external loads. The design space is filled with small virtual cubes with the help of *Altair HyperMesh*. *Altair OptiStruct* is a linear structural code that is next used to identify strain energy density and obtain the material layout which gives the load flow path and vacant space (topology optimization) where the material is unnecessary from a functional point of view.

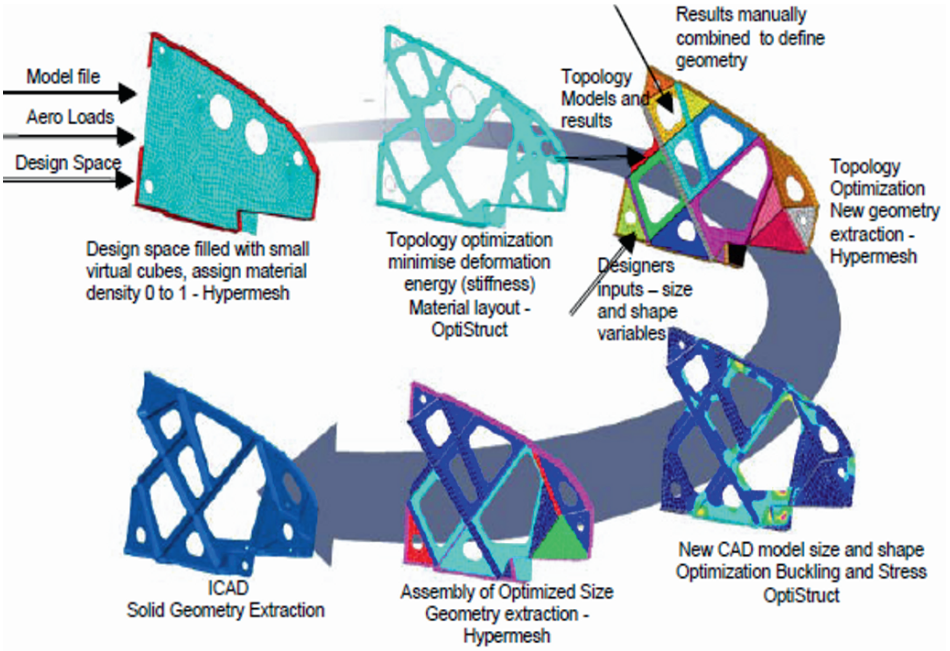

Fig. 1 Topology Optimization Process Illustrated for a Nose Rib.

Typically the design team looks at the optimized topology and provides size and shape variables and the topology results are manually combined to form new geometry. A new CAD model is then obtained for optimized buckling and stress constraints using *Optistruct*. The geometry is next extracted from *Hyper-Mesh* and the solid geometry is next extracted to provide the final optimized component. Some details of this process are explained below.

A typical rib of an aircraft wing box is shown in Fig. 2. The FE model of this base line rib is then subjected to aerodynamic drag and jack loads during landing as shown in Fig. 3 to determine the peak stress and displacement which are 97.7 MPa and 1.062 mm respectively. The first topology optimization resulted in the flow path as shown by relative density plot in Fig. 4. Inputs from engineering team are taken to select areas in material density region 0 to 0.3 and make additional cutouts and thinning the ribs and topology iterations carried out to give the final optimized rib shown in Fig. 5. This rib has same displacement and stress peak values as the base line however the weight is reduced from 8.085 kg to 3.75 kg thus giving a weight saving by ~ 46%. This technology has helped in considerable weight reduction by 500 kg in each of the Airbus 380 wings[4] and similar reductions in F-35 Joint Strike Fighter[5].

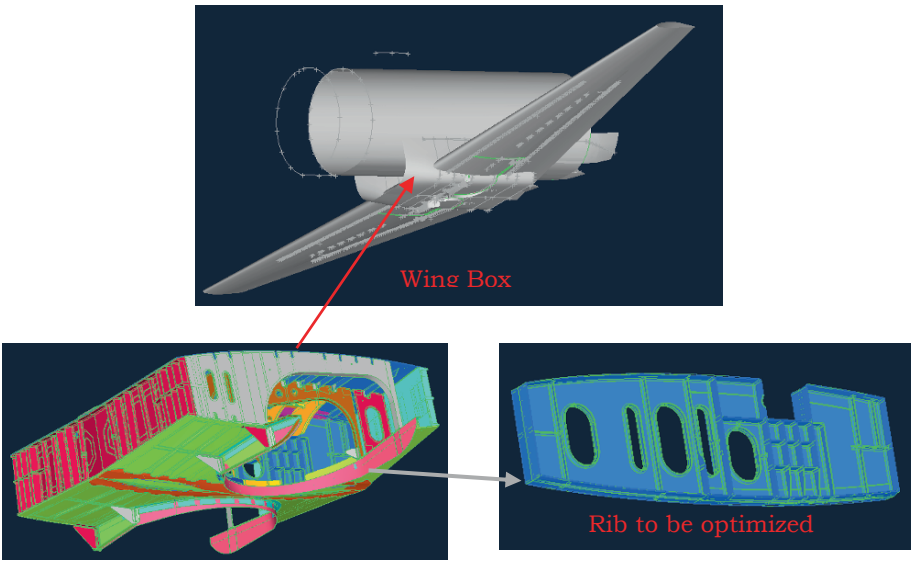

Fig. 2 Base Line Wing Box Rib for Optimization.

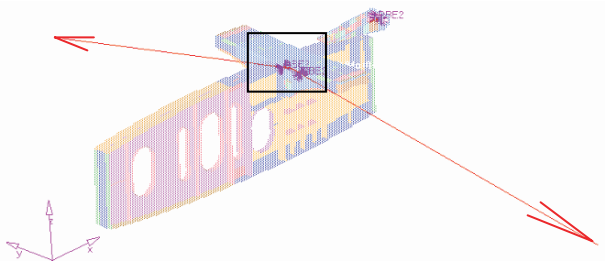

Fig. 3 FE Model of Rib and Loads.

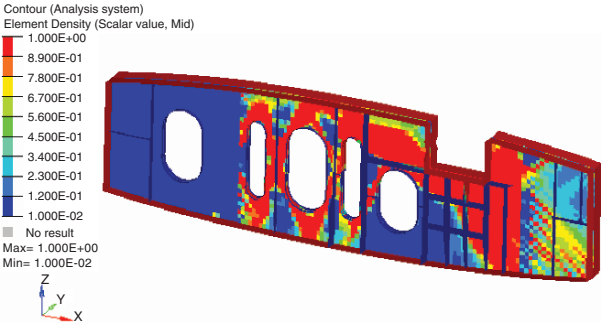

Fig. 4 Topology Optimization and Relative Material Density.

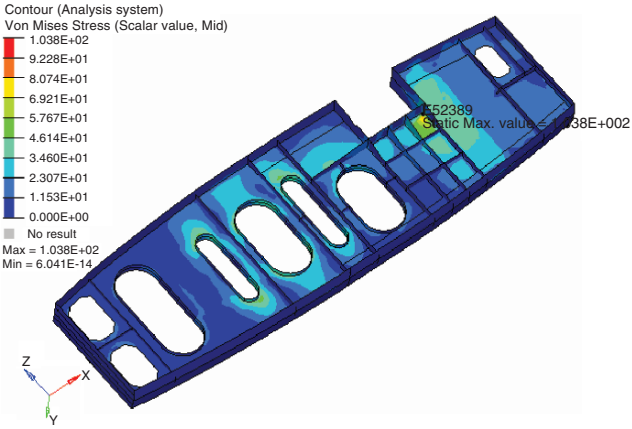

Fig. 5 Optimized Rib.

3. Shape optimization of nonlinear structures

Fig. 6 shows a rotating bladed disk with a sector model and cyclic symmetry boundary conditions. The first five natural modes are 344, 707, 1230, 1295 and 1630 Hz.

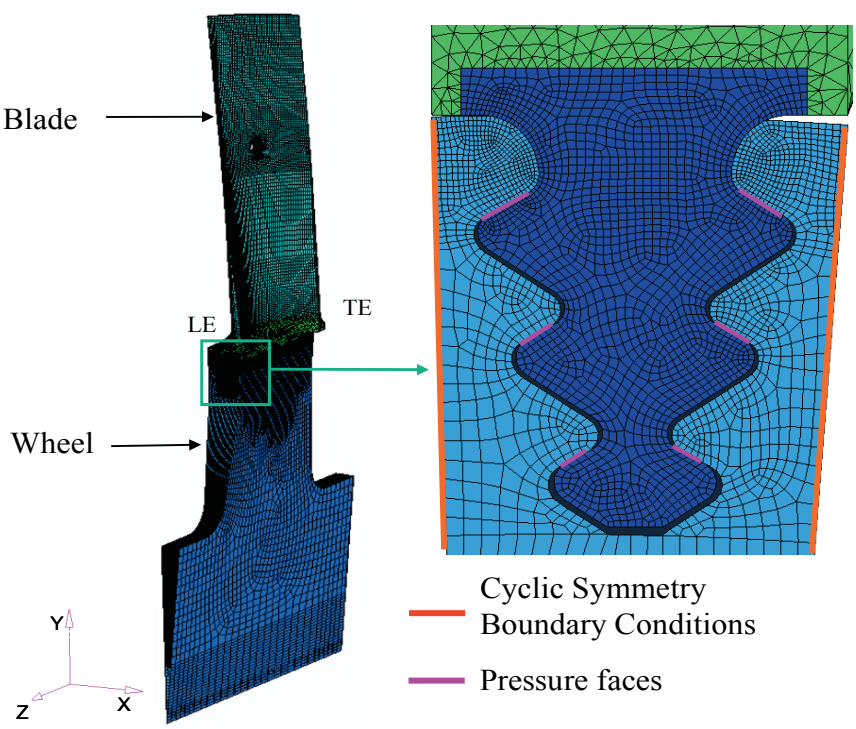

Fig. 6 Cyclic Symmetry Bladed Disk Model for Shape Optimization.

Because of high operational speed 8500 rpm, the blade is subjected to high centrifugal stresses. At the blade notch the stresses go beyond elastic limit into plastic range. A nonlinear analysis with the material property defined in Fig. 7 was conducted with the help of *Ansys release* 9 code[9].

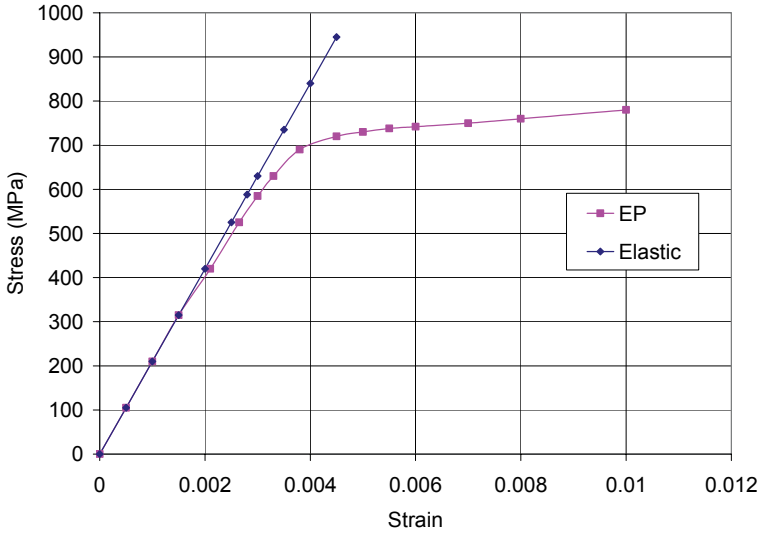

Fig. 7 Material Nonlinearity of the Bladed Disk.

The stress field obtained is shown in Fig. 8. Average stress is 216.86 MPa, however the peak stress is 768 MPa confined to the notch region rapidly decreasing to average stress region.

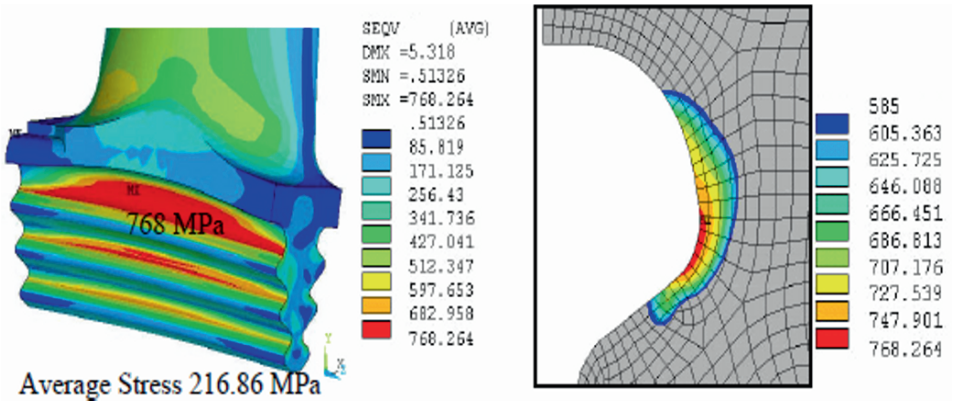

Fig. 8 Globally Elastic and Locally Plastic Blade Stress Field.

To improve the performance of this blade the base line shape of the bladed disk groove may be improved by an optimization process. *Altair HyperStudy* is used for this purpose. The blade root shapes are varied within the constraints as shown in Fig. 9.

The objective function is the peak stress with the above shape (design) variables. *Altair HyperStudy* is used for optimization with *Ansys* as solver for the nonlinear problem. Fig. 10 shows the iterations during the optimization and the convergence of the design for optimum shape of the blade groove. The baseline shape and final optimized shape are given in Fig. 11.

The optimized shape result for stress is given in Fig. 12. The maximum stress decreased marginally from 768 to 746 MPa by 22 MPa (2.86%) from baseline elasto-plastic analysis for 8500 RPM; however the peak plastic strain reduced from 0.0153 to 0.01126 by 26.4%. This is the major advantage in optimization for a blade root shape. Many existing machines have roots designed by experience and there can be considerable margin in lowering peak strains and therefore enhanced life. Alternatively new designs can be made by simulation rather then extensive testing of several prototypes.

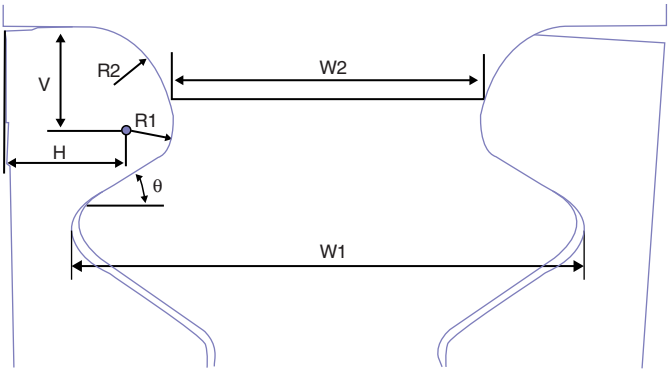

Minimum Value (mm)	Maximum Value (mm)
W1 = 22.17	W1 = 25.76
W2 = 13.65	W2 = 13.86
R1 = 1.70, H = 5.67, V = 4.13, R2 = 4.0	R1 = 2.14, H = 4.85, V = 4.06, R2 = 3.37
$\theta = 29.86^0$	$\theta = 16.25^0$

Fig. 9 Shape Variables.

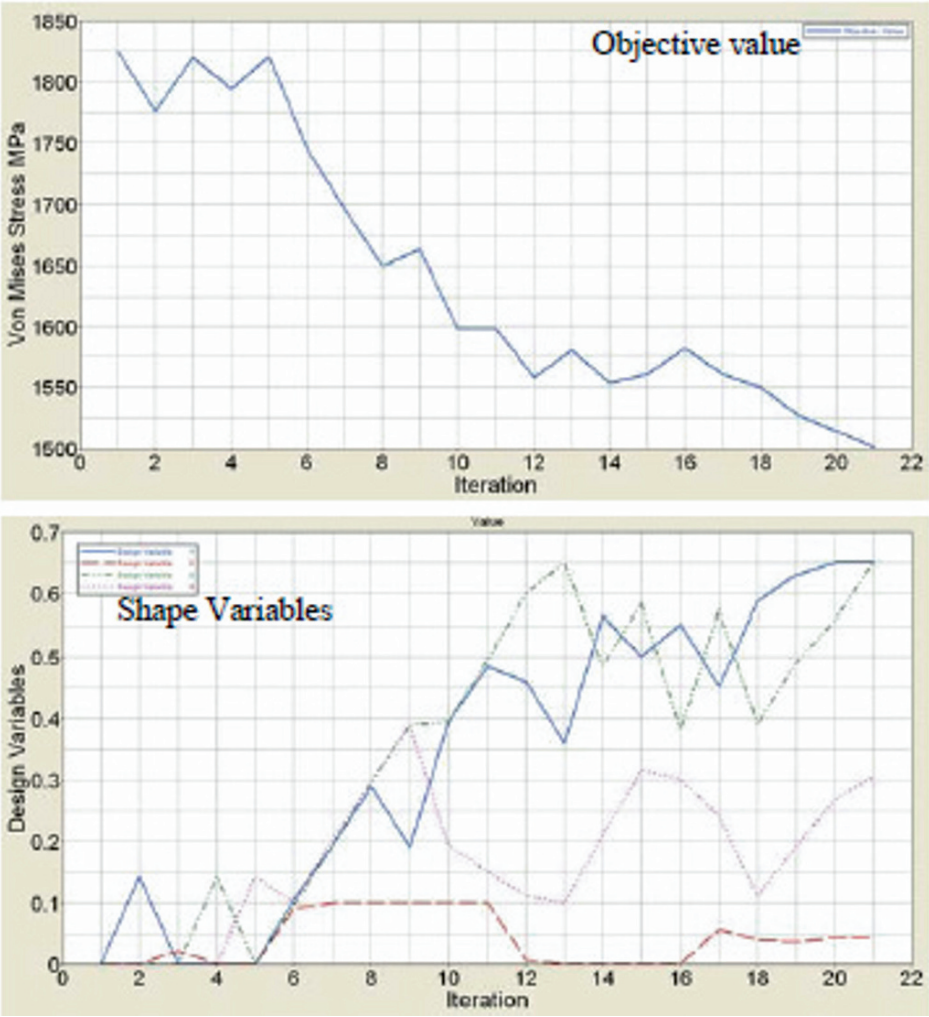

Fig. 10 Variation of Objective and Shape Variables During Optimization.

The last stage steam turbine blades are usually the limiting blades to extract power from the flow path because their natural frequencies reach a low value of 110 Hz as the blade length increases with reduction in pressure from high pressure stages to low pressure stages. Because 2 per rev excitations can destroy the machines due to excitation from inherent misalignments it becomes necessary to keep the mean stresses to as low value as possible. Since the long blades in low pressure stage are already subjected to stresses close to or above the yield region, the peak stress rapidly rises above elastic limit along the material hardening characteristic. It then becomes imperative to limit the plastic

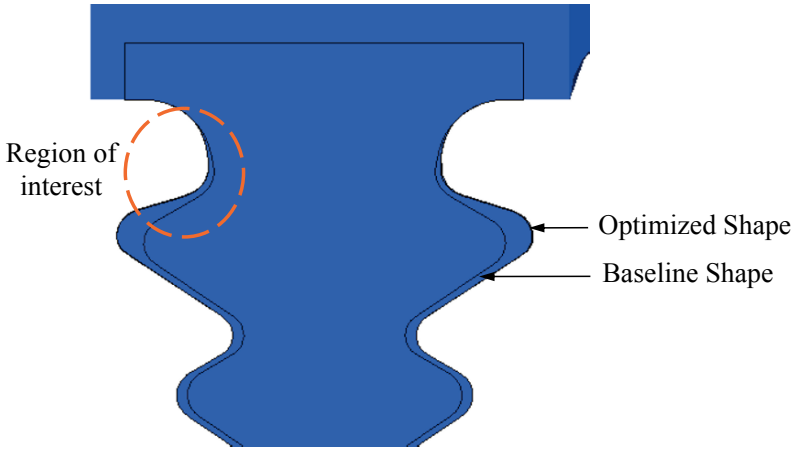

Fig. 11 Optimized Shape for Minimum Peak Stress.

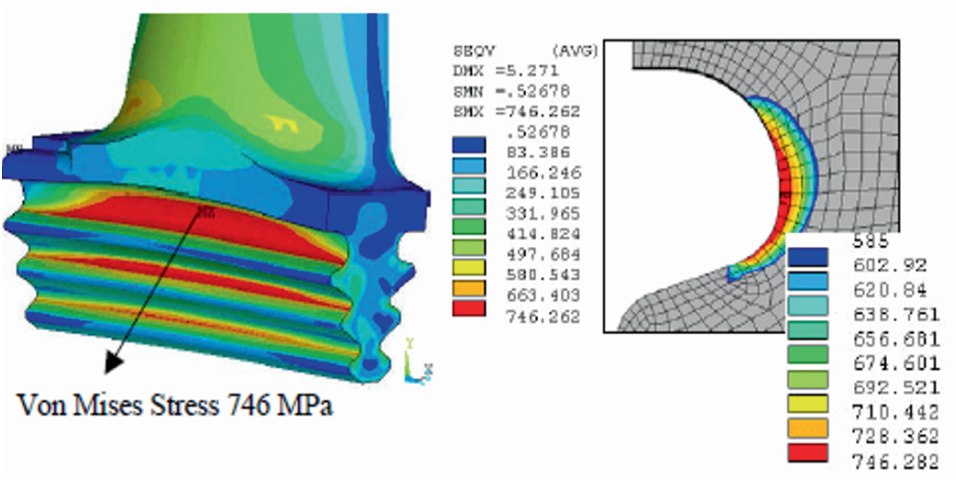

Fig. 12 Optimized Shape Stress Result.

strain as the structure is controlled by local strain rather than the stress. The above procedure illustrates how to achieve this low strain value by *Altair HyperStudy*.

4. Concluding remarks

Optimization techniques are now increasingly employed to enable large size structures under limiting conditions of operation (globally elastic and locally plastic) for minimum weight and maximum permissible stress field. Such optimum designs are particularly applicable in aerospace engineering applications.

ACKNOWLEDGEMENTS

The author is thankful to many of his colleagues who performed variety of optimization problems in Altair India, of particular mention, Mr. J. L. Ravindra, Mr. Umesh Kachole and Mr. Suresh Shankaranarayana Rao. The author is also thankful to Altair Engineering India.

References

1. S. S. Rao, 1996. *Engineering Optimization Theory and Practice*, John Wiley & Sons, Inc. New York.
2. K. Deb, 2006. *Genetic Algorithms for Engineering Product Design*, Altair CAE Users Conference, Innovation through Simulation, Bangalore, India.
3. *Altair OptiStruct, User's Manual v7.0*, 2003. Altair Engineering Inc., Troy, MI.
4. G. Schuhmacher, 2006. *Optimizing Aircraft Structures*, Concept to Reality, Winter Issue, p. 12.
5. R. M. Taylor et al., 2006. *Detail Part Optimization on the F-35 Joint Strike Fighter*, AIAA 2006-1868, *47th AIAA/ASME/ASCE/AHS/ASC Structures, Structural Dynamics, and Material Conference*, Newport, Rhode Island.
6. *Altair HyperMesh, User's Manual v7.0*, 2003. Altair Engineering Inc., Troy, MI.
7. *Altair HyperStudy, User's Manual v7.0*, 2003. Altair Engineering Inc., Troy, MI.
8. J. S. Rao, S. Suresh, 2006. *Blade Root Shape Optimization*, The Future of Gas Turbine Technology, 3rd International Conference, S2-T2-3, Brussels, Belgium.
9. ANSYS Release 9.0, 2004. *Documentation*, Ansys Inc.

SH WAVE PROPAGATION IN LATERALLY HETEROGENEOUS MEDIUM

A. ROY*
Department of Applied Mathematics, University of Calcutta, 92 A.P.C. Road, Kollkata-700009, India

Abstract. The present work reports some of the recent investigations in the field of Investigations of our group in wave propagation in laterally heterogeneous media. Such studies have practical applications in developing building code in earth prone area or in wave-guide problem. We present a new analytical approach to the title problem. This is an improved version of our earlier work with M. Mitra and R.K. Bhattacharya[1].

We consider the SH wave propagation through two different elastic media in vertical contact with each other while the medium on the right or left is horizontally layered. One can assume the contact surface to be inclined to each other. Unlike the usual approach of finding the approximate form of the reflection transmission coefficient by the use of the representation theorem, we use the exact solution of the wave equation in each medium. Various boundary conditions at the horizontal and vertical/inclined contact surface are satisfied exactly. Boundary conditions give rise to a set of coupled integral equation connecting the unknown constants of the solution. The source may be a line source or simply a plane incident wave. Iterative solutions of the integral equations provide various wave arrivals which include the scattered waves unlike previous works. Exact computations of various wave arrivals may help in developing accurate building codes in earthquake prone area.

Keywords: lateral heterogeneity, vertical/inclined surface

* roy_arabinda1@yahoo.co.in

E. İnan et al. (eds.), *Vibration Problems ICOVP-2007*,

1. Introduction

During the past forty years various theoretical methods have been developed to compute the reflection/transmission coefficients of surface waves across vertical discontinuities. These methods are basically based on i) the use of the representation theorem[2-5], ii) some approximation to the boundary conditions at the vertical contact surface[6], iii) representation of the surface wave field as a superposition of plane homogeneous and inhomogeneous waves[7-8]. Scattered waves from the step like irregularities have been studied in [9], [10]. In all the above works except the last three the vertical contact surface conditions are approximately satisfied neglecting the scattering effect.

2. Mathematical formulation

We consider the SH wave propagation in two layered media (Fig. 1) vertical contact with each other.

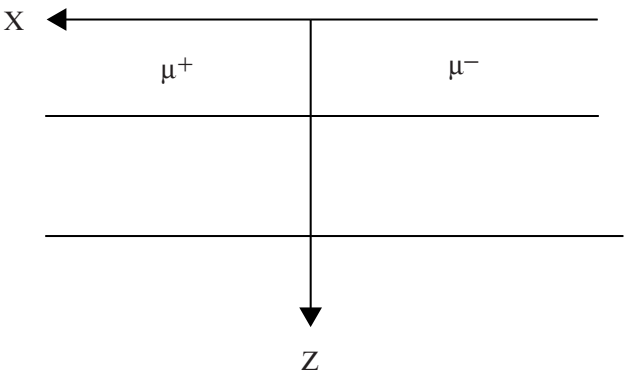

Fig. 1 Two layered media.

In all layers two dimensional SH displacement v satisfies the wave equation and the solution in the i^{th} layer s taken as

$$v_i^{\pm}(x,z) = e^{-i\omega t}\left[\int_0^{\infty}\left[A_i^{\pm}(\zeta)e^{-iz\sqrt{\zeta^2-\omega^2/\beta_i^2}} + B_i^{\pm}(\zeta)e^{iz\sqrt{\zeta^2-\omega^2/\beta_i^2}}\right]\cos(\zeta x)\right]d\zeta$$
$$+\left[C_i^{\pm}(\zeta)e^{-i|x|\sqrt{\zeta^2-\omega^2/\beta_i^2}}\cos(\zeta z)\right]d\zeta + v_0(x,z)$$

where β is the SH wave velocity, ω is the angular frequency and the constants $A_i^{\pm}(\zeta)$ represent waves in the i^{th} medium in $x>0$ and $x<0$ moving away

from the horizontal surface, $C_i^{\pm}(\zeta)$ corresponding waves moving away from the vertical contact surface and $v_0(x,z)$ is the source effect.

Boundary conditions are:

a) Continuity of displacement and stress across horizontal boundary $z = z_i$

$$v_i(x, z_i - 0) = v_{i+1}(x, z_i + 0)$$
$$\mu_i \frac{\partial v_i(x, z_i - 0)}{\partial z} = \mu_{i+1} \frac{\partial v_{i+1}(x, z_{i+1} + 0)}{\partial z}$$

b) Continuity of displacement and stress across vertical contact surface $x = 0$

$$v_i^+(0+, z) = v_i^-(0-, z)$$
$$\mu_i^+ \frac{\partial v_i^+(0+, z)}{\partial x} = \mu_i^- \frac{\partial v_i^-(0-, z)}{\partial x}$$

On satisfying the boundary conditions we derive a set of coupled integral equations connecting $A_i^{\pm}(\zeta)$ with $B_i^{\pm}(\zeta)$ which are solved iteratively. We specifically give the detailed calculations in the case of two layered model.

3. Conclusion

Use of the exact solution of the wave equation and the exact validation of the boundary conditions give not only the reflected and transmitted surface waves as all kind of scattered waves in the model considered. The systematic evaluation of various wave arrivals by the new formulation may be of practical use.

Though we have only considered SH waves our formulation can be easily extended to the case of P and SV wave. Our analysis can be easily modified for the inclined contact surface. Such inclined contact surface is present in the ocean-continental regions.

References

1. A. Roy, M. Mitra, R. K. Bhattacharya, 2002. D.S.T. report.
2. J. A. Hudson, L. Knopoff, 1964. *Transmission and reflection of surface waves at a corner*, Journal of Geophysical Research, **69**, 281.
3. L. Knopoff, J. A. Hudson, 1964. *Transmission of Love waves past a continental margin*, Journal of Geophysical Research, **69**, 1649-1653.
4. A. Mal, L. Knopoff, 1965. *Transmission of Rayleigh at a corner*, Bulletin of the Seismological Society of America, **55**, 455-466.

5. E. N. Its, I. B. Yanovskaya, 1985. *Propagation of surface Waves in a half space with vertical inclined or curved interfaces*, Wave Motion, **7**, 79-84.
6. V. I. Keilis Borok (editor), 1989. *Seismic Surface Waves in a laterally inhomogeneous earth*.
7. B. G. Buchin, A. Levshin, 1980. *Propagation of Love waves across a vertical discontinuity*, Wave Motion, **2**, 293-302.
8. S. Gregersen, I. E. Alsop, 1974. *Amplitude of horizontally refracted waves*, Bulletin of the Seismological Society of America, **66**, 1855-1872.
9. S. K. Bose, 1975. *Transmission of SH waves across a rectangle step*, Bulletin of the Seismological society of America, **65**, 1779-1786.
10. A. N. Das, M. L. Ghosh, 1992. *SH wave propagation across a vertical step in two joined elastic half space*, Journal of Technical Physics, **33**, 411-420.

LATERAL DYNAMICS OF A RAILWAY TRUCK ON FLEXIBLE TANGENT TRACK

A. K. SAHA*
Department of Mechanical Engineering, Charotar Institute of Technology, Changa, TA: Petlad, Dist: Anand, Changa-388421, Gujarat, India

R. KARMAKAR AND R. BHATTACHARYYA
Department of Mechanical Engineering, Indian Institute of Technology, Kharagpur-721302, India

Abstract. A railway vehicle becomes unstable beyond a critical speed. Assessment of the critical speed is important for safety and passenger comfort. Bond graph model of a railway truck-wheelset system on flexible tangent track has been created with eighteen degrees of freedom considering six degrees of freedom for each wheelset and the truck unit without any linearity approximation for the wheelsets. Kalker's linear creep theory has been used for rail-wheel contact forces. The bond graph model of a single wheelset created earlier has been used for the front and rear wheelsets to model the truck-wheelset system. The model is created and simulated for a given set of nominal parameter values with rigid track condition. Truck-critical speeds and stability bahaviour are studied through simulations. Critical speed of a truck is found to be higher than that of a wheelset at the same axle load and conicity for nominal primary suspension and wheelbase. Contrary to the variation of critical speed of a single wheelset with increasing conicity critical speed of a truck decreases with increasing conicity.

Keywords: truck-wheelset, lateral dynamics, bond graph, conicity, primary suspension

*Corresponding author, saha_ak2001@yahoo.co.in

E. İnan et al. (eds.), *Vibration Problems ICOVP-2007*,

1. Introduction

In a rail vehicle the car body is supported on two trucks through secondary suspensions, each truck being supported by two wheelsets on track through primary suspensions. A railway vehicle becomes unstable beyond a critical speed. This instability called hunting results in violent lateral vehicle oscillation with the wheel flanges repeatedly hitting the rails. Assessment of the critical speed is important for safety and passenger comfort. A single wheelset itself becomes unstable above a critical speed because of speed dependant creep forces at the rail wheel contact surface. However, critical speed of a truck is higher than wheelset critical speed. Since the car body has pivoted connection with the bolsters supported on the truck through secondary suspensions, vehicle critical speed is likely to be close to truck critical speed, and thus much attention has been paid to truck instability in the literature[1,2]. In a previous work[3] the authors developed a six degrees of freedom bond graph[4] model for a single wheelset on tangent track using Kalker's linear creep theory[5] without any linearity approximation.

This work presents a bond graph model of a railway truck-wheelset system on flexible tangent track with eighteen degrees of freedom considering six degrees of freedom for each wheelset and the truck unit without any linearity approximation for the wheelsets. Kalker's linear creep theory has been used for rail-wheel contact forces. The bond graph model of a single wheelset created earlier has been used for the front and rear wheelsets to model the truck-wheelset system. The model is created and simulated for a given set of nominal parameter values with rigid track condition to study truck instability behaviour.

2. Idealized truck and equivalent suspension

The model is developed on the basis of the truck-wheelset system on equivalent primary linear and torsional suspension. Considering motion of a wheelset relative to the truck in the XY-plane, the actual suspension can be replaced by an equivalent one consisting of a linear and torsional spring combination, as shown in Figs. 1a and 1b. Fig. 2 shows the truck frame on equivalent primary suspensions.

3. Modeling approach

The model is developed on the basis of the truck-wheelset system on equivalent primary linear and torsional suspension shown in Fig. 2 as follows.

1. Find the velocity components of the points g_f, g_r and g_t in the direction of the truck frame axes x_T, y_T and z_T considering these to be points fixed on the truck and also points fixed on the wheelsets.
2. Find the differences between similar velocity components of the truck and the wheelset and attach the corresponding equivalent primary linear suspension to be acted upon by the velocity difference.
3. Find the difference between corresponding angular velocity component of the truck and the wheelset and attach primary torsional suspensions to be acted upon by the velocity difference.

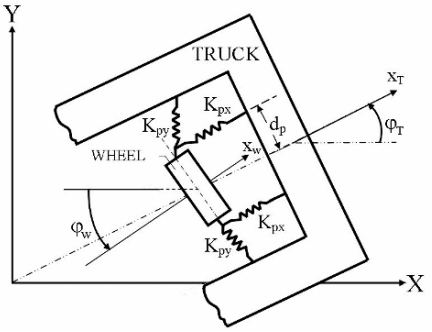

Fig. 1a Actual primary axial and lateral spring configurations.

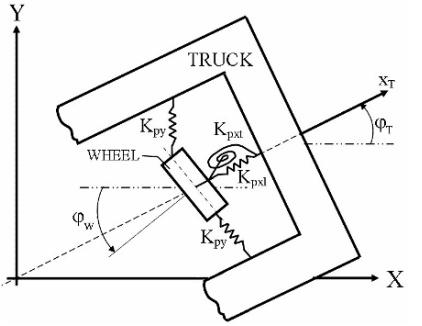

Fig. 1b Equivalent linear and torsional suspension springs in x_T direction.

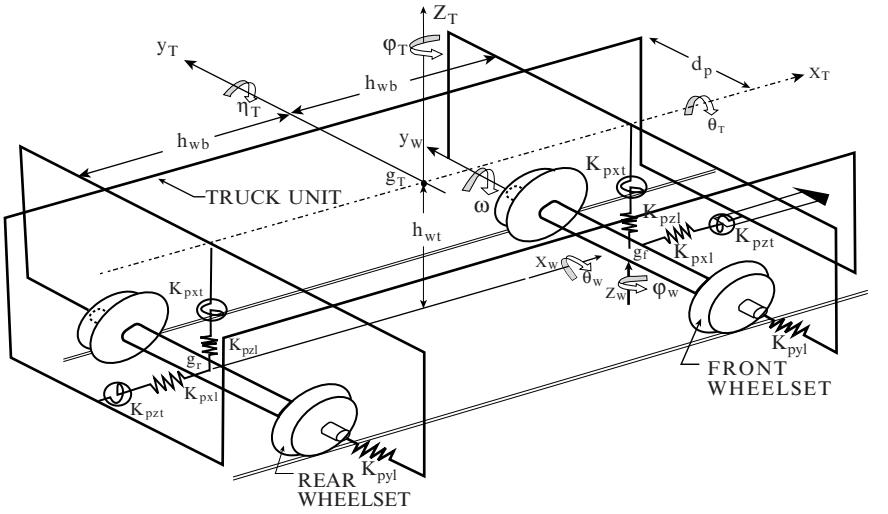

Fig. 2 Truck-wheelset with equivalent linear and torsional suspensions.

4. Velocity components along axes of the truck frame

Velocity components of points g_f, g_r and g_t can be obtained from inertial linear and angular velocities of the truck and wheelset centre of mass and truck geometrical parameters. Truck and wheelset inertial motions are represented as follows.

Let $\dot{X}_T, \dot{Y}_T$ and $\dot{Z}_T$ be inertial velocities of truck centre of mass, $\dot{\theta}_T, \dot{\eta}_T$ and $\dot{\phi}_T$ angular velocities of the truck about x_T, y_T and Z_T, and $\dot{X}_{wf}$, $\dot{Y}_{wf}$ and $\dot{Z}_{wf}$ inertial velocities of front wheelset centre of mass and $\dot{X}_{wr}, \dot{Y}_{wr}$ and $\dot{Z}_{wr}$ inertial velocities of rear wheelset centre of mass. Also $\dot{\theta}_{wf}$ and $\dot{\phi}_{wf}$ designate the angular velocities of the front wheelset about x_w and Z_w axes, and $\dot{\theta}_{wr}$ and $\dot{\phi}_{wr}$ are the angular velocities of the rear wheelset about x_w and Z_w axes, respectively.

The velocity components of g_f fixed on truck in x_T, y_T and Z_T direction are given as follows.

$$\begin{aligned}
\dot{g}_{fT}\Big|_{x_T} &= \dot{X}_T \cos\phi_T + \dot{Y}_T \sin\phi_T - \dot{\eta}_T h_{wt}, \\
\dot{g}_{fT}\Big|_{y_T} &= -\dot{X}_T \sin\phi_T + \dot{Y}_T \cos\phi_T + \dot{\phi}_T h_{wb} + \dot{\theta}_T h_{wt}, \\
\dot{g}_{fT}\Big| Z_T &= \dot{Z}_T - \dot{\eta}_T h_{wb}
\end{aligned} \tag{1}$$

The velocity components of g_f fixed on front wheelset, are obtained as

$$\begin{aligned}
\dot{g}_{fw}\Big|_{x_T} &= \dot{X}_w \cos\phi_T + \dot{Y}_w \sin\phi_T \\
\dot{g}_{fw}\Big|_{y_T} &= -\dot{X}_w \sin\phi_T + \dot{Y}_w \cos\phi_T \\
\dot{g}_{fw}\Big| Z_T &= \dot{Z}_{wf}
\end{aligned} \tag{2}$$

Similarly, the velocity components of g_r fixed on truck and the velocity components of g_r fixed on rear wheelset are obtained.

5. Bond graph model

In reference [3], bond graph model of a wheelset has been created with six degrees of freedom without any linearity approximation using bond graph modeling and simulation software SYMBOLS 2000[6]. This software provides

the facility for creation of subsystem bond graph capsules with its equations and parameter descriptions. In this work the wheelset bond graph[3] has been converted to a capsule with effort input glue ports for each of the wheelset motion variables $\dot{X}_w, \dot{Y}_w, \dot{Z}_w, \dot{\phi}_w, \dot{\theta}_w$ and used to model the truck-wheelset system.

Model of the truck-wheelset system has two parts. Interface between truck motion and front wheelset motion and interface between truck motion and rear wheelset motion. The total model the truck with wheelset capsules is shown in Fig. 3.

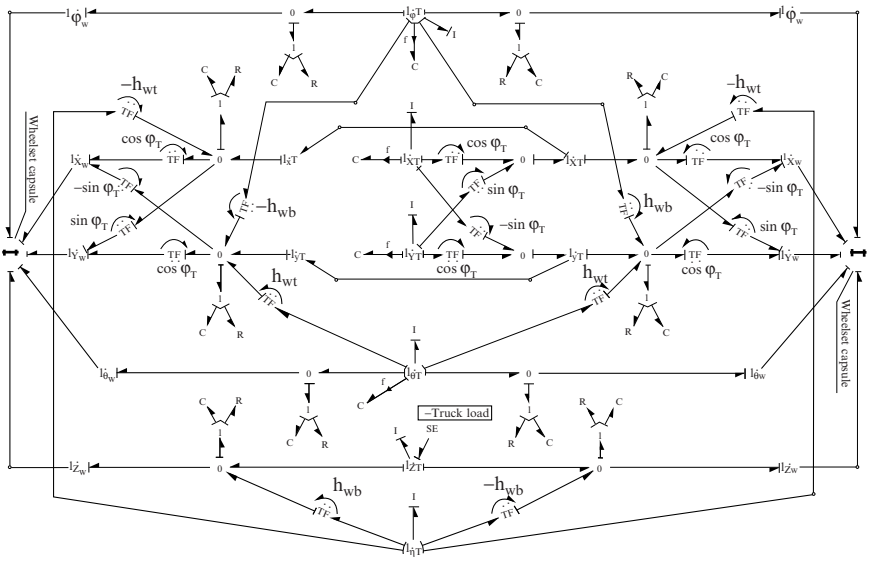

Fig. 3 Bond graph model of the truck with wheelset capsules.

Bond graph of the truck created as explained above is extended as shown in Fig. 4 for simulation with different truck speed along the track. The spring-damper combination with high parameter values is used to remove differential causality.

Bond graph Modeling and Simulation software SYMBOLS 2000[6] is used to create an integrated model of the truck-wheelset system, generate the system equations and simulate the same.

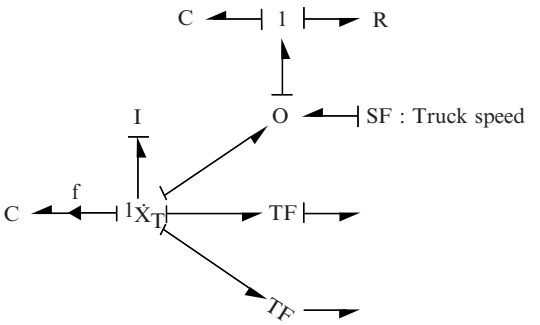

Fig. 4 Extension to Fig. 3. for truck simulation.

6. Simulation

Simulation studies are performed for the truck-model with nominal geometrical and inertia parameter values of wheelset and truck to study truck instability behaviour. Variation of truck critical speed with conicity for decreasing values of primary forward spring stiffness K_{px} with the nominal values of K_{py} and for various wheel diameters are shown in Fig. 5 and Fig. 6 respectively.

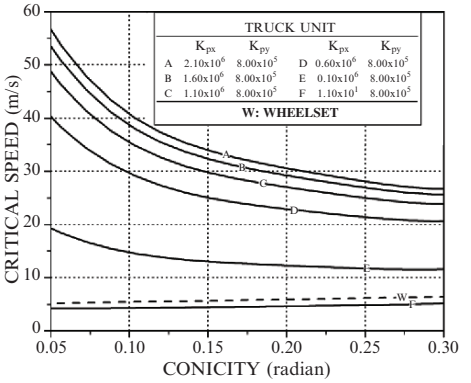

Fig. 5 Variation of critical speed with conicity for truck unit with fixed K_{py} and different values of K_{px}.

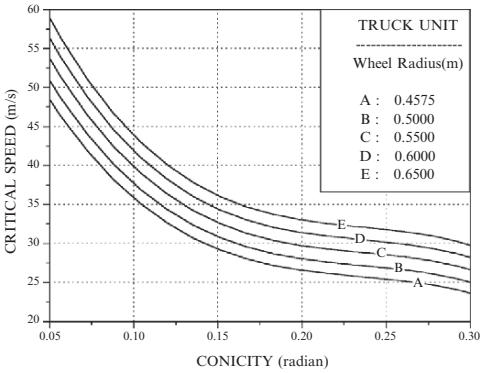

Fig. 6 Plot of critical speed – conicity for various wheel diameter.

7. Conclusions

Truck stability behaviour is studied through simulations. Truck critical speed is higher at low conicity. Critical speed of a truck is higher than that of a wheelset at the same axle load and conicity for normal primary suspension and wheel-base. Critical speed increases at high values of lateral primary damping. A truck model can be converted to a capsule and used to develop bond graph model of a carbody.

References

1. A. E. W. Hobbs, T. G. Pearce, 1974. *The Lateral Dynamics of the Linear Induction Motor Test Vehicles*. Journal of Dynamics Systems, Measurement, and Control, TRANS. ASME, 147-157.
2. A. H. Wickens, 1998. *The Dynamics of Railway Vehicles-From Stephenson to Carter*. Proc. Instn. Mech. Engrs., **212**, Part F, 209-226.
3. A. K. Saha, R. Karmakar, R. Bhattacharyya, 2003. *On the Modelling of Lateral Dynamics of a Rail-Wheelset – a Bond graph Approach*, Technical report, Department of Mechanical Engineering, Indian Institute of Technology, Kharagpur, India.
4. A. Mukherjee, R. Karmakar, *Modelling and Simulation of Engineering Systems Through Bond graphs*. CRC Press, Florida. BN.
5. J. J. Kalker, 1967. *On the Rolling contact of Two Elastic Bodies in the Presence of Dry Friction*, PhD Dissertation. University of Delft.
6. *High-Tech Consultants*: SYMBOLS 2000. STEP, IIT-Kgp, http://www.symbols2000.com.

VIBRATION AND STABILITY OF CROSS-PLY LAMINATED TWISTED CANTILEVER PLATES

S. K. SAHU*, A. V. ASHA, AND S. NAGARAJU
Department of Civil Engineering, National Institute of Technology, Rourkela-769008, India

Abstract. The buckling and vibration analysis of cross-ply laminated cantilever twisted plates are investigated. The analysis is carried out using the finite element method with first order shear deformation theory. An eight-nodded isoparametric quadratic element is employed in the present analysis with five degrees of freedom per node. The element elastic stiffness matrix, mass matrix and load vector are derived using the principle of Stationery Potential Energy. Plane stress analysis is carried out using the finite element method to determine the stresses and these are used to formulate the geometric stiffness matrix. The overall stiffness and mass matrices are obtained by assembling the corresponding element matrices using skyline technique. The eigenvalues are determined using subspace iteration scheme. Extensive results are presented to show the effects of various parameters such as aspect ratio, number of layers, angle of twist, ply orientation, etc on the buckling and vibration behavior of cross-ply laminated twisted cantilever plates. It was noticed that both the non-dimensional buckling and frequency parameter decreased with the increase in the angle of twist of the plate. The non-dimensional frequency parameters as well as buckling loads also increase with increase in the number of layers of the plate. There is significant decrease in the buckling load of the plate with increase of aspect ratio unlike the frequencies of vibration. These can be used to advantage in tailoring of laminated cross-ply twisted cantilever plates.

Keywords: vibration, stability, twisted plates, finite element method

*Corresponding author, sksahu@nitrkl.ac.in

E. İnan et al. (eds.), *Vibration Problems ICOVP-2007*,

1. Introduction

Twisted cantilever plates have significant applications in turbo-machinery, impeller and fan blades. Their range of practical applications demands a proper understanding of their vibration, static and dynamic stability characteristics. Composite structures have extensive use in aerospace, civil, marine and other engineering applications. Cross-ply laminated composites are becoming key components in many of them. The vibration and stability behavior of cross-ply laminated cantilever twisted plates therefore has tremendous technical significance in understanding their behaviour for use in structural design. Many researchers worked on the vibration and stability of untwisted cross-ply laminated plates. Putcha and Reddy[1] investigated the vibration and buckling of untwisted cross-ply plates using mixed element based on a refined plate theory. Gendy et al[2]. presented a free vibration and stability analysis of untwisted composites including cross-ply plates with hybrid/mixed formulation. Free vibration studies for laminated composite twisted cantilever plates are made by Qatu and Leissa[3] using Ritz method. Although extensive free vibration frequencies and mode shapes are presented, the results were however confined to symmetric angle ply laminates only. To the best of the author's knowledge, no work is reported on vibration and stability of pre-twisted cross-ply plates.

2. Mathematical formulation

The basic problem considered here is the vibration and stability of laminated composite cross-ply doubly curved twisted panel as shown in Fig. 1.

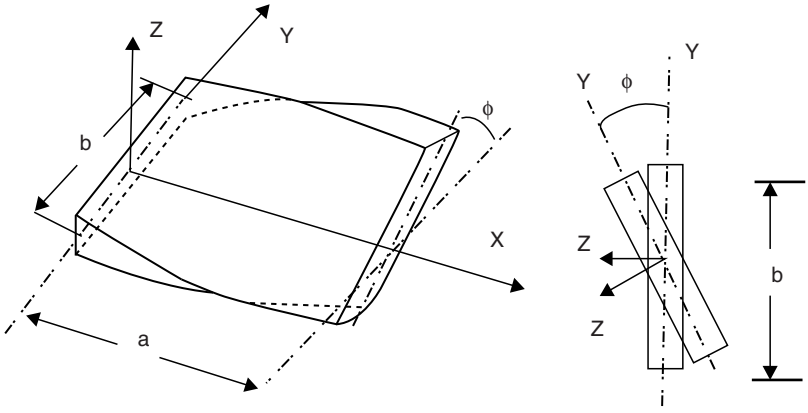

Fig. 1 Pre-twisted cantilever cross ply plate.

The governing equations for vibration and stability of twisted cross-ply plates are:

$$\textbf{Vibration} \qquad [M]+[K_e]\{q\} = \{0\} \tag{1}$$

$$\textbf{Static stability} \qquad [[K_b]-P\,[K_g]]\{q\} = \{0\} \tag{2}$$

where

$[K_e]$ = Elastic stiffness matrix with shear deformation

$[K_g]$ = Geometric stiffness or stress stiffness matrix

$[M]$ = Consistent mass matrix

A finite element analysis was performed using an eight nodded curved isoparametric shell element with five degrees of freedom *u, v, w,* θ_x and θ_y per node. The shell element can accommodate laminated materials and twisting of the panel, based on first order shear deformation theory. Standard consistency mass matrix is employed considering rotary inertia.

Strain Displacement Relations: Green-Lagrange's strain displacement relations are presented in general throughout the analysis. The linear part of the strain is used to derive the elastic stiffness matrix and the non-linear part of the strain is used to derive the geometric stiffness matrix.

Constitutive Relations: The laminated composite pre-twisted cantilever panel is considered to be composed of composite material laminae (typically thin layers). The material of each lamina consists of parallel continuous fibers embedded in a matrix. Each layer is regarded on a microscopic scale as being homogenous and orthotropic. The stress resultants are related to the mid-plane strains and curvatures for the laminated shell element as:

$$\{\sigma\} = [D]\{\varepsilon\} \tag{3}$$

or

$$\begin{Bmatrix} N_i \\ M_i \\ Q_i \end{Bmatrix} = \begin{bmatrix} A_{ij}....B_{ij}....0 \\ B_{ij}....D_{ij}....0 \\ 0.....0....S_{ij} \end{bmatrix} \begin{Bmatrix} \varepsilon_j \\ k_j \\ \gamma_m \end{Bmatrix} \tag{4}$$

The extensional, bending-stretching coupling and bending stiffnesses are expressed as

$$\left(A_{ij}, B_{ij}, D_{ij}\right) = \sum_{k=1}^{n} \int_{Z_{k-1}}^{Z_k} \left(\overline{Q_{ij}}\right)_k \left(1, z, z^2\right) dz, \quad i, j = 1, 2, 6 \tag{5}$$

The transverse shear stiffness is expressed as:

$$\left(S_{ij}\right) = \sum_{k=1}^{n} \int_{Z_{k-1}}^{Z_k} \kappa \left(\overline{Q_{ij}}\right)_k dz, \quad i, j, = 4, 5 \tag{6}$$

Derivation of Element matrices: The element elastic stiffness and consistent mass matrices are derived using standard procedure as:
Elastic stiffness matrix

$$[k_e]_e = \int_{-1}^{1} \int_{-1}^{1} [B]^T [D][B] |J| d\xi d\eta \tag{7}$$

Consistent mass matrix

$$[m]_e = \int_{-1}^{1} \int_{-1}^{1} [N]^T [P][N] |J| d\xi d\eta \tag{8}$$

where $[B], [D], [N]$ are the strain-displacement matrix, stress-strain matrix and shape function matrix and J is the Jacobian determinant. $[P]$ involves mass density parameters. The geometric stiffness matrix is a function of in-plane stress distribution in the element due to applied edge loading. Plane stress analysis is carried out using the finite element techniques to determine the stresses and these stresses are used to formulate the geometric stiffness matrices.

Geometric stiffness matrix

$$[k_g]_e = \int_{-1}^{1} \int_{-1}^{1} [G]^T [S][G] |J| d\xi d\eta \tag{9}$$

where

$$[S] = \begin{bmatrix} s & 0 & 0 & 0 & 0 \\ 0 & s & 0 & 0 & 0 \\ 0 & 0 & s & 0 & 0 \\ 0 & 0 & 0 & s & 0 \\ 0 & 0 & 0 & 0 & s \end{bmatrix}$$

and

$$[s]=\begin{bmatrix}\sigma_x^{\,0} & \tau_{xy}^{\,0}\\ \tau_{xy}^{\,0} & \sigma_y^{\,0}\end{bmatrix}=\frac{1}{h}\begin{bmatrix}N_x^{\,0} & N_{xy}^{\,0}\\ N_{xy}^{\,0} & N_y^{\,0}\end{bmatrix} \tag{10}$$

A computer program is developed to perform all the necessary computations. Reduced integration technique is adopted to avoid possible shear locking. The overall matrices $[K_b], [K_g]$ and $[M]$ are obtained by assembling the corresponding element matrices using skyline technique. Subspace iteration method is adopted throughout to solve the eigenvalue problems. The further details are omitted here for sake of brevity.

3. Results and discussions

The convergence study is made for non-dimensional fundamental frequencies of vibration of laminated composite twisted cantilever plates. From this convergence study, 10 ×10 mesh has been employed to idealize the panel in the subsequent analysis. The non-dimensional fundamental frequencies of vibration of untwisted cross-ply cylindrical shells for three lamination schemes [0°/90°], [0°/90°/0°], and [0°/90°/90°/0°] are compared with the results of the work done by Khedeir[4] and Kim[5]. As seen from Table 1, the results compare very well with the studies done by either the HSDT or the FSDT. The non-dimensional buckling load of both moderately thick and thin composite plates for a symmetric cross-ply plate (0°/90°/90°/0°) under axial compression are compared with references. The present solutions are in very good agreement with the solution using first-order transverse shear deformation theory but the effect of using a higher-order theory is not very significant in this case.

TABLE 1. Comparison of non-dimensional buckling load of simply supported cross-ply shells. $a/b=1$, $E_{11}=40$, E_{22}, $G_{12}=G_{13}=0.5\,E_{22}$, $G_{23}=0.6\,E_{22}$, $\upsilon_{12}=\upsilon_{13}=0.25$, $N_x=N\,b^2/E_{22}\,h^3$

Number of layers	HSDT Khdeir[4]	FSDT Khdeir[4]	Kim FSDT[5]	Present
3	22.312	22.315	22.318	22.0925
5	24.747	24.574	24.550	24.4087
9	25.671	25.495	25.498	25.3481

3.1. NUMERICAL RESULTS

After validation, the free vibration results are extended to laminated composite cross-ply pre-twisted cantilever plates and panels. The studies are also extended

to stability studies on cross-ply composite pretwisted cantilever plates and panels. The geometrical properties of the twisted panels are:

$$a = b = 500 \text{ mm}, h = 2 \text{ mm}, \quad E_{11} = 141.0 \text{ GPa}, \; E_{22} = 9.23 \text{ GPa}$$
$$\nu_{12} = 0.313, \quad G_{11} = 5.95 \text{ GPa}, G_{23} = 2.96 \text{ GPa}.$$

Non-dimensional frequency

$$\omega = \omega a^2 \sqrt{\frac{\rho}{E_{11} h^2}} .$$

Non-dimensional buckling load

$$\lambda = \frac{N_x b^2}{E_{22} h^3} .$$

The results of studies on the stability of twisted cantilever cross-ply laminated plates and shells are presented in two parts (1) free vibration studies and (2) buckling studies.

3.2. FREE VIBRATION STUDIES

The non-dimensional frequencies of vibration of twisted cantilever plates for different cross-ply orientations and for varying angles of twist are studied in Fig. 2. It is found that as the angle of twist increases for a particular cross-ply orientation, the frequency parameter decreases. This is true for both the

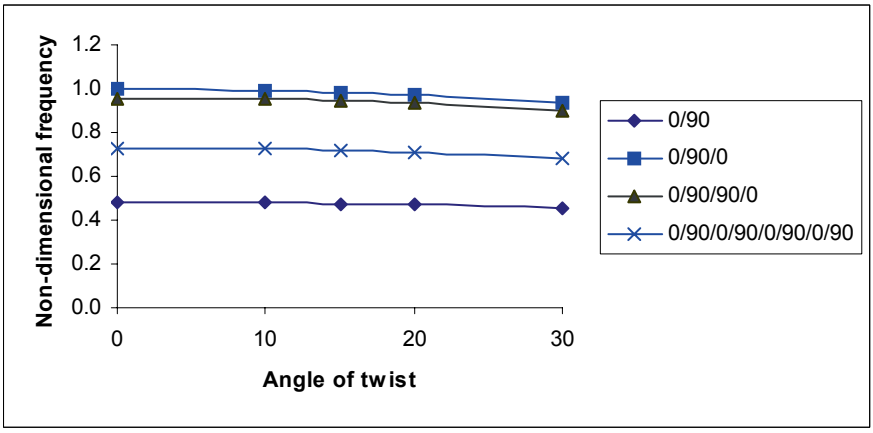

Fig. 2 Variation of non-dimensional frequency parameter with angle of twist for different number of layers of cross ply plates.

symmetric as well as anti-symmetric cross-ply plates. Fig. 3 shows the variation of non-dimensional frequency with the variation of aspect ratio. As the aspect ratio increases, non-dimensional frequency is gradually decreasing in all the ply-orientations. The non-dimensional frequency is higher in the symmetric cross-ply compared to other orientations.

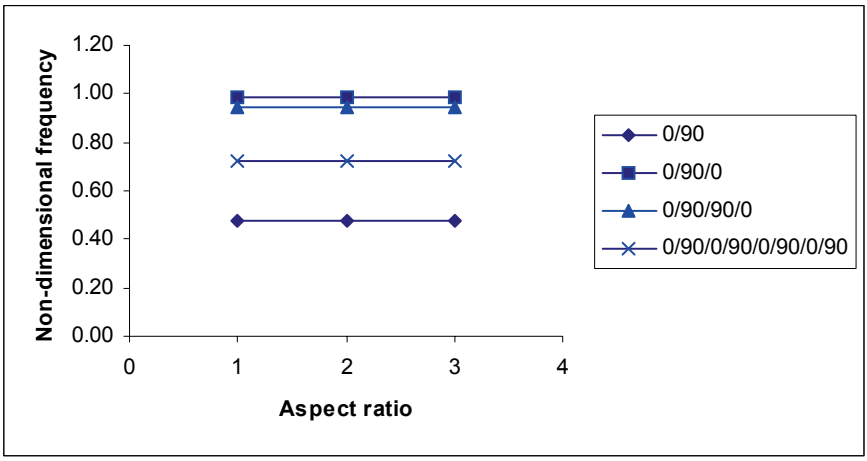

Fig. 3 Variation of non-dimensional frequency with variation of aspect ratio for twisted square plate ($\phi = 15°$).

3.3. BUCKLING STUDIES

The studies are then extended further to examine in detail the effects of various parameters on stability of composite, pre-twisted cantilever panels. The buckling loads are computed for square laminated cantilever twisted plates for different angles of twist and ply orientation as shown in Fig. 4. The non-dimensional

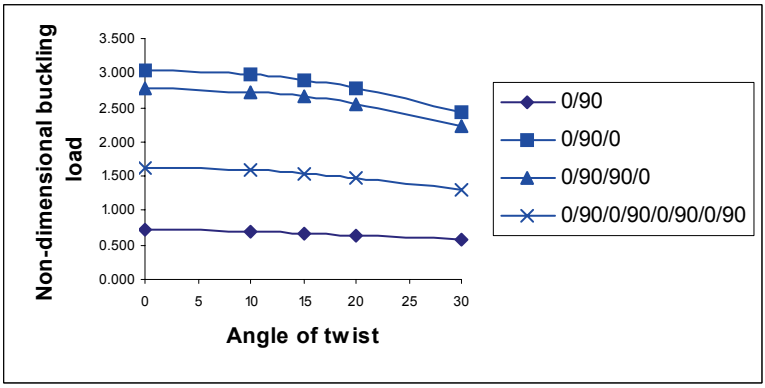

Fig. 4 Variation of non-dimensional buckling load with angle of twist for different cross-ply square plates.

buckling load is more in the case of angle of twist $\phi = 10°$ and 0/90/0 laminates. The untwisted plate shows more buckling load than the twisted plate. The least buckling load is observed in the case of $\phi = 30°$ with 0/90 laminates.

In Fig. 5, variation of non-dimensional buckling load with variation of aspect ratio of twisted square cantilever plates is studied. As the aspect ratio increases, non-dimensional buckling load decreases. This is observed for all the ply orientations. The maximum buckling load is shown by the symmetric cross-ply (0/90/0) for a particular aspect ratio.

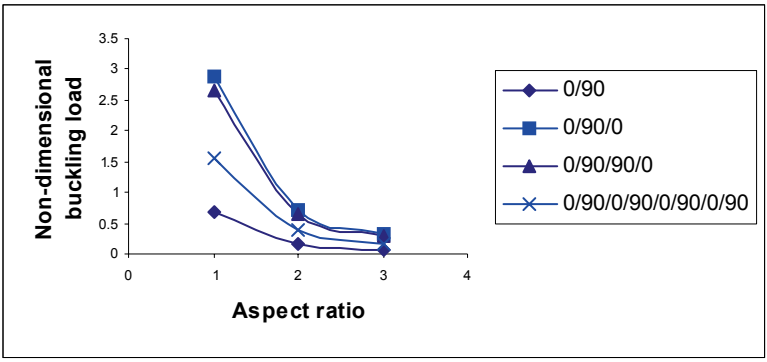

Fig. 5 Variation of non-dimensional buckling load with aspect ratio of square cantilever twisted plates.

4. Conclusion

As the angle of twist increases for a particular cross-ply orientation, the frequency parameter and non-dimensional buckling load of the plate decreases. This is true for both the symmetric as well as antisymmetric cross-ply plates. As the aspect ratio of the plate increases, non-dimensional frequency is gradually decreasing in all the ply-orientations. The untwisted plate shows more buckling load than the twisted plate. As the aspect ratio increases, non-dimensional buckling load of the plate decreases significantly. This is observed for all the ply orientations. This can be used to the advantage of tailoring of composite plates.

References

1. N. S. Putcha, J. N. Reddy, 1986. *Stability and natural vibration analysis of laminated plates by using a mixed element based on a refined plate theory*, Journal of Sound and Vibration, **104**, 285-300.
2. A. S. Gendy, A. F. Saleeb, S. N. Mikhail, 1997. *Free vibration and stability analysis of laminated composite plates and shells with hybrid/mixed formulation*, Computers and Structures, **63**, 1149-1163.
3 M. S. Qatu, A. W. Leissa, 1991. *Vibration studies for laminated composite twisted cantilever plates*, International Journal of Mechanical Sciences, **33**, 927-940.
4. A. A. Khdeir, L. Librescu, 1988. *Analysis of symmetric cross-ply laminated elastic plates using higher order theory: part II-buckling and free vibration*, Journal of Composite Structures, **9**, 259-277.
5. K. D. Kim, 1996. *Buckling behaviour of composite panels using the finite element method*, Journal of composite structures, **36**, 33-43.

FREE VIBRATION ANALYSIS OF TRUNCATED SANDWICH CONICAL SHELLS WITH CONSTRAINED ELECTRO-RHEOLOGICAL FLUID DAMPING

S. SHARNAPPA, N. GANESAN*, AND R. SETHURAMAN
Department of Mechanical Engineering, Indian Institute of Technology Madras, Chennai, 600036, India

Abstract. This article presents the frequency and damping characteristics of sandwich conical shell structures with electro-rheological fluid (ER) core. The dynamic characteristics of conical shell for different core to facing thickness ratio (t_c / t_f), length to mean radius (L/R) ratio and effect of cone angle on frequency and damping for different boundary conditions are carried out. The variation of damping characteristics of electro-rheological fluid core with electric voltage is also investigated.

Keywords: complex shear modulus, electro-rheological fluid, truncated conical shell

1. Introduction

The sandwich construction is most commonly used shell configurations for aerospace structures, space vehicles and missile construction. In recent past a lot of research has been done on the sandwich shell structures with viscoelastic core. Khatri and Asnani[1] are investigated the vibration and damping analysis of multiplayer conical shells. Khatri[2] also presented the analysis of axisymmetric vibration of multilayered conical shell with core layers of viscoelastic material. Wilkins et al[3]. have studied the free vibration analysis of orthotropic conical

*Corresponding author, nganesan@iitm.ac.in

E. İnan et al. (eds.), *Vibration Problems ICOVP-2007*,

shell with honeycomb core sandwich structures. Jia and Lien[4] studied the dynamic stability of a sandwich plate with a constrained layer and electro-rheological fluid core.

The free vibration analysis of truncated conical sandwich shell with ER fluid cores are not found in literature, the present study deals with vibration and damping analysis of conical shell with electro-rheological fluid core. There are two types of electro-rheological fluid cores are used in the present study, which are given in the reference[4].

2. Finite element formulation

A semi analytical finite element method is used with a three noded isoparametric element for the structure. The general shell element with sandwich structure, which is converted to conical shell, is shown in Fig. 1. Where α is the cone angle, L is length of the shell, $r = r(s) = a + s\sin\alpha$ is the mean radius at the coordinate point (s, θ, z), a and b are the small and big end radius of the conical shell respectively, here mean radius also expressed as $R = (a+b)/2$. The displacement field used in the present analysis for core and facings is proposed by Wilkins et al[3]. The effect of shear deformation is accounted for the facings. The displacements u, v and w in the s (meridian), θ (circumferential) and z (normal outward from the reference surface of the shell) directions respectively, at any point in core or facings.

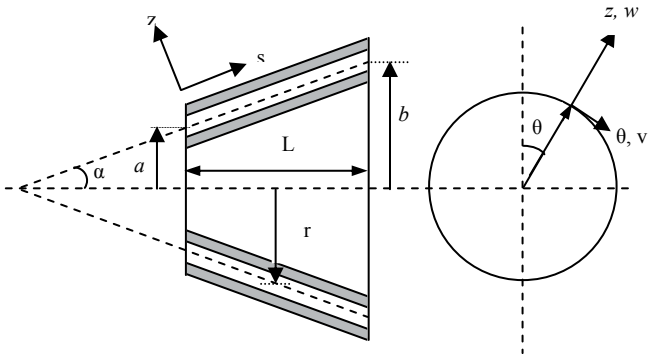

Fig. 1 Geometry of a truncated sandwich layer conical shell.

In the present analysis three noded elements with seven degrees of freedom per node is used. The vector of displacement per element u_e is expressed as $\{u_e\} = \{u_{0,1}\, v_{0,1}\, w_{0,1}\, \psi_{s,1}\, \psi_{\theta,1}\, \phi_{s,1}\, \phi_{\theta,1} \ldots \phi_{s,3}\, \phi_{\theta,3}\}$ where the subscripts 1, 2 and 3

denote the node number. Where u_0, v_0 and w_0 are the displacement components at the middle surface and ψ_s, ψ_θ and ϕ_s, ϕ_θ are the angles of rotations normal to the middle surface in meridional and circumferential directions for core and facings respectively. The strain displacement relations for core, inner and outer facings are referred in the present study are given by Ramasamy and Ganesan[5]. The strain vector is

$$\{\varepsilon\} = \{\varepsilon_{ss}\ \varepsilon_{\theta\theta}\ \gamma_{s\theta}\ \gamma_{\theta z}\ \gamma_{sz}\}^T$$

where $\varepsilon_{ss}\ \varepsilon_{\theta\theta}$ are normal strains and $\gamma_{s\theta}\ \gamma_{\theta z}\ \gamma_{sz}$ are the shear strains of the structure.

The strain vectors can be represented as

$$\{\varepsilon\} = \{\varepsilon_{ss}\ \varepsilon_{\theta\theta}\ \gamma_{s\theta}\ \gamma_{\theta z}\ \gamma_{sz}\} = [B]\{u_e\} \tag{1}$$

Here $[B]$ is the derivative of shape function matrix. The element stiffness matrix $[K_e]$ and mass matrix $[M_e]$ are expressed as follows

$$[K_e] = \int_v [B]^T [D][B]\, dv \tag{2}$$

$$[M_e] = \int_v [N]^T [N]\, \rho\, dv \tag{3}$$

The stiffness matrix $[K_e]$ consists of real part $[K]_R$ and imaginary part $[K]_I$ due to complex shear modulus of ER fluid core. Where ρ is density of the structure.

2.1. EVALUATION OF FREQUENCY AND LOSS FACTOR

The following eigen value problem gives natural frequencies

$$[K] - \omega^2 [M] = 0\,. \tag{4}$$

The ER fluid loss factor for n^{th} mode can be calculated by

$$\eta_n = \frac{\phi_n^T [K]_I \phi_n}{\phi_n^T [K]_R \phi_n} \tag{5}$$

where ϕ_n is n^{th} mode eigenvector.

The properties of this ER material available in literature are tabulated in the Table 1. The facings material used in the present study is mild steel.

TABLE 1. Complex shear modulus of ER fluids[4], where E_* is the electric field in kV/mm.

Shear modulus (G)	ER fluid core	
	Type 1 (ER1)	Type 2 (ER2)
Real part (G_R)	$\approx 1500E_*^2$	$\approx 50000E_*^2$
Imaginary part (G_I)	≈ 6900	$\approx 2600E_*^2 + 1700$

3. Results and discussions

The frequency and damping analysis of sandwich conical shell by using two types of electro-rheological (ER1 and ER2) core materials are investigated. The parametric study carried out for different core to facing (t_c / t_f) thickness and length to mean radius (L / R) ratio for clamped free (C-F) and clamped-clamped (C-C) boundary condition. The results are plotted for first axial mode of a conical shell.

3.1. CLAMPED FREE SANDWICH CONICAL SHELL

3.1.1. *Effect of Electric field on Loss Factor*

Fig. 2 shows the variation of loss factor with circumferential modes (n) for a first axial mode (m) of a clamped free sandwich conical shell with two types of electro-rheological fluid cores (ER1 and ER2). Loss factor remains constant up to $(n = 3)$ then onwards increases with increasing the circumferential modes; it

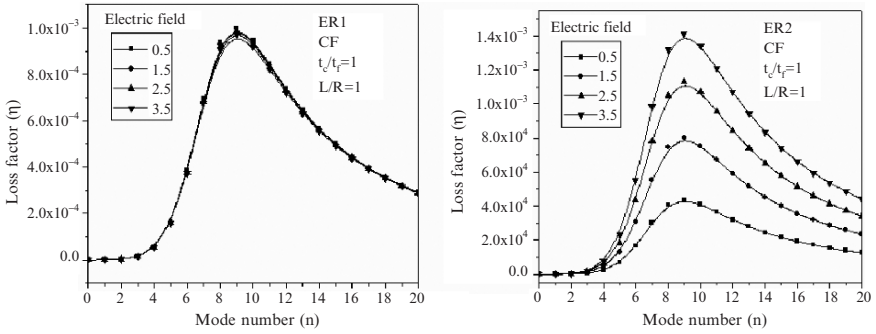

Fig. 2 Loss factor with harmonics at different electric field of an ER1 and ER2 core.

reaches a maximum value $(n=9)$ then decreases with increasing the mode numbers. The influence of electric field on loss factor in case of ER1 core is not observed much. In case of ER2 core it is noticed that increasing the electric field loss factor increases as presented by Jai and Lien[4].

3.1.2. *Effect of core to facing thickness ratio* (t_c / t_f) *on frequency and loss factor*

Fig. 3 shows the variation of frequency and loss factor with mode number of an ER1 fluid core sandwich conical shell with length to mean radius ratio $(L/R)=1$ for different core to facing thickness ratios (t_c / t_f). Frequency decreases with increasing the mode number up to $n=9$ and reaches a minimum value then onwards increases with increasing the mode number. The frequency is more and loss factor is less at lower and higher modes, this trend may be due to fact that the membrane effect is more at lower modes and bending effect is predominant at higher modes. Increasing the core to facing thickness ratio there is slight decrease in the frequency and increase in loss factor.

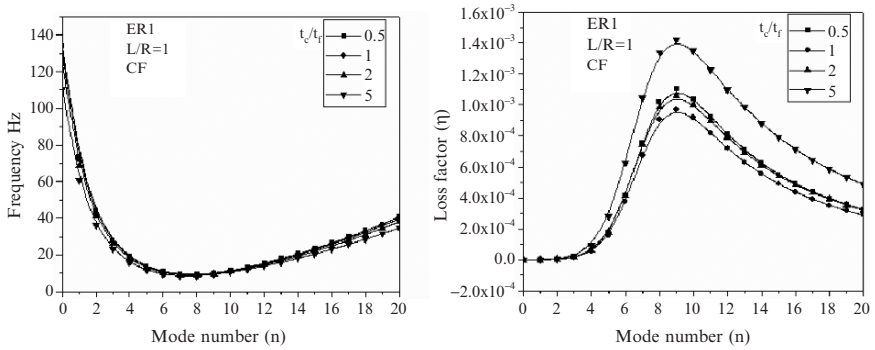

Fig. 3 Frequency and loss factor with mode number for different t_c / t_f ratios.

3.1.3. *Effect of core material on frequency and loss factor*

Fig. 4 shows the variation frequency and loss factor with mode number of a ER1 and ER2 fluid core sandwich conical shell having $L/R=5$ and $t_c / t_f = 1$ for clamped free condition. The frequencies of ER1 and ER2 core sandwich conical shell are same but the loss factor of ER2 core material is higher than the ER1 core. The reason for this may be the loss modulus of the ER2 fluid core is more than the ER1 core, so the numerator of the equation (5) increases which leads to increase in the loss factor, which is clearly observed at higher

circumferential modes. Comparing the Fig. 3 and Fig. 4 it is observed that increasing the L/R ratio the stiffness of the shell decreases which leads to decrease in the frequency of ER1 core sandwich conical shell at all circumferential modes.

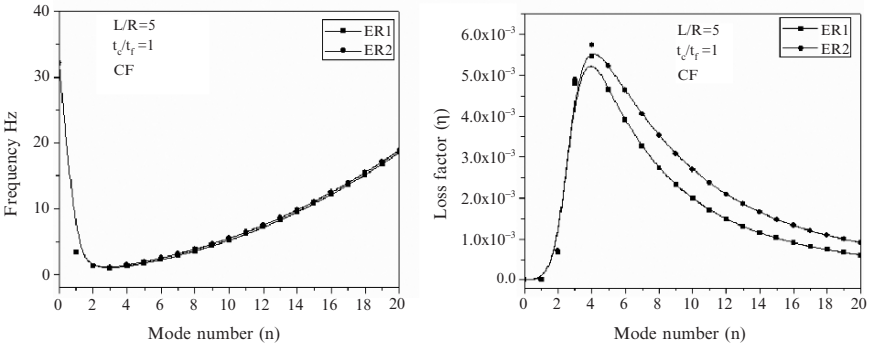

Fig. 4 Frequency and loss factor with mode number for ER1 and ER2 core material at $L/R = 5$.

3.1.4. *Effect of cone angle on frequency and loss factor*

Fig. 5 shows the effect of cone angle on frequency and loss factor of ER1 fluid core sandwich conical shell at $L/R = 1$ and $t_c/t_f = 1$ in clamped free condition. Increasing the cone angle the stiffness of the shell reduces which leads to decrease in the frequency and increase in the loss factor at all the circumferential modes.

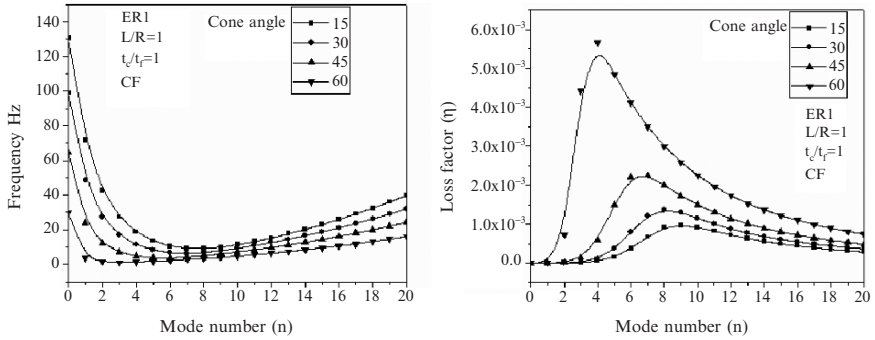

Fig. 5 Frequency and loss factor with mode number at different cone angles.

3.2. CLAMPED-CLAMPED SANDWICH CONICAL SHELL

3.2.1. *Effect of core material on frequency and loss factor*

Fig. 6 shows the variation of frequency and loss factor of ER1 and ER2 fluid core sandwich conical shell at $L/R=5$ and $t_c/t_f=1$ for clamped-clamped condition. The trend of the curves for ER1 and ER2 cores same as discussed in the section 3.1.3. Comparing the Fig. 4 and Fig. 6 the frequency of C-C shell is more but loss factor is less than the C-F shell.

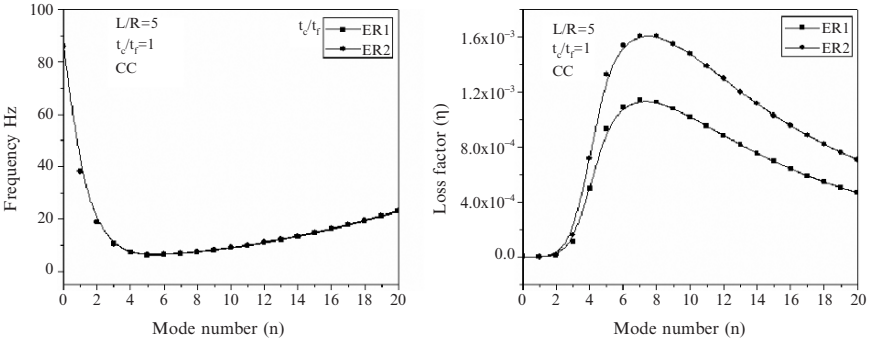

Fig. 6 Frequency and loss factor with harmonics for ER1 and ER2 core material at $L/R=5$.

4. Conclusions

The following conclusions are arrived from the above study

1. Increasing the electric filed, loss factor of ER2 core sandwich conical shell increases, the effect of electric filed on ER1 core is not observed.
2. Increasing the core to facing thickness ratio frequency decreases slightly and loss factor increases which is observed at all circumferential modes.
3. Increasing the cone angle the frequency decreases and loss factor increases.
4. In case of C-C shell the frequency is more and loss factor is less than the C-F shell.

References

1. K. N. Khatri, N. T. Asnani, 1995. *Vibration and damping analysis of multilayered conical shells*, Composite Structures, **33**, 143-157.

2. K. N. Khatri, 1996. *Axisymmetric vibration of multilayered conical shells with core layers of viscoelastic material*, Computers and Structures, **58**, 389-406.
3. D. J. Wilkins, C. W. Bert, D. M. Egle, 1970. *Free vibration of orthotropic sandwich conical shells with various boundary conditions*, Journal of Sound and Vibration, **13**, 211-28.
4. J. Y. Yeh, L. W. Chen, 2005. *Dynamic stability of a sandwich plate with a constrained layer and electrorheological fluid core*, Journal of Sound and Vibration, **285**, 637-652.
5. R. Ramasamy, N. Ganesan, 1999. *Vibration and damping analysis of fluid filled orthotropic cylindrical shells with constrained viscoelastic damping*, Computers and Structures, **70**, 363-376.

ON THE PROBLEM OF THE CHOICE OF CONTROLLED DAMPER BY THE VIBRO-ISOLATION SYSTEM

JAN ŠKLÍBA* AND MICHAL SIVČÁK
Department of Mechanical Engineering, Technical University in Liberec, Czech Republic

Abstract. In the paper there is stated a method of the correct solving of this problem: the dependency of damping force is not possible to linearise. The non-linear response is substituted by linear broken line and the tuning is made for alternatives of steepness of individual sections. By the vibro-isolation system of the ambulance coach the controlled dampers BRANO (made in Czech Republic) and SUSPA (made in Germany) were applied and by means of this method their adjustment was optimized.

Keywords: vibro-isolation system, external excitation, parametric excitation, translating vibration, rotating vibration, wave spring, cylindrical spring locating mechanism, hydraulic damper, throttle elements

1. Introduction

Our vibro-isolation system is determinated to eliminate not only the vertical vibrations of the carriage, but also the rotating vibrations around both horizontal axes (so called pitching or rolling) might be eliminated.

Such a vibro-isolation system (Fig. 1) of the ambulance couch is realized with controlled pneumatic springs and controlled hydraulic dampers. The conducting mechanism has three degrees of freedom and is formed by a parallelogram (Fig. 2), on its upper base is double Cardan suspension .On its inner frame is placed a couch with the patient.

*Corresponding author, jan.skliba@tul.cz

E. İnan et al. (eds.), *Vibration Problems ICOVP-2007*,

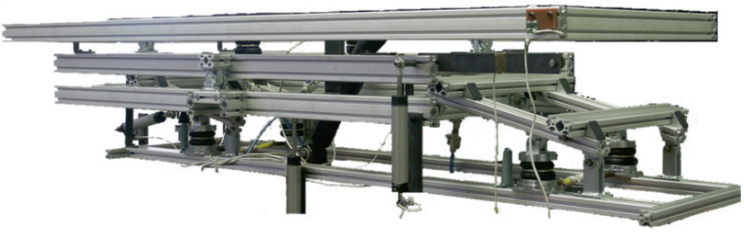

Fig. 1 Vibro-isolation system.

2. Preliminary considerations

For this system there has been deduced both a general nonlinear system[1] (1) and its proper linearised system (2) for small deflections q_i (where $\vec{q}$ is the vector of general coordinates q_i).

$$\frac{d}{dt}\frac{\partial T}{\partial \dot{q}_i} - \frac{\partial T}{\partial q_i} + \frac{\partial U}{\partial q_i} = M_{Si} + M_{Di}, \quad i = 1,\ldots,3 \tag{1}$$

$$\mathbf{A}\ddot{\vec{q}} + \left(\mathbf{B}_0 + \mathbf{B}_1(t)\right)\dot{\vec{q}} + \left(\mathbf{C}_0 + \mathbf{C}_1(t)\right)\vec{q} = \vec{E}_0 + \vec{E}_1(t) \tag{2}$$

There is used the signification: T resultant kinetic energy, U potential energy of gravity forces, $M_{S.}$ or M_{Di} - the external moments of forces of pneumatic springs or dampers, $\mathbf{A}$ mass matrix, $\mathbf{B}_0$ damping matrix, $\mathbf{C}_0$ stiffness matrix, $\mathbf{B}_1(t)$ or $\mathbf{C}_1(t)$ matrixes of parametric excitation, $\vec{E}_0$ vector of the static moment (in the equilibrium state must be $\vec{E}_0 = 0$), $\vec{E}_1(t)$ vector of external excitation.

The members of symmetrical mass matrix are functions of masses m_j, inertia moments J_{ij}, length of parallelogram arm R, and etc. The members of diagonal stiffness matrix are functions pressure P_j, gravity forces, parameters

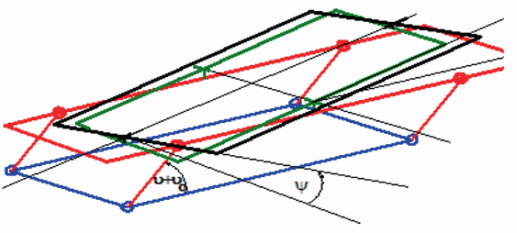

Fig. 2 Conducting mechanism.

of effective area S_{0i}, S_{1i} of the pneumatic springs, and of arms r_{pi} of their moments. The members of diagonal damping matrix are functions of steepness b_{1j}, of the damper velocity characteristic and r_{Ti} arms of dampers moment.

$$\begin{aligned}
A_{11} &= (m_R + m_4 + m_5 + m_6)R^2 + 4J_{Ry}, \\
A_{22} &= J_{5y} + J_{6y} + m_6(x_{56}^2 + z_{56}^2 + 2x_{56}x_{T6} + 2z_{56}z_{T6}), \\
A_{12} &= R[m_5(-x_{T5}\cos\vartheta_0 - z_{T5}\sin\vartheta_0) + m_6((-x_{T6} - x_{56})\cos\vartheta_0 \\
&\quad + (-z_{T6} - z_{56})\sin\vartheta_0)], \\
A_{33} &= J_{6x}, \quad A_{13} = m_6 R\cos\vartheta_0 y_{T6}, \quad A_{23} = -D_{6xy} - m_6 x_{56} y_{T6}
\end{aligned} \tag{3}$$

Matrixes of damping and stiffness are diagonal:

$$B_{011} = 4b_{1i}r_{T\vartheta i}^2\cos^2\vartheta_0, \quad B_{022} = \sum_{j=1}^{2} b_{1j}r_{T\varphi j}^2, \quad B_{033} = \sum_{j=1}^{2} b_{1j}r_{T\psi j}^2 \tag{4}$$

$$\begin{aligned}
C_{011} &= -(2m_R + m_4 + m_5 + m_6)gR\sin\vartheta_0 - 4r_{p\vartheta}^2\left(\frac{n(p_a + p_4)S_{04}^2}{V_4} + p_4 S_{14}\right) + \\
&\quad + 4p_4 S_{04} r_{p\vartheta}\sin\vartheta_0 \\
C_{022} &= -(m_5 z_{T5} + m_6 z_{56} + m_6 z_{T6})g - r_{p\varphi 1}^2\left(\frac{n(p_a + p_{51})S_{05}^2}{V_5} + p_{51}S_{15}\right) - \\
&\quad - r_{p\varphi 2}^2\left(\frac{n(p_a + p_{52})S_{05}^2}{V_5} + p_{52}S_{15}\right) \\
C_{033} &= -m_6 g z_{T6} - r_{p\psi 1}^2\left(\frac{n(p_a + p_{61})S_{06}^2}{V_6} + p_{61}S_{16}\right) - \\
&\quad - r_{p\psi 2}^2\left(\frac{n(p_a + p_{62})S_{06}^2}{V_6} + p_{62}S_{16}\right)
\end{aligned} \tag{5}$$

and for components of vector E_0:

$$\begin{aligned}
E_{01} &= \left(m_4 + m_5 + m_6 + 2m_R\right)gR\cos\vartheta_0 - 4p_4 S_{04} R\cos\vartheta_0, \\
E_{02} &= -\left(m_5 x_{T5} + m_6(x_{T6} + x_{56})\right)g - S_{05}(p_{51}r_{p\varphi 1} - p_{52}r_{p\varphi 2}), \\
E_{03} &= m_6 y_{T6} g - S_{06}(p_{61}r_{p\psi 1} - p_{62}r_{p\psi 2})
\end{aligned} \tag{6}$$

and the members of external kinematic excitation vector $\vec{E}_1(t)$ and the members of the parametric excitation matrix $\mathbf{B}_1(t)$, $\mathbf{C}_1(t)$, see [1].

There has been tested an accordance of the solution of the general nonlinear system (1) and its proper linearised system (2). It was demonstrated that the linear substitution of the pneumatic spring characteristics by the tangent at the working point are satisfactory. On the other hand side, the approximation of the nonlinear velocity characteristics of the damper with straight line in the initial point is dissatisfactory and it leads to a significant default (see Fig. 3, dotted line). It was demonstrated in paper [3]. For this reason, system (1) was replaced with system (7), in which the velocity characteristics are replaced with a segment-linear response.

$$\mathbf{A}\ddot{\vec{q}} + \left(\mathbf{B}_1(t)\right)\dot{\vec{q}} + \left(\mathbf{C}_0 + \mathbf{C}_1(t)\right)\vec{q} = \vec{E}_0 + \vec{E}_1(t) + \vec{M}_D \tag{7}$$

Therefore, we use a particular linearised system, in which the damper moments see. Eqn. (7) and Fig. 3 is deduced from this substitute. The segment linear function sufficiently describes the influence of the adjusting of the damper throttle elements (their influence on the velocity characteristic is shown in the Fig. 4):

A. Calibrated orifices
B. Prestressing of discharge and pressure valve springs
C. Stiffness of these springs

When we want to optimize the velocity characteristic of applied damper, we must respect these base properties and analyze each of these three parameters.

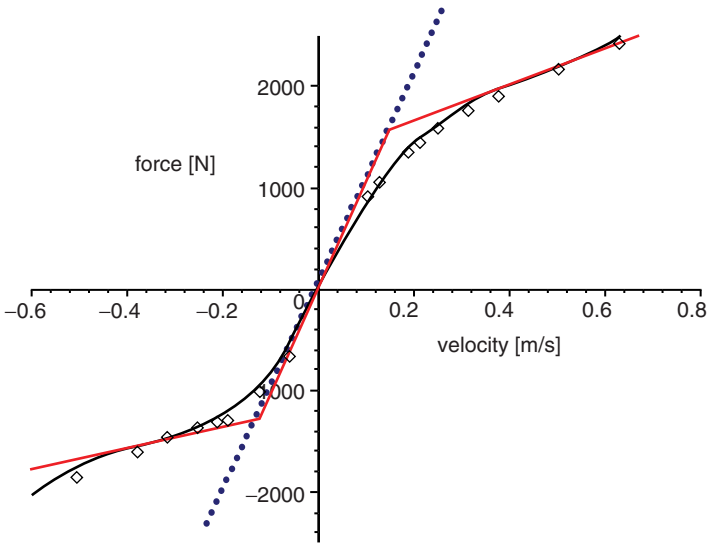

Fig. 3 Velocity characteristics.

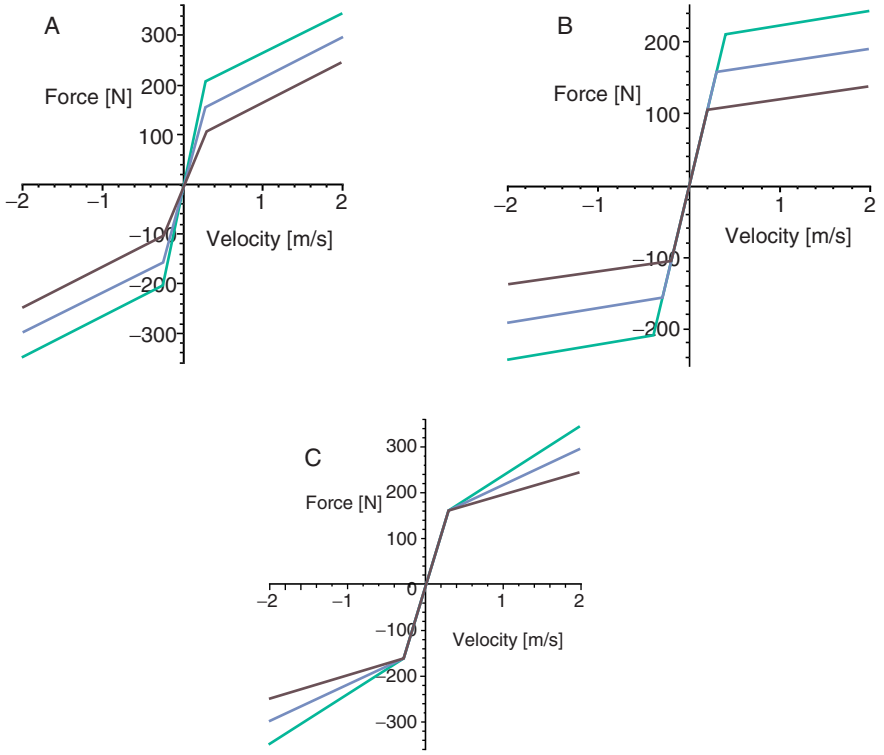

Fig. 4 The influence of damper throttle elements on the velocity characteristics.

3. Kinematic excitation

As an entry was chosen vertical kinematic excitation:

I. The quasiharmonic signal with slowly changed frequency (0-10Hz per 240s) and with constant amplitude of velocity (see. Fig. 5).
II. The jump signal (cosines half wave) (see. Fig. 6).

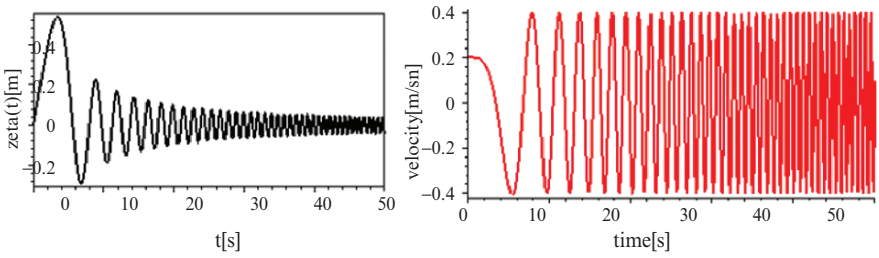

Fig. 5 The quasi-harmonic signals.

The time responses of the relative deflections θ, φ, ψ and also the absolute deflection of upper base of parallelogram z_{40} were denoted. There were also denoted velocities of these deflections.

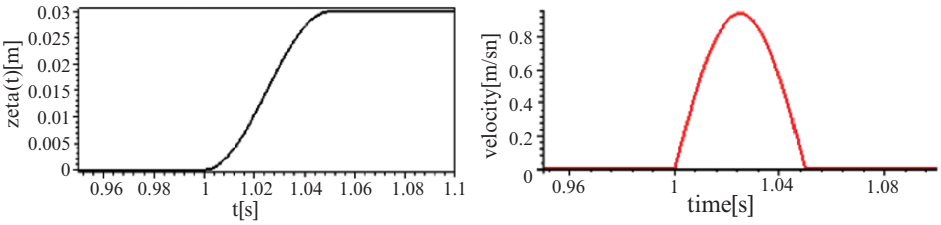

Fig. 6 The jump signals.

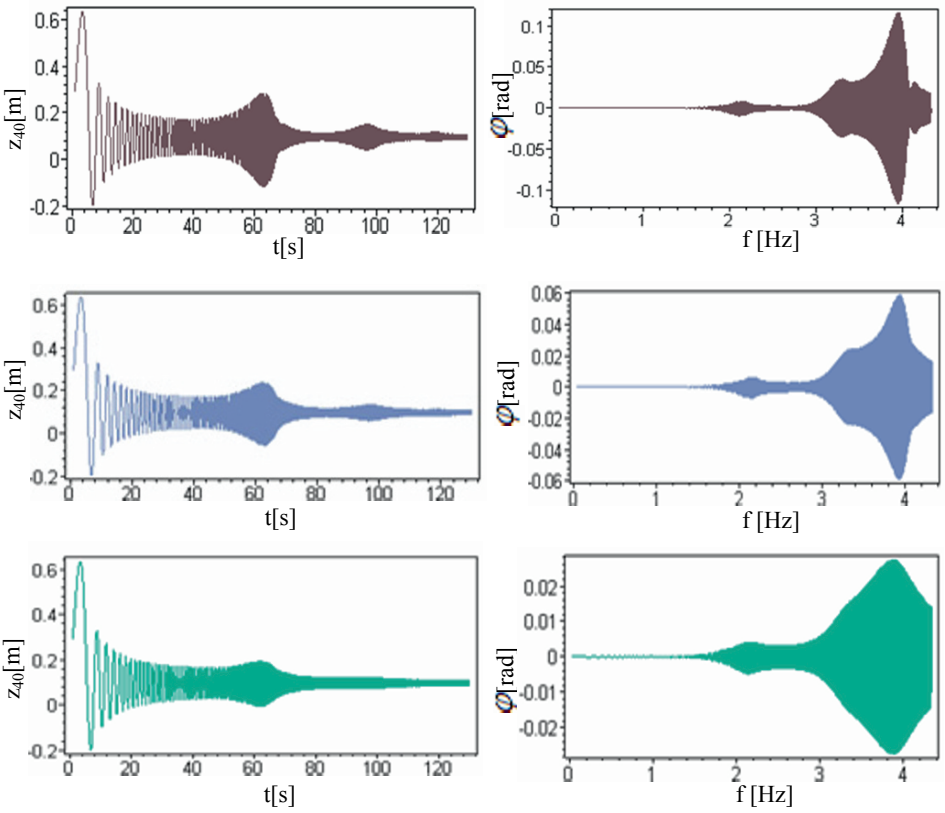

Fig. 7 Results of (A).

4. The results of numerical simulations

A. If we reduce the result cross of calibrated orifices, the gradient of the first linear section increases. The confrontations of soft, middle and hard adjustments demonstrate that the hard one is optimal (Fig. 7).

B. The highest velocity of the fracture point is consequent to the highest prestressing of valve spring. In this case the time-response of z_{40} and φ is optimal but the time response of ψ is optimal by the middle adjustment (Fig. 8).

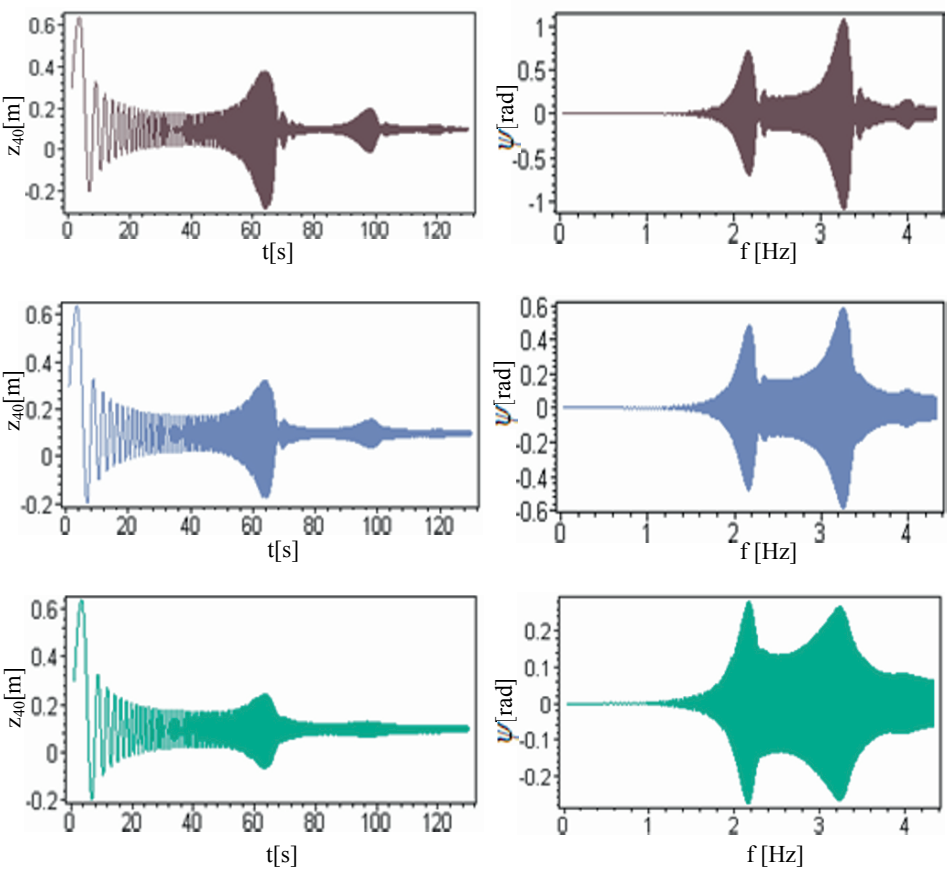

Fig. 8 Results of (B).

C. If we finally increase the springs stiffness, the gradient of the second linear section extends; then we see that the time responses of the all deflections are optimal by hard adjustment (Fig. 9).

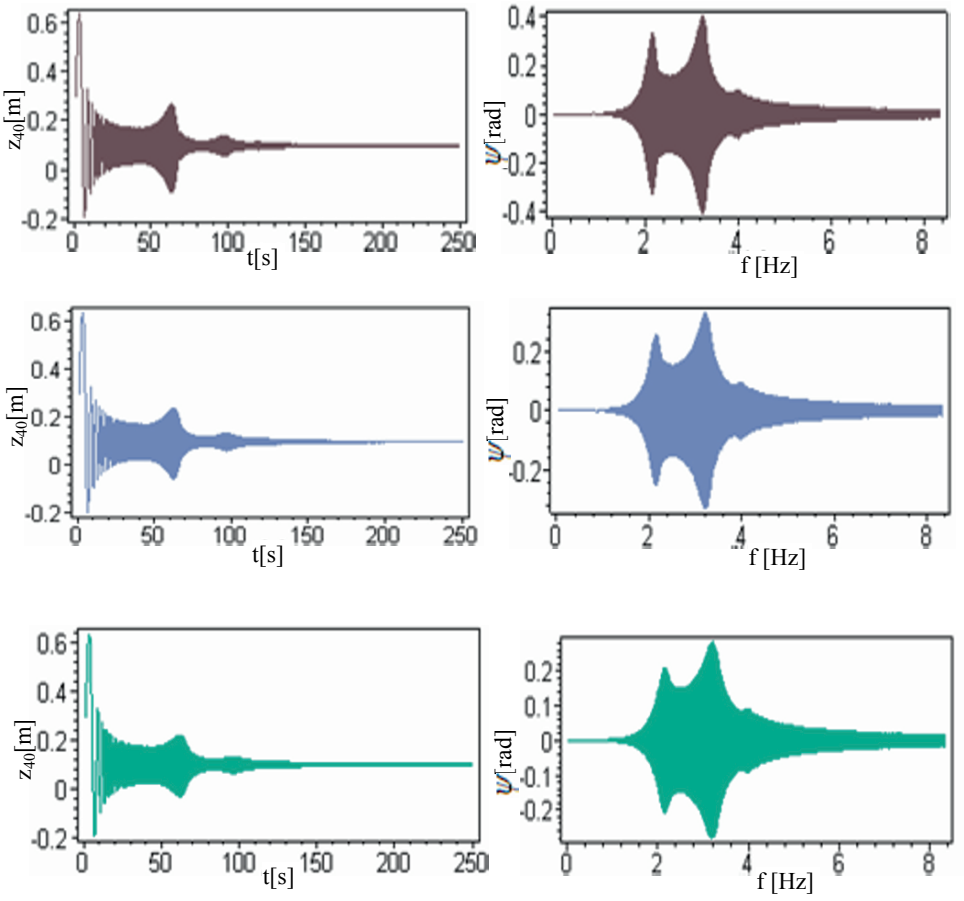

Fig. 9 Results of (C).

5. Conclusions

1. From results of numerical experiments we see, that the adjustment of the damper was chosen too soft. By this method we find the middle adjustment as optimal.
2. It is evidently, that the most effective means for change of velocity characteristic is the adjusting of prestressing of the valve spring (Fig. 10).

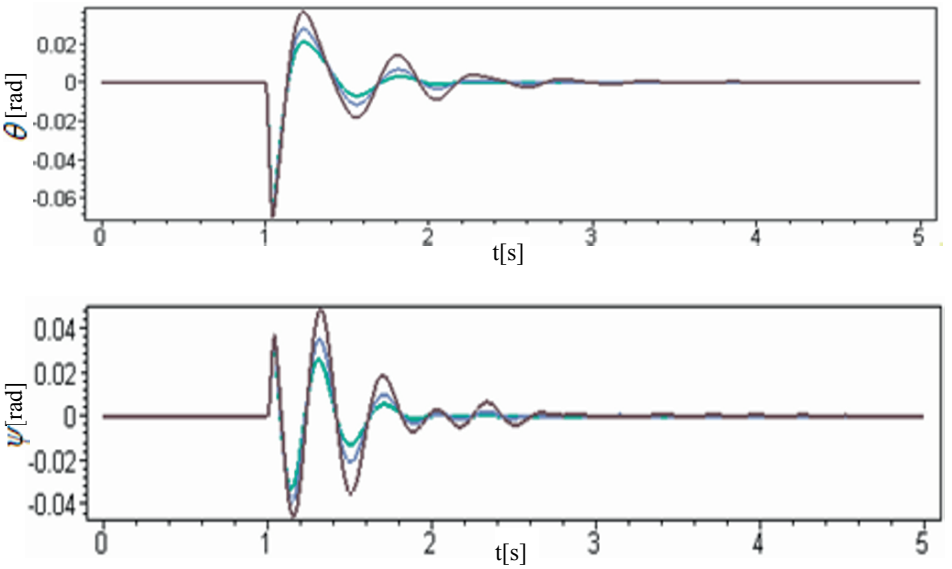

Fig. 10

ACKNOWLEDGEMENT

The research has been supported by project MSM 4674788501 “Optimalizace vlastností strojů v interakci s pracovními procesy a člověkem”.

References

1. J. Šklíba, J. Prokop, M. Sivčák, 2006. *Vibro-isolation system of an ambulance couch with three degrees of freedom*, Engineering Mechanics, **13**.
2. J. Šklíba, M. Sivčák, 2006. *Kinematic excitation of the vibro-isolation system with three degrees of freedom*, Colloquium Dynamics of machines.
3. M. Sivčák, J. Šklíba, 2006. The dependence of the vibro-isolation effect of the system with three degrees of freedom on the description applied dampers, National conference Engineering mechanics.

ON THE PROBLEM OF DEPENDENCE OF DAMPER FORCE ON THE CONCENTRATION OF FREE AIR IN WORKING LIQUID

RUDOLF SVOBODA
Techlab s.r.o., Sokolovská 207, 19000 Praha 9, Czech Republic
JAN ŠKLÍBA*
Technical University Liberec, Hálkova 6, 46117 Liberec 1, Czech Republic

Abstract. In-process of damping of vibrations with great velocities (greater then 2 m/s) the concentration of the free air in working liquid of the two-jacket hydraulic damper increases. This phenomenon is allowed by the free surface of the liquid in the accumulator of the damper and invoked by the changes of equilibrium conditions between the quantity of air evolved from liquid and the quantity of air dissolved in oil in dynamic state for greater damping velocities. In the paper two unfavourable effects of this phenomenon are analyzed: delay on the working damper characteristics, which leads to the considerable degradation of damper force, and decrease of damper valve resistance to the self-excited oscillations. These vibrations can arise in steady parts of both damper expansion and rebound phases where all transient phenomena have gone off long ago and working valves are fully open. The zones of self-excited vibrations coincide with regions of linear asymptotic instability of the system, i.e. with the areas where the real part (natural damping) of at least one of the damper eigenvalues achieves positive value.

Keywords: hydro-mechanical model of hydraulic damper, concentration of the free air in working liquid, static and dynamic damper characteristics, self-excited valve oscillation, zones of instability

*Corresponding author, jan.skliba@tul.cz

E. İnan et al. (eds.), *Vibration Problems ICOVP-2007*,

1. Introduction

Hydraulic dampers still represent one of the basic instruments for absorption of vibrations in dynamic systems. Correct determination and description of their damping properties is therefore necessary for trustworthy modeling of real dynamic systems. In calculations the dampers are substituted either indirectly (and with less accuracy) by hydraulic velocity characteristics or directly by mathematical models as a component of the precise model of a dynamic system (for instance a vibroisolating system) in which the damper is applied. Mathematical damper models are usually more detailed and can be also used separately for damper designing and development purposes.

Owing to the intended utilizations of dynamic model of hydraulic damper in calculations of real-time dynamic systems it is unacceptable to solve damper dynamics in full complexity using finite element methods for calculations of mechanical damper parts movements and finite volumes method for description of flows inside the damper. To ensure reasonable computer time all mechanical parts of the damper are modelled by simple way using concentric parameters and the flows through the valves are modelled on the bases of laws of hydraulics.

Up to now, the oil in the damper was considered as an ideal compressible liquid without addition of dissolved or diffused air (in the form of air bubbles). The air column in the accumulator was strictly separated from the liquid and the air could not penetrate to other damper areas. Such models can respect only the compression of the air in accumulator and, in case that the pressure falls under the value of saturated vapor pressure, the evolution and destruction of caves of saturated vapors in the regions above and under the piston (see [1]).

The oil as an ideal working liquid without dissolved air does not correspond to the reality. The concentration of the air in the oil dynamically changes (especially during the passage through the valves) in the whole working cycle; thus the physical oil parameters markedly change as well. Unfortunately, dynamical process of successive dissolving of the air in oil and regressive release of the dissolved air from the oil cannot be described in full complexity at present. There are experimental equipments for measuring of quantity of air evolved from the liquid, but there is still no possibility to determine quantity of air dissolved in oil in dynamic state. Moreover, we are not able to fill adequate parameters into the Stritter equation for time changes of concentration of dissolved air. This is the main reason why only an unchanging concentration of free and dissolved air can be reflected in damper models.

The presumption of constant level of air concentration in oil, which comes to stay after certain operating period, at least approximately substitutes the dynamic process of air evolving and dissolving. With respect to the fact, that the velocity of evolving of free air bubbles from the oil is roughly two times

greater then the velocity of dissolving of the air fixed on oil molecules, the presumption of constant air concentration under working conditions can be to a certain extent accepted.

2. Damper models with constant air concentration in the oil

2.1. COMBINED HYDRO-MECHANICAL MODEL OF THE DAMPER

The present standard dynamic model of hydraulic damper deals with pressures concentrated into three regions (regions above the piston, under the piston and in the accumulator – see Fig. 1). This model consists of systems of differential equations describing equations of motion of valves, dynamic balance of flows among the damper regions, evolution and destruction of columns of saturated vapours and algebraic equations describing dependence of discharge flow coefficients on corresponding Reynolds numbers. The enhanced model of hydraulic damper deals with pressures concentrated into the seven regions. In this model the flows through valves are modelled more precisely and pressure gradients in supply channels are respected for all four valves. For both standard and enhanced models the flows among regions of the damper are supposed to be one-dimensional, the liquid is compressible, in the state of unsaturated solution (it does not contain

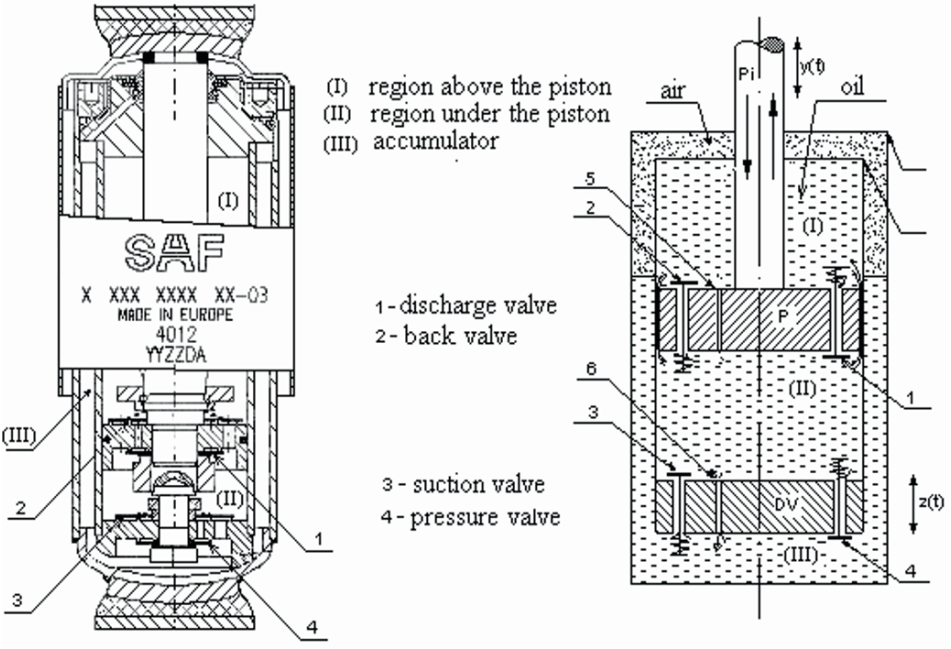

Fig. 1 A damper cross-section view and scheme of corresponding damper model.

free air), viscose. The columns of the liquid are described by concentric parameters. The entire system of equations has been presented in [2], [3]. The standard dynamic model of hydraulic damper consists of four non-linear differential equations of the second order and five non-linear differential equations of the first order, completed with seven algebraic equations; the state vector consists of thirteen components. In case of the seven-pressure model where the original system of equations is enlarged by eight differential equations describing pressures and flows in supply channels, the state vector consists of twenty one components.

2.2. DAMPER MODEL WITH CONSTANT AIR CONCENTRATION IN THE OIL

In case of damper model with constant air concentration in the oil we come out from derived equations with ideal working liquid. We suppose the air-oil mixture to be formally composed from mutually independent liquid and gaseous components; the flows of mixture by valves and other throttle elements are described in the same way as in original model by well known formula depending on pressure gradient, discharge flow coefficient α and hydraulic coefficient $K(\rho)$

$$Q = \alpha \cdot K(\rho) \cdot \sqrt{(P_{inp} - P_{out})} \,. \tag{1}$$

The concentration κ_v of the air diffused in oil in the form of bubbles is described as a ratio of volume of air and unit volume of the mixture. It is evident that in this manner defined concentration substantially depends on the actual pressure inside the damper regions and strongly changes during the working cycle. The constant air concentration we take therefore as constant air mass concentration κ_m (as a ratio of the mass of diffused air and unit mass of the mixture), which does not depend on the actual pressure.

In case of oil-air mixture the flow Q_m on passage through the valve gap into the region with different output pressure changes its volume. Corresponding input and output (volume) flows $Q_{V,inp}$, $Q_{V,out}$ can be expressed by means of mass flow Q_m according to relation (2).

$$Q_{V,inp} = \left(\frac{1-\kappa_m}{\rho_k} + \kappa_m \frac{P_0}{P_{inp}} \cdot \frac{1}{\rho_V} \right) \cdot Q_m, \;\; Q_{V,out} = \left(\frac{1-\kappa_m}{\rho_k} + \kappa_m \frac{P_0}{P_{out}} \cdot \frac{1}{\rho_V} \right) \cdot Q_m \,. \tag{2}$$

The equations of hydraulic part of the damper model with ideal working liquid were derived on condition of volume flows balance (with signs representing conventional flow directions in the damper): sum of all volume flows among damper regions is equal to zero. This balance of volume flows in the damper represents at the same time the law of preservation of mass.

In case of oil-air mixture the condition of volume flows balance is not fulfilled owing to the dependence of the mixture volume on the pressure inside the damper. The condition of volume flows balance must be replaced by the condition of mass flows balance, which now expresses the law of preservation of mass: sum of all mass flows among damper regions is equal to zero.

3. Results of analysis and calculations

Dynamic velocity characteristics of the damper for variant concentrations of the diffused air are presented in Fig. 2. With increasing concentration of the air in oil the resulting modulus of elasticity of the mixture decreases, the pressure changes in transient regions are slower and the sharp transitions of damper force in damper characteristics are getting smooth. The high compressibility of the air component of the mixture leads on the one hand to the desirable softening of damper characteristics in problematic transient zones (central parts of curves in the figure), on the other hand can cause unfavourable delay on the working damper characteristics with corresponding considerable degradation of damper force – see almost constant parts in damper characteristics for higher air concentrations.

On higher air concentration and certain combinations of definition parameters some zones with strong vibrations of self-excited type occur in the solution. These vibrations arise in steady parts of both damper expansion and rebound phases where all transient phenomena have gone off long ago and working valves are fully open. Vibration frequency corresponds to the one of

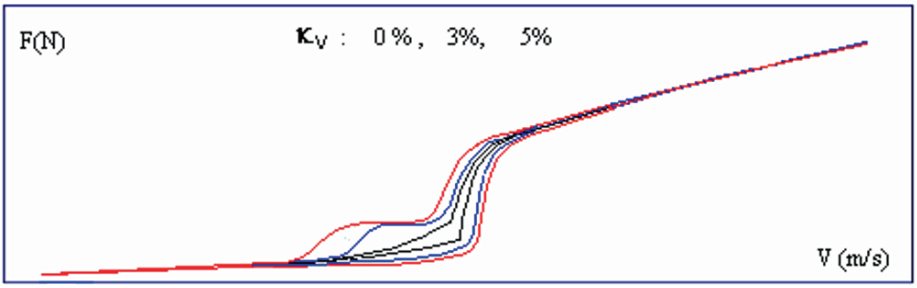

Fig. 2 Dynamic velocity characteristics for various air concentrations.

the natural frequencies of the damper. Because the damper is described by a system of non-linear differential equations, its spectral properties depend on instantaneous operating state – the actual value of the state vector $\mathbf{Y}(t)$. Natural frequencies and corresponding natural damping we get then as eigenvalues of the Jacobian matrix $\mathbf{A}$ determined by linearization of damper system equations $\mathbf{F}(\mathbf{Y},t)$ around the actual operating state $(t_0,\mathbf{Y}(t_0))$:

$$\dot{\mathbf{Y}} = \mathbf{A}(\mathbf{Y}_0,t_0).\left(\mathbf{Y}-\mathbf{Y}_0\right)+\mathbf{b}(\mathbf{Y}_0,t_0).\left(t-t_0\right),\ \mathbf{A}=\frac{\partial \mathbf{F}}{\partial \mathbf{Y}}(\mathbf{Y}_0,t_0),\mathbf{b}=\frac{\partial \mathbf{F}}{\partial t}(\mathbf{Y}_0,t_0)\,. \quad (3)$$

The regions with self-excited vibrations of damper force (Fig. 3) and other state vector components coincide with regions of linear asymptotic instability of the system, i.e. with the areas where the real part (natural damping) of at least one of the damper eigenvalues achieves positive value.

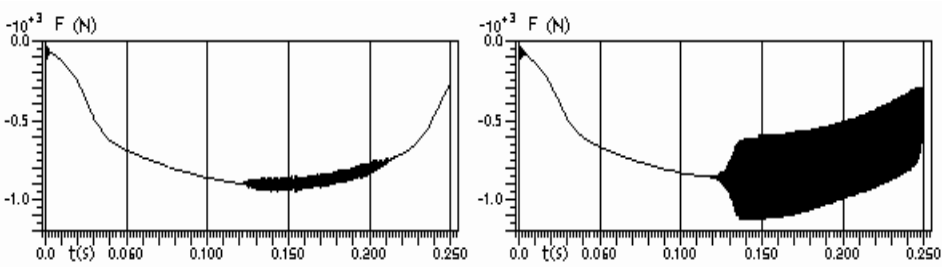

Fig. 3 Self-excited vibrations of damper force.

4. Conclusions

To come near the reality, the working liquid in the mathematical model of the damper was considered in the form of oil-air mixture with mutually independent liquid and gaseous components. The flows of mixture by valves and other throttle elements were derived on the bases of hydraulics in the same way as in original model with ideal liquid without diffused air. However, the conditions of volume flows balance are not valid hereafter and were replaced by equilibrium conditions of mass flows of the mixture among damper regions.

The high compressibility of the air component of the mixture leads on the one hand to the desirable softening of damper characteristics in problematic transient zones, on the other hand can cause unfavourable delay on the working damper characteristics with corresponding considerable degradation of damper force.

The other unfavourable effect of the high compressibility of the mixture with higher air concentrations consists in decrease of damper valve resistance to the self-excited oscillations. This type of vibrations can arise in steady parts of both damper expansion and rebound phases where all transient phenomena have gone off long ago and working valves are fully open. The zones of self-excited vibrations coincide with regions of linear asymptotic instability of the system.

ACKNOWLEDGEMENTS

This work has been supported by Ministry of Education of Czech Republic in the frame of the project No. MSM 4674788501.

References

1. H. L. Lang, 1978. *A study of the characteristics of automotive hydraulic dampers at high stroking frequencies*, PhD Dissertation, University of Michigan.
2. R. Svoboda, J. Šklíba, 2003. *Identification of non-linear stiffness of hydraulic damper valves*, Proc. of the 6th International conference on vibration problems, pp. 78-80, Liberec, Czech Republic.
3. J. Šklíba, R. Svoboda, 2005. *Specification of flow conditions in mathematical model of hydraulic damper*, 7th International conference on vibration problems ICOVP 2005, Springer Proceedings in Physics, pp. 455-462.

AUTHOR INDEX

LIST OF PARTICIPANTS

ACHARYYA A. K.
Jadavpur University
Department of Civil Engineering
Kolkata 700032
India
e-mail: anjanboni@rediffmail.com

ALIŞVERİŞÇİ F.
Yıldız Technical University
Department of Mechanical Engineering
Istanbul 34349
Turkey
e-mail: afusun@yildiz.edu.tr

ASHA A. V.
National Institute of Technology
Department of Civil Engineering
Rourkela 769008
India

BANERJEE M. M.
202 Nandan Apartment, Hillview (N), S B Gorai Road
Asansol-713304, W. B.
India
e-mail: dgp muralimb@sancharnet.in

BATABYAL A. K.
Haldia Institute of Technology
Department of Mechanical Engineering
Haldia 721657 West Bengal
India

BERA R. K.
Heritage Institute of Technology
Department of Mathematics
Anandapur, Kolkata 700107
India
e-mail: rasajit@yahoo.com

BHATTACHARJEE J. K.
Indian Association for the Cultivation of Sciences
Kolkata 700032
India
e-mail: tpjkb@mahendra.iacs.res.in

BHATTACHARYYA R.
Indian Institute of Technology
Dept. of Mechanical Engineering
Kharagpur 721302
India
e-mail: rbmail@iitkgp.ernet.in

BOOMINATHAN A.
Indian Institute of Technology
Madras, Dept. of Ocean Engineering
India

CHAKRABARTI A.
1A/14 Ramlal Agarwala Lane
Calcutta-700050
India

CHAKRABORTY D.
Jadavpur University
Department of Civil Engineering
Kolkata 700032
India
e-mail: dchakravorty@vsnl.net

CHAKROBORTY S.

SMS DEMAG Private Limited
West Bengal
India
e-mail: suvonkar.chakroborty@in.smsdemag.com

CHATTERJEE S.

Bengal Engineering and Science University, Department of Mech. Eng. Shibpur, P.O. Botanic Garden
Howrah-711103, W. B.
India
e-mail: shy@mech.becs.ac.in

CHAUDHURI S.

Vehicles Research & Development Establishment (VRDE)
Ahmednagar-414006
Maharastra State
India
e-mail: vrde_san@rediffmail.com

CHOUDHURY A.

Sikkim Manipal Institute of Technology, Department of Mechanical Engineering
Majitar Rangpo 737132, Sikkim
India
e-mail: achintya01@rediffmail.com

COHEN S. S.

McGill University
Dept. of Mechanical Engineering
Montreal, QC, H3A 2K6
Canada

DAS N. C.

Jadavpur University
Department of Mathematics
Calcutta 700032
India

DAS S. K.

Government College of Eng. and Leather Tech., Dept. of Mech. Eng.
Block-LB, Salt Lake City
Kolkata-700098
India
e-mail: das_sourabh2003@yahoo.co.in

DEMİRAY H.

Işık University
Department of Mathematics
Şile, 34980 Istanbul
Turkey
e-mail: demiray@isikun.edu.tr

DHARMARAJU N.

Bhabha Atomic Research Centre
Vibration Laboratory Section
Reactor Engineering Division
Mumbai-400085
India
e-mail: drajugn@yahoo.com

DHILEEP M.

Royal Bhutan Institute of Tech.
Department of Civil Engineering
Rinchending, Phuentsholing Bhutan
India
e-mail: dhileep@rbit.edu.bt

DUTTA D.

S.N. Bose National Centre for Basic Sciences
Saltlake, Kolkata 700098
India
e-mail: debabrata@bose.res.in

DUTTA S. C.

Bengal Eng. and Science University
Department of Civil Engineering
Shibpur, Howrah 711103
West Bengal
India
e-mail: scdind2000@yahoo.com

GAIK T. K.

Science Study Center
Universiti Teknologi Tun Hussein
Onn Malaysia, Johor
Malaysia
e-mail: tay@kuittho.edu.my

GANESAN N.

Indian Institute of Technology
Madras, Department of Mechanical
Engineering
Chennai 600036
India
e-mail: nganesan@iitm.ac.in

GUPTA N.

Motilal Nehru National Institute of
Technology, Department of
Electrical Engineering
Allahabad 211004
India
e-mail: neha.1608@gmail.com

IBRAHIM S. M.

Indian Institute of Technology
Department of Applied Mechanics
Delhi
New Delhi-110016
India

İNAN E.

Işık University
Faculty of Arts and Sciences
Şile, 34980 Istanbul
Turkey
e-mail: inan@isikun.edu.tr

JAFARALI P.

Air Frame Stress Group
Aeronautical Development Agency
Bangalore 560017
India
e-mail: jafaralnaf@rediffmail.com

KADOLI R.

National Institute of Technology
Karnataka, Dept. of Mechanical
Engineering
Surathkal Srinivasnagar 575025
India
e-mail:rkkadoli@rediffmail.com

KARMAKAR A.

Jadavpur University, Department of
Mechanical Engineering
Kolkata 700032
India
e-mail: shrikatha@yahoo.co.in

KARMAKAR R.

Indian Institute of Technology
Dept. of Mechanical Engineering
Kharagpur 721302
India

KENDRI R. G.

National Institute of Technology
Karnataka, Dept. of Mechanical
Engineering, Surathkal, PO
Srinivasnagar 575025
India

KIRIS A.
Istanbul Technical University
Faculty of Science and Letters
Maslak, 34469 Istanbul
Turkey
e-mail: kiris@itu.edu.tr

KOLLA S.
R.V.R & J.C.C.E
Guntur-522019, A.P.
India
e-mail: kolla_neha@rediffmail.com

KUMAR R. K.
Indian Institute of Tech. Madras
Dept. of Mechanical Engineering
Machine design section
Chennai 600036
India
e-mail: kishoreramisetti@iitm.ac.in

KUMAR Y. A.
R.V.R & J.C.C.E
Guntur-522019, A.P.
India

KUSHWAHA B.
Vehicles Research & Development
Establishment (VRDE)
Ahmednagar-41400
Maharastra State
India

MADHESWARAN C. K.
Structural Engineering Research
Centre, Chennai
India
e-mail: ckm@sercm.org

MAITI A.
Presidency College
Department of Mathematics
Kolkata 700073
India
e-mail: alakesh_maity@hotmail.com

MALIK P.
National Institute of Technology
Karnataka, Dept. of Mechanical
Engineering, Surathkal
Srinivasnagar, 575025
India
e-mail: pravin_malik@yahoo.com

MALLIK A. K.
Indian Institute of Technology
Kanpur, Dept. of Mechanical
Engineering, 208016
India
e-mail: akmallik@iitk.ac.in

MARVALOVA B.
Technical University of Liberec
Halkova 6, 46117, Liberec
Czech Republic
e-mail: bohda.marvalova@tul.cz

MEHER K. K.
Bhabha Atomic Research Centre
Vibration Laboratory Section
Reactor Engineering Division
Mumbai-400085
India
e-mail: vilred@magnum.barc.ernrt.in

MISRA A. K.
McGill University
Dept. of Mechanical Engineering
Montreal, QC, H3A 2K6
Canada
e-mail: arun.misra@mcgill.ca

MITRA R.
Jadavpur University
Department of Mathematics
Calcutta 700032
India
e-mail: smita1308@gmail.com

MOVCHAN A. B.
University of Liverpool
Dept. of Mathematical Sciences
U.K.
e-mail: abm@maths.liv.ac.uk

MUKHERJEE S.
National Aerospace Laboratories
Structures Division
Bangalore 560017
India
e-mail: somu@css.cmmacs.ernet.in

MUKHOPADHYAY B.
Bengal Engineering and Science
University
Howrah-711103
India

NAGARAJU S.
National Institute of Technology
Department of Civil Engineering
Rourkela 769008
India

NATARAJAN K.
Structural Engineering Research
Centre, Chennai
India

NATH Y.
Indian Institute of Technology
Department of Applied Mechanics
Delhi, New Delhi-110016
India
e-mail: nathyogendra@hotmail.com

NIYOGI A. G.
Jadavpur University
Civil Engineering
Kolkata 700032
India
e-mail: agn_ju@yahoo.com

PAL S.
Jadavpur University
Civil Engineering
Kolkata 700032
India
e-mail: palsreyashi@gmail.com

PATEL B. P.
Indian Institute of Technology
Department of Applied Mechanics
Delhi, New Delhi-110016
India

PAUL T. K.
Central Mechanical Engineering
Research Institute
Condition Monitoring Group
Durgapur 713209, W. B.
India
e-mail: tkp7494@yahoo.com

POHIT G.

Jadavpur University
Department of Mechanical Engineering
Kolkata-700032
India
e-mail: gpohit@vsnl.net

PRATHAP G.

Centre for Mathematical Modelling and Computer Simulation
Bangalore 560037
India
e-mail: gp@cmmacs.ernet.in

RAJESH S.

S.R.K.R.C.E
Bhimavaram, A.P.
India

RAO A. R.

Bhabha Atomic Research Centre
Vibration Laboratory Section
Reactor Engineering Division
Mumbai-400085
India
e-mail: vilred@magnum.barc.ernrt.in

RAO J. S.

Chief Science Officer, Altair Eng.
Mercury 2B Block, 5th Floor
Prestige Tech Park, Sarjapur
Marathhalli Outer Ring Road
Bangalore 560087
India
e-mail: js.rao@altair.com

RAY P. C.

Government College of Engineering & Leather Technology
Department of Mathematics
Block LB, Salt Lake City
Kolkata-70098
India
e-mail: raypratap1@yahoo.co.in

RAYCHAUDHURI A.

Bengal Eng. and Science University
Department of Civil Engineering
Shibpur, Howrah 711103
West Bengal
India
e-mail: anusritarayc@yahoo.com

ROY A.

University of Calcutta
Dept. of Applied Mathematics
92 A.P.C. Road
Kollkata 700009
India
e-mail: roy_arabinda1@yahoo.co.in

SAHA A. K.

Charotar Institute of Technology
Dept. of Mechanical Engineering
Changa, TA: Petlad, Dist: Anand
Changa-388421, Gujarat
India
e-mail: saha_ak2001@yahoo.co.in

SAHU S. K.

National Institute of Technology
Department of Civil Engineering
Rourkela 769008
India
e-mail: sksahu@nitrkl.ac.in

SAMANTA G. P.

Bengal Eng. and Science University
Department of Mathematics
Shibpur, Howrah 711103
India
e-mail: g_p_samanta@yahoo.co.uk

SANDESH S.

Indian Institute of Tech. Madras
Dept. of Mechanical Engineering
Machine design section
Chennai 600036
India
e-mail: sandesh@iitm.ac.in

SANKAR P.

Central Mechanical Engineering
Research Institute, Condition
Monitoring Group
Durgapur 713209, W. B.
India

SARANGI S.

Indian Institute of Technology Dept.
of Mechanical Engineering
Kharagpur 721302
India

SARKAR S.

Jadavpur University
Department of Mathematics
Calcutta 700032
India

SETHURAMAN R.

Indian Institute of Technology
Madras, Department of Mechanical
Engineering
Chennai 600036
India

SHANKAR K.

Indian Institute of Tech. Madras
Dept. of Mechanical Engineering
Machine design section
Chennai 600036
India
e-mail: skris@iitm.ac.in

SHARMA M.

National Institute of Tech.
Dept. of Mechanical Engineering
Warangal
India

SHARNAPPA S.

Indian Institute of Technology
Madras, Department of Mechanical
Engineering
Chennai 600036
India

SIVČÁK M.

Technical University in Liberec
Dept. of Mechanical Engineering
Czech Republic
e-mail: michal.sivcak@tul.cz

ŠKLÍBA J.

Technical University Liberec
Dept. of Mechanical Engineering
Hálkova 6, 46117, Liberec 1
Czech Republic
e-mail: jan.skliba@tul.cz

SUNDARAVADIVELU R.

Indian Institute of Technology
Madras, Dept. of Ocean
Engineering
India

SVOBODA R.

Techlab S. R. O.
Sokolovská 207, 19000, Praha 9
Czech Republic
e-mail: techlab@czn.cz

TANDON N.

ITMMEC, Indian Institute of
Technology, Hauz Khas
New Delhi, 110016
India
e-mail: ntandon@itmmec.iitd.ernet.in

TIONG O. C.

Universiti Teknologi Malaysia
Faculty of Science
Johor
Malaysia